Metals, Semimetals and Semiconductors for Spinelectronics

Plamen Stamenov

School of Physics, Department of Science

University of Dublin

A thesis submitted to the University of Dublin in part-fulfilment of the requirements for the degree of

Doctor of Philosophy

31th of October 2007

Declaration

This thesis is submitted by the undersigned for examination for the degree Doctor of Philosophy at the University of Dublin. It has not been submitted as an exercise for a degree at any other University or other degree-giving institution.

This thesis, apart from the advice, assistance and joint effort mentioned in the acknowledgements and in the text, is entirely my own work.

I agree, that the Library may lend or copy this thesis freely upon request.

Plamen Stamenov

I would like to dedicate this thesis to my loving family and my loyal friends ...

Acknowledgements

First and foremost I would like to thank Prof. J. M. D. Coey for accepting me in Group D, for his professional help and constructive criticism, for guiding my research efforts and providing me with ample opportunities to work at large facilities and go to international schools and conferences throughout the last five years. Also my personal thanks for his and his family's hospitality and friendliness.

Many thanks to Venky for all the help, discussions and joint work, and before all, for being a good friend.

Formal collaborators: Dr. Kathrin Dörr (IFW, Dresden), Dr. Duncan Maude (GHMFL, Grenoble), Dr. Vojislav Krstic (GHMFL, Grenoble) and Dr. Peter Bencok (ISRF, Grenoble)

There are a number of people, whose samples have suffered in my hands, and therefore deserve a special mention. These are, in alphabetical order: Cora, Ciara, Lucio, Jonathan, Kaan, Oscar, Robbie and Venky. My results are their results, too.

There are a number of people that have spent time in the Group D Labs, doing Post Grads or Post Docs, with whom we've laboured together over this or that piece of equipment, sample or theoretical problem. In alphabetical order: Adriele, Anna, Cathy, Chris, Ciara, Ciaran, Cora, Darragh, Eoin, Fernando, Franklyn, Janko, Jason, Jerome, Jonathan, Fiona, Gen, Greg, Guenole, Karl, Karsten, Katie, Kentaro, Lucio, Marita, Martin, Matt, Mazhar, Nandu, Oscar, Peter, Rethi, Robbie, Sebastiaan, Simone, Steve, Treasa and Zhu. I am probably skipping someone.

There are a number of people from other groups and departments and institutions, whom I've interacted with. Again in alphabetical order: Alex, Ivan, Michel and Stefano.

Many thanks to our technical staff for their professionalism and friendliness. One more time in alphabetical order: David, Ciaran, Joe, Jackie, John, Mick, Michael, Pat and Tracy.

Thanks to all summer and project students (too numerous to mention explicitly) for keeping me busier than usual, while they've been here.

Deepest thanks to Maria for absolutely everything.

Abstract

The development of the new field of spin electronics depends upon the existence of materials and structures that may be used as effective spin-polarised current injectors, transmitters, manipulators and detectors. Potential high-efficiency injection structures include tunnel, Schottky, hetero and p-n junctions, barriers employing ferromagnetic metals (ideally half-metals) and magnetic or semimagnetic semiconductors. As media with long carrier mean free path and spin-coherence length, an eventual transmitter, few possibilities are currently explored. These are classical IV, III-V, II-VI semiconductors, and semimetals such as bismuth and graphite. Various means are used to manipulate and detect spin-polarised currents - optical (optical pumping, magnetic circular dichroism and Kerr effect), electrostatic (FET with spin-orbit coupling) and galvanic (different types of Hall effect and magnetoresistive devices).

The experiments described in this thesis are devised to explore the first two bits in the above 'spin chain'. They include the possibility to use Schottky barriers as efficient spin-injectors, including the more fundamental aspect of spin-polarisation measurement employing Schottky barriers; the modelling of the electronic transport through tunnel junctions with high magnetoresistive ratios; the possibilities for direct magnetic detection of spin polarisation injected through metal-metal junctions; the fundamental transport and magnetisation properties of graphite (a good example of a semi-metal) and the magnetic properties of multi-walled carbon nanotubes; and the magneto-transport through Co:ZnO (a candidate for room temperature semimagnetic semiconductor).

In the first chapter, the theory of Schottky junctions is presented. The standard results of essentially all available theoretical approaches are discussed with extensions for spin-polarised metals and/or semiconductors. The magnetic field effects on Schottky junctions are studied systematically. Experimental results on various approaches towards the detection of spin-polarisation using Schottky barriers are then presented. A novel effect - the magneto-photovoltaic effect in ferromagnetic Schottky junctions, is envisaged, modelled and illustrated experimentally.

In the second chapter, the theory of tunnelling to and from normal metals and ferromagnets via insulators is provided. Particular aspects, like coherent and incoherent tunnelling are looked at from a magnetic standpoint. The bias and temperature dependence of the tunnelling current

are treated in detail. Inelastic tunnelling is also considered, in order to complement the adiabatic tunnelling picture and explain the fine details of the derivative spectra of real junctions. Micromagnetic effects are also considered. Here again a novel effect - the high-field anisotropy of the tunnelling magnetoresistance, is envisaged, modelled and illustrated experimentally.

In the third chapter, the problem of direct magnetic detection of injected spin polarisation in all-metal junctions is considered. The measurement capabilities, of a commercial SQUID magnetometer system, to perform the measurement are analysed in detail. Concurrently occurring effects, like adiabatic depolarisation, and some measurement artefacts are also considered. Experimental limits are set on the observability of the injected polarisation and the associated spin diffusion length, at low temperature in aluminium.

In the fourth chapter, the magnetic and magneto-transport properties of highly oriented graphite and multi-walled carbon nanotubes are considered. Extensions of the existing transport data on graphite are performed in the high-field, low-temperature, quantum regime. A simple model of the novel non-linear diamagnetism of carbon nanotubes is developed.

In the fifth chapter, the magnetic and magneto-transport properties of Co-doped ZnO, co-doped with Al, are investigated. No evidence that the system is intrinsically a magnetic semiconductor is found. Experimental evidence is established, that the system is two-phase with Co precipitates. A novel anisotropy of the magnetoresistance is characterised in detail and scaling is suggested.

In the interest of readability, appendixes are associated with each of the chapters, and contain pieces of information, which is either supplementary, and unnecessary for the flow of ideas in the main text, or are important, but too heavy (either in terms of size or complexity) for the main text.

Contents

Nomenclature **xliii**

1 Introduction **1**

2 Schottky Junctions **5**

2.1 Schottky Theory . . . 5

2.1.1 Introduction . . . 5

2.1.1.1 General Points . . . 5

2.1.1.2 Contacts . . . 7

2.1.2 Models . . . 10

2.1.2.1 Semiempirical models . . . 11

2.1.2.2 Fermi-level pinning by interface states . . . 12

2.1.2.3 Generalized models . . . 12

2.1.3 Distribution and Screening . . . 13

2.1.3.1 Metals . . . 13

2.1.3.2 Semiconductors . . . 14

2.1.4 Current Components . . . 15

2.1.4.1 Schottky Model . . . 16

2.1.4.2 Bethe Model . . . 18

2.1.4.3 Sze Model . . . 18

2.1.4.4 Tunnelling Current . . . 21

2.1.4.5 Minority Components . . . 21

2.1.4.6 Scattering . . . 24

2.1.5 Imperfections and Complications . . . 26

2.1.5.1 Oxide Layer . . . 26

2.1.5.2 Scattering and Reflection . . . 27

2.1.5.3 Schottky effect . . . 28

2.1.5.4 Common Treatment . . . 29
2.1.5.5 Other Imperfections . . . 29
2.1.5.6 Parameters extraction . . . 32
2.1.6 Magnetic Field Effects . . . 41
2.1.6.1 Field Effects in TE . . . 41
2.1.6.2 Field Effects in DD . . . 43
2.1.6.3 Magnetic effects in CS . . . 45
2.1.6.4 Magnetic effects on DGR . . . 50
2.1.6.5 Magnetisation Effects . . . 51
2.1.6.6 Quantising fields . . . 53
2.1.6.7 Impact Ionisation . . . 54
2.1.7 Photo-Illumination . . . 55
2.1.7.1 Simple Treatment . . . 56
2.1.7.2 Photo-emission . . . 56
2.1.7.3 External photoemission . . . 57
2.1.7.4 Generation in the depletion region . . . 57
2.1.7.5 Photo-capacitance . . . 61
2.2 Transport Measurements . . . 61
2.2.1 Initial Characterisation . . . 61
2.2.2 Field Dependence . . . 68
2.2.3 Bridge Techniques . . . 70
2.3 Magneto-Optics . . . 78
2.4 Plausibility . . . 83
2.5 Ohmic Contacts . . . 85
2.6 Conclusions . . . 95

3 Tunnelling in Ferromagnet/Insulator/Ferromagnet structures 97

3.1 The theory of tunnelling . . . 97
3.1.1 Basic Analysis . . . 97
3.1.2 Image Forces . . . 99
3.1.3 Effective Hamiltonian . . . 102
3.1.4 Independent Particle . . . 107
3.1.5 Mani Particle . . . 111
3.1.6 Zero Bias . . . 112
3.1.7 Inelastic Tunnelling . . . 117

3.2 Ferromagnetic Junctions . . . 121
3.2.1 DOS Effects . . . 121
3.2.2 Matrix Element . . . 122
3.2.3 Anisotropy Effects . . . 130
3.2.4 Broadening . . . 131
3.2.4.1 Finite Lifetime . . . 131
3.2.4.2 Thermal Smearing . . . 132
3.2.4.3 Modulation broadening . . . 134
3.2.5 Interface Roughness . . . 135
3.2.6 Diffuse Scattering . . . 136
3.2.7 Inelastic Transport . . . 139
3.3 Magneto-transport . . . 141
3.3.1 Advances in TMR . . . 141
3.3.2 Derivative Spectra . . . 143
3.3.2.1 Deconvolution . . . 143
3.3.3 Temperature Effects . . . 147
3.3.4 Spin anisotropy . . . 153
3.3.5 Bias Dependance . . . 157
3.3.6 Differential Capacitance . . . 164
3.3.7 Micromagnetic Effects . . . 166
3.3.8 Inelastic transport . . . 176

4 Spin Injection **183**
4.1 Historical Remarks . . . 183
4.2 Drift-diffusion approximation . . . 184
4.3 Spin Temperature . . . 186
4.4 Spin Injection Experiments . . . 188

5 Zinc Oxide **201**
5.1 Magneto theory . . . 201
5.2 Semimagnetic Semiconductors . . . 208
5.3 Magneto-transport reports . . . 209
5.4 Magnetotransport data . . . 210
5.5 Al co-doping . . . 214
5.6 AMR data . . . 218
5.7 Magnetisation Data . . . 226

6 Magnetism of Carbon **231**

6.1 Brief account of the magnetism of Carbon . . . 231

6.2 Theoretical Consideration . . . 234

6.2.1 Historical remarks . . . 234

6.2.2 dHvA and ShdH oscillations . . . 235

6.2.3 Magnetic Zener Breakdown . . . 237

6.3 Diamagnetism of Graphite . . . 238

6.4 Conventional magneto-transport . . . 240

6.5 Oscillatory and Kinetic and Thermodynamic Effects . . . 244

6.6 Theoretical Considerations . . . 254

6.6.1 Persistent Currents . . . 254

6.7 Experimental Results on MW Carbon Nanotubes . . . 257

6.8 Examples of peculiar data . . . 265

6.9 Conclusions on the Magnetism of Graphite and Carbon Nanotubes . . . 265

7 Conclusions and Outlook **269**

A Appendix A **271**

A.1 Currents in Insulators . . . 271

A.1.1 FN Tunnelling . . . 271

A.1.2 PF emission . . . 272

A.1.3 SC Limited Current . . . 272

A.1.4 Ballistic Transport . . . 273

A.2 Full Depletion . . . 274

A.3 Derivations . . . 276

A.3.1 Diffusion . . . 276

A.3.2 Thermionic Emission . . . 277

A.3.3 Tunnelling . . . 279

A.4 Accumulation . . . 282

A.5 Calibrations . . . 284

A.6 Experimental Procedures . . . 287

A.6.1 Schottky preparation . . . 287

A.6.2 I-V Curve Tracer . . . 289

A.6.3 Transport Setup . . . 289

B Appendix B **293**

B.1 Transfer Hamiltonian . . . 293

B.2 Sample Preparation . . . 296

B.3 Measurement . . . 296

B.4 Superconductor Tunnelling . . . 299

B.5 PPMS Controller . . . 301

B.5.1 Control . . . 302

B.5.2 Data Taking . . . 303

B.5.3 Cycles . . . 303

B.5.4 Branching . . . 304

B.5.5 Expressions . . . 304

C Appendix D **307**

C.1 Experimental setup and samples for direct magnetic detection of spin injection . 307

C.2 Materials used in the spin injection experiment . . . 308

C.3 Magnetisation measurements . . . 312

C.3.1 Gradiometers for magnetisation measurements . . . 312

C.3.2 Second-order gradiometer analysis . . . 312

C.3.3 Data regression algorithms . . . 314

C.3.4 Various imperfections . . . 316

C.3.4.1 Sample shape and size . . . 316

C.3.4.2 Sample position and orientation . . . 326

C.3.4.3 Non-uniform magnetisation distribution . . . 328

C.3.5 Calculation details . . . 333

C.3.6 Experimental details . . . 335

C.3.7 Experimental precautions . . . 335

C.3.8 Conclusions . . . 336

D Appendix E **337**

D.1 Sample preparation and characterisation . . . 337

E Appendix C **341**

E.1 Samples Information . . . 341

E.2 Magnetisation Measurements . . . 341

E.3 Transport Measurements . . . 342

E.4 Many-carrier transport model . . . 342

F List of Publications **345**

References **393**

List of Figures

2.1 Simplified energy diagram for two semi-infinite slabs separated by vacuum. 8

2.2 Simplified energy diagram for a Schottky junction at zero external bias for the case of $\Phi_m \gg \Phi_s$. 9

2.3 Simplified energy diagram for a Schottky junction at zero external bias for the case of $\Phi_m \ll \Phi_s$. 9

2.4 Simplified energy diagram for a Schottky junction under external bias V_a. 10

2.5 Various current contributions in a Schottky barrier. 16

2.6 Relationships between charge density, electric field, electric potential, chemical potential and carrier energy for an arbitrary Schottky contact. Not to scale. 18

2.7 Influence of a insulating layer at the interface. 26

2.8 Simplified effective circuit representing a real diode. 32

2.9 Schematic representation of two most probable photoexcitation processes: internal photoemission (1) and generation in the depletion region (2). 55

2.10 Current-voltage characteristic of a Ohmic back contact to Si. Actually two of them on both sides of a chip. 62

2.11 Magnetoresistance of n-type Si substrate at 300K. 62

2.12 Thermal activation plot for moderately doped n-type Si (The dopant is phosphorous, at a level of $5 \cdot 10^{17}$ cm^{-3}). The slope corresponds to $E_d = 0.042(1)$ eV. 63

2.13 Current-voltage characteristics of set of Schottky junctions. Compliance limits are shown with red lines. 64

2.14 Comparison between magnetic, nonmagnetic Schottky junctions and a standard -6 V Zener diode at $\nu = 30$ Hz. 65

2.15 Comparison between magnetic, nonmagnetic Schottky junctions and a standard -6 V Zener diode at $\nu = 20$ kHz. Bad (capacitive) contacts are easily noticed. 65

2.16 Current-Voltage characteristics of pressed contacts of various metals on GaAs. 66

2.17 Current-Voltage characteristics of pressed contacts of various metals on Nb:STO. . . . 66

2.18 Set of current voltage characteristics measured with a source-meter. The junctions are fabricated by thermal evaporation on a n-Si¡100¿ wafer. 67
2.19 Fit to experimental data, taken at 300 K, for a CoFe/Si Schottky junction. 68
2.20 Fit to experimental data, taken at 300 K, for a Cu/Si Schottky junction. 68
2.21 Set of reconstructed current-voltage characteristics at 300 K. 69
2.22 Set of reconstructed current-voltage characteristics at 300 K. 69
2.23 A cut at constant bias voltage $U = -8$V for a Cu diode. 70
2.24 Bridge measurement of a Cu vs. Co diode at zero bias. 70
2.25 Bridge measurement of a Cu vs. CoFe diode at zero bias. 71
2.26 Bridge measurement of a Cu vs. Cu diode at zero bias. 71
2.27 Bridge measurement of two Cu junctions, one in, one out of the magnet. 73
2.28 Bridge measurement of two Co junctions, one in, one out of the magnet. 73
2.29 Bridge measurement of two CoFe junctions, one in, one out of the magnet. 73
2.30 Deviation of the measured current derivative from its zero-field value, for a Cu/Si Schottky junction. 74
2.31 Deviation of the measured current derivative from its zero-field value, for a Co/Si Schottky junction. 74
2.32 Deviation of the measured current derivative from its zero-field value, for a CoFe/Si Schottky junction. 75
2.33 Negated product of the current and its second derivative with respect to voltage for a CoFe/Si Schottky junction. The derivative is constructed numerically from the $I - V$ characteristic of the device. 77
2.34 Reverse bias break down of a CoFe Schottky junction. 77
2.35 Schematic of a Schottky junction under illumination. 78
2.36 Simplified effective circuit under internal biasing (a), and under auxiliary biasing (b). . 78
2.37 Photo-illumination characteristics of Au and Co on Si. 79
2.38 Photo-illumination characteristics of Au and Co on Si at 61 K and 300 K. 80
2.39 Photo-illumination characteristics of Au and Co on Si at 61 K and 300 K. Note the extreme photo-sensitivity at low temperatures. 81
2.40 Open-circuit photovoltage vs. applied field for GaAs diodes at 300 K. 81
2.41 Short-circuit photocurrent vs. applied field for GaAs diodes at 300 K. 82
2.42 Open circuit photovoltage vs. applied field for GaAs diodes at 300 K. 82
2.43 Magneto-photovoltaic effect in a Co diode at 300 K. 82
2.44 Magneto-photovoltaic effect in a various diodes at 100 K. 83

2.45 Magneto-photovoltaic effect in a various diode at 200 K. 84
2.46 Electron work functions of the 3d metals. After reference Eastman (1970) 85
2.47 $I - V$ characteristic of rare-earth-transition metal/Si junctions, measured at ambient temperature. 86
2.48 Low bias $I - V$ characteristic of rare-earth-transition metal/Si junctions, measured at ambient temperature. 86
2.49 Low bias $I - V$ characteristic $GdCo_2$/Si junction, measured at 300 K. 87
2.50 Low bias $I - V$ characteristic $CeCo_5$/Si junction, measured at 300 K. 87
2.51 Low bias $I - V$ characteristic $GdFe_3$/Si junction, measured at 300 K. 88
2.52 Low bias $I - V$ characteristic Y/Si junction, measured at 300 K. The sample has been annealed to promote diffusion across the interface. 88
2.53 $I - V - T$ characteristic $GdCo_2$/Si junction. 90
2.54 $I - V - T$ characteristic $GdFe_3$/Si junction. 90
2.55 $I - V - T$ characteristic $CeCo_5$/Si junction. 90
2.56 Low bias $\ln I - 1/T$ characteristic of a $GdCo_2$/Si junction, via a cut at 0.2 V. Two different activation energies are clearly distinguishable. 92
2.57 Low bias $\ln I - 1/T$ characteristic of a Gd_5Si_4/Si junction, via a cut at 0.1 V. Only one activation energy is clearly distinguishable. 92
2.58 Low bias $\ln I - 1/T$ characteristic of a Ce_2Co_17/Si junction, via a cut at 0.2 V. The higher activation energy of 0.469(2) eV does not correspond to $E_g/2$. 93
2.59 Low bias $\ln I - 1/T$ characteristic of a $GdFe_2$/Si junction, via a cut at 0.2 V. The higher activation energy of 0.429(1) eV does not correspond to $E_g/2$. 93
2.60 Low bias $\ln I - 1/T$ characteristic of a $GdFe_3$/Si junction, via a cut at 0.1 V. The higher activation energy of 0.227(1) eV does not correspond to $E_g/2$. 94

3.1 Energy diagrams of two similar metal electrodes separated by vacuum (left) and by and insulator (right). 98
3.2 Energy diagrams of two dissimilar metal electrodes before (left) and after (right) they have been brought into intimate contact with an insulator slab. 98
3.3 Potential profiles, for an arbitrary tunnel junction at equilibrium. The nominal barrier height is 1 eV, and barrier width is 2 nm. 100
3.4 Potential profiles, for an arbitrary tunnel junction at applied voltage $V_a = 0.5$ V. The nominal barrier height is 1 eV, and barrier width is 2 nm. 101

3.5 Current density as a function of applied voltage, calculated by both direct integration and the Simmons approximation. The nominal barrier height is 1 eV, and barrier width is 2 nm. . . . 102

3.6 Schematic representation of the decomposition of the scattering problem within the global transfer matrix method. . . . 103

3.7 Schematic diagram of the modified wavefunctions in the effective Hamiltonian approach. 105

3.8 Schematic diagram of two constant energy surfaces of $E = E_{\mathrm{F}}$ and their projections on the plane of the tunnel interface. . . . 111

3.9 Weak-localisation-like zero bias anomaly for negative residual electron-electron interaction. Parameters have been selected as: $\lambda_{\mathrm{D}} = 10$ nm, and $D = 1\mathrm{m}^2/\mathrm{s}$. . . . 115

3.10 Energy diagrams of two similar metal electrodes separated by vacuum (left) and by and insulator (right). . . . 118

3.11 The effective bias V_{eff} as a function of applied bias V_{a} for inelastic tunnelling via an excitation with $\hbar\omega^{\mathrm{in}} = 0.2$ eV, at $T = 300$ K. . . . 120

3.12 The static polarisation as a function of the MC ratio for tunnelling between identical ferromagnetic electrodes, within Julliere's model. . . . 122

3.13 Schematic representation of the two channel model within the WKB approximation. . . . 123

3.14 Schematic representation of the integration over the states available for tunnelling under applied bias. . . . 125

3.15 Schematic representation of the states available for tunnelling for $k_{\mathrm{Fl}} < k_{\mathrm{Fr}}$ (top panel), and $k_{\mathrm{Fl}} > k_{\mathrm{Fr}}$ (bottom panel). . . . 125

3.16 Magnetoconductance for a δ-barrier, between ferromagnets, with a difference of the spin-resolved Fermi-levels of ΔE_{F}, within the simplified WKB approach to tunnelling. . . . 126

3.17 Junction magneto-conductance, evaluated within the adiabatic approximation, for an average barrier height of 2.5 eV, as a function of bias, for various Fermi level differences ΔE_{F}. . . . 127

3.18 Actual Fermi convolution kernel and its approximations by Gaussian, Lorentzian and Voigt functions. The thermal energy is set at $kT = 0.1$ eV. . . . 133

3.19 Deduced Gaussian broadening of the Fermi convolution kernel, as a function of thermal energy kT. . . . 133

3.20 Deconvoluted from experimental data taken at $T = 300$ K data, differential resistivity; compared with the experimental data measured at $T = 2.0$ K. The arrows point to artefacts due to the finite size of the representation used for deconvolution. . . . 145

3.21 Recovered differential resistivity, for CoFeB tunnel junction in the antiparallel configuration, with different methods for cleaning of the singular value vector of the deconvolution matrix for the matrix system 3.3.10, compared with experimental data for $T = 300$ K. 146

3.22 Reconstructed vectors **a** and **b** for a unannealed CoFeB junction. Note that **a** is associated with $\mathcal{M}(E)$, and (b) with $\frac{\mathrm{d}}{\mathrm{d}E}\mathrm{M}(E)$ 147

3.23 Differential resistance as a function of applied bias and temperature, for an unannealed CoFeB/MgO/CoFeB junction, in the parallel state. The projections of the data points on the three main phase-space planes are shown. 148

3.24 Differential resistance as a function of applied bias and temperature, for an annealed CoFeB/MgO/CoFeB junction, in the parallel state. The projections of the data points on the three main phase-space planes are shown. 148

3.25 Temperature dependence of the differential resistance (derivative voltage) at zero bias, extracted from the data on figures 3.23 and 3.24. The solid lines represent a second order polynomial fit and a $\beta-$spline, for the unannealed and annealed cases, respectively. 149

3.26 Temperature dependence of the first-order resistance derivative spectra for an annealed CoFeB/MgO/CoFeB junction in the antiparallel state. 149

3.27 Temperature dependence of the first-order resistance derivative spectra for an annealed CoFeB/MgO/CoFeB junction in the parallel state. 150

3.28 Temperature dependence of the first-order resistance derivative spectra for an unannealed CoFeB/MgO/CoFeB junction in the antiparallel state. 150

3.29 Temperature dependence of the first-order resistance derivative spectra for an unannealed CoFeB/MgO/CoFeB junction in the parallel state. 150

3.30 Voltage dependence of the differential resistance (the experimental derivative voltage) of a single CoFeB/MgO/CoFeB junction, in the parallel state, measured at different temperatures. The data is identical to the one of figure 3.31. 151

3.31 Voltage dependence of the differential conductance of a single CoFeB/MgO/CoFeB junction in the parallel state, measured at different temperatures. The inset shows a close-up of the small bias region. 151

3.32 Voltage dependence of the differential resistance (the experimental derivative voltage) of a double CoFeB/MgO/CoFeB junction, in the antiparallel state, measured at different temperatures. 152

3.33 Temperature dependence of the FWHM of the central resistance peak of figure 3.33, as a function of temperature. The deviations from linearity are largely due to the improper modeling of the voltage dependence with a single resistance peak, and not the quality of the raw experimental data. 152

3.34 Modulation of the differential resistance, upon rotation of applied field of $\mu_0 H = 14$ T, in the plane of the junction, as a function of the applied bias V_a, for a CoFeB/MgO/CoFeB junction, measured at $T = 2$ K. 153

3.35 Modulation of the differential resistance, upon rotation of applied field of $\mu_0 H = 14$ T, in a plane orthogonal to the plane of the junction, as a function of the applied bias V_a, for an annealed CoFeB/MgO/CoFeB junction, measured at $T = 2$ K. The amplitude of the color-depth is 50 μV or about 0.5%. 154

3.36 Modulation of the differential resistance, upon rotation of applied field of $\mu_0 H = 14$ T, in a plane orthogonal to the plane of the junction, as a function of the applied bias V_a, for an unannealed CoFeB/MgO/CoFeB junction, measured at $T = 2$ K. The amplitude of the color-depth is 25 μV or about 0.25%. 154

3.37 Base functions for the current dependence of the modulation of the differential resistance of unannealed and annealed CoFeB/MgO/CoFeB tunnel junctions, at various fields (5,7, 10, 14 T), and temperatures (2, 10 K). The arrows point towards artefacts produced upon sample reloading cycle (the samples have been taken out of the system and then put back). 155

3.38 Base function for the voltage dependence of the modulation shown on figure 3.35. Best fit is achieved with a set of four Lorentzians of width ≈ 0.35 eV, and approximately equivalent spacings of 0.25 eV. 156

3.39 Same as figure 3.38, for a temperature of 10 K. The middle two peaks are refined as one, because of the additional thermal broadening, and worse signal to noise ratio. . . . 157

3.40 $I - V$ characteristics of a CoFeB/MgO/CoFeB single tunnel junction, in the parallel state, at different temperatures. 158

3.41 $I - V$ characteristics of a CoFeB/MgO/CoFeB double tunnel junction, in the parallel state, at different temperatures. 159

3.42 Logarithmic derivative in the antiparallel state, for an unannealed CoFeB/MgO/CoFeB junction, measured at $T = 2$ K. 159

3.43 Conductance in the parallel, and in the antiparallel state, for an unannealed CoFeB/MgO/CoFeB junction, measured at $T = 2$ K. 160

3.44 Conductance in the parallel, and in the antiparallel state, for an annealed CoFeB/MgO/CoFeB junction, measured at $T = 2$ K. 160

3.45 The difference in differential conductance between the parallel and the antiparallel state, and the average conductance, for an unannealed CoFeB/MgO/CoFeB junction, measured at $T = 2$ K. 161

3.46 The difference in differential conductance between the parallel and the antiparallel state, and the average conductance, for an annealed CoFeB/MgO/CoFeB junction, measured at $T = 2$ K. 161

3.47 The average conductance, for an annealed CoFeB/MgO/CoFeB junction, measured at $T = 2$ K, together with 4^{th} order polynomial fit at high bias. 162

3.48 The the difference between the actual average conductance and the polynomial fit of figure 3.47, for an annealed CoFeB/MgO/CoFeB junction, measured at $T = 2$ K, revealing the contribution of the inelastic processes within the barrier region. 163

3.49 Voltage dependence of the differential resistance (the experimental derivative voltage) for a single CoFeB/MgO/CoFeB junction, in the parallel state, together with two fits to the model of Altshuler & Aronov (1979). 163

3.50 Bias dependence of the differential capacitance for a single CoFeB/MgO/CoFeB junction, measured at a frequency of $f = 1.234$ kHz, at a temperature of 2 K, for both the parallel and antiparallel states. Parallel plates capacitance model estimate is shown with an arrow. 165

3.51 Linearly scaled capacitance compared with the junction conductance, for the antiparallel case of figure 3.50. 166

3.52 Magnetic field and current dependencies of the first derivative of the voltage drop, for an annealed CoFeB/MgO/CoFeB junction, measured at two different temperatures and at two different orientations. 167

3.53 Magnetic field orientation in plane and current dependencies of the voltage drop and its first and second derivative with respect to current, for an annealed CoFeB/MgO/CoFeB junction, measured several different field magnitudes. The angle range is $\theta \in [-5\,^\circ, 365\,^\circ]$, 90 $^\circ$ per division. The current range is $J \in [-100\ \mu\text{A}, 100\ \mu\text{A}]$, 50 μA per division. . . 168

3.54 Magnetic field and current dependencies of the voltage drop and its first and second derivative with respect to current, for an annealed CoFeB/MgO/CoFeB junction, measured at $T = 2.0$ K at various angles θ between the current and the applied field. The field range is $\mu_0 H \in [-3\text{ T}, 3\text{ T}]$, 1 T per division. The current range is $J \in [-100\ \mu\text{A}, 100\ \mu\text{A}]$, 50 μA per division. 169

3.55 Magnetic field and current dependencies of the voltage drop and its first and second derivative with respect to current, for an annealed CoFeB/MgO/CoFeB junction, measured at $T = 2.0$ K at various angles θ between the current and the applied field. The field range is $\mu_0 H \in [-3\text{ T}, 3\text{ T}]$, 1 T per division. The current range is $J \in [-100\ \mu\text{A}, 100\ \mu\text{A}]$, 50 μA per division. Continued from figure 3.54. 170

3.56 Magnetic field and current dependencies of the voltage drop and its first and second derivative with respect to current, for an annealed CoFeB/MgO/CoFeB junction, measured at $T = 2.0$ K at various angles θ between the current and the applied field. The field range is $\mu_0 H \in [-3\text{ T}, 3\text{ T}]$, 1 T per division. The current range is $J \in [-100\ \mu\text{A}, 100\ \mu\text{A}]$, 50 μA per division. Continued from figure 3.55. 171

3.57 Magnetic field and current dependencies of the voltage drop and its first and second derivative with respect to current, for an unannealed CoFeB/MgO/CoFeB junction, measured at $T = 2.0$ K at various angles θ between the current and the applied field. The field range is $\mu_0 H \in [-3\text{ T}, 3\text{ T}]$, 1 T per division. The current range is $J \in [-100\ \mu\text{A}, 100\ \mu\text{A}]$, 50 μA per division. 171

3.58 Magnetic field and current dependencies of the voltage drop and its first and second derivative with respect to current, for an unannealed CoFeB/MgO/CoFeB junction, measured at $T = 2.0$ K at various angles θ between the current and the applied field. The field range is $\mu_0 H \in [-3\text{ T}, 3\text{ T}]$, 1 T per division. The current range is $J \in [-100\ \mu\text{A}, 100\ \mu\text{A}]$, 50 μA per division. Continued from figure 3.57. 172

3.59 Magnetic field and current dependencies of the voltage drop and its first and second derivative with respect to current, for an unannealed CoFeB/MgO/CoFeB junction, measured at $T = 2.0$ K at various angles θ between the current and the applied field. The field range is $\mu_0 H \in [-3\text{ T}, 3\text{ T}]$, 1 T per division. The current range is $J \in [-100\ \mu\text{A}, 100\ \mu\text{A}]$, 50 μA per division. Continued from figure 3.58. 173

3.60 Magnetic field and current dependencies of the differences (the hysteretic difference between ramping the external field $+3\text{ T} \rightarrow -3\text{ T}$ and $-3\text{ T} \rightarrow +3\text{ T}$) between the voltage drop and its first and second derivative with respect to current, for an annealed and unannealed CoFeB/MgO/CoFeB junctions, measured at $T = 2.0$ K at two different angles θ between the current and the applied field. The field range is $\mu_0 H \in [-3\text{ T}, 3\text{ T}]$, 1 T per division. The current range is $J \in [-100\ \mu\text{A}, 100\ \mu\text{A}]$, 50 μA per division. Continued from figure 3.60. 174

3.61 Dependence of the zero-bias differential resistivity on the angle of the applied magnetic field θ, in the plane of the junction, for an unannealed CoFeB/MgO/CoFeB junction, measured at 2 K. 174

3.62 Dependence of the zero-bias differential resistivity on the angle of the applied magnetic field, for an unannealed CoFeB/MgO/CoFeB junction, measured at 2 K. 175

3.63 Dependence of the zero-bias differential resistivity on the angle of the applied magnetic field, for an annealed CoFeB/MgO/CoFeB junction, measured at 2 K. 175

3.64 Zero-bias differential resistance as a function of applied field for an annealed CoFeB/MgO/CoFeB junction. The model assumes uniaxial directional anisotropy. 175

3.65 Exchange bias parameter H_a extracted from fits as the ones shown on figure 3.64 for an annealed CoFeB/MgO/CoFeB junction. The fits are described in the text. 176

3.66 Barrier height extracted with an automatic evaluation and fitting procedure employing the model of Simmons (1969) at each field value, for unannealed and annealed CoFeB/MgO/CoFeB tunnel junctions, measured at $T = 2.0$ K, with magnetic field applied parallel to the current direction. 177

3.67 Second differential resistance profile for an annealed CoFeB/MgO/CoFeB tunnel junction, measured at $T = 2.0$ K, in the antiparallel state, with the automatically detected extrema marked. 178

3.68 Second differential resistance profile for an annealed CoFeB/MgO/CoFeB tunnel junction, measured at $T = 2.0$ K, in the parallel state, with the automatically detected extrema marked. 178

3.69 Maxima detected second differential resistance with respect to current for an annealed CoFeB/MgO/CoFeB tunnel junction, measured at $T = 2.0$ K, with the magnetic field applied perpendicular to the plane of the junction. 180

3.70 Minima detected second differential resistance with respect to current for an annealed CoFeB/MgO/CoFeB tunnel junction, measured at $T = 2.0$ K, with the magnetic field applied perpendicular to the plane of the junction. 180

3.71 Maxima detected second differential resistance with respect to the applied voltage V_a, for an annealed CoFeB/MgO/CoFeB tunnel junction, measured at $T = 2.0$ K, with the magnetic field applied perpendicular to the plane of the junction. 181

3.72 Minima detected second differential resistance with respect to the applied voltage V_a for an annealed CoFeB/MgO/CoFeB tunnel junction, measured at $T = 2.0$ K, with the magnetic field applied perpendicular to the plane of the junction. 181

4.1 Schematic representation of the experimental setup used for magnetic detection of diffused spin polarisation. . . . 188

4.2 Scaled magnetic response, measured as a function of applied field, measured at the centre of the Al strip of Sample 1 (Fe injectors), at $T = 2$ K. . . . 189

4.3 Magnetisation distribution expected for a Sample 1 with Fe injection electrodes, for either left-hand or right-hand-side injection. Parameters are given in the text. . . . 189

4.4 Coupled flux profiles generated by the injected magnetisation distributions shown on figure 4.3, together with the ones due to the substrate contribution and the adiabatic depolarisation of the central Al conductor (not to scale). . . . 190

4.5 Calculated coupled flux profiles for positive (green), negative (red) and zero (black) current bias, for $\lambda_{sd} = 3.5$ cm, and assuming 10 % injection efficiency. . . . 190

4.6 Raw coupled flux profiles for different voltage biases of Sample 1 (Fe electrodes), measured at $T = 4.23$ K and $\mu_0 H = 100$ mT. . . . 191

4.7 Raw coupled flux profiles for Sample 1 (Co electrodes), measured at $T = 1.8$ K and $\mu_0 H = 20$ mT. Note the flux-jump experienced and the scale of the voltage response for an individual flux quantum Φ_0. . . . 192

4.8 Spatial profiles of the flux coupled to the gradiometer at $T = 1.8$ K and 10 Kfor applied current of 0 (green and magenta), +10 mA (black and blue) and -10 mA (red and cyan) for Sample 2 with Fe injection electrodes. The Sample is situated at $z = 5.4$ cm. Note that at 10 K the profiles are completely anti-symmetric with respect to applied current. . . . 192

4.9 Field reversal symmetry of the inductive (antisymmetric) and the non-inductive (symmetric) with respect to current components of the coupled flux, measured on Sample 1 (Fe electrodes) at $T = 1.8$ K. . . . 193

4.10 Temperature dependence of the non-inductive part of the pick-up for Sample 1 (Fe electrodes). . . . 193

4.11 Current dependence of the symmetric and antisymmetric parts of the coupled flux, measured for Sample 1 (Zn electrodes), at $T = 1.8$ K, and $\mu_0 H = 100$ mT. . . . 194

4.12 Spatial profiles of the non-inductive component of the AC detected coupled flux, for Sample 1 (Ni electrodes), measured at $T = 1.8$ K. . . . 194

4.13 Field dependence of the non-inductive component of the coupled flux for Sample 1 (Ni electrodes, measured at $T = 1.8$ K.) . . . 195

4.14 Voltage-current characteristics of Sample 1 with different injection electrodes, measured at $T = 1.8$ K. Note the small nonlinearities in some of the curves. . . . 195

4.15 Symmetrised with respect to current coupled flux profile of Sample 1, measured at $T = 1.8$ K. . . . 196
4.16 Difference of the zero-current coupled flux profiles measured at $T = 10$ K and at 1.8 K for Sample 1. . . . 196
4.17 Coupled flux profiles for positive (green), negative (blue) and zero (red and black) current bias, measured at $T = 1.8$ K for Sample 1 (Fe electrodes). . . . 197
4.18 Synchronously detected (AC method) coupled flux at the fundamental frequency of 1.133 kHzwith positive, negative and zero current bias, for Sample 2 (Fe electrodes). The measurement is performed at applied field of 20 mT and at $T = 1.8$ K. . . . 197

5.1 An illustration of the various contributions towards the magnetoresistance in semiconductors. . . . 202
5.2 An illustration of the anomalous contributions towards the magnetoresistance and the Hall effect. . . . 204
5.3 An illustration of the anisotropic magnetoresistance contribution in a crystalline system. 204
5.4 An illustration of the weak localization magnetoresistance contribution in a disordered system. . . . 207
5.5 An illustration of the oscillatory contributions towards the magnetoresistance and the Hall effect. . . . 208
5.6 Resistance as a function of temperature for an Undoped ZnO sample, measured at zero applied field. . . . 210
5.7 Temperature dependence of the resistance of a 5 % Co doped ZnO film. Note the logarithmic temperature scale. . . . 210
5.8 Magnetic hysteresis of a 25 % Co doped ZnO thin film prepered in conditions analogous to the one system of figure 5.22. . . . 211
5.9 Resistance as a function of field, at various temperatures (shown), for an undoped ZnO sample. . . . 211
5.10 Magnetoresistance of a 5 % Co doped ZnO film, demonstrating peculiar behaviour at low temperatures. The magnetic field is applied out of the plane of the film. . . . 212
5.11 Same as figure 5.10, with the magnetic field applied in the plane of the film. . . . 212
5.12 A fit to the magnetoresistance of a 5 % Co doped ZnO film prepared at 600 °C, using a combined model, taking into account two band contribution and ionised impurity scattering. . . . 213

5.13 Quantum oscillations in a 5 % Co doped ZnO film prepared at 600 °C, measured at $T = 1.8$ K. The peaks corresponding to two different extremal cross sections of the Fermi surface are indicated. . . . 213

5.14 An illustration of the degeneration of the electron gas upon increasing of the carrier concentration via Al co-doping. . . . 214

5.15 Apparent carrier concentration as a function of nominal Al concentration. Note the saturation over about 0.2 % nominal Al content. . . . 215

5.16 Illustration of the Burstein-Moss shift in Al co-doped ZnCoO. . . . 216

5.17 Activation of the carriers in 5 % Co doped, 0.1 % Al co-doped ZnO film. The activation energy is 7.9 meV. . . . 216

5.18 Activation of the carriers in undoped ZnO film. The activation energy is 2.9 meV. . . . 216

5.19 Hall resistance of a 5 % Co doped, 0.5 % Al co-doped ZnO film. Note the miniscule changes of the gradient with temperature. . . . 217

5.20 Hall coefficient as a function of temperature for a series of different Al co-dopant concentrations. . . . 217

5.21 Magnetoresistance measured at $T = 2.0$ K , for a series of different Al co-dopant concentrations. . . . 218

5.22 Magnetoresistance of a bi-layer structure (5 / 25 % Co doped ZnO), showing 'butterfly' shape, characteristic of the magnetic hysteresis of the Co clusters of the 25 % Co doped layer. . . . 218

5.23 Resistance of a 5 % Co doped ZnO film prepared at 600 °C, as a function of magnetic field at various angles out of plane of the film, measured at $T = 1.8$ K. . . . 219

5.24 Resistance of a 25 % Co doped ZnO film prepared at 500 °C, as a function of magnetic field at various angles out of plane of the film, measured at $T = 1.8$ K. . . . 219

5.25 Angular dependence of the anisotropy of the magnetoresistance for a 4 % Co doped ZnO film, measured at $T = 2.0$ K and $\mu_0 H = 1$ T. . . . 220

5.26 Field dependence of the second order anisotropic conductance coefficient for a 4 % Co doped ZnO film. . . . 220

5.27 Field dependence of the fourth order anisotropic conductance coefficient for a 4 % Co doped ZnO film. . . . 221

5.28 Intuitive expectation for the field dependence of the second anisotropic magnetoresistance coefficient, at low temperature. . . . 221

5.29 Temperature dependence of the second order anisotropic conductance coefficient for a 5 / 25 % Co doped ZnO bi-layer film. . . . 221

5.30 Temperature dependence of the second order anisotropic conductance coefficient for a 4 % Co doped ZnO film. . . . 222
5.31 Temperature dependence of the fourth order anisotropic conductance coefficient for a 4 % Co doped ZnO film. . . . 222
5.32 Field temperature scaling for the second order anisotropic conductance coefficient for a 4 % Co doped ZnO film. . . . 223
5.33 Second order anisotropic resistance coefficient as a function of field and temperature, for a 0.2 % Al co-doped, nominally 5 % Co in ZnO sample, deposited on c-cut sapphire. 223
5.34 Second order anisotropic conductance coefficient as a function of field and temperature, for a 1.0 % Al co-doped, nominally 5 % Co in ZnO sample, deposited on c-cut sapphire. 224
5.35 Second order anisotropic conductance coefficient as a function of field and temperature, for a 0.2 % Al co-doped, nominally 5 % Co in ZnO sample. . . . 224
5.36 Fourth order anisotropic conductance coefficient as a function of field and temperature, for a 0.2 % Al co-doped, nominally 5 % Co in ZnO sample. . . . 224
5.37 Sixth order anisotropic conductance coefficient as a function of field and temperature, for a 0.2 % Al co-doped, nominally 5 % Co in ZnO sample. . . . 225
5.38 Magnitude of the second order anisotropy coefficient as a function of applied magnetic field for the temperatures shown. The electron effective mass is fixed at $m^\star = 0.24\ m_e$, and the Dingle temperature is chosen to be $T_D = 5$ K. . . . 225
5.39 Magnitude of the second order anisotropy coefficient as a function of applied magnetic field for the temperatures shown. The electron effective mass is fixed at $m^\star = 1.21\ m_e$, and the Dingle temperature is chosen to be $T_D = 20$ K. . . . 226
5.40 Magnetic moment as a function of temperature for a 5 % Co doped ZnO film on Al_2O_3 substrate, prepared at 450 °C. The individual curves are measured at the temperatures indicated. . . . 226
5.41 Low field part of the data set shown on figure 5.40, at the extreme temperatures. Note the very different magnetisation behaviour in the two cases. . . . 227
5.42 High field slopes of the magnetic moment vs temperature curves from figure 5.40, showing essentially constant with respect to the measurement errors value of 0.154 Am^2/T. 227
5.43 Magnetic moment as a function of temperature for a 5 % Co doped ZnO prepared at 450 °C, after substraction of the diamagnetic contribution of the substrate. . . . 228
5.44 Saturating moment at $\mu_0 H = 5$ T as a function of inverse temperature, as extracted from the data set of figure 5.43. Note the paramagnetic and the ferromagnetic contributions. . . . 228

5.45 Temperature dependence of the coercive field for the data set shown on figure 5.43. Note the pronounced exponential behaviour and the coercivity offset due to the hysteresis of the superconducting magnet used for the measurements. 229

6.1 The coordinates on a graphene sheet. 233
6.2 The crystallographic structure of graphite. 234
6.3 The crystallographic structure of graphite. 236
6.4 Magnetisation of HOPG (grade ZYB) in different orientations, measured at 300 K. . . 238
6.5 Magnetisation of HOPG (grade ZYH) in different orientations, measured at 300 K. . . 239
6.6 Magnetisation of HOPG (grade ZYA) with field applied along the c-axis, measured at 1.8 K K. The inset shows the oscillating part of the magnetisation, after the substraction of the linear susceptibility slope. 239
6.7 Magnetisation of HOPG (grade ZYA) with the field applied perpendicular to the c-axis in different orientations, measured at 1.8 K K. The inset shows the saturating part of the magnetisation, after the substraction of the linear susceptibility slope. 240
6.8 Resistivity as a function of magnetic field along the c-axis of HOPG, in the high temperature limit. The lines are fits to a three carrier model. The data is regressed simultaneously with the one of figure 6.9. 241
6.9 Hall resistivity as a function of magnetic field along the c-axis of HOPG, in the high temperature limit. The lines are fits to a three carrier model. The data is regressed simultaneously with the one of figure 6.8. 241
6.10 Resistivity as a function of magnetic field along the c-axis of HOPG, in the high temperature limit, at small fields. The lines are fits to a three carrier model. The data is regressed simultaneously with the one of figure 6.11. 242
6.11 Hall resistivity as a function of magnetic field along the c-axis of HOPG, in the high temperature limit, at small fields. The lines are fits to a three carrier model. The data is regressed simultaneously with the one of figure 6.10. 242
6.12 Carrier densities for the different carrier types in HOPG as a function of temperature. The line through the minority holes data is just a guide to the eye. 243
6.13 Carrier densities for the different carrier types in HOPG as a function of temperature. The splines through the data are just guides to the eye. 243
6.14 Scattering frequencies of majority and minority carriers in HOPG as a function of temperature. 244
6.15 Resistance as a function of magnetic field along the c-axis of HOPG, at various temperatures. 245

6.16 Hall resistance as a function of magnetic field along the c-axis of HOPG, at various temperatures. . . . 245
6.17 Resistance as a function of magnetic field perpendicular to the c-axis of HOPG and to the applied current, at various temperatures. . . . 245
6.18 Hall resistance as a function of magnetic field perpendicular to the c-axis of HOPG and to the applied current, at various temperatures. . . . 246
6.19 Resistance as a function of magnetic field perpendicular to the c-axis of HOPG and parallel to the applied current, at various temperatures. . . . 246
6.20 Hall resistance as a function of magnetic field perpendicular to the c-axis of HOPG and parallel to the applied current, at various temperatures. . . . 247
6.21 Resistance as a function of temperature, at various magnetic fields along the c-axis of HOPG. . . . 247
6.22 Hall resistance as a function of temperature, at various magnetic fields along the c-axis of HOPG. . . . 247
6.23 Resistance as a function of temperature, at various magnetic fields perpendicular to the c-axis of HOPG and to the applied current. . . . 248
6.24 Hall resistance as a function of temperature, at various magnetic fields perpendicular to the c-axis of HOPG and to the applied current. . . . 248
6.25 Resistance of HOPG in the basal plane, as function of the applied field of up to 23 T. . 249
6.26 Normal and Hall resistance as a function of magnetic field along the c-axis of HOPG. The arrows point towards the appearance of the oscillations corresponding to the minority carriers. . . . 250
6.27 Conductivity oscillations in HOPG at 0.3 K, and the allocation of the different periods observed. . . . 250
6.28 Inverse domain image of the ShdH oscillations in the intermediate frequency region. . . 250
6.29 Inverse domain image of the ShdH oscillations in the low frequency region. . . . 251
6.30 Relative phase of the ShdH oscillations in HOPG, measured at 0.3 K. The vertical lines are guide to the eye. The arrows point towards the minority carrier oscillations. . 251
6.31 Relative phase of the ShdH oscillations in HOPG, measured at 0.5 K. The vertical lines are guide to the eye. The arrows point towards the minority carrier oscillations. Note the slightly different scale. . . . 251
6.32 Relative phase of the ShdH oscillations in HOPG, measured at 2.8 K. The vertical lines are guide to the eye. The arrows point towards the minority carrier oscillations. . 252

6.33 Relative phase of the ShdH oscillations in HOPG, measured at 4.0 K. The vertical lines are guide to the eye. The arrows point towards the minority carrier oscillations. . 252
6.34 Temperature dependence of the amplitude of the ShdH oscillations in HOPG. 252
6.35 Hall conductivity as a function of field, revealing the absence of explicit quantisation in the conductivity. 253
6.36 Band-pass filtered (3 - 5 T) majority electrons' component of the oscillatory conductivity GREEN and a fit using the L-K approximation RED, with parameters: $T = 0.3$ K, $m^\star = 0.039 m_e$, $T_D = 5$ K, $A_{ext} = 4.2 \cdot 10^{16} m^{-2}$, $\phi = -\pi/2$. 253
6.37 Magnetisation of a nanotube ensemble at different temperatures. 258
6.38 Raw SQUID response profile for a nanotubes compact. 258
6.39 Fitting a simple model to the magnetisation curve of an ensemble of nanotubes. 258
6.40 Components of the magnetisation of a nanotube ensemble. 259
6.41 Oscillatory component of the magnetisations for a nanotube ensemble at different temperatures. 259
6.42 Measured and deduced magnetisation components for a nanotube ensemble at $T = 5$ K. 260
6.43 Calculated magnetisation components for a nanotube ensemble at $T = 5$ K. 260
6.44 Measured temperature dependence of the magnetisation for a nanotube ensemble in a field of $\mu_0 H = 5$ T, and a fit to it with a simple model, with a $T_D = 110$ K. 261
6.45 Measured temperature dependence of the magnetisation for a nanotube ensemble in a field of $\mu_0 H = 0.5$ T, and a fit to it with a simple model, with a $T_D = 58$ K. 261
6.46 Measured temperature dependence of the magnetisation for a nanotube ensemble at two different applied fields. 262
6.47 Calculated temperature dependence of the magnetisation for a nanotube ensemble at two different applied fields. 262
6.48 Comparison of dHvA oscillations in HOPG and carbon nanotubes, without de-drifting. 263
6.49 Comparison of dHvA oscillations in HOPG and carbon nanotubes, with de-drifting. . . 263
6.50 Oscillations in the thermodynamic and the kinetic coefficients. 264
6.51 Resistance of nanotubes compact at different temperatures. 264
6.52 Resistance of a nanotubes compact at 1.8 K, and a fit to it. The inset shows a low field zoom-in of the same dataset, demonstrating the initial quadratic field dependence of the resistance. 265
6.53 Magnetisation of an ensemble of predominantly single and double walled carbon nanotubes at different temperatures. 265

6.54 Magnetisation of an ensemble of predominantly single and double walled carbon nanotubes as a function of temperature at a field of $\mu_0 H = 5$ T. 266
6.55 Magnetisation of an ensemble of micron-sized carbon whiskers at different temperatures. 266

A.1 Potential distribution across the depleted region for n-type non-degenerate semiconductor. Constants are set as follows: $\epsilon_s = 10\epsilon_0$, $N_d = 10^{-15}$ cm^{-3} and $\phi_i = 1$ V. 275
A.2 Electric field distribution across the depleted region for n-type non-degenerate semiconductor. Constants are set as follows: $\epsilon_s = 10\epsilon_0$, $N_d = 10^{-15}$ cm^{-3} and $\phi_i = 1$ V. . . 275
A.3 Potential distribution across the depleted region for n-type non-degenerate semiconductor. Constants are set as follows: $\epsilon_s = 10\epsilon_0$, $N_d = 10^{-17}$ cm^{-3} and $\phi_i = 1$ V. 284
A.4 Coordinate system and sign convention used in the description of the Schottky junction theory. 284
A.5 Spectral calibration of the S1000 fibre-optics spectrometer. 285
A.6 Spectral calibration of the S2000 fibre-optics spectrometer. 285
A.7 Intensity calibration of the KL1500 lamp used in the experiments. 286
A.8 Intensity calibration of the KL1500 lamp used in the experiments. 286
A.9 Absorber calibration in the NUV - VIS - NIR range. 287
A.10 Absorber calibration in the NUV - VIS - NIR range. 287
A.11 Diode mounting configuration, used for ambient temperature diode characterisation. . . 288
A.12 Block diagram of the $I - V$ curve tracer used for fast diode characterisation. 289
A.13 Block diagram of the $I - U$ curve curve measurement configurations for low device impedance (a), and for high device impedance (b). 290
A.14 Block diagram of the AC/DC bridge device comparison setup. 290
A.15 Temperature, as monitored by a 4-wire AC-bridge measurement on Class A, Pt 100, standard resistor. During the scan the field was ramped continuously at a rate of 0.1 T/min. 291

B.1 Schematic diagram of the setup used for four-wire DC resistance and AC differential resistance measurements. 297
B.2 Voltage dependence of the differential resistance of a 1 kΩ standard resistor. The noise band is shown for a time constant of 0.1 s. 297
B.3 Electromagnetic interference as coupled to a standard BNC connector, in a normal laboratory environment, in the frequency window where mains interference is dominant. 298
B.4 Electromagnetic interference as coupled to a standard BNC connector, in a normal laboratory environment. 299

C.1 Schematic representation of the two types of samples used to investigate the possibilities for direct magnetic detection of injected spin polarisation. 308

C.2 Magnetic moment as a function of temperature, measured in a field of 1 T, for a 4N pure Al sample of mass 211.5 mg. 309

C.3 The dataset of figure C.2, replotted in order to illustrate the quadratic temperature dependence of the magnetic susceptibility. 309

C.4 The dataset of figure C.2, replotted in order to illustrate the low temperature Curie-like temperature dependence of the magnetic susceptibility. 310

C.5 A fit to the dataset of figure C.2, including the temperature dependence of the Pauli susceptibility and the Curie-like low temperature upturn. 310

C.6 Magnetic susceptibility as a function of temperature for a borosilicate glass sample. . . 311

C.7 Magnetic susceptibility as a function of temperature for a 5N pure fused SiO_2 rod sample. The data has not been corrected for an absolute sensitivity calibration factor of 1.085(1) valid at the time of the measurement. 311

C.8 Spatial frequency domain spectrum of the second-order gradiometer used (solid line), compared to the background drifts and noise spectrum (dotted line). The inset shows the geometry of gradiometer and the reference frame used. 313

C.9 The total coupled flux due to a point dipole of $1 \cdot 10^{-6}$ Am^2: situated in the centre of the system and oriented along the z-axis (top panel); radially offset at $\rho = 0.5$ cm and oriented along the z-axis (middle panel); radially offset at $\rho = 0.5$ cm and oriented perpendicular to the z-axis (bottom panel). Linear fits around the right-hand-side maximal derivative position are also shown, together with the actual z-axis spans used. 315

C.10 Calculated total coupled flux quoted in 10^{-11} Wb (numbers on top), and deviations relative to a point dipole (numbers on bottom) for different geometrical distributions of magnetic moment. The three columns correspond to the three standard data reduction procedures discussed in the text. The total sample moment is set to $1 \cdot 10^{-6}$ Am^2. The sizes are 0.5 cm in all dimensions, as appropriate, apart from the film on substrate examples where the substrate thickness is 0.5 mm and the ratio of the paramagnetic moment of the film to the diamagnetic moment of the substrate is 1:2. Continued on pages 320 and 321. 319

C.11 Continued from page 319. 320

C.12 Continued from page 320. 321

C.13 Autocorrelation function (solid line) and the squared correlation function (dotted line) for the response function of the gradiometer used. The distances at which two point dipoles are independent are given with arrows. 322

C.14 Calculated and deconvoluted z-axis profile of the magnetisation distribution, by multi-parameter regression (top panel), and by abruptly filtered SVD deconvolution (bottom panel, bars) and smoothly filtered SVD (bottom panel, line); for a system of three point dipoles of magnitudes 1, -0.5 and -0.25, situated at positions z = 0, 0.45 and 3.19 cm , respectively. The simulated random noise background is 0.1 % of the signal amplitude. 323

C.15 Normalised total magnetic moment response of various deconvolution procedures, compared with the standard iterative regression procedure, for a system consisting of a spring of 99.9 % pure Ag wire (ϕ 0.5 mm, m = 124.5 mg), elongated to different lengths d. Note relative stability of response of the smooth-filtered SVD deconvolution procedure. 325

C.16 Single coil response function at different radial offsets ρ. The inset shows the dependence of the width of the response peak on the radial offset (dots) and a quadratic fit for its dependence on ρ (line). The radius of the coil is $r_c = 0.97$ cm. 327

C.17 The response of the three standard regression procedures to a point dipole of $1 \cdot 10^{-6}$ Am^2, radially displaced at a distance ρ. 328

C.18 Magnetisation curves for pieces of CrO_2 commercial magnetic recording tape situated at a radial offset ρ = 2.5 mm, and oriented parallel (top panel) and perpendicular (bottom panel) to the z-axis. Both the axial m_z and radial m_ρ components of the magnetic moment are extracted. 329

C.19 Base-set functions for a point dipole situated at a radial offset ρ = 2.5 mm: on axis component F_z (solid line) and radial component F_ρ (dotted line). 330

C.20 Response of the three standard regression procedures to a system of two point dipoles of $0.5 \cdot 10^{-6}$ Am^2 each, one of which is situated at the centre of the system and the other one is placed at a distance Z along the z-axis. 330

C.21 (a) Arbitrary non-linear magnetisation curve (solid line) of a system of two point dipoles situated 0.5 mm apart, one of which positive and saturating in applied field, and the other one negative and linear in applied field. The calculated response of the iterative regression procedure is shown as (dots). Note the large deviations around zero total magnetic moment. (b) Magnetisation curve at 300 K for 100 nm thick $Sn_{0.95}Co_{0.05}O$ film on R-cut Al_2O_3 substrate (0.5 x 5 x 5 mm). Please, note the deviations pointed out in the regions where the total z-axis dipole moment m_z is close to zero. 331

C.22 Response of the geometrical average data regression procedure, for a system of two point dipoles of opposite signs and various magnitudes, for different distance d between them. 332

C.23 Response of the linear data regression procedure, for a system of two point dipoles of opposite signs and various magnitudes, for different distance d between them. 332

C.24 Response of the iterative data regression procedure, for a system of two point dipoles of opposite signs and various magnitudes, for different distance d between them. 333

C.25 Measured and deconvoluted z-axis profile of the magnetisation distribution, by constrained to positive dipole density multi-linear fitting (top panel, bars) and SVD deconvolution (top panel, line), by multi-parameter regression (middle panel), and by abruptly filtered SVD deconvolution (bottom panel, bars) and smoothly filtered SVD (bottom panel, line); for a system of four dipoles of relative magnitudes 0.48, 1.00, 0.61 and 0.31, situated at positions z = 3.3, 6.2, 7.2 and 9.6 cm, respectively. The sample consists of pieces of standard CrO_2 magnetic recording tape. Total moment is $4.4 \cdot 10^{-6}$ Am^2. 334

D.1 Approximate thickness determination from the optical transmission of a seres of 5 % Co doped ZnO films made at different occasions. 338

D.2 Optical absorption spectrum in the NIR-VIS-NUV region. The data is a combination of two data sets measured with S1000 and S2000, fibre-optic coupled spectrometers. . . 339

List of Tables

2.1 Reduced results of magneto-photovoltaic measurements of various Schottky diodes with Si base, at two different temperatures. 83

2.2 Minimal barrier heights without further corrections, and total resistances at -0.1 V and 0.1 V for various Schottky junctions on silicon. Subscript $_{ann}$ denotes an annealed sample of the same batch. 91

2.3 Barrier heights ϕ_{b} and recombination activation energies E_{r} for various Schottky junctions on silicon. Values are denoted by - when only one characteristic energy can be extracted. 94

3.1 Peak parameters (effective band positions and dispersions) at two different temperatures for an annealed CoFeB/MgO/CoFeB junction. 157

3.2 Anisotropy coefficients of the tunnelling magnetoresistance, at zero bias, for a unannealed CoFeB/MgO/CoFeB junction, extracted from data measured at $T =$ 2.0 K 158

3.3 Anisotropy coefficients of the tunnelling magnetoresistance, at zero bias, for a annealed CoFeB/MgO/CoFeB junction, extracted from data measured at $T =$ 2.0 K 158

3.4 Fitting parameters for the fits visualised figure 3.65. 176

3.5 Peak parameters of the maxima of second derivative profile (by automated extraction) for an annealed CoFeB/MgO/CoFeB junction in the antiparallel state, measured at $T = 2.0$ K. The positions denoted by * correspond to the boundaries of the dataset. 179

3.6 Peak parameters of the maxima of second derivative profile (by automated extraction) for an annealed CoFeB/MgO/CoFeB junction in the parallel state, measured at $T = 2.0$ K. The positions denoted by * correspond to the boundaries of the dataset. 179

5.1 Apparent carrier concentrations in various ZnO thin films deposited on C-cut and R-cut sapphire. 215

6.1 Extracted material parameters for HOPG and multi-walled carbon nanotubes. *The actually detected frequencies are: 10.9 T, 14.3 T, 18.2 T and 26.3 T. 249

6.2 Extracted material parameters for HOPG and multi-walled carbon nanotubes. . 267

Nomenclature

Roman Symbols

A	independent Richardson constant
a_0	Bohr radius
$A^\star$	Richardson constant
$A^{\star\star}$	effective Richardson constant
B	magnetic field
B_a	Anisotropy field
$\mathbf{c}$	annihilation operator for s-like states
c	$\approxeq 2.9979 \times 10^8$ m/s the velocity of light in vacuum
C_j	junction capacitance (measured in C/m^2)
$\mathbf{d}$	annihilation operator for d-like states
D	diffusion coefficient
d_0	mean electron-hole pair distance
$D^\star$	ambipolar diffusion coefficient
e	$\simeq 2.718\ldots$
E	energy general
E_c	corelation energy
E_ex	exchange energy
E_F	Fermi energy

E_{g}	main energy gap
E_{r}	recombination current activation energy
f	probability
F_{N}	Norde function
Γ	gamma function
$\mathbf{G}$	global transfer matrix
g	Lande g-factor
G_{N}	reformulated Norde function
h	Planck's constant
$\hbar$	reduced Planck's constant
I_{g}	generation current
I_{r}	recombination current
I_{S}	saturation current
$\mathbf{j}$	probability current density operator
J	current density
j	probability density current
J_{d}	diffuse transmission current
J_{d}	dipolar energy integral
J_{ex}	exchange energy integral
J_{S}	saturation current density
J_{s}	specular transmission current
$\mathbf{k}$	wave vector
k	Boltzmann's constant
k_0	Thomas-Fermi wave vector

k_{F}	Fermi wave vector
$k_{\parallel}$	component of the momentum parallel to the interface
l	mean free path
L_{D}	Debye length
$m^{\star}$	effective mass
m_{e}	the free electron mass
$m^{\star\star}$	reduced electron and hole mass
N	available density of states (measured in m^{-1})
n	electron carrier concentration
n_0	electronic number density
n_{t}	concentration of traps
$\mathbf{P}$	phase matrix
P	total electronic polarisation
p	hole carrier concentration
Q	area density of the electric charge
q	unsigned electronic charge
r	resistance area product
r_{d}	drift-diffusion region resistance area product
R_{l}	leakage resistance
R_{s}	series resistance
r_{s}	the radius of the single electron sphere
$\mathbf{S}$	scattering matrix
$\mathbf{s}$	spin vector
S	surface area

T	absolute temperature
T_{C}	Curie temperature
T_{K}	Kondo temperature
$\overline{v}$	mean thermal velocity
V_{a}	applied voltage
v_{b}	ballistic velocity of carriers
V_{bf}	band flattening voltage
V_{bi}	build-in potential
v_{D}	drift velocity
v_{d}	diffusion velocity
v_{F}	Fermi velocity
V_{n}	voltage difference between c-band and the Fermi Level
v_{R}	Richardson velocity
v_{r}	recombination velocity
v_{S}	sound velocity
V_{t}	voltage equivalent of temperature
x_{a}	accumulation layer width
x_{d}	depletion layer width
x_{i}	insulator thickness
x_{p}	diffusion length for holes

Greek Symbols

α	absorption length for light
α^{c}	conduction electron spin polarisation
α^{s}	static spin polarisation

β	spin-asymmetry of the diffusion coefficient
χ	electron affinity (measured in J)
Δ	the Laplace operator
δ	Dirac's delta function
$\delta\eta$	spin-split of the chemical potential
Δ_{ex}	exchange splitting
Δ_{s}	superconducting gap parameter
ϵ	electrical permittivity
$\mathcal{E}$	electric field
ϵ_0	$\equiv \frac{1}{\mu_0 c^2} \approxeq 8.831 \times 10^{-12}$ F/m the permittivity of vacuum
ϵ_{i}	insulator permittivity
Φ	work function (measured in J)
ϕ	electric potential
Φ_0	energy barrier as seen from the metal (measured in J)
ϕ_{b}	barrier height as seen from the semiconductor (measured in V)
$\bar{\phi}_{\mathrm{b}}$	average barrier height
Φ_{g}	chemical potential of the surface gap states
Γ	band broadening factor
γ	quantum mechanical level degeneracy
ι	ratio of donor-like states density to total density
κ	dimensionless magnetic susceptibility
$\Lambda_{\mathrm{e-e}}$	effective constant of the residual e-e interaction
λ_{D}	De Broglie wavelength
λ_{e}	elastic mean free path

$\lambda^\star$	ambipolar diffusion length
$\lambda_{\mathrm{s-f}}$	spin-flip length
λ_{T}	Thomas-Fermi screening length
η	electrochemical potential
μ	carrier mobility
μ_0	$\equiv 4\pi 10^{-7}$ H/m the permeability of vacuum
μ_{B}	Bohr magneton
$\mu^\star$	ambipolar or effective mobility
∇	the gradient operator
ν	frequency
$\eta^\star$	photon-electron conversion number
ω_{op}	optical phonon frequency
ϕ_{M}	magnetic flux
π	$\simeq 3.1415\ldots$
Ψ	electron wave function
ψ	digamma function
ϕ_{M}^0	flux quantum
θ	azimuthal angle
ρ	mass density
ϱ	Boltzmann distribution function
$\Sigma_{\mathrm{e-e}}$	self-energy due to e-e interaction
ς	slope of the dependence of the Φ_0 on Φ_{m}
$\bar{\sigma}_{\mathrm{b}}$	dispersion of the barrier height
σ_{j}	junction conductivity (measured in S/m^2)

σ_{t}	trap centre cross section
Θ	macroscopic deformation field
τ_{a}	athermal scattering time
τ_{b}	characteristic tunnelling time
τ_{d}	mean diffusion time
$\tau_{\mathrm{e-e}}$	mean electron-electron relaxation time
$\tau_{\mathrm{h-h}}$	mean hole-hole relaxation time
τ_{ph}	electron-phonon characteristic scattering time
τ_{r}	mean time before recombination
$\tau_{\mathrm{s-f}}$	spin-flip time
Υ	ideality factor
ϑ	power exponent
ω_{c}	cyclotron frequency
ω_{L}	Larmor precession frequency
ψ_{s}	surface potential
Ξ	deformation potential
Ψ	wave function
$\psi_{\mathbf{k}}$	Bloch state of momentum $\mathbf{k}$

Superscripts

$^{\mathrm{DD}}$	denotes Drift Diffusion
$^{\mathrm{TE}}$	denotes Thermionic Emission

Subscripts

$_{\uparrow}$	denotes spin up
$_{\downarrow}$	denotes spin down

c	denotes conduction band
DG	denotes direct gap
e	denotes electrons
el	denotes elastic
g	denotes gap states
h	denotes holes
i	denotes intrinsic
in	denotes inelastic
m	denotes metal
mag	denotes magnons
n	denotes electrons
OC	denotes open-circuit
orb	denotes orbital
ox	denotes oxide
p	denotes holes
s	denotes semiconductor
SC	denotes short-circuit
t	denotes traps
v	denotes valence band

Other Symbols

$\otimes$	convolution product
$\angle$	angle
$\mathcal{A}$	internal quantum yield
$\parallel$	parallel

$\perp$	perpendicular
$\mathcal{B}$	blocking factor
$\mathcal{C}$	scattering integral
$\mathcal{D}$	density of states (measured in $\mathrm{J}^{-1}\ \mathrm{m}^{-3}$)
$\mathcal{E}$	electric field
$\mathcal{F}_n$	Fermi integral of order n
$\mathcal{G}$	Greens function
$\mathcal{H}$	Hamiltonian
$\mathcal{I}$	light intensity
$\mathcal{M}$	diffuse matrix element
$\mathcal{P}$	tunnelling polarisation coefficient
$\Re$	real part
$\mathcal{S}$	spectral function
$\mathcal{T}$	matrix element of a transition
$\mathcal{V}$	scattering amplitude power

Chapter 1

Introduction

Spin electronics is, by idea, a borderline activity. It combines and concepts, methods, materials and devices between the fields of magnetism and electronics. This is, however, not a mechanical mixture of the two sciences. Even though it may appear as an attractive possibility to simply double the capacity of modern day conventional digital electronics, by somehow adding a spin degree of freedom, it is practically impossible, and also commercially unjustifiable. Because of the 'Moore's Law' - the exponential increase of the capacity of practical CMOS technology, with an average doubling time of about 18 months, by the time a simple spin-doubling of a conventional electronic technology has taken place, the conventional technology, itself, would have multiplied far more effectively.

Spin electronics, however, promises more than simple capacity doubling. It offers new magnetic functionality, namely devices ranging from magnetic field sensors to magnetic on-chip actuators. The 'icon' of magnetism - the hysteresis loop, offers alternatives to existing technologies for memory devices. The intrinsically weak interaction of the electron spin with its surroundings naturally leads to the concept of 'dissipationless' spin currents and therefore the possibility of realising computation, essentially limited in dissipation by thermodynamic entropy production (a particularly attractive idea, since even the best modern laptop computers can hardly survive a long-haul flight, without recharging).

Spin electronics is, also, not a new science. It's first 'child' - the Giant MagnetoResistance (GMR) stack has already proven to be a commercially-viable device, through its application in hard-drive read-heads. In recognition of the maturity of the field and the seminal character of the early work on giant magnetoresistance, this year's Nobel prize (2007) has been awarded to Prof. Albert Fert from Université Paris-Sud, France (an honorary Doctor of Sciences of the University of Dublin), and Prof. Peter Grünberg from Forschungszentrum Jülich, Germany, for "for the discovery of Giant Magnetoresistance".

The GMR stack, is however, a two-terminal device, passive from the electronic standpoint. Even its improved-performance successor, the Tunnel MagnetoResistance (TMR) stack is still nothing but a tunnelling resistor (for most practical applications). Spin triode devices (i.e. spin transistors), have long been touted for the next generation spin electronics, as they are the building blocks for the physical realisation of almost all logic elements, and thus would provide the key towards true digital spin circuitry.

In order to realise three (or more) terminal devices utilizing spin polarised electronic currents, materials and structures have to be found to act as effective spin-polarised current injectors, transmitters, manipulators and detectors. Potential high efficiency injection structures include tunnel, Schottky, hetero and p-n junctions, barriers employing ferromagnetic metals (ideally half-metals) and magnetic or semimagnetic semiconductors. As media with long carrier mean-free path and spin-coherence length - an eventual transmitter - a few possibilities are currently explored, including classical IV, III-V, II-VI semiconductors, and semimetals as bismuth and graphite. Various means are used to manipulate and detect spin-polarised currents - optical (optical pumping, magnetic circular dichroism and Kerr effect), electrostatic (FET with spin-orbit coupling) and galvanic (different types of Hall effect and magnetoresistive devices).

The dominant part of what follows is a description, albeit an incomplete and deformed one, of the experimental and analytical efforts of the author and his collaborators, on investigating different routes for improving the efficiencies of primarily the first two building blocks - spin injectors and spin-transmitting media.

As the coherent generation and control of spin populations in bulk non-magnetic materials (for example conventional semiconductors like Si and GaAs), is normally associated with external action, external magnetic fields and polarised photo-illumination among others, the source of which is in most cases difficult or impractical to integrate on a chip, the most promising approach spin manipulation is spin injection through various types of interfaces (junctions). Various possibilities are present.

One is to take a ferromagnetic metal and realise a Schottky junction via intimate contact with a semiconductor. There are several major disadvantages of such an approach, which are described later in the text. Probably the most pertinent is the impossibility to realise substantial current densities through structures which, by necessity, involve at least two rectifying diodes in opposition. The possibility still exists, of course, to realise structures where only one of the end elements (either the spin-injector or the spin-detector) is a Schottky barrier.

The above problem is slightly alleviated by the use of tunnel junctions, which have far more (anti)symmetric current-voltage characteristics, allowing for comparable magnitudes of

the injection and detection currents. Tunnel junctions though, have several other disadvantages: they are more difficult and expensive to produce, more difficult to control and generally permit relatively small current densities to flow safely.

Even ferromagnetic/paramagnetic metal junctions are not free from spin-injection problems, with the efficiency of the injection depending on the matching of the electronic structure of the two materials. And though relatively large current densities are permissible through such junctions, they impose an all metal construction, thus making it difficult to say control spins electrostatically (i.e. via gating the device).

A possibility still remains of injection (detection) of spin populations via hetero or p-n junctions between a ferromagnetic semiconductor and a non-magnetic one. The problem in this case lies in the difficulty of finding a suitable candidate for magnetic or semimagnetic semiconductor. Most well-established candidates like EuS and (Ga,Mn)As, have Curie points far below room temperature, thus being disqualified for widespread practical application. New potential candidates like, for example, Co and Fe doped ZnO and SnO_2, among many others, have not yet been proved, to be intrinsically magnetic, without being highly degenerate, of a single carrier type, exhibiting rather low mobilities and little useful magneto-transport properties at and above room temperature. Aspects of all four possibilities mentioned above are treated in chapters 2, 3, 4 and 5, of this thesis.

The other two remaining steps, the transmission and manipulation of spins, would in principle, pose very different requirements on the materials aspects of the problem. An efficient spin transmitting medium must obviously have a large, preferably macroscopic spin-diffusion length, and be spin-ballistic on the mesoscopic or microscopic scales. Therefore a light material (in terms of atomic number), with small effective mass, high mobility, and small carrier concentration is necessary, in order to minimise the spin-orbit scattering, the phonon scattering and make electrostatic control possible. Good potential candidates are graphite and other carbon polymorphs like carbon nanotubes and whiskers. While their basic material properties are well established, some details of their transport and magnetism reman a subject of open scientific debate and research. An account of these is given in chapter 5 of this thesis.

Chapter 2

Magnetic and Nonmagnetic Schottky Junctions

2.1 Main results of the theory of Schottky junctions

2.1.1 Introduction to spin injection in semiconductors

2.1.1.1 General points

Spin electronics is a quickly growing field at the border between magnetism and semi-conductor physics, which is trying to exploit the spin-degree of freedom of the electron (or any other quasi-particle in the solid) to realise new devices with fundamentally novel or enhanced properties. Ziese & Thornton (2001) While, spin-electronics is primarily focused on exploiting normal and magnetic semiconductors, the first and the most common two terminal spin electronic device, the spin valve, consists of at least two ferromagnetic layers (usually metals) the magnetisation of which can be switched independently, ideally changing the resistance of the device. The magnitude of the total current at a given bias is thus dependent on the mutual orientation of the magnetisations of the ferromagnetic layers, provided that the current flowing through the layers is at least partially spin-polarised. The actual static α^{s} or current α^{c} polarisation close to the Fermi level are given by:[1]

$$\begin{aligned} \alpha^{\mathrm{s}} &= \frac{n_{\uparrow} - n_{\downarrow}}{n_{\uparrow} + n_{\downarrow}} \\ \alpha^{\mathrm{c}} &= \frac{\langle n_{\uparrow} v_{\mathrm{F}\uparrow}^2 \rangle - \langle n_{\downarrow} v_{\mathrm{F}\downarrow}^2 \rangle}{\langle n_{\uparrow} v_{\mathrm{F}\uparrow}^2 \rangle + \langle n_{\downarrow} v_{\mathrm{F}\downarrow}^2 \rangle} \end{aligned} \tag{2.1.1}$$

where $n_{\updownarrow}$ are the concentrations up spin up/down electrons at the Fermi level and $v_{\mathrm{F}\updownarrow}$ are the spin up/down Fermi velocities. For an arbitrary number of electronic bands crossing the

[1] The notation is explained in the nomenclature section.

Fermi level, $n_{\updownarrow}$ are defined as:

$$n_{\updownarrow} = \frac{1}{(2\pi)^3} = \sum_a \int \delta(E_{a\updownarrow}(\mathbf{k}))\mathrm{d}^3k \tag{2.1.2}$$

where $E_{a\updownarrow}(\mathbf{k})$ is the band dispersion of the a-th subband of spin $\uparrow$ or $\downarrow$, $\delta(x)$ is the Dirac delta function and the integration is taken over the volume of one primitive cell in k-space. Both ratios are close to unity for the case of a half-metallic material (see for example Mazin (1999)). As both $n_{\updownarrow}$ and $v_{\updownarrow}$ are, in principle, energy dependent electronic structure parameters, it is important to note that it is possible to have a ferromagnetic (paramagnetic) material with total equilibrium polarisation in zero (or finite) magnetic field $P = \int_0^{E_\mathrm{F}} (n_\uparrow(\epsilon) - n_\downarrow(\epsilon))\mathrm{d}\epsilon \neq 0$, while $\alpha^\mathrm{s} = 0$. Conversely, it is, in principle, possible to have a case with $P = 0$ but $\alpha^\mathrm{s} \neq 0$.

The sense of the averaging of v:

$$\langle n_{\updownarrow} v_{\mathrm{F}\updownarrow}^2 \rangle = \frac{1}{(2\pi)^3} \sum_a \int v_{\mathrm{F}\updownarrow}(\mathbf{k})\delta(E_{a\updownarrow}(\mathbf{k}))\mathrm{d}^3k \tag{2.1.3}$$

follows from the classical spin-dependent Boltzmann transport theory where the spin up/down currents are taken to have the same relaxation times $\tau_\uparrow = \tau_\downarrow$, like:

$$J_{\updownarrow} = \frac{q^2 \tau_{\updownarrow} v_{\mathrm{F}\updownarrow}^2 n_{\updownarrow} \mathcal{E}}{kT} \tag{2.1.4}$$

where $\mathcal{E}$ is the applied electric field, q is the modulus of the electronic charge, and the polarisation is calculated as the ratio:

$$\alpha^\mathrm{c} = \frac{J_\uparrow - J_\downarrow}{J_\uparrow + J_\downarrow} \tag{2.1.5}$$

I should be also noted that, while in structures based on metals the conduction takes in most cases in an energy window of about $2kT$ around the Fermi level E_F, Kittel (1996) in structures featuring semi-conductors or insulators it is possible to have hot-electron transport at higher energies at separate quasi-fermi-levels for spin-up or spin-down electrons (holes), therefore α^s and α^c are not characteristics universally applicable to any material or transport problem. Moreover, there are experimental techniques for spin-polarisation evaluation, like for example the point-contact Andreev-reflection[1], where at least in the idealised situation, the transport is ballistic (i.e. without inelastic and elastic scattering) and the velocity averaging concerns only the component $v_{\updownarrow x}$:

$$J \updownarrow = \frac{q^2}{(2\pi)^3} \sum_a \int_{v_{\updownarrow x}>0} v_{\updownarrow x} \delta E_{a\updownarrow}(\mathbf{k})\mathrm{d}\mathbf{k} \tag{2.1.6}$$

and therefore the appropriate definition for the spin-polarisation is:

$$\alpha^\mathrm{b} = \frac{\langle n_\uparrow v_{\mathrm{F}\uparrow} \rangle - \langle n_\downarrow v_{\mathrm{F}\downarrow} \rangle}{\langle n_\uparrow v_{\mathrm{F}\uparrow} \rangle + \langle n_\downarrow v_{\mathrm{F}\downarrow} \rangle} \tag{2.1.7}$$

[1] often abbreviated as PCAR, consists of measurement of differential conductance spectra of a point contact between a superconducting tip and the ferromagnet of interest

Ferromagnetic metal/non-magnetic semiconductor contacts are of interest for two main reasons:

(a) they may provide ways of efficient spin-injection into semiconductors, and

(b) they may enable estimation of spin-polarisation at elevated temperatures.

Injection of spin-polarised currents into semi-conductors is problematic because of the conductivity mismatch or the vastly different Fermi surfaces as pointed-out by Schmidt *et al.* (2000). There are several ways to avoid this problem, some of which are the injection of hot electrons through a tunnel barrier Rashba (2000) or Schottky barrier Albrecht & Smith (2002, 2003) at appropriate combination of the respective work functions or at high-bias Yu & Flatté (2002a,b). Very limited success has been achieved, and only very small and ambiguous chirality-dependent photocurrents have been observed upon switching the magnetisation direction of the Ni or Fe electrode of a GaAs based Schottky junctions by Hirohata *et al.* (1999). Alternatively, reflection from a ferromagnet may be used to generate spin-polarisation in the semiconductor side of a Schottky junction Ciuti *et al.* (2002), or spin-filtering in ferromagnet/semiconductor hetero-structures Bland *et al.* (2003) or through a ferromagnetic insulator tunnel barrier Smith & Silver (2001). Nuclear polarisation via the hyperfine interaction has been demonstrated at Fe/AlGaAs and MnAs/AlGaAs interfaces by Epstein *et al.* (2003); Kawakami *et al.* (2001). Further, optically excited ferromagnetic resonance has been observed in FeCo/GaAs Schottky junctions (Buess *et al.* (2004)). Electron spin polarisation via proximity effect has been shown in Fe/GaAs Schottky junction (Epstein *et al.* (2002)). Room temperature spin injection from Fe into GaAs has been detected optically by Hanbicki *et al.* (2003); Isakovic *et al.* (2002); Zhu *et al.* (2001); and from MnAs into GaAs by Stephens *et al.* (2004). More recently, spin accumulation has been predicted theoretically (Bauer *et al.* (2005)) and demonstrated via the electrical Hanle effect at the Fe/n-type GaAs interface (Lou *et al.* (2006)).

For the remainder of this chapter, the main interest will be focused around the possibility of realisation of spin-polarisation measurement employing ferromagnet/semiconductor junctions, and the possibility of realisation of highly transparent ohmic spin-injectors onto standard semiconductor materials, like Si.

2.1.1.2 Types of metal-semiconductor contacts

Disregarding the detailed nature of the contact between a metal and a semiconductor, an insight into the formation of rectifying and ohmic contacts can be obtained by analysing the problem within the so called rigid bands model. The formation of the contact can be thought of as

virtual bringing of two semi-infinite material slabs together in vacuum. The initial stage of such a thought-process is visualised on 2.1, neglecting the band bending that naturally occurs immediately at the surface of the material slabs. The symbols have their usual meanings,

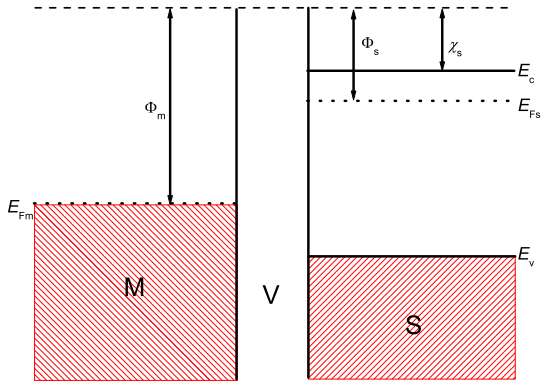

Figure 2.1: Simplified energy diagram for two semi-infinite slabs separated by vacuum.

namely: E_{Fm} and E_{Fs} are the Fermi level in the metal and the semiconductor, Φ_{m} and Φ_{s} are the two respective work functions, χ_{s} is the electron affinity in the semiconductor, E_{c} and E_{v} are the bottom of the conduction and top of the valence bands in the semiconductor.

Upon virtual contact the conduction and valence bands in the semiconductor will bend close to the interface in order to reach an identical equilibrium Fermi level on both sides of the junction $E_{\mathrm{Fm}} = E_{\mathrm{Fs}}$. A barrier will thus form for electrons trying to pass through the junction, provided $\Phi_{\mathrm{m}} \gg \Phi_{\mathrm{s}}$, as is often the case for common metals like Au, Cu, Ta, Fe, etc. on silicon. A build-in equilibrium potential (and corresponding electric field) will exist at the interface of magnitude:

$$qV_{\mathrm{bi}} = \Phi_{\mathrm{m}} - \Phi_{\mathrm{s}} \tag{2.1.8}$$

The barrier, as seen from the metal will thus be:

$$\Phi_0 = \Phi_{\mathrm{m}} - \chi_{\mathrm{s}} \tag{2.1.9}$$

This situation is visualised on figure 2.2

It should be noted, that the above approximation is often not valid for polar interfaces between metals and binary semiconductors (like GaAs, GaP and InSn, among others), as in those cases the Fermi-level at the interface is 'pinned' by the large densities of surface states and the Schottky barrier heights become practically insensitive to the work function of the metal used. Moreover, as discussed in detail by Tersoff (1984), the gap states have a continuum nature, and result in a locally metallic character of the semiconductor near the interface. In

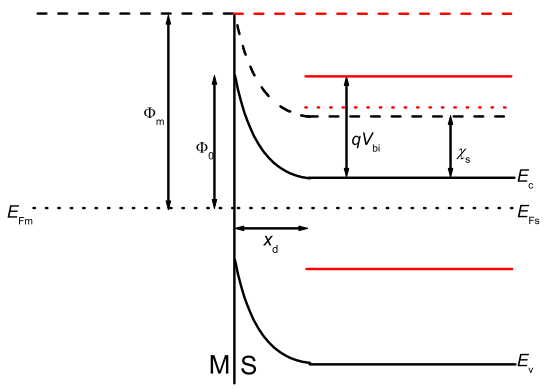

Figure 2.2: Simplified energy diagram for a Schottky junction at zero external bias for the case of $\Phi_m \gg \Phi_s$.

such cases, simple modelling is inapplicable and the barrier heights must be evaluated using first-principles calculations (Berhod *et al.* (2003)).

In the opposite situation, when $\Phi_m \ll \Phi_s$, there would be very small or no barrier formed as illustrated on figure 2.3. This case is quite uncommon in practise, and the work functions of few metals are low enough to form truly ohmic contact to silicon. Examples include U, Th and Gd. As ohmic contacts are important from practical standpoint, as for example as back

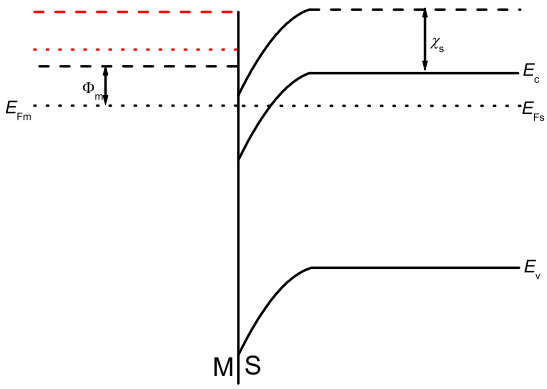

Figure 2.3: Simplified energy diagram for a Schottky junction at zero external bias for the case of $\Phi_m \ll \Phi_s$.

contacts to Schottky diodes, another way has been found to create them. Namely, high surface doping, to degenerate n^+ or even highly-degenerate n^{++} levels, leads (as will be explained later in paragraph 2.1.4.1) to the formation of only a very narrow depletion region that is tunnelling-transparent for the electrons incident at the interface from both sides of the junction. Thus the resulting contact can be highly ohmic and of fairly low resistance.

All of the above cases have been illustrated for an n-type semiconductor for simplicity. The variety of contacts of metal to p-type semiconductor is far more abundant and includes contacts with the formation of inversion layer in the semiconductor close to the interface, which in some cases can behave as a 2DEG [1].

In order to understand qualitatively the rectifying behaviour of a Schottky junction under externally applied bias V_a, one can analyse the situation as shown schematically on figure 2.4. It is clear that a positive shift of the chemical potential[2] at the semiconductor side will lead to a Schottky barrier lowering, and therefore to increased transmission probability and current flow. Conversely, a negative shift of the chemical potential[3] will lead to an increased barrier height, decreased transmission probability and smaller current. Accompanying the change of barrier height, there will be a small change in the width of the depletion region $x_d(V_a)$, which will be discussed in more detail later in paragraph 2.1.4.1.

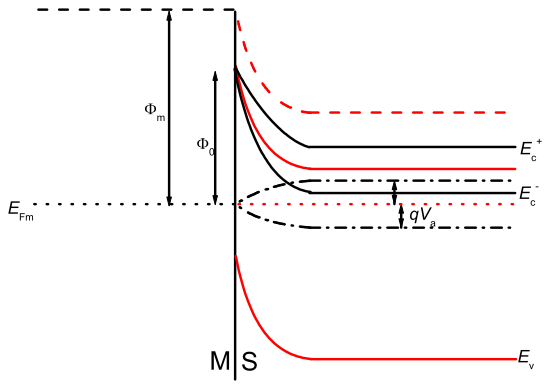

Figure 2.4: Simplified energy diagram for a Schottky junction under external bias V_a.

2.1.2 Models for Schottky barrier formation

The Schottky barrier height is, probably, the most important parameter associated with metal-semiconductor contacts. Nevertheless, for a lot of real physical situations, the exact mechanisms which determine the value of ϕ_b remain unclear. Therefore, it is useful to briefly summarise the main models for barrier formation and comment on the limits of their applicability.

[1] Two Dimensional Electron Gas
[2] The current is dominated by electron flow from the semiconductor to the metal.
[3] The current is dominated by electron flow from the metal to the semiconductor.

2.1.2.1 Semiempirical models

Mott-Schottky rule for noninteracting surfaces. As it was already mentioned, as a first approximation, the work done by an electron crossing the interface can be assumed equal to the work done when first extracting the electron to the vacuum state from the semiconductor and then and then placing the electron in the metal. Therefore, the barrier height is simply given by:

$$\Phi_0 = \Phi_\mathrm{m} - \chi_\mathrm{s} \tag{2.1.10}$$

which is known as the Schottky-Mott rule. In other words the slope

$$\varsigma = \frac{\mathrm{d}\Phi_0}{\mathrm{d}\Phi_\mathrm{m}} \tag{2.1.11}$$

often referred to as the *interface index*, is equal to 1, within this model. Even for elemental semiconductors, like Si and Ge, the slope ς is found to be closer to zero rather than unity (see Heine (1965)).

Bardeen model: the effect of surface states. In an effort to explain $\varsigma \approx 0$, it can be argued that the small density of surface states due to the presence of a surface and the truncation of the periodic atomic potential, that lyes in the gap of the semiconductor band structure, can actually pin the Fermi level. If these surface states are occupied up to an energy Φ_g, the barrier height can be approximated by requiring overall neutrality(see Berthod (1998)), like:

$$\Phi_0 \approx \varsigma\left(\Phi_\mathrm{m} - \chi_\mathrm{s}\right) + \left(1 - \varsigma\right)\Phi_\mathrm{g} \tag{2.1.12}$$

where ς becomes:

$$\varsigma = \frac{1}{1 + \frac{q^2 \mathcal{D}_\mathrm{g} x_\mathrm{g}}{\epsilon_\mathrm{g}}} \tag{2.1.13}$$

and $\mathcal{D}_\mathrm{g}$ is the surface density of gap states, and x_g is the distance on which the charge disturbance due to them is screened. For many semiconductors $\mathcal{D}_\mathrm{g}$ is in the range $10^{-3} \ldots 10^{-2}\mathrm{eV}^{-1}\mathrm{\AA}^{-2}$, and x_g is approximately 1 nm. Thus values of ς as low as 0.1 can be explained.

Heine model: the metal induced gap states. At any metal-semiconductor interface there are four kinds of electronic states:

1. states which are propagating on both sides of the junction;
2. states which propagate on the metal side and decay on the semiconductor side;
3. states which propagate on the semiconductor side and decay on the metal side;
4. states that decay on both sides.

The importance of the second kind of states was elaborated by Heine (1965). It is argued that these states, with energies within the semiconductor gap, decay exponentially in the semiconductor, over some characteristic length λ_g. Thus an alternative expression can be written for ς, which depends on the density of metal induced gap states $\mathcal{D}_g$ and the Thomas-Fermi screening length λ_T like:

$$\varsigma = \frac{1}{1 + q^2 \mathcal{D}_g(E_{Fm}) \left(\frac{x_g}{\epsilon_s} + \frac{\lambda_T}{\epsilon_0} \right)} \tag{2.1.14}$$

and is thus influenced by the charge screening properties of both the metal and the semiconductor.

2.1.2.2 Fermi-level pinning by interface states

It is important to note, that peculiar cases do exist, like for example clean GaAs surfaces, where there are no *intrinsic* surface-induced gap states present, though, the Fermi level can be shown to be pinned for junctions with most metals (see Gunea *et al.* (1983); Schlüter (1978)). Therefore it is suggested that *extrinsic* states exist generated by defects at the interface. In view of the above, it should be mentioned that some semiconductors tend to form binary and ternary compounds with metals at relatively low temperatures (typical examples are the silicides of Pt, Pd, Rh, Ni, Co, Ti, Cr, Mo, Zr etc. above about 400 °C), which further masks the nature of the states resulting from the interface (Andrews & Phillips (1975); Brillson (1978)). In cases when the detailed chemical character of the interface cannot be neglected, the simple, semiempirical models fail and *ab initio* methods become a necessity. There are also attempts at semi-analytical estimation of the barrier height dependence on applied voltage $\phi_b(V_a)$ in the case of near-interface states by Bozhkov & Zaitsev (2005a).

2.1.2.3 Generalized models

Of the more involved models, the ones taking into account the decoupling between the metal and the semiconductor side of the junctions due to a native oxide layer, are the most commonly used (see for example reference Sze & Cheng (1995)). In this case, the interface index ς can be approximated as:

$$\varsigma \approx \frac{1}{1 + q^2 \mathcal{D}_s \varpi} - (E_g + \chi_s - \Phi_b - \Phi_m) \frac{q^2 \mathcal{D}_s \lambda_s}{\epsilon_s (1 + q^2 \mathcal{D}_s \varpi)} \tag{2.1.15}$$

where λ_s is the penetration depth of the interface states in the semiconductor, and the inverse interface capacitance ϖ is defined as:

$$\varpi = \frac{\lambda_T}{\epsilon_m} + \frac{\delta}{\epsilon_{ox}} \tag{2.1.16}$$

where δ is the thickness of the native oxide layer, ϵ_{m} is the effective permittivity of the metal and ϵ_{ox} is the permittivity of the oxide layer. It is easily seen, that in the limit of strong decoupling $\frac{q^2\mathcal{D}_{\mathrm{s}}\delta}{\epsilon_{\mathrm{ox}}} \gg 1$, the interface index $\varsigma \to 0$, and in the limit of strong coupling, the expression reduces to the one for the Bardeen model.

2.1.3 Carrier distribution and screening in metals and semiconductors

2.1.3.1 The metal case

The theory of metal-semiconductor junctions can be developed similarly to the one of abrupt heterojunctions Chatterjee & Marshak (1981), with few specific details, mainly due to the fact the screening lengths L_{D}[1], for the non-degenerate case, defined as (Woan (2000)):

$$L_{\mathrm{D}} = \sqrt{\frac{\epsilon kT}{q^2 n}} \tag{2.1.17}$$

in metals are generally much shorter than in semiconductors, due to their higher carrier concentrations n and much smaller wave vector dependent effective Thomas-Fermi dielectric constant $\epsilon_{\mathrm{m}}(\mathbf{k}) = \epsilon_0\left(1 + \frac{q^2}{\epsilon_0\mathbf{k}^2}\frac{\partial n_0}{\partial \eta}\right)$ at the interface (q being the electron wave vector and η being the chemical potential) where $\frac{\partial n_0}{\partial \eta}$ may be negative[2]. In other words, their carrier concentration is, by far, harder to influence by external fields on scales longer than $1/k_0$ [3], where k_0 is the Thomas-Fermi wave vector defined as:

$$k_0 = \sqrt{\frac{q^2}{\epsilon_0}\frac{\partial n_0}{\partial \eta}} \tag{2.1.18}$$

For a bulk metal film $\frac{\partial n_0}{\partial \eta}$ is practically equal to the density of states at the Fermi level $\mathcal{D}(E_{\mathrm{F}})$ and is given by (Ashcroft & Mermin (1976)):

$$\mathcal{D}(E_{\mathrm{F}}) = \frac{m^\star k_{\mathrm{F}}}{\hbar^2\pi^2} \tag{2.1.19}$$

where k_{F} is the Fermi wave vector and parabolic dispersion is implied. Therefore the ratio

$$\frac{k_0^2}{k_{\mathrm{F}}^2} = \frac{16}{3\pi^2}^{2/3}\frac{r_{\mathrm{s}}}{a_0} \tag{2.1.20}$$

where $r_{\mathrm{s}} = \left(\frac{3}{4\pi n}\right)^{1/3}$ and $a_0 = \frac{\epsilon_0 h^2}{\pi m_{\mathrm{e}} q^2}$ is the Bohr radius[4]; is normally about 2 to 6 for metals. Thus the charge disturbance, at the metal side of a heterojunction, is only felt a few monolayers away from the interface.

[1] Also known as Debye length.
[2] n_0 is the electronic number density (Ashcroft & Mermin (1976))
[3] $1/k_0 \approx 46.87$ pm for a generic metal with free electron mass ($m^\star = m_{\mathrm{e}}$).
[4] $a_0 \approx 52.981$ pm

2.1.3.2 The semiconductor case

Due to their substantially lower carrier concentrations, charge disturbances of the plasma in semiconductors have much longer characteristic lengths L_D that may reach tens of microns in intrinsic materials. The exact electric field profiles depend on details like doping level and applied field. Fully self-consistent quantum-mechanical solution for the field and charge distribution is quite difficult and often unnecessary. As the characteristic length-scale is much longer than the atomic scale $L_\mathrm{D} \gg a_0$, it is acceptable in most cases to apply macroscopic thermodynamics and electrodynamics.

A specific complication, for the semiconductor case, comes from the fact that under external bias, the electrons and the holes are not in thermodynamic equilibrium with each other, that is to say that the characteristic electron-electron and hole-hole scattering times are much shorter than the mean time before recombination or $\tau_{\mathrm{e-e}} \ll \tau_\mathrm{r}$ and $\tau_{\mathrm{h-h}} \ll \tau_\mathrm{r}$. Therefore it is generally impossible to introduce a common Fermi level and solve in a simple fashion the electrostatic problem (say, for the charge distribution away from the metal-semiconductor interface, under applied bias V_a). Nevertheless, it is still acceptable to introduce quasi-Fermi levels E_Fn and E_Fp, separate for electrons and holes, as they are very close to thermodynamic equilibrium within themselves. For the most common cases of non-degenerate electron and hole gas (the limiting case of Boltzmann statistics) the carrier concentrations are thus given by:

$$\begin{aligned} n &= n_\mathrm{i} \exp \frac{E_\mathrm{F} - E_\mathrm{i} + qV_\mathrm{a}}{kT} = N_\mathrm{c} \exp \frac{E_\mathrm{F} - E_\mathrm{c} + qV_\mathrm{a}}{kT} \\ p &= n_\mathrm{i} \exp \frac{E_\mathrm{i} - E_\mathrm{p} - qV\mathrm{a}}{kT} = N_\mathrm{v} \exp \frac{E_\mathrm{v} - E_\mathrm{F} - qV\mathrm{a}}{kT} \end{aligned} \tag{2.1.21}$$

where n_i is the intrinsic carrier concentration, E_c and E_v are the band edges of the conduction and valence bands, and N_c and N_v are the equilibrium concentrations (density of states) of electrons and holes. Similar expressions may be written for quantum-mechanically degenerate electron gas:

$$\begin{aligned} n(x) &= N_\mathrm{c}(x) \mathcal{F}_{1/2} \left(\frac{E_\mathrm{F}(x) - E_\mathrm{c}(x) + qV_\mathrm{a}(x)}{kT} \right) \\ p(x) &= N_\mathrm{v}(x) \mathcal{F}_{1/2} \left(\frac{E_\mathrm{v}(x) - E_\mathrm{F}(x) - qV\mathrm{a}(x)}{kT} \right) \end{aligned} \tag{2.1.22}$$

where $\mathcal{F}_{1/2}$ is the Fermi-Dirac integral of order $\frac{1}{2}$ [1] and this time the spatial dependencies are explicit. Here it is not useful to introduce n_i as it is not constant across the depleted layer [2].

[1] Fermi-Dirac integral of order $\frac{1}{2}$ is defined as: $\mathcal{F}_{1/2}(\eta) = \frac{2}{\sqrt{\pi}} \int_0^\infty \frac{\sqrt{\xi}}{1+\mathrm{e}^{\xi-\eta}} \mathrm{d}\xi$.

[2] The usefulness of n_i for the standard theory follows primarily from the so-called mass-action law $pn = n_\mathrm{i}^2$, which is not valid for the case of a degenerate semiconductor.

The effective density of states for electron and holes can be written as:

$$\begin{aligned} N_{\mathrm{c}}(E) &= \gamma_{\mathrm{c}} \frac{1}{2\pi^2} \left(\frac{2m_{\mathrm{c}}^{\star}}{\hbar^2} \right)^{3/2} \sqrt{E - E_{\mathrm{c}}} \\ N_{\mathrm{v}}(E) &= \gamma_{\mathrm{v}} \frac{1}{2\pi^2} \left(\frac{2m_{\mathrm{v}}^{\star}}{\hbar^2} \right)^{3/2} \sqrt{E_{\mathrm{v}} - E} \end{aligned} \tag{2.1.23}$$

for the nondegenerate case (see Woan (2000)), and as

$$\begin{aligned} N_{\mathrm{c}} &= \gamma_{\mathrm{c}} \left(\frac{2\pi m_c^{\star} kT}{h^2} \right)^{3/2} \\ N_{\mathrm{v}} &= \gamma_{\mathrm{v}} \left(\frac{2\pi m_v^{\star} kT}{h^2} \right)^{3/2} \end{aligned} \tag{2.1.24}$$

for the degenerate case, where $m_c^{\star}$ and $m_v^{\star}$ are their respective effective masses, and γ_{c} and γ_{v} are their respective degeneracies[1], both normally close to 2.

Apart from the charge density due to mobile carriers $n(x)$ and $p(x)$, correct evaluation of the electric potential should include the contributions from ionised impurities N_{d}^{+} and N_{a}^{-}. Their explicit statistics is:

$$\begin{aligned} N_{\mathrm{d}}^{+}(x) &= \frac{N_{\mathrm{d}}}{1 + \gamma_{\mathrm{d}} \exp\{\left[E_{\mathrm{F}}(x) - E_{\mathrm{d}}(x) + qV_{\mathrm{a}}(x)\right]/kT\}} \\ N_{\mathrm{a}}^{-}(x) &= \frac{N_{\mathrm{a}}}{1 + \gamma_{\mathrm{a}} \exp\{\left[E_{\mathrm{a}}(x) - E_{\mathrm{F}}(x) - qV_{\mathrm{a}}(x)\right]/kT\}} \end{aligned} \tag{2.1.25}$$

where γ_{d} and γ_{a} are the degeneracy factors of donors and acceptors[2], respectively, and the positions of the impurity levels E_{d} and E_{a} are defined on the same energy scale as E_{v} and E_{c}.

Within the above approximations, it is now possible to solve self-consistently the problem for the charge/field distribution[3] under applied bias(Domaingo & Schürrer (2004); Lake (1997); Yung-Song Lou (1994)). Examples are to follow in section 2.1.4.

2.1.4 Main current components in a Schottky barrier

In order to understand the potential of the Schottky junction as a spin-polarised current injector or a spin-filter one should analyse the main transport mechanisms visualised on figure (2.5) borrowed from Rhoderick & Williams (1988). Where the different contributions are as follows:

(a) Thermionic emission of electrons from the semiconductor over the top of the barrier into the semiconductor;

(b) Quantum-mechanical tunnelling through the barrier;

[1] γ_{c} and γ_{v} are close to 2 if the conduction and valence bands are not spin-split, and close to 1 otherwise.
[2] γ_{d} and γ_{a} are close to 2 if the impurities are not spin-split, and close to 1 otherwise.
[3] Sometimes referred to as the Boltzmann-Poisson System.

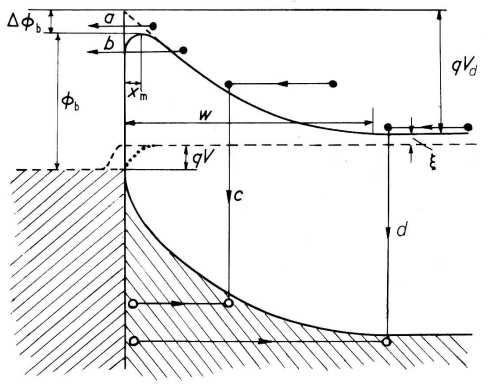

Figure 2.5: Various current contributions in a Schottky barrier.

(c) Recombination in the space-charge region;

(d) Recombination in the neutral region.

There are two classical models describing the current flowing through such a barrier - the Schottky theory, which assumes large depletion region with respect to the mean free path and assumes the drift diffusion limitations as the bottleneck of the process. The Bethe theory, just the contrary, assumes that all the electrons moving towards the metal with high enough energy, cross the barrier, thus the transport process is emission limited. Before continuing further the schematic and the standard sign notation in the theory of Schottky junctions should be examined as given on figure A.4.

2.1.4.1 The Schottky model

For the first case the macroscopic one-dimensional continuity equation can be expressed in the form:

$$J_n = q(\mu_n n\mathcal{E} + D_n \frac{\mathrm{d}n}{\mathrm{d}x}) \tag{2.1.26}$$

where J_n is the current density, n is the carrier concentration, $\mathcal{E}$ is the electric field strength, μ_n is the carrier mobility and $D_n = \frac{kT\mu_n}{q}$ is the diffusion coefficient. The equation can be used to express the current if the electrostatic potential and the carrier concentration are given as a function of the applied voltage, which is achieved by solving the Poisson equation:

$$\frac{\mathrm{d}^2\phi}{\mathrm{d}x^2} = -\frac{\rho}{\epsilon_\mathrm{s}} = -\frac{q}{\epsilon_\mathrm{s}}(p - n + N_\mathrm{d}^+ N_\mathrm{a}^-) \tag{2.1.27}$$

where ϕ is the electric field potential, p is the hole concentration, N_d^+ and N_a^- are the concentrations of the ionised donors and acceptors, respectively. This differential equation cannot be

solved analytically, without certain assumptions, the simplest one of which is the full depletion approximation - the donors are considered fully ionised in the region close to the interface (the depletion layer) with the metal of width:

$$x_{\mathrm{d}} = \sqrt{\frac{2\epsilon_{\mathrm{s}}(\phi_{\mathrm{i}} - V_{\mathrm{a}})}{qN_{\mathrm{d}}}} \tag{2.1.28}$$

for an applied voltage V_{a}. In most interesting cases the full depletion approximation is well justified (see appendix A.2). It should be noted, however, that numerical solutions of the nonlinear Poisson equation are achievable for all interesting cases. A computationally effective and robust algorithm has been described by Mayergoyz (1986). The barrier height and the build-in potential given for a n-type semiconductor, respectively, by $\phi_{\mathrm{b}} = \frac{\Phi_{\mathrm{m}} - \chi_{\mathrm{s}}}{q}$ and $\phi_{\mathrm{i}} = \phi_{\mathrm{b}} - \frac{kT}{q} \ln \frac{N_{\mathrm{c}}}{N_{\mathrm{d}}}$, where N_{c} is the effective density of states in the conduction band in the semiconductor, N_{d} is the density of donor states. Φ_{m} and χ_{s} are, as customary, the work function of the metal and the electron affinity of the semiconductor. More generally, the limiting value for the barrier height for n/p type substrate is given by:

$$q\phi_{\mathrm{b_n}} = (\Phi_{\mathrm{M}} - \chi_{\mathrm{c}}) \tag{2.1.29}$$

$$q\phi_{\mathrm{b_p}} = E_{\mathrm{g}} - (\Phi_{\mathrm{M}} - \chi_{\mathrm{s}}) \tag{2.1.30}$$

The space charge per unit area, associated with the depletion layer $Q_{\mathrm{s}} = qN_{\mathrm{d}}x_{\mathrm{d}}$ is equal to the charge deposited in the metal Q_{m} and given by:

$$Q_{\mathrm{s}} = \sqrt{2q\epsilon_{\mathrm{s}}N_{\mathrm{d}}\left(\phi_{\mathrm{i}} - V_{\mathrm{a}}\right)} \tag{2.1.31}$$

And the associated capacitance per unit area $C_{\mathrm{j}} \equiv \frac{|\partial Q_{\mathrm{s}}|}{\partial V_{\mathrm{a}}}$ can be expressed as:

$$C_{\mathrm{j}} = \frac{\epsilon_{\mathrm{s}}}{x_{\mathrm{d}}} = \sqrt{\frac{q\epsilon_{\mathrm{s}}N_{\mathrm{d}}}{2(\phi_{\mathrm{i}} - V_{\mathrm{a}})}} \tag{2.1.32}$$

Accordingly, one of the popular methods for the determination of the barrier height ϕ_{b}, consists of extrapolating the dependence $C_{\mathrm{j}}(V_{\mathrm{a}})$ towards zero capacitance $C_{\mathrm{j}}(\phi_{\mathrm{b}}) \to 0$ (see for example Garbarczyk *et al.* (1978); Zhu *et al.* (2006)). The analysis can be generalized to include, apart from charge exchange between the donor centres and the conduction band of the semiconductor, also exchange with the valence band of the semiconductor and the conduction band of the metal; and forms the basis of the Schottky capacitance spectroscopy (see for example Barret *et al.* (1983)). The relationships between charge density ρ, electric field $\mathcal{E}$, electric potential ϕ, chemical potential η and carrier energy E are visualised on figure 2.6.

Using the full depletion approximation, the current density can thus be expressed like:

$$J_{\mathrm{n}} = \frac{q^2 D_{\mathrm{n}} N_{\mathrm{c}}}{kT} \sqrt{\frac{2q(\phi_{\mathrm{b}} - V_{\mathrm{a}})N_{\mathrm{d}}}{\epsilon_{\mathrm{s}}}} \exp\left(-\frac{q\phi_{\mathrm{b}}}{kT}\right) \left[\exp\left(\frac{qV_{\mathrm{a}}}{kT}\right) - 1\right] \tag{2.1.33}$$

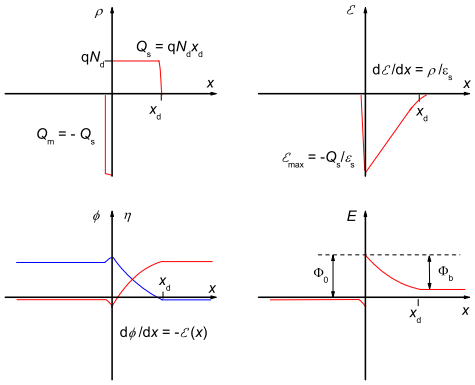

Figure 2.6: Relationships between charge density, electric field, electric potential, chemical potential and carrier energy for an arbitrary Schottky contact. Not to scale.

Schematic derivation of this expression is given in section A.3.1.

2.1.4.2 The Bethe Model

Alternatively, as required in the second model, the current density may be calculated estimating the number of electrons with high enough energies to go over the barrier like:

$$J_{\mathrm{n}} = \int_{E_{\mathrm{c}}(x=+\infty)}^{q\phi_{\mathrm{n}}} qv_x \frac{\mathrm{d}n}{\mathrm{d}E}\mathrm{d}E \tag{2.1.34}$$

A simple, yet, unnecessarily detailed calculation, the schematics of which are given in appendix A.3.2, leads to the result:

$$J_{\mathrm{n}} = \frac{4\pi q m_{\mathrm{c}}^{\star} k^2}{h^3} T^2 \exp\left(-\frac{q\phi_{\mathrm{b}}}{kT}\right)\left[\exp\left(\frac{qV_{\mathrm{a}}}{kT}\right) - 1\right] \tag{2.1.35}$$

where the constant pre-factor $A^{\star} = \frac{qN_{\mathrm{c}}\overline{v}}{4} = \frac{4\pi m^{\star} q k^2}{h^3}$ is the Richardson constant, and $m_{\mathrm{c}}^{\star}$ is the electron effective mass in the semiconductor Sze (1981). For semiconductors, for which the effective mass approximation is valid, $m_{\mathrm{c}}^{\star} = \sqrt{l^2 m_y m_z + m^2 m_z m_x + n^2 m_x m_y}$, where $[l, m, n]$ is the normal vector to the interface in the own coordinate system of the effective mass ellipsoid, and m_x, m_y and m_z are the eigenvalues of the effective mass tensor Rhoderick & Williams (1988). For silicon, with the junction parallel to a {111} plane $m_{\mathrm{c}}^{\star} = 6\sqrt{(m_{\mathrm{t}}^2 + 2m_{\mathrm{t}}m_{\mathrm{l}})/3}$, which evaluates for $m_{\mathrm{l}} = 0.92m_e$ and $m_{\mathrm{t}} = 0.19m_{\mathrm{e}}$ Kittel (1996) at $m_{\mathrm{Si\{111\}}}^{\star} = 2.15$. The respective value of the Richardson constant is $A_{\mathrm{Si\{111\}}}^{\star} = 258\ \mathrm{Acm^{-2}K^{-2}}$.

2.1.4.3 The Sze model

Apart from the above two models further refinement was made by Crowell & Sze (1966a) which consists of effectively putting the two mechanisms (diffusion and thermionic emission) in series.

This modifies 2.1.35 into the form:

$$J_{\mathrm{n}} = \frac{qN_{\mathrm{c}}v_{\mathrm{r}}}{1+v_{\mathrm{r}}/v_{\mathrm{d}}} \exp\left(-\frac{q\phi_{\mathrm{b}}}{kT}\right)\left[\exp\left(\frac{qV_{\mathrm{a}}}{kT}\right)-1\right] \tag{2.1.36}$$

where v_{r} is the so-called 'recombination velocity', which in the simplest case when no backscattering of electrons in the semiconductor is assumed[1], equals $v_{\mathrm{r}} = \overline{v}/4$, as in this case (simple Maxwellian velocity distribution):

$$v_{\mathrm{r}} = \frac{\int_0^\infty v_{\mathrm{x}} \exp\left(-\frac{m^\star v_{\mathrm{x}}^2}{2kT}\right) \mathrm{d}v_{\mathrm{x}}}{\int_{-\infty}^\infty \exp\left(-\frac{m^\star v_{\mathrm{x}}^2}{2kT}\right) \mathrm{d}v_{\mathrm{x}}} = \sqrt{\frac{kT}{2\pi m^\star}} \approx v_{\mathrm{R}} \tag{2.1.37}$$

where v_{R} is the Richardson velocity. More precisely, the actual velocity distribution close to the interface is drifted Maxwellian (see Shibkov *et al.* (1992); Tang & Adams (1989))

$$v_{\mathrm{r}} = \frac{\int_0^\infty v_{\mathrm{x}} \exp\left(-\frac{m^\star (v_{\mathrm{x}}-v_{\mathrm{d}})^2}{2kT}\right) \mathrm{d}v_{\mathrm{x}}}{\int_{-\infty}^\infty \exp\left(-\frac{m^\star (v_{\mathrm{x}}-v_{\mathrm{d}})^2}{2kT}\right) \mathrm{d}v_{\mathrm{x}}} \tag{2.1.38}$$

therefore the recombination velocity is no longer independent of the drift-diffusion velocity v_{d}.

The 'effective diffusion velocity' v_{d} is associated with the drift-diffusion of electrons from the edge of the depletion region to the top of the barrier, and is defined like:

$$\begin{aligned} v_{\mathrm{d}}^{-1} &= \int_{x_{\mathrm{m}}}^{x_{\mathrm{d}}} \frac{q}{\mu_{\mathrm{n}} kT} \exp\left(-\frac{q\phi_{\mathrm{b}} - E_{\mathrm{c}}(x)}{kT}\right) \mathrm{d}x \\ &\approx \frac{L_{\mathrm{D}}^2}{D_{\mathrm{n}} x_{\mathrm{d}}} \left(1 - \mathrm{e}^{-\frac{x_{\mathrm{d}}^2}{L_{\mathrm{D}}^2}}\right) \end{aligned} \tag{2.1.39}$$

where E_{c} is the energy of the bottom of the conduction band and x_{m} is the position of the maximum of the potential barrier with respect to the interface so that $\phi(x_{\mathrm{m}}) = \max(\phi(x))$, and is equal to essentially zero if the image forces are neglected.

It is easy to verify that in the limit of $v_{\mathrm{d}} \gg v_{\mathrm{r}}$, equation 2.1.36 reduces to essentially 2.1.35 and the thermionic emission model applies, for example, when either the mobility μ_{n} is large, there is no efficient recombination at the interface (the interface is close to ideal) or the barrier height ϕ_{B} is large. Alternatively, in the limit of $v_{\mathrm{d}} \ll v_{\mathrm{r}}$, equation 2.1.36 is roughly equivalent to 2.1.33 and the diffusion limitation is dominant. This is a situation often met when either the mobility μ_{n} is small, there are a lot of recombination centres close to the interface or the barrier

[1] Which is equivalent to assuming, that the interface is highly transparent for the electrons, which is often not the case for a disordered surface region of the semiconductor, or in the presence of thin insulating layer. Therefore the effective recombination velocity v_{r} may be quite different from the ideal $\overline{v}/4$.

height ϕ_B is small. More precisely the condition for the validity of the thermionic emission theory ($v_d \gg v_r$) can be expressed as $\mu_n \mathcal{E}_{max} \gg \overline{v}/4$ or in either if these equivalent forms:

$$q\mathcal{E}_{max} \gg \frac{m_c^\star \overline{v}}{4\tau_n} \tag{2.1.40}$$

$$\lambda_n q\mathcal{E}_{max} \gg \frac{2kT}{\pi} \tag{2.1.41}$$

where $\mathcal{E}_{max}$ is the maximal electric field in the barrier, τ_n and λ_n are the mean free time and the mean free path of the electrons in the semiconductor defined via the usual relations $\mu_n = q\tau_n/m_c^\star$ and $\overline{v} = \sqrt{8kT/\pi m_c^\star}$. The conditions 2.1.40 and 2.1.41 are equivalent to the criterion that the mean free path must exceed the distance over which the barrier drops by an amount of kT, originally stated by Bethe.

Minor corrections to the above model have been done by Darling (1996); Lou & Wu (1994); Wu (1982), in the form of transmission coefficient for the electrons passing through a thin interfacial oxide layer (or general layer rich in gap states) f_{ox} (which is discussed in section 2.1.4.4) by means of tunnelling and an additional voltage drop across the interface V_{ox}. The majority current becomes:

$$J_n = \frac{f_{ox} q N_c v_r}{1 + f_{ox} v_r / v_d} \exp\left(-\frac{q\phi_b}{kT}\right) \exp\left(-\frac{qV_{ox}}{kT}\right) \left[\exp\left(\frac{qV_a}{kT}\right) - 1\right] \tag{2.1.42}$$

and the voltage drop V_{ox} can be estimated as:

$$V_{ox} = \frac{Q_{ox}(V_a)}{C_{ox}} \tag{2.1.43}$$

with C_{ox} given by:

$$C_{ox} = \frac{\epsilon_{ox}}{\delta} \tag{2.1.44}$$

where δ is the width of the oxide layer and ϵ_{ox} is permittivity. The charge density $Q_{ox}(V_a)$ can be estimated as an integral over the gap energies, like:

$$Q_{ox} = -q \int_{E_v}^{E_c} \mathcal{D}_{ox}(E) \mathcal{F}_t(E) \mathrm{d}E + q\iota \int_{E_v}^{E_c} \mathcal{D}_{ox}(E) E \tag{2.1.45}$$

where $\mathcal{D}_{ox}$ is the density of oxide-induced interfacial states, ι is the ratio of the donor-like interface states to their total density and $\mathcal{F}_t$ is the Hall-Schottky/Read factor, which for a trap of energy E_t, interacting with one conduction and one valence band, is given by:

$$\mathcal{F}_t = \frac{\overline{v}_n \sigma_n \gamma_1 n + \overline{v}_p \sigma_p \gamma_1 p_1}{\overline{v}_n \sigma_n (\gamma_1 n + \gamma_0 n_1) + \overline{v}_p \sigma_p (\gamma_0 p + \gamma_1 p_1)} \tag{2.1.46}$$

where σ_n and σ_p are the electron and hole capture cross sections, γ_0 is the trap centre degeneracy factor when empty of electrons, γ_1 is the trap centre degeneracy when occupied with one

electron, and n_1 and p_1 are defined as:

$$n_1 = n_\mathrm{i} \exp\left(\frac{E_\mathrm{t} - E}{kT}\right) \tag{2.1.47}$$

$$p_1 = n_\mathrm{i} \exp\left(\frac{E - E_\mathrm{t}}{kT}\right) \tag{2.1.48}$$

The density of states in the semiconductor gap $\mathcal{D}_\mathrm{ox}$ is often approximated by a set of few (often one to three) Gaussian-convoluted levels:

$$\mathcal{D}_\mathrm{ox}(E) = \sum_{i=1}^{3} \mathcal{D}_i^0 \exp\left(-\frac{E - E_i}{\sqrt{2}\Delta E_i}\right)^2 \tag{2.1.49}$$

where $\overline{v}_\mathrm{n}$ and $\overline{v}_\mathrm{p}$ are the thermal velocities of electrons and holes; E_i are the energies, ΔE_i are the broadening factors and $\mathcal{D}_i^0$ are the partial densities of the respectful levels. This parametric representation can be, in principle, used to calculate the dependence of $V_\mathrm{ox}(V_\mathrm{a})$ and parametrically fit experimental data. Because of the large number of free parameters, the practical application of the Wu model is limited and all cases requires the external knowledge of some of the parameters of the junction, in order to reach convergence.

2.1.4.4 Tunnelling current

For thin enough barriers, at low temperature, and in reversed bias, another contribution may become important - the tunnelling current. Given the barrier shape the current can be estimated by solving the Schrödinger equation:

$$-\frac{\hbar^2}{2m^\star}\frac{\mathrm{d}^2\Psi}{\mathrm{d}^2 x} + q\phi(x)\Psi = E\Psi \tag{2.1.50}$$

with mixed boundary conditions at infinity, yielding:

$$J_\mathrm{n} \approx q v_\mathrm{R} n \exp\left(-\frac{4}{3}\frac{\sqrt{2m_\mathrm{c}^\star}}{\hbar}\sqrt{q\phi_\mathrm{b}}x_\mathrm{d}\right)\exp\left[\left(\frac{qV_\mathrm{a}}{kT}\right) - 1\right] \tag{2.1.51}$$

where $v_\mathrm{R} = \sqrt{\frac{kT}{2\pi m_\mathrm{c}^\star}}$ is the Richardson velocity (Yu *et al.* (1998)). A schematic derivation of the tunnelling current density is given in appendix A.3.3

2.1.4.5 Minority current components

From the minor current components, one important contribution is created by the recombination in the depleted region. This process can be considered as a direct transition through the band-gap. After Grove (1967); Wittmer (1990, 1991), the current density can be estimated as:

$$J_\mathrm{n} = \frac{q n_\mathrm{i} x_\mathrm{d}}{2\tau_\mathrm{r}} \exp\left(-\frac{E_\mathrm{g}}{2kT}\right)\exp\left[\left(\frac{qV_\mathrm{a}}{2kT}\right) - 1\right] \tag{2.1.52}$$

where τ_r is the mean free time before recombination and n_i is the intrinsic carrier concentration; and is likely to be relatively more important in high barriers, in materials of low carrier lifetime, at low temperature and at low bias voltage. This is equivalent to assuming that the product of the hole concentration p and the electron concentration n can be described like $pn = n_i^2 \exp(qV_a/kT)$ throughout the depletion region width x_d. It is a common cause of error as it changes the effective activation energy, measured in the temperature dependencies.

The minority carrier currents are inversely proportional to the appropriate barrier heights:

$$\begin{aligned} J_p &\propto \exp\left(-\frac{\Phi_p}{kT}\right) \\ J_n &\propto \exp\left(-\frac{\Phi_b}{kT}\right) \end{aligned} \tag{2.1.53}$$

where $\Phi_p = E_g - \zeta$ and $\zeta = E_c - E_d$ is the energy of the donors with respect of the bottom of the conductance band in the semiconductor. Along with the dominant current due to the electrons, there is a small flux of injected holes; the injection ratio ξ defined as:

$$\frac{J_p}{J_n} = \xi \propto \exp\left(-\frac{\Phi_p - \Phi_b}{kT}\right) \tag{2.1.54}$$

is normally much less than unity within the thermionic emission model.

In the drift-diffusion model the injection ratio depends on the mobilities of both electrons and holes and can be approximated like:

$$\xi = \frac{\mu_p}{\mu_n}\left(\frac{n_i}{N_D}\right)^2 \frac{J}{J_S} \tag{2.1.55}$$

The associated additional surface charge accumulation density can be expressed as (see Scharfetter (1965)):

$$Qa = q\frac{n_i^2}{N_d}\frac{D_p}{v_r}\frac{J}{J_S} \tag{2.1.56}$$

and may result in additional contribution to the junction capacitance $C_j\left(\frac{J}{J_S}\right)$.

For an example of current transient and quasi-static measurements of injection ratio in metal-semiconductor contacts see Alavi *et al.* (1987); Low (1955); Many (1954) and Wagner & Chuang (1985).

The injection ratio in not a constant and above certain current density grows linearly with the current. The injection ratio is further increased in the presence of a thin insulating layer at the metal-semiconductor interface. It has therefore profound implications on the high bias transport characteristics of Schottky junctions. Detailed analysis of both low and high-level injection has been performed by Hassan (2000); Ng *et al.* (1990), and confirmed later by numerical simulations (see Prokopyev & Mesheryakov (1999)) or semi-analytical calculations (see Prokopyev & Mesheryakov (2005)), in the spirit of the Sze model.

For low-level injection the minority carrier $J-V$ characteristic can be expressed as:

$$J_{\mathrm{low}} = J_{\mathrm{Sp}}\left[\exp\left(\frac{V_{\mathrm{a}} - J_{\mathrm{low}} r_{\mathrm{d}}}{V_{\mathrm{t}}}\right) - 1\right] \tag{2.1.57}$$

where r_{d} is the drift-diffusion region resistance area product, approximated like:

$$r_{\mathrm{d}} = \frac{x_{\mathrm{d}}}{q\mu_{\mathrm{p}} N_{\mathrm{a}}} \tag{2.1.58}$$

and J_{Sp} is the saturation current for holes, given approximately by:

$$J_{\mathrm{Sp}} = \frac{4\pi q m_{\mathrm{v}}^{\star} k^2}{h^3} T^2 \exp\left(-\frac{\Phi_{\mathrm{p}}}{kT}\right) \tag{2.1.59}$$

For high-level injection, there is a correction on the voltage drop on the depleted region V_{d} that depends on the carrier concentration close to the interface $n(0)$ like:

$$V_{\mathrm{d}} = \frac{D_{\mathrm{n}} - D_{\mathrm{p}}}{\mu_{\mathrm{n}} + \mu_{\mathrm{p}}} \ln\left[\frac{n(x_{\mathrm{d}})}{n(0)}\right] \tag{2.1.60}$$

and the carrier concentration close to the interface is determined by the solution of the modified continuity equation like:

$$n(0) = \frac{-C_1 + \sqrt{C_1^2 - 4J_{\mathrm{Sp}} C_2}}{2J_{\mathrm{Sp}}} \tag{2.1.61}$$

where the coefficients C_1 and C_2 are given by:

$$C_1 = J_{\mathrm{Sp}} N_{\mathrm{a}} + \frac{qD^{\star} n_{\mathrm{i}}^2}{\lambda^{\star}} \frac{\sinh\left(\frac{x_{\mathrm{d}}}{\lambda^{\star}}\right) + \frac{v_{\mathrm{r}}\lambda^{\star}}{D^{\star}} \cosh\left(\frac{x_{\mathrm{d}}}{\lambda^{\star}}\right)}{\cosh\left(\frac{x_{\mathrm{d}}}{\lambda^{\star}}\right) + \frac{v_{\mathrm{r}}\lambda^{\star}}{D^{\star}} \sinh\left(\frac{x_{\mathrm{d}}}{\lambda^{\star}}\right)} \tag{2.1.62}$$

$$C_2 = \frac{n_{\mathrm{i}}^2 J_{\mathrm{high}}}{\mu_{\mathrm{n}} + \mu_{\mathrm{p}}}\left[\mu_{\mathrm{p}} + \frac{\mu_{\mathrm{n}}}{\cosh\left(\frac{x_{\mathrm{d}}}{\lambda^{\star}}\right) + \frac{v_{\mathrm{r}}\lambda^{\star}}{D^{\star}} \sinh\left(\frac{x_{\mathrm{d}}}{\lambda^{\star}}\right)}\right] \tag{2.1.63}$$

where v_{r} is the recombination velocity close to the interface, $\lambda^{\star}$ is the ambipolar diffusion length defined as:

$$\lambda^{\star} = \sqrt{D^{\star}\tau^{\star}} \tag{2.1.64}$$

where $D^{\star}$ is the ambipolar diffusion coefficient defined as:

$$D^{\star} = \frac{\mu_{\mathrm{n}} D_{\mathrm{p}} + \mu_{\mathrm{p}} D_{\mathrm{n}}}{\mu_{\mathrm{n}} + \mu_{\mathrm{p}}} \tag{2.1.65}$$

and $\tau^{\star}$ is the ambipolar life time, that can be approximated for the limit of high level injection like:

$$\tau^{\star} = \tau_{\mathrm{n}} + \tau_{\mathrm{p}} \tag{2.1.66}$$

And finally, the applied voltage should equal the sum of the partial drops like:

$$V_{\mathrm{a}} = V_{\mathrm{t}} \ln\left(-\frac{J_{\mathrm{high}}}{J_{\mathrm{Sp}}}\right) + V_{\mathrm{d}}(J_{\mathrm{high}}) - J_{\mathrm{high}} R_{\mathrm{s}} \tag{2.1.67}$$

where R_s is any additional series resistance associated with the structure (to be discussed in more detail later, in section 2.1.5.5). The analysis of the injection process in the intermediate region is quite involved and often an arbitrary switch function $s(x)$ is used to smooth the transition between the low-level injection case and the high-level injection case like:

$$J_p = s(n(0))J_{low} + [1 - s(n(0))]\, J_{high} \tag{2.1.68}$$

the requirements over the switch function being:

$$\begin{aligned} s(n(0)) \quad &\rightarrow \quad 1 \qquad n(0) \ll N_a \\ &\rightarrow \quad 0 \qquad n(0) \gg N_a \end{aligned} \tag{2.1.69}$$

two examples of useful switch functions (one power law, one exponential) being:

$$s(n(0); N_a, e_1, e_2) = \frac{1}{1 + \left(\frac{e_1 n(0)}{N_a}\right)^{e_2}} \tag{2.1.70}$$

$$s(n(0); N_a, e_1, e_2) = \frac{1 - \tanh\left(\frac{e_1 n(0) - N_a}{e_2}\right)}{2} \tag{2.1.71}$$

where e_1 and e_2 are arbitrary constants (to be refined experimentally) defining the smoothness of the transition.

A modification of equation 2.1.55 has been suggested by Hassan (2000), which is valid for both high and low levels of injection for thin barriers for which the hole diffusion length is similar to the width of the depletion region $x_p \sim x_d$:

$$\xi = \frac{4\frac{\mu_p}{\mu_n} p_0}{2\left(1 - \frac{\mu_p}{\mu_n}\right) p_0 + \left(1 + \frac{\mu_p}{\mu_n}\right) N_d} \tag{2.1.72}$$

where $p_0 = p(0)$ is the hole concentration at the interface, estimated as:

$$p_0 = \frac{N_d}{2}\left[\sqrt{1 + \frac{4n_i^2\left(\frac{J}{J_S} + 1\right)}{N_d^2}} - 1\right] \tag{2.1.73}$$

which can be readily shown, to reduce to equation 2.1.55, in the limit of $\frac{J}{J_S} \gg 1$. In the opposite limit, via Taylor expansion around $J = 0$, the injection ratio can be demonstrated to be virtually constant up to a small linear correction, for low current densities for which $\frac{J}{J_S} \ll 1$.

2.1.4.6 Phonon-scattering and other quasiparticle scattering

So far the influence of elastic and inelastic electron scattering has not been explicitly taken into account in the derivations of the various current components. It is intuitively clear, that only

an *ideal rectifier* would dissipate no power (for example to Joule heating) in all parts of its $I-V$ characteristic[1]. For any real junction, there would be a significant amount of Joule dissipation (not only related to series resistance), which means that there would be a non-negligible phonon (or other quasi-particles, for example magnons should the junction consist of ferromagnetic materials, or photons in direct-gap systems with non-vanishing photoluminescence) generation. The detailed analysis of these phenomena goes beyond the scope of this section.

Here an example is due on the formal treatment of phonon-scattering within the one-dimensional Boltzmann equation, say along the x-axis. The Boltzmann equation for the distribution function $\varrho(E, v_x, x, t)$ can be written as:

$$\frac{\partial \varrho}{\partial t} + v_x \frac{\partial \varrho}{\partial x} - q\mathcal{E}\left(v_x \frac{\partial \varrho}{\partial E} + \frac{1}{m_x^\star}\frac{\partial \varrho}{\partial v_x}\right) = \mathcal{C}[\varrho] \tag{2.1.74}$$

where $\mathcal{C}$ is the scattering integral, broken down to elastic and inelastic scattering integrals:

$$\mathcal{C}[\varrho] = \mathcal{C}_{\mathrm{el}}[\varrho] + \mathcal{C}_{\mathrm{in}}[\varrho] \tag{2.1.75}$$

which are estimated (assuming elastic scattering from acoustic phonons and inelastic scattering from optical phonons) as follows:

$$\mathcal{C}_{\mathrm{el}} = 2\pi \frac{kT\Xi^2}{4\hbar\rho\overline{v}_{\mathrm{S}}^2} \int \mathcal{D}(E)\left[\varrho(E, v_x', x, t) - \varrho(E, v_x, x, t)\right] \mathrm{d}v_x' \tag{2.1.76}$$

$$\begin{aligned}\mathcal{C}_{\mathrm{in}} = 2\pi \frac{\Theta^2}{8\rho\omega_{op}} \int & \mathcal{D}(E^-)\left[N_{\mathrm{op}}\varrho(E^-, v_x') - (N_{\mathrm{op}}+1)\varrho(E, v_x')\right] \\ & + \mathcal{D}(E^+)\left[(N_{\mathrm{op}}+1)\varrho(E^+, v_x') - N_{\mathrm{op}}\varrho(E, v_x)\right] \mathrm{d}v_{\mathrm{x}}'\end{aligned} \tag{2.1.77}$$

where Ξ is the deformation potential and Θ is the deformation field, $\overline{v}_{\mathrm{S}}$ is the average sound velocity in the semiconductor, ρ is the mass density, $E^\pm = E \pm \hbar\omega_{\mathrm{op}}$, ω_{op} is the optical phonon frequency and the optical phonon number density is defined, in the usual Bose statistics way, like:

$$N_{\mathrm{op}} = \frac{1}{\mathrm{e}^{\frac{\hbar\omega_{\mathrm{op}}}{kT}} - 1} \tag{2.1.78}$$

Equation 2.1.74 should be solved in a system with the Poisson equation:

$$\frac{\partial \mathcal{E}}{\partial x} = \frac{q}{\epsilon_{\mathrm{s}}}\left[N_{\mathrm{d}}(x) - \int\int \mathcal{D}_{\mathrm{s}}(E)\varrho(E, v_x, x, t)\ \mathrm{d}E\ \mathrm{d}v_x\right] \tag{2.1.79}$$

and thus the temporal (in general, phase space) evolution of the distribution function ϱ obtained, which allows for the estimation of observable parameters like $J_{\mathrm{n}}(V_{\mathrm{a}})$. In practise, the numerical solution is usually done either with multi-grid methods or by expansion over a base

[1] At reverse bias, because the leakage current is vanishing, and at forward bias, because the voltage drop is vanishing.

set of functions. Imposing boundary conditions at the metal-semiconductor interface and deep in the neutral part of the semiconductor side of the junction is problematic and an issue of contemporary investigations (see Domaingo & Schürrer (2004); Katkar & Tait (2004)). The generation of optical phonons (and in a similar fashion of magnons) influences the $I-V$ characteristic at low temperature $kT \ll \hbar\omega_{\mathrm{op}}$ and at bias comparable to the characteristic energy of the phonon $qV_{\mathrm{a}} \sim \hbar\omega_{\mathrm{op}}$. This is the essence of the popular experimental method of derivative spectroscopy, applicable to tunnel and narrow Schottky junctions.

2.1.5 Various imperfections and complications

There is a large number of 'non-idealities' that influence the transport properties and make the analysis of experimental data difficult for an arbitrary Schottky junction. In the following paragraphs some of those will be discussed in more detail.

2.1.5.1 Existence of an oxide layer

One of the most common imperfection in non-UHV cleaved junctions is the formation of an oxide layer at the interface between the metal and the semiconductor. The existence of a thick insulating layer leads to a reformulation of the current limiting conditions and is discussed in greater detail in appendix A.1. To a first approximation, the presence of a naturally oxidised layer may be modelled as a thin tunnel barrier between the metal and the semiconductor, taking part of the total voltage drop, thus decreasing the actual applied voltage on the Schottky barrier itself. In the rigid zones approximation this is visualised on figure (2.7), following Rhoderick & Williams (1988).

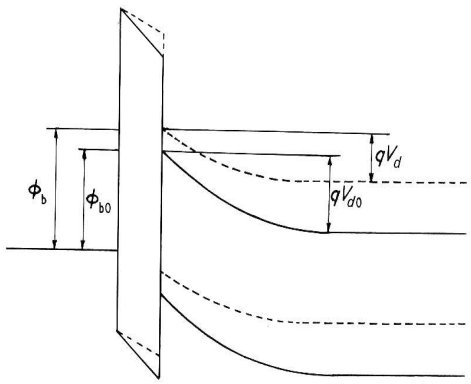

Figure 2.7: Influence of a insulating layer at the interface.

The Poisson equation for the electrostatic problem can be solved again within the full depletion approximation (A.2). In analogy to 2.1.28 the solution is obtained by expressing x_d from the quadratic equation:

$$q\left(V_\mathrm{bi}-V_\mathrm{a}\right)=\frac{qN_\mathrm{d}x_\mathrm{d}^2}{2\epsilon_\mathrm{s}}+\frac{qN_\mathrm{d}x_\mathrm{d}x_\mathrm{ox}}{\epsilon_\mathrm{ox}} \tag{2.1.80}$$

where x_ox is the thickness and ϵ_ox is the dielectric constant of the oxide layer. The explicit form can be compared with 2.1.28, which becomes a limiting case when $x_\mathrm{ox}\to 0$ and $\epsilon_\mathrm{ox}=\epsilon_\mathrm{s}$. The explicit form is:

$$x_\mathrm{d}=x_\mathrm{ox}\left(1-\frac{\epsilon_\mathrm{s}}{\epsilon_\mathrm{ox}}\right)+\sqrt{\frac{2\epsilon_\mathrm{ox}^2(\phi_\mathrm{i}-V_\mathrm{a})}{\epsilon_\mathrm{s}qN_\mathrm{d}}} \tag{2.1.81}$$

which shows that in most cases the additional oxide layer increases the depletion layer width. The increased width, naturally, leads to decreased (to be compared with 2.1.32) capacitance:

$$C_\mathrm{j}=\frac{\epsilon_\mathrm{s}}{L_\mathrm{D}}\sqrt{\frac{kT}{2q(\phi_i^\star-V_\mathrm{a})}} \tag{2.1.82}$$

where L_D is the effective dielectric thickness and $\phi_\mathrm{i}^\star=\phi_\mathrm{i}+\Delta\phi$, where $\Delta\phi$ is the resulting shift of the barrier potential. The current density in this case may be expressed like:

$$J_\mathrm{n}=J_\mathrm{s}\exp\left(\frac{qV_\mathrm{a}-2q\Delta\phi\left(1-\sqrt{1+\frac{\phi_\mathrm{i}-V_\mathrm{a}}{\Delta\phi}}\right)}{kT}\right) \tag{2.1.83}$$

where the shift of the barrier potential is expressed as $\Delta\phi=\frac{qN_\mathrm{d}d^2}{\epsilon_\mathrm{s}}\left(\frac{\epsilon_\mathrm{s}}{\epsilon_\mathrm{ox}}\right)^2$, ϵ_ox being the permeability of the oxide tunnel barrier. Because of the potential drop in the interfacial layer the barrier height is being lowered. The current density is reduced because of the additional barrier by an amount nearly proportional to $\Delta\phi$. More detailed analysis can be found in reference Gomila (1999).

2.1.5.2 Phonon scattering and quantum reflection

It is, in principle, possible for electrons to scatter from optical phonons in the region between the top of the barrier and the metal, that is 'covered' by neither the drift-diffusion, nor the thermionic emission theories (see Crowell & Sze (1966b)). For sufficiently sharp barriers, or in the limit of small x_d, when $x_\mathrm{d}\sim\lambda_\mathrm{D}$, where λ_D is the De Broglie wavelength for the conduction electrons $\lambda_\mathrm{D}=\frac{h}{m^\star v_\mathrm{F}}$ Menzel (1960), there is a finite probability of non-adiabatic reflection of electrons with energies larger than the barrier height ϕ_B. The combined effect of the above two mechanisms is often taken into account using a modified Richardson constant:

$$A^{\star\star}=\frac{f_\mathrm{ph}f_\mathrm{q}}{1+f_\mathrm{ph}f_\mathrm{q}(v_\mathrm{r}/v_\mathrm{d})}A^\star \tag{2.1.84}$$

where $f_{\rm ph}$ is the probability of scattering by optical phonons, and $f_{\rm q}$ is the average transmission probability. Both $f_{\rm ph}$ and $f_{\rm q}$ depend in a complicated way on the maximal electric field $E_{\rm max}$, the temperature T and the electron effective mass $m^\star$. The modified Richardson constant has been evaluated by Crowell & Sze (1966a) to be $A^{\star\star}_{{\rm Si}\{111\}} = 96$ Acm^{-2}K^{-2}, considerably (about three times) lower that the standard value.

2.1.5.3 The Schottky effect

Another detrimental effect is the lowering of the barrier height, due to image charges in the metal (also known as the Schottky effect). The resulting change may be estimated like:

$$\Delta\phi_{\rm b} = \sqrt{\frac{q\mathcal{E}_{\rm max}}{2\pi\epsilon_{\rm s}}} \tag{2.1.85}$$

where $\mathcal{E}_{\rm max}$ is the maximal electric field strength in the interface region given by:

$$\mathcal{E}_{\rm max} = \sqrt{\frac{2qN_{\rm d}}{\epsilon_{\rm s}}\left(V_{\rm bi} - V_{\rm a} - \frac{kT}{q}\right)} \tag{2.1.86}$$

with the build-in potential defined as:

$$V_{\rm bi} = V(x_{\rm d}) - V(0) \tag{2.1.87}$$

where, it is assumed that the potential drop across the metal is negligible, the electric field near the interface is constant, and the band bending is reasonably high Lundstrøm & Schuelke (1982). It is clear that the $V_{\rm bi}$ is proportional to the barrier height $\phi_{\rm B} \approx V_{\rm bi}$. Also, the maximum electric field can be expressed simply in terms of the build-in potential and the barrier width like:

$$\mathcal{E}_{\rm max} = \frac{V_{\rm bi} - V_{\rm a} - kT/q}{x_{\rm d}} \tag{2.1.88}$$

For small band bending, when the flat band state is approached, equation 2.1.86 is no longer valid. A more exact solution for $\mathcal{E}_{\rm max}$ should be used instead in this case (see Bozhkov & Zaitsev (2005b)):

$$\mathcal{E}_{\rm max} = \sqrt{\frac{2qN_{\rm d}}{\epsilon_{\rm s}}\left[V_{\rm t}\exp\left(-\frac{V_{\rm bi} - V_{\rm a}}{V_{\rm t}}\right) + V_{\rm bi} - V_{\rm a} - \frac{kT}{q}\right]} \tag{2.1.89}$$

which is easily seen to give the correct limit of $\lim_{V_{\rm a}\to V_{\rm bf}} \mathcal{E}_{\rm max} = 0$, at $V_{\rm a} = V_{\rm bf}$, where $V_{\rm bf} \approx V_{\rm bi}$ is the voltage for which the flat band condition is achieved (or when $V_{\rm a} \approx V_{\rm bi}$).

The classical image-charge concept is, of course, strictly valid for large distances from the metal-semiconductor interface. More detailed analysis is necessary, for example using *ab initio* methods, in order to assertain the influence of the exact interface reconstruction in real junctions. An example of such calculations for GaAs based Schottky junctions is given by Berthod (1998).

As the barrier lowering $\Delta\phi_b$ is voltage dependent, it may cause departures from the expected current-voltage characteristics even in otherwise perfect junctions. Though as the barrier lowering is only seen by electrons approaching the barrier from the from the semiconductor side, it does not influence to a first approximation the $C-V$ methods for estimation of the barrier height.

2.1.5.4 Common treatment

Usually, the various imperfections are 'hidden' behind a 'fudge' factor Υ called the 'ideality factor' as:

$$J = J_S \left[\exp\left(\frac{qV_a}{\Upsilon kT} - 1 \right) \right] \tag{2.1.90}$$

or simply for large enough bias $V_a \gg kT/q$ like:

$$J \approxeq J_S \exp\left(\frac{qV_a}{\Upsilon kT} \right) \tag{2.1.91}$$

where J_S is the saturation current, usually obtained by extrapolation to the limit of $V_a = 0$ and Υ is defined as

$$\Upsilon \equiv \frac{q}{kT} \frac{\partial V_a}{\partial(\ln J)} \tag{2.1.92}$$

Obviously, the closer Υ is to unity, the better is the applicability of the thermionic emission model to the particular case of interest. For example $\Upsilon \approx const$ for the common case of quasi-linear barrier lowering due to the image force[1].

As another example, the theoretical ideality factor for a Schottky junction with an oxide layer can be estimated to be:

$$\Upsilon = \frac{1}{1 - \sqrt{\frac{\Delta\phi}{\Delta\phi + \phi_i - V_a}}} \tag{2.1.93}$$

and is therefore always greater than unity.

2.1.5.5 Other imperfections of real Schottky diodes

It is important to note, that before any of treatment can be done to the experimental data, that would result in the determination of the barrier height, there are two other (often important) imperfections of real diodes that must be accounted for. One is the series resistance of the semiconductor substrate R_s. While R_s is geometry dependent and therefore can be minimised by decreasing the substrate thickness, as well as by increasing its doping level; it is still imperative to correct for the voltage drop on R_s at high bias, where voltage drop on the Schottky junction

[1] In this case Υ can shown to alter the saturation current density J_S in similar fashion $J_S \approx A^\star T^2 \exp\left(-\frac{V_{bi}}{\Upsilon V_t}\right)$, which is valid not only in the linear regime, if Υ is made a function of applied voltage $\Upsilon = \Upsilon(V_a)$ (see Bozhkov & Zaitsev (2006)).

can become negligible. The I-V characteristic for an otherwise ideal diode, incorporating a large series resistance R_s becomes:

$$I = I_S \left(\exp \left[\frac{q(V_a - IR_s)}{\Upsilon kT} \right] - 1 \right) \tag{2.1.94}$$

Equation 2.1.94 can be solved analytically for V_a to give:

$$V_a = IR_s + \frac{\Upsilon kT}{q} \ln \left(\frac{I + I_S}{I_S} \right) \tag{2.1.95}$$

which can be fitted (for example by non-linear least squares) to experimental data (see Ayyildiz *et al.* (1996); Badila & Georgescu (2002)).

It is, also, possible to obtain analytical solution in the case, when direct gap recombination is included as a current contribution I_r, for example using equation 2.1.52. The explicit form was obtained by McLean *et al.* (1986) and reads:

$$V_a = IR_s + \frac{2kT}{q} \ln \left[\sqrt{\frac{I}{I_S} + \left(1 + \frac{I_r}{2I_S} \right)^2} - \frac{I_r}{2I_S} \right] \tag{2.1.96}$$

Equation 2.1.96 can be used to fit experimental data and extract most probable values for I_S, I_r and R_s. Further, the barrier height ϕ_B and the mean carrier lifetime in the depleted region τ_r can be estimated using:

$$\begin{aligned} \phi_b &= \frac{kT}{q} \ln \left(\frac{SA^\star T^2}{I_s} \right) \\ \tau_r &= \frac{Sqn_i x_d}{2I_r} \end{aligned} \tag{2.1.97}$$

where S is the junction area. If the trap (recombination centre) concentration n_t is known by other means, the capture cross section σ_t can be estimated like:

$$\sigma = \frac{1}{\overline{v} \tau n_t} \tag{2.1.98}$$

where $\overline{v}$ is the thermal velocity of the carriers.

It is possible, in some cases, to measure R_s directly, by substituting the Schottky contact with an ohmic one as will be discussed later in paragraph 2.2.

Another similar problem is the leakage resistance R_l, often associated with increased reverse-bias current. R_l is likely, but not necessarily, determined by the finite lateral size of real junction and the defects located at the edges of the active area of real diodes. The total current for an ideal diode with leakage resistance R_l can be written as (see Chattopadhyay (1996)):

$$I = I_S \left(\exp \left[\frac{q(V_a - IR_s)}{kT} \right] - 1 \right) + \frac{V_a - IR_s}{R_l} \tag{2.1.99}$$

where the effective shunt resistance is considered connected in parallel to the ideal diode. And solved for $\ln(\frac{I}{I_S})$ in the limit of $V_a \gg V_t$ to yield:

$$\ln\left(\frac{I}{I_S}\right) = \ln\left\{\exp\left(-\frac{qV_a}{kT}\right) + \frac{V_a}{I_S R_l}\right\} - \ln\left(1 + \frac{R_s}{R_l}\right) \tag{2.1.100}$$

Alternatively, the shunt resistance can be considered connected in parallel to the entire diode structure, yielding a different expression for the total current:

$$I = I_S\left(\exp\left[\frac{q(V_a - IR_s)}{kT}\right] - 1\right) + \frac{V_a}{R_l} \tag{2.1.101}$$

Instead of looking for a solution in the limit $V_a \gg V_t$ as in (Chattopadhyay (1996)), which yields the trivial solution for $\ln(\frac{I}{I_S})$:

$$\ln\left(\frac{I}{I_S}\right) = \ln\left\{\exp\left(-\frac{qV_a}{kT}\right) + \frac{V_a}{I_S R_l}\right\} \tag{2.1.102}$$

an analytical solution can be obtained, in special functions, for $V_a(I)$ in the form:

$$V_a = R_l\left(I_S + I\right) - \frac{kT}{q}\mathrm{W}\left\{\frac{q}{kT}I_S R_l \exp\left[-\frac{q}{kT}\left(IR_s - \left(I + I_S\right)R_l\right)\right]\right\} \tag{2.1.103}$$

where $\mathrm{W}(x)$ is the Lambert's function defined as the inverse of $x\exp(x)$[1]. Thus a fit can be, in principle, done to an experimentally measured dependence $V_a(I)$. The leakage resistance is likely to affect the behaviour of real diodes in the low voltage limit (i.e. when the diodes are actually shut) and further narrows the region of applicability of the standard Schottky device modelling.

Here, it should be noted that analytical solution of the quasi-ideal diode with series resistance only problem, in terms of total current I, have been obtained before (though rather late in historical aspect) using the W function by Banwell & Jayakumar (2000) in the form:

$$I = \frac{\Upsilon V_t}{R_s}\mathrm{W}\left[\frac{I_S R_s}{\Upsilon V_t}\exp\left(\frac{V_a - I_S R_s}{\Upsilon V_t}\right)\right] - I_S \tag{2.1.104}$$

which in the high current limit $I \gg I_S$ reduces to:

$$I = \frac{\Upsilon V_t}{R_s}\mathrm{W}\left[\frac{I_S R_s}{\Upsilon V_t}\exp\left(\frac{V_a}{\Upsilon V_t}\right)\right] \tag{2.1.105}$$

Analytical and semi-analytical solutions exist for other types of effective circuit combinations of series and parallel resistors and a quasi-ideal diode (see Donoval *et al.* (1998); Ortiz-Conde & Sánchez (2005)). Because of their increasing complexity and large number of fitting parameters, actual implementation for processing experimental data is problematic.

A better understanding of the complexity of the reverse problem (the determination of the intrinsic junction parameters from the set of measured external parameters) is gained by

[1] The Lambert's W function is defined as $\mathrm{W}(a) = \mathrm{root}((xe^x - a), a)$.

schematically associating an effective circuit to the real device. A simple example is shown on figure 2.8, where R_s and R_l are the series and leakage resistances, C_j is the depletion layer capacitance, D_{dd} and D_{ti} are the effective model representations of the drift-diffusion and thermionic-emission limits and R_r is to represent the recombination currents in the junction. Because of the nonlinearity of some of the effective components and the over-determination of the associate system of governing equations, unique solution is not always obtainable without *a priori* assumptions about some of the system parameters. The forward (direct) problem, though difficult, has in principle, an unique solution, obtainable either by analytical expansion or numerically.

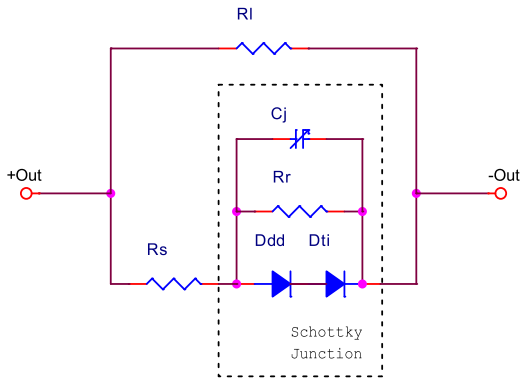

Figure 2.8: Simplified effective circuit representing a real diode.

2.1.5.6 Methods for extraction of Schottky barrier parameters

Because of their abundant practical application, the main Schottky junction parameters and the methods of their determination, have been the subject of a large number of publications. As the most important parameters of real diodes and their non-idealities were already discussed in section 2.1.5.5, a concise systematisation of the methods will follow.

Methods based on data manipulation. The simplest approach to the determination of Schottky barrier heights for almost ideal diodes is based on the high-applied voltage $V_a > (3..5)V_t$ quasi-ideal diode approximation:

$$I = I_S e^{\frac{V_a}{\Upsilon V_t}} \tag{2.1.106}$$

thus a plot of $\ln I$ versus V_a should yield a straight line, whose intercept can be used to define I_S and therefore extract ϕ_b provided that the effective Richardson constant A^{**} is known. This approach is however difficult to apply in diodes with large series resistance as there may be no linear part of the dependence $\ln I(V_a)$, at all.

In some cases, the temperature dependence of the of the current at fixed voltage can be used to extract estimates of the barrier height by plotting $\ln I$ against $1/T$, by choosing a bias setpoint $qV_\mathrm{a} \gg kT$ or measuring at moderate reverse bias (see Pipnis *et al.* (1998)). Neglecting, in this fashion, all but the thermal activation of the saturation current J_S, the procedure is, by necessity, confined to narrow regions of temperature T and applied bias V_a. A stricter approach, is to determine estimates of the saturation current at each individual temperature $J_\mathrm{S}(T)$ and then extract an estimate of the barrier height from a plot of $\ln J_\mathrm{S}(T)$ as a function of $1/T$. This however is not a problem-free procedure as current components other than pure thermionic emission (tunnelling, recombination, etc.) generally increase in magnitude with lowering the temperature and increasing the bias window. Thermionic emission can in a few cases be favoured by increasing the temperature (above ambient), though this is, generally, bound to produce irreversible changes of barrier height, due to diffusion and chemical reactions at the interface which are exponentially activated in temperature.

There are cases in which changes in temperature are not favoured at all, as the junction parameters at particular temperature (for example ambient temperature) are of particular interest. The so-called Norde plot can be often used in such situations (see Norde (1979)), which consists of plotting a function $F_\mathrm{N}(V_\mathrm{a})$ defined as:

$$F_\mathrm{N}(V_\mathrm{a}) = \frac{V_\mathrm{a}}{2} - \frac{kT}{q} \ln\left(\frac{I}{SA^{\star\star}T^2}\right) \tag{2.1.107}$$

where S is the surface area of the junction. The plot of $F_\mathrm{N}(V_\mathrm{a})$ against V_a should have a slope of $-\frac{1}{2}$ if there is no series resistance, an asymptotic slope of $+\frac{1}{2}$ at high applied voltage, when there is a large series resistance R_s, and a minimum in between. If the position of the minimum is V_0 then the Schottky barrier height may be estimated as:

$$\phi_\mathrm{b} = F_\mathrm{N}(V_0) + \frac{V_0}{2} - \frac{kT}{q} \tag{2.1.108}$$

Further, if I_0 is the current at bias V_0, the series resistance can be evaluated at:

$$R_\mathrm{s} = \frac{V_\mathrm{t}}{I_0} \tag{2.1.109}$$

This type of analysis neglects the recombination processes and the lowering of the barrier height, among other imperfections.

A slightly improved version of this model has been developed by Lien *et al.* (1984), and consists of evaluating a family of Norde functions:

$$F_\mathrm{N}(V; a) = \frac{V_\mathrm{a}}{a} - \frac{kT}{q} \ln\left(\frac{I(V_\mathrm{a})}{SA^{\star\star}T^2}\right) \tag{2.1.110}$$

for range of values of the parameter a from the estimated ideality factor Υ to ∞. For a monotonic experimental dependence $V_\mathrm{a}(I)$, the Norde function can be rewritten as:

$$G_\mathrm{N}(I;a) = F_\mathrm{N}(V_\mathrm{a};a) \tag{2.1.111}$$

The reformulated Norde function $G_\mathrm{N}(I;a)$ has a minimum at $I = I_0$ such that:

$$\frac{\mathrm{d}G_\mathrm{N}(I_0;a)}{\mathrm{d}I} = 0 = \frac{1}{a}\frac{\mathrm{d}V_\mathrm{a}(I_0)}{\mathrm{d}I} - \frac{V_\mathrm{t}}{I_0} \tag{2.1.112}$$

and the minimum $I_0(a)$ is thus given by:

$$I_0(a) = \frac{V_\mathrm{t}}{R_\mathrm{s}}a - \frac{\Upsilon V_\mathrm{t}}{R_\mathrm{s}} \tag{2.1.113}$$

Therefore, a linear regression over $I_0(a)$ should be able to provide values for both R_s and Υ. The advantage of this modification of the Norde method is in exploiting a larger amount of data points from the $I(V_\mathrm{a})$ characteristic of the device under investigation, rather that few points close to a single extremum of the standard $F_\mathrm{N}(V_\mathrm{a})$ (see Prokopyev & Mesheryakov (2003)).

The influence of the barrier height lowering has been reviewed by McLean (1986), in the linear regime when the dependence of the barrier height on applied voltage can be expressed as:

$$\phi_\mathrm{b}(V_\mathrm{a}) = \phi_\mathrm{b}(0) - \Delta\phi + \varkappa V_\mathrm{a} \tag{2.1.114}$$

where $\Delta\phi$ is the barrier height lowering at zero bias $\Delta\phi_\mathrm{b}(0)$ given by equation 2.1.85:

$$\Delta\phi = \frac{\sqrt{2}}{2\pi}\frac{q}{\epsilon_0}\sqrt{\frac{qN_\mathrm{d}V_\mathrm{bi}}{\epsilon_0}} \tag{2.1.115}$$

and $\varkappa$ is a coefficient that can be evaluated at:

$$\varkappa = \frac{\sqrt{2}}{4\pi}\frac{q}{\epsilon_0}\sqrt{\frac{qN_\mathrm{d}V_\mathrm{bi}}{\epsilon_0}}\frac{1}{V_\mathrm{bi}} \tag{2.1.116}$$

The Norde function can be thus expressed as:

$$F_\mathrm{N}(V_\mathrm{a}) = \phi_\mathrm{b} - \Delta\phi - \frac{V_\mathrm{a}}{2}(1 - 2\varkappa) \tag{2.1.117}$$

and the minimal slope has, therefore, increased to $\varkappa - \frac{1}{2}$. It can be shown that the barrier height is overestimated like:

$$\phi_\mathrm{b} - \Delta\phi = F_\mathrm{N}(V_0) + (1 - 2\varkappa)\left(\frac{V_0}{2} - \frac{kT}{q}\right) \tag{2.1.118}$$

The overestimation, therefore, can be as large as few times V_t.

A method that is supposed to deal effectively with the series resistance R_s has been developed by Chattopadhyay (1995). The idea is based on the assumption that the limiting current

mechanism is the thermionic emission and that a single surface potential ψ_s determines the probability with which electrons are emitted into the metal. The current density can be thus written as:

$$J_n = A^\star T^2 \exp\left(-\frac{qV_n}{kT}\right) \exp\left(-\frac{q\psi_s}{kT}\right) \tag{2.1.119}$$

where $qV_n = E_c - E_F$ is the energy spacing between the bottom of the conduction band and the Fermi level. The surface potential is a function of the current density and the applied voltage V_a, among other parameters:

$$\psi_s = \psi_s\left(J_n, V_a\right) \tag{2.1.120}$$

To a first approximation ψ_n can be expanded as:

$$\psi_s = \phi_b - V_n - \frac{1}{\Upsilon}\left(V_a - J_n R_s\right) \tag{2.1.121}$$

and the approximation should be valid for small V_a. Locally around a fixed point (J_f, V_f) in (J_n, V_a) space ψ_s can be expanded in a two argument Taylor series like:

$$\psi_s\left(J_n, V_a\right) = \psi_s\left(J_f, V_f\right) + \left(J_n - J_f\right)\left(\frac{\partial \psi_s}{\partial J_n}\right) + \left(V_a - V_f\right)\left(\frac{\partial \psi_s}{\partial V_a}\right) + \ldots \tag{2.1.122}$$

and the coefficients determined experimentally. It is easily seen that ϕ_b can be thus expressed like:

$$\phi_b(V_f) = \psi_s\left(J_f, V_f\right) - \frac{\partial \psi_s}{\partial V_a} V_f + V_n - V_t \tag{2.1.123}$$

and therefore an effective dependence of the barrier height on applied voltage (within the thermionic emission model) obtained. Within the regions where $\frac{\partial \psi_s}{\partial V_a}$ is constant the barrier height lowering is proportional to the applied voltage, similar to equation 2.1.114, as intuitively expected. The point (J_f, V_f), where the ϕ_b is evaluated should be the highest applied voltage V_a for which $\frac{\partial \psi_s}{\partial V_a}$ is still linear.

Methods can be developed based on the derivative $\frac{dV_a}{dI}$, or the differential resistance, obtained either experimentally by modulation techniques or by numerical differentiation (see Lee *et al.* (1998)). Differentiation of both sides of equation 2.1.95 yields:

$$\frac{dV_a}{dI} = \frac{V_t}{I + I_S} + R_s \tag{2.1.124}$$

or approximately (for $I \gg I_S$):

$$\frac{dV_a}{dI} \approx \frac{V_t}{I} + R_s \tag{2.1.125}$$

and, therefore, by fitting a straight line to the dependence $\frac{dV_a}{dI}\left(\frac{1}{I}\right)$, estimates of I_S and R_s may be obtained (see Werner (1988)). The method has a big advantage in the case of otherwise ideal junctions with large series resistance, measured at large applied currents I by lock-in techniques.

Examples exist, also of finite difference methods, like the one of Wong & Lam (2001), that reduce the problem of an quasi-ideal junction with series resistance R_s to a simple linear regression for its determination. This can be done by solving the diode equation for V_a in the limit of large voltage $V_\mathrm{a} \gg V_\mathrm{t}$ like:

$$V_\mathrm{a}(I) = \Upsilon V_\mathrm{t} \ln\left(\frac{I}{I_\mathrm{S}}\right) + R_\mathrm{s} I \tag{2.1.126}$$

and estimating the proportional difference:

$$\begin{aligned} \mathrm{d}V_\mathrm{a}(\upsilon) &= V_\mathrm{a}(\upsilon I) - V_\mathrm{a}(I) \Rightarrow \\ \mathrm{d}V_\mathrm{a}(\upsilon) &= \Upsilon V_\mathrm{t} \ln \upsilon + (\upsilon - 1) R_\mathrm{s} I \end{aligned} \tag{2.1.127}$$

which is a linear function of the current I. It is therefore possible to choose υ and perform linear regression on the resulting dependence $\mathrm{d}V_\mathrm{a}(I)$ to determine the slope $(\upsilon - 1) R_\mathrm{s}$ and the intercept $\Upsilon V_\mathrm{t} \ln \upsilon$. The values of R_s and Υ can be thus deduced.

It is possible, also, to extract the series resistance by employing the partial dissipation power, or the integral $\int V_\mathrm{a}\mathrm{d}I$. Solving the standard expression $I(V_\mathrm{a})$ for V_a within the thermionic emission model like:

$$\begin{aligned} I &= I_\mathrm{S}\left[\exp\left(\frac{V_\mathrm{a} - I R_\mathrm{s}}{\Upsilon V_\mathrm{t}}\right) - 1\right] \Leftrightarrow \\ V_\mathrm{a} &= \Upsilon V_\mathrm{t} \ln\left(\frac{I + I_\mathrm{S}}{I_\mathrm{S}}\right) + I R_\mathrm{s} \end{aligned} \tag{2.1.128}$$

it is possible to integrate analytically, to yield:

$$\int V_\mathrm{a}\mathrm{d}I = \Upsilon V_\mathrm{t}\left[I \ln\left(\frac{I}{I_\mathrm{S}} + 1\right) + I_\mathrm{S} \ln\left(\frac{I}{I_\mathrm{S}} + 1\right)\right] - \Upsilon V_\mathrm{t}\,(I + I_\mathrm{S}) + \frac{I^2 R_\mathrm{s}}{2} + const \tag{2.1.129}$$

For large enough currents $I \gg I_\mathrm{S}$ the above expression can be simplified to:

$$\int V_\mathrm{a}\mathrm{d}I \approx (\mathrm{e} - 1)\Upsilon V_\mathrm{t} I + \frac{I^2 R_\mathrm{s}}{2} + const \tag{2.1.130}$$

and the integration constant can be shown to be $const = 0$, as the power dissipated at $I = 0$ is vanishing. The definite integral can be thus taken between any two points I_1 and I_2 satisfying the condition $I_1, I_2 \gg I_\mathrm{S}$ to yield:

$$\frac{1}{I_2 - I_1}\int_{I_1}^{I_2} V_\mathrm{a}\mathrm{d}I = (\mathrm{e} - 1)\Upsilon V_\mathrm{t} + \frac{R_\mathrm{s}}{2}(I_2 - I_1) \tag{2.1.131}$$

Thus, by calculating the power integral between two appropriately chosen current values, the series resistance R_s and the ideality factor Υ can be extracted. This result is analogous, but

more precise than the integral methods described by Kaminski *et al.* (1997) and Ortiz-Conde *et al.* (1995). This method is analytically equivalent to asserting that:

$$\frac{\mathrm{d}V_\mathrm{a}}{\mathrm{d}I} \approx R_\mathrm{s} + (\mathrm{e}-1)\Upsilon V_\mathrm{t} \tag{2.1.132}$$

at high current bias. Numerically, the same level of uncertainty can be achieved by both the integral and the differential forms for the same number of experimental data points.

As intuitively clear, the measurement error impact of current and voltage on the extraction of R_s, can be traded-off for each other. This is, most easily, seen by taking the log-derivative of the current I, again writing condition of $I \gg I_\mathrm{s}$, like:

$$\frac{\mathrm{d}}{\mathrm{d}I} I = \frac{1}{V_\mathrm{t}} \frac{\mathrm{d}V_\mathrm{a}}{\mathrm{d}I} - \frac{R_\mathrm{s}}{\Upsilon V_\mathrm{t}} \tag{2.1.133}$$

Thus, the R_s can be determined, as the negated ratio of the intercept to the slope of the dependence $\partial_I \ln I(\partial_I V_\mathrm{a})$, as described by Kaminski *et al.* (1997). Though, in principle equivalent to the previously described methods, the error budget is larger for the current, rather than the voltage, and this makes this method favourable for diodes with higher impedance.

As higher derivatives of the $I-V$ characteristic carry, on theory, more information about the device being characterized, higher derivative methods may seem attractive. From practical point of view, the noise-expansion in numerical differentiation limits the order of useful derivatives to about 2. For derivatives that are measured experimentally, by employing modulation techniques, because of modulation broadening and useful signal-to-noise ratio, often, the upper limit for the derivative order is, also, set at 2.

It should be mentioned, that a class of methods exists, initiated by Mikhelashvili & Eisenstein (1999); Mikhelashvili *et al.* (1999, 2001) that is based on the voltage (or current) spectra of the power exponent, defined as:

$$\vartheta(V_\mathrm{a}) = \frac{\mathrm{d}(\ln I)}{\mathrm{d}(\ln V_\mathrm{a})} \tag{2.1.134}$$

For an quasi-ideal diode, $\vartheta(V_\mathrm{a})$ is linear function of V_a at small voltages $V_\mathrm{a} \ll V_\mathrm{bi}$, has a maximum at a voltage that depends on the series resistance R_s and decays exponentially to an asymptotic limit of $\lim_{V_\mathrm{a}\to\infty} \vartheta(V_\mathrm{a}) = 1$, because of the finite series resistance $R_\mathrm{s} \neq 0$. When there is a finite leakage resistance $R_\mathrm{l} \neq \infty$ the initial asymptotic behaviour is similar in the limit $\lim_{V_\mathrm{a}\to 0} \vartheta(V_\mathrm{a}) = 1$. The details of the dependence $\vartheta(V_\mathrm{a})$ are quite model dependent and vary with the number of various imperfections (for example, Schottky barrier lowering, recombination, tunnelling) included in the calculation.

Methods based on nonlinear regression Direct nonlinear regression based on equation 2.1.96 has been suggested and implemented by Bennet (1987). There are two basic possibilities for error minimisation (see Ferhat-Hamida *et al.* (2001); Ortiz-Conde *et al.* (1999, 2000)):

(a) Vertical error minimisation. The deviations between the measured values for the current I_i^{exp} and the simulated I_i^{sim} are minimised:

$$\delta I = \sum_{i=1}^{a} \left(\frac{I_i^{\mathrm{exp}} - I_i^{\mathrm{sim}}}{I_i^{\mathrm{sim}}} \right)^2 \tag{2.1.135}$$

(b) Lateral error minimisation. The deviations between the measured values for the voltage V_i^{exp} and the simulated V_i^{sim} are minimised:

$$\delta V = \sum_{i=1}^{a} \left(\frac{V_i^{\mathrm{exp}} - V_i^{\mathrm{sim}}}{V_i^{\mathrm{sim}}} \right)^2 \tag{2.1.136}$$

where a is the number of data points used for the least squares regression. Which one is to be preferred, depends on the measurement uncertainties of the current and voltage data and the derivatives of the parameters of interest with respect to I and V.

A class of methods exists based on fitting equation 2.1.96 and 2.1.99 to experimental data, ranging from least squares minimisation to genetic algorithms (see Almashary (2004); Jervase *et al.* (2001); Ortiz-Conde *et al.* (2001)). A common disadvantage to all of them, being that there is no guarantee for the uniqueness of the obtained solution for the set of fitting parameters. Errors can be, generally, kept to within 2 %, provided the initial guess values are to within 100 % of the actual ones, but reliability is poor.

It is also possible to account for lateral inhomogeneity of the barrier height by assuming some kind of statistical distribution of local barrier heights (see Bozhkov & Zaitsev (2007); Osvald & Dobročka (1996)). This is normally done by choosing an *a priori* distribution kernel of lognormal or normal type (see Chand (2002)), for example:

$$\hat{\rho}_{\mathrm{b}} \left(\varphi; \bar{\phi}_{\mathrm{b}}, \bar{\sigma}_{\mathrm{b}} \right) = \frac{1}{\sqrt{2\pi}\bar{\sigma}_{\mathrm{b}}} \exp\left(-\frac{\left(\varphi - \bar{\phi}_{\mathrm{b}} \right)^2}{2\bar{\sigma}_{\mathrm{b}}^2} \right) \tag{2.1.137}$$

where $\bar{\phi}_{\mathrm{b}}$ is the average barrier height and $\bar{\sigma}_{\mathrm{b}}$ is its dispersion. The total current can thus be written as the convolution product of $\hat{\rho}_{\mathrm{b}}$ and J_{n} or $\hat{\rho}_{\mathrm{b}} \otimes J_{\mathrm{n}}$ like[1]:

$$I \left(\bar{\phi}_{\mathrm{b}}, \bar{\sigma}_{\mathrm{b}}, r_{\mathrm{s}} \right) = S \int_{-\infty}^{\infty} \hat{\rho}_{\mathrm{b}} \left(\varphi; \bar{\phi}_{\mathrm{b}}, \bar{\sigma}_{\mathrm{b}} \right) J_{\mathrm{n}} \left(\varphi; r_{\mathrm{s}} \right) \mathrm{d}\varphi \tag{2.1.138}$$

[1] This is strictly valid, for incoherent transport, or at high temperature and when the direct tunnelling can be neglected. The mathematical treatment of the problem for laterally inhomogeneous thin tunnel-Schottky barrier is still in its infancy (see Bezák & Selim (2001)). The complications arise from the specular reflection from, and diffraction through, the stochastic longitudinal and transverse distribution of potential. Electric field dependent localisation effects are to be expected in the limit of strong back-scattering of electrons from a stochastic δ-barrier.

where $r_s = R_a S$ is the resistance area product of the series resistance contribution and J_n can be defined simply (see Osvald (2006a)), but not necessarily, as:

$$J_n(\varphi; r_s) = A^{\star\star} T^2 \exp\left(-\frac{q\varphi}{kT}\right)\left[\exp\left(\frac{q\left(V_a - J_n r_s\right)}{kT}\right) - 1\right] \tag{2.1.139}$$

As the total current becomes an implicit function of the applied voltage V_a and R_s, like:

$$I = I\left(V_a, R_s; \bar{\phi}_b, \bar{\sigma}_b\right) \tag{2.1.140}$$

it can be used to fit experimental data and extract estimates for one or more parameters (for example $\bar{\phi}_b$, $\bar{\sigma}_b$ and R_s). This method is, of course, most useful for large area junctions where the local barrier heights are more likely to be statistically normally distributed (see Chand & Kumar (1997)), when measurements are done at various temperatures. The voltage V_m at which the current I has a minimum as a function of temperature T may be determined by differentiating both sides of equation 2.1.138, and can be used to define the distribution of barrier heights $\overline{\sigma}_b$ as:

$$V_m = \overline{\phi}_b + 2V_t - \frac{\overline{\sigma}_b^2}{V_t} + R_s S A^{\star\star} T^2 e^2 \exp\left[-\left(\frac{\overline{\sigma}_b}{V_t}\right)^2\right] \tag{2.1.141}$$

together with an estimate of the average barrier height $\overline{\phi}_b$ (see Osvald (2006b)).

It is often assumed that the integration in equation 2.1.138 can be carried out from $-\infty$ to ∞, which leads to the simple result for the effective barrier height:

$$\phi_b^\star = \bar{\phi}_b - \frac{\hat{\sigma}_b^2}{V_t} \tag{2.1.142}$$

It should be noted that though approximately correct and simple analytically, this is not the exact form of the integration. As there ate no zero or negative barrier heights in the problem, that are physically significant, the integration in 2.1.138 should be carried out in the interval $0 \ldots 2\bar{\phi}_b$. The upper limit due to the fact that very high barriers are not likely to contribute much to the total transmission. In this case the modification affects the saturating current like:

$$I_S^\star = I_S \frac{\mathrm{erf}(f_+) - \mathrm{erf}(f_-)}{2} \tag{2.1.143}$$

where $I_S^\star$ is the effective saturation current, $\mathrm{erf}(x)$ is the error-function[1] and f_+ and f_- are defined as:

$$\begin{aligned} f_+ &= \left(\frac{\bar{\sigma}_b^2}{V_t} + \bar{\phi}_b\right)\frac{1}{\bar{\sigma}_b\sqrt{2}} \\ f_- &= \left(\frac{\bar{\sigma}_b^2}{V_t} - \bar{\phi}_b\right)\frac{1}{\bar{\sigma}_b\sqrt{2}} \end{aligned} \tag{2.1.144}$$

[1] $\mathrm{erf}(x)$ is defined as $\mathrm{erf}(x) \equiv \frac{2}{\sqrt{\pi}} \int_0^x e^{\zeta^2} d\zeta$

This correction only becomes important (the difference exceeds about 10 %) for low enough temperatures:

$$T < \frac{\bar{\sigma}_{\mathrm{b}}^2 q}{k}\left(0.9\sqrt{2}\sigma + \bar{\phi}_{\mathrm{b}}\right) \tag{2.1.145}$$

It is important to note, that the inhomogeneity of the barrier height is not, necessarily, associated with physical lateral inhomogeneity of the metal-semiconductor interface. As pointed-out by Bondarenko *et al.* (1998), even atomically flat, abrupt and defect-free contacts, in the absence of surface states, inevitably have a natural inhomogeneity of the Schottky barrier height, determined by the charge desertisation of the donor impurities for high enough donor concentration $N_{\mathrm{d}} \sim 10^{18}$ cm^{-3}. Such a situation occurs because the average distance between donor centres becomes comparable with the depletion width or $N_{\mathrm{d}}^{-1/3} \sim x_{\mathrm{d}}$, and therefore some of the donors situated at one and the same distance x from the interface will be ionised, and some will not. Therefore, in this limit, not only does the full depletion approximation lose ground, but the one dimensional modelling should be, altogether, substituted with at least a two-dimensional one.

The detailed evaluation of the width of the barrier height distribution $\bar{\sigma}_{\mathrm{b}}$, can be done using the parallel diodes model, by breaking-up the surface area of the junction S into small elements S_i for which, the effective barrier ϕ_{b}^i can be evaluated by inversing the classical thermionic emission model or equation 2.1.35, like:

$$\phi_{\mathrm{b}}^i = kT \ln\left[\frac{1}{(2\pi)^3}\frac{A^\star T^2}{J_{\mathrm{n}}^i}\left(\mathrm{e}^{\frac{V_{\mathrm{a}}}{kT}} - 1\right)\right] \tag{2.1.146}$$

where the factor $\frac{1}{(2\pi)^3}$ appears because of the change of dimensionality of the problem. Without going into the details of the derivation, it is easy to see, that the distribution of ϕ_{b} will be a finite-width quasi-gaussian peak, rather than a δ-function. The width of the distribution can be expected to be of the order of kT, as the change of conductance can be expected to be of the order of couple of conductance quanta $\sigma_0 = \frac{q^2}{\hbar}$, as couple of donors do (or do not) ionise within the area S_i, and therefore the logarithm in expression 2.1.146 gives values of the order of unity. The above effect is the fundamental reason, why it is difficult to define the barrier height at ambient temperature, to better than about 10 meV, even for moderate doping concentrations $N_{\mathrm{d}} \sim 10^{15}$ cm^{-3}.

Combined methods An example of a combined method may be given for the case of thermionic-field emission. At low temperature $\frac{kT}{E_{00}} \ll 1$ or high doping levels, the electronic current can be modelled as (see Jang *et al.* (2003)):

$$I = SJ_{\mathrm{S}} \exp\left(\frac{qV_{\mathrm{a}}}{E_{00}}\right) \tag{2.1.147}$$

which is valid for intermediate voltages $E_{00} < qV_a < q\phi_b$. This allows for simple vertical regression of the voltage dependence of the saturation current density $J_S(T)$ to be extracted as a function of temperature[1], together with the constant E_{00}. The extracted saturation current density can be then fitted by, for example, nonlinear least-squares algorithm to the nonlinear equation:

$$J_S(T) \approx \frac{A^\star \sqrt{\pi}\sqrt{E_{00}}\sqrt{\Phi_b - (E_c - E_F)}}{kT \cosh \frac{E_{00}}{kT}} \exp\left[-\frac{E_c - E_F}{kT} - \frac{\Phi_b - (E_c - E_F)}{E_{00}}\right] \tag{2.1.148}$$

and the barrier height Φ_b and the position of the Fermi level with respect to the conduction band $E_c - E_F$ can be thus determined.

2.1.6 Effects of external and internal magnetic fields on Schottky junctions

As a first order approximation the effect of an external magnetic field on the junction may be considered as effective change of the barrier height due to the Zeeman splitting of the quasi-Fermi level in the metal Ziese & Thornton (2001). While it is arguable whether or not the splitting of the chemical potential in the metal would dominate, or potentially large Lande g-factors in the semiconductor would lead to larger effects; it is still instructive to look at its possible implications on the two main models for the current limiting process 2.1.35 and 2.1.33. Some of the effects, described below, can be considered kinetic analogs to the weak Pauli paramagnetism of the quasi-free electron gas in nonmagnetic metals. Energy averaging of the material parameters is assumed throughout. The exact sense of the implied energy averaging operations is dependent upon the excitation mechanism (normally thermal activation over the barrier or alternatively photo activation, when the junction is irradiated by external light source).

2.1.6.1 Magnetic field effects within the thermionic-emission model

In the thermionic emission model this can be described introducing spin-polarised currents:

$$J_\updownarrow = q \int_{E_c}^{q\phi_n} v_{F\updownarrow} \frac{dn_\updownarrow}{dE} dE \tag{2.1.149}$$

which when the energy of the excitations is not too large may be approximated by the energy averages (at the quasi-Fermi level) as $J_\updownarrow = q\langle v_{F\updownarrow} n_\updownarrow \rangle_{E_F}(q\phi_n - E_c \pm g_m \mu_B B)$ The magneto-conductance ratio:

$$MC = \frac{(J_{\uparrow B} + J_{\downarrow B}) - (J_{\uparrow 0} + J_{\downarrow 0})}{(J_{\uparrow 0} + J_{\downarrow 0})} \tag{2.1.150}$$

[1] Provided, of course, that measurements have been performed in the broad-enough temperature window, where the thermionic-field emission model is valid.

can thus be approximated, for the case of small fields, with:

$$MC \approx -\frac{\langle v_{\mathrm{F}} n_{\uparrow}\rangle - \langle v_{\mathrm{F}} n_{\downarrow}\rangle}{\langle v_{\mathrm{F}} n_{\uparrow}\rangle + \langle v_{\mathrm{F}} n_{\downarrow}\rangle}\frac{g_{\mathrm{m}}\mu_{\mathrm{B}}B}{kT} \approx -\alpha_{\mathrm{m}}^{\mathrm{c}}\frac{g_{\mathrm{m}}\mu_{\mathrm{B}}B}{kT} \tag{2.1.151}$$

As is easily noticed, the effect is small, of the order of 1 per cent in 5 T (easily achievable field with a superconducting magnet) and room temperature.

A slightly modified version of the above model (applied to the case of a magnetic semiconductor) was suggested by Köhler *et al.* (2004); Ziese *et al.* (2005), where the exchange splitting existing in the conduction band of ferromagnetic semiconductors Δ_{ex} is included explicitly in the energy splitting within rigid bands approximation:

$$E_{\mathrm{c}\uparrow(\downarrow)} = E_{\mathrm{c}} - (+)\frac{\Delta_{\mathrm{ex}}}{2} - (+)g_{\mathrm{s}}\mu_{\mathrm{B}}B \tag{2.1.152}$$

where E_{c} is the average conduction band edge and $g_{\mathrm{s}} \approx 2$ is the gyromagnetic ratio in the semiconductor. The spin-polarised current density becomes:

$$J_{\uparrow(\downarrow)} = \frac{A^{\star}T^2}{2}\exp\left(-\frac{\phi_{\mathrm{b}} - (+)\Delta_{\mathrm{ex}}/2 - (+)g_{\mathrm{s}}\mu_{\mathrm{B}}B}{kT}\right)\left[\exp\left(\frac{qV_{\mathrm{a}}}{\Upsilon kT}\right) - 1\right] \tag{2.1.153}$$

where $A^{\star}$ and Υ have their usual meanings. The total current density is thus given by:

$$J = (J_{\uparrow} + J_{\downarrow}) = A^{\star}T^2\exp\left(-\frac{\phi_{\mathrm{B}}}{kT}\right)\cosh\left(\frac{\Delta_{\mathrm{ex}} + 2g_{\mathrm{s}}\mu_{\mathrm{B}}B}{2kT}\right)\left[\exp\left(\frac{qV_{\mathrm{a}}}{\Upsilon kT}\right) - 1\right] \tag{2.1.154}$$

For realistic externally-applied magnetic fields $g_{\mathrm{m}}\mu_{\mathrm{B}} \ll \Delta_{\mathrm{ex}}$ and equation 2.1.154 can be expanded into Taylor series and only the first three terms kept:

$$J = (J_{\uparrow}+J_{\downarrow}) = A^{\star}T^2\exp\left(-\frac{\phi_{\mathrm{b}}}{kT}\right)\cosh\left(\frac{\Delta_{\mathrm{ex}}}{2kT}\right)\left[1 + \alpha^{\mathrm{c}}\frac{g_{\mathrm{s}}\mu_{\mathrm{B}}B}{kT} + \left(\frac{g_{\mathrm{s}}\mu_{\mathrm{B}}B}{kT}\right)^2\right]\left[\exp\left(\frac{qV_{\mathrm{a}}}{\Upsilon kT}\right) - 1\right] \tag{2.1.155}$$

where the spin polarisation in the absence of external magnetic field is approximated (for the case of parabolic band dispersions) as:

$$\alpha^{\mathrm{c}} = \tanh\left(\frac{\Delta_{\mathrm{ex}}}{2kT}\right) \tag{2.1.156}$$

As it can be easily seen, while $\alpha^{\mathrm{c}}g_{\mathrm{s}}\mu_{\mathrm{B}}B \ll kT$ the resulting magnetoresistance (magneto-conductance) is linear in applied magnetic field and inversely proportional to the temperature:

$$MC \approx \alpha_{\mathrm{s}}^{\mathrm{c}}\frac{g_{\mathrm{s}}\mu_{\mathrm{B}}B}{kT} \tag{2.1.157}$$

The change of sign between 2.1.151 and 2.1.157 can potentially result in partial cancellation of the magnetoresistance (magneto-conductance) effects in a diffused barrier where zero-applied-field polarisation is not vanishing at both sides of the junction. In the limiting case of a metal

and semiconductor having similar gyromagnetic ratios $g_{\rm m} \approx g_{\rm s}$ and comparable polarisations close to the interface $\alpha^{\rm s}$, the net effect may tend to zero.

Before continuing further, an important consequence of the conservation of the component of the Fermi momentum $k_{\rm F}$ parallel to the interface and the thermionic emission theory should be mentioned. That is that electrons are emitted into the metal in a narrow cone of directions of angle $\theta_{\rm e} \approx \overline{v}/v_{\rm F}$ in the limit of low temperatures and high mobilities $\overline{v} \ll v_{\rm F}$. The same is true for electrons incident at the interface from the metal. It is therefore useful to keep the quantization direction (the applied field direction) normal to the interface, thus reducing geometric factors associated with the finite angles between $k_{\rm F}$ and B.

2.1.6.2 Field effects within the drift-diffusion model

For the case of drift-diffusion limited transport, the derivation of the magneto-conductance ratio is more involved and features completely new behavior, namely the effect is non-zero even when the metal is completely spin-symmetric[1]:

$$MC \approx \frac{D_\uparrow \sqrt{\frac{2N_{\rm d}}{\epsilon_{\rm s}}(q\phi_{\rm b} - g_{\rm m}\mu_{\rm B}B) + C} + D_\downarrow \sqrt{\frac{2N_{\rm d}}{\epsilon_{\rm s}}(q\phi_{\rm b} + g_{\rm m}\mu_{\rm B}B) + C} - (D_\uparrow - D_\downarrow)\sqrt{\frac{2N_{\rm d}}{\epsilon_{\rm s}}q\phi_{\rm b} + C}}{(D_\uparrow + D_\downarrow)\sqrt{\frac{2N_{\rm d}}{\epsilon_{\rm s}}q\phi_{\rm b} + C}} \tag{2.1.158}$$

where $D_\updownarrow$ is the spin-dependent diffusion coefficient and C is a constant with respect magnetic field energy barrier. It is well justified for experimentally achievable applied magnetic fields $g_{\rm m}\mu_{\rm B}B \ll q\phi_{\rm b}$ to expand in Taylor series with respect to B. The resulting linear approximation to MC is given by:

$$MC \approx \beta_{\rm s}\frac{g_{\rm m}\mu_{\rm B}B}{2q\phi_{\rm b}} \tag{2.1.159}$$

where $\beta_{\rm s}$ is the spin-asymmetry of the diffusion coefficient in the semiconductor, defined as:

$$\beta_{\rm s} = \frac{D_\uparrow - D_\downarrow}{D_\uparrow + D_\downarrow} \tag{2.1.160}$$

Therefore, measurement of magneto-conductance (magnetoresistance) can, in principle, yield information about spin-asymmetries in non-magnetic semiconductors.

It is important to note the fundamental difference between the magnetic field effects within the thermionic emission and the drift-diffusion models, that originates in the very different limiting carrier velocities assumed, and therefore very different saturating current densities:

$$\begin{aligned} J_{\rm S}^{\rm TE} &= qN_{\rm c}v_{\rm R}\exp\left(-\frac{\phi_{\rm b}}{V_{\rm t}}\right) \\ J_{\rm S}^{\rm DD} &= qN_{\rm c}v_{\rm D}\exp\left(-\frac{\phi_{\rm b}}{V_{\rm t}}\right) \end{aligned} \tag{2.1.161}$$

[1] Only as far as electronic density of states is concerned. Complete spin-symmetry, of course, requires the equality of all transport coefficients, like for example, characteristic scattering times.

where the Richardson velocity v_{R} and the drift velocity v_{D} are given by:

$$\begin{aligned} v_{\mathrm{R}} &= \sqrt{\frac{kT}{2\pi m_{\mathrm{c}}^{\star}}} \\ v_{\mathrm{D}} &= \mu_{\mathrm{n}}\mathcal{E}_{\max} \approx \frac{q\tau_{\mathrm{n}}\phi_{\mathrm{b}}}{m_{\mathrm{c}}^{\star}x_{\mathrm{d}}} \end{aligned} \tag{2.1.162}$$

where τ_{n} is the mean free time of the conduction electrons in the semiconductor. Therefore in the case of thermionic emission, the Zeeman energy $g\mu_{\mathrm{B}}B$ is compared with the thermal energy kT, while for the case of drift-diffusion limited transport, the relevant scale is the kinetic energy $q\phi_{\mathrm{b}}$.

Another drift-diffusion related magnetic field effect is the geometric magnetoresistance related change of mobility. The electron mobility in a direction transverse to the applied magnetic field B is given by (see Swami & Tantry (1972)):

$$\mu_{\mathrm{n}}(B) = \mu_{\mathrm{n}}(0)\left(1 - \mu_{\mathrm{n}}^{2}(0)B^{2}\right) \tag{2.1.163}$$

and, therefore, the resulting diffusion constant (using the Einstein relation $\mu = \frac{qD}{kT}$) is:

$$D_{\mathrm{n}}(B) = D_{\mathrm{n}}(0)\left(1 - \frac{q^{2}}{k^{2}T^{2}}D_{\mathrm{n}}^{2}(0)B^{2}\right) \tag{2.1.164}$$

which is the truncated expansion of the well-known Townsend expression from the theory of gas plasmas (see Bickerton & von Engel (1955)):

$$D_{\mathrm{n}}(B) = \frac{D_{\mathrm{n}}(0)}{1 + \left(\omega_{\mathrm{L}}\tau_{\mathrm{n}}\right)^{2}} \tag{2.1.165}$$

where $\omega_{\mathrm{L}} = \frac{qB}{mc^{\star}}$ is the Larmor frequency, and $\tau_{\mathrm{n}} = \frac{\mu_{\mathrm{n}}}{qm_{\mathrm{c}}^{\star}}$ is the mean electronic life time.

The saturation current density $J_{\mathrm{S}}^{\mathrm{DD}}$ is therefore magnetic field dependent and can thus be approximated as:

$$J_{\mathrm{S}}^{\mathrm{DD}}(B) \approx J_{\mathrm{S}}^{\mathrm{DD}}(0)(1 - \mu_{\mathrm{n}}^{2}B^{2}) \tag{2.1.166}$$

Therefore, the magneto-conductance will be given by:

$$MC \approx -\mu_{\mathrm{n}}^{2}B^{2} \tag{2.1.167}$$

and because of its quadratic field dependence can potentially yield effects as large as 384 % in 14 T, in high-mobility silicon ($\mu_{\mathrm{n}} \leq 1400$ cm^2/Vs). The large possible effects pose special requirements on field alignment, so as to avoid magnetic field components transverse to the current direction[1]. Nevertheless, for very large mobilities, the validity of the drift-diffusion

[1] In reality, the mobilities close to the interface are often much smaller $\mu_{\mathrm{n}} \leq 100$ cm^2/Vs, due to disorder scattering.

model is limited and the magneto-conductance reduces to the expressions discussed earlier in section 2.1.6.1. Moreover, the electron mobility is generally not constant and decreases at large electric fields (above about 0.1 MV/m, for silicon), which are commonplace in the depletion region of Schottky junctions.

It should be noted, also, that analogous effects, due to bulk magnetoresistance, exist in the neutral region of the semiconductor side of Schottky junctions. For diodes with large series resistance R_s, this may result in significant and bias dependent magneto-conductance $MC(B;V_a)$.

2.1.6.3 Magnetic effects within the Crowell-Sze model

The realisation of the fact that the saturation current depends on the recombination velocity v_r, which is only to a first approximation equal to the Richardson velocity v_R, leads to the conclusion that that potential influence of the magnetic field on the current transport in Schottky junctions can appear through magnetic field dependence of the recombination velocity.

Starting with equation 2.1.38, which can be integrated analytically to give:

$$v_r = \frac{1}{2}v_d\left[1+\operatorname{erf}\left(\frac{2}{\sqrt{\pi}}\frac{v_d}{v_R}\right)\right]+v_R\exp\left(-\frac{1}{4\pi}\frac{v_d^2}{v_R^2}\right) \tag{2.1.168}$$

which simplifies in the limit of small diffusion velocity $v_d \ll v_R$ (by keeping only the first therm of the Taylor expansion) to:

$$v_r = v_R + \frac{v_d}{2}\left(1+\frac{v_d}{v_R}\right) \tag{2.1.169}$$

and in the limit of large drift-diffusion velocity $v_d \gg v_R$ to

$$v_r = v_d \tag{2.1.170}$$

The impact external magnetic field in second case has already been analysed as it is equivalent to the one for the drift-diffusion model, as in the sense of this approximation $v_d \approx v_D$ and:

$$J_S = qN_c v_d \exp\left(-\frac{\phi_b}{V_t}\right) \tag{2.1.171}$$

The first case is more informative as it gives the first order drift-diffusion correction to the thermionic emission theory. The saturation current density as a function of the external magnetic field B can be approximated as:

$$J_S(B) = \left[qN_c v_R + \frac{q^2 N_c}{2m_c^\star}\tau_n(B)\mathcal{E}_{max}(B)\right]\exp\left(-\frac{\phi_b(B)}{V_t}\right) \tag{2.1.172}$$

therefore, the magnetic field can potentially have impact via altering the barrier height ϕ_b, by changing the maximal electric field in the junction $\mathcal{E}_{max}$ (as a function of the barrier height or

the depletion layer width), or by influencing the carriers mean free time τ_c (which may mean changing the mean collision time or the mean recombination time). Changes, in the depletion layer width as a function of magnetic field, have been reported by Nakagawa *et al.* (2005), in heterojunctions, though the reason behind the effect is still not clear.

Simplified analysis can be pursued on the basis of the full depletion approximation starting from equation 2.1.28. Apart from the direct dependence of the depletion layer width x_d on the barrier height $\phi_b(B)$, which can be potentially a function of the external magnetic field[1], there may be indirect dependence going beyond the full-depletion approximation, as the magnetic field-induced shifts in energy would be mostly influential in the regions where the band bending is small[2]. Moreover, such magnetic field effects would be vanishingly small in nonmagnetic semiconductors.

It is in principle possible to influence the depletion layer width x_d via its dependence on the permittivity of the semiconductor ϵ_s. For a fully degenerate semiconductor, the correction to the permittivity is proportional to the density of states at the Fermi level, which is very unsensitive to external magnetic field as $g_s\mu_B B \ll E_F$ and therefore:

$$\epsilon_s(\mathbf{k}) \approx \epsilon_0 \left(1 + \frac{k_F}{k^2}\frac{m_c^\star q^2}{\hbar^2 \epsilon_0}\right) \tag{2.1.173}$$

This is a consequence of the fact that for small magnetic fields, or high temperatures the spin-split density of states can be approximated like:

$$\mathcal{D}_\updownarrow(E) = \frac{1}{2}\mathcal{D}(E \pm g_s\mu_B B) \tag{2.1.174}$$

which can be expanded in Taylor series around $B = 0$:

$$\mathcal{D}_\updownarrow(E) = \frac{1}{2}\mathcal{D}(E) \pm \frac{1}{2} g_s\mu_B B \frac{\partial}{\partial E}\mathcal{D}(E) + \frac{1}{4} g_s^2 \mu_B^2 B^2 \frac{\partial^2}{\partial E^2}\mathcal{D}(E) + \ldots \tag{2.1.175}$$

as the total carrier density can be approximated like:

$$n \approx \int_{-\infty}^{\infty} \left[\mathcal{D}_\uparrow(E) + \mathcal{D}_\downarrow(E)\right] f(E) \mathrm{d}E \tag{2.1.176}$$

where $f(E)$ is the Fermi distribution function, for the degenerate case:

$$f(E) = \frac{1}{\mathrm{e}^{\frac{E-\eta}{kT}} + 1} \tag{2.1.177}$$

[1] This case has been covered already in the treatment of the magnetic field effects within the Bethe model (see section 2.1.6.1)

[2] This may happen at the edge of the edge of the depletion region, where the full depletion approximation is not well satisfied

or simply the Boltzmann distribution for the nondegenerate case:

$$f(E) = \mathrm{e}^{-\frac{E-\eta}{kT}} \tag{2.1.178}$$

Therefore, in both the degenerate and the nondegenerate cases, the total carrier density can be expanded as:

$$n(B) \cong n(0) + g_{\mathrm{s}}^2 \mu_{\mathrm{B}}^2 B^2 \int_{-\infty}^{\infty} f(E) \frac{\partial^2}{\partial E^2} \mathrm{D}(E) \mathrm{d}E \tag{2.1.179}$$

and is essentially constant with applied magnetic field B, independently of the carrier gas degeneration[1]. Consequently, the permittivity ϵ_{s} is almost constant, up to a very small quadratic correction in field:

$$\epsilon_{\mathrm{s}}(B) = \epsilon_0 \left\{ 1 + \frac{k_{\mathrm{F}}}{k^2} \frac{m_{\mathrm{c}}^{\star} q^2}{\hbar^2 \epsilon_0} \left[1 + O\left(B^2\right) \right] \right\} \tag{2.1.180}$$

and the depletion layer width would not be influenced by it.

It is clear, also, that sizeable effects are expected when the mean recombination time is influenced by external magnetic field, only from regions close to the metal-semiconductor interface, where the electric field $\mathcal{E}(x)$ is large. There is little experimental evidence for external magnetic effects on Schottky diodes, related to recombination rate changes (see Miller & Lobb (1994)). The transitions involved, are considered to be within the singlet and triplet states formed by a donor-acceptor pair, or within ground and exited states of a single recombination centre. As a toy model, a simple system of two spins $\mathbf{s}_1$ and $\mathbf{s}_2$ of $|\mathbf{s}_{1,2}| = \frac{1}{2}$ can be considered, with the total spin equal to $\mathbf{s} = \mathbf{s}_1 + \mathbf{s}_2$. As the recombination process should satisfy the conservation of energy, momentum, angular momentum and spin, if the initial state has $|\mathbf{s}| = 1$, the most probable transition before recombination is to a state with $|\mathbf{s}| = 0$, i.e. from a triplet state to a singlet state. Also, the transition probability is generally higher for initial states with $s_z = 0$ rather than for states with $s_z = \pm 1$, if standard isotropic exchange and dipolar interactions couple the two spins. Therefore, should a level crossing occur for some value of the applied magnetic field, either between $|\mathbf{s}| = 1$ and $|\mathbf{s}| = 0$ levels, or between $s_z = \pm 1$ and $s_z = 0$ levels; it will result in enhanced recombination probability, or more generally in a change between low and high recombination probability[2].

[1] This cancellation of the linear order in B is not the case for other thermodynamic observables such as the total electronic polarisation $P = \int_{-\infty}^{\infty} \left[\mathcal{D}_{\uparrow}(E) - \mathcal{D}_{\downarrow}(E) \right] f(E) \mathrm{d}E \approx g_{\mathrm{s}} \mu_{\mathrm{B}} B \int_{-\infty}^{\infty} f(E) \frac{\partial}{\partial E} \mathcal{D}(E) \mathrm{d}E$, and leads to the concept of Pauli paramagnetic susceptibility.

[2] This effect should be differentiated from the popular electrically detected magnetic resonance (EDMR) due to spin-dependent recombination (see for example reference Hornmark *et al.* (2000)). The latter depends crucially on the application of RF fields in order to achieve resonant transitions for a given applied magnetic field. The effect, under consideration here, does not require RF fields, as it depends (for example) on the thermodynamic population of the donor magnetic levels in conditions close to equilibrium.

The field B_{rec} for which such an enhanced recombination may occur for the above toy system, can be determined by finding the eigenvalues of the model Hamiltonian:

$$\mathcal{H} = -g\mu_{\mathrm{B}}\mathbf{B}\cdot\mathbf{s} + \frac{J_{\mathrm{ex}}}{2}\left[s(s+1) - \frac{3}{2}\right] - \frac{J_{\mathrm{d}}}{2}\left[3s_z^2 - s(s+1)\right] \tag{2.1.181}$$

where J_{ex} is the isotropic exchange energy integral, and $J_{\mathrm{d}} = \frac{\mu_0\mu_{\mathrm{B}}^2}{d_0^3}$ is the dipole coupling energy integral, and d_0 is average distance between the spins (analogous to the characteristic distance of the electron-hole pair or the trap radius). There are four eigenvalues ($\mathbf{B} \parallel z$):

$$\begin{aligned}
&-\frac{3}{4} && (s=0, s_z=0)\\
&\frac{J_{\mathrm{ex}}}{4} - \frac{J_{\mathrm{d}}}{2} - g\mu_{\mathrm{B}}B && (s=1, s_z=+1)\\
&\frac{J_{\mathrm{ex}}}{4} + J_{\mathrm{d}} && (s=1, s_z=0)\\
&\frac{J_{\mathrm{ex}}}{4} - \frac{J_{\mathrm{d}}}{2} + g\mu_{\mathrm{B}}B && (s=1, s_z=-1)
\end{aligned} \tag{2.1.182}$$

The explicit angular dependence of B_{rec} can be shown to be given by:

$$B_{\mathrm{rec}}(\theta) = \frac{2J_{\mathrm{ex}} - J_{\mathrm{d}}}{2g\mu_{\mathrm{B}}\sqrt{\cos^2\theta + \left[\frac{2J_{\mathrm{ex}} - J_{\mathrm{d}}}{2(J_{\mathrm{ex}} + J_{\mathrm{d}})}\right]\sin^2\theta}} \tag{2.1.183}$$

where $\theta = \angle(\mathbf{B}, \mathbf{z})$ is the angle between the applied magnetic field and the z-axis (the normal to the plane of the junction).

Therefore, in the limit of $\theta \to 0$ the critical field becomes:

$$B_{\mathrm{rec}} = \frac{2J_{\mathrm{ex}} - J_{\mathrm{d}}}{2g\mu_{\mathrm{B}}B} \tag{2.1.184}$$

an therefore can be estimated for $g \approx 2$, $J_{\mathrm{ex}} \approx 0.2$ meVand $J_{\mathrm{d}} \approx 0.4$ meV(see Miller & Lobb (1994)) to be about 0.1 T. For Schottky diodes with large density of potentially different recombination centres, the effect described above, may give rise to detectable and exhibiting nontrivial field dependence changes in conductance, at fixed bias, or change in voltage drop, at fixed current.

While the effects related to direct influence of applied magnetic field on the recombination processes are generally small, in low-doping levels semiconductor-metal junctions, large magnetic field effects may appear if geometric confinement of the injected carriers is introduced by an in-plane external magnetic field. The substantial difference between bulk and surface recombination rates would, in this case, result in large change in saturation current density $J_{\mathrm{S}}(B)$. This is the governing principle of operation of the conventional magneto-diodes (see

Kamarinos & Viktorovitch (1976); Mohaghegh *et al.* (1981)). For low (ideally near-intrinsic) carrier concentrations in the semiconductor the ambipolar diffusion cannot be neglected and the saturation current density for reverse bias operation may be approximated like:

$$J_{\mathrm{S}} = \left(1 + \frac{\mu_{\mathrm{p}}}{\mu_{\mathrm{n}}}\right)\left[q\left(n_{\mathrm{i}} + \delta n\right)\frac{D^{\star}}{\lambda^{\star}} + A^{\star\star}T^{2}\exp\left(-\frac{V_{\mathrm{bi}}}{V_{\mathrm{t}}}\right)\right] \tag{2.1.185}$$

where $\delta n(B)$ is the excess carrier density due to magnetoconcentration (the Suhl effect). It is intuitively clear that variation in density should grow as the ambipolar diffusion length becomes comparable with the width of the depletion region x_{d} or the physical width of the base[1] of the diode. In other words, the effect would become more pronounced when $\frac{\lambda^{\star}}{x_{\mathrm{d}}} \sim 1$, or for short semiconductor base Schottky diode structures. The exact details of the dependence $\delta n(B)$ are strongly geometrically dependent, though for small fields[2] B, the linear term in the Taylor expansion would dominate and therefore:

$$\delta n(B) \propto B \tag{2.1.186}$$

The maximal value of δn is determined by the ambipolar mobility $\mu^{\star} = \frac{\mu_{\mathrm{n}}\mu_{\mathrm{p}}}{\mu_{\mathrm{n}}+\mu_{\mathrm{p}}}$ and the mean recombination time τ_{r} like:

$$\max\left(\delta n\right) = n_{\mathrm{i}}\mu^{\star}\frac{V_{\mathrm{a}}\tau_{\mathrm{r}}}{x_{\mathrm{d}}^{2}} \tag{2.1.187}$$

Therefore, the magneto-conductance is linear in field in small fields $\mu^{\star}B \ll 1$ and can be expressed as:

$$MC = \frac{\delta n}{n_{\mathrm{i}}} \approx \left(\mu^{\star}\right)^{2}\frac{V_{\mathrm{a}}\tau_{\mathrm{r}}}{x_{\mathrm{d}}^{2}}B \tag{2.1.188}$$

Conversely, at high fields $\mu^{\star}B \gg 1$ the magneto-conductance should saturate to a constant value[3] of:

$$MC \approx \mu^{\star}\frac{V_{\mathrm{a}}\tau_{\mathrm{r}}}{x_{\mathrm{d}}^{2}} \tag{2.1.189}$$

Detailed analysis of magnetoconcentration in particular geometries have been reported by Jacšić & Durić (2000); Savitski & Sokolovsky (1995). The influence of the Suhl effect is vanishing for junctions with negligible surface recombination, large base thickness and when the magnetic field $\mathbf{B}$ is aligned normal to the metal-semiconductor interface.

[1] Whichever of the two is smaller, as in any case the conduction should become unipolar at the ohmic contact of the diode.

[2] At high fields and high mobilities $\mu_{\mathrm{n,p}}B \gg 1$ explicit Landau level quantisation has to be taken into account.

[3] Neglecting effects of the applied magnetic field B on either τ_{r} or x_{d}, that would result in higher order corrections, that can be neglected, for the sake of simplicity, but would otherwise prevent $MC(B)$ from saturating, or cause a non-monotonic behaviour thereof.

2.1.6.4 Magnetic field effects on the direct gap recombination

The direct gap recombination has an applied voltage dependence that leads to an increase of the ideality factor of diodes where it is a non-negligible current component. The limiting case being $\Upsilon \to 2$, if the recombination current density $J_r \gg J_S$ is much larger than the saturation current density. In the intermediate case $J_r \lesssim J_S$, a significant magnetic field dependence of the direct gap recombination would lead to a non-monotonic magnetic field dependence of the current density as a function of the applied voltage V_a.

Starting with equation 2.1.52, the recombination current saturation density can be written as:

$$J_r = \frac{q n_i x_d}{2\tau_r} \tag{2.1.190}$$

Any field dependence would possibly arise from one of the following:

1. A magnetic field dependence of n_i is not to be expected, except for the case of a magnetic semiconductor, or a non-magnetic semiconductor with a very large difference between the Lande factors for electrons g_c and holes g_v. For the case of small $g_{c,v}\mu_B B \ll kT$ and non-quantising magnetic fields, the effect may be expressed as:

$$\frac{n_i(B)}{n_i(0)} = \exp\left(-\frac{(g_c - g_v)\mu_B B}{2kT}\right) \approx 1 - \frac{(g_c - g_v)\,\mu_B B}{2kT} \tag{2.1.191}$$

   where equations 2.1.23 have been used for the case of $n_i = n_e = n_h$. Therefore, the resulting in magneto-conductance may be estimated as:

$$MC \approx -\frac{(g_c - g_v)\,\mu_B B}{2kT} \tag{2.1.192}$$

   which is, in most cases, an order of magnitude smaller effect than the ones associated with the magnetic field dependence of the saturation current density $J_S(B)$.

2. Magnetic field effects on x_d have already been analysed in section 2.1.6.3. The magneto-conductance in this case should be similar to the one expected within the drift-diffusion model.

3. As the mean recombination time τ_r can be expressed as:

$$\tau_r = \frac{1}{\overline{v}\sigma_t n_t} \tag{2.1.193}$$

   where $\overline{v}$ is the mean thermal velocity and n_t is the trap concentration; magnetic influence is possible only via the electron and hole capture cross section σ_t(B) of the mid-gap traps. If the capture cross section is isotropic, the effect of external magnetic field would be vanishing, as the quasi-particles (both electrons and holes) velocity distribution is

changed mostly in direction and negligibly in magnitude. For anisotropic capture cross section with tensor component parallel to the applied magnetic field (and parallel to the current) $\sigma_{\parallel}^{\mathrm{t}}$, and transverse component $\sigma_{\perp}^{\mathrm{t}}$; the effective cross section $\sigma_{\mathrm{t}}(B)$ may be estimated like:

$$\sigma_{\mathrm{t}}^2(B) = \left[\frac{1}{1+(\mu^\star B)^2}\right]^2 \left(\sigma_{\parallel}^{\mathrm{t}}\right)^2 + \left\{1 - \frac{1}{\left[1+(\mu^\star B)^2\right]}\right\} \left(\sigma_{\perp}^{\mathrm{t}}\right)^2 \tag{2.1.194}$$

where $\mu^\star$ is the effective mobility and uniform rotation of the electron velocity distribution has been assumed. Expansion into Taylor series to first order in $(\mu^\star B)^2$ yields:

$$\sigma_{\mathrm{t}}(B) = \sigma_{\parallel}\left(1 - \frac{\left(\sigma_{\perp}^{\mathrm{t}}\right)^2 - \left(\sigma_{\parallel}^{\mathrm{t}}\right)^2}{\left(\sigma_{\parallel}^{\mathrm{t}}\right)^2}\right)(\mu^\star B)^2 \tag{2.1.195}$$

As $J_{\mathrm{r}}(B) \propto \sigma_{\mathrm{t}}(B)$, and the effective mobility can be estimated like[1] $\mu^\star = \sqrt{\mu_{\mathrm{n}}\mu_{\mathrm{p}}}$, the magneto-conductance can be shown to be:

$$MC \approx \frac{\left(\sigma_{\perp}^{\mathrm{t}}\right)^2 - \left(\sigma_{\parallel}^{\mathrm{t}}\right)^2}{\left(\sigma_{\parallel}^{\mathrm{t}}\right)^2}\mu_{\mathrm{n}}\mu_{\mathrm{p}}B^2 \tag{2.1.196}$$

Therefore, the effect is proportional to the anisotropy of the scattering cross section and quadratic in applied field.

2.1.6.5 Magnetisation effects on quasi-tunnel-barriers and conductivity mismatch

For sufficiently thin Schottky barriers (for example, in the case of δ-doped surface layer in the semiconductor), the tunnelling current dominates the transport and the current density can be evaluated, following Bratkovsky & Osipov (2003); Osipov & Bratkovsky (2004a,b), like:

$$J_{\updownarrow} = \frac{q}{h}\int \mathrm{d}E\left[f\left(E - E_{\mathrm{Fm}\updownarrow}\right) - f\left(E - E_{\mathrm{F}}\right)\right]\int \mathrm{d}^2 k_{\parallel}\frac{\mathcal{T}_{\updownarrow}(k_{\mathrm{s}})}{(2\pi)^2} \tag{2.1.197}$$

where $f(E)$ is the Fermi function:

$$f(E) = \frac{1}{\mathrm{e}^{E-E_{\mathrm{F}}}+1} \tag{2.1.198}$$

and $\mathcal{T}_{\updownarrow}(k)$ is the transmission probability for spin-up ($\uparrow$) and spin-down ($\downarrow$) electrons and it is assumed that the scattering is purely elastic (the energy is conserved) and that the component of the momentum parallel to the interface $k_{\parallel}$ is conserved. The transmission probability $\mathcal{T}_{\updownarrow}$ can be evaluated for a triangular or rectangular barrier to be:

$$\mathcal{T}_{\updownarrow}(k) = 16a\frac{m_{\mathrm{m}\updownarrow}^\star m_{\mathrm{s}}^\star k_{\updownarrow x}k_x}{\left(m_{\mathrm{s}}^\star k_{\updownarrow x}\right)^2 + \left(m_{m\updownarrow}^\star k_{\mathrm{s}}\right)^2}\mathrm{e}^{-bk_{\mathrm{s}}\delta} \tag{2.1.199}$$

[1] This is strictly justified, only for intrinsic conduction with $n_{\mathrm{e}} = n_{\mathrm{h}} = n_{\mathrm{i}}$.

where $m^{\star}_{\mathrm{m}\updownarrow}$ is the spin-dependent effective mass in the metal, $m^{\star}_{\mathrm{s}}$ is the effective mass in the semiconductor, $k_{\updownarrow x}$ is the x-component of the momentum in the metal, k_x is the x-component of the momentum in the semiconductor, k_{s} is the average momentum in the semiconductor, and a and b are dimensionless coefficients evaluating at ($a \approx 1.2\sqrt[3]{k_{\mathrm{s}}\delta}$, $b = 4/3$) for triangular barrier; and ($a = 1$, $b = 2$) for rectangular barrier. Apart from the approximate analytical solution it is, of course, possible to solve the tunnelling problem numerically, for example employing Monte Carlo integration (see Shen *et al.* (2004)).

Special attention should be paid to the pre-factor in equation 2.1.199. It is because of the very different effective masses and carrier momenta, in metals and semiconductors, that the so called *conductivity mismatch* arises. This limits the possibilities for direct coherent transmission of spin-polarised electrons through thin barriers. For similar reason, it can be also argued that a magnetisation orientation dependence would arise in the saturation current J_{S} of a Schottky diode having large direct tunnelling current component. Of course, any non-equilibrium polarisation created at the metal/semiconductor interface will diffuse (or potentially drift in non-zero applied voltage V_{a}) into the volume of the semiconductor, provided that the bulk diffusion constants $D_{\uparrow}$ and $D_{\downarrow}$ are sufficiently large (see Korošak & Cvikl (2004)). From quantum-mechanical point of view, the states that do not propagate from the metal to the semiconductor or *vice versa* should decay exponentially away from the barrier and contribute to the density of metal-induced gap states mentioned in section 2.1.2.1.

So far, the influence of spin-flip and other inelastic scattering mechanisms has been neglected. In the limit of very strong spin-flip scattering, the quantum-mechanical coherence would be lost over lengths larger than the spin-flip length $\lambda_{\mathrm{s-f}} \propto \overline{v}\tau_{\mathrm{s-f}}$ and over times comparable with the spin-flip time $\tau_{\mathrm{s-f}}$, and the standard diffusive description of the transport is more applicable.

There is however a possibility (which is often thought to be realisable in practice) that $\tau_{\mathrm{s-f}} \gg \tau_{\mathrm{ph}}$, where τ_{ph} is the characteristic time for scattering by phonons. It is in this case, when the up and down spin channels can be treated as independent and the analysis done on the basis of the two-current model.

One more remark is due on the nature of the tunnelling process from the metal to the semiconductor and *vice versa*. In this simplified treatment, the influence of the potentially different symmetry of the unoccupied states (the holes) in the semiconductor have not been taken into account, as the conduction through the majority carriers (the electrons) dominates the transport at moderate biasing. It is possible, however, to envisage a situation, at high bias $qV_{\mathrm{a}} \gg E_{\mathrm{g}}$ when there would be non-negligible tunnelling probability for holes. The problem becomes a one of a single-component wave function in the metal and two-component wave

function in the semiconductor. The transmission coefficient $\mathcal{T}$, thus, may be a non-monotonic function of the applied potential V_a (see for example on p-type Schottky barrier Kalameĭtsev *et al.* (1997)). Though the analytical treatment becomes exceedingly involved, following simple physical arguments, increased recombination current is to be expected in such a situation[1]. It is also clear, that incoherent tunnelling and scattering by phonons or other quasi-particles would mask such effects and render them experimentally undistinguishable.

2.1.6.6 Schottky barriers in quantising magnetic fields

Situations can occur, at low temperature, and high magnetic fields, when $\mu_n B > 1$ and Landau level quantisation of the electrons may occur in the barrier region or in the neutral part of the base in Schottky diodes. Because of the large electric potentials and fields, present in the barrier region, the Landau quantisation, does not lead to an oscillatory behaviour of the conductivity of real junctions (as $\hbar\omega_c \ll \Phi_b$, where $\omega_c = \frac{qB}{m^*}$), rather than a large but purely quadratic magnetoresistance, as pointed by Kotelnikov *et al.* (1993) and Harrison (1961).

The analysis of the effect can be done on the basis of the zero bias conductivity of the barrier σ_j, neglecting mixed magnetic field - electric bias dependence of the build-in electric field $\mathcal{E}_{bi}$, or in other words, accepting that the self-consistent electric field is not influenced by external magnetic field. The junction conductivity can be evaluated as:

$$\sigma_j = \frac{q^2}{\pi\hbar\lambda_B^2} \sum_{i=0}^{i_{max}} N_i \tag{2.1.200}$$

where λ_B is the diffusive magnetic length:

$$\lambda_B = \sqrt{\frac{\hbar}{qB}} \tag{2.1.201}$$

the maximal level index is given by[2]:

$$i_{max} = \left\lfloor \frac{\eta}{\hbar\omega_c} - \frac{1}{2} \right\rfloor \tag{2.1.202}$$

and the occupation probabilities N_i are estimated as (see Kotelnikov *et al.* (1994)):

$$N_i = \exp\left[-\frac{\eta}{\hbar\omega_c} \gamma_c \frac{1}{2\pi^2} \sqrt{\frac{2m_c^\star}{\hbar^2}} \int_{\eta-\hbar\omega_c\left(i+\frac{1}{2}\right)}^{\Phi_b} \mathrm{d}E \frac{\sqrt{E-\eta+\hbar\omega_c\,(i+1/2)}}{q\mathcal{E}_{bi}} \right] \tag{2.1.203}$$

By expansion into Taylor series over $\hbar\omega_c$ it can be shown, that the above expressions lead to quadratic in field corrections to the conductivity in the limit $\Phi_b \gg \hbar\omega_c$.

[1] This situation bears some resemblance with the phenomenon of Andreev reflection at the normal-metal-superconductor interface, the gap being equivalent, essentially, to the formation energy of the Cooper pairs.

[2] Here $\lfloor x \rfloor = \mathrm{floor}(x)$ denotes the integer part of x.

2.1.6.7 Magnetic field effects on the impact ionisation in Schottky junctions

Impact ionisation is a common phenomenon in Schottky structures at high reverse bias. It is the main operating regime of the Zener diodes. Most studies have been perfumed using narrow-gap semiconductors like HgCdTe (see for example Zav'ialov & Radantsev (1994)). Within the framework of the band theory, the electric field induced breakdown can be understood as inter-band tunnelling within the same material caused by band-tilting in large external electric fields, and is possible in fields for which (see Ashcroft & Mermin (1976)):

$$q\mathcal{E}\hbar v_{\mathrm{F}} \gg E_{\mathrm{g}}^2 \tag{2.1.204}$$

where the Femi velocity v_{F} can be estimated at $v_{\mathrm{F}} \approx \frac{E_{\mathrm{F}} a_0}{\hbar}$. Therefore the condition for Zener breakdown can be written as:

$$q\mathcal{E}a_0 \gg \frac{E_{\mathrm{g}}^2}{E_{\mathrm{F}}} \tag{2.1.205}$$

Similar situation may appear in large magnetic fields for which:

$$\hbar\omega_{\mathrm{c}} \gg \frac{E_{\mathrm{g}}^2}{E_{\mathrm{F}}} \tag{2.1.206}$$

The band-gap E_{g} does not have to be the direct, nor the main one in the band structure of the semiconductor. In semiconductors like GaAs, in the band structure of which, two different spin-split hole levels exist, both electric and magnetic field breakdown (or a mixed effect of magnetic field controllable electrical breakdown) are possible. This has been demonstrated experimentally by Sun *et al.* (2004) for Schottky barriers on semi-insulating GaAs. The required large electric fields are only readily achievable in intentionally undoped semiconductors. The presence of a large build-in field $\mathcal{E}_{\mathrm{bi}}$ in a Schottky contact is, to a first approximation, expected to reduce the external electric field necessary to overcome the ionisation threshold as:

$$q\left(\mathcal{E} + \mathcal{E}_{\mathrm{bi}}\right) a_0 \gg \frac{E_{\mathrm{g}}^2}{E_{\mathrm{F}}} \tag{2.1.207}$$

therefore rendering the high-field effects easier to observe experimentally.

The actual magneto-conductance is, of course, geometry and crystallographic orientation dependent. For the case $B \parallel \mathcal{E}$, at low temperature $kT \ll \phi_{\mathrm{b}}$, the magneto-conductance may be expressed as (see Zav'ialov & Radantsev (1994)):

$$MC \approx \sqrt{\frac{E_{\mathrm{g}}}{2m^\star}} \frac{B}{\mathcal{E}} \frac{\cosh\left(\sqrt{\frac{E_{\mathrm{g}}}{2m^\star}} \frac{B}{\mathcal{E}} \frac{g^\star}{2} \frac{m^\star}{m_{\mathrm{e}}}\right)}{\sinh\left(\sqrt{\frac{E_{\mathrm{g}}}{2m^\star}} \frac{B}{\mathcal{E}}\right)} \tag{2.1.208}$$

The behaviour is approximately quadratic in field, at least at low fields for which $\sqrt{\frac{E_{\mathrm{g}}}{2m^\star}} \frac{B}{\mathcal{E}} \lesssim 1$, which makes it hard to differentiate between the contribution of the magnetoresistance of

the diode base and the true field effect, at high current densities in reverse bias (i.e. in the breakdown regime).

2.1.7 Schottky junctions under external illumination

Under external broad-band illumination, additional current contributions are present close to the interface of a Schottky junction. Those are due to the finite probability for a non-equilibrium carrier (uni-polar generation) or electron-hole pair (bipolar generation) to be drifted away from the interface by the build-in electric field, of maximum $\mathcal{E}_{\max}$, before recombination (with characteristic time $\tau_{\rm r}$) would occur. This would be more likely for high barriers as $\mu_{\rm n}\mathcal{E}_{\max}/x_{\rm d} \gg \tau_{\rm r}$ would be satisfied. Schematic representations of the two processes are visualised on figure 2.9.

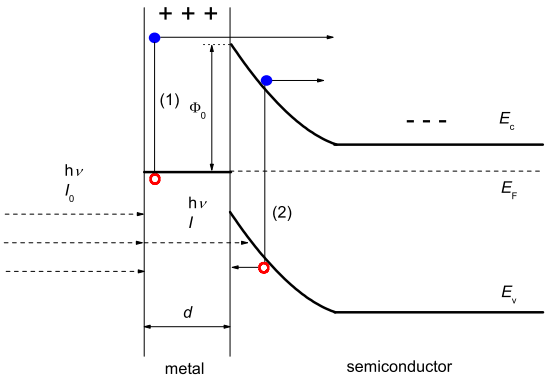

Figure 2.9: Schematic representation of two most probable photoexcitation processes: internal photoemission (1) and generation in the depletion region (2).

It is clear that the maximal achievable voltage would not generally exceed $V_{\rm bi}$ even at low temperatures and high illumination intensities. On the contrary, it is expected that the maximal voltage would be independent of illumination intensity in such conditions. Also the quasi-neutrality condition demands that the following continuity equation is satisfied at any point x across the interface:

$$I_{\rm g}(x) - I_{\rm r}(x) - I(x) = 0 \tag{2.1.209}$$

or that the charge generated per unit time, $I_{\rm g}$ minus the charge recombined per unit time $I_{\rm r}$ must be equal to the current that has left the point of space x after Lehovec (1948).

2.1.7.1 Simple overview treatment

An oversimplified treatment of the photo-voltaic effect in may be achieved by modifying 2.1.33, 2.1.35 and 2.1.36 to include the generated photo-current density J_{g} (which is assumed in the negative direction) as:

$$J_{\mathrm{n}} = J_{\mathrm{d}} \left[\exp\left(\frac{qV_{\mathrm{a}}}{kT} \right) - 1 \right] + J_{\mathrm{g}} \tag{2.1.210}$$

where J_{d} is called the 'dark current density'. The short-circuit current density in such a model is simply equal to the generated photo-current or $J_{\mathrm{SC}} = J_{\mathrm{g}}$. The open-circuit voltage can be obtained from 2.1.210 by setting $J_{\mathrm{n}} = 0$ to be:

$$V_{\mathrm{OC}} = \frac{kT}{q} \ln\left(1 + \frac{J_{\mathrm{g}}}{J_{\mathrm{d}}} \right) \tag{2.1.211}$$

A couple of different effects are considered to dominate the electronic transport in such conditions.

2.1.7.2 Internal photo-emission

One is the so-called internal photo-emission process, which in analogy to the external photo-emission, consists of the 'knocking-out' of electrons from the metal side of the junction into the semiconductor and obeys the modified Einstein condition:

$$q\mathcal{E}_{\max} x_{\mathrm{d}} < h\nu - \Phi_{\mathrm{m}} + \chi_{\mathrm{s}} + \frac{1}{2} m_{\mathrm{c}}^{\star} \overline{v} \tag{2.1.212}$$

which is written for the case of n-type semiconductor. As it can be seen from relation 2.1.212, this process will be more probable for low barrier heights ϕ_{b}. A more detailed analysis on this effect is by analogy borrowed from the theory of the external photo-effect as originally described by Fowler (1931). According to Fowler's hypothesis, the amount of electrons emitted per quantum of absorbed light is proportional to the number of electrons per unit volume of the metal whose kinetic energy normal to the surface augmented by $h\nu$ is sufficient to overcome the potential step at the surface. This statement is, once again, justified by the conservation of momentum parallel to the interface as in paragraph 2.1.6.1. The rough dependence of the density of available states can be easily evaluated as a convolution of a quasi-free electron model density of states $\mathcal{D}(E)$ and the Fermi-Dirac distribution function like:

$$\mathcal{D}^{\star}(\nu) = \int_{0}^{\infty} \frac{\mathcal{D}(x)}{\mathrm{e}^{\frac{x + (\phi_{\mathrm{b}} - h\nu)}{kT}} + 1} \mathrm{d}x \tag{2.1.213}$$

where the density $\mathcal{D}(E)$ can be evaluated like:

$$\mathcal{D}(E) = \sum_{\varkappa} \frac{1}{4\pi^3} \int \delta(E - E_{\varkappa}(\mathbf{k})) \mathrm{d}\mathbf{k} \tag{2.1.214}$$

where the integration is taken over the volume of any primitive cell in $\mathbf{k}$-space and $E_{\varkappa}(\mathbf{k})$ is the dispersion relation for the $\varkappa$-th band. Assuming that the bands can be characterized by a set of effective masses $m^{\star}_{\varkappa}$ the dispersions will be given by $E_{\varkappa}(\mathbf{k}) = \mathbf{k}^2/2m^{\star}_{\varkappa}$ Ashcroft & Mermin (1976).

For the case of primitive metals, a more precise projected density of states was evaluated by Fowler (1931) as:

$$\mathcal{D}^{\star}(\nu) = \frac{2\pi kT}{m^{\star}} \left(\frac{2kT}{m^{\star}}\right)^{1/2} \left(\frac{m}{h}\right)^{3} \int_{0}^{\infty} \frac{\log\{1 + \mathrm{e}^{-x+(h\nu-\Phi_{\mathrm{b}})/kT}\}}{x + (\Phi_{\mathrm{b}} - h\nu)/kT} \mathrm{d}x \tag{2.1.215}$$

For the case of low temperatures $T \to 0$, the above dependence can be approximated like:

$$\mathcal{D}^{\star}(\nu) \propto \begin{array}{ll} (h\nu - \Phi_{\mathrm{b}})^2 & (h\nu > \Phi_{\mathrm{b}}) \\ 0 & (h\nu < \Phi_{\mathrm{b}}) \end{array} \tag{2.1.216}$$

As generally the photo current per quantum of light absorbed $I^{\star}_{\mathrm{g}}(\nu)$ is proportional to the projected density of states $\mathcal{D}^{\star}(\nu)$, within the approximation of equation 2.1.216, the linear extrapolation of $\sqrt{I^{\star}_{\mathrm{g}}(\nu)}$ towards zero produces an estimate of the barrier height as:

$$\Phi_{\mathrm{b}} \approx \lim_{\sqrt{I^{\star}_{\mathrm{g}}(\nu)} \to 0} V_{\mathrm{OC}}\,(h\nu) \tag{2.1.217}$$

2.1.7.3 External photoemission

It should be noted that external photoemission measurements can also yield information about the Schottky barrier height (see for example Eddrief *et al.* (2002)). The evaluation is usually done by measuring the initial position of the Fermi level with respect to the valence-band maximum $E_{\mathrm{F}} - E_{\mathrm{v}}$ on a clean semiconductor surface, and then the band-bending of the valence band with respect to the Fermi-level, upon covering the semiconductor with a metal layer of increasing thickness. Alternatively the difference $E_{\mathrm{c}} - E_{\mathrm{F}}$ can be also traced. This type of studies, normally, require the use of synchrotron sources, because of the high energy resolution requirements.

2.1.7.4 Generation in the depletion region

An alternative mechanism is the generation of electron-hole pairs in the depletion layer at the semiconductor side, which is important for frequencies ν of the incoming photons larger than one necessary for direct-gap transition $\nu_{\mathrm{DG}} = E_{\mathrm{g}}/h$. While in direct gap semiconductors (like in the case of GaAs) it is possible for a photon of high enough energy to generate electron-hole pair, in indirect-gap materials (i.e. silicon) such a transition should include a phonon (or another momentum carrying quasi-particle) in order to satisfy the conservation of the total

momentum. This makes the above mechanism less probable for indirect-gap materials. It should be mentioned that, provided the energy and momentum conservation laws are satisfied, photons can also ionise donor and acceptor levels, and also generate carriers which contribute to the total current.

Following Lehovec (1948) the photo-current density can be written by solving the drift-diffusion equation 2.1.26 in the presence of an additional generation term as:

$$J_{\mathrm{n}} = -\mathfrak{I}\frac{q}{h\nu}\eta^{\star}\left[\exp\left(-\frac{x}{\alpha}\right) - \exp\left(-\frac{x_{\mathrm{d}}}{\alpha}\right)\right] + q(\mu_n n\mathcal{E} + D_n\frac{\mathrm{d}n}{\mathrm{d}x}) \tag{2.1.218}$$

with the appropriate boundary conditions, yielding a solution of the form:

$$J_{\mathrm{g}} = -\mathfrak{I}\frac{q}{h\nu}\eta^{\star}\mathcal{A} \tag{2.1.219}$$

where $\mathfrak{I}$ is the intensity of the light when entering the semiconductor, $\eta^{\star}$ is the number of electrons released by one photon and a factor $\mathcal{A}$, closely related to the quantum yield, defined as:

$$\mathcal{A} = \left[1 + \frac{kT}{q\mathcal{E}_{\max}\alpha}\right]^{-1} - \exp\left(\frac{x_{\mathrm{d}}}{\alpha}\right) \tag{2.1.220}$$

where α is the absorption length of the light in the semiconductor. Of course, when the light is not monochromatic, equation 2.1.219 should be rewritten as and integral over the frequency spectrum of the radiation incident on the junction:

$$J_{\mathrm{g}} = -\int_{\nu_{\min}}^{\nu_{\max}} \mathfrak{I}(\nu)\frac{q}{h\nu}\eta^{\star}(\nu)\mathcal{A}(\nu)\mathrm{d}\nu \tag{2.1.221}$$

As it can be easily seen, using equation 2.1.211, only the short-circuit current will be a linear superposition of the partial currents form resulting each frequency interval $\mathrm{d}\nu$. The photo-voltage under polychromatic illumination, in this simple treatment, is always smaller than the sum of the individual differential effects.

An approximate solution to the drift-diffusion equation 2.1.218 can be found to be (see Rochon & Fortin (1975, 1976)):

$$J_{\mathrm{n}} = -\mathfrak{I}\frac{q}{h\nu}\left(1 - \mathrm{e}^{-\frac{2x_{\mathrm{d}}}{\alpha(\nu)}}\right) \tag{2.1.222}$$

Or taking into account the finite hole diffusion length x_{p} (primarily determined by recombination processes):

$$J_{\mathrm{n}} = -\mathfrak{I}\frac{q}{h\nu}\left(\frac{1 - \mathrm{e}^{-\frac{2x_{\mathrm{d}}}{\alpha(\nu)}}}{1 + \frac{x_{\mathrm{p}}}{\alpha(\nu)}}\right) \tag{2.1.223}$$

As in principle the absorption length in the semiconductor is a function of the magnetic field B, there can be a dependence of the open circuit photovoltage, upon any dipole excitations in the semiconductor that are influenced by external magnetic field, of the kind:

$$V_{\mathrm{OC}} \propto \ln\left(\frac{1}{\alpha(\nu, B)}\right) \tag{2.1.224}$$

Thus the photo-voltage spectra can reflect the details of the electronic structure of the semiconductor (i.e. via Landau-level quantisation in large magnetic fields).

The same is true for the photo-current, and an interesting demonstration is the observation of Franz-Keldysh oscillations in Schottky photo-diodes (see for example Aspnes & Studna (1973); Shamir *et al.* (2001)). The relative change in absorption can be expressed as:

$$\frac{\Delta\alpha(\nu)}{\alpha(\nu)} \propto \exp\left[\frac{-2\Gamma\left(h\nu - E_{\mathrm{g}}\right)^{1/2}}{(\hbar\theta)^{3/2}}\right] \cos\left[\frac{4}{3}\frac{\left(h\nu - E_{\mathrm{g}}\right)^{3/2}}{(\hbar\theta)^{3/2}} + \zeta\right] \frac{1}{(h\nu)^2\left(h\nu - E_{\mathrm{g}}\right)} \tag{2.1.225}$$

where Γ is the band broadening factor, ν is the frequency of the light quanta, ζ is an arbitrary phase factor, and the electro-optic energy is defined via:

$$(\hbar\theta)^3 = \frac{q^2\hbar^2\mathcal{E}^2}{2m^{\star\star}} \tag{2.1.226}$$

where $\mathcal{E}$ is the total electric field in the absorption region and $m^{\star\star}$ is the reduced mass of electrons and holes:

$$m^{\star\star} = \frac{m_{\mathrm{e}}^{\star} m_{\mathrm{h}}^{\star}}{m_{\mathrm{e}}^{\star} + m_{\mathrm{h}}^{\star}} \tag{2.1.227}$$

Therefore, by fitting the oscillations of the photo-current as a function of photon energy, close to the band-gap E_{g} of the semiconductor, it is possible to extract information about the build-in electric field $\mathcal{E}_{\mathrm{bi}}$ close to the metal-semiconductor interface, where optical absorption is strongest and the total electric field is given by:

$$\mathcal{E} = \frac{V_{\mathrm{a}} + V_{\mathrm{bi}} - V_{\mathrm{t}}}{x_{\mathrm{d}}} \tag{2.1.228}$$

With a sufficient spectral resolution it is, also possible to determine individual reduced masses for different types of holes (see for example Shamir *et al.* (2001)).

It should be noted, that the principle effect is the result of the quantisation of the magnetic levels, which increases the energy gap and hence reduce the absorption. The magnetic field also retards the motion of the electron along the electric field, thus further reducing the absorption (Reine *et al.* (1966)).

For weak absorption $x_{\mathrm{d}}/\alpha \ll 1$, the hole diffusion length x_{p} should also be taken into account, and the photocurrent spectrum becomes an oscillating function of ν (see Dmitruk *et al.* (1997)):

$$J_{\mathrm{n}} \propto -\mathfrak{I}\frac{q}{h\nu}\left[\frac{x_{\mathrm{p}}}{\alpha} + \frac{x_{\mathrm{d}}}{\alpha}\left(1 + b(\nu)\right)\right] \tag{2.1.229}$$

where $b(\nu)$ is defined as:

$$b(\nu) = \frac{\cos(y)}{y} - \sin(y) - y\mathrm{Ci}(y) \tag{2.1.230}$$

$$y = \frac{\epsilon_\mathrm{s} 2\sqrt{2m^\star}\,(h\nu - E_\mathrm{g})^{3/2}}{x_\mathrm{d} h q^2 N_\mathrm{d}} \tag{2.1.231}$$

and avails for the experimental determination of x_p by fitting the spectral photocurrent response of the Schottky junction[1]. Or alternatively, the photon flux $\mathfrak{I}$ for a constant photovoltage can be plotted against $\alpha(\nu)$ and x_p extracted, as the negated intercept. This is the basis of the Goodman method for determination of minority carrier diffusion lengths as described by Choo (1995); Goodman (1961).

It is important to note that the spectrum $\mathfrak{I}(\nu)$ of the light reaching the junction is affected by the reflection and absorption of light in the metal electrode, which makes it necessary to keep the metal film layer thickness as low as possible (about 10 nm for Au). The spectral intensity reaching the junction is given by:

$$\mathfrak{I}(\nu) = \mathfrak{I}_0(\nu)\,(1 - \mathcal{R}(\nu, d) - \mathcal{A}(\nu, d)) \tag{2.1.232}$$

where $\mathfrak{I}_0(\nu)$ is the spectral intensity reaching the structure, $\mathcal{R}(\nu, d)$ is the reflection coefficient, $\mathcal{A}(\nu, d)$ is the absorption coefficient and d is the metal film thickness.

Using the short-circuit current J_SC and the open circuit voltage V_OC a model-dependent estimate of the barrier height can be extracted. As an example for the thermionic emission model 2.1.35, following the derivation of Chen *et al.* (1993b), modified to reflect the limit of large illumination intensity the barrier height ϕ_b may be expressed as:

$$\phi_\mathrm{b} = V_\mathrm{OC}(\mathfrak{I}) - \frac{kT}{q} \ln\left(\frac{J_\mathrm{SC}(\mathfrak{I})}{A^\star T^2}\right) \tag{2.1.233}$$

It is clear that at low temperatures the pre-factor in the second term in 2.1.233 is becoming decreasingly important and as the logarithm is generally of the order of unity or less, up to a correction of a few meV, the open-circuit photo-voltage V_OC is constant (independent of the light intensity $\mathfrak{I}$). Therefore the barrier height may be simply expressed as:

$$\phi_\mathrm{b} = \lim_{\substack{\mathfrak{I} \to \infty \\ T \to 0}} V_\mathrm{OC}(\mathfrak{I}) \tag{2.1.234}$$

[1] This effect is analogous to the spectral oscillations or 'thickness fringes' observed when a solid film's thickness is comparable with the wavelength of the incoming electromagnetic radiation. More generally, both reflectance and absorbance are influencing the real and imaginary parts of the optical refractive index and are thus rendering it a function of the electric field distribution in the semiconductor, which can be influenced by both minority and majority carrier processes.

For a realistic junction, the limit of $T \to 0$ is defined as temperatures below which the conduction band is depleted from carriers or $T \approx (E_c - E_d)/k$ and the limit of $\mathfrak{I} \to \infty$ is reached for intensities for which the rate of recombination is overwhelmed by the rate of generation. As pointed out by Chen *et al.* (1994) in cases when the recombination current is large, there can be substantial deviations of the barrier heights determined by photo-voltage measurements and those obtained by internal photo-emission.

2.1.7.5 The time-decay of photo-voltage

An important question from experimental point of view concerns the temporal behaviour of the photo-voltage as the illumination is switched-on, switched off or changed in general. As Schottky junctions, in general, exhibit substantial, and voltage dependent, barrier capacitance $C_j(V_a)$ given by equation 2.1.32. Following Chen *et al.* (1993a), the change of depletion region charge for a time interval dt is given by:

$$dQ_j = C_j dV_a \tag{2.1.235}$$

and as the discharging (charging) current can be written as $J_d = -\frac{dQ}{dt}$ the discharging (charging) time can be expressed like:

$$t_d = \int_{V_a(0)}^{V_a(t_d)} \frac{C_j(V)}{J_d} dV \tag{2.1.236}$$

where J_d is the sum of all current components in the junction, apart from the photo-current on discharging at zero light intensity, and the sum of all current components on charging-up. It is, therefore, easy to understand that the discharging times can be exceedingly large for cases with high effective capacitance (i.e. small number of recombination centres, low temperatures, thin depletion regions and low leakage currents).

2.2 Transport measurements on Schottky junctions

2.2.1 Initial characterisation of magnetic and nonmagnetic Schottky junctions

The details of the sample preparation are given in appendix A.6.1. An important step in characterising the Schottky diode structures is the estimation of the series resistance contribution (the resistance of the participating in the active transport part of the semiconductor substrate) and the linearity of the non-rectifying back contact. An example of indium-alloyed contact on n-type silicon is given on figure (2.10).

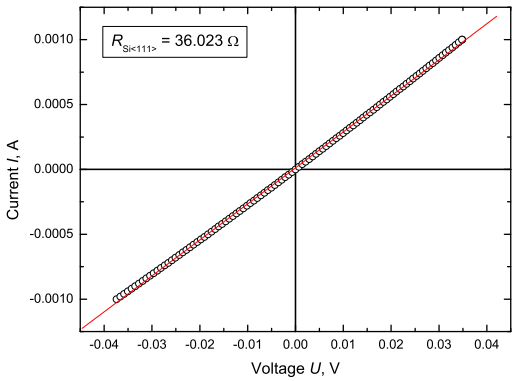

Figure 2.10: Current-voltage characteristic of a Ohmic back contact to Si. Actually two of them on both sides of a chip.

The series resistance due to the semiconductor substrate has a substantial influence on the current-voltage characteristics of the Schottky diodes, especially at high currents and low temperatures. Because of the voltage drop on the substrate, the bias on the junctions is different from the measured one by an amount that is non-linear in applied voltage and magnetic field. Initial estimates of the series resistance are required in virtually all procedures for extracting junction parameters, based on non-linear minimisation.

Observation of small effects, due to intrinsic magnetoresistance effects in the barrier region, is readily obscured by large series resistance and magnetoresistance. The magnetoresistance ratio can be as high as 25 % in 5 T at 300 K for medium n-doped Si, see figure (2.11), and about 5 % in 5 T for GaAs.

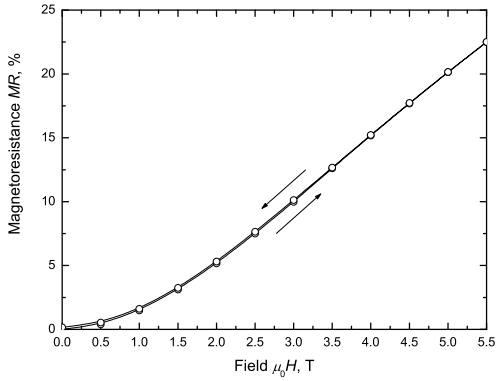

Figure 2.11: Magnetoresistance of n-type Si substrate at 300K.

Another complication due the series resistance contribution is related to its temperature de-

pendence. Observation of small effects at high (ambient and above ambient) temperature can be hindered by temperature instability and the exponential character of the thermal activation of carriers in the base of the diode. The activation laws differ depending on the degree of compensation of the semiconductor. For weak compensation and at sufficiently low temperatures $kT \ll E_g$, the carrier concentration can be approximated as (see for example Prohorov (1988)):

$$n = \frac{1}{\sqrt{2}}\sqrt{N_d N_c}\exp\left(-\frac{E_d}{2kT}\right) \tag{2.2.1}$$

for higher degree of compensation, the Fermi level is essentially coincident with the donor level $E_F \approx E_d$ and therefore the thermal activation obtains the form:

$$n = N_c \frac{N_d - N_a}{2N_a}\exp\left(-\frac{E_d}{kT}\right) \tag{2.2.2}$$

At high temperatures $kT \sim E_g$, the carrier activation is dominated by simultaneous electron-hole pair generation through the fundamental gap and therefore reads:

$$n = N_c \exp\left(-\frac{E_g}{kT}\right) \tag{2.2.3}$$

An example of activation plot, for medium n-type doped Si, is shown on figure 2.12. The temperature sensitivity exceeds 1 % per K, which imposes strict requirements at the temperature control and stabilisation of all experiments performed. The activation energy obtained, corresponds to low degree of compensation, low temperature limit of $E_d = 0.042(1)$ eV, which agrees well with the value expected for low dopings of P in Si (see Collection (2007)) $E_d = 0.045(1)$ eV.

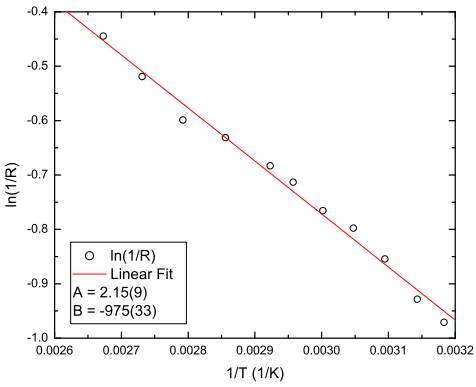

Figure 2.12: Thermal activation plot for moderately doped n-type Si (The dopant is phosphorous, at a level of $5 \cdot 10^{17}$ cm^{-3}). The slope corresponds to $E_d = 0.042(1)$ eV.

When many diodes have to be fabricated, it is important, that their rough characterisation, at ambient conditions, is a fast timesaving process. An example of such a measurement, using

a fast alternating current and voltage hysteresiograph (details are provided in appendix A.6.2), is shown on figure (2.13). This technique allows, also, for the estimation of the junction

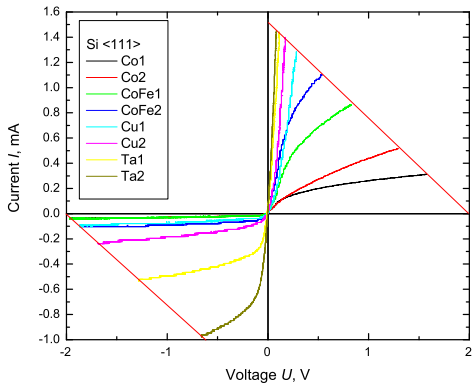

Figure 2.13: Current-voltage characteristics of set of Schottky junctions. Compliance limits are shown with red lines.

capacitance and breakdown voltage. $I - V$ traces for Si base diodes, measured at ambient temperature and different voltage sweep rates, are shown at figures 2.14 and 2.15. There are couple of points that differentiate the various diodes tested (see figure 2.14):

1. The Au/Si junction behaviour is closest to ideal (can be readily compared with a commercial Zener diode), though the ideality factor deduced $\Upsilon \approx 1.8$ is close is rather close to 2[1].

2. The Cu/Si junction exhibits an ideality factor $\Upsilon \approx 2$, which suggests recombination current to be the limiting factor. Further, a large decrease in differential conductance is observed over about 0.2 V, which may be due to drift-diffusion or tunnelling limitations on the forward current density, possibly a consequence of large diffusion of Cu atoms across the metal-semiconductor interface.

3. The Co/Si and CoFe/Si junctions exhibit large forward, as well as, large reverse current densities, which suggests that tunnelling may be the dominant current limiting mechanism. This may be attributed to the formation of Fe or Co silicides in the interface, smoother composition gradients across the interface and deterioration of the rectifying behaviour of the junctions[2].

[1] Ideality factors larger than about 1.04 for Si based Schottky diodes are associated with the inapplicability of the thermionic emission theory and a necessity to extend the modelling to account for tunnelling, recombination and other current components.

[2] This should not be directly associated with the barrier heights of abrupt 3d-metal silicide/Si junctions, which are found to be in the region 0.5 - 0.8 eV. See for example (Rhoderick & Williams (1988))

A comparison of the high-frequency $I - V$ curve traces, measured at $\nu = 20$ kHz, reveals a much larger reverse bias capacitance for Co/Si and CoFe/Si junctions, which suggests a much narrower depletion region in these Schottky junctions, which suggests a larger effective concentration of donor centres N_d and/or smaller effective dielectric constant ϵ_s close to the interface. Both of these speculations are consistent with the already noted (point 3 above) dominance of the tunnelling current component in these junctions.

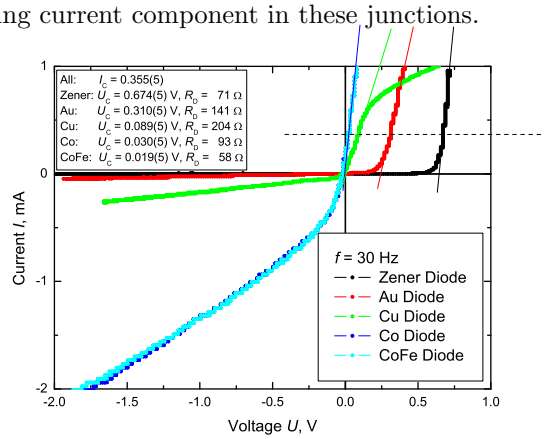

Figure 2.14: Comparison between magnetic, nonmagnetic Schottky junctions and a standard -6 V Zener diode at $\nu = 30$ Hz.

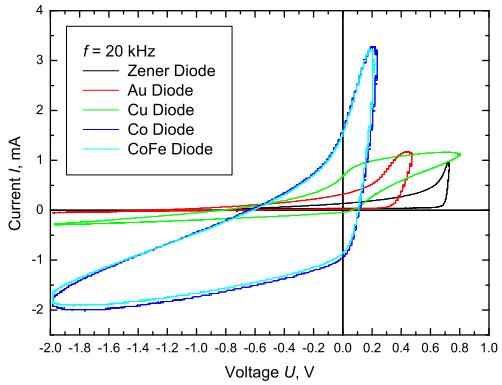

Figure 2.15: Comparison between magnetic, nonmagnetic Schottky junctions and a standard -6 V Zener diode at $\nu = 20$ kHz. Bad (capacitive) contacts are easily noticed.

The $I - V$ characteristics of contacts of various metals to medium n-doped GaAs and Nb:SrTiO (Nb:STO) are shown on figures 2.16 and 2.17, respectively. The junctions are prepared by touching a sharpened needle of the metal of interest to the cleaned semiconductor surface. Small area tunnelling and point contacts prepared in this way, only last for few seconds, if special care is not taken to stabilise them. This time is only sufficient for quick, low-resolution

characterisation. Largely different contact behaviours are found, ranging from close to ideal diode rectification, to almost pure tunnelling (evidenced by the nonlinear, antisymmetric with respect to bias reversal current dependencies).

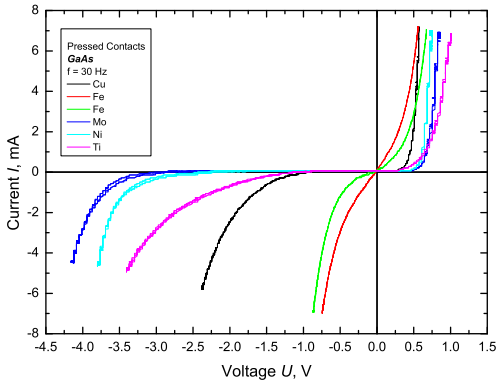

Figure 2.16: Current-Voltage characteristics of pressed contacts of various metals on GaAs.

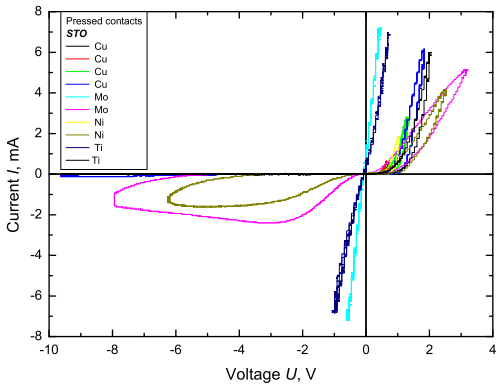

Figure 2.17: Current-Voltage characteristics of pressed contacts of various metals on Nb:STO.

A simple, but not free from artefacts, method for observation of the current-voltage characteristic of any non-linear device is the direct current (voltage) source - volt (ampere) meter measurement. A current source is to be preferred at high impedances and because of the lower noise levels that can be achieved. The method has limitations, due to low-frequency noise and interferences (for example thermoelectric, photoelectric and induced voltages), that is not effectively low-pass filtered by the time-integration performed for data point in the traces[1].

On figure (2.18) the different character of the magnetic and non-magnetic junctions is easily

[1]Low frequency interference is often the limiting factor for experiments performed with insufficient temperature or magnetic field stabilisation.

seen. The reason for the current saturation however is due to the drift-diffusion and tunnelling-thermionic emission limitation in some of the junctions, and is not direct consequence of the ferromagnetic character of the corresponding metals. These substantial differences in the dominant transport mechanism necessitate the use of both the thermionic emission model and the drift-diffusion model for data analysis.

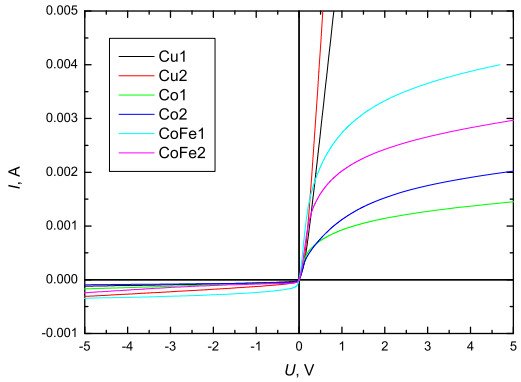

Figure 2.18: Set of current voltage characteristics measured with a source-meter. The junctions are fabricated by thermal evaporation on a n-Si¡100¿ wafer.

The analysis of the experimental data is therefore based on a combined model taking into account thermionic emission, recombination, tunnelling and drift limitations, as well as, series resistance. In rationalised terms, the model reads:

$$V_{\mathrm{a}} = IR_{\mathrm{s}} + 2V_{\mathrm{t}} \ln \left[\sqrt{\frac{I}{I_{\mathrm{S}}} + \left(1 + \frac{I_{\mathrm{r}}}{2I_{\mathrm{S}}}\right)^2} - \frac{I_{\mathrm{r}}}{2I_{\mathrm{S}}} \right] + V_{\mathrm{t}} \exp\left(\frac{I + I_{\mathrm{d}}}{I_{\mathrm{t}}}\right) \tag{2.2.4}$$

where I_{t} and I_{d} are current parameters governing the saturation of the forward current at high applied voltage V_{a}. The last term in equation 2.2.4 is necessary, as the ratio $\frac{E_{00}}{kT} \approx 0.25$ is not small enough to consider the thermionic emission to be the dominant current mechanism. An example of the fitting of such a model to experimental data is shown at figure 2.19 for the case of CoFe/Si Schottky barrier. Though convergence is poor, for the large number of fitting parameters, the following diode parameters could be deduced: barrier height $\phi_{\mathrm{b}} \approx 0.67$ V, series resistance $R_{\mathrm{s}} \approx 30\ \Omega$, recombination velocity $v_{\mathrm{r}} \approx 1.6 \cdot 10^4$ m/s, all of which agree well with the expected values. Namely, $\phi_{\mathrm{b}} \in (0.6, 0.85)$ V (see for example Rhoderick & Williams (1988)), $v_{\mathrm{r}} \in (1 \cdot 10^3, 5 \cdot 10^4)$ m/s, and $R_{\mathrm{s}} \in (25, 35)\ \Omega$.

The uniqueness of the deduced fitting parameters is not guaranteed, and it is a commonplace to find a local minimum of the error measure, instead of the global one, corresponding to the most probable model parameters. Such a situation is illustrated on figure 2.20. Even though the

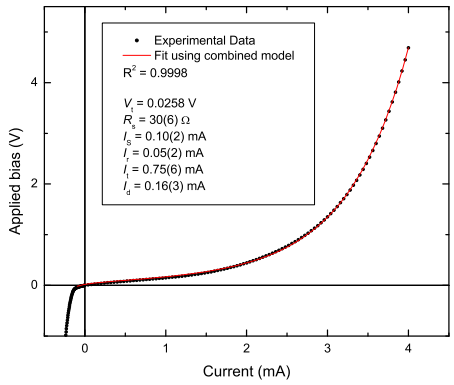

Figure 2.19: Fit to experimental data, taken at 300 K, for a CoFe/Si Schottky junction.

barrier height is only logarithmically sensitive to the saturation current density J_S, variations of the fitting parameters of 25 %, which are common even when analysing datasets obtained at fixed temperature, may lead to about 5 % of statistical uncertainty of the deduced values of the Schottky barrier height ϕ_b. Therefore, resolving small effects (due, for example, to the influence of external magnetic field on the effective barrier height), is difficult, and often impossible.

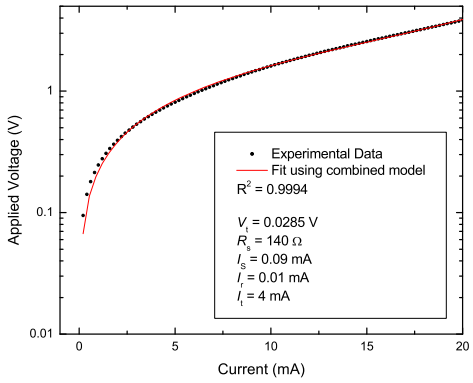

Figure 2.20: Fit to experimental data, taken at 300 K, for a Cu/Si Schottky junction.

2.2.2 Measurements of field dependence

For the measurement of the field dependence of the current-voltage characteristics, a method with a much better signal-noise ratio and stability must be applied, namely, measurement of the AC differential conductance at an arbitrary DC bias and consecutive numerical integration. The resulting reconstructed diode characteristics have significantly smaller errors in the small bias region, which facilitates the eventual resolution of small effects due to the application of

external magnetic field. On figure (2.21) and (2.22), two illustrative examples for the cases of CoFe and Cu on Si, are presented. The observed magnetic-field-induced changes are, however too big to be attributed the Zeeman splitting effect described in section 2. It is easily noticed that the effect is more pronounced at high DC biases, or when the current is high, which is in favour of magnetoresistance contribution of the semiconductor substrate.

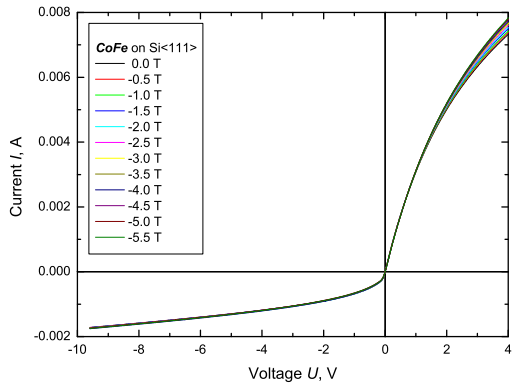

Figure 2.21: Set of reconstructed current-voltage characteristics at 300 K.

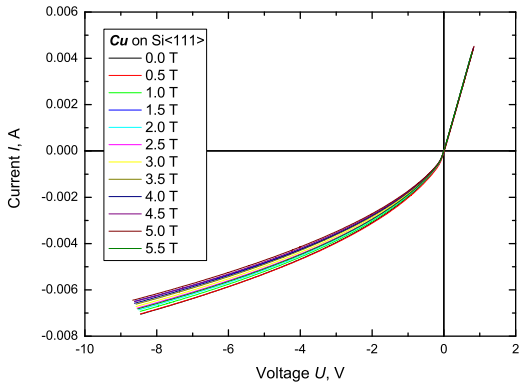

Figure 2.22: Set of reconstructed current-voltage characteristics at 300 K.

The magnetoresistance of the semiconductor base is not the only effect observed, as for example at high negative bias (for example $V_a = -8$ Vfor a nonmagnetic Cu/Si diodes), as evidenced by figure 2.23, current changes linear with the applied field B are observed. The magnitude of the magnetic field induced changes can be as large as 0.5 % per T, even in non-ferromagnetic metal/semiconductor junctions, and therefore cannot be associated with electronic polarisation of either the metal or the semiconductor side.

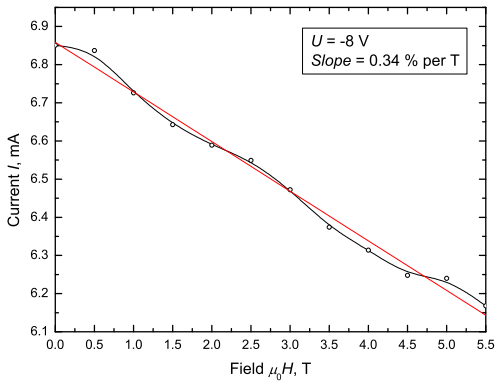

Figure 2.23: A cut at constant bias voltage $U = -8$V for a Cu diode.

2.2.3 Bridge techniques for characterisation of the field effects

It is possible to do a comparison at an arbitrary fixed bias (for example $V_a = 0$ V) between two separate Schottky junctions. This is most readily achievable by measuring the difference between the differential resistances or conductances of the junctions, in an AC bridge, while the junctions are situated together in the same magnetic field and isothermal environment. Similar bridge comparisons are shown on figures 2.24, 2.25 and 2.26; for Cu/Si vs. Co/Si, Cu/Si vs. CoFe/Si and Cu/Si vs. Cu/Si, respectively. In the latter case of two close to identical junctions, only very long time-scale temperature drifts are apparent, without any systematic field dependence of the difference of differential resistances, as expected[1]. The behaviour of

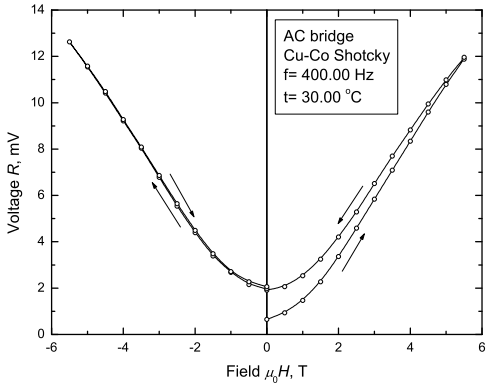

Figure 2.24: Bridge measurement of a Cu vs. Co diode at zero bias.

differences of differential resistances for the magnetic-nonmagnetic junction combinations are

[1]It should be noted that the temperature stability has been verified only down to 20 mK with the magnetic field being swept at a rate of 0.1 T/min. For more details see appendix A.6.3

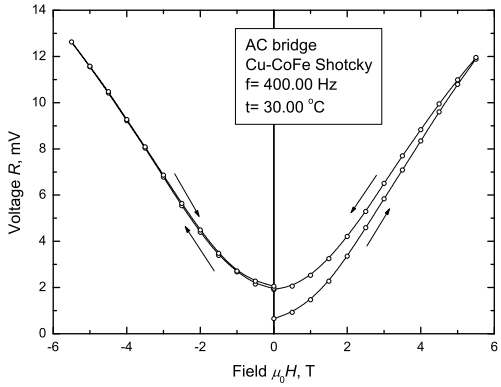

Figure 2.25: Bridge measurement of a Cu vs. CoFe diode at zero bias.

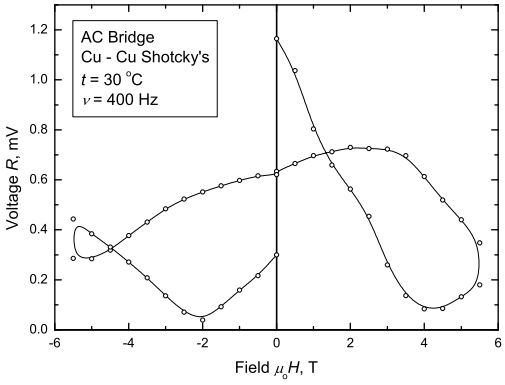

Figure 2.26: Bridge measurement of a Cu vs. Cu diode at zero bias.

determined primarily by the magnetoresistance of the semiconductor bases[1]. The much slower field ramp rate during the second half of the field evolution guarantees the already specified temperature tolerances.

A major disadvantage of the above method is the difficulty in finding a pair of magnetic/nonmagnetic Schottky junctions with close to identical zero bias (more generally, fixed bias) differential resistances. While, it may be possible to find two different values of the applied voltage V_a which result in identical differential resistances for the pair of diodes, as the different transport mechanisms have various weights at different biases, the resulting disbalance of the measurement bridge would be a complicated function of field and the actual bias voltages. It is therefore difficult to assert the differences have purely magnetic origin, and are not just a manifestation of the series magnetoresistance of the base of the diodes, made apparent by the difference of the voltages dropped at the interfacial regions in the two diodes under consideration.

A further improvement of the measurement technique is making direct difference between the differential conductance of two diodes one inside the region of the applied magnetic field, sharing the same isothermal bath. By this method taking advantage of excellent temperature stabilisation and noise cancellation, differences as small as 10^{-5} are easily resolved. Results for Cu, Co and CoFe junctions on n-type Si are shown on figures 2.27, 2.28, 2.29, respectively. A closer look at the Co and CoFe differences reveals a crossover point around 1-2 V, positive bias, that is attributed to the transition between thermionic emission limitation on the current transport over the barrier to the drift-diffusion limited case. The maximal possible value of the effect of 2.5 % at 5 T and 300 K under the thermionic emission model is exceeded in all cases, either in positive or negative bias. This fact one more time reinforces the role played by the drift-diffusion and tunnelling limitations for the active transport through Schottky diodes at room temperature.

In order to clarify the detail of the bias (current) dependence of the changes of differential conductance, the bias profile, obtained at $B = 0$ T, may be substracted from the ones obtained at higher fields. In this fashion, small magnetic field related effects can be characterized, as the majority of the background has already been substracted by the bridge circuitry. The results of this operation are shown at figures 2.30, 2.31 and 2.32, for Cu/Si, Co/Si and CoFe/Si Schottky junctions, respectively. For the Cu/Si diode, only a small, linear in field deviation is observed, virtually constant with V_a for voltages less than about -3 V, and higher than 0.25 V.

[1] I should be noted, also that the quick, initial energisation of the superconducting magnet used, leads to about 3 K increase in temperature of the magnet bore, which is not effectively compensated by the water-bath providing the isothermal measurement environment and by the magnet cooling system.

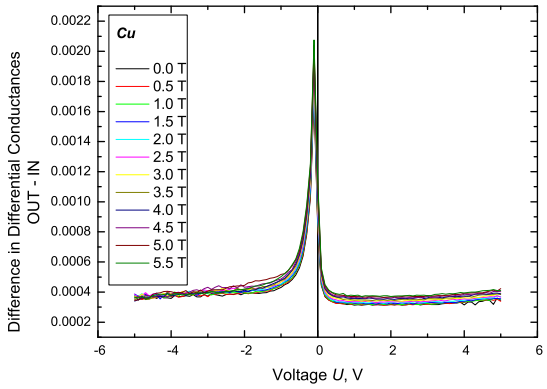

Figure 2.27: Bridge measurement of two Cu junctions, one in, one out of the magnet.

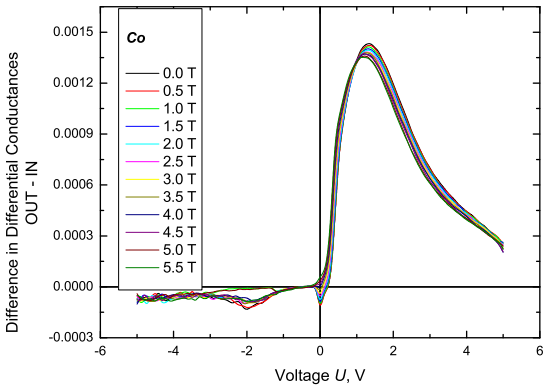

Figure 2.28: Bridge measurement of two Co junctions, one in, one out of the magnet.

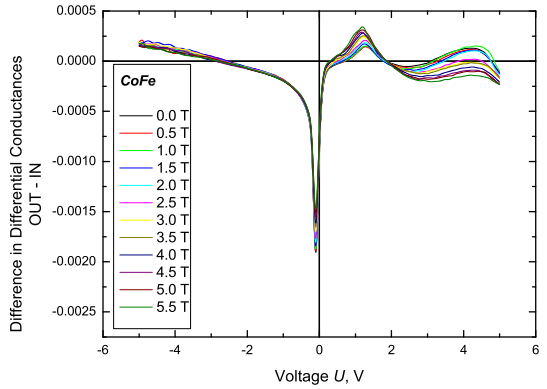

Figure 2.29: Bridge measurement of two CoFe junctions, one in, one out of the magnet.

The magnetic field dependencies for the Co/Si and CoFe/Si are about four times stronger, and have completely different bias dependencies: in the first case two positive peaks are resolvable, situated at 0.1 V and 0.4 V; in the latter case, -0.2 V and 1.2 V. Both diodes exhibit a broad depression at high positive bias. Invoking the base magnetoresistance as the cause of all observed effects is clearly impossible.

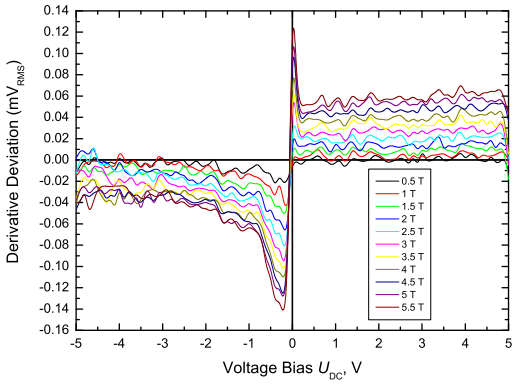

Figure 2.30: Deviation of the measured current derivative from its zero-field value, for a Cu/Si Schottky junction.

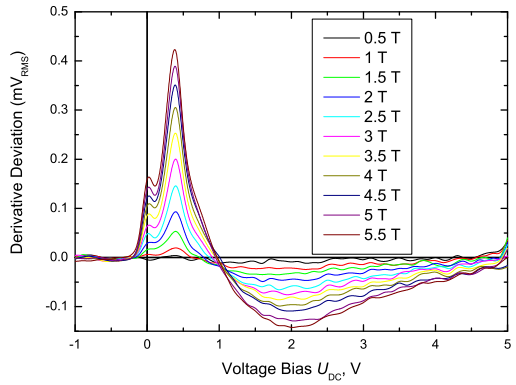

Figure 2.31: Deviation of the measured current derivative from its zero-field value, for a Co/Si Schottky junction.

Starting with equation 2.1.94, and differentiating with respect to R_s, the effect due to series resistance change, would be expected to be proportional to the total current:

$$\frac{\partial V_a}{\partial R_s} = I \tag{2.2.5}$$

A more detailed analysis may be based on the derivatives of the $I - V$ characteristic. The

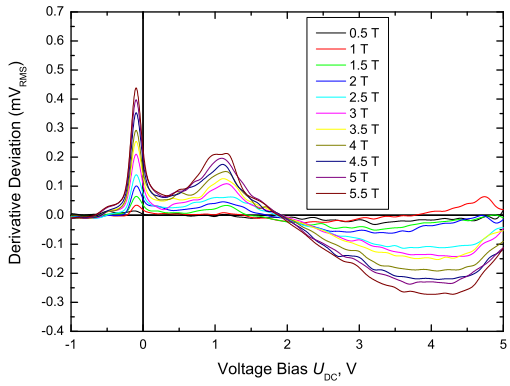

Figure 2.32: Deviation of the measured current derivative from its zero-field value, for a CoFe/Si Schottky junction.

differential resistance for a quasi-ideal Schottky diode can be shown to be equal to:

$$\frac{\partial V_{\mathrm{a}}}{\partial I} = R_{\mathrm{s}} + \frac{\Upsilon k T}{q} \frac{1}{I + I_{\mathrm{s}}} \tag{2.2.6}$$

and, therefore, its magnetic field dependence can be expected to be independent of the total current I and only a function of the field dependence of the series resistance R_{s}, as:

$$\frac{\partial}{\partial B} \frac{\partial V_{\mathrm{a}}}{\partial I} = \frac{\partial R_{\mathrm{s}}}{\partial B} \tag{2.2.7}$$

within this approximation. This result is, obviously, independent of the inclusion of recombination current or leakage current components in the total current I, which are not explicit functions of B. This is not incompatible with the experimental data for Cu/Si Schottky junctions.

An exact comparison with the experimental results should be based on the differential conductance. The solution for the total current I and its derivative with respect to voltage $\frac{\partial I}{\partial V_{\mathrm{a}}}$ can be quite difficult even for the case of quasi-ideal diode. It is, though, easy to inverse the solution for the differential resistance and obtain the form:

$$\frac{\partial I}{\partial V_{\mathrm{a}}} \approx \frac{I + I_{\mathrm{S}}}{V_{\mathrm{t}} + (I + I_{\mathrm{S}})\, R_{\mathrm{s}}} \tag{2.2.8}$$

which corresponds closely to the behaviour exhibited by the Cu/Si junction if the experimental broadening of the derivative spectrum is taken into account[1]. Or in other words, taking the change of series resistance R_{s} to be to first order:

$$\mathrm{d}R_{\mathrm{s}} = \frac{\partial R_{\mathrm{s}}}{\partial B} \mathrm{d}B \tag{2.2.9}$$

[1]The experimental spectrum is a convolution of the device characteristic and the δ-response function of the equipment. In the case under consideration, the modulation broadening (the broadening due to the finite differentiation voltage) is the dominant factor.

the form of the magnetic field induced change in differential conductance becomes:

$$\mathrm{d}\left(\frac{\partial I}{\partial V_\mathrm{a}}\right) \approx -\frac{\left(I+I_\mathrm{S}\right)^2}{\left[V_\mathrm{t}+\left(I+I_\mathrm{S}\right)R_\mathrm{s}\right]^2}\frac{\partial R_\mathrm{s}}{\partial B}\left|B\right| \tag{2.2.10}$$

Applying similar analytical description for the more detailed Schottky diode models becomes exceedingly difficult and doesn't bring any new physical insights to the problem. In a more general approach, it is possible to evaluate the magnetoresistance of the diode base by noting that the series resistance leads to a diminished voltage drop on the actual junction like:

$$V_\mathrm{a} \rightarrow V_\mathrm{a} - IR_\mathrm{s} \tag{2.2.11}$$

therefore upon the application of the magnetic field, to a linear approximation, a voltage differential is created of the form (neglecting all magnetic field related effects, but the change in series resistance):

$$\mathrm{d}V_\mathrm{a} = -I\frac{\partial R_\mathrm{s}}{\partial B}\mathrm{d}B \tag{2.2.12}$$

The total differential of the differential conductance can thus be written like:

$$\mathrm{d}\left(\frac{\mathrm{d}I(V_\mathrm{a})}{\mathrm{d}V_\mathrm{a}}\right) = \frac{\partial^2 I}{\partial V_\mathrm{a}^2}\mathrm{d}V_\mathrm{a} \tag{2.2.13}$$

Substituting equation 2.2.12 into 2.2.13 yields:

$$\mathrm{d}\left(\frac{\mathrm{d}I(V_\mathrm{a})}{\mathrm{d}V_\mathrm{a}}\right) = -\frac{\partial^2 I}{\partial V_\mathrm{a}^2}I(V_\mathrm{a})\frac{\partial R_\mathrm{s}}{\partial B}\mathrm{d}B \tag{2.2.14}$$

Therefore the changes in the derivative spectra (that are actually experimentally measured in the differential bridge method) are proportional to the second derivative of the $I(V_\mathrm{a})$ dependence, proportional to the current itself, the magnetoresistance of the base and the applied field B. This means that the effect will be vanishing if the current is zero, which agrees with the analysis already made for the differential resistance. Example of the voltage dependence of the experimental product $-I(V_\mathrm{a})\frac{\partial^2 I}{\partial V_\mathrm{a}^2}$ for a CoFe/Si junction is given at figure 2.33. Upon comparison with figure 2.32, it is easily seen that it has little to do with the observed magnetic field effects.

The harshness of the problem with the magnetic field dependence of the series resistance, at high current densities, can be further illustrated by the strong magnetic field dependence of the reverse bias current of the junctions, as illustrated on figure 2.34. It is easily seen that at high negative potentials, there is a competition between the junction breakdown process and the magnetoresistance of the substrate (combined with heating effects at very high currents).

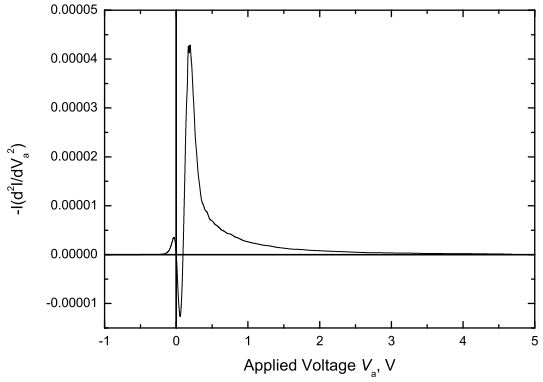

Figure 2.33: Negated product of the current and its second derivative with respect to voltage for a CoFe/Si Schottky junction. The derivative is constructed numerically from the $I - V$ characteristic of the device.

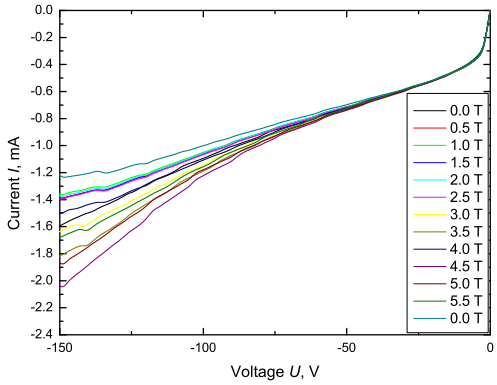

Figure 2.34: Reverse bias break down of a CoFe Schottky junction.

2.3 Magneto-Optical Measurements on Schottky junctions

A simple way to avoid large contributions from the magnetoresistance of the semiconductor substrate is to substitute the active current measurements with photovoltaic (or photo-galvanic) ones. Measurement schematic is shown on figure 2.35. The main difference between internal

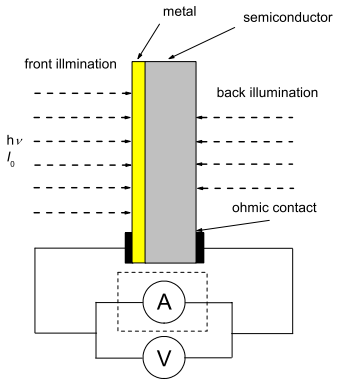

Figure 2.35: Schematic of a Schottky junction under illumination.

biasing (photo-current) and external biasing (auxiliary current source) is visualised on figure 2.36. While, in the first case, the current flows virtually entirely within the depletion region

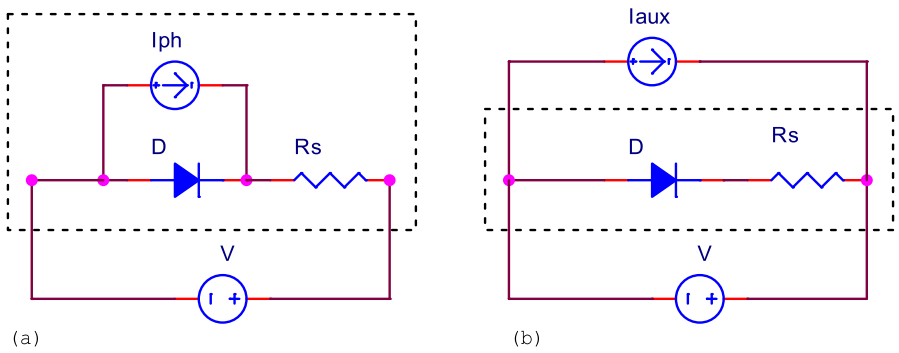

Figure 2.36: Simplified effective circuit under internal biasing (a), and under auxiliary biasing (b).

only, and the series resistance of the semiconductor substrate is adding only to the already high resistance of the measuring voltmeter. In the latter case, the series resistance is, as usual, adding to the voltage drop that the external measuring circuit detects. For a fixed balancing current requirements of the measuring voltmeter circuit I_b having an internal resistance of R_v,

and voltage drop across the diode V_a, this can be formulated like:

$$\begin{aligned} I_b^{int} &= \frac{V_a}{R_v + R_s} \\ I_b^{ext} &= \frac{(V_a + V_s)(R_v + R_d + R_s)}{R_v (R_d + R_s)} \end{aligned} \tag{2.3.1}$$

where R_d is the effective resistance of the idealised diode. The ratio of the voltage drop across the series resistance R_s under internal biasing, to the one under external biasing, becomes:

$$\frac{V_s^{int}}{V_s^{ext}} \approx \frac{V_a}{V_a + V_s} \frac{R_s R_v}{(R_s + R_v)^2} \tag{2.3.2}$$

where it has been assumed that $R_d \ll R_v$. It is easily seen, that this ratio is in all interesting cases much less than unity.

For the case of the photovoltaic method of determination of changes in the barrier height, the measurement is essentially electrostatic as the photocurrent is compensating the drift-current within the depleted region in the semiconductor, and therefore the virtual voltage drop is predominantly on the barrier, as its resistance tends to the tunnelling limit. Quite the opposite way photo-galvanic measurement is almost exactly short-circuit measurement, so the bias on Schottky barrier tends to zero.

A simple way to characterise the dependency of the photo-voltage on the light illumination (with continuous spectrum) is shown on figure (2.37). Different thickness of white absorber is placed between the light source and the junction. As the illumination depends exponentially on the absorber thickness (at least in the limit of small absorption and neglecting multiple diffuse scattering events), the actual relation photo-voltage vs. illumination may be deduced. For a large range of fluencies that is a linear relationship.

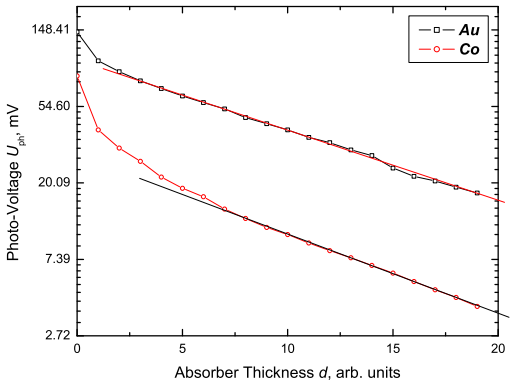

Figure 2.37: Photo-illumination characteristics of Au and Co on Si.

More information is obtained by measuring photo-illumination characteristics at low as well as high temperatures. Examples are shown on a linear scale on figure 2.38 and on a

logarithmic scale on figure 2.39. While at ambient temperature, the logarithmic character of the illumination dependence is clearly dominating, at low temperatures (61 K is close to the minimal possible for moderately doped Si based diodes), the photo-voltages not only saturate, but also decrease at high intensity. The decrease in photo-voltage may attributed to either effects related to the undesired changes in spectrum, accompanying the increase of absorption thickness or nonlinearities in the measurement circuitry at very low biasing currents[1]. The first case is more likely due to the fact that the absorbers are not perfectly 'grey' in the spectral region of interest as evidenced by figures A.9 and A.10. The region of saturated illumination dependence

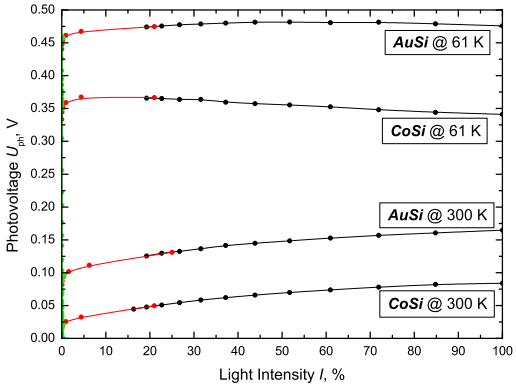

Figure 2.38: Photo-illumination characteristics of Au and Co on Si at 61 K and 300 K.

of the photovoltage, is advantageous for further magnetic field dependence investigations as it relaxes to a great extent the requirements for illumination intensity stabilisation and thus simplifies the experimental setup.

In order to determine the spin polarisation around the quasi-Fermi level at a given temperature, the change of the photo-voltage or the photocurrent with applied magnetic field, under constant illumination may be investigated. Results for different ferromagnetic and non-magnetic metals deposited on n-type Si and GaAs are shown on figures (2.40, 2.41) and (2.42). It is impossible to account for the observed effects of few percent in 5.5 T at 300 K in the framework of the thermo-ionic emission model. As the large shifts of the photo voltage are not accompanied by corresponding change of the short-circuit current, the influence of the bulk magnetoresistance of the substrate can be excluded as a factor. A reasonable explanation may

[1]There is a minimal conductance of effective source circuit (the diode under illumination) for which the response of the voltmeter used is linearly proportional to the photo-voltage of interest. While, for conductances smaller but comparable to the minimal one (roughly equal to $1/R_v$, where R_v is the internal resistance of the voltmeter circuitry) the behaviour is non-linear but stable, for conductances much smaller than the minimal, the response is divergent. In this regime the Schottky device under test cannot be considered 'connected' to the voltmeter.

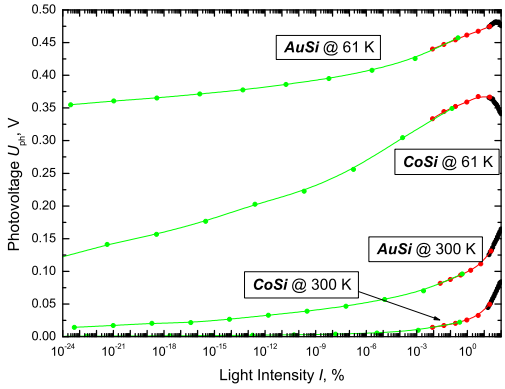

Figure 2.39: Photo-illumination characteristics of Au and Co on Si at 61 K and 300 K. Note the extreme photo-sensitivity at low temperatures.

be found only in the drift-diffusion limit, but whether the change in photo-voltage may be attributed to a change of the barrier height, or simply due to different diffusion coefficients for spin-up and spin-down electrons, remains an open question. The fact that all shifts observed on GaAs substrates are within the experimental uncertainty of 0.1 % is related to the well-known fact that the Schottky barrier height at the metal to GaAs interface is determined predominantly by interface states and not by the difference of the work-functions. An example

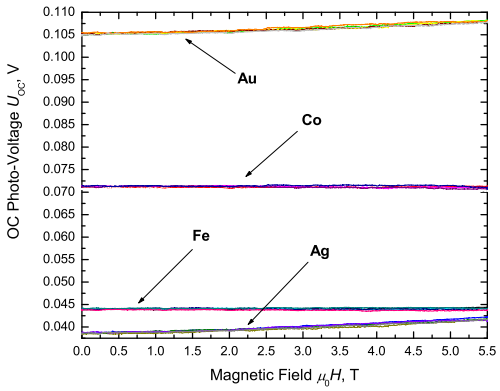

Figure 2.40: Open-circuit photovoltage vs. applied field for GaAs diodes at 300 K.

of measurement of magneto-photovoltaic effect for a Co diode is shown at figure 2.43. The experimentally observed slope of 0.316(1) % per T, would correspond to a spin-polarisation of about 71 %, which is higher than the expected value of about 40 %. As the expected effects are generally quite small, it is useful to extend the measurement range to higher fields. Data for Au, Ag, Fe and Co on Si Schottky junctions is shown on figures 2.44 and 2.45, obtained

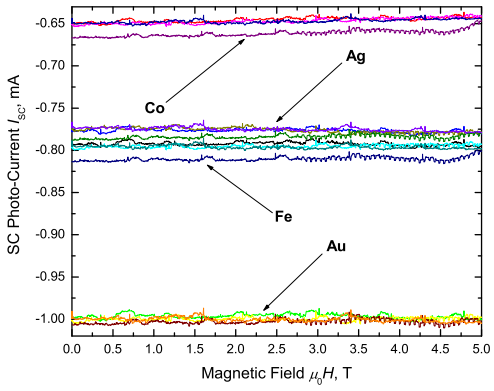

Figure 2.41: Short-circuit photocurrent vs. applied field for GaAs diodes at 300 K.

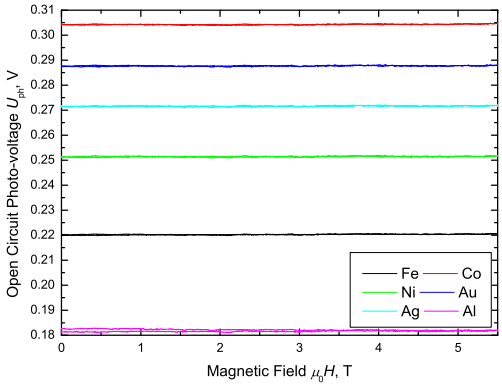

Figure 2.42: Open circuit photovoltage vs. applied field for GaAs diodes at 300 K.

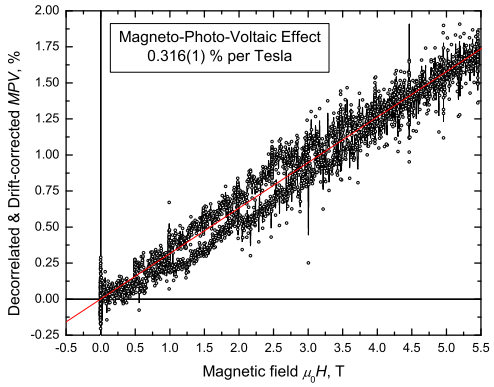

Figure 2.43: Magneto-photovoltaic effect in a Co diode at 300 K.

at 100 K and 200 K, respectively. Results are summarised in table 2.3. The first surprising result is the much smaller deduced polarisation for the Co/Si junction as compared to the 300 K experiment (see figure 2.43). Another unexpected result is the non-zero polarisation for the Ag/Si interface. Even more surprizing is the increase in slope from +0.12 %/T at 100 K, to +0.37 %/T at 200 K, for the Ag/Si Schottky barrier. All of these can, though, be attributed to the lack of saturation in the photovoltage as a function of illumination intensity at high temperatures, in all junctions, and even at low temperature for some junctions (for example Ag/Si).

Metal Si	MPV (%/T) 100 K	MPV (%/T) 200 K	α (%) 100 K	α (%) 200 K
Co	+0.33	+0.13	+25	+19
Fe	-1.23	-0.51	-91	-76
Au	+0.02	+0.01	+3	+2
Ag	+0.12	+0.37	+8	+55

Table 2.1: Reduced results of magneto-photovoltaic measurements of various Schottky diodes with Si base, at two different temperatures.

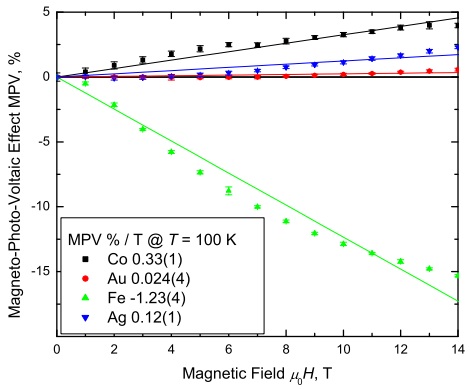

Figure 2.44: Magneto-photovoltaic effect in a various diodes at 100 K.

2.4 Conclusions on the Plausibility of Spin Polarisation Measurements Using Schottky Diodes

While direct active transport measurement of the spin-polarisation is generally unrealisable, there may be a particular system metal-semiconductor, where all of the following requirements are satisfied:

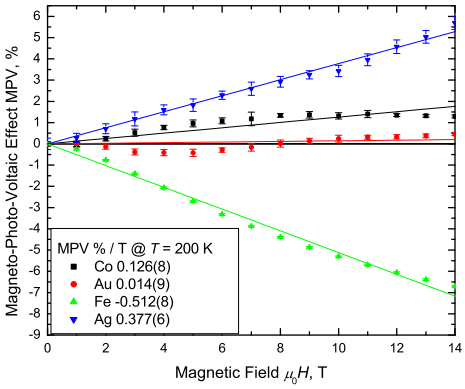

Figure 2.45: Magneto-photovoltaic effect in a various diode at 200 K.

(a) The magnetoresistance in the bulk-semiconductor is small and preferably linear, even in fields of 5 - 10 T.

(b) Low Schottky barrier height, so that the measurement can be performed at low temperatures.

(c) The substrate should be still conductive at the lowest temperature of operation of the junction, and have small temperature dependence of the resistivity.

(d) The junction complies sufficiently well with the thermo-ionic emission model, and does not include a thin oxide interfacial layer.

(e) The Schottky barrier height should be determined by the difference of the work functions of the two materials in the junction and not by interface pinning.

The conditions that must be satisfied for a successful photovoltaic measurement of the spin-polarization are as follows:

(a) The Schottky barrier height should be sufficiently different from the band gap of the semiconductor, as to avail for the separation of the internal photoemission and the direct gap contributions by experiment.

(b) The metal layer has to be sufficiently transparent at the frequencies of interest, and in the same time sufficiently thick to preserve bulk behavior.

(c) The temperature dependence of the Schottky barrier height should be sufficiently small.

(d) The Schottky barrier height should be determined by the difference of the work functions of the two materials in the junction and not by interface pinning.

2.5 Ohmic contacts of ferromagnetic metals and alloys to semiconductors

Efficient spin injection into semiconductors has been the tantamount of spin electronic during the last couple of decades. Recent works (see for example Min *et al.* (2006)), promise reasonable efficiency of spin injection into standard semiconductors (like Si) via a low-work-function metal/insulator/semiconductor tunnel junctions (modified Schottky contacts). Very low barrier heighs below 0.1 eV have been reported in the system Pt/Er/Si by Tang *et al.* (2003). As a number of standard hard-ferromagnetic alloys are based on Pt (for example CoPt), a properly designed CoPt/Er/Si junction is a good potential candidate for spin injection into silicon[1]. Very low and even 'negative' Schottky barriers have been reported and heavily argued upon in the Ti/Si system (see the dialogue Osvald (2004); Tao & Zhu (2004); Tao *et al.* (2004)). An excellent review of older works on rare-earth overlayers on silicon is also available (see Netzer (1995)). Unlike Si, GaAs (and most other compound semiconductors) based Schottky junctions have barrier heights well in excess of 0.5 eV, even with metals with metals with very small work functions like Ga (see Hirose *et al.* (1988b); Myburg *et al.* (1998); Tersoff & Harrison (1987)) due to the predominant role that the intrinsic surface states play in the determination of the barrier height as argued by Eastman & Freeouf (1975).

Data on the work functions of 3d metals is shown on figure 2.46 after references Eastman (1970); Fukuda *et al.* (1977); Li & Li (2004). All work functions are found to be between 3.4 an 5.2 eV. Therefore, all 3d metals should create Schottky barriers on top of silicon if the interface index $\varsigma \sim 1$.

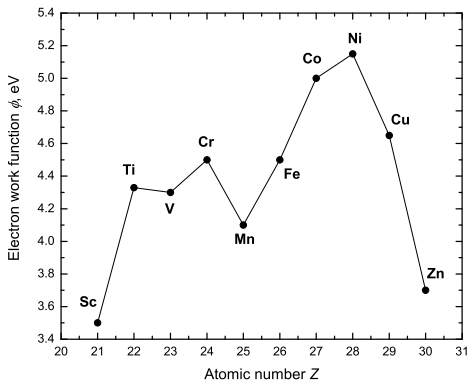

Figure 2.46: Electron work functions of the 3d metals. After reference Eastman (1970)

[1]It should be noted that there exist a great deal of discrepancy with previous studies on 3d and noble metal contacts to silicon (see for example Hirose *et al.* (1988a))

The initial characterisation of the rare-earth-3d metal/Si junctions has been carried out using the standard 4-wire DC measurement technique described in appendix A.6.3. Data taken in the bias range ±1 V, at ambient temperature and in the dark, is shown on figure 2.47. Similar dataset in a narrowed bias window is visualised on figure 2.48.

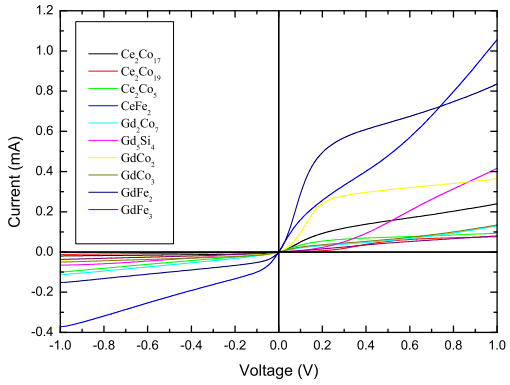

Figure 2.47: $I - V$ characteristic of rare-earth-transition metal/Si junctions, measured at ambient temperature.

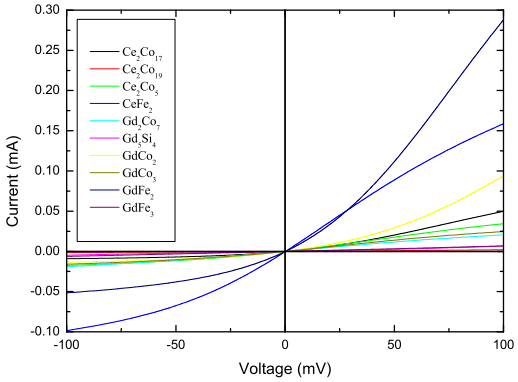

Figure 2.48: Low bias $I - V$ characteristic of rare-earth-transition metal/Si junctions, measured at ambient temperature.

Cleary, the various 3d metals form very different junctions on Si. An example of a Schottky barrier is $GdCo_2$/Si, the low-bias $I - V$ characteristic of which is shown on figure 2.49. The voltage dependence is non-linear and asymmetric with a relatively high zero-bias differential resistance $R_0 = 5.65$ kΩ.

Another characteristic example is $CeCo_5$/Si Schottky junction with very large tunnelling component, shown at figure 2.50. The prominent tunnelling current contribution diminishes the zero-bias differential resistance to $R_0 = 4.55$ kΩ.

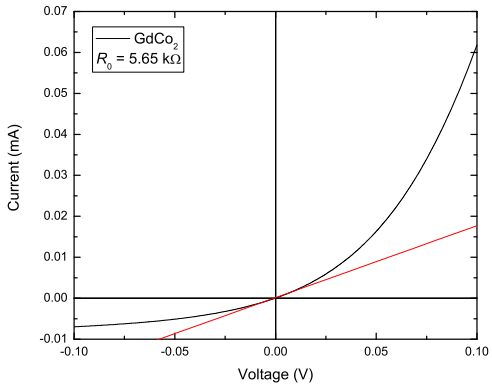

Figure 2.49: Low bias $I - V$ characteristic $GdCo_2$/Si junction, measured at 300 K.

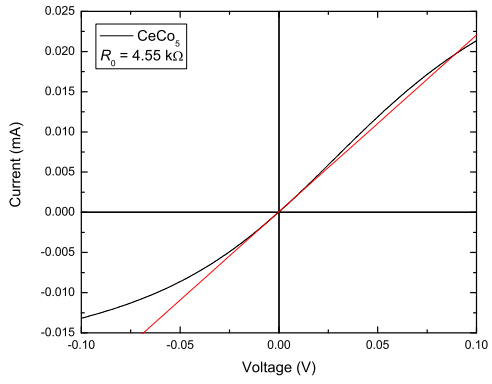

Figure 2.50: Low bias $I - V$ characteristic $CeCo_5$/Si junction, measured at 300 K.

Dominant tunnelling current component cannot be associated directly with low zero-bias differential resistances, as demonstrated on figure 2.51 for a $GdFe_3$/Si interface. The value of the zero-bias resistance is $R_0 = 22.5$ kΩ, which is about four times higher than the one observed on Schottky junctions of the same area S.

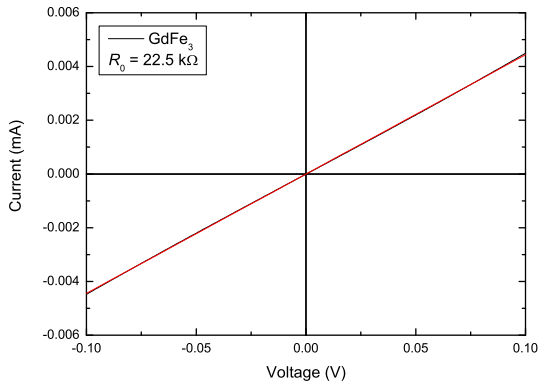

Figure 2.51: Low bias $I - V$ characteristic $GdFe_3$/Si junction, measured at 300 K.

Upon high-temperature annealing, via diffusion and/or silicide formation, true low-resistance-ohmic-contacts can be achieved. Following the same line of though as Ottaviani *et al.* (1980) in the case of transition metal-silicide/silicon Schottky barriers, negative correlation may be expected between barrier height and eutectic temperature of the silicide (of such exists). An example of a Y/Si junction annealed for 1 h at a pressure of 10^{-6} mBar and temperature of 1000 °C, is shown on figure 2.52. The resistance is limited by the series resistance of the semiconductor base and equal to $R_0 = 10.9$ Ω.

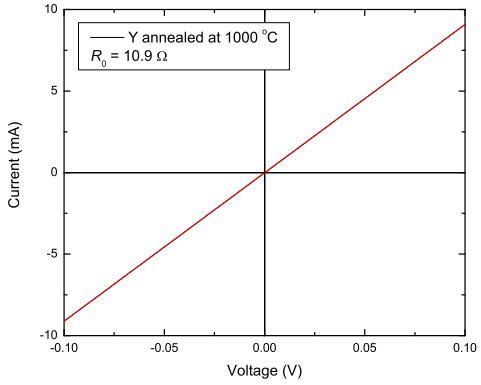

Figure 2.52: Low bias $I - V$ characteristic Y/Si junction, measured at 300 K. The sample has been annealed to promote diffusion across the interface.

More information is obtained from the analysis of the temperature dependences of the $I-V$ characteristics of the devices which represents a general 2D-surface in $I-V-T$ space. Examples are shown at figures 2.53, 2.54 and 2.55, for $GdCo_2$/Si, $GdFe_3$/Si and $CeCo_5$/Si junctions, respectively. The measurement of 'thick' set of data points allows for a subsequent numerical 2D-spline interpolation and the extraction of arbitrary cuts though parameter space, in particular, $I(T)\big|_{V=const}$ and $V(T)\big|_{I=const}$. Those can be used for subsequent fitting and diode parameter extraction as already described in section 2.1.5.6.

The actual data extraction for real diodes, can be complicated by the fact that often the finite bias voltage V_a and temperature dependence of series resistance R_s must be corrected for. The analysis can be based on the modified diode model:

$$I = SA^{\star\star}T^2 \exp\left(-\frac{q\phi_b}{kT}\right)\left\{\exp\left[\frac{q\left(V_a - IR^\star \exp\left(\frac{E_d}{kT}\right)\right)}{kT}\right]-1\right\} \tag{2.5.1}$$

where $R^\star$ is the saturation resistance of the semiconductor base[1], and only thermionic emission and series resistance have been taken into account. For its limited nature this model is only applicable at temperatures for which the thermionic emission is the dominant process or $kT \gg E_{00}$, but not too high so that a large recombination current component can develop, or $kT \ll E_g/2$.

Explicit solution for ϕ_b can be readily obtained from equation 2.5.1 in the form:

$$\phi_b = V_t\left\{-\ln I + \ln\left(SA^{\star\star}\right) + 2\ln T + \ln\left[\exp\left(\frac{V_a - IR^\star \exp\left(\frac{E_d}{kT}\right)}{V_t}\right)-1\right]\right\} \tag{2.5.2}$$

It is easily seen that the dominant term is $-\ln I$, so that if a plot of $-\ln I\left(\frac{1}{T}\right)$ is created the slope is to a large extent determined by $\frac{q\phi_b}{k}$. The remaining terms define further corrections that can be introduced, provided $R^\star$, E_d and the effective value of S are known from independent investigations[2].

A systematisation of the results on all measured junctions is presented in table 2.5. While useful, the information in this table is not free from artefacts. The main disadvantage of the simple model 2.5.2 is neglect of the recombination current component. As the recombination current has a different activation energy (normally about $E_g/2$), it should generally appear as a different slope in the activation plots at high temperature, as compared with the low-temperature limit. For recombination through the main gap in the semiconductor E_g, this

[1] Here, the through the gap activation of carriers in the semiconductor base has been neglected, therefore limiting the region of applicability of the model to low temperatures, for which $kT \ll E_g$.

[2] Because of their relatively small impact on the temperature dependence of the current I at fixed bias V_a and the large degree of linear dependency in the respective terms, both $R^\star$ and E_d are difficult to determine unambiguously by fitting the entire non-linear equation 2.5.2 to experimental data.

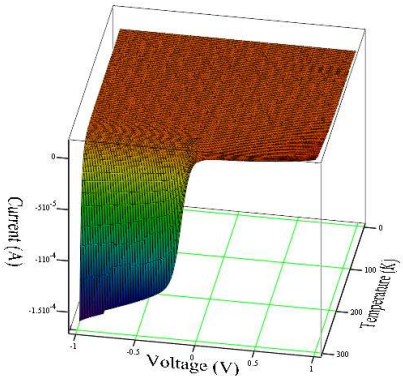

Figure 2.53: $I - V - T$ characteristic $GdCo_2$/Si junction.

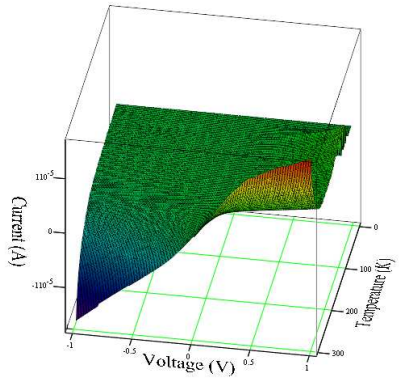

Figure 2.54: $I - V - T$ characteristic $GdFe_3$/Si junction.

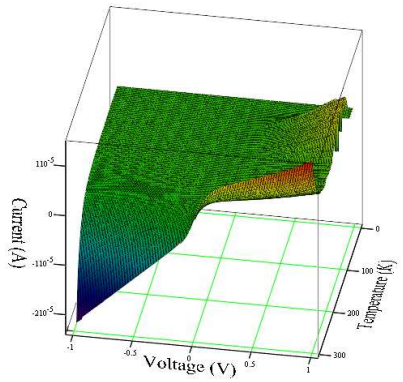

Figure 2.55: $I - V - T$ characteristic $CeCo_5$/Si junction.

leads to a temperature dependence of the form:

$$E_g = 2kT \left\{ -\ln I + \ln I_r + \ln \left[\exp\left(\frac{V_a - IR^\star \exp\left(\frac{E_d}{kT}\right)}{2kT} \right) - 1 \right] \right\} \tag{2.5.3}$$

Thus it is clear, that the gradient of the dependence $-\ln I\left(\frac{1}{T}\right)$ should be close to $E_g/2k$ at high enough temperature $kT \gg E_g/2$.

Metal	ϕ_b (V)	$R_{-0.1V}$ (Ω)	$R_{+0.1V}$ (Ω)
$GdCo_2$	0.42	14250	1617
Gd_5Si_4	0.19	29640	19250
$GdFe_3$	0.17	22330	22270
$GdFe_2$	0.26	1307	659.3
Gd_2Co_7	0.20	9474	4850
$GdCo_5$	0.20	7838	4868
Gd	0.38	$3.39 \cdot 10^6$	$1.75 \cdot 10^6$
Gd_{ann}	0.01	461.3	399.8
Ce_5Co_{19}	0.23	79680	56380
$CeCo_5$	0.25	7546	4684
$CeFe_2$	0.76	1145	768.41
Ce_2Co_{17}	0.38	7478	3237
Y	0.14	248.8	50.5
Y_{ann}	0.03	11.0	10.9
Fe	0.26	4756	2645
Co	0.36	16339	2775
Ni	0.45	5531	3189

Table 2.2: Minimal barrier heights without further corrections, and total resistances at -0.1 V and 0.1 V for various Schottky junctions on silicon. Subscript $_{ann}$ denotes an annealed sample of the same batch.

More generally, the recombination current component is likely to have chief activation energy $E_r \in [E_d, E_g/2]$. The above relations result in what may be called 'two-exponent model' for the thermal activation of non-ideal Schottky barriers. The details of the recombination processes for current conversion at the metal-semiconductor interface are hidden behind two constants I_r and E_r.

An example of a junction where there are clearly two very different activation energies is shown on figure 2.56. The higher of the two activation energies observed 0.641(2) eV is in excellent agreement with the fundamental gap of Si of $E_g/2 \approx 0.64$ eV. The lower of the two, or 0.192(3) eV corresponds to the effective barrier height for thermionic emission of electrons from Si into $GdCo_2$.

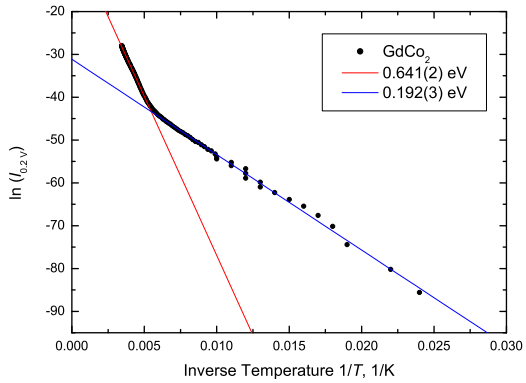

Figure 2.56: Low bias $\ln I - 1/T$ characteristic of a $GdCo_2$/Si junction, via a cut at 0.2 V. Two different activation energies are clearly distinguishable.

Though common, it is not obligatory, that the recombination process would be distinguishable on a thermal activation plot. In some Schottky junctions, only one process is dominating in the whole experimentally accessible temperature range. Similar behaviour is demonstrated by a Gd_5Si_4/Si diode on figure 2.57 with a deduced barrier height of 0.526(1) eV. This situation is also occurring when the two activation energy scales $q\phi_b$ and E_r are similar.

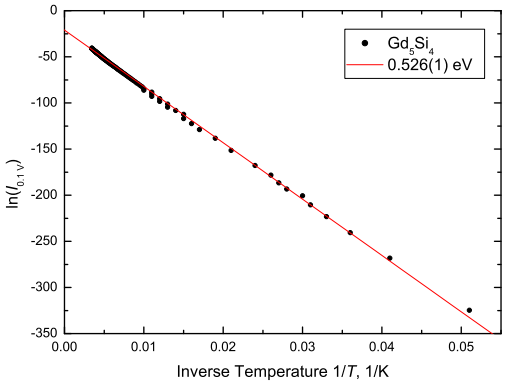

Figure 2.57: Low bias $\ln I - 1/T$ characteristic of a Gd_5Si_4/Si junction, via a cut at 0.1 V. Only one activation energy is clearly distinguishable.

There are cases, when there are two distinguishable activation energies, but $E_r \nsim E_g/2$. The unambiguous association of E_r with a particular transport process is thus often impossible. Examples are given on figures 2.58, 2.59 and 2.60 for Ce_2Co_{17}/Si, $GdFe_2$/Si and $GdFe_3$/Si, Schottky diodes respectively. In some cases, it is possible to have very similar metal alloys, forming very different Schottky barriers, both in terms of barrier height ϕ_b and recombination energy E_r, as in the example of $GdFe_2$ and $GdFe_3$, where the first diode has $\phi_b = 0.195(2)$ V and

$E_r = 0.429(1)$ eV, and the latter has $\phi_b = 0.227(1)$ V and $E_r = 0.097$ eV. Results for Schottky

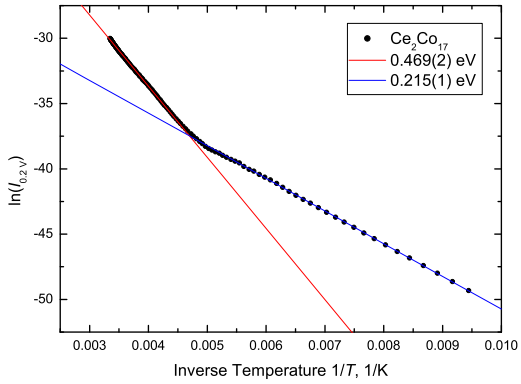

Figure 2.58: Low bias $\ln I - 1/T$ characteristic of a Ce_2Co_17/Si junction, via a cut at 0.2 V. The higher activation energy of 0.469(2) eV does not correspond to $E_g/2$.

junctions where the modified parameter extraction algorithm has been successfully applied are summarised in table 2.5.

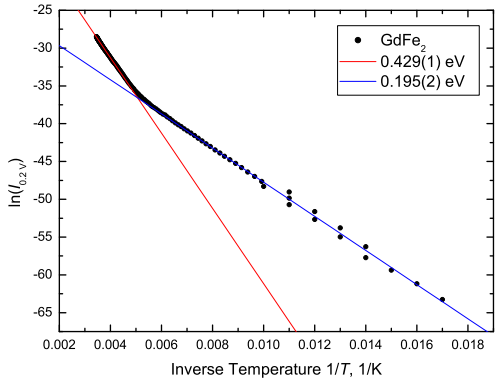

Figure 2.59: Low bias $\ln I - 1/T$ characteristic of a $GdFe_2$/Si junction, via a cut at 0.2 V. The higher activation energy of 0.429(1) eV does not correspond to $E_g/2$.

The lowest effective thermionic emission barrier heights of ferromagnetic metal on Si(001) are exhibited by $CeCo_5$ (0.048 eV), $GdCo_5$ (0.097 eV) and $GdFe_3$ (0.097 eV), all significantly lower than their 3d-metal and silicide counterparts (about 0.5 eV, see Kaltsas *et al.* (1996) and references therein). The barrier height deduced for Gd of about 0.4 eV agrees well with the one reported by Tu *et al.* (1981). Also, Y was found to form ohmic contact to Si after annealing, confirming the findings of Norde *et al.* (1981). Nevertheless all junctions have non-negligible recombination current component with activation energy of around an below 0.5 eV. This is

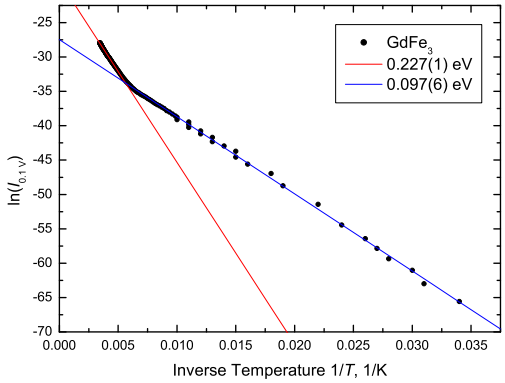

Figure 2.60: Low bias $\ln I - 1/T$ characteristic of a $GdFe_3$/Si junction, via a cut at 0.1 V. The higher activation energy of 0.227(1) eV does not correspond to $E_g/2$.

Metal	ϕ_b (V)	E_r (eV)	Metal	ϕ_b (V)	E_r (eV)
$GdCo_2$	0.192(3)	0.641(2)	Gd	0.489(2)	-
Gd_5Si_4	0.526(1)	-	$CeCo_5$	0.048(3)	0.503(6)
$GdFe_3$	0.097(6)	0.227(1)	Ce_5Co_{19}	0.536(1)	-
$GdFe_2$	0.195(2)	0.429(1)	Ce_2Co_{17}	0.215(1)	0.469(2)
Gd_2Co_7	0.435(1)	-	$CeFe_2$	0.220(1)	-
$GdCo_5$	0.096(2)	0.376(3)	Y	0.091(2)	0.181(1)

Table 2.3: Barrier heights ϕ_b and recombination activation energies E_r for various Schottky junctions on silicon. Values are denoted by - when only one characteristic energy can be extracted.

likely to affect the efficiency of spin injection through such junctions and limit their usefulness at ambient conditions. Barrier height have been demonstrated to be lowered further by high-temperature diffusion to a minimum of about 0.016 eV for Y/Si contact, with a significant gain of linearity, conductivity and thermal stability. This attempt crosses the border to the world of tunnel-barrier contacts and may potentially provide a tool for realising efficient, both, charge and spin injection in for the constantly decreasing gate size of field effect transistors on silicon. Though, this methods is prone to excessive impurity spin-scattering in the diffused region, which may also lead to poor overall injection efficiency.

2.6 General remarks on the applications of Schottky junctions

Ferromagnetic metal-normal semiconductor contacts have prospects for application as injectors and detectors of spin-polarised electronic currents. Behind their illusive simplicity, a number of underlying physical phenomena remain unexplored or not fully understood. The complexity of the overall problem is due to the mixture of quantum and classical effects often exhibited in the same junctions.

Here, mostly experimental and partially theoretical investigations have been presented focused in two directions:

1. The observation and explanation of the effects of external magnetic fields on magnetic and non-magnetic Schottky junctions.

2. The transport characterisation of potential spin-injectors into standard semiconductors.

On both directions, a number of different metal-semiconductor combinations have been prepared and studied, both by standard electronic transport methods and photo-transport methods. A classification of most of the possible magnetic field effects has been done, simple theoretical framework for their analysis and discrimination has been developed and evidence for their practical importance provided. A previously unreported phenomenon - the junction magneto-photo-voltaic effect has been observed. Low Schottky barrier material combinations have been explored.

Chapter 3

Tunnelling in Ferromagnet/Insulator/Ferromagnet structures

3.1 The theory of tunnelling

An attempt will be made to summarise the key points from the theory of tunnelling, necessary for the understanding and modelling of the various aspects of the electronic transport in magnetic tunnel junctions.

3.1.1 Basic analysis and definitions

The influence of tunnelling on the electronic transport in Schottky junctions was already treated in sections 2.1.4.4 and A.3.3. While normally, the tunnelling current is not the dominant current component (at least at moderate forward bias and semiconductor doping levels, and at high enough temperatures, among other requirements) in Schottky diodes; in artificially constructed metal/insulator/metal tunnel junctions, it should be, ideally, the main contribution to the total current, and thus deserves further theoretical elaboration.

The idealised energy diagrams of two similar metal electrodes separated by vacuum and by an insulator, at equilibrium, are illustrated at figure 3.1. Standard notation is implied, with χ_i being the electron affinity of the insulator and x_i its thickness. To zeroth approximation, the influence of the insulator is to lower the height of the potential barrier ϕ_b existing between the two metal electrodes by an amount χ_i, so that it becomes:

$$q\phi_\mathrm{b} = \Phi_\mathrm{m} - \chi_\mathrm{i} \tag{3.1.1}$$

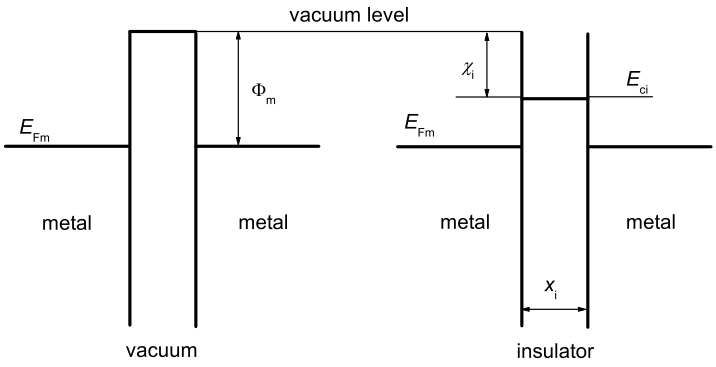

Figure 3.1: Energy diagrams of two similar metal electrodes separated by vacuum (left) and by and insulator (right).

Similar elementary analysis for the case of dissimilar metals with work functions Φ_m^l and Φ_m^r where, for definitiveness, the right-hand side electrode is chosen to have larger work function ($\Phi_m^l < \Phi_m^r$) is sketched on figure 3.2. Again, the validity of the Mott-Schottky rule for noninteracting surfaces is implied, and therefore the potential profile can be evaluated as:

$$q\phi(x) = \Phi_m^l - \chi_i + \left(\Phi_m^r - \Phi_m^l\right)\frac{x}{x_i} \tag{3.1.2}$$

within the insulator thickness x_i.

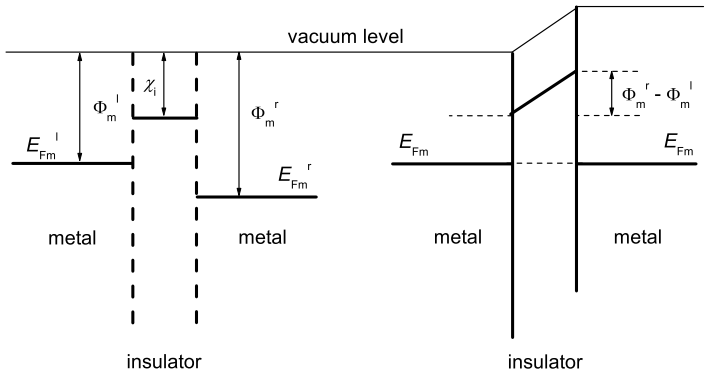

Figure 3.2: Energy diagrams of two dissimilar metal electrodes before (left) and after (right) they have been brought into intimate contact with an insulator slab.

In reality, the situation is far more complicated. Often, the tunnel junctions used in experiments, have insulating layers, which are amorphous or have a low degree of crystallinity. The

applicability of a simple band-picture for the theoretical description of such cases is limited by the existence of states in the forbidden zone (within the energy gap for a infinite single crystal) of the insulator. The position and the density of these states can influence both the barrier formation and the transport characteristics.

For a thick barrier, to a good approximation, the band-picture, may be considered applicable, by taking into account the effective density of the so-called 'disorder-induced' states in the insulator slab. This leads to renormalisation of the current density, as well as, the tunnelling magnetoresistance for magnetic tunnel junctions as schematically demonstrated by Tsymbal & Pettifor (1998).

Moreover, at small insulator thicknesses, the localised disorder-conductance paths (not too dissimilar to microscopic thickness variations or pin-holes) result in conductance that is dominated by several localised channels (defined by lower thickness and/or particular disorder configurations). The analysis of such a structure is far more complicated, but generally the behaviour can be understood in terms of quasi-one-dimensional tunnelling through an effective potential barrier, the height of which decreases with disorder, assuming, of course, the junction area is large enough for a statistical treatment of the problem (see Tsymbal & Pettifor (1998)).

3.1.2 The influence of image forces

The exponential sensitivity of the tunnelling current towards changes in the barrier height (see equation A.3.29), requires detailed handling of all effects that could possibly alter the barrier shape and/or the average barrier height, in order to avoid errors of orders of magnitude in the theoretical description of the transport characteristics of tunnel junctions. One such effect is associated with the existence of image forces as argued by Simmons (1969).

For distances x large compared with the typical interatomic spacings or $x \gg a_0$, the problem may be treated using classical electrodynamics. An electron approaching (in vacuum) a sufficiently large and thick flat metal surface, polarises it, and thus and additional force P^{i} and associated electric potential ϕ^{i} exist given by:

$$\phi^{\mathrm{i}} = \int_{\infty}^{x} P^{\mathrm{i}} \mathrm{d}x \tag{3.1.3}$$

$$\phi^{\mathrm{i}} = -\frac{1}{4\pi\epsilon_0}\frac{q^2}{4x} \tag{3.1.4}$$

The additional electric potential ϕ^{i} for the two electrode system visualised on figure 3.1 may

be evaluated using the conventional mirror image methods as the convergent series[1]:

$$\phi^{\mathrm{i}}(x) = -\frac{q^2}{8\pi\epsilon_{\mathrm{i}}}\left\{\frac{1}{2x} + \sum_{n=1}^{\infty}\left[\frac{nx_{\mathrm{i}}}{(nx_{\mathrm{i}})^2 - x^2} - \frac{1}{nx_{\mathrm{i}}}\right]\right\} \tag{3.1.5}$$

where ϵ_{i} is the permittivity of the insulator., and $x = 0$ is set at the interface between the left electrode and the insulator.

The sum in the right-hand side of equation 3.1.5 can be resolved in special functions as:

$$\sum_{n=1}^{\infty}\left[\frac{nx_{\mathrm{i}}}{(nx_{\mathrm{i}})^2 - x^2} - \frac{1}{nx_{\mathrm{i}}}\right] = -\frac{1}{2x_{\mathrm{i}}}\left[\psi\left(-\frac{x - x_{\mathrm{i}}}{x_{\mathrm{i}}}\right) + \psi\left(\frac{x + x_{\mathrm{i}}}{x_{\mathrm{i}}}\right) - 2\psi(1)\right] \tag{3.1.6}$$

where $\psi(x)$ is the digamma function[2]. Convenient approximation of the above formulation has been suggested by Simmons (1963) in the form:

$$\phi^{\mathrm{i}} \approx -\frac{q^2}{16\pi\epsilon_{\mathrm{i}}}\frac{0.795\ x_{\mathrm{i}}}{x\,(x_{\mathrm{i}} - x)} \tag{3.1.7}$$

which is far more tractable, while preserving reasonable accuracy, as evidenced on figure 3.3.

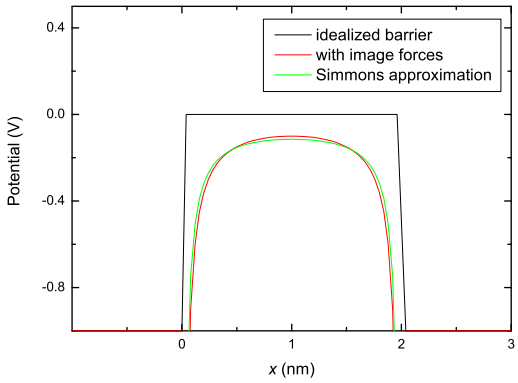

Figure 3.3: Potential profiles, for an arbitrary tunnel junction at equilibrium. The nominal barrier height is 1 eV, and barrier width is 2 nm.

At nonzero external bias V_{a}, the electric potential within the barrier can be expressed as the direct superposition of the already existing potential with the applied one as follows:

$$\phi(x) = \phi_{\mathrm{b}} - \phi^{\mathrm{i}}(x) - qV_{\mathrm{a}}\frac{x}{x_{\mathrm{i}}} \tag{3.1.8}$$

Similar situation is visualised on figure 3.4.

The extremities of the barrier on both sides x_{l} and x_{r} can be evaluated by finding the cross section of barrier with the quasi-Fermi level of the negatively charged electrode. This can be

[1] Here n is just a 'dummy' summation index.

[2] The digamma function $\psi(x)$ may be defined as $\psi(x) = \frac{\mathrm{d}}{\mathrm{d}x}\ln[\Gamma(x)]$, where the gamma function $\Gamma(x)$ can be expressed as $\Gamma(x) = \int_0^{\infty} t^{x-1}e^{-t}\mathrm{d}t$.

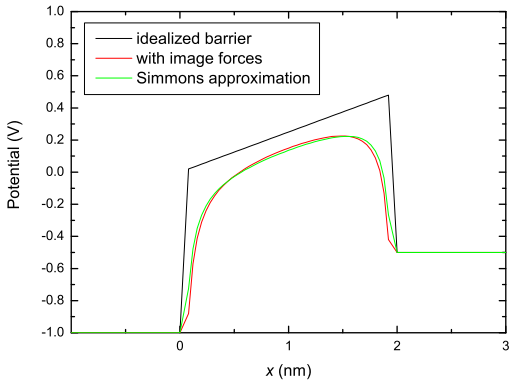

Figure 3.4: Potential profiles, for an arbitrary tunnel junction at applied voltage $V_\mathrm{a} = 0.5$ V. The nominal barrier height is 1 eV, and barrier width is 2 nm.

done either numerically, or using the approximate analytical forms derived by Simmons (1963): For $V_\mathrm{a} \lesssim \phi_\mathrm{b}$:

$$x_\mathrm{l} \approx \frac{3\cdot 10^{-10}\mathrm{eVm}}{q\phi_\mathrm{b}}\frac{\epsilon_0}{\epsilon_\mathrm{i}} \tag{3.1.9}$$

$$x_\mathrm{r} \approx x_\mathrm{l} + x_\mathrm{i}\left\{1 - \frac{23\cdot 10^{-10}\mathrm{eVm}}{x_\mathrm{i}}\frac{\epsilon_0}{\epsilon_\mathrm{i}}\left[3q\phi_\mathrm{b} + \frac{10\cdot 10^{-10}\mathrm{eVm}}{x_\mathrm{i}}\frac{\epsilon_0}{\epsilon_\mathrm{i}} - 2qV_\mathrm{a}\right]^{-1}\right\} \tag{3.1.10}$$

For $V_\mathrm{a} > \phi_\mathrm{b}$:

$$x_\mathrm{l} \approx \frac{3\cdot 10^{-10}\mathrm{eVm}}{q\phi_\mathrm{b}}\frac{\epsilon_0}{\epsilon_\mathrm{i}} \tag{3.1.11}$$

$$x_\mathrm{r} \approx \left(q\phi_\mathrm{b} - \frac{14\cdot 10^{-10}\mathrm{eVm}}{x}\frac{\epsilon_0}{\epsilon_\mathrm{i}}\right)\frac{x_\mathrm{i}}{qV_\mathrm{a}} \tag{3.1.12}$$

Out of equilibrium, at a nonzero bias V_a, the current density J may be expressed, within the WKB approximation as (see for example Simmons (1969)):

$$J = \frac{q}{h}\frac{1}{2\pi\left(a\Delta x\right)^2}\left\{\overline{\phi_\mathrm{b}}\exp\left(-k_0^{\mathrm{WKB}}\Delta x\right) - \left(\overline{\phi_\mathrm{b}} + qV_\mathrm{a}\right)\exp\left(-k^{\mathrm{WKB}}\Delta x\right)\right\} \tag{3.1.13}$$

where $\Delta x = x_\mathrm{r} - x_\mathrm{l}$ and the momenta within the WKB approximation, k_0^{WKB} and k^{WKB} are defined as follows:

$$k_0^{\mathrm{WKB}} = \frac{4\pi a}{h}\sqrt{2m_\mathrm{i}^\star\overline{\phi_\mathrm{b}}} \tag{3.1.14}$$

$$k^{\mathrm{WKB}} = \frac{4\pi a}{h}\sqrt{2m_\mathrm{i}^\star\left(\overline{\phi_\mathrm{b}} + qV_\mathrm{a}\right)} \tag{3.1.15}$$

where a is a dimensionless coefficient which depends on the barrier shape ($a = 1$ for a strictly rectangular barrier, but is also generally close to unity), and the average barrier height $\overline{\phi_\mathrm{b}}$ can

be estimated as follows:

$$\overline{\phi_{\mathrm{b}}} = \frac{1}{\Delta x}\int_{x_{\mathrm{l}}}^{x_{\mathrm{r}}} \phi_{\mathrm{b}} \mathrm{d}x \tag{3.1.16}$$

Once again, the integral 3.1.16 can be either evaluated numerically, using the relation:

$$\overline{\phi_{\mathrm{b}}} = \phi_{\mathrm{b}} - V_{\mathrm{a}} - \frac{q^2}{16\pi\epsilon_{\mathrm{i}}}\frac{1}{\Delta x}\left\{\ln\left(\frac{x_{\mathrm{r}}}{x_{\mathrm{l}}}\right) + \ln\frac{\Gamma\left[\frac{x_{\mathrm{i}}-x_{\mathrm{r}}}{x_{\mathrm{i}}}\right]\Gamma\left[\frac{x_{\mathrm{i}}+x_{\mathrm{l}}}{x_{\mathrm{i}}}\right]}{\Gamma\left[\frac{x_{\mathrm{i}}+x_{\mathrm{r}}}{x_{\mathrm{i}}}\right]\Gamma\left[\frac{x_{\mathrm{i}}-x_{\mathrm{l}}}{x_{\mathrm{i}}}\right]} + 2\psi(1)\frac{\Delta x}{x_{\mathrm{i}}}\right\} \tag{3.1.17}$$

which is supposed to be exact within the quasi-classical approximation; or alternatively, the approximate form derived by Simmons (1969) may be used:

$$\overline{\phi_{\mathrm{b}}} \approx \phi_{\mathrm{b}} - V_{\mathrm{a}}\frac{x_{\mathrm{l}}+x_{\mathrm{r}}}{2x_{\mathrm{i}}} - \frac{2.86\cdot 10^{-10}\mathrm{eVm}}{\Delta x}\frac{\epsilon_0}{\epsilon_{\mathrm{i}}}\ln\frac{x_{\mathrm{r}}\left(x_{\mathrm{i}}-x_{\mathrm{l}}\right)}{x_{\mathrm{l}}\left(x_{\mathrm{i}}-x_{\mathrm{r}}\right)} \tag{3.1.18}$$

For most purposes the exact barrier shape is irrelevant and the Simmons approximation for $\overline{\phi_{\mathrm{b}}}$ is fully sufficient to model the rough $I-V$ characteristics of tunnel junctions. This is demonstrated on figure 3.5, via an example of a symmetric junction of two identical metal electrodes with an insulator ($\epsilon_{\mathrm{i}} = 5\epsilon_0$). The barrier height is been chosen to be 1 V, and the current density is evaluated for biases in the interval $[10^{-6}\phi_{\mathrm{b}}, 2\phi_{\mathrm{b}}]$. The excellent correspondence of the Simmons approximation to the results of the exact numerical integration is evident for both the low-voltage $V_{\mathrm{a}} \ll \phi_{\mathrm{b}}$ linear (ohmic) regime, and for the high-voltage $V_{\mathrm{a}} \gtrsim \phi_{\mathrm{b}}$ exponential region of the $I-V$ characteristic.

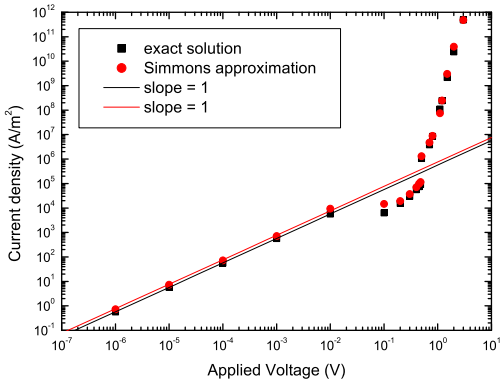

Figure 3.5: Current density as a function of applied voltage, calculated by both direct integration and the Simmons approximation. The nominal barrier height is 1 eV, and barrier width is 2 nm.

3.1.3 Effective tunnelling Hamiltonian model

Starting once again from the effective Schrödinger equation A.3.21:

$$\left[\frac{\hbar^2 k^2}{2m^\star} + q\phi(x)\right]\Psi(x) = E\Psi(x) \tag{3.1.19}$$

an exact matching procedure, would require the general solutions, which are in regions where $E - q\phi(x) > 0$ are superposition of 'forward' and 'backword' plain waves:

$$\Psi(x) = a\mathrm{e}^{ikx} + b\mathrm{e}^{-ikx} \tag{3.1.20}$$

and in regions where $E - q\phi(x) < 0$ exponentially decaying and growing waves:

$$\Psi(x) = a\mathrm{e}^{-\varkappa x} + b\mathrm{e}^{-\varkappa x} \tag{3.1.21}$$

where $\varkappa = -ik$; to be connected at the boundaries of the different without discontinuity in either $\Psi(x)$ or its first derivative $\frac{\mathrm{d}\Psi(x)}{\mathrm{d}x}$. The coefficients a and b in the different regions are most easily determined by employing a method analogous to the global transfer matrix already used within the WKB approximation in section A.3.2. For the model system depicted on figure 3.6, on the boundary between regions with numbers u and $u+1$, can be done using reflection matrix $\mathbf{R}_{u,u+1}$ defined for all values of k as:

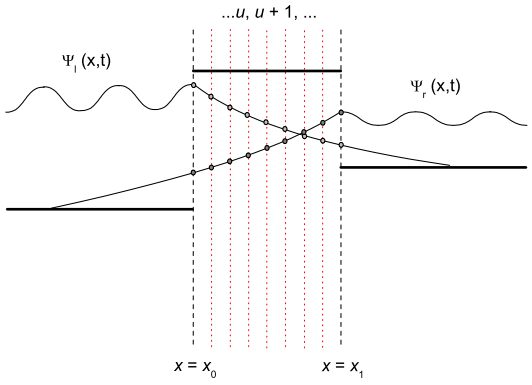

Figure 3.6: Schematic representation of the decomposition of the scattering problem within the global transfer matrix method.

$$\mathbf{R}_{u,u+1} = \frac{1}{2k_u}\begin{pmatrix} (k_u + k_{u+1})\exp\left[i\left(-k_u + k_{u+1}\right)x_u\right] & (k_u - k_{u+1})\exp\left[i\left(-k_u - k_{u+1}\right)x_u\right] \\ (k_u - k_{u+1})\exp\left[i\left(k_u + k_{u+1}\right)x_u\right] & (k_u + k_{u+1})\exp\left[i\left(k_u - k_{u+1}\right)x_u\right] \end{pmatrix} \tag{3.1.22}$$

with the vectors of the amplitude coefficients related as:

$$\begin{pmatrix} a_u \\ b_u \end{pmatrix} = \mathbf{R}_{u,u+1}\begin{pmatrix} a_{u+1} \\ b_{u+1} \end{pmatrix} \tag{3.1.23}$$

More generally, for a number of regions, the total reflection matrix $\mathbf{R}$ is given simply by the product of the individual reflection matrices $\mathbf{R}_{u,u+1}$ like:

$$\mathbf{R} = \prod_{u=0}^{nu} \mathbf{R}_{u,u+1} \tag{3.1.24}$$

where $u \in [0, nu-1]$ and nu is the number of the rightmost region of the potential 'landscape'. For a model system consisting of three regions 0, 1 and 2, representing respectively; left-hand-side metal electrode, insulator and right-hand side metal electrode; the tunnelling probability Θ can be expressed as the ratio of the probability currents j_2 and j_0 defined via the amplitudes of the travelling waves as:

$$j_u = \frac{\hbar k_u}{m_u^\star} |a_u|^2 \tag{3.1.25}$$

to yield the familiar result (see section A.3.27):

$$\Theta = \frac{j_2}{j_0} = \frac{16 k_0 k_2 \varkappa_1^2}{(k_0^2 + \varkappa_1^2)(k_2^2 + \varkappa_1^2)} \mathrm{e}^{-2\varkappa_1 \Delta x} \tag{3.1.26}$$

with $\varkappa$ defined in the usual way:

$$\varkappa_u = \frac{\sqrt{2m_u^\star (q\phi_u - E)}}{\hbar} \tag{3.1.27}$$

with the potential ϕ_u assumed constant within each the region u, but varies from region to region[1].

Another approach to the problem has been suggested by Bardeen (1961). The smallness of the tunnelling probability (for realistic parameters $\Theta \sim 10^{-5} - 10^{-10}$, see Kane (1969)), brings about the idea of using approximate solutions for the wavefunction which continue to decay after tunnelling through the potential barrier, instead of being travelling waves. The following states can be chosen for the left and right-hand sides of the system:

$$\begin{aligned} \Psi_\mathrm{l}(x) &= a_{1\mathrm{l}} \mathrm{e}^{-\varkappa_1 x}; \quad x \geq x_0 \\ \Psi_\mathrm{r}(x) &= b_{1\mathrm{r}} \mathrm{e}^{\varkappa_1 x}; \quad x \leq x_1 \end{aligned} \tag{3.1.28}$$

so that Ψ_l is to matched to the correct solution for $x \leq x_0$, but decays for all $x \geq x_0$; and Ψ_r is to be matched to the correct solution for $x \geq x_1$, but decays for all $x \leq x_0$; and both states do not satisfy the starting Schrdinger equation with the original Hamiltonian, say $\mathcal{H}_0$. The the simplified situation is sketched on figure 3.7.

If then the electron is assumed to be initially in the state Ψ_l and have a final state Ψ_r, then conventional time-dependent perturbation theory can be employed for the time-dependent wavefunction $\Psi(x,t)$:

$$\Psi(x,t) = c(t)\Psi_\mathrm{l}(x)\mathrm{e}^{-\frac{iE_\mathrm{l}t}{\hbar}} + d(t)\Psi_\mathrm{r}\mathrm{e}^{-\frac{iE_\mathrm{r}t}{\hbar}} \tag{3.1.29}$$

where $c(t)$ and $d(t)$ are probability amplitude coefficients and E_l and E_r are the energies of the electron on left and right-hand side of the structure, respectively.

[1] This method is convenient for numerical realisation in case of 'smoothly' varying potential $\phi(x)$, by breaking down the system into discrete regions of constant potential ϕ_u.

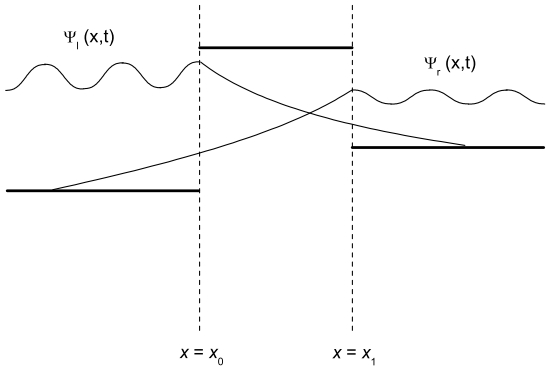

Figure 3.7: Schematic diagram of the modified wavefunctions in the effective Hamiltonian approach.

Substituting the wavefunction 3.1.29 into the time dependent Schrödinger equation:

$$i\hbar\frac{\partial\Psi}{\partial t} = \mathcal{H}\Psi \tag{3.1.30}$$

yields:

$$i\hbar\frac{\partial c}{\partial t}\Psi_{\rm l}{\rm e}^{-\frac{iE_{\rm l}t}{\hbar}} + c\Psi_{\rm l}{\rm e}^{-i\frac{E_{\rm l}t}{\hbar}} + i\hbar\frac{\partial d}{\partial t}\Psi_{\rm r}{\rm e}^{-\frac{iE_{\rm r}t}{\hbar}} + d\Psi_{\rm r}{\rm e}^{-\frac{iE_{\rm rt}}{\hbar}} = c{\rm e}^{-\frac{E_{\rm l}t}{\hbar}}\mathcal{H}\Psi_{\rm l} + d{\rm e}^{-i\frac{E_{\rm r}t}{\hbar}}\mathcal{H}\Psi_{\rm r} \tag{3.1.31}$$

which can be simplified by noting that $c \approx 1$ and $d \approx 0$, as the probability of finding the electron on the left-hand side is, normally, much greater than the same on the right-hand side, as well as $\frac{\partial c}{\partial t} \approx 0$ because of particle conservation (the normalisation condition demands that the total probability is conserved or $\frac{\rm d}{{\rm d}t}\left(cc^\star + dd^\star\right) = 0$)[1], and therefore:

$$i\hbar\frac{\partial d}{\partial t}\Psi_{\rm r}{\rm e}^{-\frac{iE_{\rm r}t}{\hbar}} = \left(\mathcal{H} - E_{\rm l}\right)\Phi_{\rm l}{\rm e}^{-\frac{iE_{\rm l}t}{\hbar}} \tag{3.1.32}$$

Using the fact the fact that $\Psi_{\rm l}$ and $\Psi_{\rm r}$ can be normalised so that:

$$\int \Psi_{\rm l}\Psi_{\rm l}^\star {\rm d}x = \int \Psi_{\rm r}\Psi_{\rm r}^\star {\rm d}x = 1 \tag{3.1.33}$$

with the integration taken over the length of the system (or over the entire x-axis, equation 3.1.32 can be rewritten as:

$$i\hbar\frac{\partial d}{\partial t} = {\rm e}^{\frac{i\left(E_{\rm r}-E_{\rm l}\right)t}{\hbar}}\int \Psi_{\rm r}^\star\left(\mathcal{H} - E_{\rm l}\right)\Psi_{\rm l}{\rm d}x \tag{3.1.34}$$

which is, to within a constant, equivalent to the standard expression from time-dependent perturbation theory (see for example Woan (2000)), for a single initial state $\Psi_{\rm l}$ and a single final state $\Psi_{\rm r}$, with a Hamiltonian that can be broken down as:

$$\mathcal{H}(t) = \mathcal{H}_0 + \mathcal{H}_1(t) \tag{3.1.35}$$

[1] Here, * denotes complex conjugate.

and wavefunction $\Psi(x,t)$ with the final state amplitude given by:

$$d(t) = -\frac{i}{\hbar}\int_0^t \langle \Psi_\mathrm{r}|\mathcal{H}_1(t')|\Psi_\mathrm{l}\rangle \mathrm{e}^{\frac{i(E_\mathrm{r}-E_\mathrm{l})t'}{\hbar}}\mathrm{d}t' \tag{3.1.36}$$

The constant is of course zero, as in the initial moment of time $d(0) = 0$.

The matrix element for the transition from the left-hand side to the right-hand side is thus given by:

$$\mathcal{T}_\mathrm{rl} = \int \Psi_\mathrm{r}^\star \left(\mathcal{H} - E_\mathrm{l}\right)\Psi_\mathrm{l}\mathrm{d}x \tag{3.1.37}$$

and therefore the perturbation is expressed as:

$$\mathcal{H}_1 = \mathcal{H} - E_\mathrm{l} \tag{3.1.38}$$

and the unperturbed Hamiltonian satisfies:

$$\mathcal{H}_0\Psi_\mathrm{l} = E_\mathrm{l}\Psi_\mathrm{l} \tag{3.1.39}$$

with the associated necessary condition ($\mathcal{H}_1 \ll \mathcal{H}_0$) for validity of the perturbation approach:

$$\frac{\mathcal{H} - E_\mathrm{l}}{E_\mathrm{l}} \ll 1 \tag{3.1.40}$$

which means, also, that the initial and final energies need not be too different:

$$\frac{E_\mathrm{r} - E_\mathrm{l}}{E_\mathrm{l}} \ll 1 \tag{3.1.41}$$

The problem can be analysed further, by noting that the integral in equation 3.1.37 receives nonzero contributions only from the interval $x > x_1$ and thus can be symmetrised by extending it with a term of zero contribution in the interval $x > x_0$, like:

$$\mathcal{T}_\mathrm{rl} = \int_{x_0<x<x_1}^{\infty} \Psi_\mathrm{r}^\star \left(\mathcal{H} - E_\mathrm{l}\right)\Psi_\mathrm{l} - \Psi_\mathrm{l}\left(\mathrm{H} - E_\mathrm{r}\right)\Psi_\mathrm{r}^\star \mathrm{d}x \tag{3.1.42}$$

Integrating by parts the right-hand side of equation 3.1.42, an expression much like the conventional probability density current can be recognised in:

$$T_\mathrm{rl} = -\frac{\hbar^2}{2m^\star}\left(\Psi_\mathrm{r}^\star\frac{\mathrm{d}\Psi_\mathrm{l}}{\mathrm{d}x} - \Psi_\mathrm{l}\frac{\mathrm{d}\Psi_\mathrm{r}^\star}{\mathrm{d}x}\right)_{x_0<x<x_1} \tag{3.1.43}$$

as in the standard definition (see for example Woan (2000)):

$$j(x) = -\frac{i\hbar}{2m}\left(\Psi^\star\frac{\partial\Psi}{\partial x} - \Psi\frac{\partial\Psi^\star}{\partial x}\right) \tag{3.1.44}$$

and therefore:

$$\mathcal{T}_\mathrm{rl} = -i\hbar j_\mathrm{rl} \tag{3.1.45}$$

where j_{rl} is considered continuous across the barrier region and a single effective mass has been assumed in all regions (the correct generalisation is out for the scope of the present discussion and will be treated later).

The probability density current incident (left-hand side) on the barrier can be estimated using equation 3.1.25 to be:

$$j_0 = \frac{\hbar k_0}{m^\star}|a_0|^2 \tag{3.1.46}$$

Fermi's golden rule may be employed to deduce the transmitted current on the right-hand side as:

$$j_2 = \frac{2\pi}{\hbar}|\mathcal{T}_{\mathrm{rl}}|^2\mathcal{D}(E_{\mathrm{r}}) \tag{3.1.47}$$

and thus $\Theta = \frac{j_2}{j_0}$ can be evaluated if the matrix element $\mathcal{T}_{\mathrm{rl}}$ is known. The matrix element, itself, can be evaluated employing different methods. If the direct matching procedure is used, $\mathcal{T}_{\mathrm{rl}}$ may be written as:

$$\mathcal{T}_{\mathrm{rl}} = \frac{\hbar^2\varkappa_1}{m^\star}b^\star_{1\mathrm{r}}a_{1\mathrm{l}} \tag{3.1.48}$$

and thus, the result already obtained by direct matching, as equation 3.1.26, is recovered. Therefore the first-order time-dependent perturbation theory (or in other words, the effective Hamiltonian approach to the tunnelling problem) recovers the same result as the simple matching of the partial wavefunctions in the different regions.

The effective Hamiltonian approach seems, at first, to introduce into the solution for the current J a proportionality to the density of states $\mathcal{D}$ via equation 3.1.47. Nevertheless, no direct proportionality to the density of states is obvious in the final result 3.1.26. Whether or not, and in what circumstances, the energy dependence of the density of states of the electrodes influences the tunnelling current, is a very important question, from experimental point of view, which is the subject of section 3.1.4.

3.1.4 Independent-particle tunnelling

The limitations of the independent-particle model of tunnelling have been analysed in detail by Harrison (1961). Below, just an outline of the original argumentation will be given.

The quantum states in the structure can be chosen to be represented by linear combinations of one dimensional Bloch waves (see for example Kittel (1996)):

$$\psi_k(x) = u_k(x)\exp(ikx) \tag{3.1.49}$$

with $u_k(x)$ having the periodicity of the crystal lattice. These states may be represented by their associated plane waves $\tilde{\psi}(k)$. As the Bloch states ψ_k must be matched continuously at all boundaries in the system, the associated plane waves $\tilde{\psi}(k)$ are, in principle not smooth and

discontinuous. Set of functions $\tilde{\alpha}(E,\mathbf{k})$ and $\tilde{\beta}(E,\mathbf{k})$ may be introduced such that $\tilde{\beta}\tilde{\psi}$ and $\tilde{\alpha}\frac{\partial\tilde{\psi}}{\partial x}$ are continuous at all boundaries.

A generalized form of the probability density current may be introduced as:

$$j_x = -\frac{i\hbar}{2m^\star}\left[\tilde{\psi}^\star\tilde{\alpha}\frac{\partial}{\partial x}\tilde{\beta}\tilde{\psi} - \tilde{\psi}\tilde{\alpha}\frac{\partial}{\partial x}\tilde{\beta}\tilde{\psi}^\star\right] \tag{3.1.50}$$

so that it is conserved on all boundaries within the system. The velocity $v_x(k_x)$ associated with any particular state $\tilde{\psi}(k)$ is thus given by:

$$v_x = \frac{\hbar}{m^\star}\tilde{\alpha}\tilde{\beta}k_x \tag{3.1.51}$$

and can be also evaluated via the isotropic effective mass independent particle approximation as:

$$v_x = \frac{p_x}{m^\star} = \frac{1}{\hbar}\frac{\partial E}{\partial k_x} \tag{3.1.52}$$

and therefore the effective wave-number $\tilde{\alpha}\tilde{\beta}k_x$ can be evaluated as:

$$\tilde{\alpha}\tilde{\beta}k_x = \frac{m^\star}{\hbar^2}\frac{\partial E}{\partial k_x} \tag{3.1.53}$$

and for the case of elastic tunnelling should be matched at the interfaces. As pointed out by Harrison (1961), the associated plane waves obey the wave equation:

$$\frac{\partial^2\tilde{\psi}}{\partial x^2} + k_x^2\tilde{\psi} = 0 \tag{3.1.54}$$

in regions of constant band structure $E(\mathbf{k})$. The method can be generalized for continuously varying band structure by using a wave equation with the effective wave number $\tilde{\alpha}\tilde{\beta}k_x$ as:

$$\tilde{\beta}\frac{\partial}{\partial x}\frac{\tilde{\alpha}}{\tilde{\beta}}\frac{\partial}{\partial x}\tilde{\beta}\tilde{\psi} + \tilde{\beta}\tilde{\alpha}k_x^2\tilde{\psi} = 0 \tag{3.1.55}$$

where $\tilde{\psi}(x)$, $\tilde{\alpha}(x)$, $\tilde{\beta}(x)$ and $k_x(x)$ have to be varying slowly on a scale set by the kernel of $u(x)$, in order for the above approximations to be valid. Equations 3.1.54 and 3.1.55 are strictly valid for real wave numbers $\mathbf{k}$, and in order to threat tunnelling problems, must be generalized by analytic continuation for complex $\mathbf{k}$. The same, of course, concerns the band structure $E(\mathbf{k})$.

In order to proceed, various methods can be used to find the wave functions (direct matching, WKB approximation, etc.), calculate the matrix element $\mathcal{T}_{\mathrm{lr}}$ and calculate the electronic current density, employing time-dependent perturbation theory:

$$J = \frac{4\pi q}{\hbar}\sum_{k_\mathrm{t}}\int_{-\infty}^{\infty}|\mathcal{T}_{\mathrm{lr}}|^2\mathcal{D}_\mathrm{l}\left(k_\mathrm{t}\right)\mathcal{D}_\mathrm{r}\left(k_\mathrm{t}\right)\left(f_\mathrm{l}-f_\mathrm{r}\right)\mathrm{d}E \tag{3.1.56}$$

where k_t is the wavenumber component perpendicular to the x-axis (the transverse momentum), and f_l and f_r are the probabilities of occupation of the respective states. As the matrix element

is generally proportional to the density current operator between the states on both sides of the junction through equation 3.1.45, and the probability current density operator $\mathbf{j}$ can generally be expressed as[1]:

$$\mathbf{j} = \Re\left(\Psi^{\star}\mathbf{v}\Psi\right) \tag{3.1.57}$$

and if the tunnelling velocity is taken in the form of equation 3.1.51, then the matrix element $\mathcal{T}_{\mathrm{lr}}$ would be proportional to the inverse of the density of states as:

$$\mathcal{T}_{\mathrm{lr}} \propto \frac{\partial E}{\partial k_x} \tag{3.1.58}$$

therefore the total current will not, generally, be directly proportional to the density of states as the direct dependence in equation 3.1.56 would be compensated by the indirect dependence through the matrix element:

$$J \propto |\mathcal{T}|^2 \mathcal{D}_{\mathrm{l}} \mathcal{D}_{\mathrm{r}} \propto \left(\frac{\partial E}{\partial k_x}\right)^2 \left(\frac{\partial E}{\partial k_x}\right)^{-1} \left(\frac{\partial E}{\partial k_x}\right)^{-1} \tag{3.1.59}$$

and no particular dependence sharp dependence on applied bias expected in the tunnelling current and its derivatives.

The same lack of direct dependence, can be shown explicitly by estimating the matrix element $\mathcal{T}_{\mathrm{lr}}$ within the WKB approximation. The wavefunctions can be chosen as linear superposition of the forms (see for example Menzel (1960)):

$$\tilde{A}_u \frac{1}{\sqrt{\tilde{\alpha}\tilde{\beta}k_x}} \exp\left(i\int k_x \mathrm{d}x\right) \tag{3.1.60}$$

with the boundaries of the integrals taken between the classical turning points and the limits of the extend of the side electrodes, with normalisation constants $\tilde{A}_u$. One more time, as the effective wave number $\tilde{\alpha}\tilde{\beta}k_x$ is inversely proportional to the density of states, within the independent-particle approximation, there is no structure from the density of states appearing in the bias dependence of the current integral:

$$J = \gamma\frac{q}{h}\sum_{k_{\mathrm{t}}}\int_{-\infty}^{\infty} \exp\left(-\gamma\int_{x_0}^{x_1}|k_x|\mathrm{d}x\right)\left(f_{\mathrm{l}} - f_{\mathrm{r}}\right)\mathrm{d}E \tag{3.1.61}$$

with the quantum degeneracy $\gamma = 2$, in the non-spin-polarised case.

Equation 3.1.61 seems, at first, to be in direct contradiction with the experimental facts pointed out even in the earliest experiments in tunnelling to and from superconductors (see for example Giaever (1960a,b)), which evidenced that details from the density of states do appear in the bias dependence of the current and its derivatives. As pointed out by Harrison (1961),

[1] $\Re(x)$ denotes real part of x.

the key is in the breakdown of the independent-particle approach for highly correlated systems (like superconductors). The common assertion that in such experiments the density of states is the quasi-particle one (gapped Cooper pairs) and the matrix element is the one expected for normal metals due to Bardeen (1961), leads to lack of current conservation on the boundary of between, say, a normal metal and a superconductor, within the one-particle approach[1]. This phenomenon is the topic of section 3.1.5. For tunnelling between normal metals, semimetals and semiconductors, a breakdown of the independent-particle model is not expected, and therefore simple proportionality of the, say, differential conductance to the density of states is highly unlikely.

A more 'visual' and informative description is obtained by substituting the sum in equation 3.1.61 with and integral over the projection of constant energy surface onto the plane of the tunnel interface like:

$$J = \gamma \frac{q}{h} \frac{1}{(2\pi)^2} \int_{-\infty}^{\infty} \mathrm{d}E \, (f_\mathrm{l} - f_\mathrm{r}) \int 2\pi k_\mathrm{t} \mathrm{d}k_\mathrm{t} \exp\left(-\gamma \int_{x_0}^{x_1} |k_x| \mathrm{d}x \right) \tag{3.1.62}$$

thus the integral over $\mathrm{d}^2 k_\mathrm{t}$ is essentially the overlap of the projections of the constant energy surfaces on both sides of the junction on a plane parallel to the interface in k-space. It follows that, if at least one of the energy surfaces is small, as it is often the case in semiconductors and semimetals, the exponential factor becomes practically constant the current becomes proportional to area of overlap of the projections of the constant energy surfaces. If, on the other hand, both surfaces are large, as is the case in simple metals, the exponential factor dominates, allowing only states with small k_t to contribute to the current density integral, or which is the same, only electrons moving approximately normal to the tunnel interface need be taken into account as already mentioned in section 2.1.6.1. A situation with two comparable ellipsoidal Fermi surfaces is illustrated on figure 3.8.

It is important to check whether or not the absence of the density of states in the expression for the current 3.1.62 is associated with the smoothness of the transition between the different regions of the junction, implied by the WKB approximation. The analysis may be done on the base of equation 3.1.26, if the band structure is neglected, by recollecting, that the one dimensional density of states (per unit energy and length) $\mathcal{D}$ and the wavenumber k_x, are connected within the effective mass approximation as:

$$\mathcal{D} = \gamma \frac{1}{2\pi} \left(\frac{\partial E}{\partial k_x} \right)^{-1} = \gamma \frac{1}{2\pi} \frac{m^\star}{\hbar^2} \frac{1}{k_x} \tag{3.1.63}$$

[1] This phenomenon is also known as Andreev reflection, and its investigation yields valuable information for the degree of spin-polarisation in experiments involving low-bias tunnelling between ferromagnetic and superconducting electrodes.

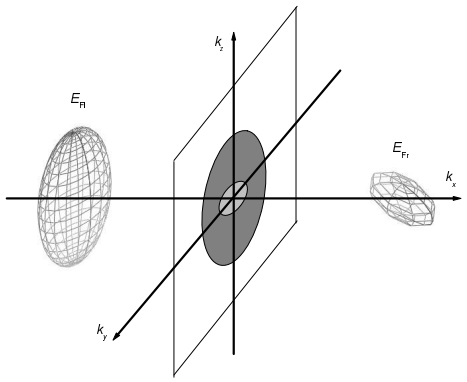

Figure 3.8: Schematic diagram of two constant energy surfaces of $E = E_F$ and their projections on the plane of the tunnel interface.

Alternatively, following Harrison (1961), the effective wavenumber $\tilde{\alpha}\tilde{\beta}k_x$ may be used, by introducing the effective wavelength $\tilde{\lambda}$ like:

$$\tilde{\lambda} = \frac{\tilde{\beta}}{\tilde{\alpha}k_x} = \tilde{\beta}^2 \frac{1}{\gamma} 2\pi \frac{\hbar^2}{m^\star} \mathcal{D} \tag{3.1.64}$$

and $\tilde{\beta}^2$ may physically viewed as the proportional to the value of the normalised Bloch kernels $|u_k(x)|^2$ at the boundaries of the unit cells where the matching of the Bloch states must be performed. The product of the matrix element and the densities of states on both sides of the tunnel junction may thus be reconstructed as:

$$|\mathcal{T}_{lr}|^2 \mathcal{D}_l \mathcal{D}_r = \gamma_l \gamma_r \frac{1}{\pi^2} \frac{\tilde{\lambda}_0 \tilde{\lambda}_1^2 \tilde{\lambda}_2}{\left(\tilde{\lambda}_0^2 + \tilde{\lambda}_1^2\right)\left(\tilde{\lambda}_1^2 + \tilde{\lambda}_2^2\right)} \mathrm{e}^{-2\varkappa_1 \Delta x} \tag{3.1.65}$$

and therefore, an *inverse proportionality* is to be expected between the tunnelling current density and the density of states, not a direct one within the independent-particle approach for strictly abrupt junctions. For junctions, where the transition region at all interfaces are comparable or larger than one electron wavelength, the WKB approximation becomes exceedingly good and no structure from density of states would appear in the tunnel conductance. This is equivalent to asserting, that the density of states influences the bias dependence of the tunnelling current, only via the non-adiabatic processes of quantum reflection and transmission, for independent quasiparticles. Quite the contrary, the adiabatic (long times, long wavelengths) transport seems to be insensitive to details in the density of states.

3.1.5 Many-particle tunnelling

While, within the independent-particle approach to tunnelling, the energy dependence of the density of states does not influence the differential conductance; a many-particle view on the

problem, generally opposes this consequence. In a long-range-correlated electronic system (for example a superconductor or a ferromagnet), the situation is dramatically different.

As an example, tunnelling between a superconductor and a normal metal may be considered. Following Bardeen (1961), the analysis may be qualitatively be made, considering the position dependence of the superconductor energy-gap, and realising, that the gap is essentially non-existent in the insulator. In other words, the long-range corelation in the electronic system, responsible for the modification of the electronic structure in the superconducting state, would not extend beyond the barrier region, thus relieving the tunnelling matrix element from the obligation to be inversely proportional to the density of states. Since the tunnelling matrix element $\mathcal{T}_{\mathrm{lr}}$, to a good approximation, does only depend on the wavefunction within the barrier region (see equation 3.1.43), it should be virtually the same in both the normal and the superconducting state. As the matrix element in the normal state is generally a smooth function of energy (bias), the final result can be expected to be *directly proportional* to the density of states, as suggested by equations 3.1.47 and 3.1.56. A brief overview of the theory of tunnelling between ferromagnetic metals and superconductors is given in appendix B.4. By analogy, similar behaviour should be expected, from junctions, where one or two of the electrodes are ferromagnetic. Should the insulator be nonmagnetic, the magnetic (exchange, dipole, etc.) correlation, would be expected to decay rapidly in the barrier region, thus leaving open the possibility of the energy-dependence of the density of states spin-polarisation to enter the problem[1].

3.1.6 Zero and finite bias anomalies

Deviations from the conventional parabolic voltage dependence (see Brinkman *et al.* (1970)) of the differential tunnelling conductivity are not uncommon. Often these, so called, 'anomalies' take the form of either a peak or a dip centred at $V_{\mathrm{a}} = 0$. The systematic reports of 'zero-bias anomalies' in normal metal tunnel junctions, are too numerous to be referenced explicitly (see for example Rowell & Shen (1966); Wallis & Wyatt (1972)). Reports exist of large shifts, of the order of tens of millivolts of the conductance anomalies from zero bias (for example see Xiang *et al.* (2003b)), attribute similar effects to large differences of the density of states on both sides of the tunnel junction[2]. There are a number of varied phenomena and models thereof, which

[1] It is instructive, to consider the opposite situation, where the long-range magnetic corelation is only weakly perturbed in the barrier region. It would follow that the quasi-electrons can adiabatically tunnel through the barrier region, smoothly adjusting their spin orientation in order to match the local order parameter. Therefore, no strong non-adiabatic quantum reflection would be expected, with its associated density of states dependence.

[2] Large artificial shifts from zero-bias may potentially exist in magnetic tunnel junctions, when substantial difference in temperature of the lattice and/or the electronic subsystem is tolerated. Because of the large expected thermopower (see McCann & Fal'ko (2004)), of the order of $1 - 100$ μV/K, moderate effective temperature gradients can potentially lead to observable internal voltage (current) bias.

have been investigated. Below is a historical reference to most of them.

One early example is the model of Appelbaum (1966), its physical interpretation by Anderson (1966) and its further refinement by Appelbaum *et al.* (1967); Appelbaum (1967); Appelbaum & Brinkman (1970), which suggest that magnetic impurities and the associated localised states may give rise to a peak in conductance close to zero-bias. At one low temperature, such localised states are considered to be momentum reservoirs and thus influence the tunnel current indirectly. The problem is similar to the one of Kondo scattering in the theory of low-temperature conductivity of metals with magnetic impurities. Recently, a large temperature, as well as bias dependance of the differential resistance CoFe/AlO_x/CoFe junctions with substantial amount of magnetic impurities incorporated in the barrier oxide, has also been attributed to the Kondo effect by Lee *et al.* (2007). Also, extension for the case of ferromagnetic electrodes has been performed by Inoue *et al.* (2002).

According to the model of Appelbaum (1966) there can be a logarithmic anomaly of either positive (for antiferromagnetic coupling between the localised states and the conduction electrons), or negative sign (ferromagnetic coupling), of the form:

$$\frac{\Delta\sigma_{\mathrm{j}}}{\sigma_{\mathrm{j}}} \propto -4J_{\mathrm{ex}}\frac{s}{s+1}\left[\mathcal{D}_{\mathrm{l}}\left(E_{\mathrm{F}}\right)+\mathcal{D}_{\mathrm{r}}\left(E_{\mathrm{F}}\right)\right]\ln\left(\frac{kT\pm g\mu_{\mathrm{B}}B}{E_0}\right) \tag{3.1.66}$$

where the symbols have their usual meanings. Or more precisely, at $B \neq 0$ and $kT \ll g\mu_{\mathrm{B}}B$, there would be up to three peaks - one at zero bias and two centred at $\pm\Delta V = \frac{g\mu_{\mathrm{B}}B}{q}$. The model has been validated by a number of experimental observations (see for example Appelbaum & Shen (1971); Losee & Wolf (1969); Shen & Rowell (1967, 1968)), for small amplitudes of the observed effects, while discrepancies have been noticed for large amplitudes, in both the temperature and field dependencies (see Christopher *et al.* (1968)). Though, strong evidence exists (see Mezei (1969); Nielsen (1969, 1970)) that zero-bias anomalies with small characteristic voltage widths are due to impurity scattering, magnetic field-independent broad peaks in the differential conductance spectra often observed in practice, cannot be explained within the model of Appelbaum (1966).

A slightly different model, based on the same idea for scattering and localisation has been developed by Altshuler & Aronov (1979, 1993); Altshuler *et al.* (1980) and has found some experimental verification (see Imry & Ovadyahu (1982); Sood (1982)). In analogy to the treatment of weak localisation magnetoresistance in bulk materials, the residual electron-electron interaction combined with impurity scattering would lead to a change in the spectral function (and therefore to the density of states, or generally the conductivity as in equation B.1.9), close to the Fermi level. As customary (see Landau *et al.* (1989)), the density of states can be

expressed as the momentum (in principle, and spin) integral of the spectral function:

$$\mathcal{S}\left(\mathbf{k},s;E\right) = -\mathrm{Im}\left[\mathcal{G}\left(\mathbf{k},s;E\right)\right] \tag{3.1.67}$$

$$\mathcal{D}\left(E\right) = \gamma\frac{1}{\left(2\pi\right)^3}\int \mathcal{S}(\mathbf{k},s;E)\mathrm{d}^3\mathbf{k} \tag{3.1.68}$$

where $\mathcal{G}\left(\mathbf{k},s;E\right)$ is the retarded electronic Green function, which can be expressed as:

$$\mathcal{G}\left(\mathbf{k},s;E\right) = \left(E-\varepsilon_{\mathbf{k}}-E_{\mathrm{F}}+\frac{ih}{\tau_{\mathrm{e-e}}}-\Sigma_{\mathrm{e-e}}\left(\mathbf{k},s;E\right)\right)^{-1} \tag{3.1.69}$$

where $\Sigma_{\mathrm{e-e}}$ is the self-energy due to the electron-electron interaction. If the modification to the density of states, associated with the electron-electron interaction is $\Delta\mathcal{D}\left(E\right)$, then the magnitude of the peak(dip) in the junction conductivity may be expressed in a way analogous to equation 3.2.37:

$$\frac{\Delta\sigma_{\mathrm{j}}}{\sigma_{\mathrm{j}}} = \frac{1}{kT}\int \mathrm{d}E\frac{\Delta\mathcal{D}}{\mathcal{D}}\left\{\frac{1}{\cosh^2\frac{E-qV_{\mathrm{a}}}{2kT}}+\frac{1}{\cosh^2\frac{E+qV_{\mathrm{a}}}{2kT}}\right\} \tag{3.1.70}$$

Without going into the details of the evaluation of the self-energy $\Sigma_{\mathrm{e-e}}$, the physical picture is simple. In the presence of impurity scattering, the electron-electron interaction leads to week localisation on an energy scale determined by $h/\tau_{\mathrm{e-e}}$. The relative correction to the density of states (for small temperatures $|qV_{\mathrm{a}}| \gg kT$ and moderate scattering, so that

$$\frac{\hbar}{\tau_{\mathrm{e-e}}} \gg |qV_{\mathrm{a}}| \gg \frac{\hbar}{\tau_{\mathrm{e-e}}}\Lambda_{\mathrm{e-e}}^{\frac{2}{3}}\left(\frac{\hbar}{E_{\mathrm{F}}\tau_{\mathrm{e-e}}}\right)^{\frac{4}{5}} \tag{3.1.71}$$

is given by:

$$\frac{\Delta\mathcal{D}}{\mathcal{D}}(E) = \Lambda_{\mathrm{e-e}}\frac{4\pi q^2 L_{\mathrm{D}}^2}{\epsilon_0}\frac{1}{2\sqrt{2}\pi^2}\frac{\sqrt{kT}}{\hbar D}^{\frac{3}{2}}\sqrt{\frac{|E|}{kT}} \tag{3.1.72}$$

where $\Lambda_{\mathrm{e-e}}$ is the effective constant (dimensionless) of the residual electron-electron interaction, which can be either positive (residual repulsion) or negative (residual attraction), therefore producing a dip or a peak in differential conductivity. In the limit of very low temperature $T \to 0$, equation 3.1.72 simplifies to:

$$\frac{\Delta\mathcal{D}}{\mathcal{D}}(E) = \frac{\Lambda_{\mathrm{e-e}}}{2\sqrt{2}\pi^2}\frac{\sqrt{|E|}}{(\hbar D)^{\frac{3}{2}}} \tag{3.1.73}$$

and represents a cusp-like feature centred at zero bias. Both low temperature limit, and the temperature broadened case are demonstrated on figure 3.9, for $\lambda_{\mathrm{D}} = 10$ nm, and $D = 1\mathrm{m}^2/\mathrm{s}$.

On intuitive grounds, it can be expected, that strong magnetic field can split (lift the degeneracy of) the quasiparticle spectrum and result in a set of three peaks (dips), one of which remains at $V_{\mathrm{a}} = 0$, while the other two would be centred at $q\Delta V = \pm g\mu_{\mathrm{B}}B$. This

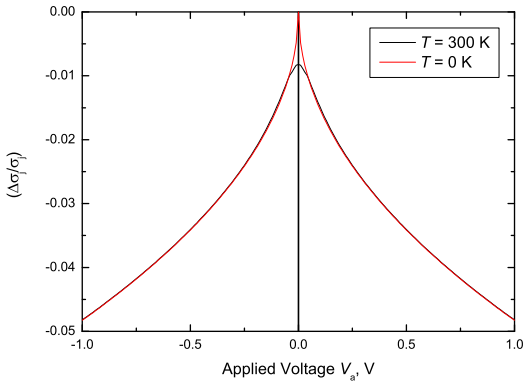

Figure 3.9: Weak-localisation-like zero bias anomaly for negative residual electron-electron interaction. Parameters have been selected as: $\lambda_{\mathrm{D}} = 10$ nm, and $D = 1\mathrm{m}^2/\mathrm{s}$.

is, indeed, the case, as has been proven explicitly by Altshuler & Aronov (1983). In contrast with the zero-bias anomaly, which is smeared only by thermal effects, the Zeeman-split ones are broadened and suppressed by the spin-flip scattering, so that the bias and temperature windows are restricted like:

$$\begin{aligned} (qV_{\mathrm{a}} \pm g\mu_{\mathrm{B}}B) &\lesssim \frac{\hbar}{\tau_{\mathrm{s-f}}} \\ kT &< \frac{\hbar}{\tau_{\mathrm{s-f}}} \end{aligned} \tag{3.1.74}$$

The physical reason for the appearance of the appearance of the non-zero bias anomalies is the high spatial correlation of the wavefunctions of the spin-up and spin-down electrons (or holes), when the Fermi energy of one of the sub-bands is equal the other modulo the Zeeman splitting, and therefore can interfere effectively, leading to what is often called, a finite bias projection of a zero-bias singularity in the electronic spectral function. More generally, scattering contributes to the imaginary part of the self energy, but as Kramers-Kronig relations are to be obeyed between its real and imaginary parts[1], the real part is also affected by scattering processes.

It should be noted, that an analogous, but spin-polarised, treatment has been realised by Sheng *et al.* (2004), for the case of impurity scattering and electron-phonon interaction. Both the calculation procedure and the resulting estimates of the bias dependence of the tunnel current are very close to the ones found within the model of Altshuler & Aronov (1979).

It is not difficult to envisage a situation where the role of the magnetic field B is taken over by the magnetisation of ferromagnetic electrodes, and therefore the characteristic energy scale, instead of being the Zeeman splitting $g\mu_{\mathrm{B}}B$, is the effective exchange energy E_{ex}. In this case,

[1]This is strictly true in linear generalized susceptibility theory, and is reasonably justified in low order perturbation theory.

the finite bias anomalies would also depend on the mutual orientation of the magnetisations of the two electrodes, as the energy differences depend on the projections of the spins on the magnetisation axis. The peaks (dips) positions are thus expected to vary as:

$$q\Delta V = \pm E_{\mathrm{ex}} \cos\left(\theta/2\right) \tag{3.1.75}$$

where θ is the angle between the magnetisations of the electrodes. Of course, energy conservation must be satisfied, and the additional resistance (as is often the case), which means additional dissipation, would lead to the generation of magnons. What type of magnon relaxation mechanism would dominate (one magnon, two magnon, etc.), depends on the actual magnon and electron dispersions involved. Within the effective mass approximation, as typical quasi-electrons have masses of the order of $m_{\mathrm{e}}^{\star} \sim m_{\mathrm{e}}$, and typical magnons have effective masses of the order of $m_{\mathrm{mag}}^{\star} \sim 100 \cdot m_{\mathrm{e}}$, the direct exchange of energy (via inelastic collisions) is limited (the process from the point of view of the quasi-free electron model is close to elastic), indirect processes such as the ones described above, can actually dominate the electronic energy relaxation, as they represent the influence of predominantly elastic scattering on the dissipation of energy and momentum.

A different approach to taking into account the scattering of electrons by other quasi-particles has been developed by Adler *et al.* (1975). In the conventional approach to tunnelling the quasi-electrons are often considered to obey the equilibrium distribution functions in both electrodes and their finite relaxation times neglected. In this fashion, the unavailability of states for tunnelling does not enter the problem. The phase-space conservation and finite relaxation times, may potentially cause important corrections to the tunnelling probabilities and thus influence the junction conductivity. While in quasi-equilibrium, the current density has the simple form:

$$J \propto \int \mathrm{d}E \left[f\left(E - E_{\mathrm{F}} - qV_{\mathrm{a}}\right) - f\left(E - E_{\mathrm{F}}\right)\right] \mathcal{T}\left(E\right) \tag{3.1.76}$$

in steady-state out-of-equilibrium, the electronic relaxation dynamics enters the problem:

$$J \propto \int \mathrm{d}E \left[f\left(E - E_{\mathrm{F}} - qV_{\mathrm{a}}\right) - f\left(E - E_{\mathrm{F}}\right)\right] \left[1 - \mathcal{B}\left(E, V_{\mathrm{a}}, T\right)\right] \mathcal{T}\left(E\right) \tag{3.1.77}$$

where $\mathcal{B}\left(E, T\right)$ is the so-called blocking factor, defining the probability of a given quantum state (in this example in energy, but more generally in k-space and energy) is dynamically occupied and unavailable, and is given to a linear approximation by:

$$\mathcal{B}\left(E, T\right) = \frac{\frac{1}{\tau_{\mathrm{b}}}}{\frac{1}{\tau_{\mathrm{b}}} + \frac{1}{\tau\left(E, V_{\mathrm{a}}, T\right)}} \tag{3.1.78}$$

where τ_b is the inverse of the tunnelling rate and can be broken down into separate relaxation times for the left, $\tau_\mathrm{b}^\mathrm{l}$ and right, $\tau_\mathrm{b}^\mathrm{r}$ electrode; and $\tau\left(E, V_\mathrm{a}, T\right)$ is the hyperbolic average of the various inelastic scattering times - τ_ph, τ_mag, etc., in both electrodes.

Differentiating the relation for the current 3.1.77, with blocking of the tunnelling states included, leads to the following expression for the relative change of junction conductance:

$$\frac{\Delta\sigma_\mathrm{j}}{\sigma_\mathrm{j}} = \int \mathrm{d}E \frac{\partial f\left(E,T\right)}{\partial E}\left[\frac{\tau_\mathrm{l}\left(E-qV_\mathrm{a},T\right)}{\tau_\mathrm{b}^\mathrm{l}} + \frac{\tau_\mathrm{r}\left(E-qV_\mathrm{a},T\right)}{\tau_\mathrm{b}^\mathrm{r}}\right] \tag{3.1.79}$$

which represent a negative quasi-gaussian peak with a temperature dependence similar to the one described in section 3.2.4. It is easily seen that the magnitude of the relative change in tunnel conductance at $V_\mathrm{a} = 0$ is given by:

$$\frac{\Delta\sigma_\mathrm{j}}{\sigma_\mathrm{j}}(0) \propto \frac{\tau_\mathrm{b}}{\tau(0,T)+\tau_\mathrm{b}} \tag{3.1.80}$$

and, as expected, tends to zero with decreasing τ_b, as the electrons relax faster to their equilibrium energy E_F in the electrodes. As in impure, or otherwise imperfect junctions, a quasi-electron may scatter $10^2 - 10^3$ times while tunnelling through the barrier[1], and the resulting conductance anomaly due to the relaxation 'bottleneck' can be as large as few percent. When quasi-electrons of particular energies, momenta, or spin are difficult to relax to equilibrium upon tunnelling (or in other words regions of phase space exist often called 'hot spots'), small changes in conductance are generally expected.

3.1.7 Inelastic tunnelling

From a quantum-mechanical point of view, excitations in the barrier, or the electrodes, change the number of states available for tunnelling, having particular energy and momentum. The situation is shown schematically on figure 3.10.

Thus the $I - V$ characteristic, and its derivatives, would normally contain information about those excitations, their abundance and energy-momentum dispersions. A simple optical analogue can be constructed. Considering a monochromatic photon beam, incident on a region in space with time varying refractive index (as for example in an acoustooptical modulator), for simplicity, in one dimension. If the initial beam is represents the plain electromagnetic wave:

$$\mathcal{E}_\mathrm{t} = \mathcal{E}_0 \cos\left(2\pi\nu_0 t\right) \tag{3.1.81}$$

[1] As the tunnelling probabilities are small, the time an electron takes to tunnel through the barrier may be very large - $10^{-6} - 10^{-7}$ seconds.

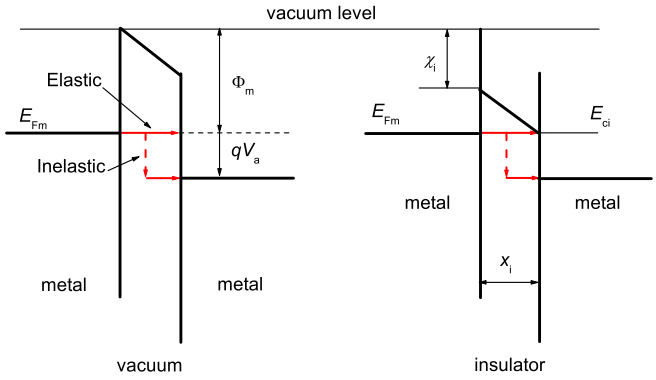

Figure 3.10: Energy diagrams of two similar metal electrodes separated by vacuum (left) and by and insulator (right).

where $\mathcal{E}_t$ is the transverse component of the electric field vector and ν_0 is the incoming photon frequency, the transmitted beam would be expected to change in intensity and spectral distribution, even when only the real part of the refractive index is subject to modulation[1]. The outgoing beam would be modulated like:

$$\mathcal{E}_t = \mathcal{E}_0 \cos(2\pi\nu_0 t)\left[1 + \frac{\Delta\mathcal{E}}{\mathcal{E}_0}\cos(2\pi\nu_m t)\right] \tag{3.1.82}$$

where $\frac{\Delta\mathcal{E}}{\mathcal{E}_0}$ and ν_m are the dept and frequency of the modulation, respectively. The outgoing spectral composition would thus be given by:

$$\mathcal{E}_t = \mathcal{E}_0 \cos(2\pi\nu_0 t) + \frac{1}{2}\Delta\mathcal{E}\cos[2\pi(\nu_0+\nu_m)t] + \frac{1}{2}\Delta\mathcal{E}\cos[2\pi(\nu_0-\nu_m)t] \tag{3.1.83}$$

or the primary beam and its anti-Stokes and Stokes scattered components. In almost complete analogy, Raman-like scattering is expected to influence the conductance spectra of tunnel junctions.

Within the Fermi's golden rule approximation, the probability per unit time for tunnelling in the elastic and inelastic cases can be written as (see Jaklevic & Lambe (1969); Kirtley *et al.* (1976)), athermally:

$$w_{lr}^{el} = \frac{2\pi}{\hbar}|\mathcal{T}_{lr}|^2\,\delta(E_l - Er) \tag{3.1.84}$$

$$w_{lr}^{in} = \frac{2\pi}{\hbar}|\mathcal{T}_{lr}|^2\,\delta(E_l - Er + \hbar\omega_{in}) \tag{3.1.85}$$

[1]Because of the Kramers-Kronig theorem the real an imaginary parts of the refractive index are related locally in frequency space. Noting, of course, that the refractive index,itself, is not a generalized susceptibility, but is related via s nonlinear operation to one, i.e. $\sqrt{\frac{\epsilon}{\epsilon_0}}$, for non-magnetic media.

with $\omega_{\rm in}$ being the characteristic of the quasi-particle excitation in the barrier region. Within the WKB approximation, while in the elastic case, the tunnelling matrix element is proportional to the weighted overlap:

$$\mathcal{T}_{\rm lr}^{\rm el} \propto \langle \Psi_{\rm l} | f^{\rm WKB} | \Psi_{\rm r} \rangle \tag{3.1.86}$$

with only the electronic wavefunction participating; in the inelastic case, the products of the electronic wavefunctions and the ones of the quasiparticle, interacting with the electron in-elastically $\psi_{\rm in}$, like:

$$\mathcal{T}_{\rm lr}^{\rm in} \propto \langle \Psi_{\rm l} \psi_0^{\rm in} | f^{\rm WKB} | \Psi_{\rm r} \psi_2^{\rm in} \rangle \tag{3.1.87}$$

where $\psi_0^{\rm in}$ and $\psi_2^{\rm in}$ are the wavefunctions of the quasiparticle interacting in-elastically with the tunnelling electron, in a state 'before', and 'after' tunnelling (not necessarily leftmost and rightmost region).

As $f^{\rm WKB}$ may be expanded into a non-perturbed part and perturbation (assuming the change in the barrier height due to the inelastic interaction is small) like:

$$\begin{aligned} f^{\rm WKB} &= \exp\left(-\frac{\gamma}{\hbar}\int_{x_{\rm l}}^{x_{\rm r}} {\rm d}x \sqrt{m^\star \left\{q\left[\phi(x,0)+\Delta\phi(x,V_{\rm a})\right]-E_{\rm F}+E_{\rm t}\right\}}\right) \\ &\approx \exp\left(-\frac{\gamma}{\hbar}\int_{x_{\rm l}}^{x_{\rm r}} {\rm d}x \sqrt{m^\star \left[q\phi(x,0)-E_{\rm F}+E_{\rm t}\right]}\right) + \\ &-\frac{1}{2}\exp\left(-\frac{\gamma}{\hbar}\int_{x_{\rm l}}^{x_{\rm r}} {\rm d}x \sqrt{m^\star \left[q\phi(x,0)-E_{\rm F}+E_{\rm t}\right]}\right)\frac{\gamma}{\hbar}\int_{x_{\rm l}}^{x_{\rm r}} {\rm d}x \frac{qm^\star}{\sqrt{m^\star \left[q\phi(x,0)-E_{\rm F}+E_{\rm t}\right]}}\Delta\phi(x,V_{\rm a}) \end{aligned} \tag{3.1.88}$$

keeping constant and linear terms, only. The first term in equation 3.1.88, is the usual elastic contribution to the transmission probability, while the second one represents an approximation to the inelastic contribution. Therefore, further, averaging the barrier height over the width of the barrier region, and setting $\gamma = 2$, the matrix element may be written as:

$$\mathcal{T}_{\rm lr} \quad \propto \quad \exp\left(-\varkappa_1 \Delta x\right) \quad - \quad \exp\left(-\varkappa_1 \Delta x\right) \sqrt{\frac{m^\star}{2\hbar^2 \overline{\phi}_{\rm b}}} \left\langle \psi_0^{\rm in} \left| \int_{x_{\rm l}}^{x_{\rm r}} \phi^{\rm in}(x, V_{\rm a}) {\rm d}x \right| \psi_2^{\rm in} \right\rangle \tag{3.1.89}$$

Thus the contribution to the total current from the inelastic process with characteristic energy $\hbar\omega_{\rm in}$ may be written within the finite temperature WKB approximation like:

$$J^{\rm in} \propto J^{\rm el} \frac{m^\star}{2\hbar^2 \overline{\phi}_{\rm b}} \left| \left\langle \psi_0^{\rm in} \left| \int_{x_{\rm l}}^{x_{\rm r}} \phi^{\rm in}(x, V_{\rm a}) {\rm d}x \right| \psi_2^{\rm in} \right\rangle \right|^2 \int_{-\infty}^{\infty} f(E)\left[1 - f(E + qV_{\rm a} - \hbar\omega^{\rm in})\right] {\rm d}E \tag{3.1.90}$$

where the anti-stokes component has been neglected, as the quasiparticles being excited by the tunnelling electrons may in most situations be considered having their ground state occupation

probabilities. The occupation integral in equation 3.1.90, can be handled directly, so finally the expression for the inelastic component of the tunnelling current becomes:

$$J^{\mathrm{in}} \propto J^{\mathrm{el}} \frac{m^{\star}}{2\hbar^2 \overline{\phi}_{\mathrm{b}}} \left| \left\langle \psi_0^{\mathrm{in}} \left| \int_{x_1}^{x_{\mathrm{r}}} \phi^{\mathrm{in}}(x, V_{\mathrm{a}}) \mathrm{d}x \right| \psi_2^{\mathrm{in}} \right\rangle \right|^2 \cdot \left(qV_{\mathrm{a}} - \hbar\omega^{\mathrm{in}}\right) \frac{\exp \frac{qV_{\mathrm{a}} - \hbar\omega^{\mathrm{in}}}{kT}}{\exp \frac{qV_{\mathrm{a}} - \hbar\omega^{\mathrm{in}}}{kT} - 1} \tag{3.1.91}$$

the second factor from which represents a 'switch on' from essentially zero inelastic tunnelling current, at small bias $qV_{\mathrm{a}} < \hbar\omega^{\mathrm{in}}$, to a linear growth over the threshold bias, or an effective voltage bias V_{eff} for the inelastic tunnelling component, visualised on figure 3.11, for $\hbar\omega^{\mathrm{in}} = 0.2$ eV and $T = 300$ K. The The behaviour of the effective bias shown, leads to a step-like

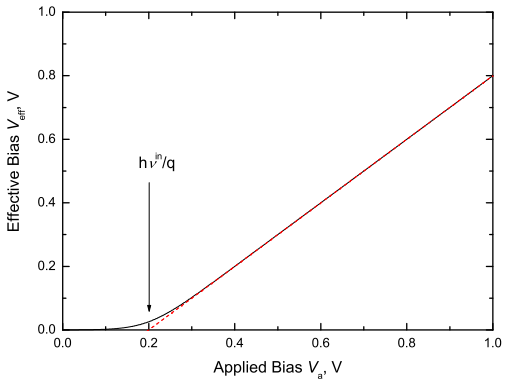

Figure 3.11: The effective bias V_{eff} as a function of applied bias V_{a} for inelastic tunnelling via an excitation with $\hbar\omega^{\mathrm{in}} = 0.2$ eV, at $T = 300$ K.

feature at the characteristic energy in the differential conductance $\sigma_{\mathrm{j}}^{\mathrm{in}}$, and to a peak in its voltage derivative. This is the basis of the so-called inelastic tunnelling spectroscopy, which, in most cases, consists of measuring, or obtaining by numerical differentiation, the second voltage derivative of the current through a tunnel barrier and analysing the peaks in the resulting spectrum in terms of the various possible excitations. The approximate convolution function may be obtained by the consecutive differentiation of equation 3.1.91 in the form:

$$\frac{\partial^2 J}{\partial V_{\mathrm{a}}^2} \propto \mathrm{e}^{\frac{qV_{\mathrm{a}} - \hbar\omega^{\mathrm{in}}}{kT}} \frac{\left(\frac{qV_{\mathrm{a}} - \hbar\omega^{\mathrm{in}}}{kT} - 2\right) \mathrm{e}^{\frac{qV_{\mathrm{a}} - \hbar\omega^{\mathrm{in}}}{kT}} + \left(\frac{qV_{\mathrm{a}} - \hbar\omega^{\mathrm{in}}}{kT} + 2\right)}{\left(\mathrm{e}^{\frac{qV_{\mathrm{a}} - \hbar\omega^{\mathrm{in}}}{kT}} - 1\right)^3} \tag{3.1.92}$$

and represents a quasi-gaussian peak of FWHM of about 5.4 kT.

3.2 Application to ferromagnetic junctions

3.2.1 Density of states effects

An interpretation of junction magnetoresistance (JMR), in a constant tunnelling matrix element model, has been reported first by Jullière (1975). Neglecting the spin-flip events at the interfaces, which may only be realistic for very small or zero bias, the junction conductance depends on the fractions of the total number of tunnelling electrons on both sides of the potential barrier with spins parallel to the magnetisation, $\frac{n^{\mathrm{l}}_{\uparrow}}{n^{\mathrm{l}}}$ and $\frac{n^{\mathrm{r}}_{\uparrow}}{n^{\mathrm{r}}}$, close to the Fermi level, like:

$$\frac{\partial J_{\uparrow\uparrow}}{\partial V_{\mathrm{a}}} \propto \frac{n^{\mathrm{l}}_{\uparrow}}{n^{\mathrm{l}}}\frac{n^{\mathrm{r}}_{\uparrow}}{n^{\mathrm{r}}} + \left(1-\frac{n^{\mathrm{l}}_{\uparrow}}{n^{\mathrm{l}}}\right)\left(1-\frac{n^{\mathrm{r}}_{\uparrow}}{n^{\mathrm{r}}}\right) \tag{3.2.1}$$

for parallel orientation of the magnetisations of the electrodes, and like:

$$\frac{\partial J_{\uparrow\downarrow}}{\partial V_{\mathrm{a}}} = \frac{\partial J_{\downarrow\uparrow}}{\partial V_{\mathrm{a}}} \propto \frac{n^{\mathrm{l}}_{\uparrow}}{n^{\mathrm{l}}}\left(1-\frac{n^{\mathrm{r}}_{\uparrow}}{n^{\mathrm{r}}}\right) + \frac{n^{\mathrm{r}}_{\uparrow}}{n^{\mathrm{r}}}\left(1-\frac{n^{\mathrm{l}}_{\uparrow}}{n^{\mathrm{l}}}\right) \tag{3.2.2}$$

for antiparallel orientation of the magnetisations. Therefore the normalised magneto-conductance ratio may be approximated as:

$$MC = \frac{\frac{\partial J_{\uparrow\uparrow}}{\partial V_{\mathrm{a}}} - \frac{\partial J_{\uparrow\downarrow}}{\partial V_{\mathrm{a}}}}{\frac{\partial J_{\uparrow\uparrow}}{\partial V_{\mathrm{a}}}} = \frac{2\alpha^{\mathrm{s}}_{\mathrm{l}}\alpha^{\mathrm{s}}_{\mathrm{r}}}{1+\alpha^{\mathrm{s}}_{\mathrm{l}}\alpha^{\mathrm{s}}_{\mathrm{r}}} \tag{3.2.3}$$

where $\alpha^{\mathrm{s}}_{\mathrm{l}}$ and $\alpha^{\mathrm{s}}_{\mathrm{r}}$ are defined, in the usual way, as the static polarisations of the left and the right electrode, respectively, at the Fermi level. As a simple consequence of Julliere's model, in a tunnelling system with two identical ferromagnetic electrodes, the magnetisation of one of which can be controlled independently from the other[1], the MC ratio may be used as a measure of the static polarisation of the ferromagnetic material at the Fermi level. Of course, only the absolute value of the static spin polarisation may be extracted as:

$$|\alpha^{\mathrm{s}}| = \frac{1}{2-MC}\sqrt{2MC-MC^2} \tag{3.2.4}$$

This estimate is a good starting point for cases where the independent spin channel model is applicable, and is visualised on figure 3.12.

The transfer Hamiltonian approach has been generalized for the case of spin-polarised electrodes (see for example Zhang & Levy (1999)), depicting a bit more complicated picture, than originally envisaged by Julliere. First, at least two different bands should be present close to the Fermi level, in order to have non-vanishing MC in the adiabatic approximation. Second, the spin-polarised current density, and therefore the magneto-conductance, depend not only on the inverse density of states of the electrodes, but also on the hybridisation between the

[1] For example, by means of shape anisotropy or via exchange biasing with an antiferromagnet.

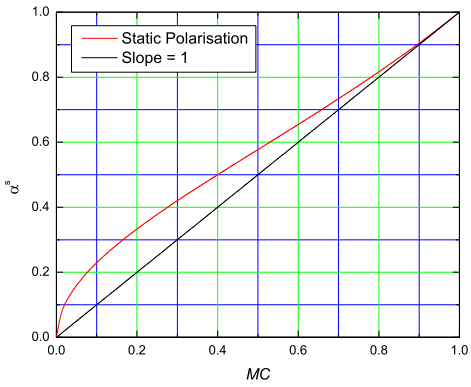

Figure 3.12: The static polarisation as a function of the MC ratio for tunnelling between identical ferromagnetic electrodes, within Julliere's model.

different bands. A schematic derivation of the tunnelling current within this approach is given in appendix B.1.

3.2.2 Tunnelling matrix element effects

Within the model of Jullière (1975), the matrix element is considered independent of energy and spin. This is incompatible with the view adopted by Harrison (1961) in the independent-particle tunnelling problem as described in section 3.1.4, and the density of states does not enter the problem directly. A different analysis is necessary, taking into account the different radii of the Fermi spheres for spin up and spin down[1]. Such a derivation may be carried-out more simply, compared with unnecessary detailed first principle calculations an example of which for Fe/MgO/Fe, atomically flat and abrupt, tunnel junctions is given by Butler *et al.* (2001) and Zhang *et al.* (2004a).

Following Hachaturov (2005b) and Chui (1997); Davis & MacLaren (2000)[2], the differential conductivity of the tunnel junction, at zero applied bias $V_\mathrm{a} = 0$ and zero temperature $T = 0$, may be expressed as:

$$\sigma_\mathrm{j}(0) = \left.\frac{\partial J}{\partial V_\mathrm{a}}\right|_{V_\mathrm{a}=0} = \frac{1}{(2\pi)^2}\frac{q^2}{h}\int 2\pi k_\mathrm{t}\mathrm{d}k_\mathrm{t}\exp\left(-\frac{\gamma}{\hbar}\int_{x_1}^{x_\mathrm{r}}\sqrt{2m^\star\left[q\phi(x,0) - E_\mathrm{F} + E_\mathrm{t}\right]}\mathrm{d}x\right) \quad (3.2.5)$$

where $E_\mathrm{t} = \frac{k_\mathrm{t}^2\hbar^2}{2m^\star}$ is the kinetic energy associated with the transverse wavenumber k_t. The integral over d^2k_t is, as customary, taken over the overlap of the projections of the two (left-

[1]The Fermi surfaces are considered as spheres, only for simplicity. Adopting more general shapes is a refinement of the model, but does not introduce any new concepts.

[2]An analogous treatment for tunnelling in semiconductor hetero-structures has been performed by Voskoboynikov *et al.* (1998).

hand-side and right-hand-side) Fermi surfaces on a plane parallel to the junction interface. Further, if the spin is conserved upon tunnelling (the two channel model is valid), the differential conductance of the up and down spin channels would be related as the transverse Fermi surface cross sections for spin-up and spin-down electrons, in the case when the magnetisations of the two electrodes are parallel and the total conductance is to equal the sum of the conductances of the individual channels. For the anti-parallel case, the conductance is smaller, as it is proportional to the sum of the smaller of the two cross sections (either spin-up or spin-down). The situation is illustrated on figure 3.13.

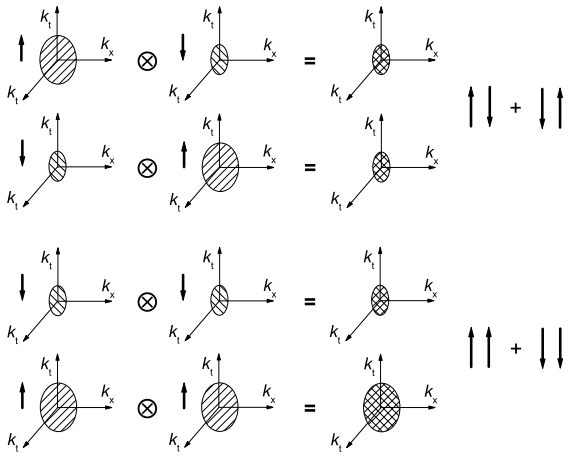

Figure 3.13: Schematic representation of the two channel model within the WKB approximation.

It is clear that within this approximation, the difference in differential conductance between the parallel and the anti-parallel state of the magnetisation of the electrodes, would be proportional to the difference of the cross sections of the spin up, and spin down, Fermi surfaces at $E_{\mathrm{F}}^{\uparrow}$ and $E_{\mathrm{F}}^{\downarrow}$:

$$\pi \left(k_{\mathrm{F}\uparrow}^2 - k_{\mathrm{F}\downarrow}^2 \right) \propto E_{\mathrm{F}}^{\uparrow} - E_{\mathrm{F}}^{\downarrow} \tag{3.2.6}$$

and therefore, the magneto-conductance is due to the portion of electrons, with quasi-momentum k_{t} in the region $k_{\mathrm{t}} \in [k_{\mathrm{F}\downarrow}, k_{\mathrm{F}\uparrow}]$. It follows, that there would be a minimal angle at which the electrons incident at the interface would contribute to the MC ratio. The angle θ_{min} may be estimated as:

$$\theta_{\mathrm{min}} = \arcsin\left(\frac{k_{\mathrm{F}\downarrow}}{k_{\mathrm{F}\uparrow}}\right) = \arcsin\left(\sqrt{\frac{E_{\mathrm{F}\downarrow}}{E_{\mathrm{F}\uparrow}}}\right) \tag{3.2.7}$$

and has values of more than 20° for common ferromagnetic metals. This is an important consequence, as the electrons that determine the conductivity and its higher derivatives are normally the ones approaching the barrier at almost normal incidence.

The conventional definition of junction magneto-conductance:

$$MC = \frac{\sigma_{\mathrm{j}}^{\uparrow\uparrow} - \sigma_{\mathrm{j}}^{\uparrow\downarrow}}{\sigma_{\mathrm{j}}^{\uparrow\uparrow}} \tag{3.2.8}$$

may be used with equation 3.2.5, by changing variables from $\mathrm{d}^2 k_{\mathrm{t}}$ to $\mathrm{d}E_{\mathrm{x}}$ over the Fermi sphere, to obtain an expression for the zero-bias $V_{\mathrm{a}} = 0$ magneto conductance:

$$MC(0) = \frac{\int_0^{E_{\mathrm{F}\uparrow} - E_{\mathrm{F}\downarrow}} f^{\mathrm{WKB}}\left(E_x, 0\right) \mathrm{d}E_x}{\int_0^{E_{\mathrm{F}\uparrow}} f^{\mathrm{WKB}}\left(E_x, 0\right) \mathrm{d}E_x + \int_0^{E_{\mathrm{F}\downarrow}} f^{\mathrm{WKB}}\left(E_x, 0\right) \mathrm{d}E_x} \tag{3.2.9}$$

where f^{WKB} is the tunnelling probability within the WKB approximation, given by the familiar expression:

$$f^{\mathrm{WKB}}\left(E_x, 0\right) = \exp\left(-\frac{\gamma}{\hbar} \int_{x_{\mathrm{l}}}^{x_{\mathrm{r}}} \sqrt{2m^{\star}\left[q\phi(x,0) - E_{\mathrm{F}} + E_{\mathrm{t}}\left(E_x\right)\right]} \mathrm{d}x\right) \tag{3.2.10}$$

Therefore, the zero-bias magneto-conductance ratio for a δ-barrier[1], defined as $\phi(x,0) = \phi_{\mathrm{b}}\delta(x)$, may be expressed simply as:

$$MC = \frac{E_{\mathrm{F}\uparrow} - E_{\mathrm{F}\downarrow}}{E_{\mathrm{F}\uparrow} + E_{\mathrm{F}\downarrow}} \tag{3.2.11}$$

For ease of evaluation of the current density in different spin channels, an approximation of the exact integral over the projection of the constant energy surfaces on both sides of the junction may be done following Hachaturov (2005a). The original evaluation procedure is based on the approximations of the area of integration in a fashion shown at figure 3.14, after Floyd & Walmsley (1978). In the limit $T \to 0$ the different current density components can be thus written as:

$$j_{s_{\mathrm{l}},s_{\mathrm{r}}}(V_{\mathrm{a}}) = \frac{2\pi q m^{\star}}{h^3}\left[qV_{\mathrm{a}} \int_{CO(V_{\mathrm{a}})}^{E_{\mathrm{Fl}} - qV_{\mathrm{a}}} f^{\mathrm{WKB}}\left(E_x, V_{\mathrm{a}}\right) \mathrm{d}E_x + \int_{E_{\mathrm{Fl}} - qV_{\mathrm{a}}}^{E_{\mathrm{Fl}}} \left(E_{\mathrm{F}} - E_x\right) f^{\mathrm{WKB}}\left(E_x, V_{\mathrm{a}}\right) \mathrm{d}E_x\right] \tag{3.2.12}$$

with the cutoff function $CO\left(V_{\mathrm{a}}\right)$ defined as:

$$CO\left(V_{\mathrm{a}}\right) = \begin{cases} 0, & s_{\mathrm{l}} \geq s_{\mathrm{r}} \\ \left(E_{\mathrm{Fl}} - E_{\mathrm{Fr}} - qV_{\mathrm{a}}\right)\theta_{\mathrm{H}}\left(E_{\mathrm{Fl}} - E_{\mathrm{Fr}} - qV_{\mathrm{a}}\right), & s_{\mathrm{l}} < s_{\mathrm{r}} \end{cases} \tag{3.2.13}$$

where θ_{H} is the Heaviside step function[2]. The above cutoff function is a manifestation of the observation made by Hachaturov (2005a), that in the adiabatic transition of electrons from a

[1] Actually, for a δ-barrier, the WKB approximation is poorly defined in the region of the barrier. As the requirements for adiabaticity are violated both in spatial and temporal sense.

[2] The Heaviside step function is defined as: $\theta_{\mathrm{H}}(x) = \begin{cases} 0, & x \leq 0 \\ 1, & x > 0 \end{cases}$.

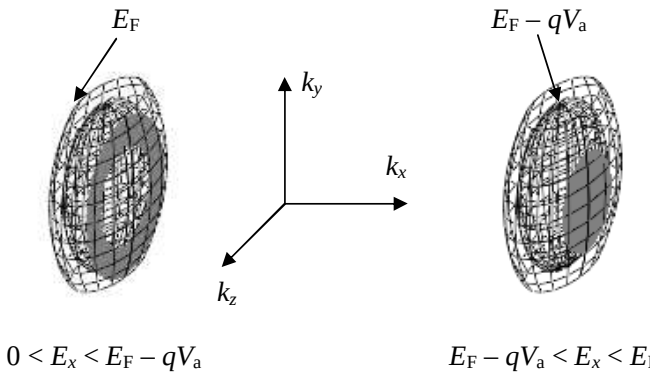

Figure 3.14: Schematic representation of the integration over the states available for tunnelling under applied bias.

metallic electrode with a larger Fermi wavenumber to a one with a smaller Fermi wavenumber, there is a restriction on the minimal longitudinal kinetic energy of the form $E_x \geq E_{\mathrm{Fl}} - E_{\mathrm{Fr}} - qV_{\mathrm{a}}$ for $E_{\mathrm{Fl}} > E_{\mathrm{Fr}}$. Similar situation is illustrated on figure 3.15.

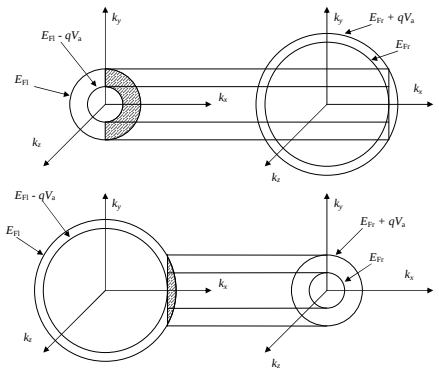

Figure 3.15: Schematic representation of the states available for tunnelling for $k_{\mathrm{Fl}} < k_{\mathrm{Fr}}$ (top panel), and $k_{\mathrm{Fl}} > k_{\mathrm{Fr}}$ (bottom panel).

In order to calculate the differential magneto-conductance (magnetoresistance), the expression for the equation 3.2.12 may be differentiated with respect to V_{a}, yielding:

$$\sigma_{\mathrm{j}}^{s_{\mathrm{l}},s_{\mathrm{r}}} = \frac{2\pi q m^{\star}}{h^3}\left[\int_{E_{\mathrm{Fl}}-qV_{\mathrm{a}}}^{E_{\mathrm{Fr}}} (E_{\mathrm{Fl}} - E_x)\frac{\partial f^{\mathrm{WKB}}}{\partial V_{\mathrm{a}}}\mathrm{d}E + q\int_{CO(V_{\mathrm{a}})}^{E_{\mathrm{Fl}}-qV_{\mathrm{a}}}\left(f^{\mathrm{WKB}} + V_{\mathrm{a}}\frac{\partial f^{\mathrm{WKB}}}{\partial V_{\mathrm{a}}}\right)\mathrm{d}E_{\mathrm{x}} + \right.$$
$$\left. + q^2 V_{\mathrm{a}} f^{\mathrm{WKB}}\theta_{\mathrm{H}}\left(E_{\mathrm{Fl}} - E_{\mathrm{Fr}} - qV_{\mathrm{a}}\right)\delta_{s_{\mathrm{l}}-1,s_{\mathrm{r}}}\right] \quad (3.2.14)$$

Using the conventional definition 3.2.11, together with the above expression, gives for the differential magneto-conductance, the following expression:

$$MC = \frac{q\int_0^{E_{\mathrm{Fl}}-E_{\mathrm{Fr}}-qV_{\mathrm{a}}}\left(f^{WKB}+V_{\mathrm{a}}\frac{\partial f^{\mathrm{WKB}}}{\partial V_{\mathrm{a}}}\right)\mathrm{d}E_x - q^2V_{\mathrm{a}}f^{WKB}}{\sigma_{\mathrm{j}}^{\uparrow\uparrow}(V_{\mathrm{a}})+\sigma_{\mathrm{j}}^{\downarrow\downarrow}(V_{\mathrm{a}})}\theta_{\mathrm{H}}\left(E_{\mathrm{Fl}}-E_{\mathrm{Fr}}-qV_{\mathrm{a}}\right) \quad (3.2.15)$$

or in a more transparent form:

$$MC \approx \frac{q\tilde{f}^{\mathrm{WKB}}\left(\Delta E_{\mathrm{F}}-2qV_{\mathrm{a}}\right)+qV_{\mathrm{a}}\frac{\partial}{\partial V_{\mathrm{a}}}\tilde{f}^{\mathrm{WKB}}\left(\Delta E_{\mathrm{F}}-qV_{\mathrm{a}}\right)}{\sigma_{\mathrm{j}}^{\uparrow\uparrow}(V_{\mathrm{a}})+\sigma_{\mathrm{j}}^{\downarrow\downarrow}(V_{\mathrm{a}})}\theta_{\mathrm{H}}\left(\Delta E_{\mathrm{F}}-qV_{\mathrm{a}}\right) \quad (3.2.16)$$

where $\Delta E_{\mathrm{F}} = E_{\mathrm{F}\uparrow} - E_{\mathrm{F}\downarrow}$ is the difference of the Fermi levels for spin-up and spin-down electrons, and $\tilde{f}^{WKB}$ is the average transmission probability.

In the textbook limit of a δ-barrier, there is no voltage dependence of the transmission probability $\frac{\partial}{\partial V_{\mathrm{a}}}\tilde{f}^{\mathrm{WKB}} = 0$, while the probability $\tilde{f}^{\mathrm{WKB}}$ is kept constant. Therefore, expression 3.2.16 is further simplified to:

$$MC\left(V_{\mathrm{a}}\right) = \frac{\Delta E_{\mathrm{F}}-2qV_{\mathrm{a}}}{\Delta E_{\mathrm{F}}}\theta_{\mathrm{H}}\left(\Delta E_{\mathrm{F}}-qV_{\mathrm{a}}\right) \quad (3.2.17)$$

which is visualised on figure 3.16. Therefore, within this simplified model changes linearly in

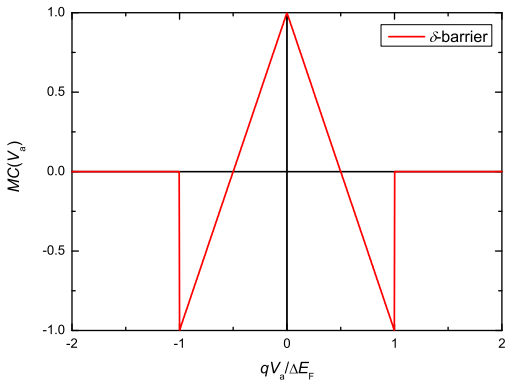

Figure 3.16: Magnetoconductance for a δ-barrier, between ferromagnets, with a difference of the spin-resolved Fermi-levels of ΔE_{F}, within the simplified WKB approach to tunnelling.

the applied voltage interval $[0, \frac{\Delta E_{\mathrm{F}}}{q}]$, between the extremal values of $\pm\frac{E_{\mathrm{F}\uparrow}-E_{\mathrm{F}\downarrow}}{E_{\mathrm{F}\uparrow}+E_{\mathrm{F}\downarrow}}$ as in equation 3.2.11, and in contrast with the Julliere's model 3.2.3, does not depend explicitly on the static density of states polarisation.

Apart from the above approximations, it is possible, to evaluate numerically the magneto-conductance, taking into account, the difference in the Fermi levels for spin-up and spin-down electrons ΔE_{F}, the barrier lowering, due to image forces, finite temperatures (only as smearing

of the distribution functions). Results of such an approach are shown on figure 3.17. A couple of peculiarities, already mentioned, remain independent of the level of approximation. The magneto-conductance has a non-monotonic bias dependence, changing sign at a voltage of the order of $\Delta E_{\mathrm{F}}/2q$[1]. At high enough bias, which depends on ΔE_{F} and the barrier profile, there is change of slope as a function of bias. Thus, the simple, adiabatic, approximation should be

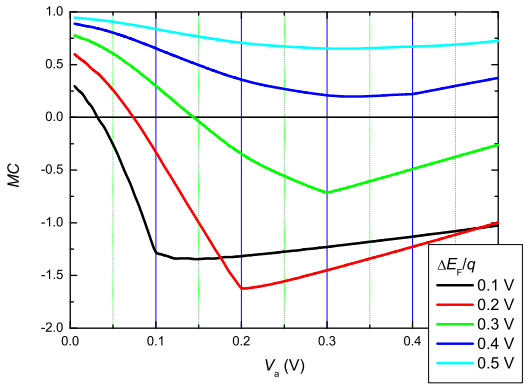

Figure 3.17: Junction magneto-conductance, evaluated within the adiabatic approximation, for an average barrier height of 2.5 eV, as a function of bias, for various Fermi level differences ΔE_{F}.

capable of describing the rough large-scale details of the bias behaviour of the conductance and magneto-conductance. And more exact models, may be treated as corrections to it, at least as far as macroscopic and mesoscopic tunnel junctions are concerned, with transition regions between the various layers of at least 2 - 3 atomic monolayers. The initial drop-off of MC and its subsequent increase can, in this fashion, be associated with the relatively weak bias dependence of the transmission probability at small applied voltage, and the exponential increase at high bias, combined with the bias dependence of the topology of the states available for tunnelling, which contribute to the magneto-conductance (magnetoresistance).

In other words, while the differential conductance, within the adiabatic approximation is a smooth, close to quadratic function of bias, due to the fact that, mostly electrons approaching the tunnel barrier at small angles $\theta \sim v_{\mathrm{T}}/v_{\mathrm{F}} \ll 1$ contribute to the current density; the magneto-conductance does, in principle, have a non-monotonic bias dependence, as the electrons responsible for its formation are the ones moving at relatively large angles $\theta \sim \Delta E_{\mathrm{F}}/E_{\mathrm{F}}$. The electrons having small transverse momentum k_{t} are present on both sides of the junction independently of their spin direction and thus have little effect on establishing a difference

[1]The Fermi energy difference E_{F} should not be directly associated with the exchange splitting Δ_{ex}. The actual values of ΔE_{F}, suitable for approximation of the electronic structure of a given material do not have to be equal to Δ_{ex}.

in transmission probability between the states with parallel and anti-parallel magnetisation orientations of the junction electrodes.

Inversion of the sign of the tunnelling magnetoresistance at elevated bias ($V_\mathrm{a} \gtrsim \frac{\Delta E_\mathrm{F}}{q}$), consistent with the model of Hachaturov (2005b), have been reported by Sharma *et al.* (1999), for Ta_2O_5 and Al_2O_3 barriers and NiFe electrodes.

Similar, non-monotonic behaviour may be recovered, also, by direct solution of the Schrödinger equation within the quasi-free electron model (see Liu & Guo (2000)). In the direct matching approach, generally, oscillating in bias solutions are obtained for $MC(V_\mathrm{a})$, often with a magnitude of the second extremum, larger than the one at $V_\mathrm{a} = 0$ V, originating from the non-monotonic and oscillatory behaviour of the transmission coefficient as a function of the longitudinal kinetic energy, which survives the integration over the transverse momentum. These observations have been later reaffirmed by Montaigne *et al.* (2001), taking into account the barrier shape modification due to the image forces. Below a brief account will be given of the classical model of Slonczewski (1989), which though very schematic is often a reasonable starting point for the estimation of the junction magnetoresistance of well defined sharp tunnel structures with electrodes of high electronic mobility with quasi-parabolic dispersions, and also serves as a base for more detailed treatments (see for example Slonczewski (2005)).

The analysis is a spin-polarised version of the derivation described in section 3.1.3. The spin components of the wavefunction in a Pauli-like description may chosen as:

$$\Psi_{\uparrow 0} = \frac{1}{\sqrt{k_\uparrow}} \mathrm{e}^{ik_\uparrow x} + a_\uparrow \mathrm{e}^{-ik_\uparrow x}, \quad \Psi_{\downarrow 0} = a_\downarrow \mathrm{e}^{-ik_\downarrow x} \tag{3.2.18}$$

$$\Psi_{\updownarrow 1} = b_\updownarrow \mathrm{e}^{-k_\updownarrow x} + c_\updownarrow \mathrm{e}^{k_\updownarrow x} \tag{3.2.19}$$

$$\Psi_{\updownarrow 2} = d_\updownarrow \mathrm{e}^{ik_\updownarrow (x - x_\mathrm{b})} \tag{3.2.20}$$

in the different regions, with a, b, c and d being constants that are to be determined by a direct matching procedure. If, for simplicity, it is assumed that the quantisation axis (determined by the direction of the order parameter, or in this case the magnetisation) is rotated at an angle θ from the left electrode to the right one, or $\theta = \angle\left(\vec{P}_\mathrm{l}, \vec{P}_\mathrm{r}\right)$. In order to be able to execute the matching of wavefunctions and derivatives at the interface between the regions 1 and 2, the change in quantisation axis should be taken into account with the spinor rotation:

$$\begin{pmatrix} \Psi_\uparrow \\ \Psi_\downarrow \end{pmatrix}_1 = \begin{pmatrix} \cos(\theta/2) & \sin(\theta/2) \\ -\sin(\theta/2) & \cos(\theta/2) \end{pmatrix} \begin{pmatrix} \Psi_\uparrow \\ \Psi_\downarrow \end{pmatrix}_2 \tag{3.2.21}$$

Without going through the algebraic difficulties of the matching procedure, the final expressions (the spin-polarised versions of equation 3.1.26) for the transmissivity of the barrier may

be written for the case of a single band ferromagnet (a half-metal) in both electrodes, as:

$$\Theta = \frac{8k_{\uparrow}\varkappa_1^2}{\left(k_{\uparrow}^2+\varkappa_1^2\right)^2}\mathrm{e}^{-2\varkappa_1\Delta x} \tag{3.2.22}$$

where $\varkappa_1$ is the effective attenuation coefficient in the barrier.

The analytical expressions for the transmissivity become more complicated with increasing the number of bands present at the Fermi level, but the case of two bands ($\uparrow$ and $\downarrow$) is still tractable, leading to:

$$\Theta = \frac{8\left(\varkappa^2+k_{\uparrow}k_{\downarrow}\right)\left(k_{\uparrow}+k_{\downarrow}\right)}{\left(k_{\uparrow}^2+\varkappa_1^2\right)\left(k_{\downarrow}^2+\varkappa_1^2\right)}\mathrm{e}^{-2\varkappa_1\Delta x} \tag{3.2.23}$$

If only tunnelling at small applied bias is of interest ($V_{\mathrm{a}} \to 0$) is of interest, the above expressions yield junction conductivities of the forms:

$$\sigma_{\mathrm{j}}(\theta) = \sigma_{\mathrm{j}}(0)\left[1+\cos(\theta)\right] \tag{3.2.24}$$

$$\sigma_{\mathrm{j}}(\theta) = \sigma_{\mathrm{j}}(0)\left[1+\mathcal{P}^2\cos(\theta)\right] \tag{3.2.25}$$

$$\sigma_{\mathrm{j}}(\theta) = \sigma_{\mathrm{j}}(0)\left[1+\mathcal{P}_{\mathrm{l}}\mathcal{P}_{\mathrm{r}}\cos(\theta)\right] \tag{3.2.26}$$

for the three simple cases of a half-metal electrodes, identical two-band ferromagnet on both sides of the barrier, and different ferromagnets on both sides of the barrier (which are all assumed to have normal parabolic energy dispersions, so that the quasi-free electron model is valid). The polarisation coefficients $\mathcal{P}$ depend on the static density of states polarisation, but are also a function of the barrier attenuation, like:

$$\mathcal{P}_{\mathrm{l(r)}} = \frac{k_{\uparrow\mathrm{l(r)}}-k_{\downarrow\mathrm{l(r)}}}{k_{\uparrow\mathrm{l(r)}}+k_{\downarrow\mathrm{l(r)}}}\cdot\frac{\varkappa^2-k_{\uparrow\mathrm{l(r)}}k_{\downarrow\mathrm{l(r)}}}{\varkappa^2+k_{\uparrow\mathrm{l(r)}}k_{\downarrow\mathrm{l(r)}}} \tag{3.2.27}$$

where all wave-vectors are evaluated at E_{F}.

Though of limited applicability to real tunnel junction structures (as in real materials the number of bands 'dispersing' around the Fermi level is greater and often the quasi-free electron model does not apply), the model of Slonczewski (1989) is widely used, for comparisons with experimental data. It is also historically important, as it predicts a set of phenomena related to dissipative exchange coupling between the ferromagnetic electrodes. Namely current induced magnetisation precession, and reversal, follow from this model and the conservation of angular momentum (see for example Manchon *et al.* (2007)). It is also possible to make generalisations for multiple barriers and include bias dependence of the transmission coefficients (see for example Zhang *et al.* (1997b)). Here, for completeness, an evaluation for the tunnelling conductance (due to MacLaren *et al.* (1997)) is provided, based on the conventional Landauer-Büttiker (see Landauer (1957) and Büttiker (1988)) formula for the tunnelling current:

$$\sigma_{\mathrm{j}} = \frac{q^2}{(2\pi)^2 h}\int \mathrm{d}^2k_{\mathrm{t}}\mathcal{T}(k_{\mathrm{t}}) \tag{3.2.28}$$

with $\mathcal{T}$ being a generalized version of 3.1.26:

$$\mathcal{T}(k_{\mathrm{t}}) = \frac{16k_0\varkappa_1^2k_2}{\varkappa_1^2\left(k_0+k_2\right)^2\left(1+\exp(2\varkappa_1\Delta x)\right)^2+\left(\varkappa_1^2-k_0k_2\right)^2\left(1-\exp(2\varkappa_1\Delta x)\right)^2}\mathrm{e}^{2\varkappa_1\Delta x} \quad (3.2.29)$$

with wavenumbers k_0 and k_2 given by either $k_\uparrow$ or $k_\downarrow$ define with the appropriate effective masses for each of the junction electrodes within the effective mass approximation. The above procedure defines the abrupt junction version (with a rectangular barrier), of the formalism already described in the WKB approximation due to Hachaturov (2005b), and is valid, strictly, only for atomically flat interfaces and perfectly abrupt junctions. The exact quasi-free electron model is generally well approximated by the model of Slonczewski (1989), but not the one of Jullière (1975) as demonstrated by MacLaren *et al.* (1997). Therefore, the Julliere model may only be considered to give a starting estimation of the maximal magneto-conductance ratios, and is not generally appropriate. Moreover, in view of the dominant independent electron character of the tunnelling process in real junctions with ferromagnetic electrodes, it simply lacks theoretical basis.

3.2.3 Anisotropy effects on the tunnelling conductance

Several different types of anisotropy effects exist, or are predicted to exist in magnetic tunnel junctions:

Intrinsic orbital anisotropy of the tunnel magnetoresistance, for electrodes and/or tunnel barrier of high degree of crystallinity. The junction conductivity and magneto-conductance depend on the orientation of the current density vector with respect to the crystallographic axis of the constituting ordered materials. This is probably the most trivial class of effects and has been demonstrated, as an example, for highly-epitaxial $Fe/Al_2O_3/Fe_{50}Co_{50}$ tunnel junctions by Yuasa *et al.* (2000).

Intrinsic spin anisotropy may exist in junctions with electrodes whose spin-split energy surfaces are anisotropic. This would lead to a changes of the junction conductance, as a function of the orientation of the common magnetisation vector of two ferromagnetic electrodes, at a constant current density vector. This type of transport anisotropy has not been reported before and is the subject of section 3.3.4.

Conventional projection anisotropy is arising already in the classical model of Slonczewski (1989) in the general forms given by equations 3.2.24:

$$\sigma_{\mathrm{j}}\left(\theta\right) = \sigma_{\mathrm{j}}(0)\left[1+\mathcal{P}_{\mathrm{l}}\mathcal{P}_{\mathrm{r}}\cos\left(\theta\right)\right] \quad (3.2.30)$$

As the orientations of the ferromagnetic electrodes can be complicated functions of external magnetic field, magneto-crystalline anisotropy, shape anisotropy and exchange bias, among

others, a large set of possible behaviour is observed, generally, by keeping the current density vector constant and rotating or changing the magnitude of the magnetic field. Examples include works on $Co/Al_2O_3/CoFe/NiFe$ tunnel junctions by Chiang *et al.* (2005), $Fe/Al_2O_3/Fe$ junctions by Miyazaki & Tezuka (1995), CoFe-based junction with Ru-spaced artificial ferrimagnet[1] by Tiusan *et al.* (2000) and on $Co/Al_2O_3/Co/CoO/Au$ junctions by Jaffrés *et al.* (2001).

Spin-orbit coupling induced anisotropy has been observed in tunnel junctions with a single ferromagnetic electrode, and tunnel junctions and nano-constrictions with two ferromagnetic electrodes, in the GaMnAs/GaAs system by Giraud *et al.* (2005); Gould *et al.* (2004), and Giddings *et al.* (2005); Ruüster *et al.* (2005); Saito *et al.* (2005), and attributed to the large spin-orbit coupling in the valence band of these materials, and its influence on the projected density of states. It has been suggested by Chantis *et al.* (2007), based on first principles calculations that similar effect may be observable in a Fe/vacuum/Cu junction, though such an effect has not been observed in metallic systems.

Examples of the implications of some of these anisotropy mechanisms on real junctions are discussed later in the context of experimental evidences.

3.2.4 Broadening of the spectral features

3.2.4.1 Finite lifetime athermal broadening

The interaction of the quasi-electrons with their surroundings, leads to a temporal decay of the occupation probability for any given state. For the simplest case of a propagating state, its conjugated plane wave, instead of being homogeneous and harmonic in time, possesses a decaying envelope, which to a first order may be expressed as:

$$\Psi(x,t) = \Psi_0(x,t)\exp\left(-\frac{t}{\tau}\right) \tag{3.2.31}$$

where τ is the effective lifetime due to all present factors and associated interactions, and $\Psi_0(x,t)$ is the original unperturbed state. Via Fourier transform, this decaying envelope results in a standard Lorentzian line-shape in energy which serves as a convolution kernel for all derived energy dependant integral quantities. For example, the junction conductivity σ_j would be convoluted like:

$$\sigma_\mathrm{j} = \frac{1}{\pi}\int_{-\infty}^{+\infty}\frac{\Gamma}{E^2+\Gamma^2}\sigma_\mathrm{j}\left(V_\mathrm{a}-E/q\right)\mathrm{d}E \tag{3.2.32}$$

with the energy broadening Γ being simply related to the lifetime via:

$$\Gamma = \frac{\hbar}{\tau} \tag{3.2.33}$$

[1] A system of two ferromagnetic layers with different magnetic moments antiferromagnetically coupled through a spacer.

Of course, the broadening Γ may, potentially, include contributions of various origins, defect and impurity scattering, phonon, magnon, and other quasi-particle scattering events.

3.2.4.2 Thermal smearing

The treatment of thermal smearing is more conveniently done, following Åkerman *et al.* (2003), starting from the general expression for the tunnel current density:

$$j\left(V_{\mathrm{a}},T\right)=\frac{q}{h}S^{2}\int\limits_{-\infty}^{\infty}\mathcal{M}\left(E-qV_{\mathrm{a}},E\right)N_{\mathrm{l}}\left(E-qV_{\mathrm{a}}\right)N_{\mathrm{r}}\left(E\right)\left[f\left(E-qV_{\mathrm{a}}\right)-f\left(E\right)\right]\mathrm{d}E \tag{3.2.34}$$

where $\mathcal{M}$ is the effective matrix element (which may, generally, include implicit dependence on the density of states), N_{l} and N_{r} are the available for tunnelling density of states for the left and right electrode, respectively, and S is the surface area of the junction. By differentiating the expression for the current density 3.2.34, the following relation for the differential conductivity may be obtained:

$$\begin{aligned}\sigma_{\mathrm{j}}\left(V_{\mathrm{a}},T\right)=\frac{q}{h}S^{2}\Bigg\{&\int\limits_{-\infty}^{\infty}\frac{\partial}{\partial V_{\mathrm{a}}}\left[\mathcal{M}\left(E-qV_{\mathrm{a}},E\right)N_{\mathrm{l}}\left(E-qV_{\mathrm{a}}\right)N_{\mathrm{r}}\left(E\right)\right]\left[f\left(E-qV_{\mathrm{a}}\right)-f\left(E\right)\right]\mathrm{d}E+\\&\int\limits_{-\infty}^{\infty}\left[\mathcal{M}\left(E-qV_{\mathrm{a}},E\right)N_{\mathrm{l}}\left(E-qV_{\mathrm{a}}\right)N_{\mathrm{r}}\left(E\right)\right]\frac{\partial}{\partial V_{\mathrm{a}}}\left[f\left(E-qV_{\mathrm{a}}\right)-f\left(E\right)\right]\mathrm{d}E\Bigg\}\end{aligned} \tag{3.2.35}$$

The two terms in the above equation correspond to quasi-athermal broadening, directly proportional to the applied voltage, and voltage independent thermal broadening, directly proportional to the temperature T, respectively. The athermal broadening is vanishing at small bias $V_{\mathrm{a}}\rightarrow 0$, and therefore, can be often neglected. Another good reason for neglecting the first term is that, generally, both the density of available states, and the effective matrix element, are smooth functions of energy, and therefore the derivative $\frac{\partial}{\partial V_{\mathrm{a}}}\left[\mathcal{M}\left(E-qV_{\mathrm{a}},E\right)N_{\mathrm{l}}\left(E-qV_{\mathrm{a}}\right)N_{\mathrm{r}}\left(E\right)\right]\rightarrow 0$.

The second therm in 3.2.35 may be simplified using the well known relation for Fermi functions:

$$\frac{\partial}{\partial V_{\mathrm{a}}}\left[f\left(E-qV_{\mathrm{a}}\right)-f\left(E\right)\right]=\frac{\partial}{\partial V_{\mathrm{a}}}f\left(V_{\mathrm{a}}\right)\Big|_{E-V_{\mathrm{a}}} \tag{3.2.36}$$

to yield an approximate expression for the differential conductivity at finite temperature:

$$\sigma_{\mathrm{j}}\left(V_{\mathrm{a}},T\right)=\int\limits_{-\infty}^{\infty}\sigma_{\mathrm{j}}\left(E-qV_{\mathrm{a}},0\right)\left[4kT\cosh\left(-\frac{E-qV_{\mathrm{a}}}{2kT}\right)^{2}\right]^{-1}\mathrm{d}E \tag{3.2.37}$$

or the conductivity at finite temperature is, to a large extent, a convolution of the zero-temperature limit conductivity and a quasi-Gaussian kernel (of width larger than $2kT$ as seen immediately from the argument of the hyperbolic cosine in equation 3.2.37), visualised on figure

3.18 together with its approximations by a pure Gaussian, pure Lorentzian, and a Voigt. While the approximation of the convolution kernel with a Voigt function, is clearly the best of the three, a Gaussian is a fully acceptable choice, and is simpler for analytical handling. The width

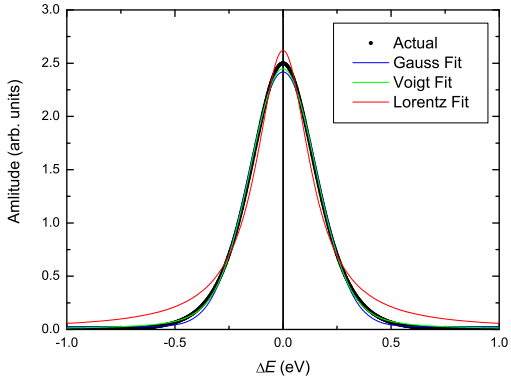

Figure 3.18: Actual Fermi convolution kernel and its approximations by Gaussian, Lorentzian and Voigt functions. The thermal energy is set at $kT = 0.1$ eV.

of the peak may be estimated numerically, as evidenced on figure 3.19, to be $2\sqrt{2\ln 2} \cdot 1.63 \cdot kT$ FWHM[1], with a resulting voltage broadening of $\Delta V \approx 3.84\frac{kT}{q}$. As the thermal voltage

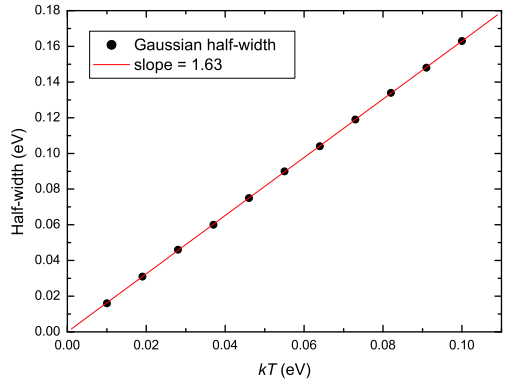

Figure 3.19: Deduced Gaussian broadening of the Fermi convolution kernel, as a function of thermal energy kT.

broadening can be as large as 0.1 V, at 300 K, it imposes a strong constraint on experimental temperatures where high-resolution derivative spectroscopy methods can be applied.

[1] Full Width at Half Maximum

3.2.4.3 Modulation broadening

Actual measurements of σ_{j} and it's derivatives is usually performed by means of modulation technique. As finite modulation amplitude, say V_ω must be applied in order to perform the measurements, and moreover the detected signal is proportional to the squared modulation amplitude V_ω^2, a careful balance is necessary between the demands for increasing modulation amplitude - better signal-to-noise ratio, and faster measurements, and the demands for increasing resolution. As an example, if the second derivative of the current is of interest (as is generally the case in the inelastic junction spectroscopy), the broadening may be evaluated (following Klein *et al.* (1973)) by expressing the measured signal, say $J_{2\omega}$ via the $J-V$ characteristic of the junction:

$$J = J\left(qV_{\mathrm{a}} + qV_\omega \cos\omega t\right) \tag{3.2.38}$$

like:

$$J_{2\omega} = \frac{2}{\tau_\omega}\int_\tau J\left(qV_{\mathrm{a}} + qV_\omega\cos\omega t\right)\cos 2\omega t \mathrm{d}t \tag{3.2.39}$$

where $\tau_\omega = \frac{2\pi}{\omega}$ is the period of the modulation oscillation. By substituting a new variable $E = qV_\omega \cos\omega t$ and performing two integrations by parts, the second harmonic of the current becomes:

$$J_{2\omega} = \frac{2}{\pi V_\omega^2}\int_{-qV_\omega}^{qV_\omega} \frac{\partial^2 J}{\partial(qV)^2}\left(qV_{\mathrm{a}} + E\right)\frac{\left(q^2V_\omega^2 - E^2\right)^{3/2}}{3} \tag{3.2.40}$$

or in other words, the measured signal becomes the convolution of the actual second derivative with an instrumental apposition function f_{instr}

$$J_{2\omega} = \frac{\partial^2 J}{\partial(qV)^2} \otimes f_{\mathrm{instr}} \tag{3.2.41}$$

with the instrumental broadening approximated as:

$$f_{\mathrm{instr}} = \frac{2}{\pi V_\omega^2}\left(qV_{\mathrm{a}} + E\right)\frac{\left(q^2V_\omega^2 - E^2\right)^{3/2}}{3}, \quad |E| \le qV_\omega \tag{3.2.42}$$

$$= 0, \quad |E| > qV_\omega \tag{3.2.43}$$

which represents a symmetric bell-shaped function of FWHM of about 1.22 qV_ω, as expected, close to $\left(\frac{\sqrt{2}-1}{2}+1\right)qV_\omega$. While theoretically possible, deconvolution with the inverse of f_{instr} is often impractical, because of the small signal to noise ratio of the second harmonic detection data. Resolution is more often gained by diminishing the modulation amplitude V_ω, and keeping the scanning step-size of V_{a} comparable to it.

3.2.5 Effects of interface roughness

There are various types of surface roughness and more generally disorder, that potentially affect the transport characteristics of tunnel junctions. Unfortunately, there is no unique way to treating disorder. Nevertheless, it is important to gain at least a rough model understanding of its implications, as it is intuitively clear, that because of the general exponential dependence of the tunnel current on thickness, the resulting effects can be quite dramatic.

Probably the simplest imperfection, to treat analytically, is the geometric roughness, or the fluctuations of the physical barrier layer thickness (preserving the atomic flatness and specular reflection/transmission conditions at the corrugated interface). The barrier thickness distribution function $f_{\mathrm{b}}(x)$ can be defined as a Gaussian kernel:

$$f_{\mathrm{b}}(x) = \frac{1}{\bar{\sigma}_x}\frac{1}{\sqrt{2\pi}}\exp\left[-\frac{(x-\bar{x}_{\mathrm{b}})^2}{2\bar{\sigma}_x^2}\right] \tag{3.2.44}$$

Therefore, if the junction conductance is proportional to k^{WKB} like:

$$\sigma_{\mathrm{j}} \propto \exp\left(-k^{\mathrm{WKB}}x_{\mathrm{b}}\right) \tag{3.2.45}$$

the effective conductance $\bar{\sigma}_{\mathrm{j}}$ would increase with increasing roughness $\bar{\sigma}_x$ in an exponential fashion:

$$\bar{\sigma}_{\mathrm{j}} \propto \int f_{\mathrm{b}}(x)\exp\left(-k^{\mathrm{WKB}}x\right)\mathrm{d}x = \exp\left[-k^{\mathrm{WKB}}\left(\bar{x}_{\mathrm{b}} - k^{\mathrm{WKB}}\bar{\sigma}_x^2\right)\right] \tag{3.2.46}$$

The effective barrier width $\tilde{x}_{\mathrm{b}}$ of a tunnel junction with interface roughness is given by:

$$\tilde{x}_{\mathrm{b}} = \bar{x}_{\mathrm{b}} - k^{\mathrm{WKB}}\bar{\sigma}_x^2 \tag{3.2.47}$$

and is always smaller that the nominal one.

A more detailed treatment, within the incoherent partial waves approach is given by Bardou (1997). The junction conductance can be considered proportional to the tunnelling probability for a rectangular barrier in each differential surface element $\mathrm{d}S$ in the plane of the tunnel junction, so that the differential current:

$$\mathrm{d}I \propto \frac{1}{1 + b\sinh^2\left(\frac{x}{\lambda_{\mathrm{a}}}\right)}\mathrm{d}S \tag{3.2.48}$$

where λ_{a} is the attenuation length given by:

$$\lambda_{\mathrm{a}} = \frac{\hbar}{\sqrt{2m_{\mathrm{e}}\left(q\phi_{\mathrm{b}} - E\right)}} \tag{3.2.49}$$

and the coefficient b is defined as the ratio:

$$b = \frac{q^2\phi_{\mathrm{b}}^2}{4E\left(q\phi_{\mathrm{b}} - E\right)} \tag{3.2.50}$$

Assuming a Gaussian thickness distribution kernel similar to 3.2.44, the resulting probability distribution, as a function of the transmission probability $\mathcal{T}$, is log-normal of the form:

$$f_J\left(\mathcal{T}\right) = \frac{\lambda_\mathrm{a}}{\bar{\sigma}_x \mathcal{T}} \frac{1}{\sqrt{2\pi}} \exp\left\{ -\frac{\lambda_\mathrm{a}^2}{2\bar{\sigma}_x^2} \left[2\ln\left(2\sqrt{\frac{b}{\mathcal{T}}} \right) - \frac{\bar{x}_\mathrm{b}}{\lambda_\mathrm{a}} \right]^2 \right\} \tag{3.2.51}$$

for small transmission coefficients $\mathcal{T} \ll \frac{b}{1+b}$. The opposite case, of large transmission, is harder to handle fully analytically, but the main physical consequence is the high probability of existence of a relatively small number of dominant high-conductance (low effective barrier height) local channels or 'hot-spots', through which the majority of the current passes. This limits the possibilities of realising tunnel junctions with stable and reproducible parameters, which are thinner than few tens of monolayers. The situation is unfavourable experimentally, as statistically rare (and therefore harder to control) events (fluctuations) tend to dominate the tunnelling transport.

3.2.6 The influence of diffuse scattering

Most analysis of tunnelling has been done on the basis of specular transmission/reflection (the conservation of the components of the momentum parallel to the tunnelling interface). Below a brief discussion is given on the implications of the abandonment of this idea.

Following Stratton (1964), the wavefunctions for the left-hand-side and right-hand-side regions may be written as:

$$\Psi_\mathrm{l}\left(E, k_\mathrm{t}\right) = \sum_{k_\mathrm{t}'} a_i\left(k_\mathrm{t}, k_\mathrm{t}'\right) \psi_\mathrm{l}\left(E, k_\mathrm{t}'\right) \tag{3.2.52}$$

$$\Psi_\mathrm{r}\left(E, k_\mathrm{t}\right) = \sum_{k_\mathrm{t}'} b_i\left(k_\mathrm{t}, k_\mathrm{t}'\right) \psi_\mathrm{r}\left(E, k_\mathrm{t}'\right) \tag{3.2.53}$$

in each labeled by i, in the already defined convention, region of space. Would the coefficients a_i be all equal (likewise for the coefficients b_i), the wavefunctions Ψ_l and Ψ_r would still be solutions of the Schrdinger equation for the corresponding regions of space, $x < x_0$ and $x > x_1$. It is intuitively clear, that the above may not be the case, should the nature of the scattering process be diffusive.

Further within the approach of Bardeen (1961), the current for the case of specular transmission is given by equation 3.1.56, or:

$$J_\mathrm{s} = \frac{4\pi q}{\hbar} \sum_{k_\mathrm{t}} \int_{-\infty}^{\infty} \left|\mathcal{T}_\mathrm{lr}\right|^2 \mathcal{D}_\mathrm{l}\left(k_\mathrm{t}\right) \mathcal{D}_\mathrm{r}\left(k_\mathrm{t}\right) \left(f_\mathrm{l} - f_\mathrm{r}\right) \mathrm{d}E \tag{3.2.54}$$

with $\mathcal{D}_\mathrm{l}\left(k_\mathrm{t}\right)$ and $\mathcal{D}_\mathrm{r}\left(k_\mathrm{t}\right)$ being density of states at fixed tangential wavenumber k_t. While for perfectly diffuse boundaries, the tangential component of the momentum does not get conserved,

and therefore the summation over the different k_t is trivial and therefore the current can be written as:

$$J_\mathrm{d} = \frac{4\pi q}{\hbar} \int_{-\infty}^{\infty} |\mathcal{M}_\mathrm{lr}|^2 \mathcal{D}_\mathrm{l} \mathcal{D}_\mathrm{r} \left(f_\mathrm{l} - f_\mathrm{r}\right) \mathrm{d}E \tag{3.2.55}$$

where $\mathcal{D}_\mathrm{l}$ and $\mathcal{D}_\mathrm{r}$ are the usual three-dimensional density of states functions on both sides of the barrier, and the diffuse transport matrix element $\mathcal{M}_{lr}$ is related to the specular one $\mathcal{T}_\mathrm{lr}$, like:

$$\mathcal{M}_\mathrm{lr} = \sum_{k_\mathrm{t}'} a_2^\star \left(k_\mathrm{t}, k_\mathrm{t}'\right) b_0 \left(k_\mathrm{t}, k_\mathrm{t}'\right) \mathcal{T}_\mathrm{lr} \left(k_\mathrm{t}'\right) \tag{3.2.56}$$

which for diffuse boundary conditions may be simplified to:

$$\left|\mathcal{M}_\mathrm{lr}\right|^2 = \sum_{k_\mathrm{t}} \left|a_2\right|^2 \left|b_0\right|^2 \left|\mathcal{T}_\mathrm{lr}\right|^2 \tag{3.2.57}$$

by making random phase approximation and therefore neglecting the interference terms that would otherwise appear[1]. As already mentioned in section 3.1.4, the matrix element $\mathcal{T}_\mathrm{lr}$ is inversely proportional to the density of states, and therefore, the density of states is not likely to reappear in a derivation of an expression for the tunnel current in the diffusive limit, based on equation 3.2.55, and the main effect is essentially a renormalisation of the magnitude of the current.

There is no unique way to define the renormalisation of the current, without making particular assumptions on distribution of the transmitted and reflected wave-vectors, after diffusive transmission or reflection. A reasonable assumption, for the perfectly diffusive case, is a uniform distribution of both the transmitted and reflected vectors over the corresponding energy hemispheres. For spherical Fermi surfaces and at normal incidence, this yields averaging over the azimuthal angle θ, of the type:

$$\int_{-\pi/2}^{\pi/2} 1 \cos\left(\theta\right) \mathrm{d}\theta = 2 \tag{3.2.58}$$

which can be compared with the one assumed for specular reflection/transmission:

$$\int_{-\pi/2}^{\pi/2} \delta\left(\theta\right) \cos\left(\theta\right) \mathrm{d}\theta = 1 \tag{3.2.59}$$

[1]The situation bears certain resemblance with coherent and incoherent transmission of light through a thin film interferometer. It is clear, that instead of the sum of interference patterns of equal angle that would appear if a light source is coherently illuminating the thin film (a separate pattern for each photon frequency), just intensity dependent transmission (no definite phase information) would remain in the diffuse case of say, a frosted film.

which is well justified if the Fermi-surfaces on both sides of the interface are large. It is, therefore, not unreasonable to expect ratios close to 2 between the diffusive and specular components of the current through a single interface:

$$\frac{J_{\mathrm{d}}}{J_{\mathrm{s}}} \approx 2 \tag{3.2.60}$$

It follows, that if the relative amount of specular transmission, at the two interfaces delimiting the tunnel barrier, is f_0^{s} and f_1^{s}, respectively (so that the relative amounts of diffusive transmission are $f_0^{\mathrm{d}} = 1 - f_0^{\mathrm{s}}$ and $f_1^{\mathrm{d}} = 1 - f_1^{\mathrm{s}}$), then the total tunnel current may be estimated as:

$$J \approx (2 - f_0^{\mathrm{s}})\,(2 - f_1^{\mathrm{s}})\,J_{\mathrm{s}} \tag{3.2.61}$$

Thus, within this simple model, the total current ranges between J_{s} in the purely specular regime, to about $4J_{\mathrm{s}}$, in the purely diffusive regime.

The analysis becomes more complicated for non-spherical Fermi surfaces, but the consequences are physically simple - anisotropy of the tunnelling current, arising from or modified by the diffusiveness of the interfaces. Of course, such effects may only be observable if a macroscopic averaging does not 'smooth' them out. In other words, for the observation of similar tunnelling anisotropy, it is a prerequisite, that at least one of the metal electrodes is single-crystalline, or, at least, well oriented crystallographically[1].

The formal theory of tunnelling for thick junctions has been elaborated by Walker (1999). The analysis is, by necessity, based an the expression for the tunnelling current with a three-dimensional wave-vector space integration, without spin splitting ($\gamma = 2$):

$$J = \gamma \frac{q}{h} \int \mathrm{d}E \left[f\left(E - qV_{\mathrm{a}}\right) - f\left(E\right) \right] \int \frac{\mathrm{d}^2 k}{\left(2\pi\right)^2} \mathcal{M}\left(E, \mathbf{k}\right) \tag{3.2.62}$$

with the transmission probability $\mathcal{M}$ given by:

$$\mathcal{M}\left(E, \mathbf{k}\right) = \left| \bar{\mathcal{V}}_{\mathrm{lr}}(\mathbf{k}) \right|^2 + \int \mathcal{K}_{\mathrm{lr}}\left(\mathbf{k}, \mathbf{k}'\right) \mathrm{d}\mathbf{k}' \tag{3.2.63}$$

where $\bar{\mathcal{V}}_{\mathrm{lr}}$ is the average scattering amplitude power and represents the specular part of the scattering; and $\mathcal{K}_{\mathrm{lr}}$ defines the probability for scattering into state with a wave-vector $\mathbf{k}'$ if the original state is a one of $\mathbf{k}$, and is proportional to the mean-square slope of the roughness of the interfaces $\overline{\delta s}$ (in principle all interfaces may have different roughness, which makes the mathematical description rather cumbersome, without introducing any new physical insights into the problem):

$$\mathcal{K}_{\mathrm{lr}}\left(\mathbf{k}, \mathbf{k}'\right) \propto \overline{\delta s}^2 \tag{3.2.64}$$

[1] This is in accordance with the generalized Neumann's principle, which states that the symmetry elements of any physical property of the device as a whole, should include all the symmetry elements of the point groups of the crystals from which the device is made, and elements of symmetry group of the device structure, as such.

This view over the problem for tunnelling through junctions with significant interface roughness is known as the tangent plane approximation, and is valid only if the interfaces are smooth (not necessarily flat) over distances larger than the characteristic wavelengths of the tunnelling electrons.

While the viewing of the tunnelling problem as consecutive scattering from a series of rough interfaces may be tractable under certain approximations, as has been demonstrated by Palasantzas *et al.* (2000), it is important to note couple of physical points without going into detailed evaluations.

Even when inelastic scattering is neglected (Leo & MacDonald (1990)), the coherent scattering from rough interfaces leads to exchange of perpendicular and transverse momentum, which influences the transport integrals, and can potentially produce asymmetry in the $I-V$ characteristics of real devices, if the different interfaces have significantly different roughnesses. Therefore interface roughness, can be considered an alternative to compositional gradients and variations across the tunnel structure, for defining directional anisotropy (and therefore partially rectifying $I-V$ characteristic) of the tunnelling contact.

The diffuse scattering component would dominate the transport at rough interfaces, as it does not suffer from the destructive interferences, which diminish the specular (fully coherent) component[1]. Therefore, the tunnelling looses its directionality if the interfaces between the insulating barrier and the metal electrodes have high roughness, and an exact treatment of the electron scattering on each rough interface is necessary, in order to develop a realistic model. Roughness, on a scale comparable with the typical electronic wavelengths in the electrodes or in the barrier, would lead to changes in the states available for tunnelling, as well as the transition probabilities between the various quantum states. The problem thus becomes fully quantum mechanical, and the use of quasi-classical, or any other adiabatic approximation, for its solution, is no longer justified. There are important consequences for nature of the tunnelling process at small applied bias, some of which are discussed in section 3.1.6.

3.2.7 Inelastic transport

The usefulness of tunnel junctions with ferromagnetic electrodes for practical applications is often limited by strong bias dependance of the junction magnetoresistance. While electronic relaxation within regions of the electrodes is generally rapid, and can be taken into account, in a quasi-equilibrium approach like the one of Hachaturov (2005a); at low and intermediate

[1] The situation bears some resemblance with the phenomenon of weak localisation in disordered metals, or more generally, localisation in a random potential. The coherent interference is dominated by backscattering, if there is no breaking of phase relationships in the scattering process.

biases, non-equilibrium population of hot electrons can be established in the barrier region, via additional (energy and momentum) relaxation mechanisms, like scattering from phonons and magnons, leading to observable effects on the transport characteristics.

Bulk magnons lead to a drop-off of the polarisation of the electrodes of the form (Shang *et al.* (1998)):

$$P(T) = P(0)\left[1 - \left(\frac{T}{T_{\mathrm{mag}}}\right)^{3/2}\right] \tag{3.2.65}$$

where T_{mag} is a characteristic energy scale for the electron-magnon coupling, which is different deep in the volume of the electrodes and close to the interface due to the so-called 'softening' of the exchange coupling. Therefore the junction magnetoresistance will be influenced, passively[1], according to the asymmetries in the electrodes, if any.

Historically, the first model of inelastic transport, aimed in explaining the bias and temperature dependences of the conductance and the TMR ratio, is the one of Zhang *et al.* (1997b). The model has several limited extensions, modifications and experimental verifications (Dartora & Cabrera (2004); Dimopoulos *et al.* (2004); Han *et al.* (2001); Tkachov (2007); Wingbermühle *et al.* (2002), among others). A brief account of this model is given below.

The conductances $\sigma_{\mathrm{j}}(V_{\mathrm{a}}, T)$ in the parallel ($\uparrow\uparrow$) and antiparallel ($\uparrow\downarrow$) alignment are approximated like:

$$\sigma_{\mathrm{j}}^{\uparrow\uparrow(\uparrow\downarrow)}(V_{\mathrm{a}}, 0) = \sigma_{\mathrm{j}}^{\uparrow\uparrow(\uparrow\downarrow)}(0,0) + \Delta\sigma_{\mathrm{j}}^{\uparrow\uparrow(\uparrow\downarrow)}(V_{\mathrm{a}}) \tag{3.2.66}$$

$$\sigma_{\mathrm{j}}^{\uparrow\uparrow(\uparrow\downarrow)}(0, T) = \sigma_{\mathrm{j}}^{\uparrow\uparrow(\uparrow\downarrow)}(0,0) + \Delta\sigma_{\mathrm{j}}^{\uparrow\uparrow(\uparrow\downarrow)}(T) \tag{3.2.67}$$

where $\Delta\sigma_{\mathrm{j}}^{\uparrow\uparrow(\uparrow\downarrow)}(V_{\mathrm{a}})$, and $\Delta\sigma_{\mathrm{j}}^{\uparrow\uparrow(\uparrow\downarrow)}(T)$ are two different functions of the applied voltage V_{a} and the lattice temperature T, respectively, and are sufficient to describe the junction behaviour only at low bias and temperature and if the magnon distribution obeys Bose-Einstein statistics.

.

The three base functions are approximated like:

$$\sigma_{\mathrm{j}}^{\uparrow\uparrow(\uparrow\downarrow)}(0,0) = \frac{4\pi q^2}{\hbar}\left[|\mathcal{T}^{\mathrm{d}}|^2 + 2s^2|\mathcal{T}^{\mathrm{J}}|^2\right] A^{\uparrow\uparrow(\uparrow\downarrow)} \tag{3.2.68}$$

$$\Delta\sigma_{\mathrm{j}}^{\uparrow\uparrow(\uparrow\downarrow)}(V_{\mathrm{a}}) = \frac{4\pi q^2}{\hbar}|\mathcal{T}^{\mathrm{J}}|^2 B^{\uparrow\uparrow(\uparrow\downarrow)}\frac{sqV_{\mathrm{a}}}{E_{\max}} \tag{3.2.69}$$

$$\Delta\sigma_{\mathrm{j}}^{\uparrow\uparrow(\uparrow\downarrow)}(T) = \frac{4\pi q^2}{\hbar}\frac{2skT}{E_{\max}}|\mathcal{T}^{\mathrm{J}}|^2 B^{\uparrow\uparrow(\uparrow\downarrow)}\left[-\ln\left(1 - \mathrm{e}^{\frac{E_{\min}^{\uparrow\uparrow(\uparrow\downarrow)}}{kT}}\right)\right] \tag{3.2.70}$$

[1] The electronic subsystem is 'feeling' the elevated temperature, and is at all times close to equilibrium with the phonon and magnon baths. As compared to the active influence, when the electrons are at an elevated effective temperature (if it is at all possible to describe the distribution function with an effective Fermi distribution, which is only a good approximation at small excitation intensities) and create magnons in the immediate proximity to the barrier, before they are relaxed to the equilibrium population.

and $A^{\uparrow\uparrow(\uparrow\downarrow)}$ and $B^{\uparrow\uparrow(\uparrow\downarrow)}$ are defined as:

$$A^{\uparrow\uparrow} = \mathcal{D}_{\mathrm{l}}^2(E_{\mathrm{F}}) + \mathcal{D}_{\mathrm{r}}^2(E_{\mathrm{F}}) \tag{3.2.71}$$

$$A^{\uparrow\downarrow} = 2\mathcal{D}_{\mathrm{l}}(E_{\mathrm{F}})\mathcal{D}_{\mathrm{r}}(E_{\mathrm{F}}) \tag{3.2.72}$$

$$B^{\uparrow\uparrow} = 2\mathcal{D}_{\mathrm{l}}(E_{\mathrm{F}})\mathcal{D}_{\mathrm{r}}(E_{\mathrm{F}}) \tag{3.2.73}$$

$$B^{\uparrow\downarrow} = \mathcal{D}_{\mathrm{l}}^2(E_{\mathrm{F}}) + \mathcal{D}_{\mathrm{r}}^2(E_{\mathrm{F}}) \tag{3.2.74}$$

where s is the localised spin at the interfaces, $\mathcal{T}^{\mathrm{d}}$ is the direct tunnelling matrix element, $\mathcal{T}^{\mathrm{J}}$ is the inelastic tunnelling matrix element and $E_{\max}$ is the bandwidth of the surface magnons, which can be mean-field approximated as:

$$E_{\max} \approx \frac{3kT_{\mathrm{C}}}{(s+1)} \tag{3.2.75}$$

with T_{C} being the Curie temperature, and $E_{\min}^{\uparrow\uparrow(\uparrow\downarrow)}$ are the minimal surface magnon energies for the two magnetisation states, that remain free parameters and are determined primarily by magnetic anisotropy and geometrical magnon wavelength limitations.

While the above model (3.2.66) has been applied successfully for the fitting of temperature dependancies of the junction magnetoresistance, the bias dependence, due to the perturbation character of the model is only capable of explaining a limited number of cases (mostly AlO_x, MgO based tunnel junctions (Dimopoulos *et al.* (2004)), where there is a limited low-bias structure and a monotonic bias behaviour), but is hardly applicable to very-high TMR ration junctions exhibiting strong bias dependence and an abundance of low-bias structure in the inelastic tunnelling spectra.

3.3 Magneto-transport in Ferromagnet/Insulator/Ferromagnet structures

3.3.1 Advances in the theory and experiment on bias dependence of the TMR

Large deviation from the models of Jullière (1975) and Slonczewski (1989) have been noted in work of Moodera *et al.* (1998) on Co and NiFe based tunnel junctions with Al_2O_3 barrier, and attributed to magnon scattering, at least in the low-bias region. Surface magnons excited by hot tunnelling electrons have been considered theoretically by Zhang *et al.* (1997a), as the cause for deterioration of the junction magnetoresistance with applied bias in similar magnetic tunnel junctions, with a reasonable agreement with experiment at low bias (less than about 200

mV). Similar assertions have been corroborated by other experimental studies (see for example Han *et al.* (2001); Murai *et al.* (2001); Tezuka *et al.* (1999)).

Further, the influence of magnetic impurities in the barrier region has been found by Jansen & Moodera (2000) and Bae & Wang (2002), to be in a rough agreement with the temperature dependence expected s-d model theory of Appelbaum (1966), for intentionally doped tunnel junctions with Al_2O_3 barrier and permalloy electrodes. A different approach has been suggested, however, by Kohlhepp *et al.* (2002); LeClair *et al.* (2001), attributing the zero-bias anomaly, observed in $Co/Al_2O_3/Co$ tunnel junctions with Cr and Ru 'dusting' layers, to a strong modification of the local density of states close to the metal-insulator interfaces. Variation of the density of states of the ferromagnetic electrodes has been also considered to be a contributing factor for diminishing tunnel magnetoresistance at high applied bias (see for example Xiang *et al.* (2003a)), with supporting data on Co and permalloy based junctions. This speculation, though, is in direct contradiction with the experimental evidence on through-vacuum tunnelling between a Co (0001) surface and amorphous CoFeSiB tip. The absence of any zero-bias anomaly reported by Ding *et al.* (2003), and theoretically modelled by Henk & Bruno (2003), is a strong suggestion that neither density of states effects, nor magnons or phonons, are likely to be responsible for the appearance of one, while defect scattering and other insulator-related phenomena remain as open possibilities.

Despite the original popularity of magnetic tunnel junctions based on AlO_x barriers, other insulators have been considered both experimentally and theoretically. One of the most popular choices over the years has proved to be MgO. High tunnelling magnetoresistance ratios (larger than 65 % for Fe/MgO/Fe) (TMR) have been reported by Faure-Vincent *et al.* (2003), exceeding the ones expected by the simple model of Jullière (1975). In-situ growth and characterisation of single-crystalline Fe/MgO/Fe tunnel junctions have also been reported, by Klaua *et al.* (2001); Wulfhekel *et al.* (2001). High, but both positive and negative TMR ratios have been revealed in the same tunnelling system by Tiusan *et al.* (2004), and interfacial states pointed as the likely origin of the TMR bias dependence. Following, have been reports of *giant* TMR ratios in MgO based barriers. Examples include CoFe/MgO/CoFe, reported by Parkin *et al.* (2004), with TMR of more than 300 % at low temperature, complemented by polarisation measurements revealing very high polarisation of more than 85 % of the electrodes, this time, within reasonable agreement with the model of Jullière (1975)[1]. Numerous other reports exist of giant tunnel magnetoresistance at room temperature (see Tsunekawa *et al.* (2005) and Yuasa

[1] This can be easily undestood, as for amorphous and small-grain size poly-crystalline electrodes and barriers, the transverse component of the momentum of the electrons is averaged in the scattering process, leading to a reasonable description of the tunnelling magnetoresistance, by a single parameter - the effective polarisation of the electrodes.

et al. (2006)). Almost fully coherent transport in the Fe/MgO/Fe, with a TMR ratio oscillating with barrier thickness, have been observed by Moriyama *et al.* (2006); Yuasa *et al.* (2004, 2005).

Amorphous ferromagnetic electrodes (for example CoFeB alloys centred around the deep eutectic of the parent alloy $Co_{80}B_{20}$) are the subject of ongoing research, and their growth, characterisation and application are described in a large number of publications (only as examples, Luo *et al.* (2005); Nagasaka *et al.* (2000) and references therein).

Reports of first and second derivative spectroscopy of CoFeB/MgO/CoFeB (like the ones of Matsumoto *et al.* (2005) and Miao *et al.* (2006); Ono *et al.* (2006)) have resolved some phonon and magnon excitations in the electrodes, have reported a systematic decrease in differential tunnelling magnetoresistance and have attributed it to changes in the barrier penetration probability, together with inelastic magnon-assisted tunnelling channels. Also, comparisons between AlO and MgO based tunnel barriers has been performed by Mizuguchi *et al.* (2006).

The importance of the micromagnetic state of the CoFeB electrodes has been pointed-out by Yuan *et al.* (2006), and also recognised theoretically for the Fe/MgO/Fe case by Yavorsky & Mertig (2006). Chemical composition close to the interface has also been found to have a significant impact on the TMR ration and its bias dependence (Tiusan *et al.* (2006b)).

Double tunnel barriers based on Fe and MgO, have also been investigated in view of optimising the so-called 'spin filtering' effect within the MgO barriers (the different decay lengths for the majority and minority carriers within the barrier) by Tiusan *et al.* (2006a).

From the theoretical point of view, it has been argued by Heiliger *et al.* (2005) that within the coherent transport approximation, the conductance and magneto-conductance of Fe/MgO/Fe structures should exhibit profound sensitivity towards the particular interface reconstruction, with justification in the density of states at the interfaces and the symmetries of the involved tunnelling states (Heilinger *et al.* (2006)).

Recently thin MgO tunnel barriers have been considered as candidates for the realisation of spin-transfer-torque devices, of both coherent precession type and magnetisation reversal type, analogous to the all-metal based nano-pillar type stacks (see for example Fuchs *et al.* (2006) and references therein).

3.3.2 Derivative spectra and their temperature broadening

3.3.2.1 Deconvolution of the temperature broadening

The temperature broadening of the differential conductivity σ_j may be handled in several different ways. A deconvolution based the approximation 3.2.37 is a relatively straight-forward procedure. The problem may be solved in discrete voltage representation.

Let the differential conductivity be measured at n_{sample} different points in the bias window $[-V_{\max}..V_{\max}]$. The vector of the measured conductivity may be thus defined as:

$$[\boldsymbol{\sigma}]_i = \sigma\left(v_i\right) \tag{3.3.1}$$

where $\mathbf{v}$ is the base vector of the applied voltage, the components of which may be simply (but not necessarily) defined as:

$$v_i = -V_{\max} + 2V_{\max}\frac{i}{n_{\text{sample}}} \tag{3.3.2}$$

If the convolution matrix is defined via equation 3.2.37 like:

$$[\mathbf{p}]_{ij}(T) = \left[4kT\cosh\left(-\frac{v_i - qv_j}{2kT}\right)^2\right]^{-1} \tag{3.3.3}$$

and therefore the vector of the conductivity at an arbitrary temperature T may be expressed as:

$$\boldsymbol{\sigma}(T) = \mathbf{p}(T)\cdot\boldsymbol{\sigma}(0) \tag{3.3.4}$$

and therefore in order to find the vector $\boldsymbol{\sigma}(0)$, if the vector $\boldsymbol{\sigma}(T)$ is known, the inverse convolution matrix (the deconvolution matrix) is needed:

$$\mathbf{p}^{-1}(T)\cdot\boldsymbol{\sigma}(T) = \boldsymbol{\sigma}(0) \tag{3.3.5}$$

In most situations, the matrix $\mathbf{p}(T)$ is either singular, or very close to singular, so that its inverse is not well defined, or at least, not well behaved numerically. One possible way around this problem is to employ the singular value decomposition (SVD) matrix inversion method (see for example Press *et al.* (1992)).

The singular values of $\mathbf{p}(T)$ may be factored-out as:

$$\mathbf{p}(T) = \mathbf{U}\text{diag}(\mathbf{s})\mathbf{V}^{\mathrm{T}} \tag{3.3.6}$$

where $\mathbf{U}$ and $\mathbf{V}$ are two orthogonal matrices, and diag($\mathbf{s}$) is a diagonal matrix, containing the singular values of $\mathbf{p}(T)$. The inverse of $\mathbf{p}$ is thus given by:

$$\mathbf{p}^{-1} = \mathbf{V}\text{diag}(s)\mathbf{U}^{\mathrm{T}} \tag{3.3.7}$$

The above inversion is as useless as the direct matrix inversion of $\mathbf{p}(T)$ if the vector of singular values $\mathbf{s}$ is left untouched. The strength of the SVD approach is, actually, in the possibility of selective filtering of the elements of the vector $\mathbf{s}$, which are rather close to zero[1], a procedure, which is discussed in detail in section C.3. Here, it will be assumed that the vector $\mathbf{s}$ is

[1] How close, is rather close, depends ultimately on the noise contribution to the actual measured data vector $\boldsymbol{\sigma}(T)$.

somehow 'filtered' from its very small singular values, resulting in a vector $\mathbf{f}$. The inverse of the convolution matrix $\mathbf{p}$ would therefore be the well-behaved:

$$\mathbf{p}^{-1} = \mathbf{V}\mathrm{diag}(f)\mathbf{U}^{\mathrm{T}} \tag{3.3.8}$$

and therefore, an approximation to the zero-temperature conductance vector may be reconstructed as:

$$\boldsymbol{\sigma}(0) = \mathbf{V}\mathrm{diag}(f)\mathbf{U}^{\mathrm{T}}\boldsymbol{\sigma}(T) \tag{3.3.9}$$

A demonstration of this procedure is shown at figure 3.20 for a unannealed CoFeB-based tunnel junction, for an antiparallel orientation of the magnetisations of the electrodes. The deconvoluted, $T = 0$ K from $T = 300$ K, spectrum is in reasonable agreement with the low temperature $T = 2.0$ K data. Large deviations are evident at the extremes of the bias window, which are due to the finite-size of the representation used for the deconvolution (in therms of infinitesimal transforms - the convolution integrals span outside the bias interval for the measured data).

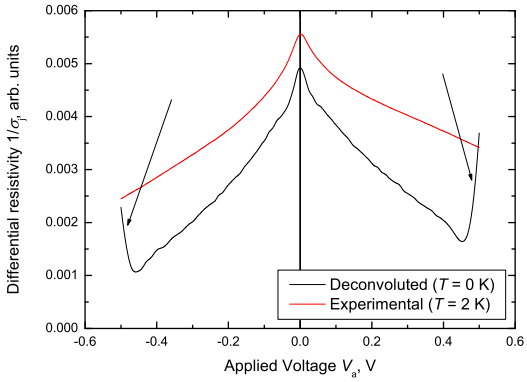

Figure 3.20: Deconvoluted from experimental data taken at $T = 300$ K data, differential resistivity; compared with the experimental data measured at $T = 2.0$ K. The arrows point to artefacts due to the finite size of the representation used for deconvolution.

The treatment of the thermal smearing of the derivative spectra, demonstrated above is not free from systematic errors, even within the simplified effective Hamiltonian tunnelling model. Non-negligible deviations are caused by the omission of the first term in equation 3.2.35, responsible for the voltage dependent part of the broadening. The analytical (and numerical) handling becomes more complicated. Instead of inversing a single matrix equation, the following system of matrix equations may be solved:

$$\left|\begin{array}{lcl} \boldsymbol{\sigma}(0) & = & \mathbf{a} + \mathbf{q}(0)\cdot\mathbf{b} \\ \boldsymbol{\sigma}(T) & = & \mathbf{p}(T)\cdot\mathbf{a} + \mathbf{q}(T)\cdot\mathbf{b} \end{array}\right. \tag{3.3.10}$$

where the matrix $\mathbf{p}(0)$ has been substituted with the unit matrix $\mathbf{1}$, and $\mathbf{q}$ is the convolution matrix corresponding to the voltage broadening component:

$$[\mathbf{q}]_{ij} = f(v_i - v_j) - f(v_i) \tag{3.3.11}$$

and $\mathbf{a}$ and $\mathbf{b}$ are vectors (in principle independent), that within the approximation that effective matrix element $\mathcal{M}(E)$ is independent of the bias voltage and only a function of energy, can be associated with $\mathcal{M}$ and $\frac{\partial}{\partial E}\mathcal{M}(E)$, respectively.

The obvious solution of the system 3.3.10 is:

$$\begin{aligned} \mathbf{b} &= [\mathbf{q}(T) - \mathbf{p}(T)\cdot\mathbf{q}(0)]^{-1} \cdot [\boldsymbol{\sigma}(T) - \mathbf{p}(T)\cdot\boldsymbol{\sigma}(0)] \\ \mathbf{a} &= \boldsymbol{\sigma}(0) - \mathbf{q}(0)\mathbf{b} \end{aligned} \tag{3.3.12}$$

provided the two vectors $\boldsymbol{\sigma}(T)$ and $\boldsymbol{\sigma}(0)$ are known. Of course, while the former can be experimentally determined, the latter may be only approximated by experimental data taken at low temperature, for which the thermal broadening is negligible. One of the data vectors is chosen at $T = 0$ K so that one matrix inversion can be avoided, namely the inversion of p at low temperature, which is problematic and often unnecessary. The remaining inversion of $[\mathbf{q}(T) - \mathbf{p}(T)\cdot\mathbf{q}(0)]$ may be done by, again, employing the SVD methodology. Similar approach is demonstrated on figure 3.21, in terms of the reconstructed solutions for the differential resistivity at $T = 300$ K.

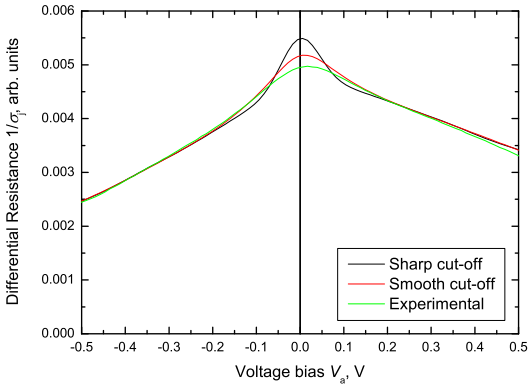

Figure 3.21: Recovered differential resistivity, for CoFeB tunnel junction in the antiparallel configuration, with different methods for cleaning of the singular value vector of the deconvolution matrix for the matrix system 3.3.10, compared with experimental data for $T = 300$ K.

The validity of the above approach is substantiated by the fact, that the vectors $\mathbf{a}$ and $\mathbf{b}$ determined as quasi-linearly-independent, relate via energy differentiation, as shown on figure 3.22.

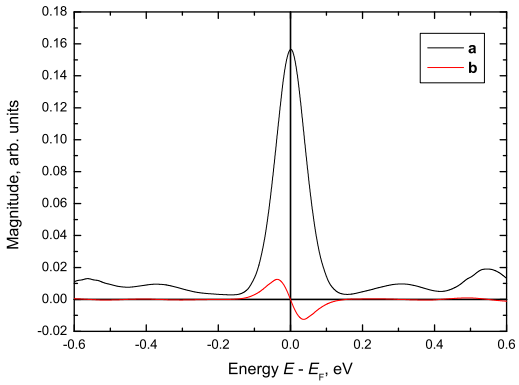

Figure 3.22: Reconstructed vectors **a** and **b** for a unannealed CoFeB junction. Note that **a** is associated with $\mathcal{M}(E)$, and (b) with $\frac{\mathrm{d}}{\mathrm{d}E}\mathrm{M}(E)$

3.3.3 Temperature effects

The weak temperature dependence of the tunnelling current, is in strong contrast with the exponential temperature sensitivity of the thermionic emission current over the barrier region, or even the normal metallic conduction through so-called 'pinholes' often present is low quality tunnel junctions, exhibiting almost linear temperature dependence in a broad region of temperatures. One exception is the Kondo scattering modification of the resistance, non-negligible only in junctions with a large amount of magnetic impurities within the insulator, which can be often described with the semi-empirical expression (see Lee *et al.* (2007) and references therein):

$$\frac{R_\mathrm{j}(T)}{R_\mathrm{j}(0)} = \left(\frac{T_0^2}{T^2+T_0^2}\right)^{s_\mathrm{K}} \tag{3.3.13}$$

where T_0 is related to the Kondo temperature T_K via:

$$T_0 = T_\mathrm{K}\frac{1}{\sqrt{2^{1/s_\mathrm{K}}-1}} \tag{3.3.14}$$

and s_K is a dimensionless free parameter of order of unity.

Therefore, temperature-independent conduction is often considered a strong indication for a dominating tunnel current component in real junctions as argued by Åkerman *et al.* (2002). Of course, a small number of carriers may still be excited over the barrier, though, for junctions with metallic (or degenerate semiconductor) electrodes, their number is exponentially small over energies of the order of $3-5\ kT$. However, this sets only a mild restriction on the minimal barrier height of the order of 200 mV, at room temperature, readily achievable in metal/insulator/metal junctions.

Various examples can be given of junctions exhibiting primarily adiabatic tunnelling behaviour. Two are shown on figures 3.23 and 3.24, identical CoFeB/MgO/CoFeB tunnel junctions, one as deposited, the other one annealed.

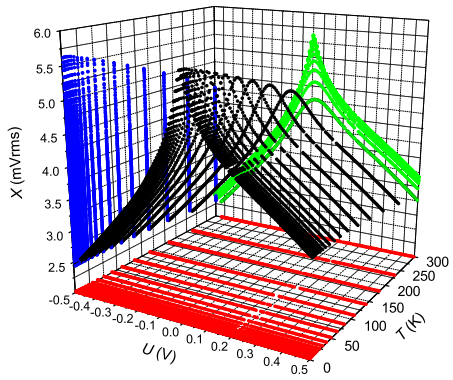

Figure 3.23: Differential resistance as a function of applied bias and temperature, for an unannealed CoFeB/MgO/CoFeB junction, in the parallel state. The projections of the data points on the three main phase-space planes are shown.

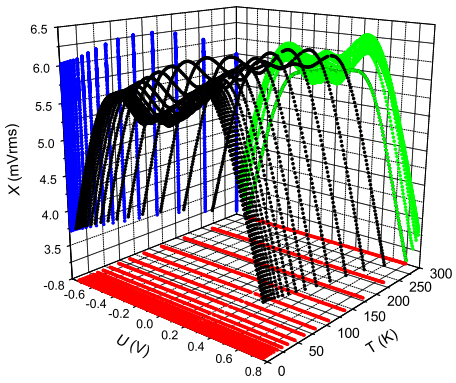

Figure 3.24: Differential resistance as a function of applied bias and temperature, for an annealed CoFeB/MgO/CoFeB junction, in the parallel state. The projections of the data points on the three main phase-space planes are shown.

For the case of an unannealed junction, the behaviour can be explained by the effect of thermal broadening on the Fermi distribution. The zero bias differential resistance peak becomes both narrower and higher. The expected temperature dependence is weak, constant minus a linear and quadratic terms, and this is indeed verified experimentally as demonstrated on figure 3.25. For the annealed case, the temperature dependence of the zero-bias differential resistance is non-monotonic, exhibiting a maximum at about 150 K, and generally weaker temperature

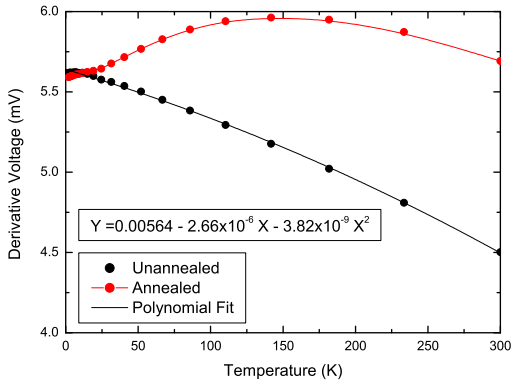

Figure 3.25: Temperature dependence of the differential resistance (derivative voltage) at zero bias, extracted from the data on figures 3.23 and 3.24. The solid lines represent a second order polynomial fit and a $\beta-$spline, for the unannealed and annealed cases, respectively.

dependence, as shown on figure 3.25. This non-trivial behaviour may therefore be related either to the improved degree of crystallinity of the barrier region, or the diffusion of magnetic impurities from the ferromagnetic electrodes. Another possible explanation may be related to the magnetic anisotropy axis developed upon annealing and the high generic junction magnetoresistance of the annealed structures. Competition of different anisotropies may, in principle, lead to small deviations of the magnetisation orientations of the junction electrodes from the parallel orientation, thus influencing the temperature dependence of the differential resistance in a broad bias window.

Other examples for both the parallel and antiparallel states of unannealed and annealed CoFeB-based junctions are shown on figures 3.26, 3.27, 3.28 and 3.29.

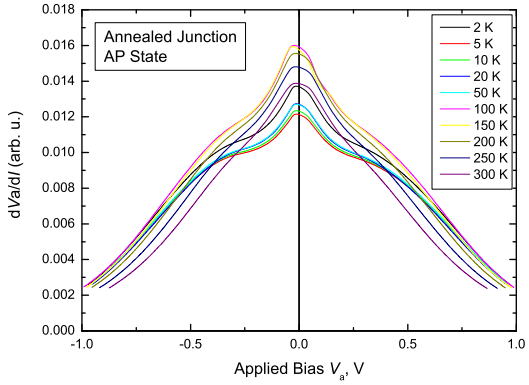

Figure 3.26: Temperature dependence of the first-order resistance derivative spectra for an annealed CoFeB/MgO/CoFeB junction in the antiparallel state.

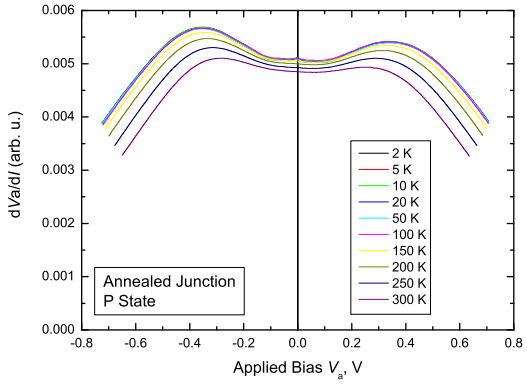

Figure 3.27: Temperature dependence of the first-order resistance derivative spectra for an annealed CoFeB/MgO/CoFeB junction in the parallel state.

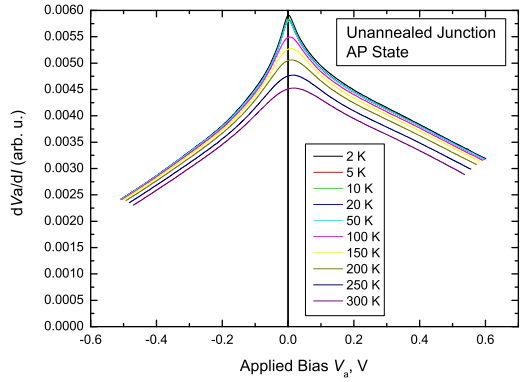

Figure 3.28: Temperature dependence of the first-order resistance derivative spectra for an unannealed CoFeB/MgO/CoFeB junction in the antiparallel state.

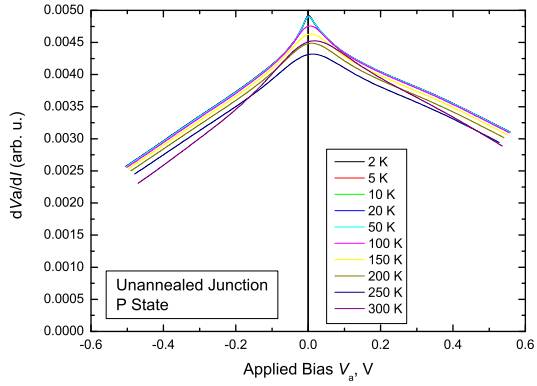

Figure 3.29: Temperature dependence of the first-order resistance derivative spectra for an unannealed CoFeB/MgO/CoFeB junction in the parallel state.

It is not uncommon, for junctions annealed at low temperatures (thus preventing large diffusion, and composition homogenisation), to exhibit little or no observable temperature dependence of the resistance, except for that due to thermal broadening. A similar situation is illustrated on figure 3.30. The behaviour is essentially unaltered, independently of whether

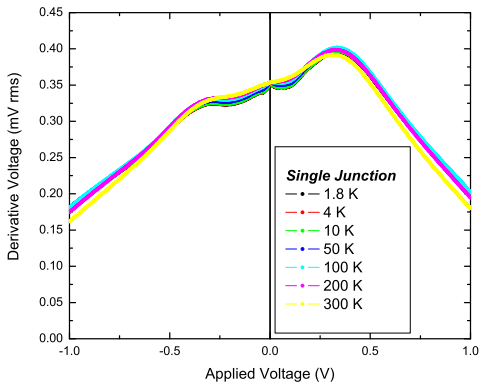

Figure 3.30: Voltage dependence of the differential resistance (the experimental derivative voltage) of a single CoFeB/MgO/CoFeB junction, in the parallel state, measured at different temperatures. The data is identical to the one of figure 3.31.

resistance or conductance are considered. As the differential resistances are generally large (of the order of 1 kΩ), for both the parallel and the anti-parallel orientations, the reciprocal relationship between differential resistance and conductance does not distort the bias dependencies observed, and can be often considered to merely negate the characteristic features in the derivative spectra, as demonstrated on figure 3.31, as compared to figure 3.30. The struc-

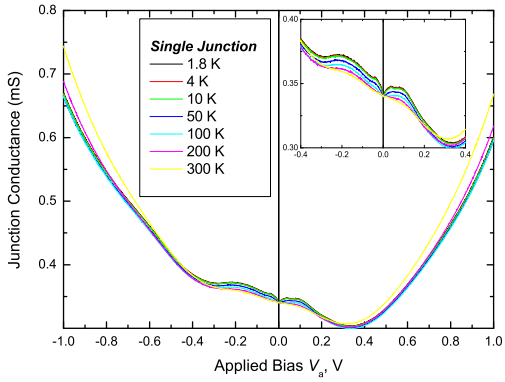

Figure 3.31: Voltage dependence of the differential conductance of a single CoFeB/MgO/CoFeB junction in the parallel state, measured at different temperatures. The inset shows a close-up of the small bias region.

ture appearing at low temperature and bias (below about ±0.4 V), is primarily due to inelastic processes, and is discussed in more detail in section 3.3.8.

The behaviour of junctions containing a very large number of scatterers, like double tunnel junctions and junctions with 'dusting' layers, can be strongly influenced by temperature. An example is given on figure 3.32. The dominating effect is thermal broadening, while the zero-bias differential resistance remains relatively constant. The FWHM of the central resistance

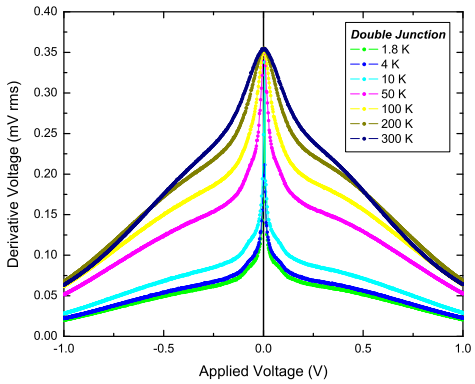

Figure 3.32: Voltage dependence of the differential resistance (the experimental derivative voltage) of a double CoFeB/MgO/CoFeB junction, in the antiparallel state, measured at different temperatures.

peak is plotted as a function of temperature on figure 3.33. The effective electronic temperature obtained is very high: $T_{\text{eff}} = 8.8\ T$, which strongly suggests hot electron injection through the double barrier. At low temperature the resistance (conductance) are almost singular, exhibiting a very sharp peak, close to zero bias, with a non-trivial shape. The nature of the resonance is

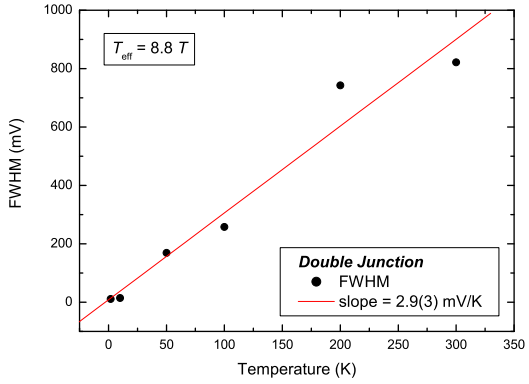

Figure 3.33: Temperature dependence of the FWHM of the central resistance peak of figure 3.33, as a function of temperature. The deviations from linearity are largely due to the improper modeling of the voltage dependence with a single resistance peak, and not the quality of the raw experimental data.

not fully understood, though Kondo-like tunneling process, similar to the ones already described (the model of Appelbaum (1966)), is a probable candidate. It is intuitively clear that a limited number of strongly quantized states would only be available for tunnelling in the barrier region. With the application of external bias V_a, the symmetry of those states changes. For example, if the original states have been superpositions of stationery Bloch waves, the ones after the application of external bias, may be considered to a good approximation superpositions of Wannier functions.

3.3.4 Intrinsic spin anisotropy

At sufficiently high external magnetic field, much larger than the various magnetic anisotropies, the magnetisation vectors of the two ferromagnetic electrodes of a magnetic tunnel junctions, may be considered parallel. As the normally dominant effects related to the angle between the magnetisations of the electrodes are suppressed, more detailed information about the anisotropy of the electronic structure begins to emerge.

A simple procedure for the observation of anisotropies related to the electronic structure may be designed. A resistance (conductance) spectrum can be measured, as a function of the angle between the current direction and the applied strong magnetic field. The large constant background resistance spectrum can then be substracted, and the resulting dataset de-trended. Insufficiently strong magnetic field would allow for substantial angular deviation between the pinned and free layers of the tunnel structure resulting in measurable changes in resistance. An example for field rotation within the plane of the junction, and orthogonal to the current direction, is given on figure 3.34. Only for sufficiently strong field $B \gg B_a$, where B_a is the

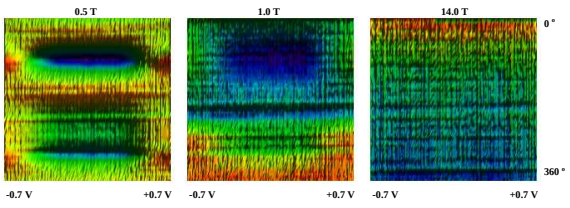

Figure 3.34: Modulation of the differential resistance, upon rotation of applied field of $\mu_0 H = 14$ T, in the plane of the junction, as a function of the applied bias V_a, for a CoFeB/MgO/CoFeB junction, measured at $T = 2$ K.

largest anisotropy field in the system, the two electrodes remain sufficiently parallel (for the above example about 2 T is sufficient to render the micromagnetic effects subject to section 3.3.7 undetectable over the noise and drift floor, or about 0.05%).

Significant effects arise when the external magnetic field is rotated out of the plane of the junction. Example are shown on figures 3.35 and 3.36, for annealed and unannealed CoFeB/MgO/CoFeB junctions, respectively. It is readily noticed, that the resulting func-

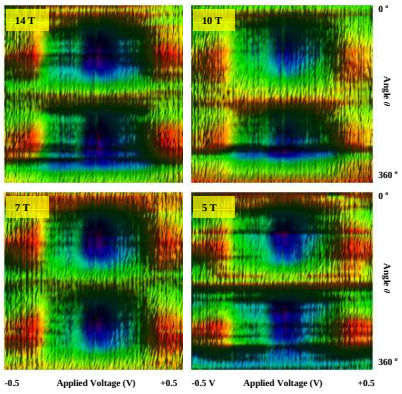

Figure 3.35: Modulation of the differential resistance, upon rotation of applied field of $\mu_0 H = 14$ T, in a plane orthogonal to the plane of the junction, as a function of the applied bias V_a, for an annealed CoFeB/MgO/CoFeB junction, measured at $T = 2$ K. The amplitude of the color-depth is 50 μV or about 0.5%.

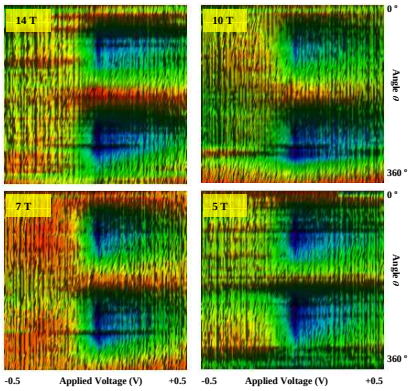

Figure 3.36: Modulation of the differential resistance, upon rotation of applied field of $\mu_0 H = 14$ T, in a plane orthogonal to the plane of the junction, as a function of the applied bias V_a, for an unannealed CoFeB/MgO/CoFeB junction, measured at $T = 2$ K. The amplitude of the color-depth is 25 μV or about 0.25%.

tional dependence may be described in terms of an angle-independent, voltage dependent base function (more generally base functions), and a trivial harmonic angular dependence (generally set of different powers of primitive harmonic functions). For a symmetric junction structure, and a single major axis crystallographic structure (tetragonal, hexagonal), this may be written

as series in the even powers of, say, $\cos\theta$:

$$\frac{\partial R_{\mathrm{j}}}{\partial V_{\mathrm{a}}}(V_{\mathrm{a}}) = A_0^{\mathrm{base}}(V_{\mathrm{a}}) + A_2^{\mathrm{base}}(V_{\mathrm{a}})\cos^2\theta + A_4^{\mathrm{base}}(V_{\mathrm{a}})\cos^4 + \ldots \tag{3.3.15}$$

where θ is the angle between the angle between the current density and field vectors, and R_{j} is the junction resistance. In the simplest case, of a true uniaxial anisotropy of the electronic structure (the Fermi surface being an uniaxial ellipsoid), or the barrier region being highly disordered, the only surviving terms will be:

$$\frac{\partial R_{\mathrm{j}}}{\partial V_{\mathrm{a}}}(V_{\mathrm{a}}) = A_0^{\mathrm{base}}(V_{\mathrm{a}}) + A_2^{\mathrm{base}}(V_{\mathrm{a}})\cos^2\theta \tag{3.3.16}$$

As the background $A_0^{\mathrm{base}}(V_{\mathrm{a}})$ can be readily substracted, the only function that remains to be experimentally determined is $A_2^{\mathrm{base}}(V_{\mathrm{a}})$. Some examples of such determinations are presented on figure 3.37, for unannealed and annealed CoFeB/MgO/CoFeB junctions. It is easily seen,

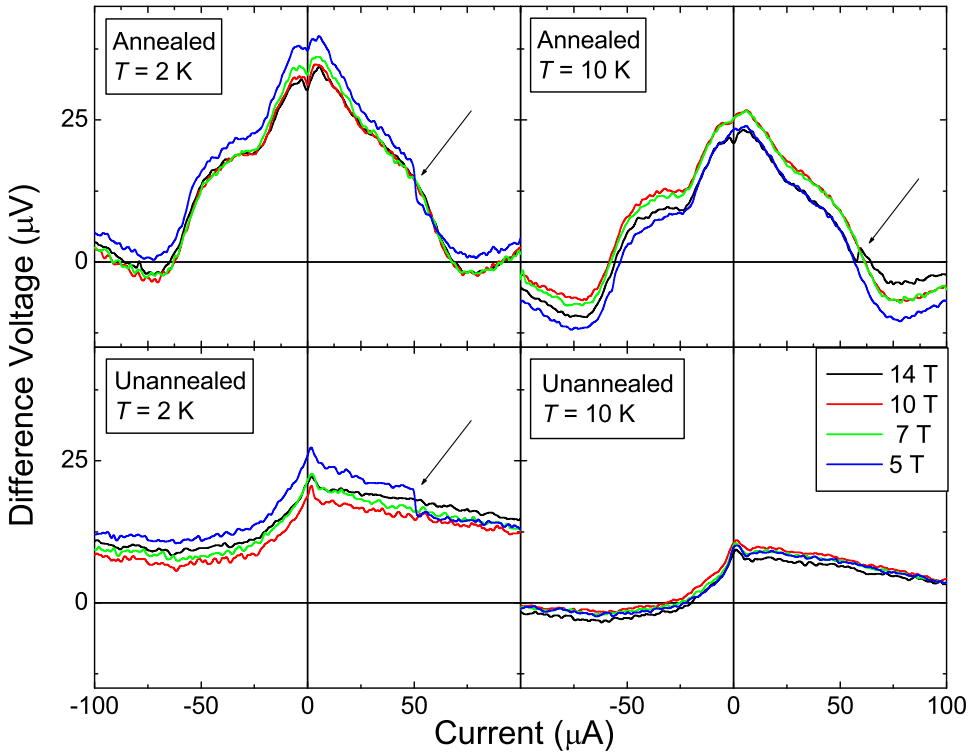

Figure 3.37: Base functions for the current dependence of the modulation of the differential resistance of unannealed and annealed CoFeB/MgO/CoFeB tunnel junctions, at various fields (5,7, 10, 14 T), and temperatures (2, 10 K). The arrows point towards artefacts produced upon sample reloading cycle (the samples have been taken out of the system and then put back).

that the base functions are field independent for large enough fields (in this case more that 3 T,

at 2 K), and temperature independent, except for the thermal smearing, as expected for effects related to the electronic structure of the electrodes.

While the zero-bias amplitude may be related directly to the anisotropy of the Fermi surfaces for spin-up and spin-down electrons, the physical interpretation of the observed structure should be related to the failure of the adiabatic approximation to describe the fine detail in the differential spectra, and the associated appearance of structure due to bands (or band edges) situated below and above the Fermi level. The physical situation bears some resemblance to the observation of structure in the tunnelling spectra of semimetals and semiconductors by Esaki & Stiles (1965, 1966a,b). Though, while in that case, the non-adiabatic tunnelling appears as the dominant component, determining an easy to observe structure in the differential resistance (conductance), in the case of magnetic, metallic tunnel structures, the non-adiabatic corrections are generally small, and have a larger energy scale.

Examples of the interpretation of the base function $A_2^{\mathrm{base}}(V_{\mathrm{a}})$ in terms of the anisotropy of the bands close to the Fermi level are shown on figures 3.38 and 3.39. The fitting is

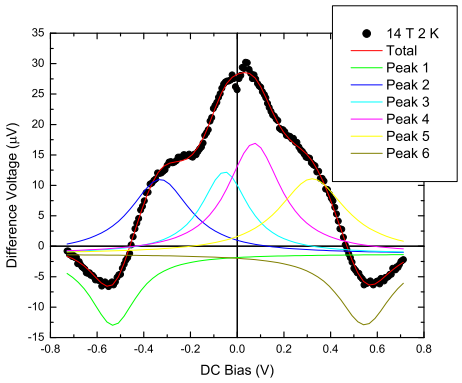

Figure 3.38: Base function for the voltage dependence of the modulation shown on figure 3.35. Best fit is achieved with a set of four Lorentzians of width ≈ 0.35 eV, and approximately equivalent spacings of 0.25 eV.

executed with Lorentzian peaks, instead of the actual single band tunnelling components, for simplicity and ease of convergence. Every peak is interpreted as a band edge of a simple band with a parabolic dispersion and ellipsoidal anisotropy. The position of the peak should, thus, be roughly determined by the position of the band edge with respect to the Fermi level, while its width is related to the width of the band (or to the effective mass in parabolic dispersion approximation). The refined peak parameters are presented in table 3.3.4. It should be noted that the existence of structure in the differential resistance as the one described above, depends critically on both the degree crystallinity and the actual crystal symmetry of the near-barrier

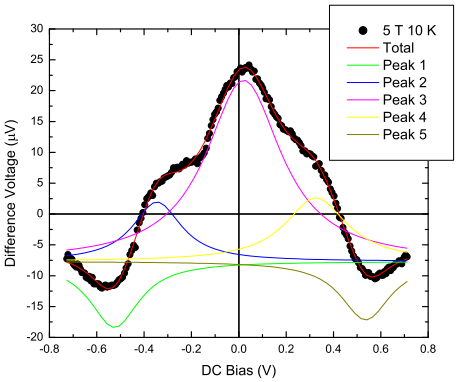

Figure 3.39: Same as figure 3.38, for a temperature of 10 K. The middle two peaks are refined as one, because of the additional thermal broadening, and worse signal to noise ratio.

Peak No.	Position (mV) 2.0 K	Position (mV) 10.0 K	Width (mV)
1	-531(5)	-525(5)	240(20)
2	-330(7)	-250(20)	310(10)
3	-50(10)	-	240(10)
4	+70(10)	-	280(50)
5	+321(9)	+326(7)	350(70)
6	+546(6)	+536(6)	270(30)

Table 3.1: Peak parameters (effective band positions and dispersions) at two different temperatures for an annealed CoFeB/MgO/CoFeB junction.

region, so that amorphous or highly disordered electrodes would not give rise to similar effects. This is illustrated on figure 3.37 and tables 3.3.4 and 3.3.4. It is clearly seen that while the average differential resistivity at zero bias for the unannealed and annealed junction is quite similar, the relative anisotropy is different by at least a factor of two.

3.3.5 Bias dependence of the tunnelling probability

Early experiments on high magnetoresistance ratio, CoFe/Al_2O_3/Co and NiFe based tunnel junctions (see for example Moodera *et al.* (1995)), have demonstrated significant decrease in magnetoresistance ratio with increasing DC bias. The origin of this decrease is to a large extent system dependent and a common treatment is difficult or impossible.

Probably the most conceptually simple way of characterising tunnel barriers, is via their $I-V$ characteristic. There is however relatively little information to be extracted from them. As the low-bias behaviour is generally linear, and the intermediate bias one, includes primarily low-

Field (T)	Average (mV)	Amplitude (mV)	Anisotropy (%)
14	4.992	-0.0120	-0.24
10	4.982	-0.0149	-0.30
7	4.971	-0.0127	-0.26
5	4.948	-0.0135	-0.27

Table 3.2: Anisotropy coefficients of the tunnelling magnetoresistance, at zero bias, for a unannealed CoFeB/MgO/CoFeB junction, extracted from data measured at $T = 2.0$ K

Field (T)	Average (mV)	Amplitude (mV)	Anisotropy (%)
14	5.160	-0.0241	-0.47
10	5.165	-0.0290	-0.56
7	5.163	-0.0263	-0.51
5	5.152	-0.0234	-0.45

Table 3.3: Anisotropy coefficients of the tunnelling magnetoresistance, at zero bias, for a annealed CoFeB/MgO/CoFeB junction, extracted from data measured at $T = 2.0$ K

odd-order non-linear terms, the characteristics are quite generic ans similar between junctions. This is illustrated on figures 3.40 and 3.41, for two very different junctions, one having a single MgO barrier, the other a double one. While, the slightly non-linear quasi-ohmic

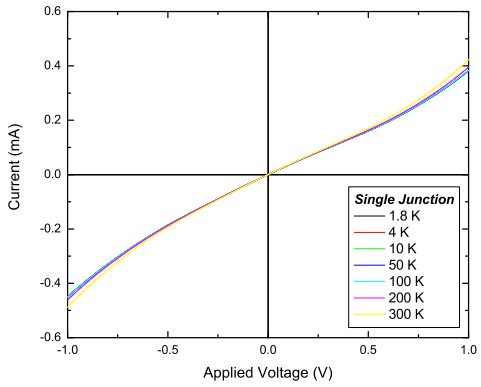

Figure 3.40: $I - V$ characteristics of a CoFeB/MgO/CoFeB single tunnel junction, in the parallel state, at different temperatures.

behaviour cannot be considered an evidence for dominating tunnelling processes, the very weak temperature dependence is a strong evidence, in this respect.

While barrier parameters, like barrier width and height, can be potentially extracted by for example the model of Simmons (1963), the width and height determined, are generally not linearly independent, so normally some junction parameters have to be determined by

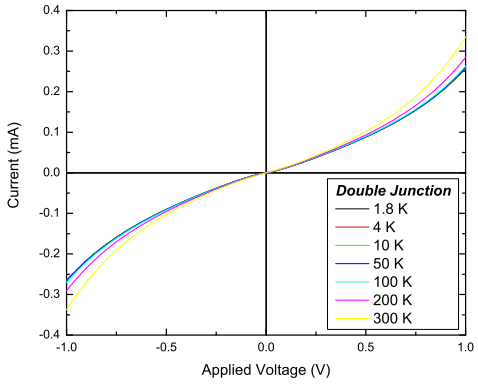

Figure 3.41: $I - V$ characteristics of a CoFeB/MgO/CoFeB double tunnel junction, in the parallel state, at different temperatures.

other methods. One possibility is the use of the logarithmic derivative $\frac{\mathrm{d}}{\mathrm{d}V_\mathrm{a}} \ln\left[\frac{J(V_\mathrm{a})}{V_\mathrm{a}}\right]$, which as argued by Rottländer *et al.* (2002), should produce a positive cusp at about $V_\mathrm{a} \approx 1.2\ \phi_\mathrm{b}$. However, when the barrier height is of the order of 1 eV, or more, it is often difficult to measure the junction $J - V$ characteristic without permanently damaging it (overheating, avalanche breakthrough, etc.). Therefore, the use of this method is quite limited (primarily to thick and low tunnel barriers). An illustration of its inapplicability to high tunnel magnetoresistance CoFeB/MgO/CoFeB junctions is given on figure 3.42.

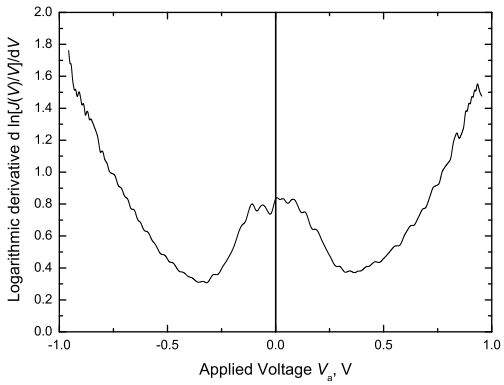

Figure 3.42: Logarithmic derivative in the antiparallel state, for an unannealed CoFeB/MgO/CoFeB junction, measured at $T = 2$ K.

A standard method for more detailed characterisation is the derivative spectroscopy, employing modulation techniques, as described in appendix B.3. In general, it is possible to measure the differential conductance as a function of applied bias, magnetic field (magnitude and orien-

tation) and temperature, among other parameters. In order to isolate the peculiarities related to the bias dependence, alone, two particular cuts in parameter space have primary importance - the voltage dependence of the conductance at low temperature $T \to 0$, for parallel and anti-parallel orientation of the junction electrodes. Out of these experimental dependances, differences and averages can be constructed, in an effort to understand the the factors that govern the magnitude of the magnetoresistance and its bias dependence.

In this respect, couple of examples are given on figures 3.43, 3.45, for unannealed (quasi-amorphous), and on figures 3.44, 3.46, for annealed (oriented polycrystalline) CoFeB junction electrodes.

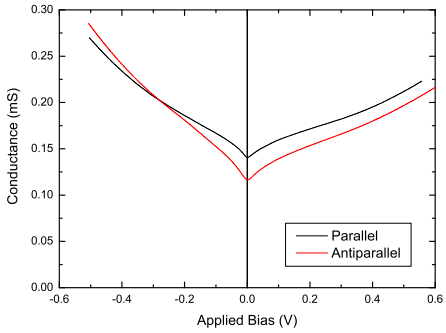

Figure 3.43: Conductance in the parallel, and in the antiparallel state, for an unannealed CoFeB/MgO/CoFeB junction, measured at $T = 2$ K.

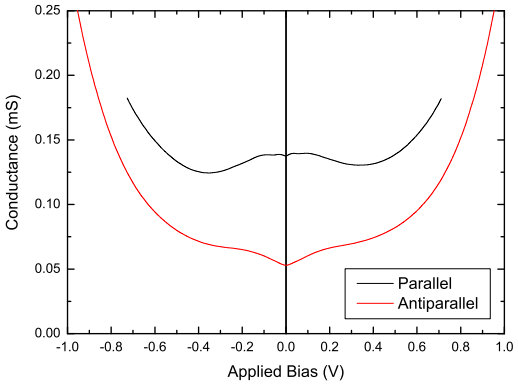

Figure 3.44: Conductance in the parallel, and in the antiparallel state, for an annealed CoFeB/MgO/CoFeB junction, measured at $T = 2$ K.

Major differences are easily noted:

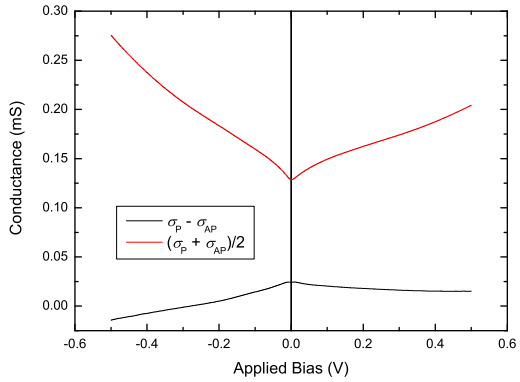

Figure 3.45: The difference in differential conductance between the parallel and the antiparallel state, and the average conductance, for an unannealed CoFeB/MgO/CoFeB junction, measured at $T = 2$ K.

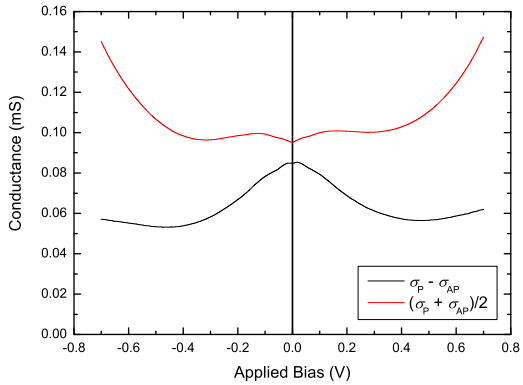

Figure 3.46: The difference in differential conductance between the parallel and the antiparallel state, and the average conductance, for an annealed CoFeB/MgO/CoFeB junction, measured at $T = 2$ K.

1. The zero-bias magneto-conductance ratios are very different, -61.7% for the annealed junction, as compared to -17.4% for the unannealed one. While this could be due to both electronic reasons - i.e. different polarisations close to the Fermi level, or micro-magnetic reasons - i.e. domain structure in the electrodes at small field.

2. The general shape of the average conductances for the parallel and antiparallel cases, and their differences are quite different. While in the unannealed junction, the low-bias conductance is dominated by a cusp-shape feature reminiscent of the localisation model of Altshuler & Aronov (1979), the annealed junction exhibits a smooth difference curve, characteristic of adiabatic tunnelling and the model of Hachaturov (2005a).

The external voltage-induced change in barrier height, generally dominates the intermediate and high bias regions, as shown on figure 3.47.

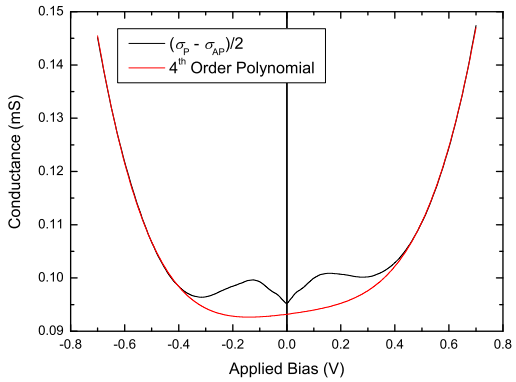

Figure 3.47: The average conductance, for an annealed CoFeB/MgO/CoFeB junction, measured at $T = 2$ K, together with 4^{th} order polynomial fit at high bias.

A deeper insight into the difference between the elastic, and inelastic contributions, to the junction conductance, may be obtained by plotting the difference of the actual conductance average between the parallel and the anti-parallel state and the polynomial fit of figure 3.47.

It is clear that the inelastic processes are most effective in the region of 0.12 eV. This behaviour is generic, and independent of the orientation of the ferromagnetic electrodes (with the exception the different effective barrier height for the parallel and antiparallel cases). The systematic deviation between the experimental average conductance and the 4th order polynomial fit used, in the low bias region, is likely due to inelastic tunnelling processes, as the background conductance, as well as the greater part of the spin-dependent conductance can be understood within the elastic adiabatic scattering approximation[1].

[1] By elastic tunnelling, a dissipation-less process within the barrier region is understood. Of course, this does

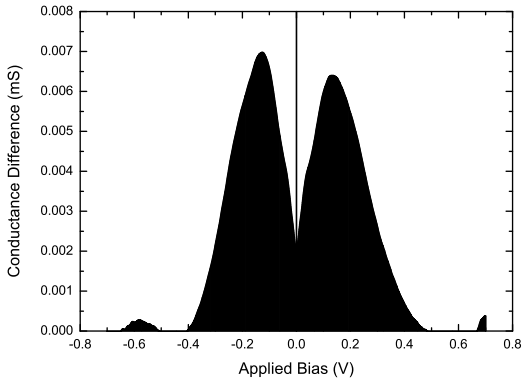

Figure 3.48: The the difference between the actual average conductance and the polynomial fit of figure 3.47, for an annealed CoFeB/MgO/CoFeB junction, measured at $T = 2$ K, revealing the contribution of the inelastic processes within the barrier region.

Reasonable agreement can be demonstrated between experimental voltage dependence of the differential resistance and the localisation model of Altshuler & Aronov (1979) in the low bias region, even without the inclusion of thermal broadening. The agreement is even better when the correct thermal smearing is introduced, as demonstrated on figure 3.49.

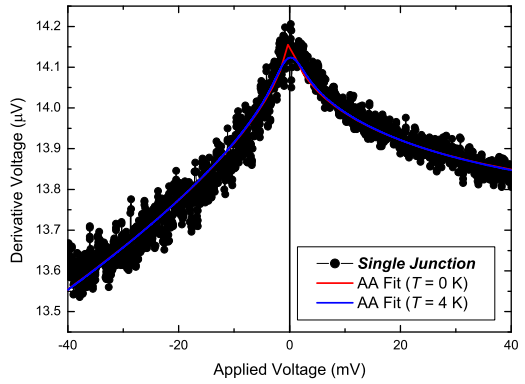

Figure 3.49: Voltage dependence of the differential resistance (the experimental derivative voltage) for a single CoFeB/MgO/CoFeB junction, in the parallel state, together with two fits to the model of Altshuler & Aronov (1979).

not exclude the possibility of inelastic electron scattering, but just limits it appearance to the regions of the electrodes close to the barrier, rather than the barrier, itself.

3.3.6 Effects of finite junction capacitance

The capacitance associated with metal/insulator/metal junctions is often neglected, partially for simplicity, partially as most experimental studies are focused on the low-frequency, quasi-static characteristics of these structures. However at sufficiently high frequency, the contribution of the junction capacitance becomes significant, and limits the magnitude of the junctions response, if the device is used as a sensor. A positive feature of the junction capacitance is the possibility to characterise the quality of the oxide barrier, the existence of electron traps close to the tunnelling interfaces, and the completeness of the oxidation process (if post-deposition oxidation is used), as demonstrated by Huang & Hsu (2004) and Hsu & Huang (2005) for AlO_x based junctions.

Probably the simplest effective model of a metal/insulator/metal tunnel junction is the 'leaky capacitor' model, i.e. a parallel connection of the junction's active differential resistance, and its differential capacitance (see for example McCarthy *et al.* (1999)). The complex impedance Z_j of such a circuit can be written as:

$$\frac{1}{Z_\mathrm{j}} = \frac{1}{R_\mathrm{j}} + i\omega C_\mathrm{j} \tag{3.3.17}$$

where all quantities have differential sense. The effective circuit capacitance, can thus be evaluated as the negated imaginary part of the complex junction impedance:

$$\Re(Z_\mathrm{j}) = R_\mathrm{j}\frac{1}{1+(\omega\tau_\mathrm{j})^2} \tag{3.3.18}$$

$$\Im(Z_\mathrm{j}) = -R_\mathrm{j}\frac{\omega\tau_\mathrm{j}}{1+(\omega\tau_\mathrm{j})^2} \tag{3.3.19}$$

where $\tau_\mathrm{j} = R_\mathrm{j}C_\mathrm{j}$ is the time constant associated with the junction. It is readily seen that in the low-frequency limit $\omega\tau_\mathrm{j} \ll 1$, the impedance is purely real, and the contrary, in the high-frequency $\omega\tau_\mathrm{j} \gg 1$ limit the behaviour is essentially capacitive. In the intermediate region, the impedance is generally complex, and care must be taken in order to avoid systematic errors in fast, high-frequency derivative spectroscopy methods for characterisation of tunnel junctions.

If both the quasi-static and the finite frequency differential impedances are known, then the junction capacitance can be determined as:

$$C_\mathrm{j} = -\frac{\Im(Z_\mathrm{j})}{\Re(Z_\mathrm{j})}\frac{1}{\omega R_\mathrm{j}} \tag{3.3.20}$$

This procedure is illustrated on figure 3.50. It is easily seen that the difference between the zero-bias values of the parallel and anti-parallel electrode configurations is close to the junction capacitance estimated from the parallel planar capacitor model:

$$C_\mathrm{j} = \frac{\epsilon_\mathrm{s} S}{\Delta x} \tag{3.3.21}$$

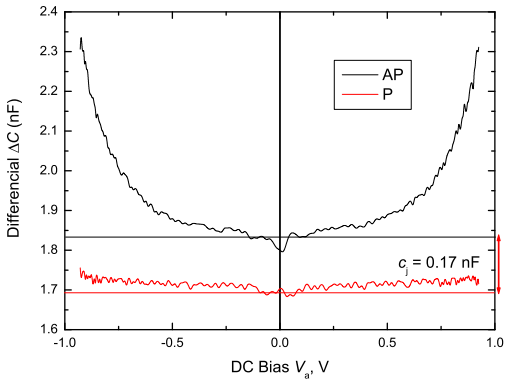

Figure 3.50: Bias dependence of the differential capacitance for a single CoFeB/MgO/CoFeB junction, measured at a frequency of $f = 1.234$ kHz, at a temperature of 2 K, for both the parallel and antiparallel states. Parallel plates capacitance model estimate is shown with an arrow.

Where ϵ_s is the permittivity of the barrier insulator. For an MgO based tunnel junction with $\epsilon_s \approx 9.65\epsilon_0$, $S \approx 45 \times 45$ μm^2 and $\Delta x \approx 12.6$ Å, the capacitance is evaluated at 0.17 nF, which sets a transit frequency[1] for the junction at about 120 MHz, when operated from a 50 Ω driver. Of course, the transit frequency can be increased by reducing the junction area, though, a decrease in barrier thickness, which is required for applications like current-induced magnetisation precession and reversal, as well as, to optimise the tunnel magnetoresistance ratio, will lead to a significant increase in junction capacitance and thus limit the useful frequency region. The bias dependance of the junction capacitance resembles the differential conductance within the WKB approximation. Thus the possibility must be considered, that because of small systematic errors in the measurement of the quasi-static differential resistance and the finite frequency differential resistance, the deduced junction capacitance may include a contribution of the active part of the impedance. This hypothesis is verified on figure 3.51. As the deduced bias dependence of the differential capacitance agrees within the experimental errors with the linearly rescaled differential conductivity of the same junction, it can be concluded that the reactive part of the tunnel diode impedance has a trivial, virtually bias independent behaviour, explained by the effect of the capacitor that the junction represents if the tunnelling current is neglected.

The above treatment can be considered correct, only in the large junction limit. Charging effects in nano-scale structures can play a significant role in determining both the quasi-static

[1]By transit frequency, here is understood the approximate limit over which the impedance of the junction would become essentially capacitive, and tunnel magnetoresistance would be difficult to detect.

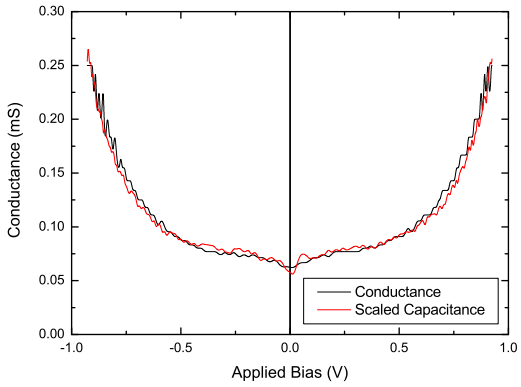

Figure 3.51: Linearly scaled capacitance compared with the junction conductance, for the antiparallel case of figure 3.50.

and high-frequency regimes[1]. In the so-called Coulomb blockade mode - when the charge accumulated on the junction significantly raises the energy required for consecutive tunnelling. Of course, in order for the charging to be effective, it is necessary for the characteristic tunnelling times to be much smaller than the time constants associated with the junction capacitance and the adjoined environmental capacitance. For an example of such treatment see Kauppinen & Pekola (1996).

Moreover, effective diffusive capacitance, associated with tunnelling through disordered metals and semiconductors as described by the model of Altshuler & Aronov (1979), can be set on the same footing as the Coulomb blockade theory of tunnelling through ultrasmall junctions. Similar treatments have been performed by Rollbühler & Grabert (2001) and Reizer (1998) for case of Coulomb blockade tunnelling between disordered conductors, and utilised as an explanation for some zero-bias anomalies.

3.3.7 Micromagnetic effects

While the macroscopic magnetisation behaviour of a complex tunnel junction stack may be quite complex, as the signal is an average over all magnetic layers; the transport may be still quite simple, as only the layers immediately neighbouring the barrier limit the electronic transport.

The direction and magnitude of the exchange bias field B_{eb}, acting on the free layer of the junction, can be investigated by extracting the angular dependence (in the plane of the junction) of say the differential resistance, for various magnitudes of the applied magnetic field, ranging from below to above B_{eb}, at sufficiently low temperatures. An illustration for a CoFeB

[1]For theoretical treatment of the problem for ultra-small capacitance junctions see Devoret *et al.* (1990); Mullen *et al.* (1988) and references thereof.

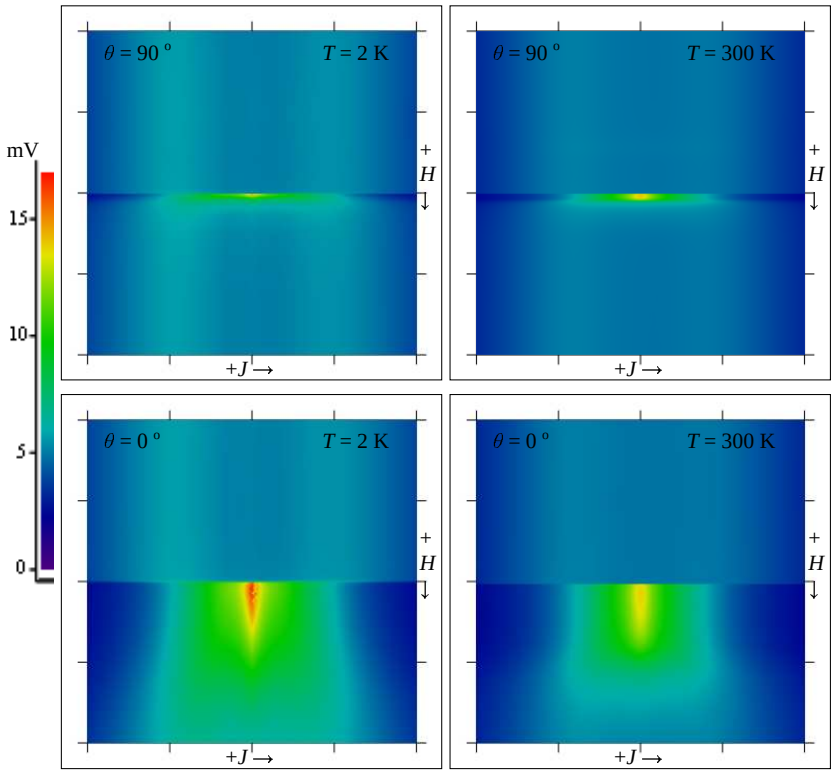

Figure 3.52: Magnetic field and current dependencies of the first derivative of the voltage drop, for an annealed CoFeB/MgO/CoFeB junction, measured at two different temperatures and at two different orientations.

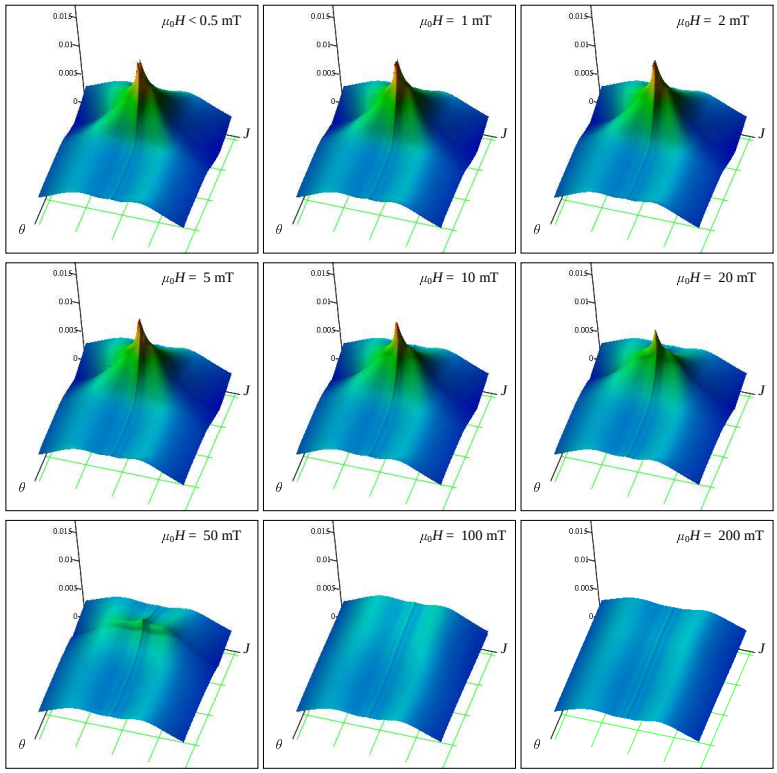

Figure 3.53: Magnetic field orientation in plane and current dependencies of the voltage drop and its first and second derivative with respect to current, for an annealed CoFeB/MgO/CoFeB junction, measured several different field magnitudes. The angle range is $\theta \in [-5\ ^\circ, 365\ ^\circ]$, 90 $^\circ$ per division. The current range is $J \in [-100\ \mu\text{A}, 100\ \mu\text{A}]$, 50 μA per division.

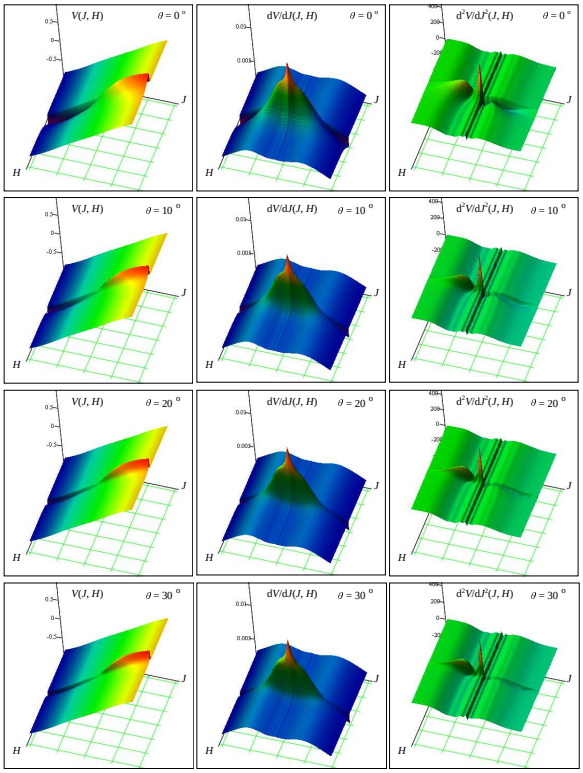

Figure 3.54: Magnetic field and current dependencies of the voltage drop and its first and second derivative with respect to current, for an annealed CoFeB/MgO/CoFeB junction, measured at $T = 2.0$ K at various angles θ between the current and the applied field. The field range is $\mu_0 H \in [-3\text{ T}, 3\text{ T}]$, 1 T per division. The current range is $J \in [-100\ \mu\text{A}, 100\ \mu\text{A}]$, 50 μA per division.

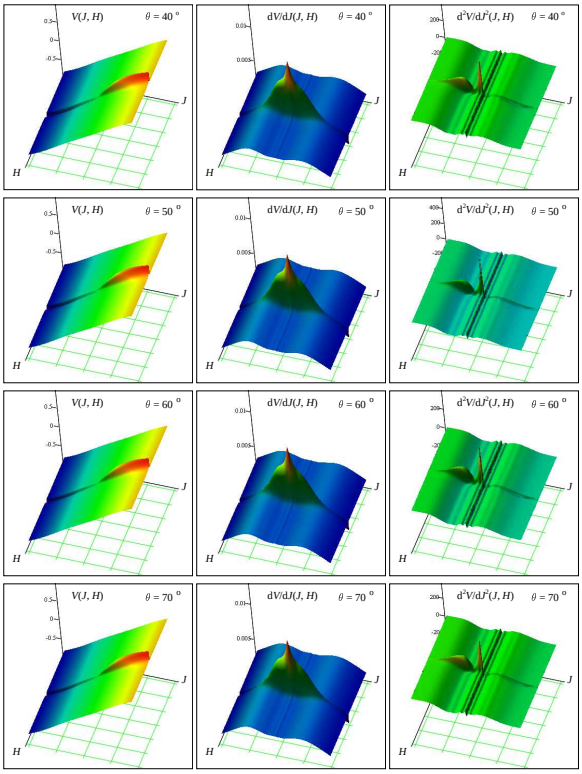

Figure 3.55: Magnetic field and current dependencies of the voltage drop and its first and second derivative with respect to current, for an annealed CoFeB/MgO/CoFeB junction, measured at $T = 2.0$ K at various angles θ between the current and the applied field. The field range is $\mu_0 H \in [-3\text{ T}, 3\text{ T}]$, 1 T per division. The current range is $J \in [-100\ \mu\text{A}, 100\ \mu\text{A}]$, 50 μA per division. Continued from figure 3.54.

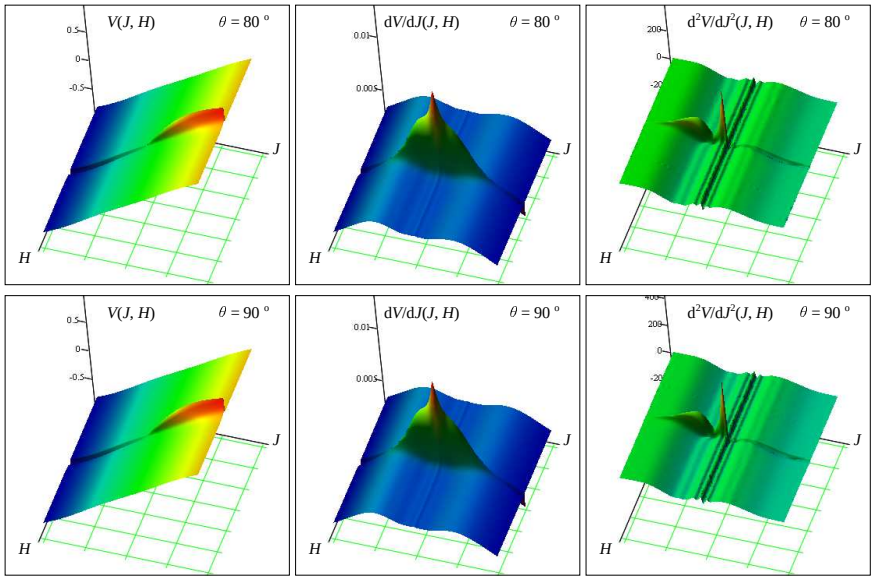

Figure 3.56: Magnetic field and current dependencies of the voltage drop and its first and second derivative with respect to current, for an annealed CoFeB/MgO/CoFeB junction, measured at $T = 2.0$ K at various angles θ between the current and the applied field. The field range is $\mu_0 H \in [-3\text{ T}, 3\text{ T}]$, 1 T per division. The current range is $J \in [-100\ \mu\text{A}, 100\ \mu\text{A}]$, 50 μA per division. Continued from figure 3.55.

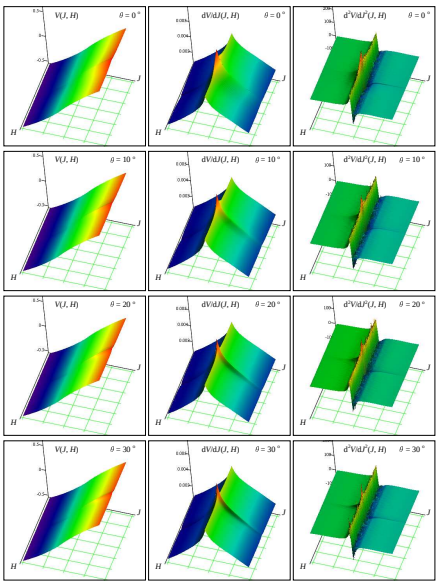

Figure 3.57: Magnetic field and current dependencies of the voltage drop and its first and second derivative with respect to current, for an unannealed CoFeB/MgO/CoFeB junction, measured at $T = 2.0$ K at various angles θ between the current and the applied field. The field range is $\mu_0 H \in [-3\text{ T}, 3\text{ T}]$, 1 T per division. The current range is $J \in [-100\ \mu\text{A}, 100\ \mu\text{A}]$, 50 μA per division.

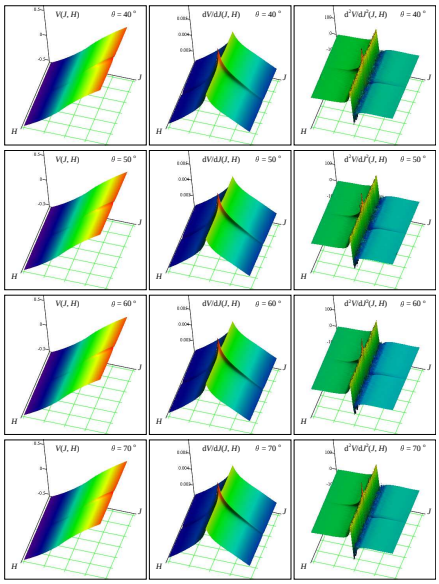

Figure 3.58: Magnetic field and current dependencies of the voltage drop and its first and second derivative with respect to current, for an unannealed CoFeB/MgO/CoFeB junction, measured at $T = 2.0$ K at various angles θ between the current and the applied field. The field range is $\mu_0 H \in [-3\text{ T}, 3\text{ T}]$, 1 T per division. The current range is $J \in [-100\ \mu\text{A}, 100\ \mu\text{A}]$, 50 μA per division. Continued from figure 3.57.

junction, with well developed anisotropy after annealing, is shown on figure 3.61. Apart of the magnitude of $B_{\text{eb}} \approx 25$ mT, acting on the free layer, the plot for the smallest applied field reveals the doubling of the directional anisotropy axis, with the two components, separated by $\Delta\theta \approx 20°$. While the origin of the doubling cannot be ascertained entirely from macroscopic transport measurements, the steps in the mutual orientation of the two electrodes, which are present upon reversal (see for example figure 3.52), are suggestive of at least two separate magnetic domains present within the free layer, at small applied magnetic fields.

In junctions without well-developed anisotropy, or exchange bias, the conductance (resistance) would be symmetric upon a π rotation of the applied magnetic field in a plane orthogonal to the barrier. For a structure with in-plane shape anisotropy, this would lead to maxima of resistance at $\theta = 0, \pi$, symmetric around both 0 and π, with θ being the angle between the current density (orthogonal to the plane of the junction) and the external magnetic field. Such a situation is demonstrated on figure 3.62 for an unannealed CoFeB/MgO/CoFeB tunnel junction. At small enough field, the magnetisation of the hard layer is confined to a particular axis in the plane of the junction. Therefore, as the magnetic field rotates, and the free layer is 'dragged' along with it, the angle between the magnetisations of the two electrodes changes,

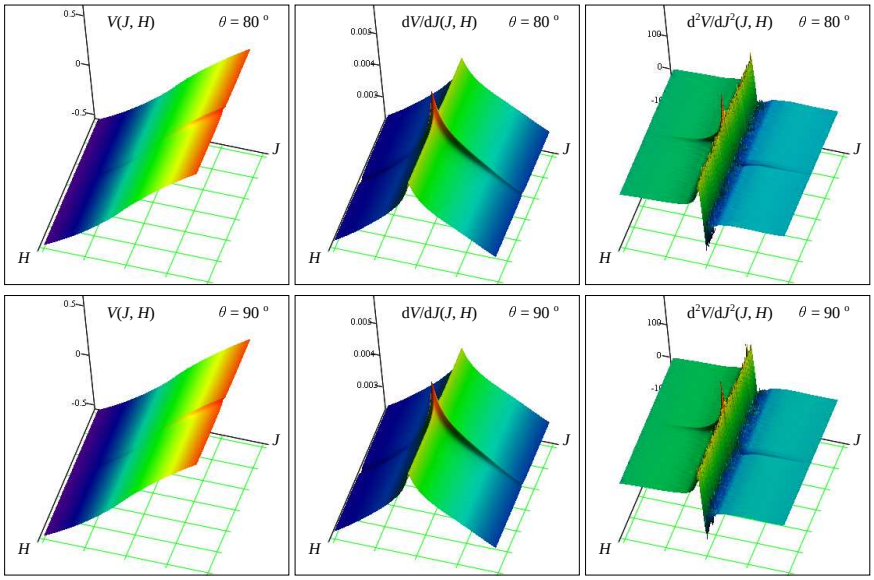

Figure 3.59: Magnetic field and current dependencies of the voltage drop and its first and second derivative with respect to current, for an unannealed CoFeB/MgO/CoFeB junction, measured at $T = 2.0$ K at various angles θ between the current and the applied field. The field range is $\mu_0 H \in [-3\text{ T}, 3\text{ T}]$, 1 T per division. The current range is $J \in [-100\ \mu\text{A}, 100\ \mu\text{A}]$, 50 µA per division. Continued from figure 3.58.

leading to a corresponding change in transport coefficients.

For annealed junctions, with well-developed exchange bias, the hard layer is preferably oriented in a particular direction within the plane of the junction. Therefore the peaks at $\theta = 0, \pi$, are asymmetric, with very fast switching of the magnetisation on one side. This case is visualised on figure 3.63, on the example of an annealed CoFeB based junction.

The situation is similar upon an evolution of the external field along the direction of the exchange bias field for the hard layer of the junction of interest. The switching and rotation scenario, in this case, is shown on figure 3.64. The model assumes uniaxial directional anisotropy (exchange bias) of magnitude H_a. From simple minimisation of the magnetostatic energies involved, and the Malus's law[1] for the current through the junction, the following model dependance may be obtained:

$$R_\text{j} = A_0 + A_1 \cos^2\left(\arctan\frac{H}{H_\text{a}}\right) \tag{3.3.22}$$

which is well verified experimentally. Moreover, the dependence of the extracted exchange bias of the hard layer H_a, has a strong dependence on the angle θ between the applied field direction and the normal to the normal to the junction, which is illustrated on figure 3.65. The

[1] In a direct analogy with the optical transmission through a polariser/analyser pair.

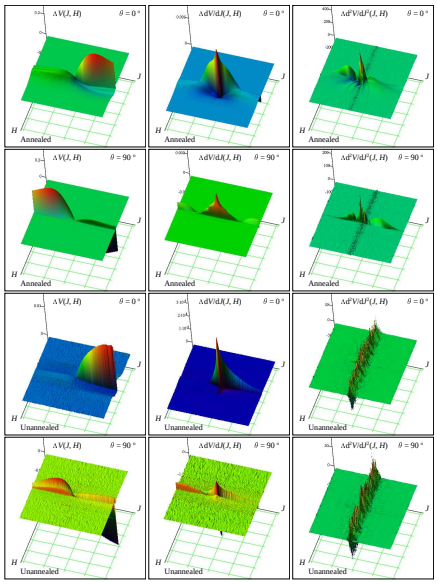

Figure 3.60: Magnetic field and current dependencies of the differences (the hysteretic difference between ramping the external field $+3\ \mathrm{T} \rightarrow -3\ \mathrm{T}$ and $-3\ \mathrm{T} \rightarrow +3\ \mathrm{T}$) between the voltage drop and its first and second derivative with respect to current, for an annealed and unannealed CoFeB/MgO/CoFeB junctions, measured at $T = 2.0$ K at two different angles θ between the current and the applied field. The field range is $\mu_0 H \in [-3\ \mathrm{T}, 3\ \mathrm{T}]$, 1 T per division. The current range is $J \in [-100\ \mu\mathrm{A}, 100\ \mu\mathrm{A}]$, 50 μA per division. Continued from figure 3.60.

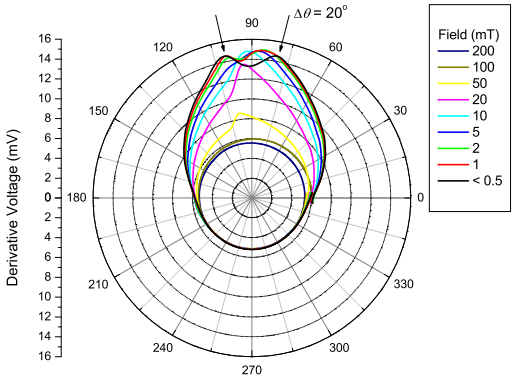

Figure 3.61: Dependence of the zero-bias differential resistivity on the angle of the applied magnetic field θ, in the plane of the junction, for an unannealed CoFeB/MgO/CoFeB junction, measured at 2 K.

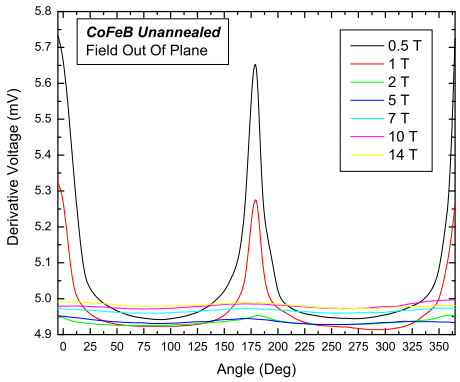

Figure 3.62: Dependence of the zero-bias differential resistivity on the angle of the applied magnetic field, for an unannealed CoFeB/MgO/CoFeB junction, measured at 2 K.

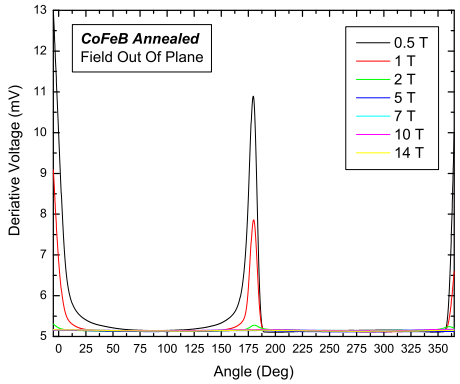

Figure 3.63: Dependence of the zero-bias differential resistivity on the angle of the applied magnetic field, for an annealed CoFeB/MgO/CoFeB junction, measured at 2 K.

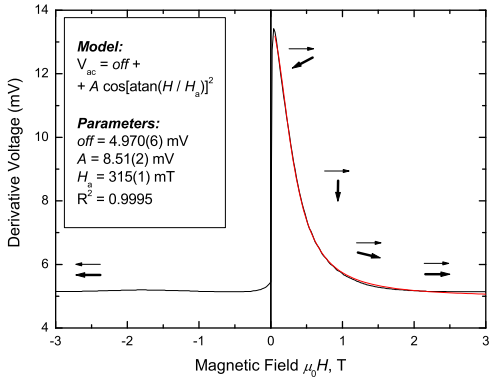

Figure 3.64: Zero-bias differential resistance as a function of applied field for an annealed CoFeB/MgO/CoFeB junction. The model assumes uniaxial directional anisotropy.

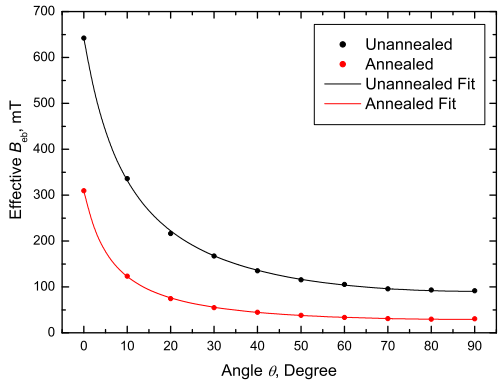

Figure 3.65: Exchange bias parameter H_a extracted from fits as the ones shown on figure 3.64 for an annealed CoFeB/MgO/CoFeB junction. The fits are described in the text.

experimental data is modelled with a generalized version of the dependence expected at $T \to 0$, namely:

$$H_{\rm eb} \sim \frac{1}{\cos\theta}, \quad T \to 0 \tag{3.3.23}$$

$$H_{\rm eb} \sim H_{\rm off} + \frac{H_{\rm amp}}{offset + \cos\theta}, \quad T > 0 \tag{3.3.24}$$

the extracted parameters for unannealed and annealed CoFeB junctions are summarised in table 3.3.7.

Parameter	Unannealed	Annealed
$H_{\rm off}$,mT	-17(4)	-3.4(9)
$H_{\rm amp}$,mT	128(4)	36.4(7)
$offset$	0.194(5)	0.116(2)

Table 3.4: Fitting parameters for the fits visualised figure 3.65.

Apart from the zero-bias differential resistivity, a barrier height evaluated via fitting to the generalized model of Simmons (1969), may be used to characterise the state of the ferromagnetic electrodes, with analogous results, though less dependent on the presence of zero-bias anomaly in the differential characteristics. An example of the results of an automatic procedure for barrier height extraction for unannealed and annealed CoFeB/MgO/CoFeB junctions is given on figure 3.66.

3.3.8 Inelastic transport

The inelastic spectroscopy data of MgO based tunnel junctions has been reported on numerous occasions (Plesiewicz & Adler (1986), Kirley & Hansma (1975)). The different bias regions have

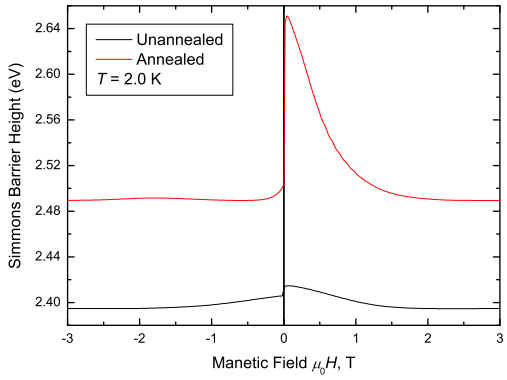

Figure 3.66: Barrier height extracted with an automatic evaluation and fitting procedure employing the model of Simmons (1969) at each field value, for unannealed and annealed CoFeB/MgO/CoFeB tunnel junctions, measured at $T = 2.0$ K, with magnetic field applied parallel to the current direction.

been ascribed to various inelastic excitations (Klein *et al.* (1973)):

1. The low-bias region, approximately $(0 - 50$ meV), is usually dominated by phonons of the electrodes lattices, reaching the barrier region. The actual energies of the observed peaks, of course, vary largely with the metal or alloy used. As an example, phonons at 150 meV, and magnons 50 meV, have been reported by Nagahama *et al.* (2003) in junctions with Fe electrodes. Magnons at 9 meV and bandwidth of 90 meV have been resolved in CoFeB based tunnel junctions by Miao *et al.* (2006). A lower cut-off of 8-9 meVhas been documented for CoMnSi magnons by Schmalhorst *et al.* (2005).

2. The intermediate bias region, approximately $(0-100$ meV), includes the phonon spectrum of the barrier lattice. For the MgO lattice, four phonon peaks have isolated - 38, 54, 66 and 82 meV. Out of which, the ones at 54 and 82 meV are more prominent and often resolvable. Similar energies are observed for MnO optical phonons, 33 meVand 61 meVby Schmalhorst *et al.* (2005).

   In ferromagnetic or antiferromagnetic insulating barriers, complex excitations may occur. For example, multiple magnons have been observed in NiO based tunnel junctions by Tsui *et al.* (1971), as well as, MnO magnons at 25 meVby Schmalhorst *et al.* (2005).

3. The high-bias region, approximately $>$ 100meV, is occupied primarily by vibrational modes of molecular impurities, the most common of which are: 310, 370 and 447 meV, corresponding to the incorporation of H_2O and derivatives; 370, 353 and 338 meV, associated with the incorporation of hydrocarbons, 190, 170, 130 and 116 meV various

carbon-containing radicals; and 453 and 459 meV, associated with the formation of surface $Mg(OH)_x$.

High energy surface magnons have been claimed to have bandwidth (sic) of about 600 meV in CoFeB/MgO/CoFeB tunnel junctions (see for example Slonczewski & Sun (2007)).

The processing of large amounts of derivative-spectroscopy data is a laborious task, which can be automated, by for example, employing gradient based peak detection algorithms or box-scan search algorithms. Examples of low-temperature, second differential resistance profiles, for an annealed CoFeB/MgO/CoFeB junction are presented on figures 3.67 and 3.68, for antiparallel and parallel orientation of the ferromagnetic electrodes, respectively; together with the automatically extracted extrema (both minima and maxima). Spectroscopic structure

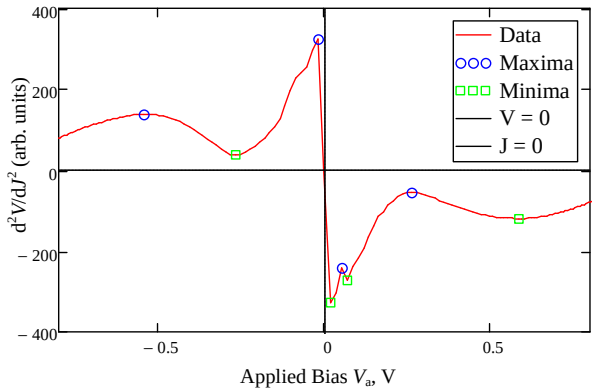

Figure 3.67: Second differential resistance profile for an annealed CoFeB/MgO/CoFeB tunnel junction, measured at $T = 2.0$ K, in the antiparallel state, with the automatically detected extrema marked.

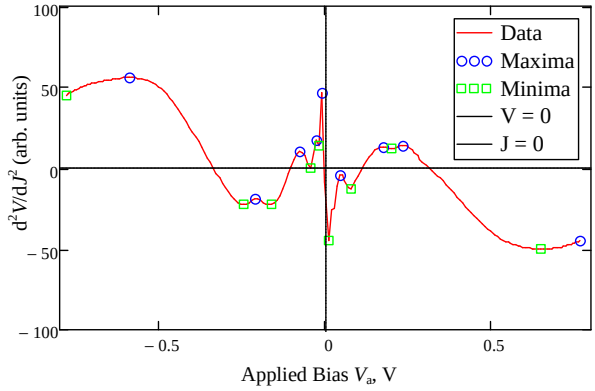

Figure 3.68: Second differential resistance profile for an annealed CoFeB/MgO/CoFeB tunnel junction, measured at $T = 2.0$ K, in the parallel state, with the automatically detected extrema marked.

is more readily resolvable on top of the relatively featureless elastic background profile in the parallel case, however at least three different features are resolvable in both cases. A summary of all automatically extracted positions of extrema in the second derivative are given in tables 3.3.8 and 3.3.8.

Position (V) Maxima	Magnitude Arb. Units	Position (V) Minima	Magnitude Arb. Units
-0.542	+139.5	-0.950⋆	+34.1
-0.018	+325.4	-0.267	+37.0
+0.053	-241.9	+0.018	-327.7
+0.263	-54.8	+0.070	-272.5
+0.947⋆	-36.4	+0.584	-119.3

Table 3.5: Peak parameters of the maxima of second derivative profile (by automated extraction) for an annealed CoFeB/MgO/CoFeB junction in the antiparallel state, measured at $T = 2.0$ K. The positions denoted by ⋆ correspond to the boundaries of the dataset.

Position (V) Maxima	Magnitude Arb. Units	Position (V) Minima	Magnitude Arb. Units
-0.583	+43.4	-0.731⋆	+40.8
-0.209	-20.8	-0.248	-23.0
-0.066	+3.4	-0.163	-23.8
-0.007	+24.6	-0.044	-6.6
+0.044	+4.5	+0.007	-32.1
+0.161	+15.6	+0.073	-4.1
+0.213	+15.5	+0.191	+15.2
+0.715⋆	-39.9	+0.670	-40.5

Table 3.6: Peak parameters of the maxima of second derivative profile (by automated extraction) for an annealed CoFeB/MgO/CoFeB junction in the parallel state, measured at $T = 2.0$ K. The positions denoted by ⋆ correspond to the boundaries of the dataset.

The positions of the extrema in the second derivatives can be tracked as a function of applied magnetic field, in order to look for any influence of the reorientation of the magnetisation directions of the electrodes on the excitations present in the tunnel junction (both phonons and magnons). Examples of such a procedure are shown on figures 3.69 and 3.70, with the current through the junction as the extracted parameter.

It is clear, however that such data may be strongly influenced by the large changes in voltage drop across the barrier, upon magnetic reorientation. Therefore, it may appear useful to recast

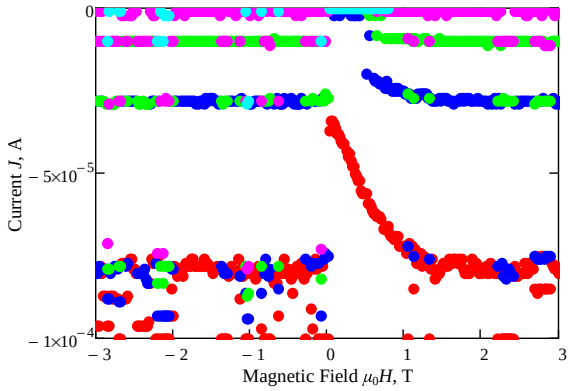

Figure 3.69: Maxima detected second differential resistance with respect to current for an annealed CoFeB/MgO/CoFeB tunnel junction, measured at $T = 2.0$ K, with the magnetic field applied perpendicular to the plane of the junction.

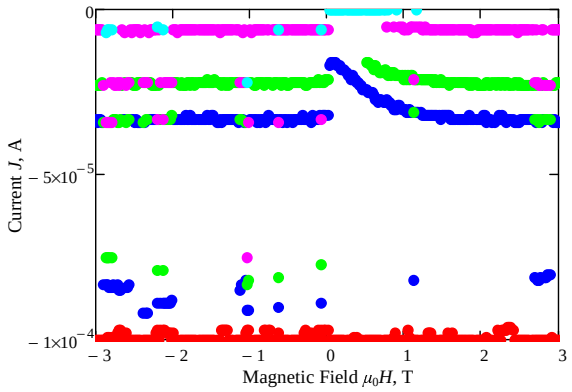

Figure 3.70: Minima detected second differential resistance with respect to current for an annealed CoFeB/MgO/CoFeB tunnel junction, measured at $T = 2.0$ K, with the magnetic field applied perpendicular to the plane of the junction.

the same datasets in terms of the voltage developed across the tunnel junction structure, as demonstrated on figures 3.71 and 3.72.

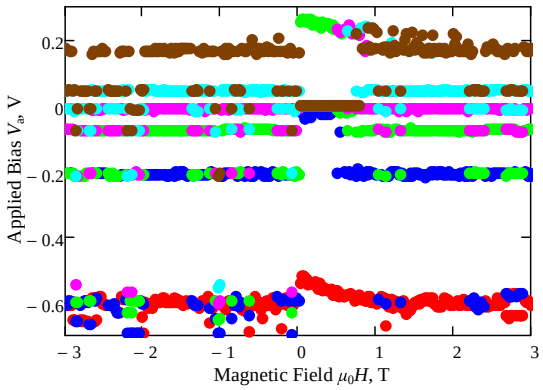

Figure 3.71: Maxima detected second differential resistance with respect to the applied voltage V_a, for an annealed CoFeB/MgO/CoFeB tunnel junction, measured at $T = 2.0$ K, with the magnetic field applied perpendicular to the plane of the junction.

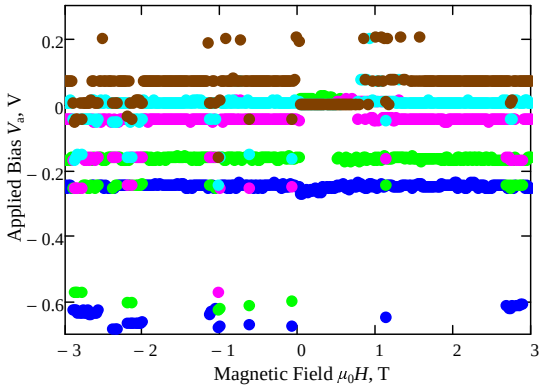

Figure 3.72: Minima detected second differential resistance with respect to the applied voltage V_a for an annealed CoFeB/MgO/CoFeB tunnel junction, measured at $T = 2.0$ K, with the magnetic field applied perpendicular to the plane of the junction.

As expected this resolves the problem to some extent, though, as well known, the lead-in series resistance voltage drop can yield non-negligible contribution to the voltage applied to the tunnel structure as a whole. The four wire technique just eliminates the series resistance of the macroscopic cabling. Complete elimination of the series resistance, is however possible only in junctions with superconducting electrodes, due to the intrinsic two-terminal nature of the tunnelling diodes. Thus a unambiguous assignment of the peaks observed in the derivative spectra to either phonons or magnons can only be done on specially prepared structures.

In conclusion, various aspects of the tunnelling processes in magnetic tunnel junctions (both elastic and inelastic) have been analysed. For most junctions adiabatic tunnelling approximations is a satisfactory assumption as evidenced experimentally. A detailed experimental investigation on the temperature, field, and orientation of the tunnelling conductance in junctions with various degrees of crystallinity of the electrodes has been carried out. All observable features of the obtained datasets have been classified and quantified. Further improvement in performance of the magnetic tunnel junction family described would require both optimisation of the micromagnetic behaviour of the electrodes, as well as the crystal structure of both the electrodes and the barrier. A further reduction in barrier thickness is highly desirable, though experimentally very challenging to obtain with sufficient, for practical applications, degree of reproducibility.

Chapter 4

Magnetic detection of spin injection

4.1 Historic remarks on spin injection

Historically, nuclear polarisation (electronic polarisation has been also alluded to) has been first suggested to be induced by hot electron currents by Feher (1959). Subsequently, experimental evidence (via FID-NMR[1]) has been obtained for spin injection from a non-magnetic metal into semiconductor with a different g-factor by Clark & Feher (1963) and corroborated theoretically by Johnson (2000); Weger (1963); Zvezdin (1966, 1967). The interest in current-induced dynamic nuclear polarisation has been recently rekindled by Hoch *et al.* (2005).

Another technique of choice (CESR[2]) has been developed into an instrument for the estimation of the relaxation times and lengths in metals and semiconductors by Chazalviel (1975). Theoretical analysis of the spin injection and diffusion process in metals and semiconductors has been performed by Aronov (1976), Aronov & Pikus (1976) and Aronov & Linda-Geller (1989). The subject has been reopened by a series of experimental attempts (electrical detection using SQUID picovoltmeters) and theoretical works on the injection and detection of spin polarisation in metals (Johnson (1993); Johnson & Byers (2003); Johnson & Silsbee (1985, 1987, 1988a,b, 1989)).

More modern experimental techniques for the observation of spin-injection usually involve micro or nano-scale patterning. Extraordinary Hall effect has been used as the detecting effect by Otani *et al.* (2000). Spin valves have also been employed in a non-local geometry, on a number of occasions (see for example Godfrey & Johnson (2006); Jedema *et al.* (2003); Kimura

[1] Free Induction Decay Nuclear Magnetic Resonance
[2] Conduction Electron Spin Resonance

et al. (2005, 2006); Urech *et al.* (2006)). Superconductor-normal metal junctions have also been used in non-local magnetoresistance experiments (Urech *et al.* (2004)).

4.2 Drift-diffusion approximation

One of the most common approximations used to simplify the problem for the spin-polarised current kinetics is drift-diffusion. In analogy with the conventional (non-spin-polarised) drift diffusion model:

$$\frac{\partial}{\partial t}\rho = \mathrm{div}\mathbf{j} \tag{4.2.1}$$

$$\mathbf{j} = \hat{\boldsymbol{\sigma}}\mathbf{E} + \hat{\mathbf{D}}\nabla\rho \tag{4.2.2}$$

$$\mathrm{div}(\hat{\boldsymbol{\epsilon}}\mathbf{E}) = \frac{\rho}{\epsilon_0} \tag{4.2.3}$$

where ρ is the charge density, $\hat{\boldsymbol{\sigma}}$ is the conductivity tensor, $\hat{\boldsymbol{\epsilon}}$ is the permittivity tensor and $\hat{\mathbf{D}}$ is the diffusivity tensor; what is often referred to as the two-component model may be written down as:

$$q\frac{\partial n_{\uparrow(\downarrow)}}{\partial t} = \mathrm{div}\mathbf{j}_{\uparrow(\downarrow)} + \frac{q}{2\tau_{\mathrm{sf}}}\left(n_{\downarrow(\uparrow)} - n_{\uparrow(\downarrow)}\right) + S_{\uparrow(\downarrow)}(\mathbf{r},t) \tag{4.2.4}$$

$$\mathbf{j}_{\uparrow(\downarrow)} = \hat{\boldsymbol{\sigma}}_{\uparrow(\downarrow)}\mathbf{E} + q\hat{\mathbf{D}}_{\uparrow(\downarrow)}\nabla n_{\uparrow(\downarrow)} \tag{4.2.5}$$

$$\mathrm{div}(\hat{\boldsymbol{\sigma}}\mathbf{E}) = \frac{q}{\epsilon_0}(n_0 - n) \tag{4.2.6}$$

$$n = n_\uparrow + n_\downarrow \tag{4.2.7}$$

$$P = n_\uparrow - n_\downarrow \tag{4.2.8}$$

where τ_{sf} is the characteristic spin-flip time, S is a spin source term, n_0 is the equilibrium carrier concentration and P is the electronic polarisation.

It is possible to solve the system 4.2.4, and obtain a dynamic equation for the electronic polarisation P, of the form[1]:

$$q\frac{\partial P}{\partial t} = \hat{\mathbf{D}}\Delta P + \hat{\boldsymbol{\mu}}(\mathbf{E}\nabla P + \nabla\mathbf{E}P) - \frac{P}{\tau_{\mathrm{sf}}} + F(\mathbf{r},t) \tag{4.2.9}$$

with the source term F being defined as

$$F(\mathbf{r},t) = \frac{1}{q}\left[S_\uparrow(\mathbf{r},t) - S_\downarrow(\mathbf{r},t)\right] \tag{4.2.10}$$

so that in a general form the partial differential equation:

$$\frac{\partial P}{\partial t} + \hat{\mathbf{D}}\Delta P + \hat{\mathbf{A}}\nabla P + \hat{C}P = 0 \tag{4.2.11}$$

[1] $\Delta = \nabla^2$

together with the appropriate boundary conditions for the polarisation P and its derivatives, governs the dynamics of the spin population, quantized along a particular z-axis direction, and within the drift-diffusion approximation. Several effects are taken into account by the corresponding terms in equation 4.2.9. These are: diffusion term, which tries to smooth the differences in polarisation between the different spatial regions; drift terms, which cause a directional propagation of the polarisation in the presence of either polarisation gradients of electric field gradients, a spin-flip term which causes an exponential decay of the polarisation at a characteristic time-scale set by τ_{sf}, if no sources are present in the system; and a source term within the region of interest (and/or) boundary conditions for the polarisation.

A more general formalism has also been suggested (see for example Johnson & Byers (2003); Johnson & Silsbee (1987)) that combines the drift terms for the charge current j_q, heat current j_Q and magnetisation current j_M, into a single tensor notation as:

$$\begin{bmatrix} j_q \\ j_Q \\ j_M \end{bmatrix} = -\sigma \begin{bmatrix} 1 & \frac{\alpha'' k^2 T}{q E_{\mathrm{F}}} & \alpha^{\mathrm{c}} \frac{\mu_{\mathrm{B}}}{q} \\ \frac{\alpha'' k^2 T}{q E_{\mathrm{F}}} & \alpha' \frac{k^2 T}{q^2} & \beta'' \frac{\mu_{\mathrm{B}}}{E_{\mathrm{F}}} \left(\frac{kT}{q}\right)^2 \\ \alpha^{\mathrm{c}} \frac{\mu_{\mathrm{B}}}{q} & \beta'' \frac{\mu_{\mathrm{B}}}{E_{\mathrm{F}}} \left(\frac{kT}{q}\right)^2 & \beta' \frac{\mu_{\mathrm{B}}^2}{q^2} \end{bmatrix} \begin{bmatrix} \nabla V \\ \nabla T \\ \nabla(-H^\star) \end{bmatrix} \tag{4.2.12}$$

where α', α'', β' and β'' are coefficients, which can be treated as phenomenological parameters, and $H^\star$ is the magnetisation potential $-\frac{M}{\chi} + \frac{B}{\mu_0}$. Though relatively simple and convenient, this notation has found little popularity.

In one dimension, say along the z-axis, equation 4.2.9 may be simplified to (see Aronov (1976)):

$$D(E)\frac{\partial^2 P(E)}{\partial z^2} - \frac{P(E)}{\tau_{\mathrm{sf}}} = 0 \tag{4.2.13}$$

where only diffusion and spin-flip are taken into account and the drift terms have been neglected, because of their smallness ($\frac{q\mathcal{E}\lambda_{\mathrm{sf}}}{E_{\mathrm{F}}} \ll 1$ for a paramagnetic material, where $\mathcal{E} is the electric field$). The problem for the spin-injection from a ferromagnetic metal into a paramagnetic one, separated by an interface situated at $z = 0$, can thus be solved in terms of equation 4.2.13 and the boundary condition at the ferromagnet-paramagnet interface (the condition at infinity is trivial $P(z) = 0$):

$$D(E)\left.\frac{\partial P(E)}{\partial z}\right|_{z=0} = -\frac{\alpha^{\mathrm{c}}}{q}\frac{1}{3}q\mathcal{E}l(E)v\left(\frac{\partial n}{\partial E}\right) = \frac{\alpha^{\mathrm{c}}}{q}J(E) \tag{4.2.14}$$

where l is the is the mean free path of the electrons. The solution of equation 4.2.13 with the boundary condition 4.2.14 has the form:

$$P(E) = -\alpha^{\mathrm{c}}\mathcal{E}\lambda_{\mathrm{sd}}(E)\frac{\partial n}{\partial E}\mathrm{e}^{-\frac{z}{\lambda_{\mathrm{sd}}(E)}} \tag{4.2.15}$$

where $\lambda_{\rm sd}(E) = \sqrt{D(E)\tau_{\rm sf}}$ is the spin-diffusion length. It should be noted that average induced polarisation is small:

$$P = \frac{\langle P(E)\rangle}{N} \sim \alpha^{\rm c}\frac{q\mathcal{E}\lambda_{\rm sd}}{E_{\rm F}} \ll 1 \tag{4.2.16}$$

Nevertheless, the induced electron magnetisation can be comparable to the paramagnetic magnetisation created by relatively moderate static magnetic fields:

$$M = g^\star\mu_{\rm B}\left.\frac{\partial N}{\partial E}\right|_{E=E_{\rm F}}(g^\star\mu_{\rm B}B + \alpha^{\rm c}q\mathcal{E}\lambda_{\rm sd}) \tag{4.2.17}$$

or in other words the energy splitting between the spin-up and spin-down chemical potentials is of the order of $E_{F\uparrow} - E_{F\downarrow} \sim \alpha^{\rm c}q\mathcal{E}\lambda_{\rm sd}$. Therefore away from the injection point $\delta\eta = \eta_\uparrow - \eta_\downarrow$ behaves as (see Urech *et al.* (2004)):

$$\delta\eta = q\alpha^{\rm c}\lambda_{\rm sd}\frac{j}{\sigma}\exp\left(-\frac{z}{\lambda_{\rm sd}}\right) \tag{4.2.18}$$

Often the magnitude of the magnetisation current is further diminished by a coefficient taking into account the spin-flip events at the injection interface, so that $\alpha^{\rm c}$ becomes a truly phenomenological factor (Johnson & Silsbee (1985, 1987)).

It has been argued by Aronov (1976) that the above spin injection effect should be readily observable in light metals (exhibiting small spin-orbit scattering), like Al (for which the spin diffusion length has been estimated at $\lambda_{\rm sd} \sim 1$ cm), by employing either CESR or NMR techniques.

4.3 Spin Temperature

In cases where there are several semi-independent subsystems of quasiparticles which are in thermodynamic equilibrium (or close to one) within the individual subsystems; it is often useful to introduce the concept of effective temperature. An example, originally envisaged by Feher (1959) may be a two-component electronic system - mobile electrons carrying spin s and quasi-bound electrons carrying spin S. Then the spin temperatures of the two sub-systems T_s and T_S can be defined (assuming Boltzmann statistics) as:

$$\frac{n_\uparrow}{n_\downarrow} = \exp\left(\frac{g_s^\star\mu_{\rm B}B}{kT_s}\right) \approxeq 1 + \frac{g_s^\star\mu_{\rm B}B}{kT_s} \tag{4.3.1}$$

$$\frac{N_\uparrow}{N_\downarrow} = \exp\left(\frac{g_S^\star\mu_{\rm B}B}{kT_S}\right) \approxeq 1 + \frac{g_S^\star\mu_{\rm B}B}{kT_S} \tag{4.3.2}$$

where $n_\updownarrow$ and $N_\updownarrow$ are the densities of spin-up and down components for the mobile and localised quasiparticles and $g_s^\star$ and $g_S^\star$ are the respective g-factors.

If there is a third system (non-spin-polarised reservoir), situated at a temperature T, the role of which may be served by say the lattice of the crystal, and both spin subsystems are coupled to the reservoir, then for reasons of conservation of angular momentum for the entire system (mobile spins, localised spins and lattice), transitions may only be possible if two simultaneous spin flips occur. If the corresponding transition probabilities are denoted as $W(\updownarrow\updownarrow \leftrightarrow \updownarrow\updownarrow)$, then:

$$n_\uparrow N_\downarrow W(\uparrow\downarrow \leftrightarrows \downarrow\uparrow) = n_\downarrow N_\uparrow W(\downarrow\uparrow \leftrightarrows \uparrow\downarrow) \tag{4.3.3}$$

and in thermal equilibrium between the mobile and localised spins, the Boltzmann rule gives:

$$\frac{W(\uparrow\downarrow \leftrightarrows \downarrow\uparrow)}{W(\downarrow\uparrow \leftrightarrows \uparrow\downarrow)} = \exp\left[\frac{(g_s^\star - g_S^\star)\,\mu_\mathrm{B} B}{kT}\right] \approxeq 1 + \frac{g_s^\star \mu_\mathrm{B} B}{kT} - \frac{g_S^\star \mu_\mathrm{B} B}{kT} \tag{4.3.4}$$

Using the above condition together with equations 4.3.1, is easily shown that the following relationship between the different temperatures in the problem is valid to first order (so that $\frac{g_s^\star g_S^\star \mu_\mathrm{B}^2 B^2}{k^2 T_s T_S} \ll 1$):

$$\frac{1}{T_S} = \frac{g_s^\star}{g_S^\star}\left(\frac{1}{T} - \frac{1}{T_s}\right) + \frac{1}{T} \tag{4.3.5}$$

Therefore it is possible to obtain both positive and negative contributions to the temperature of the localised spins (in other words depolarise or polarise the localised subsystem), if the mobile electrons are either 'hot' ($T_s > T$) or 'cold' ($T_s < T$) with respect to the reservoir. Hot electronic current is thus expected to depolarise (*adiabatically* in thermodynamic terms) the localised electrons. The above argumentation is illustrative only. A complete treatment of the problem can be obtained as a two-electron-model translation of the derivations of the nuclear case by Weger (1963) or the one by Zvezdin (1966, 1967).

Contrary to the general expectation that hot electrons are difficult to produce in metals (in view of the short electron-phonon relaxation times) it is possible for relatively moderate current densities ($\lesssim 10^6$ A/m^2) in thin films ($\lesssim 1$ μm), which are in good thermal contact with a substrate cooled to He temperatures, to sustain a non-equilibrium population for virtually indefinite time durations (see Shklovskij (1980); Wellstood *et al.* (1994)).

The influence of hot electron generation on the magnetic susceptibility of degenerate semiconductors and metals (more generally in nonadiabatic Fermi liquids) has also been of considerable theoretical interest, in view of the possibilities to use the magnetic susceptibility as a measure of the effective temperature of the electronic system (Grimaldi & Pietronero (1999); Pal (1974); Pal & Sharma (1974)).

4.4 Experiments on the direct magnetic detection of spin injection

In an attempt to measure directly the magnetic field created by the spin polarisation injected into polycrystalline aluminium from Fe, Co, Ni and Zn injection electrodes, an experiment is envisaged taking advantage of samples with a geometry optimized with respect to a particular SQUID based second-order gradiometer. A schematic diagram of the experiment is shown on figure 4.1. The idea is based on the understanding of the pick-up and spatial resolution of the magnetometer used[1], as described in appendix C.3.

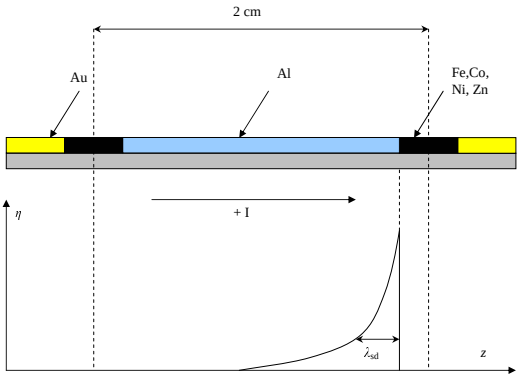

Figure 4.1: Schematic representation of the experimental setup used for magnetic detection of diffused spin polarisation.

Details on the sample preparation and measurement procedures are given in appendix C.1. Two different sample types are used - Sample 1 (on borosilicate glass) and Sample 2 (on fused quartz), the second one of which has a much improved geometrical characteristics. The geometry chosen permits the suppression of the magnetic signal associated with the ferromagnetic injection electrodes by a factor of about 60, at the centre of the Al strip, as evidenced on figure 4.2.

The magnetisation distributions that may be envisaged for current densities of 10^8 A/m^2, magnetic field $\mu_0 H \sim 0.5$ T, $T \sim 1$ K and $\lambda_{sd} \sim 1$ cm, is visualised on figure 4.3. Spin injection serves to spatially anti-symmetrise the magnetisation distribution, and it is this effect that serves the purpose for detection. The calculated response (which is the magnetisation distribution $M(z)$ convoluted with the point-spread function of the gradiometer assembly) is shown on figure 4.4, together with the partial response expected, due to the paramagnetism (the sign is assumed positive for just for illustrative purposes) of the substrate, and one should

[1] Quantum Design MPMS 5 XL

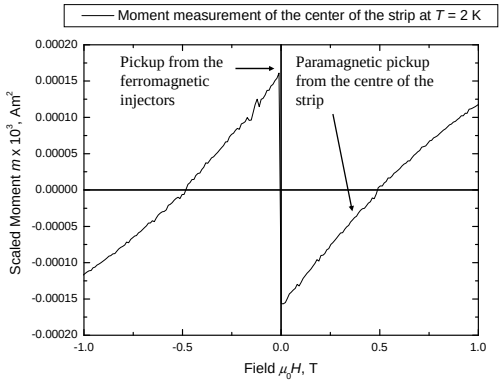

Figure 4.2: Scaled magnetic response, measured as a function of applied field, measured at the centre of the Al strip of Sample 1 (Fe injectors), at $T = 2$ K.

adiabatic depolarisation occur in the centre conducting Al strip (not to scale). An obvious way to obtain the magnetisation profiles, based on experimental data (measured coupled flux spatial distributions) would be deconvolution.

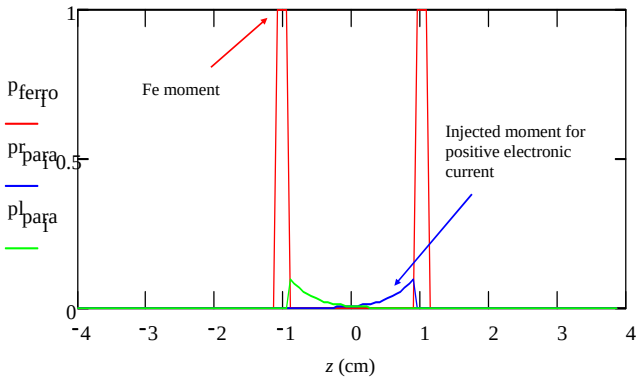

Figure 4.3: Magnetisation distribution expected for a Sample 1 with Fe injection electrodes, for either left-hand or right-hand-side injection. Parameters are given in the text.

As it is difficult to deconvolute the on-axis magnetisation distributions from raw coupled flux data see appendix C.3, it is advantageous to calculate the response expected for particular sample geometry, magnetic field, electrical current, temperature, etc. An example is shown on figure 4.5, for the dimensions of Sample 2, assuming 10 % injection efficiency and spin-diffusion length $\lambda_{sd} = 3.5$ cm, as argued by Aronov (1976) for aluminium at a lattice temperature of 1 K. It is important to note the main feature - spatially asymmetric current response in the vicinity of the injection electrodes.

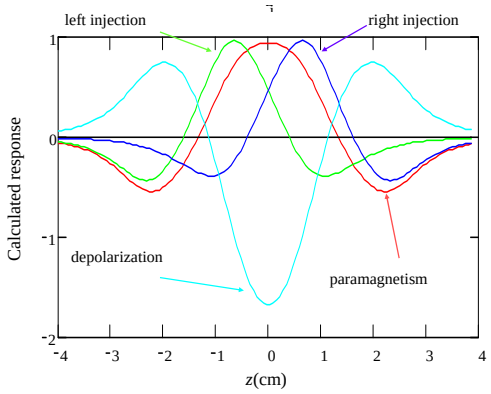

Figure 4.4: Coupled flux profiles generated by the injected magnetisation distributions shown on figure 4.3, together with the ones due to the substrate contribution and the adiabatic depolarisation of the central Al conductor (not to scale).

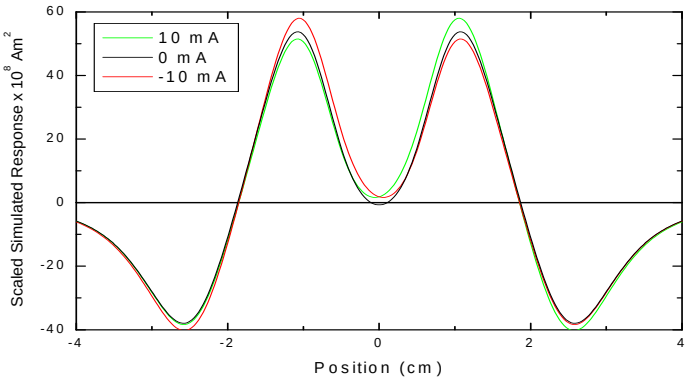

Figure 4.5: Calculated coupled flux profiles for positive (green), negative (red) and zero (black) current bias, for $\lambda_{sd} = 3.5$ cm, and assuming 10 % injection efficiency.

Example of raw experimental data is shown on figure 4.6. The coupled flux profiles are completely dominated by the background created by the ferromagnetic injection electrodes. At large enough fields (so that the magnetisation of the injectors remains stable) and at fixed temperature, this background is sufficiently reproducible and can be substracted.

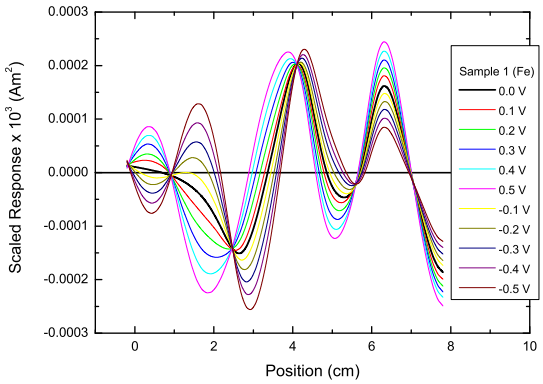

Figure 4.6: Raw coupled flux profiles for different voltage biases of Sample 1 (Fe electrodes), measured at $T = 4.23$ K and $\mu_0 H = 100$ mT.

The raw experimental data is not free from other measurement artefacts, as for example, flux jumps in the SQUID circuitry[1]. An example is shown on figure 4.7. Probably the only positive feature of the flux jump events is the possibility to establish the absolute flux sensitivity (provided the number of flux quanta spanned is known) of the secondary SQUID circuitry (which is 7.05 V/Φ_0 in this example).

In real-life samples, even though all care is taken to minimise the mutual inductance contribution to the coupled flux which is spatially symmetric as shown on figure 4.8, it is the dominant contribution for Sample 1 (Fe electrodes) at $T = 10$ K, after the zero-current background has been substracted. It is evident, though, that on lowering the temperature to 1.8 K a non-inductive contribution develops around the sample position.

The inductive contribution (antisymmetric with respect to current reversal) always present in the raw coupled flux profiles, and the symmetric with respect to current component, have different symmetry with respect to field reversal. While the inductive one is field independent, the non-inductive one is antisymmetric with respect to field as evidenced on figure 4.9.

[1] In a flux jump event, the flux-locked-loop (FLL) which utilises the SQUID device as a 'null detector' or rather a 'definite state' detector, which is normally kept locked to a single flux state, 'looses lock' and a number of flux quanta enter or escape the device. In most cases, though not always, flux jumps are due to RF interference or the signal of interest exceeding the slew rate of the feedback amplifiers of the FLL. In the case described here, the flux jumps are due to interference which couples inductively to the SQUID device via the sample leads. It is possible, also, to cause a flux jump event, by say ramping the current bias of the sample, so that the rate of change of the coupled flux exceeds the maximal slew rate.

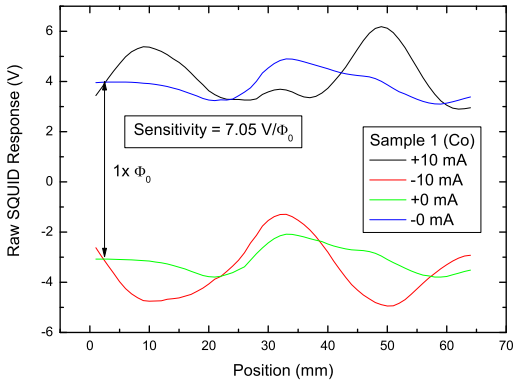

Figure 4.7: Raw coupled flux profiles for Sample 1 (Co electrodes), measured at $T = 1.8$ K and $\mu_0 H = 20$ mT. Note the flux-jump experienced and the scale of the voltage response for an individual flux quantum Φ_0.

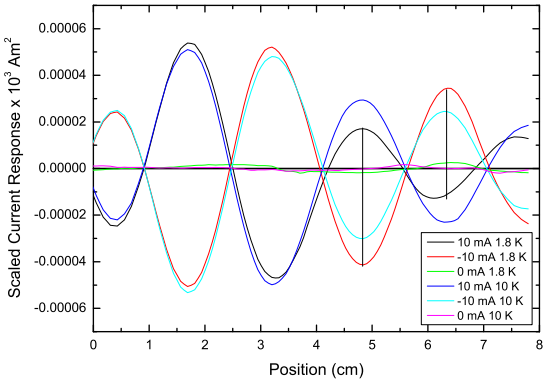

Figure 4.8: Spatial profiles of the flux coupled to the gradiometer at $T = 1.8$ K and 10 Kfor applied current of 0 (green and magenta), +10 mA (black and blue) and -10 mA (red and cyan) for Sample 2 with Fe injection electrodes. The Sample is situated at $z = 5.4$ cm. Note that at 10 K the profiles are completely anti-symmetric with respect to applied current.

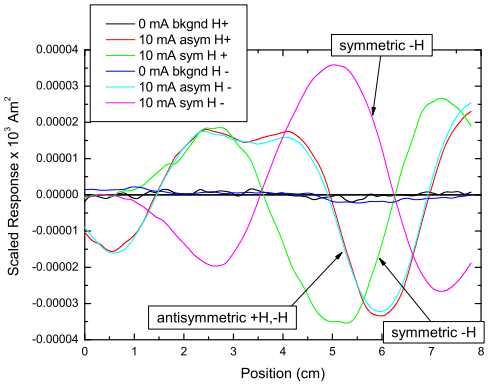

Figure 4.9: Field reversal symmetry of the inductive (antisymmetric) and the non-inductive (symmetric) with respect to current components of the coupled flux, measured on Sample 1 (Fe electrodes) at $T = 1.8$ K.

While the inductive contribution is temperature independent, the component symmetric in current shows rather strong temperature dependence, shown on figure 4.10. More information can be obtained from the current dependencies of both components, as shown on figure 4.11. Unlike the inductive component, the current-symmetric one exhibits saturating sub-linear current dependence, which is at first, quite puzzling. It is reasonable to expect a stronger than linear, and close to quadratic, current dependence should the observed effect be due to Joule heating and the actual changes in temperature small.

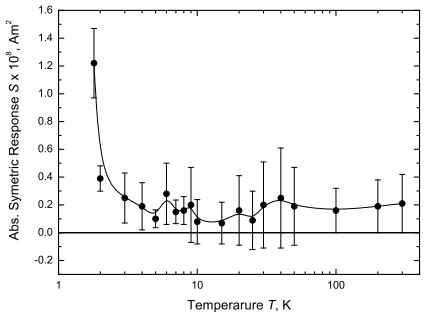

Figure 4.10: Temperature dependence of the non-inductive part of the pick-up for Sample 1 (Fe electrodes).

Apart from measuring the coupled flux directly, while applying a DC current bias on the sample, it is possible to realise a synchronous detection scheme, by modulating the current flowing through the structure, keeping it either only positive, only negative or symmetric around

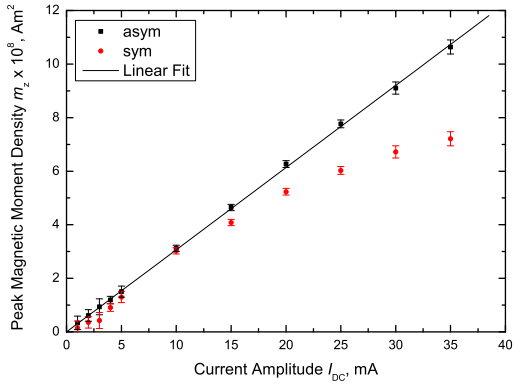

Figure 4.11: Current dependence of the symmetric and antisymmetric parts of the coupled flux, measured for Sample 1 (Zn electrodes), at $T = 1.8$ K, and $\mu_0 H = 100$ mT.

zero. The difference between the electro-magnetic susceptibility spatial profiles measured in this fashion, can be constructed free from the direct induction contribution. Examples of raw profiles and a field dependence of the amplitude of the non-inductive component obtained by this method is shown on figures 4.12 and 4.13, respectively, for Sample 1 (Ni electrodes). A linear dependence of the amplitude of the non-inductive response is clearly seen, in a contradiction with the expected saturating behaviour of the injected spin-magnetisation.

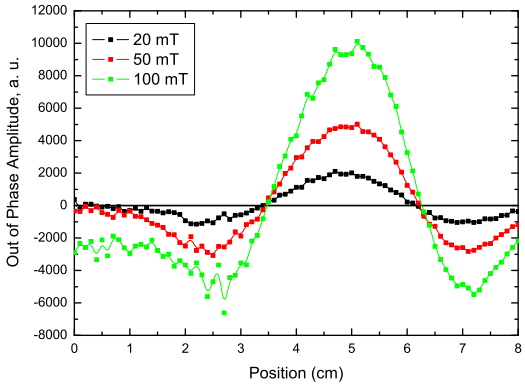

Figure 4.12: Spatial profiles of the non-inductive component of the AC detected coupled flux, for Sample 1 (Ni electrodes), measured at $T = 1.8$ K.

The analysis is further complicated by the fact, that often the inductive contribution to the flux profiles can have a high spatial gradient around the centre of the sample on the translation axis, thus producing current effects similar in spatial distribution to injected spin polarisation, as evidenced by figure 4.17. It is therefore impossible to assert, whether or not the observed effects are due to spin injection (spatially anti-symmetric), a spatially symmetric contribution

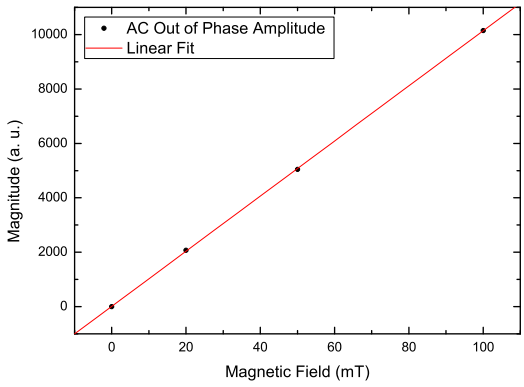

Figure 4.13: Field dependence of the non-inductive component of the coupled flux for Sample 1 (Ni electrodes, measured at $T = 1.8$ K.)

due the heating of the electronic system by the current - adiabatic depolarisation (see Zvezdin (1966)]), or are purely artefacts due to mutual inductance and lattice heating. The resistance of the individual samples (with different injection electrodes) is varying within two orders of magnitude (see figure 4.14) and provides some evidence for nonlinear effects, leaving the possibility for hot electron depolarisation open.

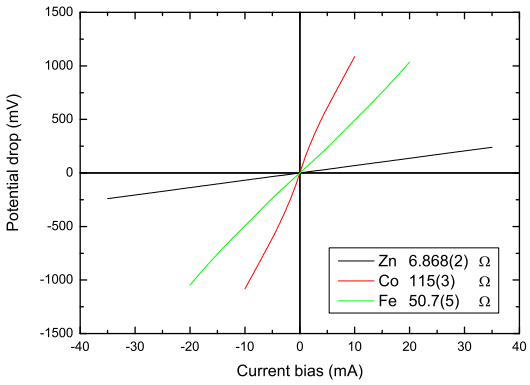

Figure 4.14: Voltage-current characteristics of Sample 1 with different injection electrodes, measured at $T = 1.8$ K. Note the small nonlinearities in some of the curves.

Strong evidence in favour of the lattice heating effect as the dominant contribution is the close resemblance (with a negative sign taken into account, due to sign of the derivative $\frac{\partial M(z)}{\partial T} < 0$) between the symmetrised with respect to current flux profile, measured at $T = 1.8$ K, shown on figure 4.15; and the difference of the zero-current coupled flux profiles, measured at $T = 10$ K and $T = 1.8$ K, shown on figure 4.16, for Sample 1 (Fe electrodes). From the scaling factor relating the two coupled flux profiles, an effective increase of sample temperature can be

estimated to be $\delta T \approx 8$ K.

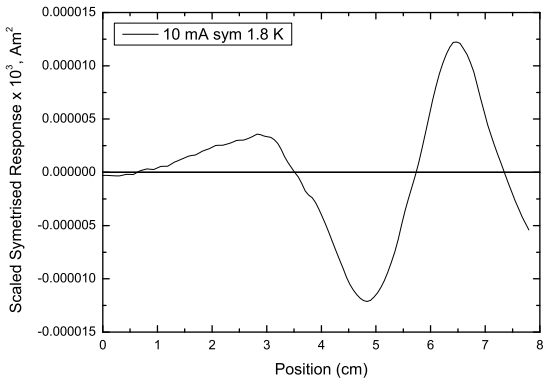

Figure 4.15: Symmetrised with respect to current coupled flux profile of Sample 1, measured at $T = 1.8$ K.

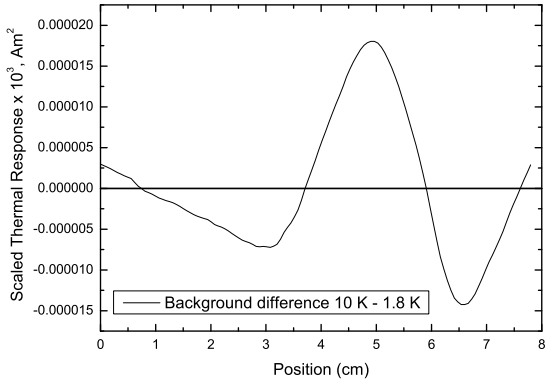

Figure 4.16: Difference of the zero-current coupled flux profiles measured at $T = 10$ K and at 1.8 K for Sample 1.

The mutual inductance and lattice heating effects can be diminished to a negligible extent if the sample support is constructed from purely diamagnetic material and the current path through it confined to the central axis of the gradiometer. Results in such a configuration (Sample 2) are shown on figure 4.18, revealing no effects other than a small residual cross inductance due to the Fe injector electrodes.

It should be noted that the construction of Sample 2 (see appendix C.1) is such that the current is flowing on two isolated conductive paths (1 mm wide) in opposing directions. One of the conductive strips is deposited in gold only, while the other consists of gold strips with the active sample region in the middle of the rod length. As electrical connections to the sample structure are only made far from its centre (9 cm away and essentially out of the sensitive

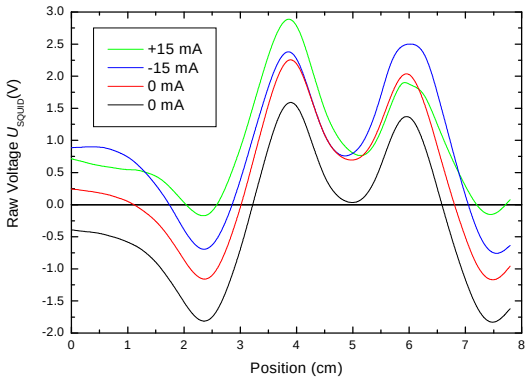

Figure 4.17: Coupled flux profiles for positive (green), negative (blue) and zero (red and black) current bias, measured at $T = 1.8$ K for Sample 1 (Fe electrodes).

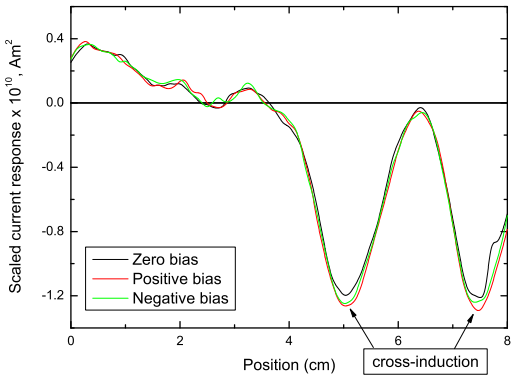

Figure 4.18: Synchronously detected (AC method) coupled flux at the fundamental frequency of 1.133 kHzwith positive, negative and zero current bias, for Sample 2 (Fe electrodes). The measurement is performed at applied field of 20 mT and at $T = 1.8$ K.

volume of the gradiometer), the geometry of Sample 2 is much closer to the ideal one. Also, the fused silica used for the support of Sample 2 has been confirmed, by low temperature magnetic susceptibility measurements, to contain less than 1 ppm of Fe impurities. The large length of the support structure results in magnetic poles, which are far from the centre of the gradiometer, and therefore yield no signal over the noise floor for fields of up to 1 T.

Some possible reasons for the lack of a measurable spin-injection effect could be:

1. poor structure of the Fe/Al interface leading to low injection efficiency;

2. smaller than expected spin-self-diffusion length in evaporated aluminium;

3. spin dephasing due to the longitudinal Hanle effect.

Below, are some remarks on the likelihood of validity of the above three points. As the expected magnetisation signal at electric fields of the order of 10^{-3} V/cm, injection efficiency of 10 %, spin-polarisation of the ferromagnetic injector at the Fermi level of 40 % and spin-diffusion length $\lambda_{sd} = 3.5$ cm (at 1 K), is equivalent to the paramagnetic magnetisation of Al in a field of 1.2 T, and equal to about 20 A/m (see Aronov (1976)); a reduction of injection efficiency to below 0.5 % would result in signal magnitude comparable or less than the sensitivity limit of the method (about 1 A/m). In a similar fashion, a spin diffusion length below about 1 mm, while preserving the injection efficiency of about 10 % would also result in signals below the detection limit. It should be noted, that in a recent review (Bass & Pratt-Jr (2007)), a large discrepancy between results for spin diffusion length in nominally pure Al has been noted. Values ranging between 300 and 450000 nm have been reported at lattice temperatures around 4 K by various methods and on samples of various degree of crystallinity. Only, a value, close to the greatest reported one would have been observable in Sample 2, by the here suggested method.

Another possible reason is the spin dephasing upon scattering of the conduction electrons from impurities and imperfections, at finite applied magnetic field. The dephasing is proportional to the magnetic field and has been shown to destroy the diffused polarisation for fields above about 10mT (see Johnson & Silsbee (1988a,b)). As a minimal field of similar magnitude is necessary, in order to keep the magnetisation of the two ferromagnetic electrodes in our samples stable upon translation of the sample with respect to the gradiometer, the absence of spin-diffusion related signal in the experiments reported here, may best be understood in terms of the Hanle effect.

In conclusion, it has been shown that, by careful design of a current-carrying structure, it is possible to achieve useful magnetisation sensitivity levels of about 1 A/m in the direct detection of current-induced spin polarisation. To the present spatial resolution of about 1 mm,

no spin injection effect is observed, after taking into account most possible artifacts. This may be attributed to the longitudinal Hanle effect. More work is required on optimizing SQUID gradiometers or scanning Hall probes to trace the spatial profiles of the injected magnetisation.

Chapter 5

Magnetic and transport properties of ZnO

5.1 Magneto-transport theory

The following known types of magnetoresistance in semiconductors should be considered relevant to dilute magnetic semiconductor systems. While most of them are generic for semiconducting materials, others are particular to magnetic systems.

Closed orbits magnetoresistance is a classical positive magnetoresistive effect, which arises in a minimum two-band picture (see section E.4) from the action of the Lorentz force on the mobile carriers[1]. For carriers in closed orbits, this term is of the form:

$$\frac{\Delta\rho^{\mathrm{CO}}}{\rho} = \frac{aH^2}{b+cH^2} \tag{5.1.1}$$

where a, b and c are parameters dependent on the carrier partial conductivities $\sigma_{1,2}$, and signed motilities $\beta_{1,2}$, like:

$$a = \sigma_1\sigma_2\left(\beta_1-\beta_2\right)^2 \tag{5.1.2}$$

$$b = \left(\sigma_1+\sigma_2\right)^2 \tag{5.1.3}$$

$$c = \left(\beta_1\sigma_1+\beta_2\sigma_2\right)^2 \tag{5.1.4}$$

This contribution is quadratic in low fields, and it saturates (also in a quadratic fashion) in high fields (see figure 5.1).

Open orbits magnetoresistance is the corresponding term for open orbits, for which the field dependence is quadratic and non-saturating:

$$\frac{\Delta\rho^{\mathrm{OO}}}{\rho} = dH^2 \tag{5.1.5}$$

[1] There is no magnetoresistance in a single-band picture.

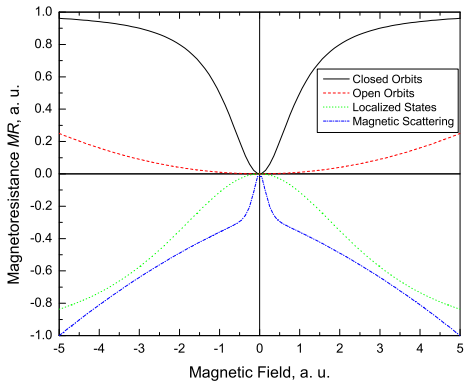

Figure 5.1: An illustration of the various contributions towards the magnetoresistance in semiconductors.

This is the most generic type of behaviour in systems with low carrier mobilities, at low magnetic fields and at high temperatures, for a very broad class of materials, and is illustrated on figure 5.1.

While most 'conventional' types of magnetoresistive effects are positive in nature, negative magnetoresistance is not uncommon in semiconductors, where it is associated mainly with impurity conduction (Goto *et al.* (1995); Woods & Chen (1964)), or with magnetic scattering (Monsterleet *et al.* (1997)). In metals negative magnetoresistance has been attributed to magnetic scattering, to weak localisation and to hopping conduction mechanisms (Belevtsev *et al.* (1998); Wang *et al.* (1999)). In a general band picture (for metals and for non-metals), it has been argued by Mott & Zinamon (1970), that if the conduction happens close to the Fermi level[1], the conductivity can be developed into Taylor series over electron energy, and the first few even-order terms kept (for reasons of time reversal symmetry):

$$\frac{\sigma(B)}{\sigma_0} = \frac{\sigma\left(E_\mathrm{F}\right)}{\sigma_0} + \frac{1}{2}\frac{1}{\sigma_0^2}\left(\mu_\mathrm{e}B\right)^2 \left.\frac{\partial^2\sigma}{\partial E^2}\right|_{E=E_\mathrm{F}} + O\left[\left(\mu_\mathrm{e}B\right)^4\right] \tag{5.1.6}$$

where μ_e is the electron mobility. Therefore the sign of the derivative $\frac{\partial^2\sigma}{\partial E^2}$ determines the sign of the magnetoresistance (negative magnetoresistance for positive derivative). Of course, in the Drude model, the conductivity derivative can be expressed in terms of the derivatives of the carrier concentration and the mobility as:

$$\frac{\partial^2\sigma}{\partial E^2} = q\left[\frac{\partial^2 n}{\partial E^2}\mu_\mathrm{e} + 2\frac{\partial n}{\partial E}\frac{\partial \mu_\mathrm{e}}{\partial E} + \frac{\partial^2\mu_\mathrm{e}}{\partial E^2}n\right]_{E=E_\mathrm{F}} \tag{5.1.7}$$

Therefore, if the Fermi level of a system is situated in a minimum of the density of states and the mobility is either relatively constant or has a minimum, then the magnetoresistance can

[1] This is certainly true for metals, pseudogap[2] materials, and sufficiently doped semiconductors.

be negative. Apart from the above argumentation, there are types of magnetoresistance, which are not readily treated within the band picture.

Hopping conduction magnetoresistance is a negative contribution of the form (valid for small fields, which do not cause very significant level-shifts as compared with the hopping integrals or $g^\star \mu_\mathrm{B} B \ll U$):

$$\frac{\Delta\rho^{\mathrm{HC}}}{\rho} = -eH^2 \tag{5.1.8}$$

where e is a temperature and system dependent positive coefficient, which is commonly found (Belevtsev *et al.* (1998)), to be proportional to T^{-1}. This term has physical relevance in the case of very strongly disordered metals and semiconductors.

Ionised impurities magnetoresistance is a negative term due to spin-flip scattering from singly-occupied localised states with $s = \frac{1}{2}$. The term

$$\frac{\Delta\rho^{\mathrm{LS}}}{\rho} = \cosh\left(\frac{H}{f}\right)^{-1} \tag{5.1.9}$$

where $f = \frac{kT}{g^\star \mu_\mathrm{B}}$, is quadratic in low fields (Boon (1973)). The characteristic shape of the field dependence of this type of magnetoresistance is illustrated on figure 5.1.

Magnetic scattering magnetoresistance is a negative term due to scattering from a paramagnetic or ferromagnetic moments, which varies as M^2 like

$$\frac{\Delta\rho^{\mathrm{MS}}}{\rho} = hM(H)^2 \tag{5.1.10}$$

where h is dimensional coefficient that depends on the strength of say the s-d scattering in the system. The magnetoresistance due to magnetic inclusions is expected to have similar magnetisation dependence, and so is the contribution from a domain structure in thin film geometry (Barabash & Stroud (2001)).

For the particular case of scattering by a paramagnetic spin system, the magnetisation of which is not saturated by a strong applied field, the contribution is negative and quadratic:

$$\frac{\Delta\rho^{\mathrm{PS}}}{\rho} = l\left(\frac{g^\star \mu_\mathrm{B} B}{k\left(T + \theta_\mathrm{C}\right)}\right)^2 \tag{5.1.11}$$

where θ_C is the asymptotic Curie temperature and l is a system dependent constant (Monsterleet *et al.* (1997)). The characteristic shape of the field dependence for this type of magnetoresistance is shown on figure 5.1. Analogous terms in the Hall coefficients represent the spontaneous (anomalous) Hall effect. A typical shape of the magnetic field dependence is illustrated on figure 5.2.

Anisotropic magnetoresistance (AMR)[1] is commonly associated with the presence of substantial d-band splitting and spin-orbit coupling in transition metals and alloys (for a review

[1] More appropriately spontaneous anisotropic magnetoresistance (Malozemoff (1985)).

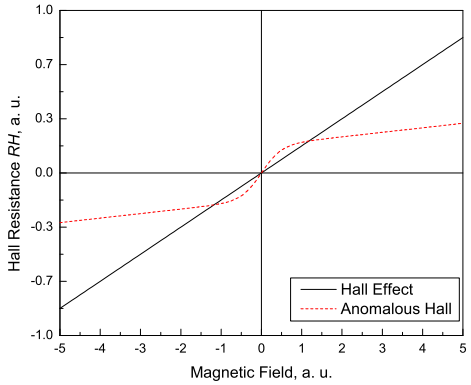

Figure 5.2: An illustration of the anomalous contributions towards the magnetoresistance and the Hall effect.

of early works see McGuire & Potter (1975)). In this case the magnetoresistance ratio is a function of the angle θ, between the current and the magnetisation of the sample (measured in the film plane for thin films), and for polycrystalline samples has the form

$$\frac{\Delta\rho^{\mathrm{AMR}}}{\rho} = \sum_{i=0,1\ldots} A_{2i}\cos^{2i}(\theta) \tag{5.1.12}$$

where A_{2i} are constants dependent on the density of d-like states at the Fermi level, sample quality, temperature, etc. The phase angle is usually defined in such way that:

$$A_2 = \frac{\rho_{\parallel} - \rho_{\perp}}{\rho_{\perp}} \tag{5.1.13}$$

where $\parallel$ and $\perp$ refer to the mutual orientation of the current density j flowing through, and the magnetisation M of the specimen. A typical angular dependence is illustrated on figure 5.3.

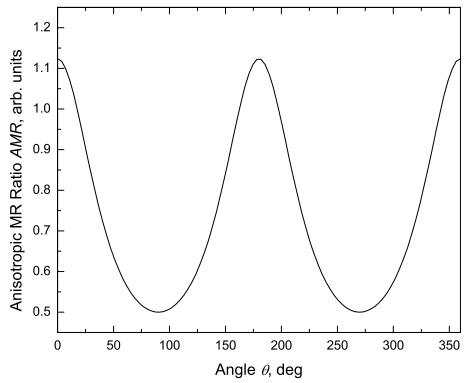

Figure 5.3: An illustration of the anisotropic magnetoresistance contribution in a crystalline system.

While in most common cases (polycrystalline alloys) only the first two terms survive, for oriented and single-crystalline samples, higher order in $\cos\theta$ terms may have to be included for proper description. The magnitudes of the amplitude coefficients have been the subject of many theoretical calculations, almost entirely for the case of 3d ferromagnetic metals and alloys (only as examples Khmelevskyi *et al.* (2003); Lopes *et al.* (2002); Malozemoff (1986); Potter (1974); Rijks *et al.* (1995)). More recent experimental observations of AMR effects in hopping conductors and semiconductors include the manganite family (Bibes *et al.* (2005); Lyanda-Geller *et al.* (2001); Ziese & Sena (1998)) and III-V semiconductors (Hayashi *et al.* (2000); Jungwirth *et al.* (2002, 2003))[1].

It should be noted, that very anisotropic terms in the magnetoresistance are contained also in the open orbits magnetoresistance of normal metals (see for example Caroline (1969); Leo (2005); Young (1982)). The expected field and angular dependence is:

$$\frac{\Delta\rho^{\mathrm{MRO}}}{\rho} = hB^2\cos^2(\theta) \tag{5.1.14}$$

and is conventionally used to detect open orbits in compensated metals for which $n_{\mathrm{e}} \approx n_{\mathrm{h}}$.

Angular oscillations of the magnetoresistance in quasi-one, and quasi-two-dimensional metals are routinely used for the experimental characterisation of their Fermi surfaces (see as examples Blundell & Singleton (1996); Danner *et al.* (1994); Kartsovnik *et al.* (1991, 1992); Kobayashi & Osada (2005); Osada *et al.* (1996)) and has been well theoretically developed (Danner *et al.* (1994); Dragulescu *et al.* (1999); Lebed & Bagnet (1997); Lebed *et al.* (2004); McKenzie & Moses (1998); Nam *et al.* (2001)). The angular dependencies are often found to scale as $\cot\theta$ and $1/\cos\theta$, and to be very characteristic of the particular material studied, however, this effect should give negligible contribution for metals and semiconductors with normal 3D dispersions.

In semiconducting systems (even in non-magnetic ones), the anisotropies of the band structure, or in simple terms, the different extremal cross sections of the constant energy surfaces can potentially lead to substantial angular dependencies of the magnetoresistance. These would resemble AMR effects, but would also have some peculiar features. Namely, terms of large orders in $\cos\theta$ are to be expected for non-cubic crystalline systems, exhibiting non-monotonic and non-saturating field dependencies, and strong and carrier concentration-governed temperature dependence. In analogy with the case of explicit Landau level formation $\mu B \gtrsim 1$ mentioned in section 5.1, an exponential decay of the amplitude of the main oscillatory component is to

[1] Even more exotic types of anisotropic magnetoresistance have recently sparkled interest - the Coulomb blockade anisotropic magnetoresistance (Wunderlich *et al.* (2006)) and the ballistic anisotropic magnetoresistance (Velev *et al.* (2005)).

be expected at high magnetic fields, due to carrier localisation, combined with an initial rise, controlled by the temperature T and the athermal scattering related Dingle temperature T_{D}, yielding for the classical limit of $\mu B \ll 1$ the scaling:

$$\frac{\Delta\rho^{\mathrm{MRA}}}{\rho} = o \exp\left[-\frac{m_{\mathrm{e}}}{m^{\star}} \frac{g^{\star}\mu_{\mathrm{B}} B}{k\,(T+T_{\mathrm{D}})}\right] \tanh^2\left[\frac{g^{\star}\mu_{\mathrm{B}} B}{k\,(T+T_{\mathrm{D}})}\right] \cos^2 \tag{5.1.15}$$

where the dimensionless coefficient o is a function of the carrier densities and mobilities in the system, as well as the anisotropies of the effective masses and mobilities.

Weak localisation magnetoresistance is another possible term[1], which is associated with the weak localization phenomenon[2], commonly observed in thin disordered metal films (see for example Altshuler & Aronov (1981); Bergmann (1983b, 1986)). The explanation lies in the coherent backscattering (destructive or constructive interference of the backscattered electronic wave) of the conduction electrons from various forms of magnetic and nonmagnetic impurities and imperfections. The maximal theoretical correction to the resistivity is of the order of

$$\Delta\rho^{\mathrm{3DWL}} \sim \frac{1}{2}\frac{\hbar}{q^2}\,(2\pi)^2\,\lambda_{\mathrm{m}} \tag{5.1.16}$$

for the 3D case or

$$\Delta\rho^{\mathrm{2DWL}} \sim \frac{1}{2}\frac{\hbar}{q^2}\,(2\pi)\,t \tag{5.1.17}$$

for the 2D case, where $\lambda_{\mathrm{m}} = \sqrt{\frac{q}{\hbar B}}$ is the diffusive magnetic length and t is the film thickness. Both expressions yield resistivity change of about 10^{-3} Ωm for film thickness of 80 nm or magnetic field of 1 T, which is of the order of the magnetoresistive changes observed in the present study. At larger fields, the weak localization contribution to the magnetoresistance will, therefore, have to move to the 3D case and yield field dependence weaker than $B^{\frac{1}{2}}$.

Details in the low field (usually below about 3 T) magnetoresistance can give information about the spin-spin (Amaral (1990); Wei *et al.* (1989)), and spin-orbit characteristic scattering times in non-magnetic metals (Bergmann & Horriat-Esser (1985)), ferromagnets (Dugaev *et al.* (2001)), semimetals (Woerlee *et al.* (1983)) and semiconductors (Hassenkam *et al.* (1997)). Detailed expressions for the 3D case are given by Bergmann (1982a):

$$\frac{\Delta\sigma}{\sigma_0} = -\left\{f^{\mathrm{3D}}\left(\frac{H_1}{H}\right) - f^{\mathrm{3D}}\left(\frac{H_2}{H}\right) + \frac{1}{2}\left[f^{\mathrm{3D}}\left(\frac{H_3}{H}\right) - f^{\mathrm{3D}}\left(\frac{H_4}{H}\right)\right]\right\} \tag{5.1.18}$$

where $\sigma_0 = \frac{q^2}{\pi h}$ is the conductance quantum and the function f^{3D} is defined as:

$$f^{\mathrm{3D}}\left(\frac{H_i}{H}\right) = \psi\left(\frac{1}{2} + \frac{H_i}{H}\right) \tag{5.1.19}$$

[1] Possibly the most modern one. The subject has been initiated in the early 80's by Abrahams *et al.* (1979). For a review of the area (see Bergmann (1984)).

[2] A more physically correct name would be weak antilocalization.

where H_i are characteristic fields, defined via the corresponding scattering times:

$$H_i = \frac{\hbar}{4qD}\frac{1}{\tau_i} \tag{5.1.20}$$

where D is the diffusion coefficient (assumed isotropic). The relevant characteristic fields are:

$$H_1 = H_{\rm el} + H_{\rm so} + H_{\rm s} \tag{5.1.21}$$
$$H_2 = \frac{4}{3}H_{\rm so} + \frac{2}{3}H_{\rm ss} + H_{\rm in} \tag{5.1.22}$$
$$H_3 = 2H_{\rm ss} + H_{\rm in} \tag{5.1.23}$$
$$H_4 = \frac{2}{3}H_{\rm ss} + \frac{4}{3}H_{\rm so} + H_{\rm in} \tag{5.1.24}$$

where $H_{\rm el}$ corresponds to elastic scattering, $H_{\rm in}$ to inelastic scattering, $H_{\rm ss}$ to magnetic (spin-spin) scattering and $H_{\rm so}$ to spin-orbit scattering. Similar expressions are valid of the 2D case, when $t < \lambda_{\rm m}$, with a different base function $f^{\rm 2D}$:

$$f^{\rm 2D}\left(\frac{H_i}{H}\right) = \ln\left(\frac{H}{H_i}\right) + \psi\left(\frac{1}{2} + \frac{H_i}{H}\right) \tag{5.1.25}$$

leading to a modification of the low-field behaviour (Averkiev *et al.* (1999); Bergmann (1982b)). An example of full theoretical calculation of the effective field parameters is the work of Pikus & Pikus (1996). An example of characteristic shapes of field dependencies of weak localisation magnetoresistance are illustrated on figure 5.4.

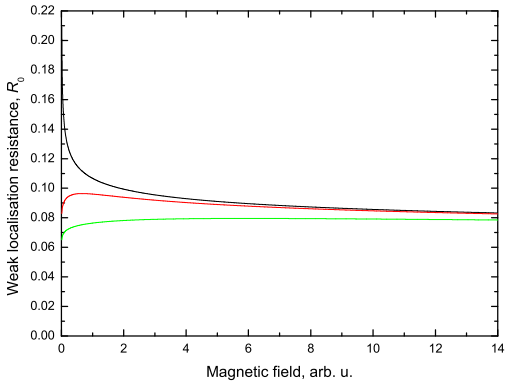

Figure 5.4: An illustration of the weak localization magnetoresistance contribution in a disordered system.

The temperature dependence of the amplitude of the weak localisation magnetoresistance is often approximated as

$$\frac{\Delta\sigma^{\rm WL}}{\sigma} \propto \ln\left(\frac{\tau_T}{\tau_{\rm el}}\right) \tag{5.1.26}$$

where $\tau_T = \frac{h}{kT}$ is the thermal scattering (or thermal diffusion) time (Bergmann (1983a)).

The weak localization magnetoresistance can also be very anisotropic. A standard reason for its anisotropy is dimensional crossover. For example, in the strong field regime, because of spin-splitting of conduction electron energies the weak localisation contribution can be positive and scaling as $\ln \frac{g^\star \mu_B B}{kT}$ in two dimensions and $\sqrt{\frac{g^\star \mu_B B}{kT}}$ in three (Grempel (1987); Lee & Ramakrishnan (1982)). Upon rotation of the applied magnetic field of fixed magnitude, say out of the plane of a thin film, the geometry can be continuously varied between the two cases (Newson & Pepper (1985)).

Another reason for anisotropy of the weak localisation magnetoresistance is the anisotropy of the tensor of the diffusion coefficients $\hat{\mathbf{D}}$. In most experimental studies, this is commonly done in a controllable fashion in multilayer systems (Baxter *et al.* (1996); Fadnis *et al.* (1993)). It is reasonable to expect that crystal anisotropy would influence the diffusion coefficients and cause similar effects. This possibility has been theoretically investigated in artificial quantum well structures by Mal'shukov *et al.* (1999).

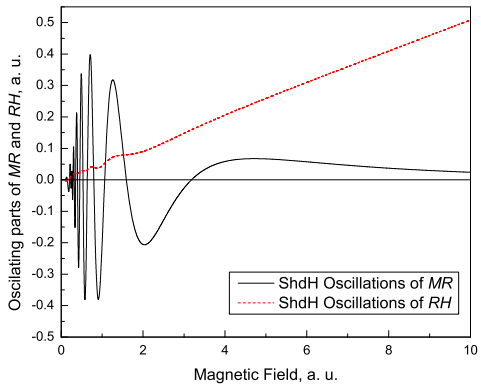

Figure 5.5: An illustration of the oscillatory contributions towards the magnetoresistance and the Hall effect.

5.2 Semimagnetic Semiconductors

Much interest, both experimental and theoretical, has been sparked by the discovery of ferromagnetism in a range of transparent oxides doped with a few percent of transition metal cations (see for example Fukumura *et al.* (2005) and Dietl *et al.* (2000); Spaldin (2004) and references therein). Examples include TiO_2, SnO_2, HfO_2, ZnO and Cu_2O doped with ions such as Cr, Mn Fe or Co. The ferromagnetism in these compounds is not an intrinsic, bulk property (Lawes *et al.* (2005)). Ferromagnetism appears only in thin films and nanocrystalline samples (Wang *et al.* (2006b)), prepared in conditions promoting extended solid solubility (Fukumura

et al. (1999)). In some cases, at least, it seems to be associated with specific crystal defects, which have not yet been definitely identified (cite). In other cases, transition metal clustering has been identified as the origin of ferromagnetic behaviour (Park *et al.* (2004)). Homogeneous dopant distributions in bulk samples and in some thin film samples give rise to paramagnetism (Fukumura *et al.* (2005)). Many of the oxides are transparent conductors, where donor electrons populate an impurity band or occupy extended states at the bottom of the conduction band. A key question that may determine the future utility of these remarkable magnetic materials is whether or not the conduction band is spin split, as it is in traditional n-type magnetic semiconductors such as EuS. A spin-split conduction band could be manifest in transport properties such as magnetoresistance or anomalous Hall effect.

5.3 Magneto-transport reports

While most experimental observations of the magnetoresistance of ZnO-based thin films report large positive effects (see for example Xu *et al.* (2006a,b)), the low temperature magnetoresistance of $Zn_{1-x}Co_xO$:Al (x ¡ 0.05) has been studied by Jin *et al.* (2001, 2002), and subdivided into a negative contribution close to zero field, attributed to weak electron localization effects, a positive contribution due to a field-dependence of the Thomas-Fermi radius and a negative term due to the decrease of spin-disorder at higher fields. Negative and predominantly isotropic magnetoresistance is often reported in $Zn_{1-x}Co_xO$ (x ¡ 0.3), combined with a 'Kondo-like' minimum in the resistivity and absence of anomalous Hall effect (Budhani *et al.* (2005)), or variable range hopping (VRH) non-activating behaviour of the resistance with temperature (Wang *et al.* (2006a)). Terms proportional to M^2, or for the case of linear response of the localised paramagnetic spins, proportional to H^2, are included in the magnetoresistance in order to explain the observations in non-ferromagnetic samples. A model has been advanced and illustrated for the case of $Zn_{1-x}Mn_xO$:Al ($x = 0.03$ and $x = 0.07$), based on the $\mathbf{k}\cdot\mathbf{p}$ approach including spin-orbit coupling and s-d exchange interactions (Andrearczyk *et al.* (2005)). Ferromagnetism or superparamagnetism found in inhomogeneous Co-ZnO magnetic semiconductor multi-layers (Ren *et al.* (2003); shen Yan *et al.* (2004)), is accompanied by 'butterfly-like' magnetoresistance curves at low temperatures, attributed to spin-dependent hopping. In thick epitaxial films it has been suggested that the magnetoresistance is due to magnetic-field-induced change in the Anderson localization length (Pakhomov *et al.* (2004)). While the question of clustering as the source of the ferromagnetism in some systems remains open, there is nevertheless evidence for successful formation of a two-dimensional electron gas in ZnMnO/ZnO heterostructure (Edahiro *et al.* (2003)) and experimental evidence for spin coherence ZnO thin films and epi-layers (Ghosh

et al. (2005)). The creation of high mobility ZnO thin film transistor by Fortunato *et al.* (2004), opens new prospects for spintronic applications based on this dilute magnetic semiconductor system.

5.4 Magnetotransport data

Resistivity curves for undoped and Co-doped ZnO films are shown on figure 5.6 and 5.7. The samples are near-degenerate semiconductors with a small temperature-dependent activation energy. Only below about 20 K is there much sign of carrier freeze-out. Hall effect measurements give a carrier density $> 10^{26}$ m^{-3}.

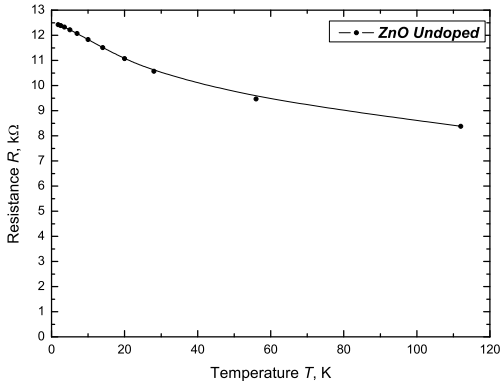

Figure 5.6: Resistance as a function of temperature for an Undoped ZnO sample, measured at zero applied field.

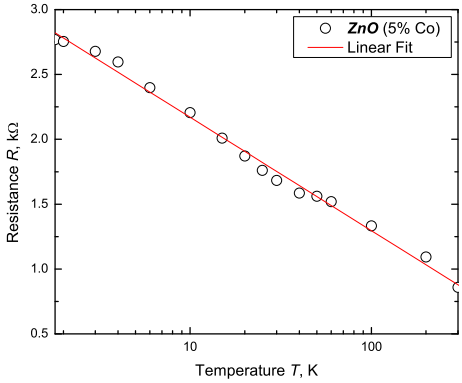

Figure 5.7: Temperature dependence of the resistance of a 5 % Co doped ZnO film. Note the logarithmic temperature scale.

Magnetoresistance curves for the x = 25 % film show a butterfly curve (see figure 5.8),

which corresponds to the 200 mThysteresis observed in the magnetisation curve at the same temperature.

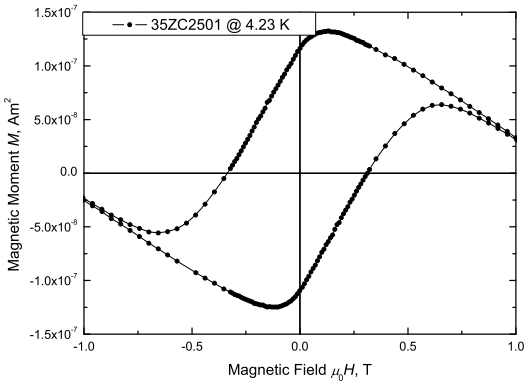

Figure 5.8: Magnetic hysteresis of a 25 % Co doped ZnO thin film prepered in conditions analogous to the one system of figure 5.22.

A set of magnetoresistance for undoped, oxygen-deficient ZnO are shown as a function of temperature in figure 5.9, for fields of up to 5 T. A small, negative magnetoresistance is apparent below 20 K.

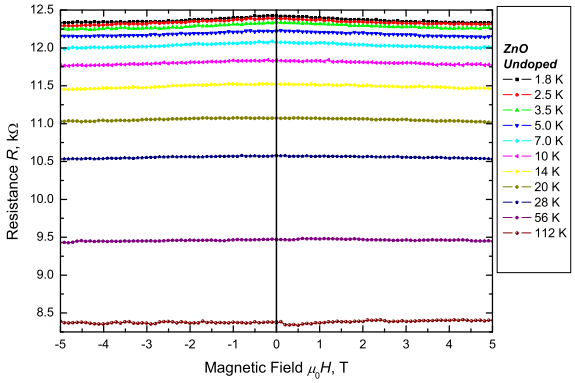

Figure 5.9: Resistance as a function of field, at various temperatures (shown), for an undoped ZnO sample.

A complete set of data on the ferromagnetic sample with $x = 0.05$ is shown on figures 5.10 and 5.11.

Data on the paramagnetic 4 % sample is shown on figure 5.12. These extend to 20 T, and a good fit of the 3.5 K curve is obtained with the four terms. The main contributions are two-band magnetoresistance and ionised impurity scattering. From the fit to the expression for the

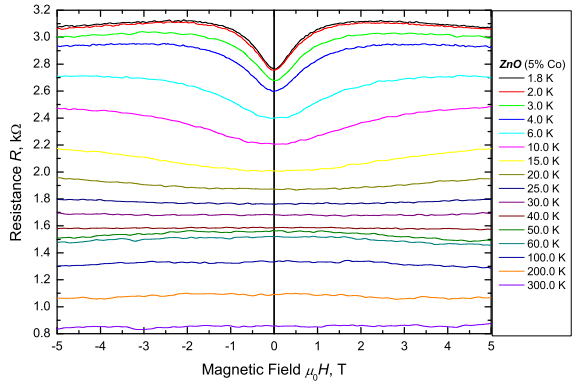

Figure 5.10: Magnetoresistance of a 5 % Co doped ZnO film, demonstrating peculiar behaviour at low temperatures. The magnetic field is applied out of the plane of the film.

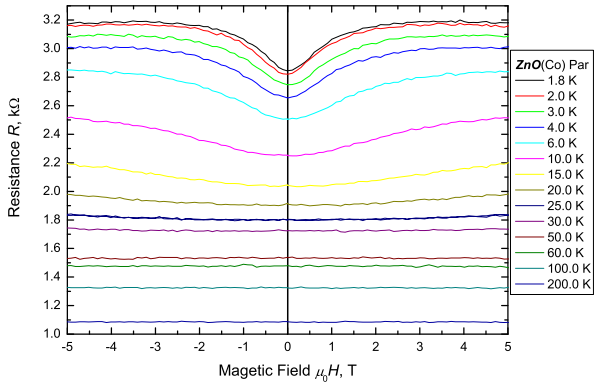

Figure 5.11: Same as figure 5.10, with the magnetic field applied in the plane of the film.

scattering from singly-occupied localised states, we find $\mu_0 f = 4.5$ T, which corresponds to a moment of $1.1 \pm 0.1\ \mu_B$, as expected. This confirms the origin of the negative magnetoresistance mechanism in the paramagnetic samples.

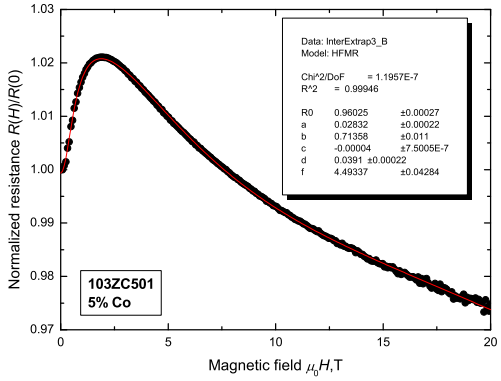

Figure 5.12: A fit to the magnetoresistance of a 5 % Co doped ZnO film prepared at 600 °C, using a combined model, taking into account two band contribution and ionised impurity scattering.

On lowering the temperature to 1.2 K, Shubnikov de Haas oscillations appear in the magnetoresistance. Two series can be resolved (see figure 5.13), with periods in $1/B$ of 0.30 T^{-1} and 0.05 T^{-1}. The corresponding extremal areas of the Fermi surface are $3.2 \cdot 10^{16}$ and $1.9 \cdot 10^{17}$ m^{-2}.

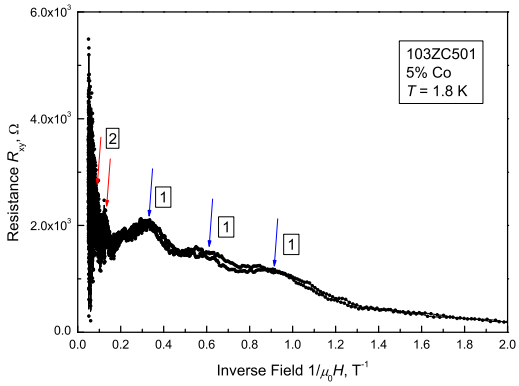

Figure 5.13: Quantum oscillations in a 5 % Co doped ZnO film prepared at 600 °C, measured at $T = 1.8$ K. The peaks corresponding to two different extremal cross sections of the Fermi surface are indicated.

The ferromagnetic sample with x = 0.04 is of poorer crystalline quality, and no quantum oscillations were observed at low temperatures. Data obtained for x = 0.25 at 2 K are included in

Fig. 5b(bottom). The data for dilute ferromagnetic samples are consistent with coherent spin-transport in a ferromagnetic matrix. The anhysteretic magnetic sample with x = 0.04 shows signs of magnetic scattering (small negative magnetoresistance contribution) in low fields (Fig 3b). The ferromagnetism here may be of the 'wandering axis' or 'random anisotropy' variety, with a short spin coherence length in zero applied field. Data for the x = 25 % films (see figure 5.8) suggest that spin-polarized electrons can tunnel coherently between well-separated cobalt clusters, which account for some in the cobalt in these materials.

The mobility in all the present ferromagnetic samples is rather small (of order 20 $cm^2V^{-1}s^{-1}$), and it decreases rapidly with increasing temperature. As a result, the magnetic term iv) in the magnetoresistance is small, and the anomalous Hall effect is practically unmeasurable. In other words, s-d scattering is not dominant in this system.

5.5 Al co-doping

Additional insights for the behaviour of the ZnO:Co system are gained by co-doping with Al. Al being a donor in this system, greatly increases the carrier concentration, thus allowing a study of the transport and magneto-transport at different positions for the Fermi level. The electron gas in this system can be made fully degenerate metallic temperature behaviour of the resistivity, with as little as 1 % of additional Al co-doping as illustrated on figure 5.14. It

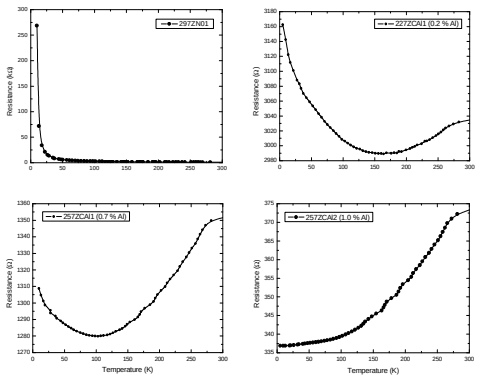

Figure 5.14: An illustration of the degeneration of the electron gas upon increasing of the carrier concentration via Al co-doping.

becomes evident also that the role of Co is not only to be an isovalent substitute for Zn^{2+}, but rather to produce deep traps within the energy gap (see table 5.5). There is evidence, as well, that films prepared on different substrate orientations, apart from growing with a different crystallographic texture, also have a slightly different electronic structure.

$n \times 10^{22}, \mathrm{cm}^{-3}$	R-cut Al_2O_3	C-cut Al_2O_3
ZnO	0.81	2.90
$Zn_{0.95}Co_{0.05}O$	0.42	0.11
$Zn_{0.95}Co_{0.05}OAl_{0.002}$	2.22	3.73

Table 5.1: Apparent carrier concentrations in various ZnO thin films deposited on C-cut and R-cut sapphire.

The Al co-doping becomes inefficient once the electron gas is fully degenerate, as shown on figure 5.15. And this may be attributed to a non-parabolicity of the conduction band at high fillings.

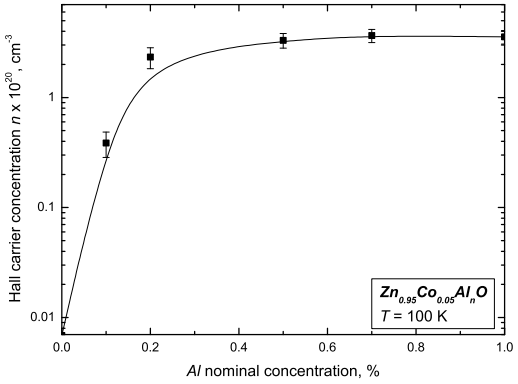

Figure 5.15: Apparent carrier concentration as a function of nominal Al concentration. Note the saturation over about 0.2 % nominal Al content.

At high doping levels (large carrier concentrations), the low-lying states in the conduction band become occupied and inaccessible for optical transitions. This causes an apparent band gap widening (Burstein-Moss effect). This is illustrated on figure 5.16. The expected functional dependence:

$$\Delta E_{\mathrm{g}} = \frac{\hbar^2}{2m^\star} \times \left(3\pi^2 n_{\mathrm{e}}\right)^{\frac{2}{3}} \tag{5.5.1}$$

is well satisfied within the experimental error and yields a mean harmonic mass defined as:

$$\frac{1}{m^\star} = \frac{1}{m_{\mathrm{e}}^\star} + \frac{1}{m_{\mathrm{h}}^\star} \tag{5.5.2}$$

with a value of $m^\star = 0.26(3)\ m_{\mathrm{e}}$ which is in good agreement with the accepted values for $m_{\mathrm{e}} = 0.23$ and $m_{\mathrm{h}} = 0.59$ for Al-doped ZnO.

Weakly co-doped films show normal semiconducting temperature activation of the carriers (see figure 5.17), though, the activation energy (7.9 meV) is strikingly different when compared with a undoped ZnO film (2.9 meV) as illustrated on figure 5.18.

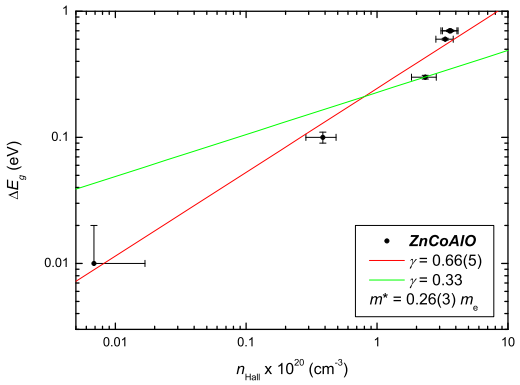

Figure 5.16: Illustration of the Burstein-Moss shift in Al co-doped ZnCoO.

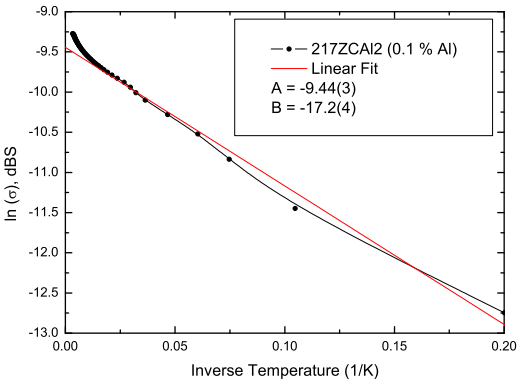

Figure 5.17: Activation of the carriers in 5 % Co doped, 0.1 % Al co-doped ZnO film. The activation energy is 7.9 meV.

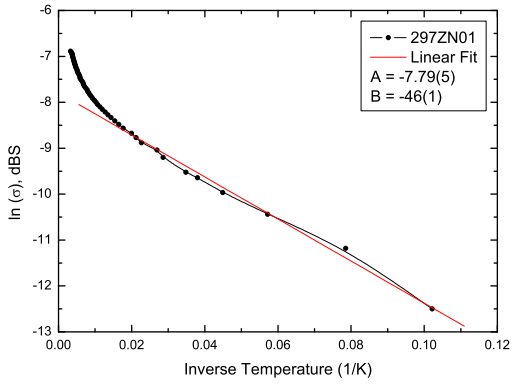

Figure 5.18: Activation of the carriers in undoped ZnO film. The activation energy is 2.9 meV.

The field dependence of the Hall effect shows no sign of anomalous contributions for all compositions, within the experimental uncertainties. For an example see figure 5.19.

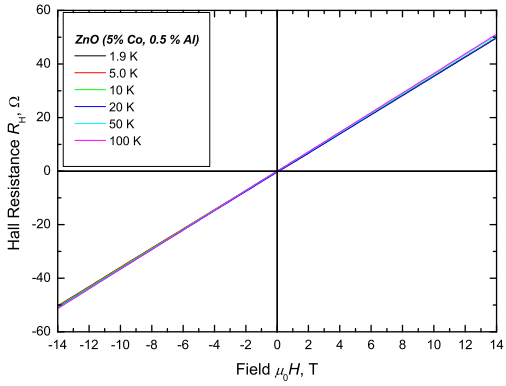

Figure 5.19: Hall resistance of a 5 % Co doped, 0.5 % Al co-doped ZnO film. Note the miniscule changes of the gradient with temperature.

The Hall coefficient shows week temperature dependence for all but the very dilute compositions (see figure 5.20), as expected for a quasi-degenerate electron gas. The magnetoresistance

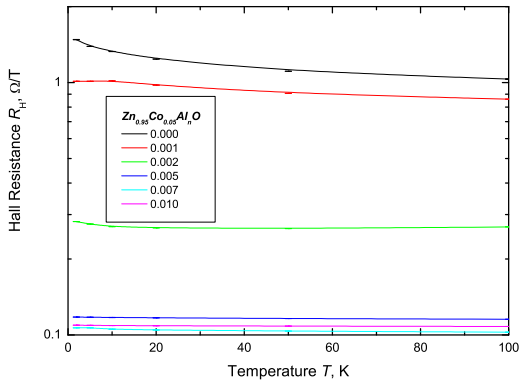

Figure 5.20: Hall coefficient as a function of temperature for a series of different Al co-dopant concentrations.

is dominated by the weak localisation contribution (see figure 5.21) and can vary substantially with small variations of the film thickness, because of the dimensional crossover already mentioned in section 5.1.

In conclusion, we can explain the magnetoresistance in a variety of doped and undoped ZnO samples in terms of four elementary terms. Our results suggest that co-doping with Al will not improve the magnetoresistance. Co-doping that creates deep traps will only exacerbate the scattering. This might be done by controlling the defects entailed by oxygen substoichiometry

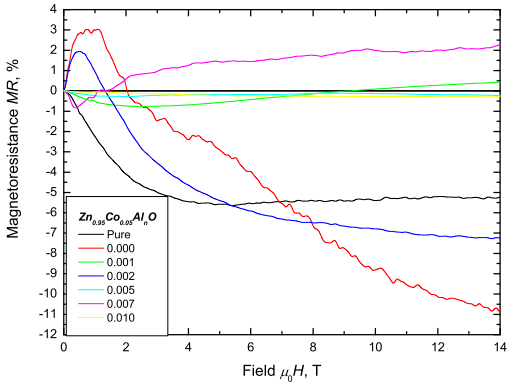

Figure 5.21: Magnetoresistance measured at $T = 2.0$ K , for a series of different Al co-dopant concentrations.

to give small, but highly mobile carrier concentrations. If these defects are responsible in some essential way for the ferromagnetism, prospects for useful magnetoresistive functionality may be dim.

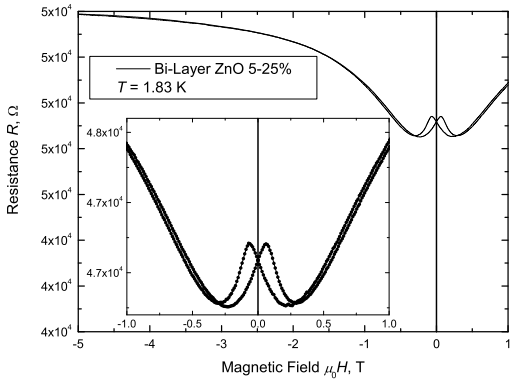

Figure 5.22: Magnetoresistance of a bi-layer structure (5 / 25 % Co doped ZnO), showing 'butterfly' shape, characteristic of the magnetic hysteresis of the Co clusters of the 25 % Co doped layer.

5.6 AMR data

The angular dependence of the magnetoresistance is the second best transport method to study the anisotropy of the Fermi surface, when ShdH oscillations are nonexistent, due to, for example, low mobility of the material system studied. The use of high magnetic fields gives the ability to differentiate between the different effects present.

Simple harmonic scaling with the out of plane angle is to be expected when the dominant

high-field transport mechanism is scattering from ionised impurities. This is, indeed, the case for moderate levels of Co doping in ZnO, as evidenced by figure 5.23. The shape of the curves remains practically unchanged.

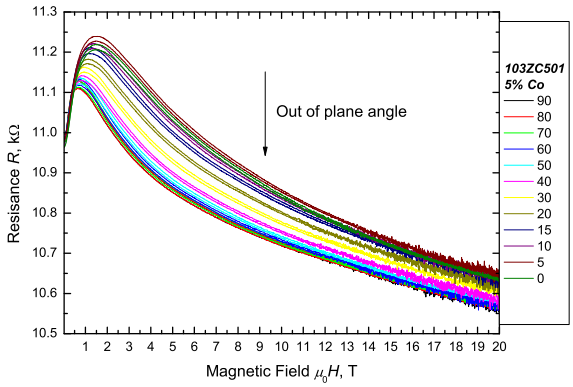

Figure 5.23: Resistance of a 5 % Co doped ZnO film prepared at 600 °C, as a function of magnetic field at various angles out of plane of the film, measured at $T = 1.8$ K.

The situation is dramatically different at large Co concentrations when there is a very significant formation of Co clusters giving rise to a non-negligible AMR effect which alters the behaviour of the total magnetoresistance with angle. Similar situation is visualised at figure 5.24 for a 25 % Co-doped ZnO sample.

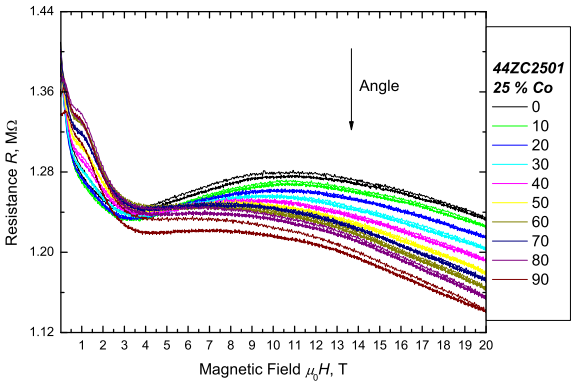

Figure 5.24: Resistance of a 25 % Co doped ZnO film prepared at 500 °C, as a function of magnetic field at various angles out of plane of the film, measured at $T = 1.8$ K.

Rotation of the applied magnetic field in the plane of the thin film gives rise to what resembles anisotropic magnetoresistance. An example for a particular field and temperature is shown on figure 5.25. Apparently, fits to the data using expression 5.1.12, can still be

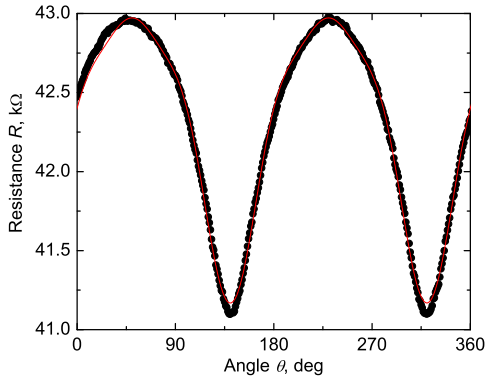

Figure 5.25: Angular dependence of the anisotropy of the magnetoresistance for a 4 % Co doped ZnO film, measured at $T = 2.0$ K and $\mu_0 H = 1$ T.

done, independently of whether or not, the observed effect is AMR or other magnetoresistance anisotropy. The coefficients of the different orders of $\cos\theta$, can then be annalised as functions of field and temperature, by performing the corresponding angular scans. Results for the first two orders coefficients are presented on figures 5.26 and 5.27, for a 4 % Co-doped ZnO sample at $T = 2.0$ K. They, obviously, do not correspond well to the naively expected scaling of

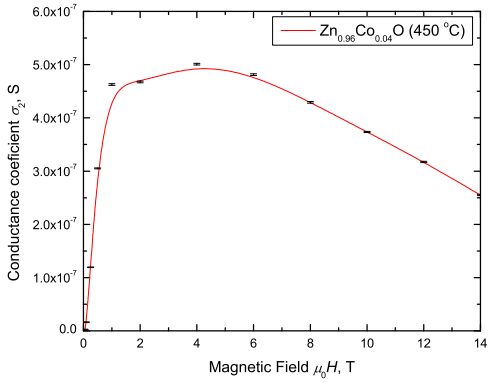

Figure 5.26: Field dependence of the second order anisotropic conductance coefficient for a 4 % Co doped ZnO film.

the AMR coefficients with the square of the magnetisation, illustrated on figure 5.28.

The temperature dependence of the second order conductance coefficients is even more spectacular, showing a well defined, and virtually sample independent, extremum at about 3 K, as evidenced by figures 5.29 and 5.30. The fourth order coefficient, however, exhibits no such an extremum, as shown o figure 5.31. It thus becomes clear, that the observed effect is related to anisotropy of the electronic structure, rather than conventional AMR.

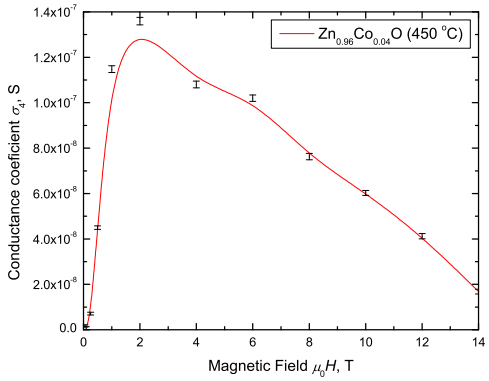

Figure 5.27: Field dependence of the fourth order anisotropic conductance coefficient for a 4 % Co doped ZnO film.

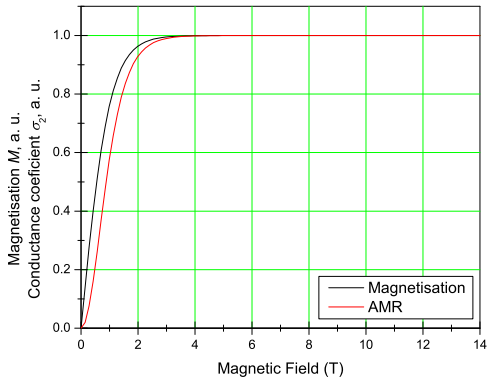

Figure 5.28: Intuitive expectation for the field dependence of the second anisotropic magnetoresistance coefficient, at low temperature.

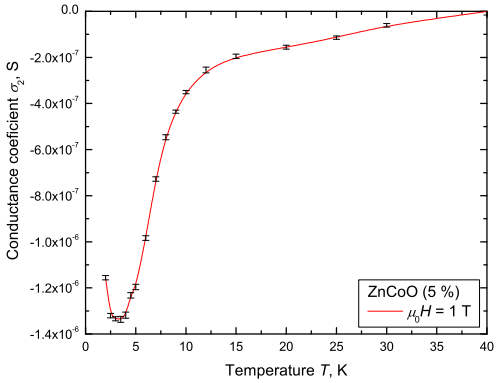

Figure 5.29: Temperature dependence of the second order anisotropic conductance coefficient for a 5 / 25 % Co doped ZnO bi-layer film.

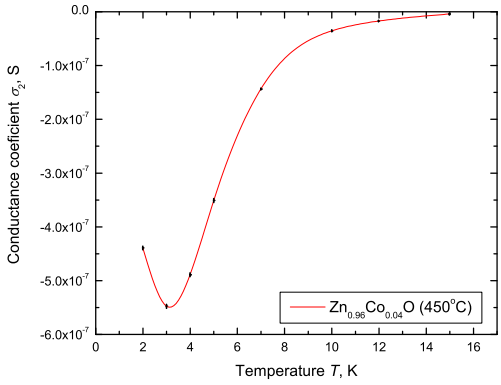

Figure 5.30: Temperature dependence of the second order anisotropic conductance coefficient for a 4 % Co doped ZnO film.

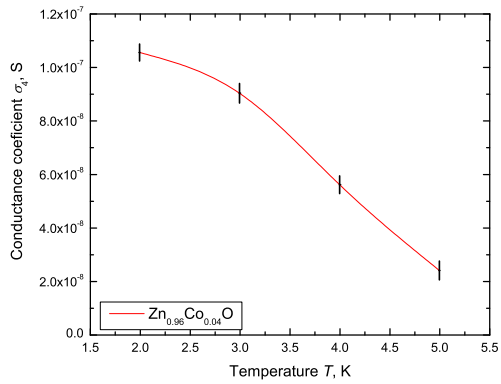

Figure 5.31: Temperature dependence of the fourth order anisotropic conductance coefficient for a 4 % Co doped ZnO film.

The field and temperature dependence of the second order coefficients for three different Al concentrations of 0, 0.2 and 1.0 %, are shown on figures 5.32, refFigG2AllS2 and refFigG5AllS2, respectively. The data for the intermediate Al doping levels is not shown as it consists of trivial experimental zeros, which brings about the idea of a purely electronic effect, varying in magnitude with the occupation of the available states is changing upon the change in carrier concentration.

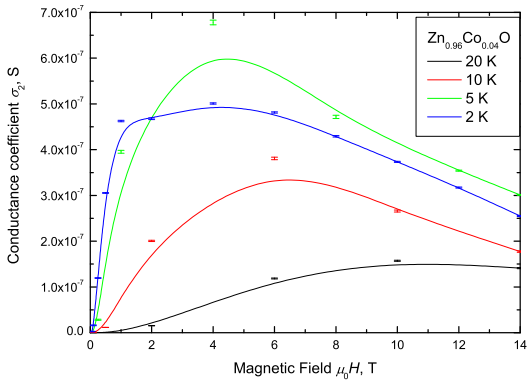

Figure 5.32: Field temperature scaling for the second order anisotropic conductance coefficient for a 4 % Co doped ZnO film.

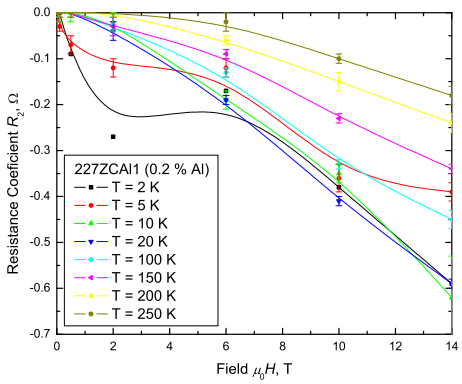

Figure 5.33: Second order anisotropic resistance coefficient as a function of field and temperature, for a 0.2 % Al co-doped, nominally 5 % Co in ZnO sample, deposited on c-cut sapphire.

It is possible, also for samples with sufficiently high mobility, to map all anisotropic conductance coefficients up to sixth order in $\cos\theta$, as shown on figures 5.35, 5.36 and 5.37.

The scaling with field and temperature can then be compared with the suggested form of equation 5.1.15, for two exemplary cases - electron effective mass $m^\star = 0.24\ m_e$ in ZnO and

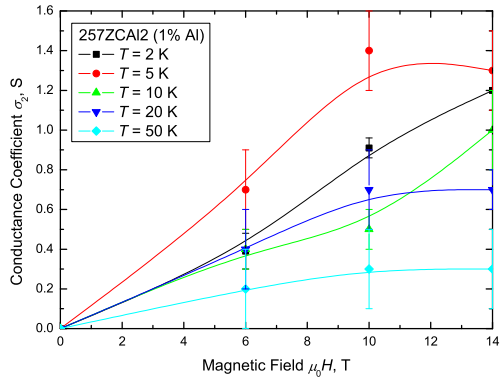

Figure 5.34: Second order anisotropic conductance coefficient as a function of field and temperature, for a 1.0 % Al co-doped, nominally 5 % Co in ZnO sample, deposited on c-cut sapphire.

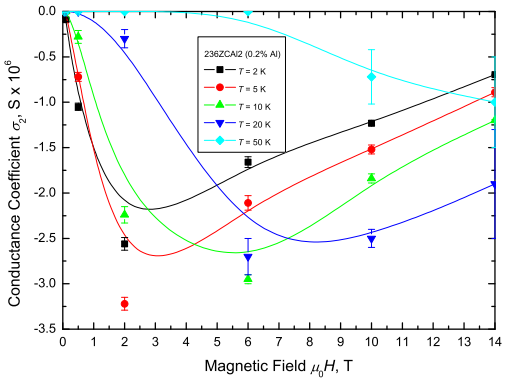

Figure 5.35: Second order anisotropic conductance coefficient as a function of field and temperature, for a 0.2 % Al co-doped, nominally 5 % Co in ZnO sample.

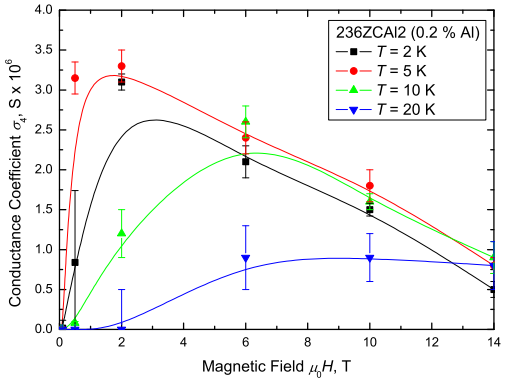

Figure 5.36: Fourth order anisotropic conductance coefficient as a function of field and temperature, for a 0.2 % Al co-doped, nominally 5 % Co in ZnO sample.

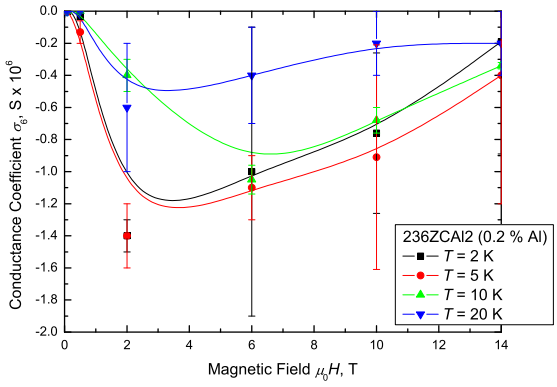

Figure 5.37: Sixth order anisotropic conductance coefficient as a function of field and temperature, for a 0.2 % Al co-doped, nominally 5 % Co in ZnO sample.

Dingle temperature of $T_{\mathrm{D}} = 5$ K, as demonstrated on figure 5.38; and hole effective mass of $m^{\star} = 1.21\ m_{\mathrm{e}}$ and Dingle temperature of $T_{\mathrm{D}} = 20$ K, shown on figure 5.39.

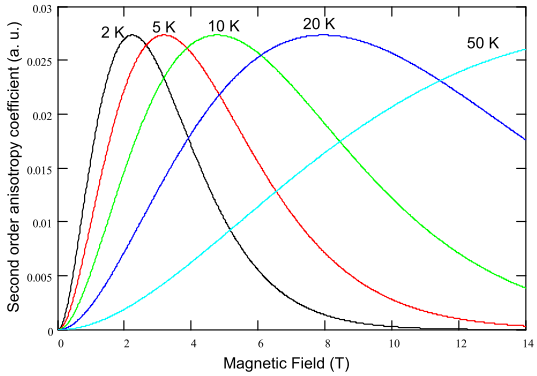

Figure 5.38: Magnitude of the second order anisotropy coefficient as a function of applied magnetic field for the temperatures shown. The electron effective mass is fixed at $m^{\star} = 0.24\ m_{\mathrm{e}}$, and the Dingle temperature is chosen to be $T_{\mathrm{D}} = 5$ K.

It may be argued that there is a reasonable correspondence between the theoretical scalings and the measured ones on at least two different occasions. Thus the magnetoresistance angular oscillations, can in principle be used to compare theoretical data for the realistic electronic structure of the material, provided a detailed calculation of the corresponding pre-factors is executed.

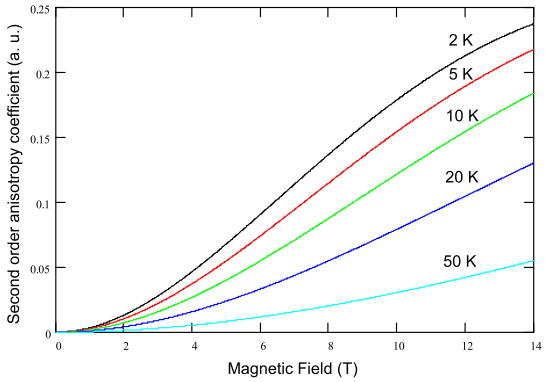

Figure 5.39: Magnitude of the second order anisotropy coefficient as a function of applied magnetic field for the temperatures shown. The electron effective mass is fixed at $m^\star = 1.21\ m_\mathrm{e}$, and the Dingle temperature is chosen to be $T_\mathrm{D} = 20$ K.

5.7 Magnetisation Data

Further evidence for the existence of hcp-Co metal clusters, apart from the Co^{2+} ions dissolved in the host matrix is presented by the low temperature magnetisation measurement. Figure 5.40 illustrates the unreduced (not raw) experimental magnetisation curves at various temperatures between 1.8 and 300 K. A zoom-in at the low field part of the dataset (see figure 5.41) at the

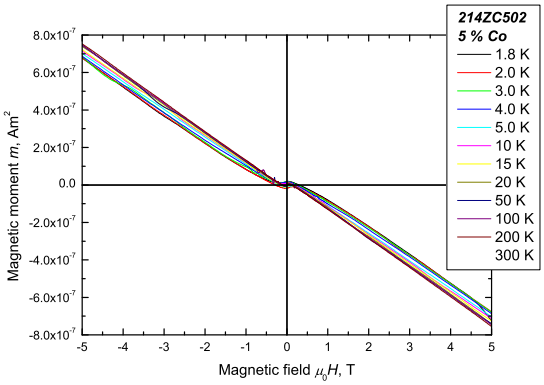

Figure 5.40: Magnetic moment as a function of temperature for a 5 % Co doped ZnO film on Al_2O_3 substrate, prepared at 450 °C. The individual curves are measured at the temperatures indicated.

two extreme temperatures reveals the developing of coercivity, which may be considered as a sign of the presence of Co clusters in the system.

In order to reduce the data further, the high field slopes would normally be substracted from the individual curves. A more reliable procedure is to first find the distribution of slopes,

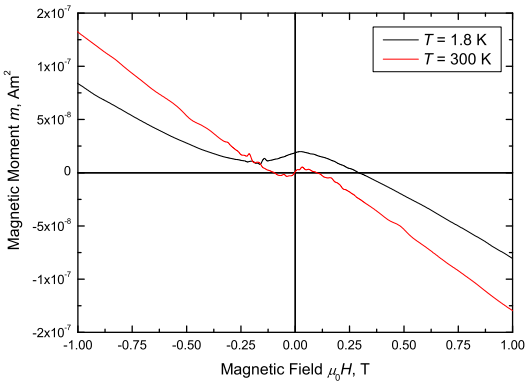

Figure 5.41: Low field part of the data set shown on figure 5.40, at the extreme temperatures. Note the very different magnetisation behaviour in the two cases.

and if that is sufficiently flat, as illustrated on figure 5.42, to substract the average slope from the entire dataset.

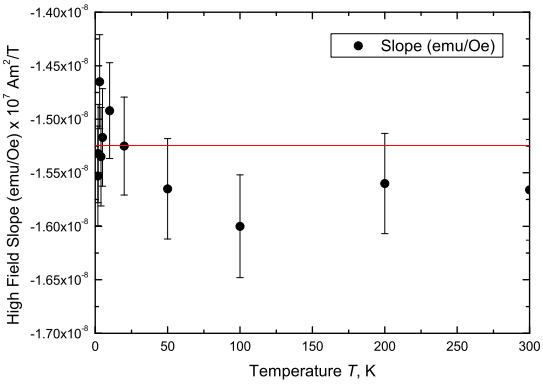

Figure 5.42: High field slopes of the magnetic moment vs temperature curves from figure 5.40, showing essentially constant with respect to the measurement errors value of 0.154 Am^2/T.

The result from such a procedure, which with a great deal of confidence, ensures that the purely diamagnetic contribution of the substrate is substracted correctly, is shown on figure 5.43.

The saturating part of the magnetic moment can then be extracted and plotted separately on an inverse temperature scale, in order to resolve the ferromagnetic and paramagnetic contributions to the magnetisation curves, as illustrated on figure 5.44 It should be noted that the paramagnetic component also saturates at high fields and low temperatures. The resulting Curie constant of the paramagnetic component and total magnetic moment value for the ferro-

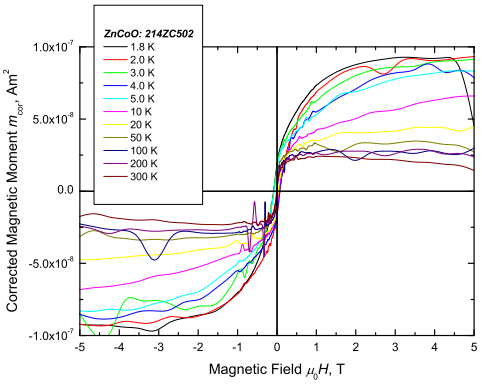

Figure 5.43: Magnetic moment as a function of temperature for a 5 % Co doped ZnO prepared at 450 °C, after substraction of the diamagnetic contribution of the substrate.

magnetic component can be then used to deduce the ratio of the masses of Co^{2+} ions and Co metal in clusters. For this example, this ratio is 3:1, in favor of the Co metal clusters.

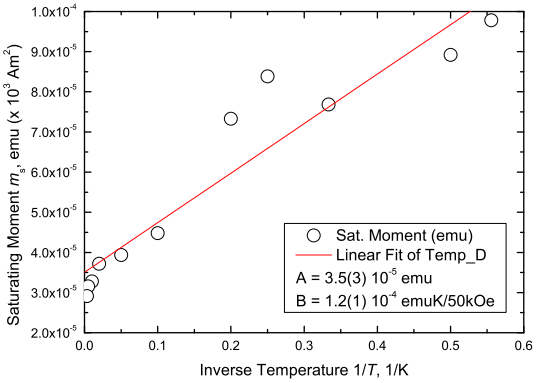

Figure 5.44: Saturating moment at $\mu_0 H = 5$ T as a function of inverse temperature, as extracted from the data set of figure 5.43. Note the paramagnetic and the ferromagnetic contributions.

From the temperature activation of the coercive field measured, an evaluation of the energy scale involved can be made (in this case uniaxial magneto-crystalline anisotropy). This can be compared to known values for the uniaxial magneto-crystalline anisotropy of bulk Co. In this fashion a rough estimate of the Co cluster size can be made. In this example, the deduced average size is about 8 nm.

In this way, by employing conventional magnetisation measurements, strong circumstantial evidence for the formation of Co metal clusters in the candidate for dilute magnetic semiconductor material Co:ZnO is found.

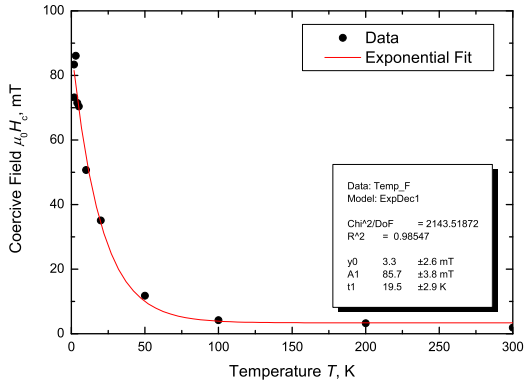

Figure 5.45: Temperature dependence of the coercive field for the data set shown on figure 5.43. Note the pronounced exponential behaviour and the coercivity offset due to the hysteresis of the superconducting magnet used for the measurements.

Chapter 6

Magnetism of Carbon

6.1 Brief account of the magnetism of Carbon

The magnetic properties of graphite and other structures composed of graphene-like sheets are a subject of renewed scrutiny, following reports of internal field Sercheli *et al.* (2002) and Han *et al.* (2004) in graphite, ferromagnetism Esquinazi *et al.* (2002) in graphite, proton-irradiated graphite Esquinazi *et al.* (2003), disordered graphite Höhne *et al.* (2004) and Makarova *et al.* (2001, 2003); Wood *et al.* (2002) fullerenes, and even superconductivity[1] Kempa *et al.* (2000); Kopelevich *et al.* (2003b) in graphite. It is difficult to be sure that small ferromagnetic moments are intrinsic effects in view of the ubiquity of low-level contamination of samples and addenda by traces of ferromagnetic iron or magnetite. There is also evidence, that magnetism can be induced by spin-polarised charge transfer at the interface between a ferromagnetic metal and carbon nanotubes Céspedes *et al.* (2004) or a graphite sheet Ostling *et al.* (1997). A variety of magnetic behaviours have been predicted theoretically for graphene-based carbon structures. For example, antiferromagnetism has been argued to exist theoretically in stacked nanographite (Hari01, Hariga01, Enoki02).

The magneto-transport properties of graphite are also a subject of renewed interest, following the theoretical speculation (Khveshchenko (2001a,b)) and experimental observation (Kopelevich *et al.* (2003a)) of what is argued to be magnetic field induced excitonic insulator transition, as well as true two-dimensional character of the electron gas, leading to quantum Hall effect, as conventionally observed in artificial gated high-mobility structures (originally discovered by v. Kiltzing *et al.* (1980), and consecutively theorised by Laughlin (1981) and Halperin (1982)). The unconventional magneto-transport data has later been attributed to pe-

[1] This is different from the superconductivity found in some graphite intercalated compounds, like for example C-S (see da Silva *et al.* (2001)).

culiarities of the graphite electronic structure modelled within the two-carrier framework (Du *et al.* (2004, 2005)).

Carbon-based solids are normally diamagnetic (Haddon (1994); Ramirez *et al.* (1994)), known exceptions being the paramagnetic behaviour of very disordered structures, like for example, glassy carbon (Wang *et al.* (2002)) and carbon nanofoam (Rode *et al.* (2004)). The main contribution is orbital diamagnetism from electrons confined in closed orbits, including the inner electron shells:

$$\kappa_{\mathrm{orb}} = -N\mu_0 q^2 \frac{\langle r_i^2 \rangle}{6m_{\mathrm{e}}} \tag{6.1.1}$$

where N is the number of atoms per unit volume, q and m_{e} are the charge and the mass of the electron and $\mu_0 = 4\pi 10^{-7}\mathrm{TmA}^{-1}$ is the free space permeability. $\langle r_i^2 \rangle$ is the mean square radius of the orbit in the xy plane, perpendicular to the applied field direction z. κ is the dimensionless SI susceptibility, which cannot exceed -1. For most solid elements it is in the range $-10^{-5} \ldots -10^{-6}$. Diamond has $\kappa = -2.2 \cdot 10^{-5}$. Compounds with benzene rings exhibit stronger diamagnetism because the π-electrons are confined in larger orbits. This helps to explain why the susceptibility of graphite is so anisotropic, with a value of $-2.6 \cdot 10^{-4}$ when the field is applied along the c-axis, but the in-plane susceptibility of $-3.8 \cdot 10^{-6}$ is less than that of diamond. Apart from macroscopic magnetisation, the magnetic susceptibility and its anisotropy can be inferred from NMR[1] and EPR[2] (see for example Goze-Bac *et al.* (2002)).

Further contributions to the susceptibility arise from the conduction electrons. In a magnetic field, the electronic energy levels condense into a few, highly degenerate Landau levels. The Landau diamagnetic susceptibility for the free-electron gas:

$$\kappa_{\mathrm{L}} = -N_{\mathrm{c}}\mu_0 \frac{\mu_{\mathrm{B}}^2}{2kT_{\mathrm{F}}} \tag{6.1.2}$$

is precisely one third as large as the Pauli paramagnetic susceptibility κ_{P}, but of opposite sign.Landau & Livshitz (1982) Here T_{F} is the Fermi temperature and N_{c} is the conduction electron density. More generally the ratio $\kappa_{\mathrm{L}}/\kappa_{\mathrm{P}}$ is $(1/3)(m_{\mathrm{e}}/m^\star)^2$, because the Landau term depends on the effective mass $m^\star$. When $m^\star$ is small, the diamagnetic contribution can outweigh the paramagnetic one. Generally, the division of the different terms in the susceptibility into diamagnetic and paramagnetic is gauge dependent, and therefore has no real physical significance (see for example Haddon (1994)). As the Landau levels are swept through the Fermi level, characteristic de Haas - van Alphen (dHvA) oscillations appear in the low temperature susceptibility.

[1] Nuclear Magnetic Resonance
[2] Electronic Paramagnetic Resonance

The electronic structure of nanotubes depends on their radius and chirality. A tube is represented by a pair of integers (n, m) or the chiral vector $\mathbf{L} = n\mathbf{a} + m\mathbf{b}$, along which the tube is wound from t[illegible] periodic boundary

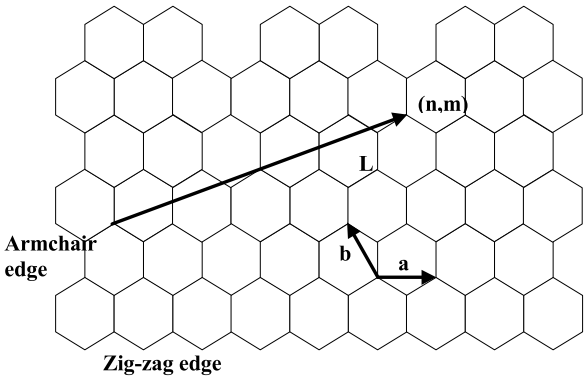

Figure 6.1: The coordinates on a graphene sheet.

conditions in this form, the structure can be calculated by means of a tight-binding model and the band structure of a 2D graphene sheet. A $\mathbf{k}\cdot\mathbf{p}$ method or effective mass approximation is also successful in describing a variety of electronic properties, including electronic wave interference patterns (Harigaya *et al.* (2002)), the Aharonov - Bohm effect (Bachtold *et al.* (1999)) and the bulk value of the diamagnetic susceptibility of ensembles of nanotubes (Fujiwara *et al.* (1999)).

The bulk magnetic susceptibility has not been measured for single-walled specimens for a specific n and m. Often measurements have been performed on very assorted mixtures of nanotubes (Bandow (1996); Bandow *et al.* (2001)). Single-walled nanotubes are grown using a transition-metal catalyst which forms a particle at the end of the tube. The ferromagnetic signal from these iron or cobalt particles may obscure the response of the tube itself. The orbital moment may, though, be deduced from the conductance through a gated nanotube in an applied magnetic field. The values of the orbital moment are estimated to be $10 \ldots 20$ Bohr magnetons (Minot *et al.* (2004)). Data are available, however, for multi-walled tubes which are mixtures of tubes of different radii and chirality. Heremans *et al.* (1994); Ramirez (1994) The anisotropy of the susceptibility and the spin gyro-magnetic ratio was studied on partially oriented ensembles Chauvet *et al.* (1995); Likodimos *et al.* (2003); Tsui *et al.* (2000) and the temperature dependence of the perpendicular component of the magnetic susceptibility is explained in terms of a simple two band electronic structure. Kotosonov (1999); Kotosonov & Kuvshinnikov (1997) The analysis of the existing data on magnetisation of ensembles of nanotubes is complicated by the following factors.

(a) The magnetisation of the ensemble is generally non-linear with field (which may be due to ferromagnetic impurities at small fields, or intrinsic, due to size effects in the tubes at high fields).

(b) The anisotropy of the magnetisation has to be inferred from partially oriented samples.

(c) The magnetisation exhibits substantial temperature dependence, which may be different for different partial orientations.

(d) is difficult to acquire substantial amounts of ultra-high purity nanotubes.

In contrast to the magnetisation measurements, which are very difficult to realise on a single nanotube, transport measurements have been reported multiple times on individually contacted samples with and without gate electrodes (see for example Minot *et al.* (2004) and Biercuk *et al.* (2004)).

Hereafter, the

6.2 Theoretical and Experimental Consideration on the Diamagnetism of Graphite

6.2.1 Historical remarks

Unlike its crystallographic structure (see figure 6.2), the electronic structure and properties of graphite has been a subject of a very large number of publications. The suggestion that the small effective mass of semimetallic systems like bismuth and graphite, may be the source of their large diamagnetic susceptibilities has been systematically studied by Adams (1953).

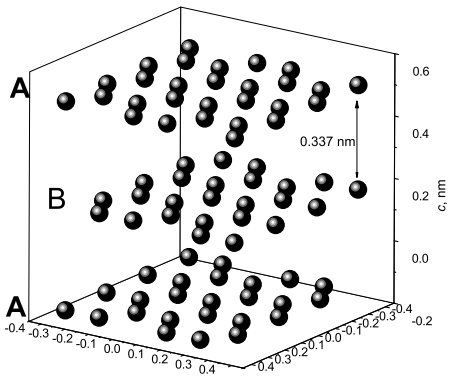

Figure 6.2: The crystallographic structure of graphite.

In the early models of the diamagnetic susceptibility of graphite, the majority of efforts have been devoted to describing the anisotropy and temperature dependence of the susceptibility based on different models for the electronic structure, by using the dispersive relations in the graphene planes:

$$\chi = \frac{\mu_{\mathrm{B}}^2}{12\pi^2}\left(\frac{m^\star}{\hbar^2}\right)^2 \int \left[\frac{\partial^2 E}{\partial k_x^2}\frac{\partial^2 E}{\partial k_y^2} - \left(\frac{\partial^2 E}{\partial k_x \partial k_y}\right)^2\right] \frac{\partial f}{\partial E} \mathrm{d}^3\mathbf{k} \tag{6.2.1}$$

and analogue ones for the case of external magnetic field being applied in the plane of the structure (see Hove (1955); McClure (1956) and references therein) and averaging using the Fermi-Dirac statistics.

Later the $\mathrm{k}\cdot\mathrm{p}$ method has been applied together with the tight-binding approximation to describe the band structure, both near the edges of the Brilloin zone, and deeper in the zone (McClure (1957)), and reproduce the main features of the experimental data on de Haas - van Alphen Effect and cyclotron resonance (McClure (1960); Noziéres (1958); Sharma *et al.* (1974)).

The energy band structure and the Fermi surface of graphite (sketched on figure 6.3) have been a subject of a very large number of publications, only as examples the following may be mentioned (Dresselhaus & Mavroides (1964); McClure (1964); Soule (1964); Tatar & Rabii (1982); Woollam (1971b)). In summary, the electron and hole Fermi surfaces are highly elongated and are aligned parallel to the c-axis of the crystal structure, with anisotropy coefficient of about 12:1, and appreciable trigonal warping. The surfaces are not ellipsoidal, and an effective mass model is only a rough approximation, being about 0.06 m_{e} and 0.04 m_{e} for majority electrons and holes, respectively. The carrier densities are about $3\cdot10^{18}$ cm^{-3} or less, at low temperatures. Minority carriers are also present with masses 0.0023 m_{e} for holes, and 0.017 m_{e} for electrons, and a concentration of about $6\cdot10^{14}\mathrm{cm}^{-1}$ (see McClure (1958)). The spin-orbit interaction constant have been estimated at 10^{-2} eV by Woollam (1970).

6.2.2 de Haas - van Alphen and Shubnikov - de Haas oscillations

Early studies of the thermodynamic and kinetic oscillatory effects in graphite (see Berlincourt & Steele (1953) and references therein), have employed simple data processing routines. In most cases only the frequency information has been retained, as extraction has been performed by peak selection and of the extrema (both minima and maxima) of the oscillatory components of susceptibility and resistance, among other physical properties measured. Generally, series of the form:

$$y = \sum_i \left[a_0^y\left(B,T,m_i^\star,E_i^0\right) + a_1^y\left(B,T,m_i^\star,E_i^0\right)\sin\left(2\pi\frac{E_i^0 m_i^\star}{q\hbar}\frac{1}{B} + \theta_i^y\right)\right] \tag{6.2.2}$$

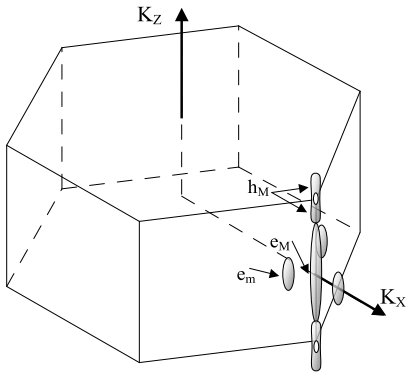

Figure 6.3: The crystallographic structure of graphite.

where y is the physical property of interest, a_0^y and a_1^y are ofset and amplitude functions, $m_i^\star$ are the effective masses, and E_i^0 are the offsets of the constant energy surfaces measured (from either the bottom of the conduction band, for electrons; or the top of the valence band, for holes) corresponding to the i-th quasiparticle type present in the system, and θ_i^y are phase offsets, which depend on both the quasiparticle and the oscillatory effect under consideration.

Later investigations have employed the Lifshitz - Kosevich theory of oscillatory galvanomagnetic effects in metals with 3D dispersions (see for example Soule (1958); Soule *et al.* (1964b)). It is customary to normalise the measured magnetoresistance by the Hall coefficient and denote it as G. The oscillating part of G can be then written as:

$$\tilde{G} = B^s \left\{ \sum_i a_i \sum_{p=1}^{\infty} b_{pi} \exp\left[p\pi^2 \frac{m_i^\star}{m_\mathrm{e}} \frac{k\,(T+T_\mathrm{D})}{g^\star \mu_\mathrm{B} B} \right] \sinh^{-1}\left(p\pi^2 \frac{m_i^\star}{m_\mathrm{e}} \frac{kT}{g^\star \mu_\mathrm{B} B} \right) \cos\left(2\pi p \frac{A_i}{q\hbar} \frac{1}{B} - \theta_r \right) \right\} \tag{6.2.3}$$

where B is the external magnetic field, a_i and b_{ip} are constant coefficients in the Fourier-like expansion, $m_i^\star$ are the effective masses describing the quasiparticle indexed by i, A_i are the extremal Fermi surface cross sections (in units $\hbar^2 \mathrm{m}^{-2}$), θ_i are the corresponding phase offsets, and T_D is the Dingle temperature defined as:

$$T_\mathrm{D} = \frac{\hbar}{\pi k \tau_\mathrm{a}} \tag{6.2.4}$$

where τ_a is an athermal characteristic scattering time. The extremal cross sections A_i and the energy offsets E_i^0 are related as:

$$A_i = m_i^\star E_i^0 \tag{6.2.5}$$

and E_i^0 can be related to the carrier densities n_i in the free-electron gas approximation:

$$E_i^0 = \frac{\hbar^2}{2m_i^\star} \left(3\pi^2 n_i\right)^{\frac{2}{3}} \tag{6.2.6}$$

and the offsets E_i^0 thus correspond to the Fermi levels for the respective quasiparticles measured with respect to the corresponding band edge.

In the derivation of the series 6.2.3, several important assumptions have been made. First, the thermal broadening must be smaller than the magnetic energy level separation or:

$$\frac{kT}{g^\star \mu_B B} \lesssim 1 \tag{6.2.7}$$

Second, the temperature should be much lower, as compared to the Fermi temperature, so that Fermi-statistics is valid:

$$\frac{kT}{E^0} \ll 1 \tag{6.2.8}$$

Third, the number of quantum levels below the Fermi level must be large, in order for the Fresnel integrals used in the derivation to be readily evaluated at infinity:

$$\frac{g^\star \mu_B B}{E^0} \ll 1 \tag{6.2.9}$$

Therefore, strong magnetic fields, low temperatures, and high Fermi levels, significantly simplify the analysis of the galvanomagnetic data.

Later studies have extended to high hydrostatic pressures (Anderson *et al.* (1967)), modifications produced by neutron irradiation (Cooper *et al.* (1970)), and High magnetic fields of about 10 T (Woollam (1971a)). Spin splitting has been studied by Woollam (1970). Recently, multiple oscillatory effects have been measured by Ocana *et al.* (2003), and phase analysis of the quantum oscillations has been performed by Luk'yanchuk & Kopelevich (2004).

6.2.3 Magnetic Zener Breakdown

In analogy with the electrical Zener effect, occurring when the externally applied electric field $\mathcal{E}$ is strong enough, so that:

$$\frac{q\,(\mathcal{E}a)\,E_F}{E_g^2} > 1 \tag{6.2.10}$$

so that the potential difference accumulated by an electron when tunnelling between two crystal planes, situated a distance of a apart, becomes comparable with the energy gap, and therefore, direct impact ionisation becomes possible; a magnetic Zener effect can be envisaged (see Ziman (1965)). Detailed reviews of the formalism of the full quantum theory of the Zener effect are available (Carlo *et al.* (1994); Quade *et al.* (1994)).

The condition for magnetic Zener breakdown can be similarly written as:

$$\frac{g^\star \mu_B B E_F}{E_g^2} > 1 \tag{6.2.11}$$

which is readily satisfied only for very high magnetic fields or very narrow gaps in the quasi-particle spectrum. When the condition 6.2.11 is satisfied, it becomes possible one quasiparticle in the crystal to tunnel into the states belonging to another one, thus forming a 'combined' trajectory over the Fermi surface[1]. In principle, the election wavefunction does have different symmetries depending on whether or not strong electric or magnetic fields are applied, and their mutual orientation (Zawadzki & Kowalski (1971)). For example, strong transverse electric field can destroy the Landau diamagnetic quantisation, while retaining the Pauli susceptibility. It is also possible for a strong magnetic field to cause semimetal-semiconductor transitions, by opening a gap in the density of available states upon explicit Landau level formation.

6.3 Diamagnetism of Graphite

In order to check the speculations about room temperature ferromagnetism in graphite, as described in the introduction, several samples of different grades HOPG were examined. Representative results for ZYB grade HOPG are shown on figure 6.4. Only one of eight samples shows any saturating component of the magnetisation at 300 K. This fact leads to the conclusion that the effects are most likely spurious and due to low-level contamination.

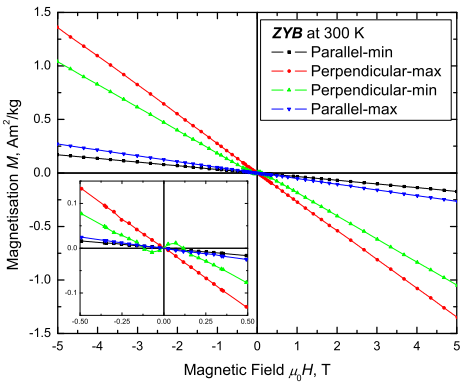

Figure 6.4: Magnetisation of HOPG (grade ZYB) in different orientations, measured at 300 K.

Though the susceptibility of graphite is has been used as a measure of its crystalline quality (Fischbach (1961); Pinnick (1954); Pinnick & Kiive (1956)), the relative variations are small as can be seen by comparing figures 6.4 and 6.5.

The magnetisation when the field is applied parallel to the c axis is predominantly linear. The characteristic for the quasi-free electron gas de Haas van Alphen oscillations can be sensed

[1] This effect should not be confused with the influence of magnetic field on the inter-band tunnelling (see as examples Argyres (1962); Bernard *et al.* (1968); Calawa *et al.* (1960); Chynoweth *et al.* (1960); Haering & Miller (1961); Roth *et al.* (1966)).

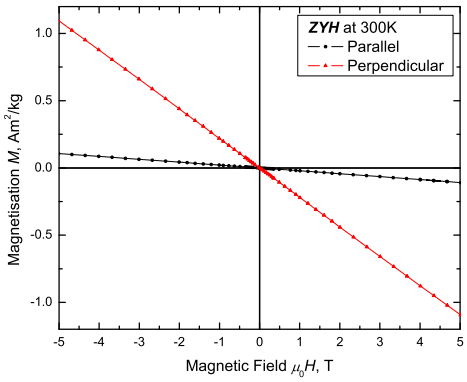

Figure 6.5: Magnetisation of HOPG (grade ZYH) in different orientations, measured at 300 K.

at low temperature as demonstrated on figure 6.6. The in-plane susceptibility is much smaller, as shown on figure 6.7, and therefore a very small saturating component can be resolved. The fact that such behaviour is not present at high temperatures leads to two possible explanations. Either the trace impurities are becoming ferromagnetic at very low temperature (which is not expected for the most common impurity - Fe) , or paramagnetic moment due to loose spins concentrated on defects of the crystalline structure is saturating, following the Langevin function, at low temperatures and high magnetic fields.

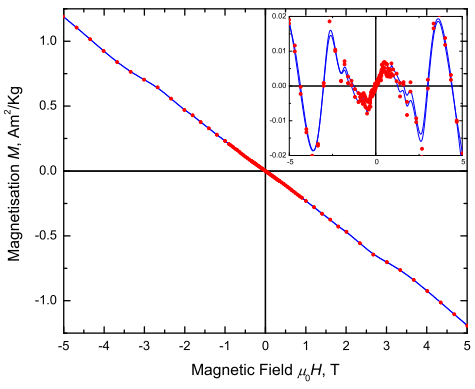

Figure 6.6: Magnetisation of HOPG (grade ZYA) with field applied along the c-axis, measured at 1.8 K K. The inset shows the oscillating part of the magnetisation, after the substraction of the linear susceptibility slope.

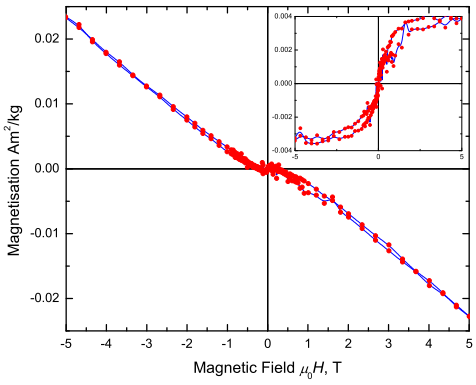

Figure 6.7: Magnetisation of HOPG (grade ZYA) with the field applied perpendicular to the c-axis in different orientations, measured at 1.8 K K. The inset shows the saturating part of the magnetisation, after the substraction of the linear susceptibility slope.

6.4 Conventional magneto-transport

The conventional transport and magneto-transport in graphite has long been a subject of interest, as a reference point for the transport properties of semimetals in general (see for example Kinchin (1953) and Morelli & Uher (1984) and references therein). In the low scattering limit, and for fields for which, there is no explicit Landau quantisation, i.e.:

$$\frac{\hbar}{\tau_{\mathrm{ph}}} < \hbar\omega_{\mathrm{c}} < kT \tag{6.4.1}$$

there exist large magnetoresistance, in graphite, which is determined by the low carrier concentrations and their small effective masses. The resistive ρ_{xx} and Hall ρ_{xy} components of the resistivity tensor can be modelled by using, for example, a multi-carrier model (see E.4), taking into consideration the dominating carrier types in graphite. Experimental results, together with fits performed simultaneously on the field dependencies, at various temperatures, of the resistive and Hall components, are visualised on figures 6.8 and 6.9, respectively.
It should be noted that, as expected, the fits become progressively worse with the lowering of the experimental temperature, because of the onset of Landau quantisation. The choice of experimental temperatures and field is far from trivial, without external information about the electronic structure. The arbitrariness of this choice is demonstrated on figures 6.10 and 6.11, where excellent fits are obtained in a severely limited field interval. The effective masses used (the effective masses are not linearly independent form the carrier concentrations and the scattering times) are: 0.06 m_{e}, for majority electrons; 0.04 m_{e}, for majority holes; and 0.02 m_{e}, for minority holes.

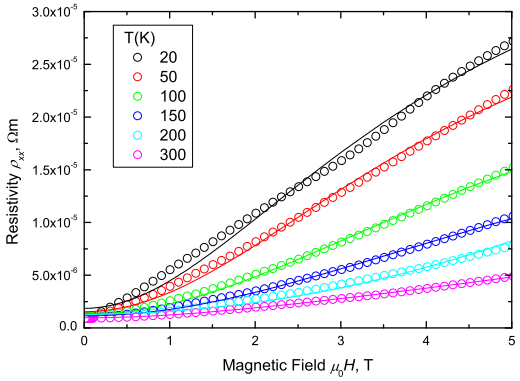

Figure 6.8: Resistivity as a function of magnetic field along the *c*-axis of HOPG, in the high temperature limit. The lines are fits to a three carrier model. The data is regressed simultaneously with the one of figure 6.9.

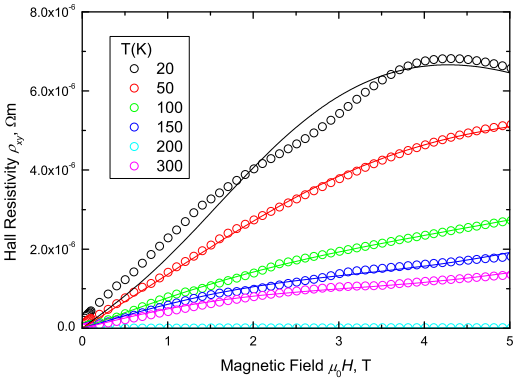

Figure 6.9: Hall resistivity as a function of magnetic field along the *c*-axis of HOPG, in the high temperature limit. The lines are fits to a three carrier model. The data is regressed simultaneously with the one of figure 6.8.

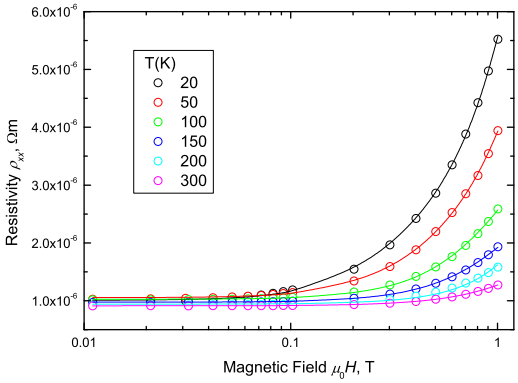

Figure 6.10: Resistivity as a function of magnetic field along the *c*-axis of HOPG, in the high temperature limit, at small fields. The lines are fits to a three carrier model. The data is regressed simultaneously with the one of figure 6.11.

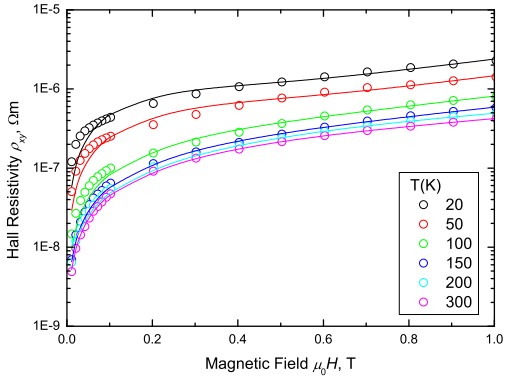

Figure 6.11: Hall resistivity as a function of magnetic field along the *c*-axis of HOPG, in the high temperature limit, at small fields. The lines are fits to a three carrier model. The data is regressed simultaneously with the one of figure 6.10.

Processed data for the temperature dependence of the carrier concentrations, extracted with the help of the three carrier model is shown on figures 6.12 and FigDensityLow, for fields of up to 5 T, and for fields less than 1 T, respectively. The high-field data is in good agreement with results reported by Du *et al.* (2004, 2005). The low-field limited data is presented, in order to illustrate the systematic errors of this type of analysis. The almost identical

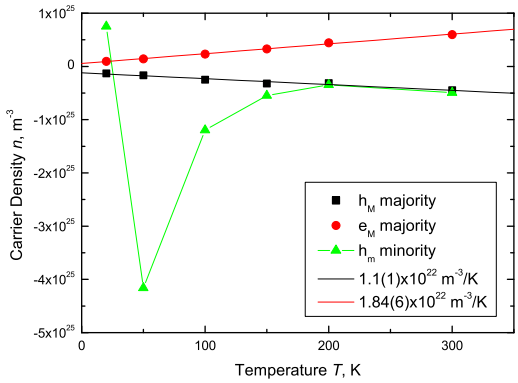

Figure 6.12: Carrier densities for the different carrier types in HOPG as a function of temperature. The line through the minority holes data is just a guide to the eye.

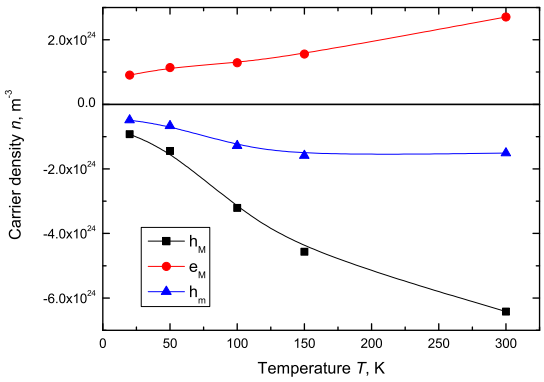

Figure 6.13: Carrier densities for the different carrier types in HOPG as a function of temperature. The splines through the data are just guides to the eye.

carrier concentrations (by absolute value) for the majority carriers, are a clear and definite demonisation of the semimetallicity of graphite. The change of sign of the carrier concentration of the minority holes is particular to the graphite sample characterised, and is due to the Fermi level crossing the energy gap at a finite temperature.

Two clearly different carrier-phonon scattering times can be resolved at high temperature, one for majority and one for minority carrier types. A plot of those as a function of temperature,

demonstrating linear temperature dependence is shown on figure 6.14. The linear temperature

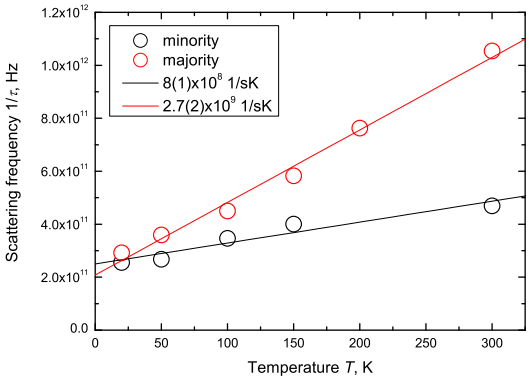

Figure 6.14: Scattering frequencies of majority and minority carriers in HOPG as a function of temperature.

dependence is a consequence of the conventional estimate for the electron-phonon scattering in metallic systems[1]:

$$\tau_{\mathrm{ph}} \simeq (k_{\mathrm{F}} a_0)\, \frac{m^\star}{m_{\mathrm{e}}} \frac{kT}{\hbar} \tag{6.4.2}$$

where a_0 is the Bohr radius, which is normally of the order of $kT/\hbar$ for most metals. In a low-carrier-density, low-effective-mass semimetal, however $\hbar\tau_{\mathrm{ph}} kT$. The values obtained for the slope of the temperature dependence are 0.021(2) $k/\hbar$, for majority carriers and 0.006(1) $k/\hbar$, for minority carriers.

6.5 Oscillatory and Kinetic and Thermodynamic Effects

A perfect illustration of the semi-metallic character of graphite is its enormous magnetoresistance at low temperature (the effects exceed 2000 %), as shown on 6.15. Below about 50 K, the quasi-free electron gas exhibits explicit Landau quantization, with Hall oscillations amounting for about 30 % of the total signal at 5 T (6.16).

When the direction of the applied magnetic field is in the plane of the graphene sheets, no oscillations can be observed, either in resistance or the Hall effect (figures 6.17 and 6.18). The magnetoresistance is still substantial at low temperatures, though the effect may be due to misalignment (the conductivity tensor anisotropy reaches about 100:1).

In the longitudinal magnetoresistance and Hall contribution, very long period oscillations can be observed (figures 6.19 and 6.20) on the account of the large anisotropy of the Fermi sur-

[1] For most common metals $a/a_0 \sim 1$, where a is the lattice constant of the material.

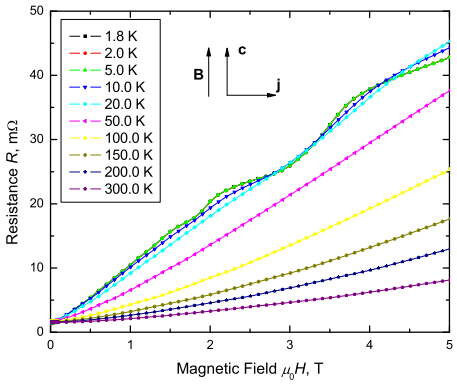

Figure 6.15: Resistance as a function of magnetic field along the c-axis of HOPG, at various temperatures.

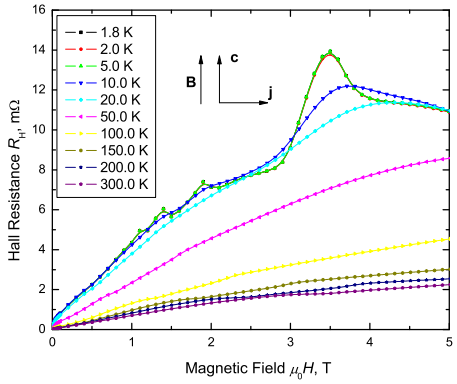

Figure 6.16: Hall resistance as a function of magnetic field along the c-axis of HOPG, at various temperatures.

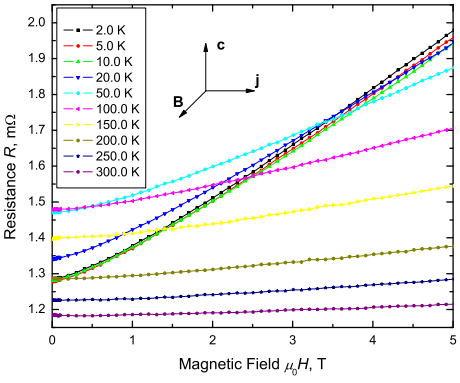

Figure 6.17: Resistance as a function of magnetic field perpendicular to the c-axis of HOPG and to the applied current, at various temperatures.

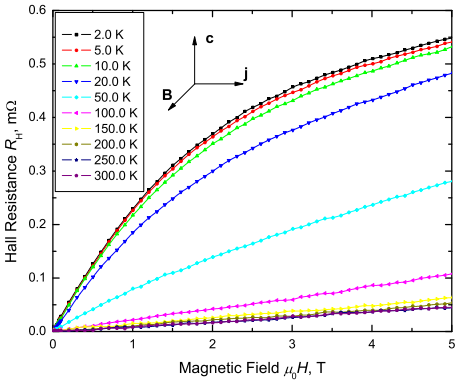

Figure 6.18: Hall resistance as a function of magnetic field perpendicular to the c-axis of HOPG and to the applied current, at various temperatures.

face, about 25:1 for the majority electron component, and 17:1 for the majority hole component.

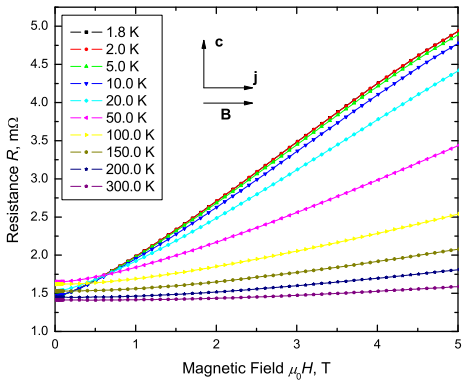

Figure 6.19: Resistance as a function of magnetic field perpendicular to the c-axis of HOPG and parallel to the applied current, at various temperatures.

Possible metal-semiconductor transition is revealed on figure 6.21 for fields as low as 0.1 T. A dramatic decrease in carrier concentration is evidenced by the enormous increase of the hall resistance (see figure 6.22). When the field is applied in the plane of the graphene sheets the effect is far less pronounced both in the resistance and Hall effect dependencies on temperature (see figures 6.23 and 6.24). It becomes evident, what has been speculated, by Kopelevich *et al.* (2003a), to be re-entrance in metallic state at very-low temperatures (field dependent series of metal-to-insulator-to metal transitions) is likely to be related to the large amplitude of the Shubnikov de Haas oscillations, due to the very small effective mass (less than 0.06 m_e).

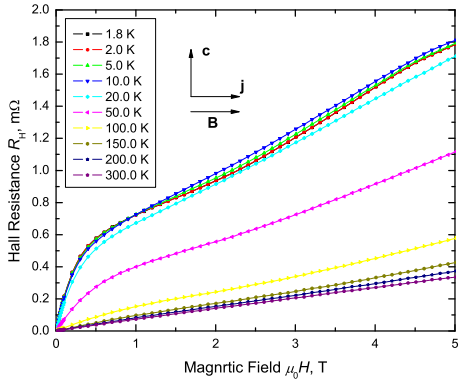

Figure 6.20: Hall resistance as a function of magnetic field perpendicular to the c-axis of HOPG and parallel to the applied current, at various temperatures.

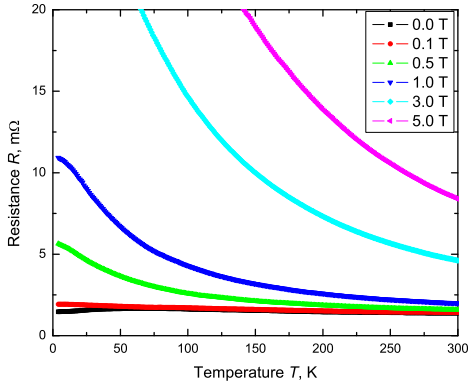

Figure 6.21: Resistance as a function of temperature, at various magnetic fields along the c-axis of HOPG.

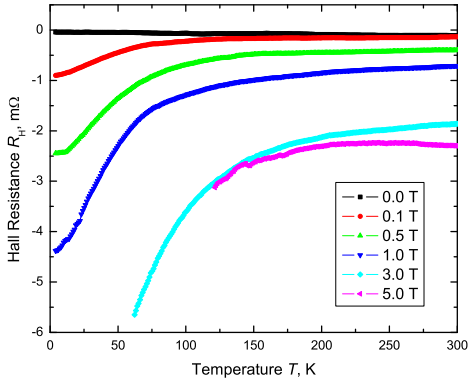

Figure 6.22: Hall resistance as a function of temperature, at various magnetic fields along the c-axis of HOPG.

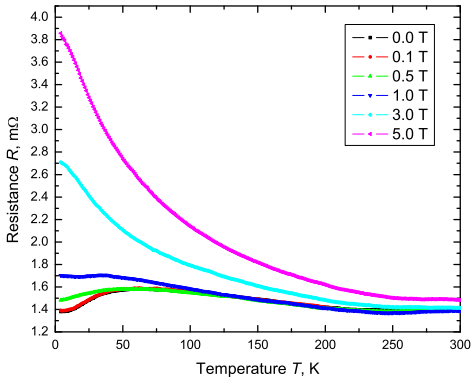

Figure 6.23: Resistance as a function of temperature, at various magnetic fields perpendicular to the *c*-axis of HOPG and to the applied current.

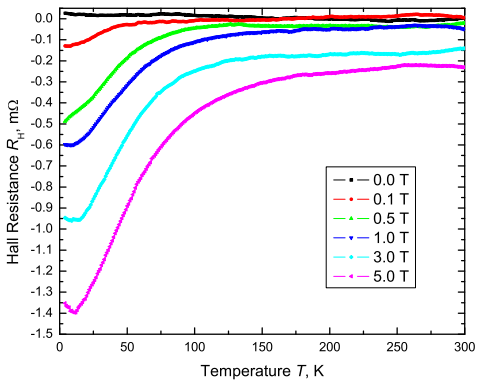

Figure 6.24: Hall resistance as a function of temperature, at various magnetic fields perpendicular to the *c*-axis of HOPG and to the applied current.

The picture of a very anisotropic quasi-free electronic system remains valid remains valid down to temperatures of 0.3 K, and fields as high as 23 T, as evidenced on figure 6.25. The magnetoresistance does not saturate in any orientation, neither shows very close to parabolic dependence on field, therefore, truly open or completely closed electron orbits if any, would not involve the majority carriers.

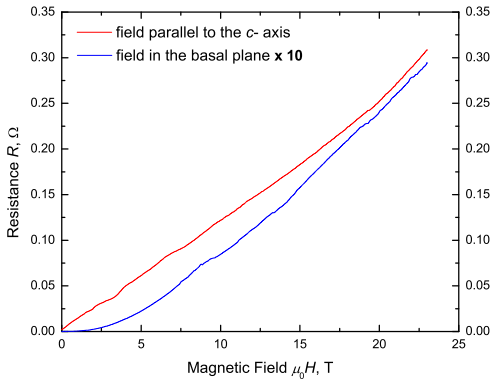

Figure 6.25: Resistance of HOPG in the basal plane, as function of the applied field of up to 23 T.

A much more detailed analysis of the oscillations of the kinetic coefficients, suggested by Landau & Liphshitz (1976), may be performed as shown on the series of figures (6.26 to 6.36). The results for the various quasi-particles may be summarised in the following list and compared to the appropriate references:

No.	Frequency	Carrier	References
1	0.33 T	minority h	0.34 T - Williamson *et al.* (1965); 0.32 T - Luk'yanchuk & Kopelevich (2004)
2	0.50 T	minority e	0.74 T - Soule *et al.* (1964a); 0.75 T - Anderson *et al.* (1967)
3	1.28 T	minority h	0.9 T - Woollam (1971b); 1.17 T - Flood (1969)
4	4.17 T	majority e	4.8 T - Soule *et al.* (1964a); 4.7 T - Cooper *et al.* (1970)
5	6.06 T	majority h	6.2 T - Woollam (1971b); 6.06 T - Cooper *et al.* (1970)
6	>10.9 T*	e + h	breakthrough

Table 6.1: Extracted material parameters for HOPG and multi-walled carbon nanotubes. *The actually detected frequencies are: 10.9 T, 14.3 T, 18.2 T and 26.3 T.

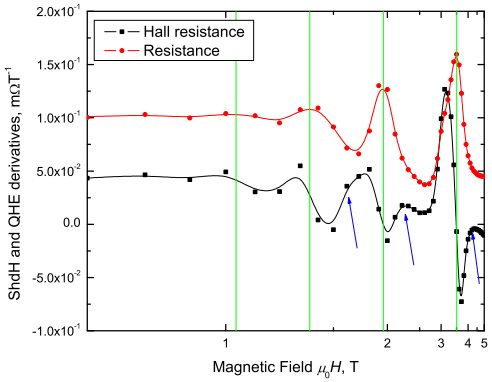

Figure 6.26: Normal and Hall resistance as a function of magnetic field along the c-axis of HOPG. The arrows point towards the appearance of the oscillations corresponding to the minority carriers.

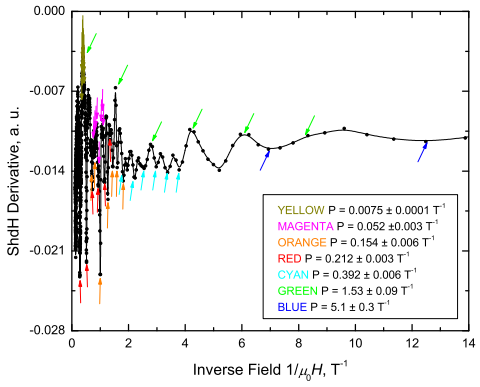

Figure 6.27: Conductivity oscillations in HOPG at 0.3 K, and the allocation of the different periods observed.

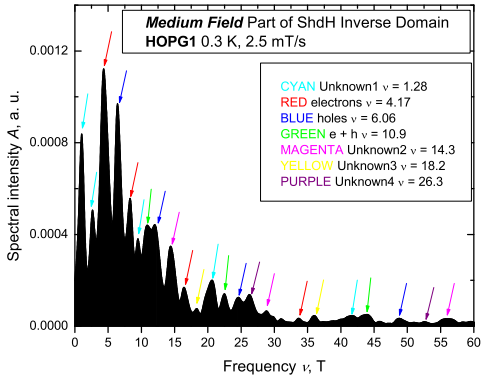

Figure 6.28: Inverse domain image of the ShdH oscillations in the intermediate frequency region.

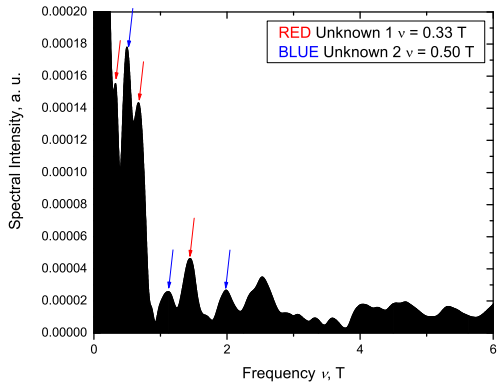

Figure 6.29: Inverse domain image of the ShdH oscillations in the low frequency region.

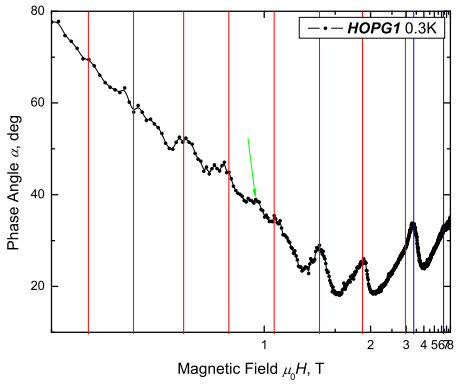

Figure 6.30: Relative phase of the ShdH oscillations in HOPG, measured at 0.3 K. The vertical lines are guide to the eye. The arrows point towards the minority carrier oscillations.

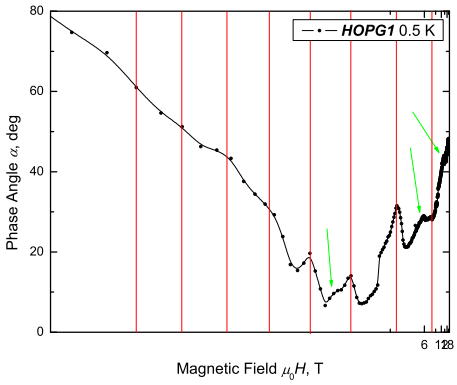

Figure 6.31: Relative phase of the ShdH oscillations in HOPG, measured at 0.5 K. The vertical lines are guide to the eye. The arrows point towards the minority carrier oscillations. Note the slightly different scale.

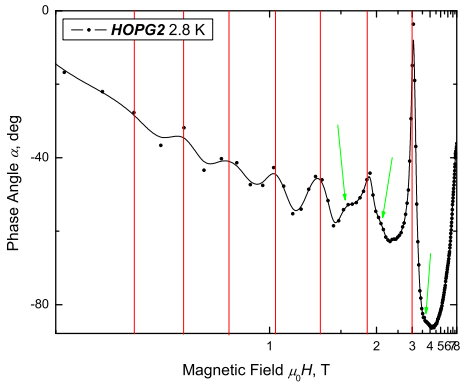

Figure 6.32: Relative phase of the ShdH oscillations in HOPG, measured at 2.8 K. The vertical lines are guide to the eye. The arrows point towards the minority carrier oscillations.

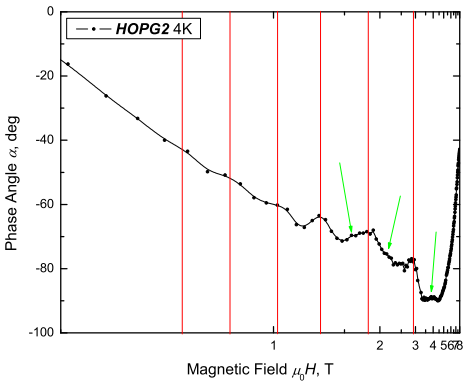

Figure 6.33: Relative phase of the ShdH oscillations in HOPG, measured at 4.0 K. The vertical lines are guide to the eye. The arrows point towards the minority carrier oscillations.

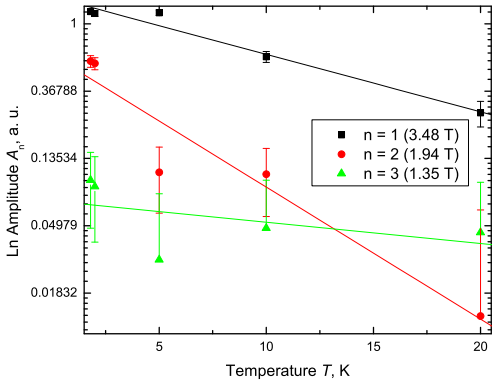

Figure 6.34: Temperature dependence of the amplitude of the ShdH oscillations in HOPG.

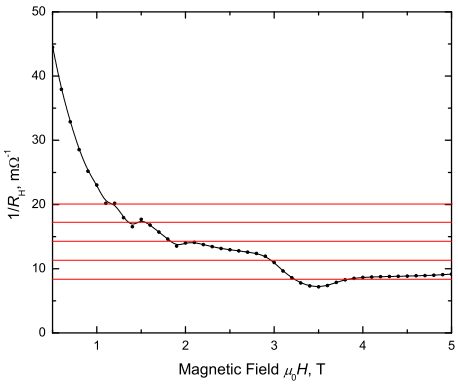

Figure 6.35: Hall conductivity as a function of field, revealing the absence of explicit quantisation in the conductivity.

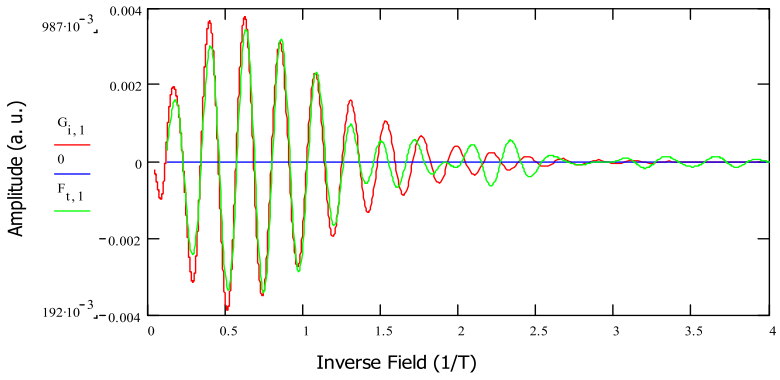

Figure 6.36: Band-pass filtered (3 - 5 T) majority electrons' component of the oscillatory conductivity GREEN and a fit using the L-K approximation RED, with parameters: $T = 0.3$ K, $m^\star = 0.039 m_\mathrm{e}$, $T_\mathrm{D} = 5$ K, $A_\mathrm{ext} = 4.2 \cdot 10^{16} m^{-2}$, $\phi = -\pi/2$.

6.6 Theoretical Considerations on the Diamagnetism of Carbon Nanotubes

6.6.1 Persistent currents and ideal conductor rings

For an insulated normal-metal ring, penetrated by a magnetic flux ϕ_{M}, at finite temperature, a equilibrium current may exist, provided phase coherence of the electronic wavefunction is preserved (Büttiker (1988)). For the gauge invariance of the magnetic vector potential $\mathbf{A}$, which is only defined to within a gradient of a scalar field, say f, the Bloch states corresponding to wave vectors $\mathbf{k}_m$ are also invariant as:

$$\mathbf{A} \rightarrow \mathbf{A} + \nabla\phi_{\mathrm{M}} \tag{6.6.1}$$

$$\psi_m \rightarrow \psi_m \exp\left(\mathrm{i}2\pi\frac{\phi_{\mathrm{M}}}{\phi_{\mathrm{M}}^0}\right) \tag{6.6.2}$$

This invariance can be incorporated as a modification on the boundary conditions as:

$$\psi_m\left(x+\Delta x\right) = \exp\left(\mathrm{i}2\pi\frac{\phi_{\mathrm{M}}}{\phi_{\mathrm{M}}^0}\right)\psi_m(x) \tag{6.6.3}$$

where the $\phi_{\mathrm{M}}^0 = \frac{h}{q}$ is the flux quantum, and Δx is the ring circumference. Therefore, the wave vectors $\mathbf{k}_m$ are flux-periodic as:

$$k_m = \frac{2\pi}{\Delta x}\left(m + \frac{\phi_{\mathrm{M}}}{\phi_{\mathrm{M}}^0}\right) \tag{6.6.4}$$

which imposes periodicity on the energy spectrum and its derivatives. For the current carried by the m-th state:

$$J_m = -q\frac{v_m}{\Delta x} = -\frac{q}{\hbar}\frac{\partial\epsilon_m}{\partial k_m}\frac{1}{\Delta x} = -\frac{\partial\epsilon_m}{\partial\phi_{\mathrm{M}}} \tag{6.6.5}$$

which, in turn, implies a change in the total energy E, of say E_{c} and a total associated current:

$$J = -\frac{\partial E}{\partial\phi_{\mathrm{M}}} \tag{6.6.6}$$

The so-called corelation energy E_{c} may be deduced from an uncertainty-principle argument to be:

$$E_{\mathrm{c}} = \frac{h}{\tau_{\mathrm{d}}} \tag{6.6.7}$$

where τ_{d} is the mean diffusion time around the ring,which may be estimated as:

$$\tau_{\mathrm{d}} \approx \frac{\Delta x^2}{\lambda_{\mathrm{e}} v_{\mathrm{F}}} \tag{6.6.8}$$

where λ_{e} is the elastic mean free path for the electrons, and v_{F} is their Fermi velocity.

For low enough temperatures, $kT \ll E_{\mathrm{c}}$, macroscopic phase coherence is preserved and the resulting periodic changes in flux, energy, etc. (the so-called Aharonov-Bohm effect) may be

observed. An exact solution of the two-dimensional ring model is available for circular geometry (Saito *et al.* (2003)). For an artificial system of metallic rings, periodic changes (both integer and half flux quanta) in the magnetisation with applied magnetic field, have been demonstrated by Pannetier *et al.* (1985) and Lévy *et al.* (1990). Analysis of persistent currents in carbon nanotubes and their implications on the magnetic properties have been performed by Szopa *et al.* (2002) and Byszewski (1997).

The following is based on the idea of Byszewski (1997) of a vector potential due to the curvature of the nanotubes. In the standard notation, the Schrdinger equations for an ensemble of N_{e} identical quasi-free electrons in a magnetic field along the z-axis of the system each has the form:

$$-\frac{\hbar^2}{2m^\star}\nabla^2\psi_j + i\frac{B_z q\hbar}{2m^\star}\left(x_j\partial_{y_j} - y_j\partial_{x_j}\right)\psi_j + \frac{B_z^2 q^2}{8m^\star}\left(x_j^2 + y_j^2\right)\psi_j - sg_{\mathrm{s}}^\star\mu_{\mathrm{B}}B_z\psi_j = E\psi_j \quad (6.6.9)$$

which is equivalent to the Schrödinger equation for a harmonic oscillator, with eigenvalues given by:

$$E_{n,s} = \frac{\hbar^2 k_z^2}{2m_{\mathrm{l}}^\star} + g_{\mathrm{t}}^\star\mu_{\mathrm{B}}B_z\left(n + \frac{1}{2}\right) - sg_{\mathrm{s}}^\star\mu_{\mathrm{B}}B_z \quad (6.6.10)$$

whare $m_{\mathrm{l}}^\star$ and $m_{\mathrm{t}}^\star$ are the longitudinal and transverse components of the effective mass tensor, and the following substitution has been made:

$$\frac{\hbar q}{m_{\mathrm{t}}^\star} = g_{\mathrm{t}}^\star\mu_{\mathrm{B}} \quad (6.6.11)$$

and here only $n = 0, 1, 2\ldots$ is the Landau level index.

The electron gas is diamagnetic only if the effective mass of the carriers is small, in other words, when $g_{\mathrm{t}}^\star > g_{\mathrm{s}}^\star$. This is borne out by the small transverse effective mass for graphite, $0.04m_{\mathrm{e}}$. The first term in the spectral equation represents the kinetic energy of translation along the z-axis, the second term represents a set of energy levels, whose degeneracy depends upon the radius of the cylinder within which the electrons are confined, and is given by

$$\gamma = \frac{qB_z R^2}{h} = \frac{R^2}{2l_{\mathrm{B}}^2} \quad (6.6.12)$$

while the last term represents the Zeeman splitting of the spin-up and spin-down levels. The degeneracy may be determined by imposing periodic boundary conditions with periods $(L_x a, L_y a)$ in the xy plane, where a is the lattice constant. The wave numbers are then quantized with $k_x = \frac{2\pi v_x}{L_x a}$, $k_y = \frac{2\pi v_y}{L_y a}$. Thus there is one degenerate state (Landau level with index n) per area $2\pi l_{\mathrm{B}}^2$ of the graphene sheet Ziman (1965)). The effect of the magnetic field along the tube axis is to confine the quasi-free electrons in a parabolic potential. When $r_{\mathrm{t}} \gg l_{\mathrm{B}}$, this is a good approximation. However the confinement in nanotubes is due to the structure of the tube itself.

The potential in which the confined electrons move in the xy plane can be approximated for low-lying states by a parabola, which will give rise to equidistant excited levels. The resulting effective potential may be represented as: $\phi_{\text{eff}}(x) = \frac{m_{\text{t}}^{\star}}{2}\left(\omega_0^2 + \omega_{\text{c}}^2\right) x^2$ where ω_0 is the frequency determined by the zero field confinement is the tube, and ω_{c} is the cyclotron frequency. In addition to the applied field $\mathbf{B}$ or vector potential $\mathbf{A}_{\text{H}} = \left(\frac{\hbar}{q l_{\text{B}}^2}\right)[-y, x, 0]$, there is a constant effective field $B_0 = \frac{\hbar\omega_0}{g_{\text{t}}^{\star}\mu_{\text{B}}}$, or vector potential $\mathbf{A}_{\text{D}} = \left(\frac{\hbar}{q r_{\text{t}}^2}\right)[-y, x, 0]$ representing the curvature of the graphene sheets Byszewski (1997). In the case of nanotubes with $r_{\text{t}} = 10$ nm, $B_0 = 7$ T; the dHvA oscillations are suppressed when $B_z < B_0$.

Macroscopic quantities such as magnetisation and susceptibility are independent of the spiral structure of the nanotubes Saito *et al.* (1998). Therefore, the basic response of the system may be calculated from thermodynamic averages based on the single-electron energy spectrum. Following Landau & Livshitz (1982), the partition function in the grand-canonical ensemble is

$$Z = N_{\text{e}} \prod_{n=0}^{\infty} \left(1 + \text{e}^{-\frac{E_n - \mu}{kT}}\right)^{\gamma} (B_z) \tag{6.6.13}$$

The chemical potential of the system μ , is pinned between two Landau levels, and it can be considered fixed at $\mu = g_{\text{t}}^2 \mu_{\text{B}} B_z \left(n_{\text{F}} + \frac{1}{2}\right)$, where n_{F} is the number of completely filled levels (the Fermi level index). Considering the two levels, just below and just above the chemical potential, the grand canonical potential is

$$\Omega = -kT \ln(Z) = -NkT \ln \left[\prod_{n=n_{\text{F}}-\frac{1}{2}}^{n=n_{\text{F}}+\frac{1}{2}} \left(1 + \text{e}^{-\frac{E_n - \mu}{kT}}\right)^{\gamma(B_z)} \right] \tag{6.6.14}$$

Furthermore, for electrons confined within a tube of radius smaller than l_{B}, corresponding to the maximum experimental field, the degeneracy $\gamma(B_z)$ can be considered a constant. The magnetisation $M = -\frac{\partial M}{\partial B_z}$ and susceptibility $\kappa = -\frac{\partial \Omega}{\partial B_z}$ as a function of temperature and magnetic field oriented along the nanotube axis are therefore:

$$M(B_z, T) = -\gamma g_{\text{t}}^{\star} \mu_{\text{B}} N_{\text{e}} \tanh\left(\frac{g_{\text{t}}^{\star}\mu_{\text{B}} B_z}{2kT}\right) \tag{6.6.15}$$

$$\kappa_{\text{L}}(B_z, T) = -\gamma g_{\text{t}}^{\star} \mu_{\text{B}} N_{\text{e}} \left[1 - \tanh^2\left(\frac{g_{\text{t}}^{\star}\mu_{\text{B}} B_z}{2kT}\right)\right] \tag{6.6.16}$$

The above remarks need a little further elaboration. Actually, explicit Landau level quantisation is missing. The curvature of the nanotubes surface removes the inversion symmetry and splits the electronic energy bands into two - circulating anticlockwise and clockwise. If an external magnetic field is then applied, instead of changing the radius of the electronic 'orbits', as in the classical Landau approach, their radius is kept constant and equal to the radius of the tubes, but their energy is changed, as in the classical Larmor approach (see for example

Byszewski & Baran (1995)). Furthermore, the circulating electrons, create sufficiently strong magnetic field, so that their spins may be considered either parallel or antiparallel to the tubes axis (via the spin-orbit interaction), and the degeneracy is lifted further.

The total susceptibility is $\kappa_{\text{tot}} = \kappa_0 + \kappa_{\text{L}}(B,T)$ where the constant term κ_0 includes the Pauli, van Vleck and orbital diamagnetic contributions cite. However, the Landau levels will be broadened by thermal effects and by non-thermal scattering of the conduction electrons by defects, which are most simply represented by a Dingle temperature $T_{\text{D}} = \frac{\hbar}{2\pi k \tau_0}$, where τ_0 is a relaxation time characterising athermal scattering by defects $T \to T + T_{\text{D}}$.

The temperature-dependence of susceptibility when the field is applied perpendicular to the tubes has been described in the tight-binding approximation, where it is associated with the orbital diamagnetism of carriers in the 2D structure Kotosonov (1999); Kotosonov & Kuvshinnikov (1997). In order to model both the field and temperature dependence of the magnetisation, we associate the calculation of $\kappa_{\parallel}$ in the confined-electron model with and a tight-binding calculation for $k_{\perp}$. In the latter case, the magnetisation perpendicular to the graphene sheet is

$$M\left(B_x,T\right) = -\frac{C\gamma_0^2 B_x}{\left(T+T_{\text{D}}\right)\left[2+\exp\left(\eta\right)+\exp\left(\eta\right)\right]} \tag{6.6.17}$$

where 3 eV, is the 2D band parameter, η is the reduced Fermi level and $C = 5.45 \cdot 10 Am^2/kgKT$. η can be evaluated using the neutrality equation for the 2D graphite model

$$\mathcal{F}_1(\eta) - \mathcal{F}_1(-\eta) = \frac{\eta_0^2}{2} \tag{6.6.18}$$

where $\mathcal{F}_1(\eta)$ is the Fermi integral, T_0 is the degeneracy temperature of the carriers, $\eta_0 = \frac{T_0}{T+T_{\text{D}}}$ and the Dingle temperature remains a free parameter. $\kappa_{\perp}$ is obtained from an average over the azimuthal angle, and the ensemble average κ is obtained form the average :

$$\tilde{M}\left[M_{\parallel}\left(H\right),\kappa_{\perp},H\right] = \int_0^{\pi/2} \sqrt{M_{\parallel}\left(H\cos\alpha\right)^2 + \left(\chi_{\perp}H\sin\alpha\right)^2}\cos\left\{\alpha - \arctan\left[\frac{\chi_{\perp}H\sin\alpha}{M_{\parallel}\left(H\cos\alpha\right)}\right]\right\}\sin\alpha d\alpha \tag{6.6.19}$$

6.7 Experimental Results on MW Carbon Nanotubes

The magnetisation of macroscopic ensembles of carbon nanotubes exhibits a strongly non-linear magnetic field and temperature dependence, as illustrated on figure 6.37. The initial low-temperature susceptibility is twice larger than the high field and high frequency one. A detailed inspection of the raw data sets, see figure 6.38, reveals no artefacts from the measurement process. Correspondingly, the next step would be to check whether the data can be fitted to

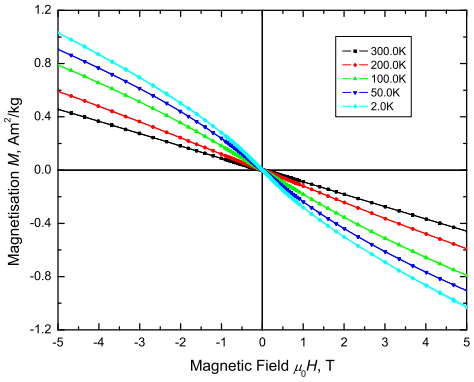

Figure 6.37: Magnetisation of a nanotube ensemble at different temperatures.

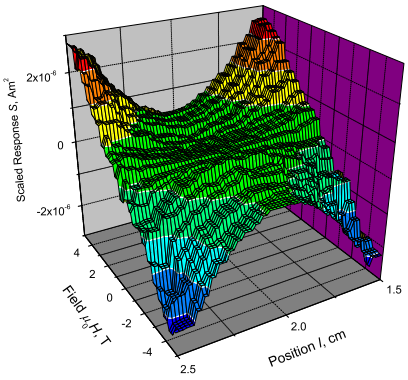

Figure 6.38: Raw SQUID response profile for a nanotubes compact.

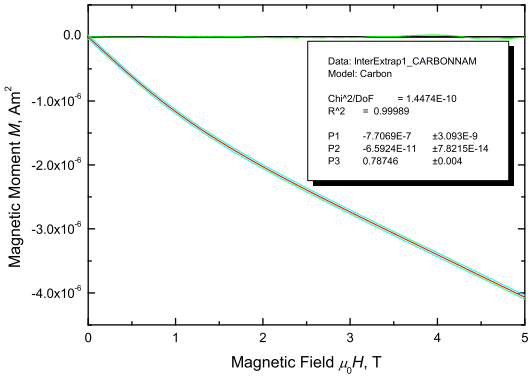

Figure 6.39: Fitting a simple model to the magnetisation curve of an ensemble of nanotubes.

the expression suggested in the previous chapter. Excellent fits are obtained, as demonstrated on figure 6.39.

A more detailed numerical calculation is visualised on figure 6.43, for both the perpendicular and parallel components of the magnetisation, as well as the ensemble average. All the important features of the experimental observations, compare with figure 6.42, are well reproduced.

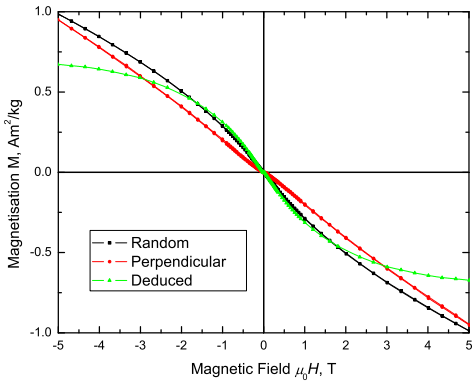

Figure 6.40: Components of the magnetisation of a nanotube ensemble.

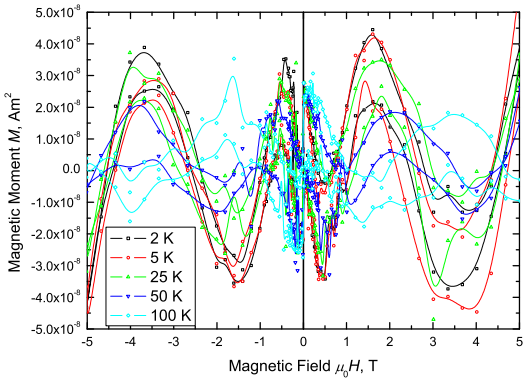

Figure 6.41: Oscillatory component of the magnetisations for a nanotube ensemble at different temperatures.

An important next step is to compare the experimental data for the temperature dependence of the magnetisation in different fields, shown on figure 6.46, with the theoretical predictions plotted on figure 6.47. There is a very good agreement, even without introducing corrections for the Van Vleck paramagnetic contributions.

Also, it is clear, that the temperature dependencies do not obey the conventional expression

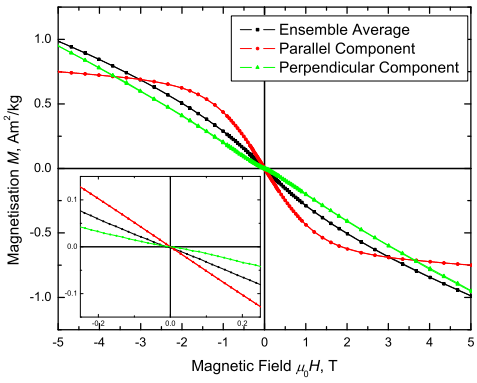

Figure 6.42: Measured and deduced magnetisation components for a nanotube ensemble at $T = 5$ K.

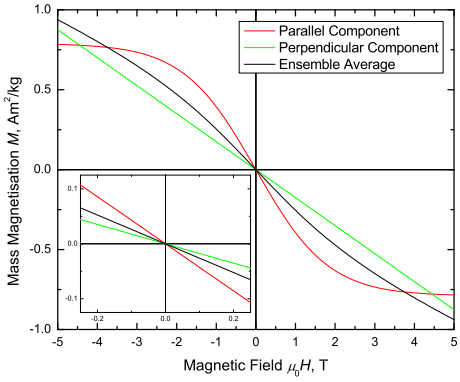

Figure 6.43: Calculated magnetisation components for a nanotube ensemble at $T = 5$ K.

(Byszewski (1997)):

$$\chi = N\frac{\mu_B^2}{kT_0}\left[1-\frac{1}{2}\left(\frac{m_e}{m^\star}\right)^2\right]\left[1-\exp\left(-\frac{T_0}{T}\right)\right] \tag{6.7.1}$$

where T_0 is the electron degeneration temperature defined via:

$$kT_0 = \frac{1}{4\pi}\frac{\hbar^2}{m^\star S_{ext}} \tag{6.7.2}$$

with S_{ext} being the reciprocal Fermi surface cross section.

Taking the correct ensemble average is also important, as otherwise two different dingle temperatures (110 Kand 58 K) are necessary, in order to fit the two temperature dependancies shown on figures 6.44 and 6.45, measured at $\mu_0 H = 5$ T and $\mu_0 H = 0.5$ T.

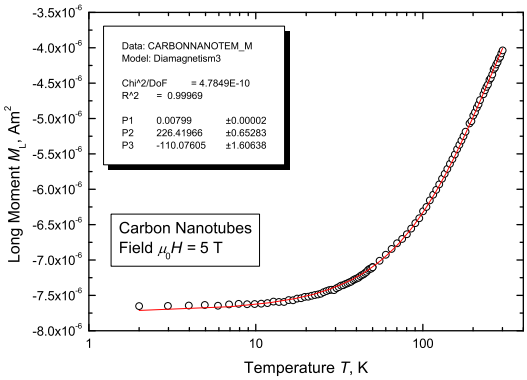

Figure 6.44: Measured temperature dependence of the magnetisation for a nanotube ensemble in a field of $\mu_0 H = 5$ T, and a fit to it with a simple model, with a $T_D = 110$ K.

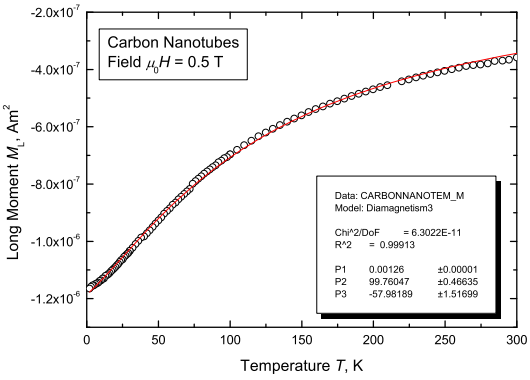

Figure 6.45: Measured temperature dependence of the magnetisation for a nanotube ensemble in a field of $\mu_0 H = 0.5$ T, and a fit to it with a simple model, with a $T_D = 58$ K.

The close correspondence of model and theory makes it possible to subtract the slowly varying contributions to the magnetisation, i. e. to do low-pass filtering of the data sets.

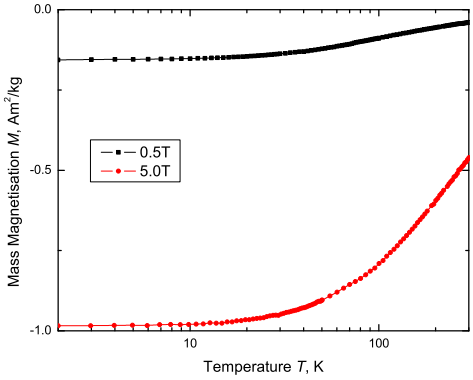

Figure 6.46: Measured temperature dependence of the magnetisation for a nanotube ensemble at two different applied fields.

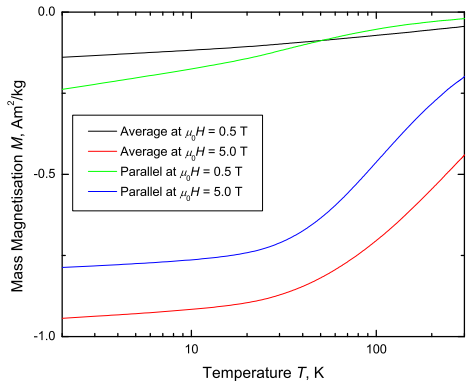

Figure 6.47: Calculated temperature dependence of the magnetisation for a nanotube ensemble at two different applied fields.

The resulting curves reveal Landau susceptibility oscillations, which may be compared to those measured in graphite on figures 6.48, 6.49 and 6.50. Comparable periodicity of the oscillations is to be expected as for relatively small nanotubes ($r \lessapprox 1$ nm), dHvA oscillations are expected only for fields, that are difficult to reach experimentally ($\mu_0 H > 30$ T), and for the electronic structure of the larger ones is very close to the one of graphite, as argued by Wang *et al.* (1992). Special attention should be paid to the largely different periods in the different orientations (related to the anisotropy of the Fermi surface) and the amplitudes of the oscillations, which are comparable for oriented nanotubes and HOPG, but trice smaller for the random ensemble of nanotubes. The latter fact strongly suggests that oscillations are only observed in the perpendicular component of the magnetisation.

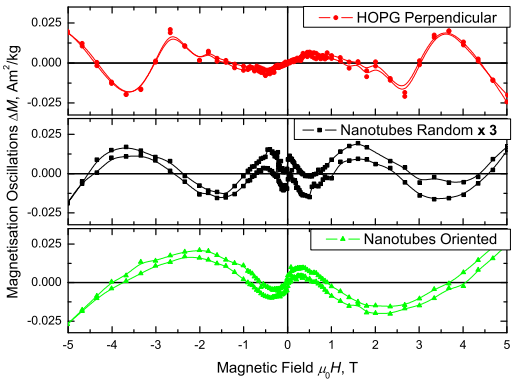

Figure 6.48: Comparison of dHvA oscillations in HOPG and carbon nanotubes, without de-drifting.

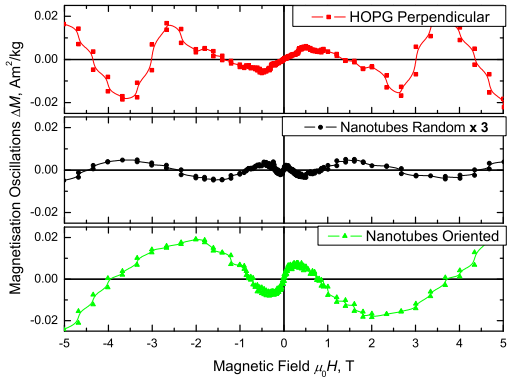

Figure 6.49: Comparison of dHvA oscillations in HOPG and carbon nanotubes, with de-drifting.

On figure 6.51 the magnetoresistance of a compact of randomly oriented multi-walled nanotubes, is demonstrated. This can be perfectly fitted to $R(H = 0) - CM^2(H)$, as shown in

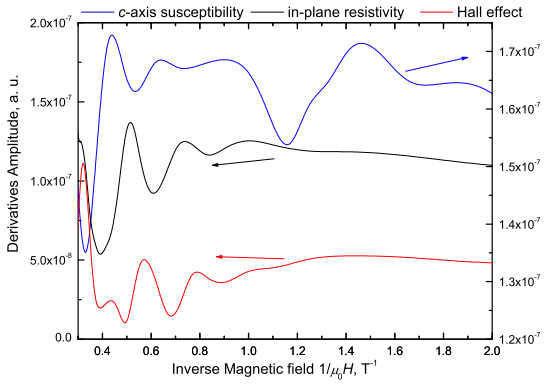

Figure 6.50: Oscillations in the thermodynamic and the kinetic coefficients.

figure 6.52, where C is a constant and M is the magnetisation. It should be noted, that the magnetoresistance of individual nanotubes is predominantly positive, quadratic and large (see for example Suzuura & Ando (2000) and references therein). The observed low temperature behavior may be attributed to powder magnetoresistance (Coey (1999)), where the tunnelling from tube to tube is enhanced by the varied diamagnetic magnetisation, which is coupled to the spin of the conduction electrons. This hypothesis agrees with the micron-scale spin-coherence observed in the transport properties of single-walled nanotubes, contacted with ferromagnetic electrodes, by Kim *et al.* (2002); Tsukagoshi *et al.* (1999), among others.

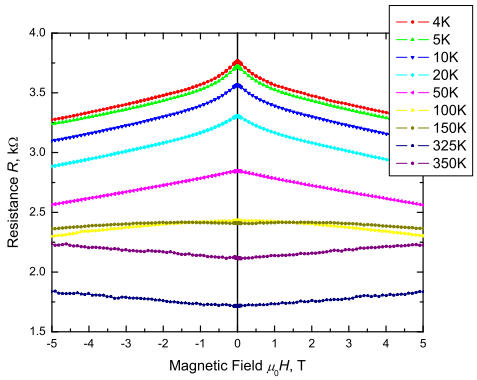

Figure 6.51: Resistance of nanotubes compact at different temperatures.

It should be noted, that measurements on nanotubes bundles and nanocrystalline graphite have been modelled with the standard two-band model and dominant weak localization magnetoresistance at low temperatures, by Song *et al.* (1994) and Zhang *et al.* (2004b), respectively. However, the magneto-resistive behaviour reported in the above reference is qualitatively dif-

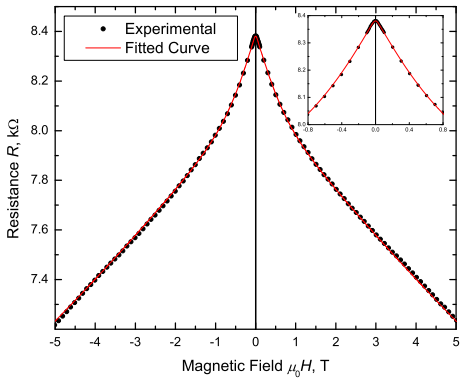

Figure 6.52: Resistance of a nanotubes compact at 1.8 K, and a fit to it. The inset shows a low field zoom-in of the same dataset, demonstrating the initial quadratic field dependence of the resistance.

ferent from the one visualised on figure 6.51, and is dominated by the transport properties of the nanotubules, rather than the contacts between them.

6.8 Examples of peculiar data

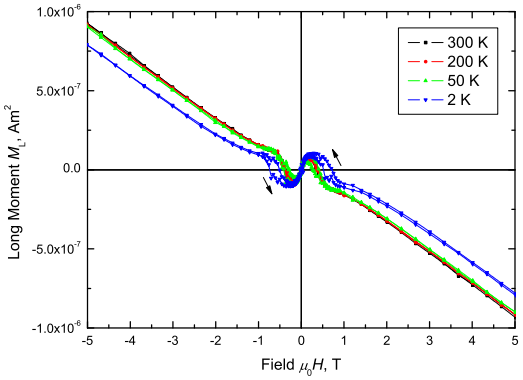

Figure 6.53: Magnetisation of an ensemble of predominantly single and double walled carbon nanotubes at different temperatures.

6.9 Conclusions on the Magnetism of Graphite and Carbon Nanotubes

A summary of the material parameters extracted is presented in table 6.9

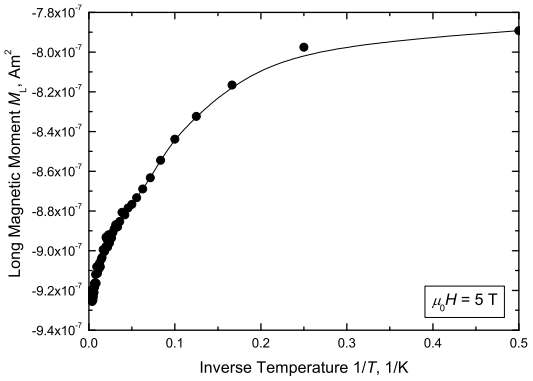

Figure 6.54: Magnetisation of an ensemble of predominantly single and double walled carbon nanotubes as a function of temperature at a field of $\mu_0 H = 5$ T.

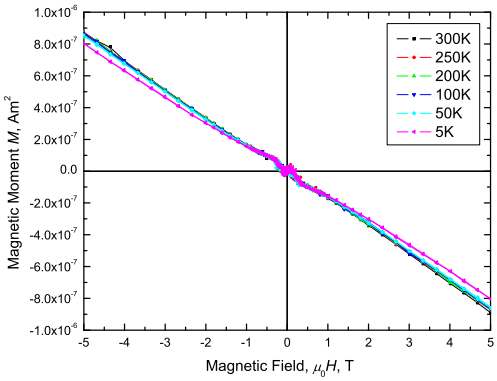

Figure 6.55: Magnetisation of an ensemble of micron-sized carbon whiskers at different temperatures.

Material	Property	Value	Units	Notes
HOPG	Magnetic susceptibility	$-3.8 \cdot 10^{-7}$	m^3kg^{-1}	Parallel to the c axis, 1.8 K
HOPG	Magnetic susceptibility	$-5 \cdot 10^{-9}$	m^3kg^{-1}	Perpendicular to the c axis
HOPG	Magnetoresistance	2280	%	Field parallel to c, 1.8 K, 5 T
HOPG	Carrier density	$3 \cdot 10^{-4}$	el/atom	At 1.8 K
HOPG	Rel. Phase of HE/MR	$\pi/4$	rad	De-phasing of the oscillations
HOPG	Electron effective mass	0.039	m_e	Majority carriers
HOPG	Anisotropy of $m^\star$	25:1	-	Majority carriers
HOPG	e-Fermi X-section	$4.2 \cdot 10^{16}$	m^2	Majority carriers
HOPG	Fermi level position	12	meV	Bottom of c-band
HOPG	Smallest gap	2	meV	Detected by breakdown
HOPG	Electron-phonon coupling	0.021(2)	$k/\hbar$	Approximate value
HOPG	Hole-phonon coupling	0.006(1)	$k/\hbar$	Approximate value
HOPG	e-temperature coefficient	$1.84(6) \cdot 10^{22}$	K^{-1}	Three-carrier model
HOPG	h-temperature coefficient	$1.1(1) \cdot 10^{22}$	K^{-1}	Three-carrier model
HOPG	e-athermal scattering freq.	$2.1(2) \cdot 10^{11}$	Hz	ZYB grade MR&Hall
HOPG	h-athermal scattering freq.	$2.5(2) \cdot 10^{11}$	Hz	ZYB grade MR&Hall
HOPG	Dingle temperature	5	K	Average (ZYB grade) from ShdH
CNT	Magnetoresistance	13	%	Random, 1.8 K, 5 T
CNT	Effective magneton	25	μ_B	Transverse at 1.8 K
CNT	2D band parameter	3	eV	Hopping integral
CNT	Free electron density	$3 \cdot 10^{-5}$	el/atom	At 1.8 K
CNT	Athermal relax. time	100	fs	Ensemble average

Table 6.2: Extracted material parameters for HOPG and multi-walled carbon nanotubes.

As a result of the experimental observations, apart from the material parameters of interest already summarised, the following general remarks should be made:

1. HOPG is, indeed, a semi-metal with a very small carrier concentration and effective mass.
2. Majority electrons in HOPG have normal 3D (though very anisotropic) dispersion.
3. Majority holes in HOPG might have 2D-like dispersion.
4. Re-entrant metallic state of HOPG at low temperatures and high fields is questionable.
5. No explicit 2D quantum Hall effect has been observed.
6. No evidence for superconductivity correlations in HOPG has been found.
7. Ferromagnetism is ambiguous (in the defect-less HOPG structure it is either due to impurities or is mimicked by saturating paramagnetic behavior of loose spins in the system).

8. Anomalous diamagnetism and magnetoresistance may be a general feature of macroscopic ensembles of nanotubes.

9. The carriers in multi-walled carbon nanotubes may be spin-polarised.

10. Small effective masses are pre-requisite for diamagnetism.

11. No ferromagnetism has been observed in multi-walled carbon nanotubes

Chapter 7

Conclusions and Outlook

In this thesis aspects of spin injection and transport have been investigated. In order of appearance they are:

1. The possibility of spin-polarisation measurements employing Schottky barriers has been treated both theoretically and experimentally. Due to the large number of concurrent magnetic field effects, the extraction of unambiguous spin-polarisation estimates is possible only in particular systems, in a limited temperature interval and requires the use of high magnetic fields. While several improvements of the experimental methodology are possible, a geneal 'recipe' for polarisation measurement cannot be established. Future work may shed light on the energy dependence (via energy-selective photo-illumination) and magnetic field dependence of the extracted spin-polarisation values.

2. The realisation of low-barrier contacts of ferromagnets to silicon. It is unlikely that only choosing a low work function metals (rare earths as an example) would be sufficient for achieving low, or no barrier. However, annealed (diffused) quasi-tunnel contacts that exhibit ohmic behaviour are relatively easy to produce. An open question remains whether these contacts would be sufficiently spin-transparent. This is the subject of a future investigation.

3. Details in the magneto-transport characteristics of tunnel junctions have been investigated. Adiabatic tunnelling seems to dominate the transport through high magnetoresistance junctions based on quasi-amorphous electrodes. The knowledge obtained about the origin of the bias dependence of the tunnelling magnetoresistance can be used to engineer the device structures further improve their response. With the use of high fields, it is possible to extract some additional parameters characterising the anisotropy of the electronic structure of the ferromagnetic junction electrodes, or characterise the barrier material.

More efforts are necessary on comparative analysis of complete bias, field, orientation, temperature varied datasets measured on different junction material combinations. This would help to further improve the modelling and increase its predictive power.

4. Direct magnetic detection of injected spin polarisation has been attempted. The experimental results shed doubt on the possibility to transport spins in Al at macroscopic distances even at He temperatures. Further improvements of the experimental equipment and methodology are necessary in order for the direct magnetic detection to become a viable characterisation tool.

5. The magneto-transport through Co:ZnO has been studied in detail. However no evidence is found in favour of this material system being a true semi-magnetic semiconductor. Just the contrary - no useful magneto-transport is observed at room temperature. In view of the two-phase character of the system and the lack of functionality, it is highly unlikely that a spin electronics application may appear.

6. The fundamental magneto-transport in graphite has been studied. The available data has been extended to higher fields, and some discrepancies in existing data resolved. Future efforts on micron and nano-scale structures are in order to achieve some useful functionality at room temperature.

7. The nonlinear diamagnetism of multi-walled carbon nanotubes has been studied experimentally and theoretically. This model system may be of interest from pedagogical point of view, as a demonstration of a simple model with a reasonable predictive power.

Appendix A

Appendix A

A.1 Current flow through insulators

Unlike metallic conductors and doped semi-conductors, because the lack of free carriers, the current flow through insulators is heavily restricted. Either mobile carriers must be first created and then transported through the insulator or the carriers must tunnel through the insulator. There are a number of different current limiting mechanisms possible, out of which, Fowler-Nordheim tunnelling, Poole-Frenkel emission, space-charge effects and ballistic transport, will be described in more detail.

A.1.1 Fowler-Nordheim tunnelling

The basic idea behind the Fowler-Nordheim model for the current limitation of the current through thick insulators is that, if somehow carriers are promoted to the conduction or valence bands of the insulator, they will be free to travel as quasi-free particles of effective mass $m^{\star}_{\mathrm{ox}}$. The critical step is therefore considered to be the tunnelling of the carriers from the contacts into the insulator. The WKB approximation[1] can be applied, yielding the following expression for the current density:

$$J_{\mathrm{FN}} = C_{\mathrm{FN}} \mathcal{E}_{\mathrm{ox}}^{2} \exp\left(-\frac{4}{3}\frac{\sqrt{2m^{\star}_{\mathrm{ox}}}}{q\hbar}\frac{(q\phi_{\mathrm{b}})^{3/2}}{\mathcal{E}_{\mathrm{ox}}}\right) \tag{A.1.1}$$

where $\mathcal{E}_{\mathrm{ox}}$ is the electric field in the oxide, ϕ_{b} is the barrier height at the interface to the conductor and C_{FN} is a constant dependent on material parameters of both the insulator and the conductor. Expression A.1.1 is widely used for explaining experimental $I(V_{\mathrm{a}})$ characteristics

[1] Wentzel-Kremers-Brillouin approximation

by plotting $\ln(J_{\mathrm{FN}}/\mathcal{E}_{\mathrm{ox}}^2)$ against $\mathcal{E}_{\mathrm{ox}}^{-1}$. The approximation is only valid for large enough fields $\mathcal{E}_{\mathrm{ox}} \geq \phi_{\mathrm{b}}$ (or thick insulators). It is often possible to determine the barrier height, provided the effective mass in the insulator is known.

A.1.2 Poole-Frenkel emission

In insulators with a lot of structural defects (examples include sputter-deposited insulators like SiO_2 and Si_3N_4, and PLD[1]-deposited semiconductors like ZnO), there is a high density of energy states close to the band edge (often called traps). According to the model of Frenkel (1938) the current is drift limited by the constant trapping and field-dependent reemission of carriers:

$$J_{\mathrm{PF}} = q n_{\mathrm{ox}} \mu_{\mathrm{ox}} \mathcal{E}_{\mathrm{ox}} \tag{A.1.2}$$

where μ_{ox} is the mobility in the semiconductor, n_{ox} is the carrier density in the insulator and is given by:

$$n_{\mathrm{ox}} = n_0 \exp\left[-\frac{q}{kT}\left(\phi_{\mathrm{b}} - \sqrt{\frac{q\mathcal{E}_{\mathrm{ox}}}{\pi\epsilon_{\mathrm{ox}}}}\right)\right] \tag{A.1.3}$$

The total current becomes:

$$J_{\mathrm{PF}} = q n_0 \mu_{\mathrm{ox}} \mathcal{E}_{\mathrm{ox}} \exp\left[-\frac{q}{kT}\left(\phi_{\mathrm{b}} - \sqrt{\frac{q\mathcal{E}_{\mathrm{ox}}}{\pi\epsilon_{\mathrm{ox}}}}\right)\right] \tag{A.1.4}$$

Experimentally Poole-Frenkel emission is dominant for shallow traps and is verified by plotting $\ln \frac{J_{\mathrm{PF}}}{\mathcal{E}_{\mathrm{ox}}}$ against $\mathcal{E}_{\mathrm{ox}}^{1/2}$.

A.1.3 Space-charge limited current

There are cases when the carriers can readily enter the insulator and, also, readily flow through it, while the carrier density is still far below the metallic limit. In such circumstances, relatively large currents can flow and the spatial changes of carrier density cause field gradients, which on their behalf limit the current density. A classic example is the space-charge limited current in vacuum tubes. Similar situation may exist in low-doping level semiconductors and insulators.

The effect can be modelled simply in one dimension, by combining Gauss law:

$$\frac{\mathrm{d}\mathcal{E}_{\mathrm{ox}}}{\mathrm{d}x} = \frac{q n_{\mathrm{ox}}}{\epsilon_{\mathrm{ox}}} \tag{A.1.5}$$

with the expression for the drift current A.1.2, yielding:

$$J_{\mathrm{SC}} = \epsilon_{\mathrm{ox}} \mu_{\mathrm{ox}} \mathcal{E}_{\mathrm{ox}} \frac{\mathrm{d}E_{\mathrm{ox}}}{\mathrm{d}x} \tag{A.1.6}$$

[1] Pulsed-Laser Deposition

Integrating from $x = 0$ where $E_{\mathrm{ox}} = 0$ to x yields:

$$\mathcal{E}_{\mathrm{ox}}(x) = \pm\sqrt{\frac{2xJ_{\mathrm{SC}}}{\epsilon_{\mathrm{ox}}\mu_{\mathrm{ox}}}} \tag{A.1.7}$$

which can be integrated once more to give the total drop of voltage V_{a}:

$$V_{\mathrm{a}} = \int_0^d \mathcal{E}_{\mathrm{ox}}(x)\mathrm{d}x \tag{A.1.8}$$

across the thickness of the insulator d. Finally, the expression for the space-charge limited current becomes:

$$J_{\mathrm{SC}} = \pm\frac{9}{8}\epsilon_{\mathrm{ox}}\mu_{\mathrm{ox}}\frac{V_{\mathrm{a}}^2}{d^2} \tag{A.1.9}$$

with the sign of J_{SC} chosen to be the same as the sign V_{a}.

A.1.4 Ballistic transport in insulators

Space-charge current limitation can take place even in the case of ballistic transport, when there is no scattering of the carriers and no mechanisms of energy loss. For low temperatures when the thermal velocity of the electrons coming from the emitter into the insulator can be neglected, the Gauss law A.1.5 can be combined with the one dimensional continuity equation:

$$J_{\mathrm{BT}} = qn_{\mathrm{ox}}v_{\mathrm{b}}^2 \tag{A.1.10}$$

where v_{b} is the ballistic velocity of the carriers, and further with energy conservation upon charging-up along the x axis:

$$\frac{m_{\mathrm{ox}}^{\star}v_{\mathrm{b}}^2}{2} = q\mathcal{E}_{\mathrm{ox}}x \tag{A.1.11}$$

to give the following differential equation for E_{ox}

$$J_{\mathrm{BT}} = \frac{\mathrm{d}\mathcal{E}_{\mathrm{ox}}}{\mathrm{d}x}\epsilon_{\mathrm{ox}}\sqrt{\frac{2q}{m_{\mathrm{ox}}^{\star}}}\sqrt{\mathcal{E}_{\mathrm{ox}}x} \tag{A.1.12}$$

which can be readily integrated from $x = 0$ to $x = d$ or over the thickness of the insulator d to give what is known in the theory of vacuum tubes as Child's law (see for example Menzel (1960)):

$$J_{\mathrm{ox}} = \frac{4}{9}\epsilon_{\mathrm{ox}}\sqrt{\frac{2q}{m_{\mathrm{ox}}^{\star}}}\frac{V_{\mathrm{a}}^{3/2}}{d^2} \tag{A.1.13}$$

A comparison between equations A.1.9 and A.1.13 reveals a substantial difference in voltage dependence, between the scattering (mobility) limited case and the ballistic case, originating from the fundamental difference in carrier behaviour in applied electric field. While for a finite

mobility $v = \frac{\mathrm{d}x}{\mathrm{d}t} \propto \mathcal{E}$, for the ballistic case $\dot{v} = \frac{\mathrm{d}^2x}{\mathrm{d}t^2} \propto \mathcal{E}$. Ballistic transport is becoming an important mechanism in modern thin-base, high-mobility Schottky diodes for which $l_\mathrm{e} \sim x_\mathrm{d}$, where l_e is the mean electron free path, evaluated as:

$$l_\mathrm{e} = \frac{3}{4}\frac{\mu_\mathrm{e}}{q}\sqrt{2\pi m_\mathrm{e}^\star kT} \tag{A.1.14}$$

For an example of ballistic transport in Schottky junctions see reference Torkhov (2001).

A.2 Validity of the full depletion approximation

For non-degenerate and fully ionised n-type semiconductor, the charge density as a function of the space-varying electric potential $\phi(x)$ can be written as:

$$\rho(\phi) = qN_\mathrm{d}\left[1 - \exp\left(\frac{q\phi}{kT}\right)\right] \tag{A.2.1}$$

where the symbols have their usual meaning. The Poisson equation can be then written as:

$$\frac{\mathrm{d}^2\phi(x)}{\mathrm{d}x^2} = -\frac{\rho(\phi)}{\epsilon_\mathrm{s}} = -\frac{qN_\mathrm{d}}{\epsilon_\mathrm{s}}\left[1 - \exp\left(\frac{q\phi(x)}{kT}\right)\right] \tag{A.2.2}$$

The numerical solution of this differential equation for $\phi(x)$ with boundary conditions $\phi(0) = -1$ V and $\phi(\infty) = 0$ can be compared with the full depletion approximation for which:

$$\frac{\mathrm{d}^2\phi(x)}{\mathrm{d}x^2} = -\frac{qN_\mathrm{d}}{\epsilon_\mathrm{s}} \tag{A.2.3}$$

within the interval $x \in [0..x_\mathrm{d}]$ and x_d is the depletion width approximated like:

$$x_\mathrm{d} = L_\mathrm{D}\sqrt{\frac{2q\left(\phi_\mathrm{i} - V_\mathrm{a}\right)}{kT}} \tag{A.2.4}$$

at zero applied field V_a and $L_\mathrm{D} = \sqrt{\frac{\epsilon_\mathrm{s}kT}{q^2N_\mathrm{d}}}$ as usual is the Debye length. The two solutions are visualised on figure A.1.

It should be noted that the full depletion approximation is sufficient to describe the potential to within few percent and establish the experimentally well verified dependence of the junction capacitance on the applied voltage:

$$C_\mathrm{j} = \frac{\epsilon_\mathrm{s}}{L_\mathrm{D}}\sqrt{\frac{V_\mathrm{t}}{2\left(\phi_\mathrm{i} - V_\mathrm{a} - V_\mathrm{t}\right)}} \tag{A.2.5}$$

when the potential difference across the semiconductor is larger than the thermal voltage $V_\mathrm{t} = kT/q$. In the opposite limiting case, when the potential drop across the semiconductor is small with respect to V_t the depletion layer width is proportional to the applied potential:

$$x_\mathrm{d} = L_\mathrm{D}\frac{\phi_\mathrm{i} - V_\mathrm{a}}{V_\mathrm{t}} \tag{A.2.6}$$

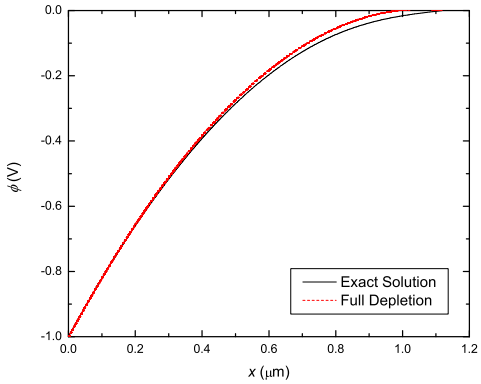

Figure A.1: Potential distribution across the depleted region for n-type non-degenerate semiconductor. Constants are set as follows: $\epsilon_s = 10\epsilon_0$, $N_d = 10^{-15}$ cm^{-3} and $\phi_i = 1$ V.

and the capacitance is virtually constant and given by:

$$C_j = \frac{\epsilon_s}{L_D} \tag{A.2.7}$$

For completeness, the spatial variation of the build-in electric field predicted by the full depletion approximation can be compared with the differential of the numerically calculated electric potential:

$$\mathcal{E}_{bi}(x) = -\frac{d\phi(x)}{dx} \tag{A.2.8}$$

They are both plotted on figure A.2 for generic material-dependent parameters.

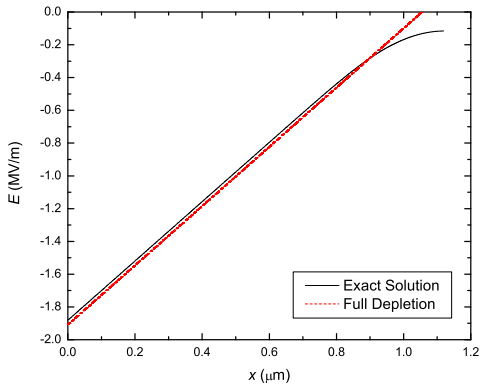

Figure A.2: Electric field distribution across the depleted region for n-type non-degenerate semiconductor. Constants are set as follows: $\epsilon_s = 10\epsilon_0$, $N_d = 10^{-15}$ cm^{-3} and $\phi_i = 1$ V.

A.3 Derivations of the main current components in a Schottky junction

A.3.1 Diffusion current

Within the drift-diffusion current model, the total current is given simply by the sum of the drift current due to build-in electric field and the externally applied field, and the diffusion current that tries to compensate the charge distribution within the depleted region. In equilibrium the two currents exactly compensate leaving the total $J_\mathrm{n} = 0$. At arbitrary positive bias the total electronic current is given by:

$$J_\mathrm{n} = q\left(-\mu_\mathrm{n} n \frac{\mathrm{d}\phi}{\mathrm{d}x} + D_\mathrm{n}\frac{\mathrm{d}n}{\mathrm{d}x}\right) \tag{A.3.1}$$

Both sides of the equation can be multiplied by $\exp(-\phi/V_\mathrm{t})$ where V_t is, as customary, the voltage equivalent of temperature $V_\mathrm{t} = kT/q$, to yield:

$$J_\mathrm{n}\exp\left(-\frac{\phi}{V_\mathrm{t}}\right) = qD_\mathrm{n}\left(-\frac{n}{V_\mathrm{t}}\frac{\mathrm{d}\phi}{\mathrm{d}x} + \frac{\mathrm{d}n}{\mathrm{d}x}\right) = qD_\mathrm{n}\frac{\mathrm{d}}{\mathrm{d}x}\left[n\exp\left(-\frac{\phi}{V_\mathrm{t}}\right)\right] \tag{A.3.2}$$

where the Einstein relation $\mu_\mathrm{n} = \frac{qD_\mathrm{n}}{kT}$ has been implied (Ashcroft & Mermin (1976)). The electronic current is then expressed as the following convolution product of $qD_\mathrm{n}n(x)$ and $\exp\left(-\frac{\phi}{V_\mathrm{t}}\right)$, within the full depletion approximation:

$$J_\mathrm{n} = \frac{qD_\mathrm{n} n\exp\left(-\frac{\phi}{V_\mathrm{t}}\right)\Big|_0^{x_\mathrm{d}}}{\int_0^{x_\mathrm{d}}\exp\left(-\frac{\phi}{V_\mathrm{t}}\right)\mathrm{d}x} = \frac{qD_\mathrm{n}N_\mathrm{c}\exp\left(-\frac{\phi_\mathrm{b}}{V_\mathrm{t}}\right)\left[\exp\left(\frac{V_\mathrm{a}}{V_\mathrm{t}}\right)-1\right]}{\int_0^{x_\mathrm{d}}\exp\left(-\frac{\phi^\star}{V_\mathrm{t}}\right)\mathrm{d}x} \tag{A.3.3}$$

where the boundaries are approximated like:

x	$n(x)$	$\phi(x)$
0	$N_\mathrm{c}\exp\left(-\phi_\mathrm{b}/V_\mathrm{t}\right)$	$\phi_\mathrm{i} + V_\mathrm{a}$
x_d	N_d	0

and $\phi^\star = \phi + \phi_\mathrm{i} - V_\mathrm{a}$ is the effective potential under applied bias. Using the expression for the potential within the full depletion approximation:

$$\phi = -\frac{qN_\mathrm{d}}{2\epsilon_\mathrm{s}}\left(x - x_\mathrm{d}\right)^2 \tag{A.3.4}$$

the effective potential $\phi^\star$ can be approximated as:

$$\phi^\star = \frac{qN_\mathrm{d}}{\epsilon_\mathrm{s}}x\left(x_\mathrm{d} - \frac{x}{2}\right) \approx \frac{qN_\mathrm{d}}{\epsilon_\mathrm{s}}xx_\mathrm{d} = \left(\phi_\mathrm{i} - V_\mathrm{a}\right)\frac{2x}{x_\mathrm{d}} \tag{A.3.5}$$

to first order for $x \ll x_\mathrm{d}$. Therefore the integral in the denominator of equation A.3.3 can be approximated, for $(\phi_\mathrm{i} - V_\mathrm{a}) > V_\mathrm{t}$, like:

$$\int_0^{x_\mathrm{d}}\exp\left(-\frac{\phi^\star}{V_\mathrm{t}}\right)\mathrm{d}x \approx x_\mathrm{d}\frac{V_\mathrm{t}}{2\left(\phi_\mathrm{i} - V_\mathrm{a}\right)} \tag{A.3.6}$$

Finally the expression for the total current becomes:

$$J_{\mathrm{n}} = qN_{\mathrm{c}}\mu_{\mathrm{n}}\mathcal{E}_{\max}\exp\left(-\frac{\phi_{\mathrm{b}}}{V_{\mathrm{t}}}\right)\left[\exp\left(\frac{V_{\mathrm{a}}}{V_{\mathrm{t}}}\right)-1\right] \tag{A.3.7}$$

where $\mathcal{E}_{\max}$ is, as already defined in 2.1.86, is the maximal field at the metal-semiconductor interface.

A.3.2 Thermionic emission current

Within the thermionic emission theory Sze (1981) the shape of the actual Schottky barrier in usually neglected, and it is assumed that all electrons with energies over the top of the barrier and moving towards the barrier will actually cross the barrier. The electronic current from right to left is thus given by:

$$J_{\mathrm{right-left}} = \int_{E_{\mathrm{c}}(x=\infty)+q\phi_{\mathrm{b}}}^{\infty} qv_x\frac{\mathrm{d}n}{\mathrm{d}E}dE \tag{A.3.8}$$

where the density of states in the interval $E\ldots E+\mathrm{d}E$ is given by (see 2.1.23):

$$\frac{\mathrm{d}n}{\mathrm{d}E} = \gamma_{\mathrm{c}}\frac{1}{2\pi^2}\left(\frac{2m_{\mathrm{c}}^{\star}}{\hbar^2}\right)^{3/2}\sqrt{E-E_{\mathrm{c}}}\exp\left(-\frac{E-E_{\mathrm{Fn}}}{kT}\right) \tag{A.3.9}$$

Within the effective mass approximation:

$$\sqrt{E-E_{\mathrm{c}}} = v\sqrt{\frac{m_{\mathrm{c}}^{\star}}{2}} \tag{A.3.10}$$

Substituting equation A.3.10 into A.3.9 and then into A.3.8 yields:

$$J_{\mathrm{right-left}} = 2\left(\frac{m_{\mathrm{c}}^{\star}}{\hbar}\right)^3\int_{-\infty}^{\infty}\exp\left(-\frac{m_{\mathrm{c}}^{\star}v_y^2}{2kT}\right)\mathrm{d}v_y\int_{-\infty}^{\infty}\exp\left(-\frac{m_{\mathrm{c}}^{\star}v_z^2}{2kT}\right)\mathrm{d}v_z \int_{-\infty}^{\infty}\exp\left(-\frac{m_{\mathrm{c}}^{\star}v_x^2}{2kT}\right)\mathrm{d}v_x\exp\left[-\frac{E_{\mathrm{c}}(x=0)-E_{\mathrm{Fn}}}{kT}\right] \tag{A.3.11}$$

which by using

$$\int_{-\infty}^{\infty}\exp\left(-\frac{m_{\mathrm{c}}^{\star}v_y^2}{2kT}\right)\mathrm{d}v_y = \int_{-\infty}^{\infty}\exp\left(-\frac{m_{\mathrm{c}}^{\star}v_z^2}{2kT}\right)\mathrm{d}v_z = \sqrt{\frac{2\pi kT}{m_{\mathrm{c}}^{\star}}} \tag{A.3.12}$$

reduces to:

$$J_{\mathrm{right-left}} = 2\left(\frac{m_{\mathrm{c}}^{\star}}{\hbar}\right)^3\frac{2\pi kT}{m_{\mathrm{c}}^{\star}}\exp\left[-\frac{E_{\mathrm{c}}(x=0)-E_{\mathrm{Fn}}}{kT}\right]\exp\left(-\frac{m_{\mathrm{c}}^{\star}v_{0_x}^2(x=\infty)}{2kT}\right)\frac{kT}{m_{\mathrm{c}}^{\star}} \tag{A.3.13}$$

where, for simplicity, the anisotropy of the effective mass has been neglected.

A. APPENDIX A

The minimal velocity v_{0_x} of an electron deep in the semiconductor that is sufficient to cross the barrier can be estimated (within effective mass approximation) as:

$$v_{0_x}(x=\infty) = \sqrt{\frac{2q\phi(x=\infty)}{m_{\mathrm{c}}^{\star}}} \tag{A.3.14}$$

Also, the energy difference $E_{\mathrm{c}}(x=\infty) - E_{\mathrm{Fn}}$ can be estimated like:

$$-\frac{E_{\mathrm{c}}(x=\infty) - E_{\mathrm{Fn}}}{q} = \phi_{\mathrm{i}} - V_{\mathrm{a}} - \phi_{\mathrm{b}} \tag{A.3.15}$$

Finally, substituting equations A.3.14 and A.3.15 into A.3.13, an estimate for $J_{\mathrm{right-left}}$ can be deduced as:

$$J_{\mathrm{right-left}} = A^{\star}T^2 \exp\left(-\frac{\phi_{\mathrm{b}}}{V_{\mathrm{t}}}\right) \exp\left(\frac{V_{\mathrm{a}}}{V_{\mathrm{t}}}\right) \tag{A.3.16}$$

The current in reverse direction $J_{\mathrm{left-right}}$ is approximately independent of the applied voltage V_{a}, as if the barrier-lowering due to image charges is neglected, the barrier height at the interface does not depend on the band-bending in the semiconductor and is always equal to ϕ_{b} [1]. Therefore $J_{\mathrm{left-right}}$ can be estimated simply to be equal to $J_{\mathrm{right-left}}$ at $V_{\mathrm{a}} = 0$ by absolute value [2]:

$$J_{\mathrm{left-right}} = -A^{\star}T^2 \exp\left(-\frac{\phi_{\mathrm{b}}}{V_{\mathrm{t}}}\right) \tag{A.3.17}$$

The total current J_{n} can be calculated simply as the sum of $J_{\mathrm{right-left}}$ and $J_{\mathrm{left-right}}$, and equals:

$$J_{\mathrm{n}} = A^{\star}T^2 \exp\left(-\frac{\phi_{\mathrm{b}}}{V_{\mathrm{t}}}\right)\left[\exp\left(\frac{V_{\mathrm{a}}}{V_{\mathrm{t}}}\right) - 1\right] \tag{A.3.18}$$

The above expression can be rewritten in therms of the Richardson velocity

$$v_{\mathrm{R}} = \sqrt{\frac{kT}{2\pi m_{\mathrm{c}}^{\star}}} \tag{A.3.19}$$

to become:

$$J_{\mathrm{n}} = qN_{\mathrm{c}}v_{\mathrm{R}} \exp\left(-\frac{\phi_{\mathrm{b}}}{V_{\mathrm{t}}}\right)\left[\exp\left(\frac{V_{\mathrm{a}}}{V_{\mathrm{t}}}\right) - 1\right] \tag{A.3.20}$$

Therefore at equilibrium $V_{\mathrm{a}} = 0$ the current densities of the thermionic currents in the positive and negative directions are both equal to $qN_{\mathrm{c}}v_{\mathrm{R}} \exp\left(-\frac{\phi_{\mathrm{b}}}{V_{\mathrm{t}}}\right)$.

[1] It should be noted that $q\phi_{\mathrm{b}}$ is only approximately equal to the barrier as seen from the electrons flowing from left to right, Φ_0.

[2] The signs of $J_{\mathrm{right-left}}$ and $J_{\mathrm{left-right}}$ are, of course, opposite.

A.3.3 Tunnelling current

Schematically, the tunnelling current component can be derived within the WKB approximation, starting from the effective Schrdinger equation:

$$\frac{\mathrm{d}^2\Psi(x)}{\mathrm{d}x^2} = \frac{2m_\mathrm{c}^\star(q\phi(x)-E)}{\hbar^2}\Psi(x) \tag{A.3.21}$$

and approximating $\Psi(x+\mathrm{d}x)$ like:

$$\Psi(x+\mathrm{d}x) = \Psi(x)\exp\left(-w\mathrm{d}x\right) \tag{A.3.22}$$

where, for an electron moving from left to right, $w = k^\mathrm{WKB}$ is given by:

$$w = \frac{\sqrt{2m_\mathrm{c}^\star\left[\phi(x)-E\right]}}{\hbar} \tag{A.3.23}$$

assuming that $\phi(x) - E$ is constant in the interval $x \ldots x + \mathrm{d}x$ Thus, for a slowly varying potential across the barrier, the wave function, at position x_d at the end of the barrier, can be expressed as:

$$\Psi(x_\mathrm{d}) = \Psi(x=0)\exp\left(-\int_0^{x_\mathrm{d}}\frac{\sqrt{2m_\mathrm{c}^\star\left[q\phi(x)-E\right]}}{\hbar}\mathrm{d}x\right) \tag{A.3.24}$$

For a triangular barrier the energy difference $q\phi(x) - E$ can be expressed like:

$$q\phi(x) - E = q\phi_\mathrm{b}\left(1-\frac{x}{x_\mathrm{d}}\right) \tag{A.3.25}$$

Therefore the tunnelling probability Θ defined as[1]:

$$\Theta = \frac{\Psi(x_\mathrm{d})\Psi^\star(x_\mathrm{d})}{\Psi(0)\Psi^\star(0)} \tag{A.3.26}$$

can be estimated like:

$$\Theta = \exp\left(-2\frac{\sqrt{2m_\mathrm{c}^\star}}{\hbar}\int_0^{x_\mathrm{d}}\sqrt{q\phi_\mathrm{b}\left(1-\frac{x}{x_\mathrm{d}}\right)}\mathrm{d}x\right) \tag{A.3.27}$$

The saturation current density can then be written as:

$$J_\mathrm{s} = qnv_\mathrm{R}\Theta \tag{A.3.28}$$

or in full:

$$J_\mathrm{s} = qv_\mathrm{R}n\exp\left(-\frac{4}{3}\frac{\sqrt{2m_\mathrm{c}^\star}}{\hbar}\sqrt{q\phi_\mathrm{b}}x_\mathrm{d}\right) \tag{A.3.29}$$

So far, the different density of states on both sides of the metal-semiconductor junction have been ignored. In a different approach, the tunnelling current can be evaluated using Fermi's

[1] Here $\star$ denotes complex conjugate.

golden rule from perturbation theory (see Woan (2000)). The current from right to left is thus proportional to the occupied density of states in the semiconductor times a matrix element of the transition $\mathcal{T}$, times the unoccupied density of states in the metal. Analogously, the current from right to left is proportional to the occupied density of states in the metal, times the same matrix element $\mathcal{T}$, times the unoccupied density of states in the semiconductor. The current density is thus expressed (following for example Shenai & Dutton (1988)) like[1]:

$$J_{\mathrm{n}} = \frac{A^{\star}T}{k}\left[\int_{0}^{\infty}\mathcal{D}_{\mathrm{s}}\mathcal{T}(\eta)\left(1-\mathcal{D}_{\mathrm{m}}\right)\mathrm{d}\eta - \int_{0}^{\infty}\mathcal{D}_{\mathrm{m}}\mathcal{T}(\eta)\left(1-\mathcal{D}_{\mathrm{s}}\right)\mathrm{d}\eta\right] \tag{A.3.30}$$

where $\mathcal{D}_{\mathrm{m}}$ and $\mathcal{D}_{\mathrm{s}}$ are evaluated at their respective electrochemical potentials $\eta \pm \Delta\eta/2$, and $\Delta\eta$ is approximately given by $\Delta\eta \approx qV_{\mathrm{a}}$. This equation forms the basis of the combined thermionic-emission-tunnelling theory.

At equilibrium $V_{\mathrm{a}} = 0$ and equation A.3.30 reduces to:

$$\int_{0}^{\infty}\left[\mathcal{D}_{\mathrm{s}}(\eta) - \mathcal{D}_{\mathrm{m}}(\eta)\right]\mathcal{T}(\eta)\mathrm{d}\eta = 0 \tag{A.3.31}$$

which is equivalent to the condition $Q_{\mathrm{s}} - Q_{\mathrm{m}} = 0$ already used when discussing the electrostatics of Schottky contacts (see 2.1.4.1). In other words, during the formation of a metal-semiconductor contact, there is a tendency towards the establishment of balance between the occupied density of states on both sides of the junction and the levelling of a common electrochemical potential η across the entire system.

The dependence of the transmission coefficient $\mathcal{T}$ on barrier height is exponential of the form (see Rhoderick & Williams (1988)):

$$\mathcal{T} \propto \exp\left(-\frac{q\phi_{\mathrm{b}}}{E_{00}}\right) \tag{A.3.32}$$

where

$$E_{00} \equiv \frac{q\hbar}{2}\sqrt{\frac{N_{\mathrm{d}}}{\epsilon_{\mathrm{s}}m_{\mathrm{c}}^{\star}}} \tag{A.3.33}$$

This explains why the tunnelling current becomes dominant in junctions incorporating heavily doped semiconductors or junctions with intentionally $\delta-$doped [2] surface layers. As a function of temperature, two distinct limits may be defined (see Crowell & Rideout (1969)):

1. $\frac{kT}{E_{00}} \gg 1$ where the thermionic emission is the dominant process and therefore the current has a strong temperature dependence;

[1] This assumes that the transmission is symmetric in both directions, from the metal to the semiconductor, and from the semiconductor to the metal.

[2] Layers of very high doping at semiconductor surfaces of width δ which are created intentionally, normally, in order to achieve ohmic contacts to metals.

2. $\frac{kT}{E_{00}} \ll 1$ where tunnelling is the dominant transport mechanism, and the temperature variation of the transmission probability is vanishing.

It can be shown, in a way already demonstrated above, that if the barrier height lowering due to the image force is neglected and at low temperature, the electronic current may be expressed as:

$$J_{\mathrm{n}} = J_{\mathrm{S}} \exp\left(\frac{qV_{\mathrm{a}}}{E_{00}}\right) \tag{A.3.34}$$

where the saturation current density can be approximated like:

$$J_{\mathrm{S}} = \frac{A^{\star}\sqrt{\pi}\sqrt{E_{00}}\sqrt{\Phi_{\mathrm{b}} - qV_{\mathrm{a}} - (E_{\mathrm{c}} - E_{\mathrm{F}})}}{kT\cosh\frac{E_{00}}{kT}} \exp\left[-\frac{E_{\mathrm{c}} - E_{\mathrm{F}}}{kT} - \frac{\Phi_{\mathrm{b}} - (E_{\mathrm{c}} - E_{\mathrm{F}})}{E_{00}}\right] \tag{A.3.35}$$

in the mixed region of thermionic-field emission (see Jang & Lee (2002); Jang *et al.* (2003)).

It is intuitively clear that applied voltage V_{a} dependence of the transmission probability, at high temperature, will follow a form similar to the one obeyed by the thermionic emission current. In practice, it is possible to approximate the exact dependence with a form like:

$$J_{\mathrm{n}} = J_{\mathrm{s}} \exp\left[\left(\frac{qV_{\mathrm{a}}}{\Upsilon kT}\right) - 1\right] \tag{A.3.36}$$

where Υ is the customary 'ideality factor' introduced in section 2.1.5.4. This has been shown to be valid in the temperature region defined by $\frac{kT}{E_{00}} \gtrsim 1$ (see Padovani & Stratton (1966)).

There are couple of corrections that can be done to the standard thermionic-emission-tunnelling theory, that are often considered (see for example Kalameĭtsev *et al.* (1997); Racko *et al.* (1996, 1997)). One is the inclusion of two different Richardson constants, A_{s} and A_{m}, and two different transmission coefficients $\mathcal{T}_{\mathrm{s-m}}$ and $\mathcal{T}_{\mathrm{m-s}}$; for the currents flowing from the semiconductor to the metal and backwards. The total current density is thus given by:

$$J_{\mathrm{n}} = \frac{T}{k}\left\{A_{\mathrm{s}}\int_0^{\infty}\mathcal{D}_{\mathrm{s}}\mathrm{T}_{\mathrm{s-m}}(E)\,(1-\mathcal{D}_{\mathrm{m}})\,\mathrm{d}E - A_{\mathrm{m}}\int_0^{\infty}\mathcal{D}_{\mathrm{m}}\mathcal{T}_{\mathrm{m-s}}(E)\,(1-\mathcal{D}_{\mathrm{s}})\,\mathrm{d}E\right\} \tag{A.3.37}$$

The other is the inclusion of an arbitrary build-in potential in the calculation of the transmission coefficients $\mathcal{T}_{\mathrm{s-m}}$ and $\mathcal{T}_{\mathrm{m-s}}$. This is most easily done numerically, by calculating the global transfer matrix:

$$\mathbf{G} = \prod_{i=0}^{ns}\mathbf{S}_i\mathbf{P}_i \tag{A.3.38}$$

where $\mathbf{S}_i$ and $\mathbf{P}_i$ are sets of scattering matrices and phase matrices, defined as:

$$\mathbf{S}_i = \frac{1}{2}\begin{bmatrix} 1 + \frac{m^{\star}_{i-1}w_i}{m^{\star}_i w_{i-1}} & 1 - \frac{m^{\star}_{i-1}w_i}{m^{\star}_i w_{i-1}} \\ 1 - \frac{m^{\star}_{i-1}w_i}{m^{\star}_i w_{i-1}} & 1 + \frac{m^{\star}_{i-1}w_i}{m^{\star}_i w_{i-1}} \end{bmatrix} \tag{A.3.39}$$

$$\mathbf{P}_i = \begin{bmatrix} \exp(-w_i d_i) & 0 \\ 0 & \exp(w_i d_i) \end{bmatrix} \tag{A.3.40}$$

where $i = [0, ns]$ where ns is the number of slices of thickness d_i, into which the total barrier width x_d has been split; and $m_i^\star$ are the effective masses within those slices, w_i are the respective momenta, defined in the usual WKB way:

$$w_i = \frac{\sqrt{2m_i^\star \left(q\phi_i - E\right)}}{\hbar} \tag{A.3.41}$$

where ϕ_i is the electric potential in each slice. Therefore the transmissions $\mathcal{T}_{\mathrm{s-m}}(E)$ and $\mathcal{T}_{\mathrm{m-s}}(E)$ can be evaluated using the global transfer matrix $\mathbf{G}$ and its inverse $\mathbf{G}^{-1}$ like:

$$\mathcal{T}_{\mathrm{s-m}} = \frac{w_{ns}}{w_0}\left(g_{11}g_{11}^\star\right)^{-1} \tag{A.3.42}$$

$$\mathcal{T}_{\mathrm{m-s}} = \frac{w_0}{w_{ns}}\left(g_{11}^{-1}g_{11}^{-1\star}\right)^{-1} \tag{A.3.43}$$

and finally the total current integral J_n evaluated.

Normally, the knowledge of the actual effective wavefunction is unnecessary, though in principle obtainable as the wavefunction may be approximated piecewise by linearly independent pair of base functions (most commonly Airy functions[1]) like:

$$\Psi_i(x) = c_\mathrm{A}\mathrm{Ai}\left(\tilde{x}_i(x)\right) + c_\mathrm{A}\mathrm{Bi}\left(\tilde{x}_i(x)\right) \tag{A.3.44}$$

where c_A and c_B are constants determined by matching the wavefunctions $\Psi_i(x)$ and their first derivatives $\partial_x\Psi_i(x)$ at the borders of each interval of width d_i, and the coordinate transforms $\tilde{x}_i(x)$ are defined as:

$$\tilde{x}_i(x) = \left(x + \frac{\phi(x) - E}{\mathcal{E}_i}\right)\left(\frac{2qm_i^\star\mathcal{E}_i}{\hbar^2}\right)^{\frac{1}{3}} \tag{A.3.45}$$

where $\mathcal{E}_i$ are the piecewise constant approximations for the electric field in the structure.

Though it is difficult to make a clear discrimination, the WKB method is to be preferred for broad and smoothly-varying barrier potentials, while the Airy functions method is technique of choice for steep field profiles (see Bruno *et al.* (2007); Vega (2006)).

A.4 Accumulation and ohmic contacts to semiconductors

For some metal/semiconductor combinations, it is possible to have $\Phi_\mathrm{s} > \Phi_\mathrm{m}$ and the Fermi level of the metal to lie between the Fermi level in the semiconductor and the conduction band edge for an n-type semiconductor (analogous situation can be similarly defined for p-type

[1] Airy functions of the first kind $\mathrm{Ai}(x)$ and the second kind $\mathrm{Bi}(x)$, defined as two linearly independent solutions of the differential equation $\partial_x^2 y(x) - y(x)x = 0$.

semiconductor Zeghbroeck (1997)). Analogously to the treatment of the electrostatic problem in section A.2 the Poisson equation for the electrostatic potential can be written like:

$$\frac{\mathrm{d}^2\phi}{\mathrm{d}x^2} = -\frac{\rho(\phi)}{\epsilon_\mathrm{s}} = \frac{qN_\mathrm{d}}{\epsilon_\mathrm{s}} \exp\left(\frac{q\phi(x)}{kT}\right) \tag{A.4.1}$$

The solution can be sought in the form:

$$\phi(x) = \frac{a}{b}\ln\left(1+bx\right) \tag{A.4.2}$$

where a and b are constant coefficients. Further, after double differentiation, boundary conditions at infinity $\mathcal{E}(\infty) = 0$ and at zero $\mathcal{E}(0) = \sqrt{\frac{2kT}{\epsilon_\mathrm{s}N_\mathrm{d}}}$ can be imposed. The first of which demanding charge neutrality deep in the semiconductor, and the second one demanding that the maximal electrostatic energy exactly equals the thermal energy, per unit volume and at equilibrium, close to the interface at $x = 0$ like:

$$\frac{\epsilon_\mathrm{s}\mathcal{E}^2(0)}{2N_\mathrm{d}} = kT \tag{A.4.3}$$

The resulting solutions for the electrostatic potential and the build-in electric field are:

$$\begin{aligned} \phi(x) &= -\frac{2kT}{q}\ln\left(1+\frac{\sqrt{2}}{2}\frac{x}{L_\mathrm{D}}\right) \\ \mathcal{E}_\mathrm{bi}(x) &= \sqrt{2}\frac{V_\mathrm{t}}{L_\mathrm{D}}\frac{1}{1+\frac{1}{\sqrt{2}}\frac{x}{L_\mathrm{D}}} \end{aligned} \tag{A.4.4}$$

where L_D, as customary, is the Debye length and $V_\mathrm{t} = \frac{kT}{q}$ is the voltage equivalent of temperature.

Solution for the electric field for an arbitrary semiconductor with $N_\mathrm{d} = 10^{17}$ cm^{-3} are shown at figure A.3 The width of the accumulation layer x_a can be obtained from equating $\phi(x_\mathrm{a}) = \phi_\mathrm{i} - V_\mathrm{a}$ at an applied bias V_a, to be:

$$x_\mathrm{a} = \sqrt{2}L_\mathrm{D}\left[\exp\left(\frac{|\phi_\mathrm{i} - V_\mathrm{a}|}{2V_\mathrm{t}}\right) - 1\right] \tag{A.4.5}$$

It is easily seen that, generally, the accumulation layer widths are shorter than the depletion layer widths, and the associated build-in electric fields are smaller for the accumulation case rather than the depletion case. Therefore, under accumulation conditions, the resulting metal-semiconductor contacts are, generally, ohmic.

It should be mentioned, that it is sometimes possible, to engineer the Fermi-level pinning at a semiconductor surface (which otherwise renders the work function of the metal, in a Schottky junction, irrelevant) and achieve both depletion and accumulation. An example is the ternary system InGaN, as proved by photoemission studies by Veal *et al.* (2006).

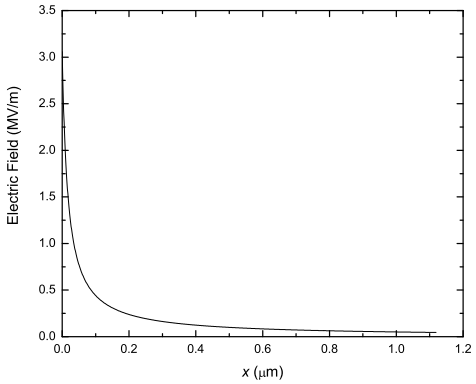

Figure A.3: Potential distribution across the depleted region for n-type non-degenerate semiconductor. Constants are set as follows: $\epsilon_s = 10\epsilon_0$, $N_d = 10^{-17}$ cm^{-3} and $\phi_i = 1$ V.

A.5 Various conventions and Instrumental calibrations

Following is a set of figures, which are important for understanding or verifying certain points in the text, though, are unnecessary burden for the reader.

The coordinate system and sign convention used in the description of the theory and experiment is standard and followed throughout most of the references in the text. Figure A.4 explicitly denotes the standard.

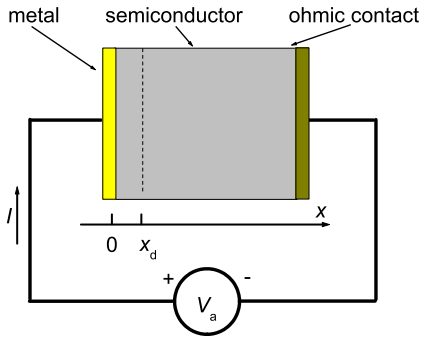

Figure A.4: Coordinate system and sign convention used in the description of the Schottky junction theory.

The spectral calibrations of the spectrometers used in characterising the 'grey' absorbers used in the photo-illumination studies of Shcottky junctions are provided at figures A.5 and A.6. The calibrations have been executed using a set of He, Na and Ne, low-pressure spectral

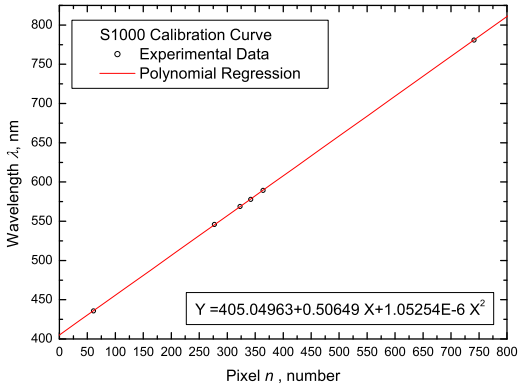

Figure A.5: Spectral calibration of the S1000 fibre-optics spectrometer.

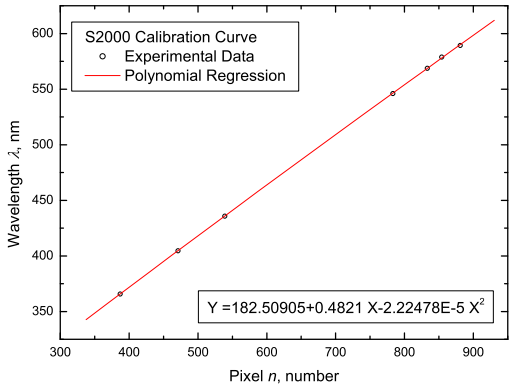

Figure A.6: Spectral calibration of the S2000 fibre-optics spectrometer.

lamps. Incandescent W based bulbs have been used for intensity calibration of the S1000 and S2000 fibre-optic coupled spectrometers. Both spectrometers exhibit high linearity and long term stability.

The intensity calibrations of the halogen lamps used for the diodes illumination are provided on figures A.7 and A.8. It is easily noted that due to absorption in the limited air-paths and attenuation in the optical fibres, for most purposes the integral spectral intensity in the near UV part of the spectrum, can be neglected below about 370 nm. The oscillation-like modulation of the spectra is related to thin-film equal-thickness fringes of interference in some of the protection coatings of the CCD detection arrays used.

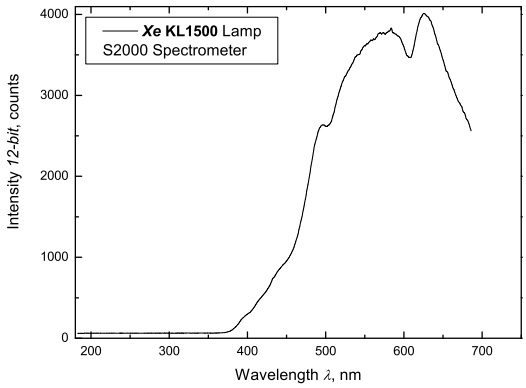

Figure A.7: Intensity calibration of the KL1500 lamp used in the experiments.

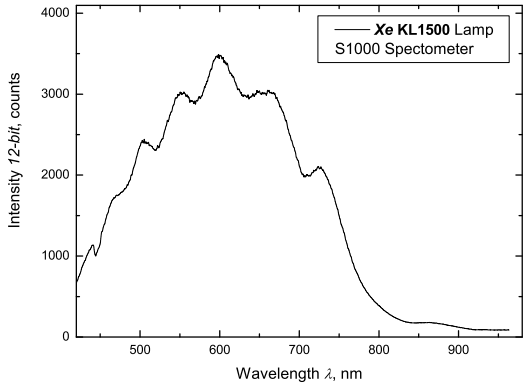

Figure A.8: Intensity calibration of the KL1500 lamp used in the experiments.

Two examples of absorption coefficient calibration on the absorbers used in the photo-illumination experiments are given at figures A.9 and A.10. On both figures, curves in red

have been measured on a S2000 fibre-coupled spectrometer and curves in black, on a S1000 spectrometer. Absorption is about 15 % and 97 % for the two absorbers used. .

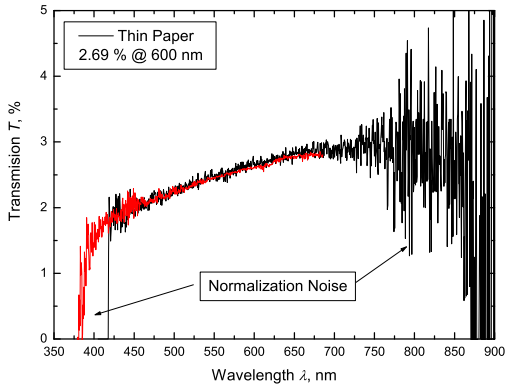

Figure A.9: Absorber calibration in the NUV - VIS - NIR range.

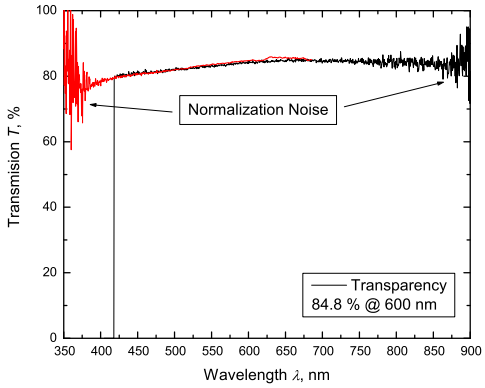

Figure A.10: Absorber calibration in the NUV - VIS - NIR range.

A.6 Details of experimental procedures

Various details of sample preparation procedures and measurement apparata and protocols are provided below.

A.6.1 Schottky junctions preparation

Commercial, moderately n-doped Si and GaAs wafers of different cuts (<100>, <111>, etc.) are used as semiconductor substrates. All wafers are cleaned in boiling acetone, boiling methanol

and 20 MΩ deionised water. For the Si substrates, standard semiconductor grade etching solution NH_4OH:HF:H_2O is used[1]. The GaAs substrates are sequentially etched in H_3PO_4:H_2O_2:H_2O optimised solution and in HCl:H_2O. All wafers are then washed in deionised water, dried in a stream of dry N_2 and immediately introduced into the vacuum chamber for deposition.

Deposition is done by Ar magnetron sputtering at 10^{-3} mBar (Shamrock Sputtering Tool) or alternatively by thermal evaporation at 10^{-7} mBar (Edwards AUTO 306). All sputtering targets and evaporation sources are of at least 4N purity. Metal alloy evaporation sources have been prepared by wighting stoechiometric amounts of the respective metals and melting the mixtures into ingots in an in-vacuum arc-melter[2] until homogeneous. Metal layer thickness is 30 nm for the diodes prepared for galvanic measurements, and 15 nm for the diodes prepared for photovoltaic measurements. Consecutively thick Ag contact pads are evaporated for the external contacts on the metallic side.

The Ohmic contacts are prepared by direct soldering with In metal at 400 K and consecutive rapid annealing at 800 K. During the entire process, the metal side of the junctions is cooled by a jet of high-purity Ar gas, in order to avoid oxidation and intermixing and large inter-diffusion of metal atoms, across the Schottky interface.

One example of a diode mounting configuration is shown on figure A.11. Other sockets and various mounting methods (i.e. wire-bonding, In soldering, silver-painting) have been employed for measurements in [3]

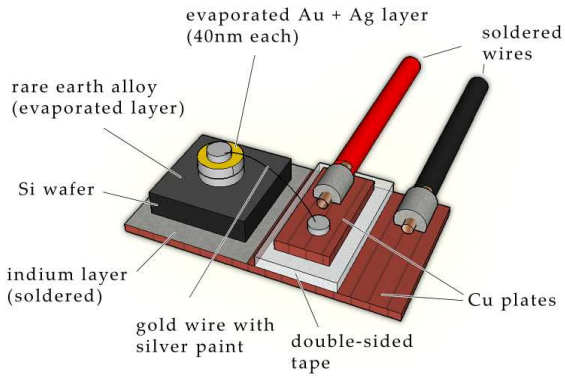

Figure A.11: Diode mounting configuration, used for ambient temperature diode characterisation.

[1] The eching solution is supplied by Honeywell Inc. USA.

[2] All ingots have been remelted at least three times.

[3] Selection is based on experimental requirements and limitations like: temperature region and thermal conductivity, available size, mechanical vibrations, external illumination, etc.

A.6.2 Description of I-V curve tracer

A block diagram of the $I-V$ curve tracer is shown at figure A.12. The arbitrary waveform generator is either 6 MHz HP/Agilent 82 or 10 MHz TTI 8. The digitising oscilloscope was 8-bit, 40 MHz Agilent 208. Current compliance is about 10 mA at 1 kHz. Voltage compliance is 10 V throughout the frequency window DC to 1 MHz. Sweeps can be performed at constant rate of change of voltage by supplying a triangular waveform of the appropriate frequency. All resistors used have tolerances better than 1 % and are low inductance, metal thin film type. Measurements were performed in the dark, at ambient conditions.

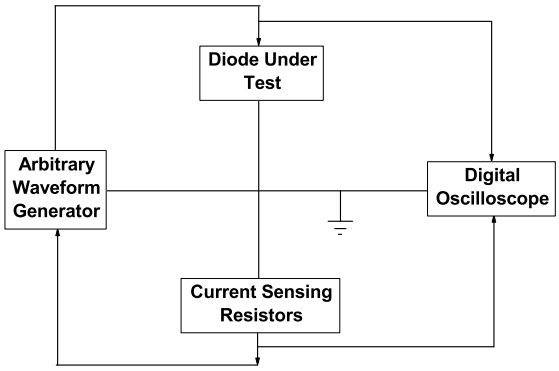

Figure A.12: Block diagram of the $I-V$ curve tracer used for fast diode characterisation.

A.6.3 Transport measurements setup

DC measurements are performed using the standard 4-wire method with source-meters (Keithley 2400, 2410 and HP228 series). Two basic connection diagrams are shown on figure A.13.

AC measurements are performed using a resistance bridge, with an isolating transformer for the AC/DC decoupling, Lock-in amplifiers (EG&G 50, 52 and 82 series), and programmable voltage source (Keithley 240). Two basic connection diagrams are shown on figure A.14.

The temperature is stabilised using a water bath (Grant) to circulate water through two planar heat sinks, between which the diodes were sandwiched. The temperature is, thus, stable to within 0.05 K. The absolute temperature is know to better than 0.5 K[1]. The maximal temperature difference between diodes, one of which is situated in, and the other out of, the

[1]The uncertainty arrises form the maximal possible thermal gradients between the temperature sensor and the devices under test.

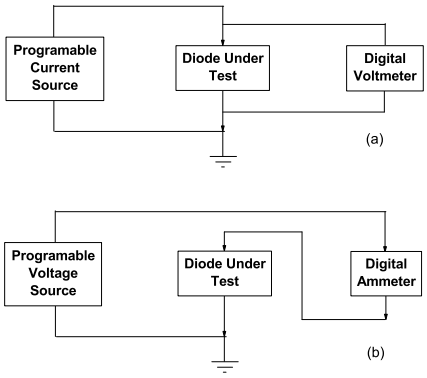

Figure A.13: Block diagram of the $I - U$ curve curve measurement configurations for low device impedance (a), and for high device impedance (b).

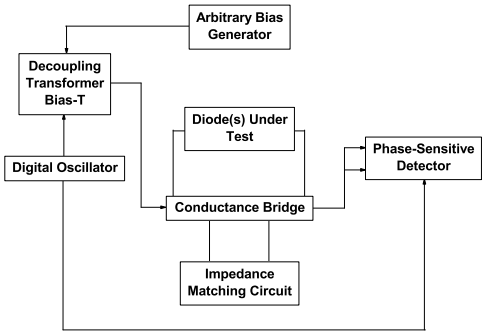

Figure A.14: Block diagram of the AC/DC bridge device comparison setup.

region of the magnet bore is measured to be below 3 K and stable to better than 0.1 K , independently of the magnetic field applied. Verification for field sweep at a rate of 0.1 T/min is shown at figure A.15. Alternatively, the samples are mounted into a He vapour-flow variable

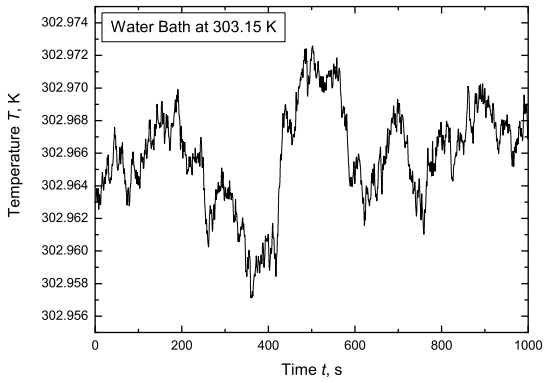

Figure A.15: Temperature, as monitored by a 4-wire AC-bridge measurement on Class A, Pt 100, standard resistor. During the scan the field was ramped continuously at a rate of 0.1 T/min.

temperature insert of providing temperatures in the region of 1.9 - 350 K, within an error margin of 0.1 Kand stability of about 0.01 K.

Magnetic field was provided with a 5.5 T wide bore superconducting magnet (Cryogenic UK) with stability of 0.05 % for a period of 1 h. The magnetic field applied was deduced from the energising current measured as a voltage drop across a high stability shunt. Alternatively, the superconducting magnet of a commercial Physical Property Measurement System (PPMS), Quantum Design Inc., is used, providing fields of up to 14 T.

The diodes are illuminated using a fibre-optic assembly, with focusing/defocusing lenses and collimators. Air-cooled, filtered xenon lamp (Xe KL1500) is used as a light source.

A. APPENDIX A

Appendix B

Appendix B

B.1 Transfer Hamiltonian approach to spin-polarised tunnelling

Bellow, a brief account of the generalisation of the transfer Hamiltonian approach is given, based on the discussion by Zhang & Levy (1999).

A simple mani-body theory to recover non-vanishing magneto-conductance within the WKB approximation for the wavefunctions of the individual quasiparticles may be constructed by using a matrix version of a second-order quantisation theory. Starting with a Hamiltonian matrix $\mathbf{H}$ for the spin-polarised electrodes of the form:

$$\mathbf{H}^{\mathrm{l,r}} = \sum_{\mathbf{k}s} {}^{\mathrm{c}}\varepsilon^{\mathrm{l,r}}_{\mathbf{k}} \mathbf{c}^{\mathrm{l,r}}_{\mathbf{k}s} \mathbf{c}^{\mathrm{l,r\dagger}}_{\mathbf{k}s} + \sum_{\mathbf{k}s} {}^{\mathrm{d}}\varepsilon^{\mathrm{l,r}}_{\mathbf{k}} \mathbf{d}^{\mathrm{l,r}}_{\mathbf{k}s} \mathbf{d}^{\mathrm{l,r\dagger}}_{\mathbf{k}s} + \sum_{\mathbf{k}s} {}^{\mathrm{t}}\varepsilon^{\mathrm{l,r}}_{\mathbf{k}} \mathbf{c}^{\mathrm{l,r}}_{\mathbf{k}s} \mathbf{d}^{\mathrm{l,r\dagger}}_{\mathbf{k}s} \tag{B.1.1}$$

where $\mathbf{c}^{\mathrm{l,r}}_{\mathbf{k}s}$ and $\mathbf{d}^{\mathrm{l,r}}_{\mathbf{k}s}$ are the annihilation operators for the left and right-hand-side electrodes for the s-like states and the d-like states, respectively, and the filling-coefficients ${}^{\mathrm{c}}\varepsilon^{\mathrm{l,r}}_{\mathbf{k}}$, ${}^{\mathrm{d}}\varepsilon^{\mathrm{l,r}}_{\mathbf{k}}$ and ${}^{\mathrm{t}}\varepsilon^{\mathrm{l,r}}_{\mathbf{k}}$ are representing the population of the s-like stated, the d-like states, and their hybridisation. The Hamiltonian of the entire tunnel junction may be thus written like:

$$\mathbf{H} = \mathbf{H}^{\mathrm{l}} + \mathbf{H}^{\mathrm{r}} + \mathbf{H}^{\mathrm{t}} \tag{B.1.2}$$

with the part $\mathbf{H}^{\mathrm{t}}$ describing the transfer of electrons from one side to the other and expressed as:

$$\mathbf{H}^{\mathrm{t}} = \sum_{\mathbf{k}\mathbf{k}'s} \left\{ \left[T^{\mathrm{c}}_{\mathbf{k}\mathbf{k}'} \mathbf{c}^{\mathrm{l\dagger}}_{\mathbf{k}s} \mathbf{c}^{\mathrm{r}}_{\mathbf{k}'s} + T^{\mathrm{c}}_{\mathbf{k}'\mathbf{k}} \mathbf{c}^{\mathrm{r\dagger}}_{\mathbf{k}'s} \mathbf{c}^{\mathrm{l}}_{\mathbf{k}s} \right] + \left[T^{\mathrm{d}}_{\mathbf{k}\mathbf{k}'} \mathbf{d}^{\mathrm{l\dagger}}_{\mathbf{k}s} \mathbf{d}^{\mathrm{r}}_{\mathbf{k}'s} + T^{\mathrm{d}}_{\mathbf{k}'\mathbf{k}} \mathbf{d}^{\mathrm{r\dagger}}_{\mathbf{k}'s} \mathbf{d}^{\mathrm{l}}_{\mathbf{k}s} \right] \right\} \tag{B.1.3}$$

where the matrix elements $T^{\mathrm{c,d}}_{\mathbf{k}\mathbf{k}'}$ are responsible for the transfer of s-like and d-like electrons, which in the WKB approximation is inversely proportional to the density of states as already mentioned in section 3.1.4:

$$T^2_{\mathrm{k}\mathrm{k}'} = \frac{C^2}{\mathcal{D}_{\mathrm{l}}\left(E_{\mathbf{k}}\right)\mathcal{D}_{\mathrm{r}}\left(E_{\mathbf{k}'}\right)} \tag{B.1.4}$$

where C is a coefficient, that depends on details of the potential barrier profile, the actual value of which is not important for the present considerations.

Further, the particle number operator $\mathbf{n}$ can be introduced in the usual way:

$$\mathbf{n}^{\mathrm{l,r}} = \sum_{\mathbf{k}s}\left\{\mathbf{c}^{\mathrm{l,r}\dagger}_{\mathbf{k}s}\mathbf{c}^{\mathrm{l,r}}_{\mathbf{k}'s} + \mathbf{d}^{\mathrm{l,r}\dagger}_{\mathbf{k}s}\mathbf{d}^{\mathrm{l,r}}_{\mathbf{k}'s}\right\} \tag{B.1.5}$$

and its time evolution described by the conventional propagator (anti-commutator with the Hamiltonian):

$$i\hbar\frac{\mathrm{d}\mathbf{n}^{\mathrm{l,r}}}{\mathrm{d}t} = \left[\mathbf{n}^{\mathrm{l,r}}, \mathbf{H}\right] \tag{B.1.6}$$

and finally the tunnelling current from left to right may be evaluated as the long-time average of $q\frac{\mathrm{d}\mathbf{n}^{\mathrm{l}}}{\mathrm{d}t}$.

In order to obtain an explicit formulation, further simplifying propositions must be made. One is to neglect the second half of the transfer Hamiltonian, namely, the tunnelling of the d-like states. In this case:

$$\mathbf{H}^{\mathrm{t}} = \sum_{\mathbf{k}\mathbf{k}'s}\left\{T^{\mathrm{c}}_{\mathbf{k}\mathbf{k}'}\mathbf{c}^{\mathrm{l}\dagger}_{\mathbf{k}s}\mathbf{c}^{\mathrm{r}}_{\mathbf{k}'s} + T^{\mathrm{c}}_{\mathbf{k}'\mathbf{k}}\mathbf{c}^{\mathrm{r}\dagger}_{\mathbf{k}'s}\mathbf{c}^{\mathrm{l}}_{\mathbf{k}s}\right\} \tag{B.1.7}$$

and the equation of motion B.1.6 simplifies to[1]:

$$i\hbar\frac{\mathrm{d}\mathbf{n}^{\mathrm{l}}}{\mathrm{d}t} = \sum_{\mathbf{k}\mathbf{k}'s} T_{\mathbf{k}\mathbf{k}'}\left[\mathbf{c}^{\mathrm{l}\dagger}_{\mathbf{k}s}\mathbf{c}^{\mathrm{r}}_{\mathbf{k}'s} - \mathrm{h.c.}\right] \tag{B.1.8}$$

The current thus becomes:

$$I = q\sum_{\mathbf{k}\mathbf{k}'s}\int \mathrm{d}E\left|T_{\mathbf{k}\mathbf{k}'s}\right|^2 \mathcal{S}^{\mathrm{r}}\left(\mathbf{k}', s; E\right)\mathcal{S}^{\mathrm{l}}\left(\mathbf{k}, s; E + qV_{\mathrm{a}}\right)\left[f_{\mathrm{r}}\left(E\right) - f_{\mathrm{r}}\left(E + qV_{\mathrm{a}}\right)\right] \tag{B.1.9}$$

where $\mathcal{S}^{\mathrm{l,r}}$ are the spectral functions of the s-like states. Those can be evaluated as the negated imaginary part of the respective Green's functions:

$$\mathcal{S}^{\mathrm{l,r}} \equiv -\mathrm{Im}\left(\mathcal{G}^{\mathrm{l,r}}\right) \tag{B.1.10}$$

The Green's function $\mathcal{G}\left(\mathbf{k}, s; E\right)$, itself, may be evaluated as the inverse of the Hamiltonian of the s-like states, within first order time-dependent perturbation theory (see Landau & Liphshitz

[1] h.c. - is used to denote Hermitian conjugate, i.e. complex conjunction and transposition.

(1976)), where the d-like states are considered to interact perturbatively with the s-like states with and energy scale of ${}^{\mathrm{d}}\varepsilon^{\mathrm{l,r}}_{\mathbf{k}}$:

$$\mathcal{G}^{\mathrm{l,r}} = \left[E - {}^{\mathrm{s}}\varepsilon^{\mathrm{l,r}}_{\mathbf{k}} - \frac{\left|{}^{\mathrm{t}}\varepsilon^{\mathrm{l,r}}_{\mathbf{k}}\right|^2}{E - {}^{\mathrm{d}}\varepsilon^{\mathrm{l,r}}_{\mathbf{k}}} \right]^{-1} \tag{B.1.11}$$

the poles of the above Green's function are situated at $E = E^{\mathrm{l,r}}_{\mathbf{k}s}$, given by:

$$E^{\mathrm{l,r}}_{\mathbf{k}s} = \frac{{}^{\mathrm{s}}\varepsilon^{\mathrm{l,r}}_{\mathbf{k}} + {}^{\mathrm{d}}\varepsilon^{\mathrm{l,r}}_{\mathbf{k}}}{2} \pm \sqrt{\left({}^{\mathrm{t}}\varepsilon^{\mathrm{l,r}}_{\mathbf{k}}\right)^2 + \left(\frac{{}^{\mathrm{s}}\varepsilon^{\mathrm{l,r}}_{\mathbf{k}} + {}^{\mathrm{d}}\varepsilon^{\mathrm{l,r}}_{\mathbf{k}}}{2}\right)^2} \tag{B.1.12}$$

and their corresponding renormalisations (calculated as residuals) are:

$$Z^{\mathrm{l,r}}_{\mathbf{k}s} = \left(1 + \frac{\left({}^{\mathrm{t}}\varepsilon^{\mathrm{l,r}}_{\mathbf{k}}\right)^2}{E^{\mathrm{l,r}}_{\mathbf{k}s} - {}^{\mathrm{d}}\varepsilon^{\mathrm{l,r}}_{\mathbf{k}s}} \right)^{-1} \tag{B.1.13}$$

Using the residuals theorem, the imaginary part of the Green's function can then be expressed as:

$$\mathrm{Im}\left(\mathcal{G}^{\mathrm{l,r}}\right) = -2\pi Z^{\mathrm{l,r}}_{\mathbf{k}s}\delta\left(E - E^{\mathrm{l,r}}_{\mathbf{k}s}\right) \tag{B.1.14}$$

In the final step of this evaluation, the sum over k-space overlap in equation B.1.9 can be substituted by an integral over energy of the overlap of the density of states, like:

$$\sum_{\mathbf{k}\mathbf{k}'} = \int \mathcal{D}_{\mathrm{l}}\left(E^{\mathrm{l,r}}_{\mathbf{k}s}\right)\mathcal{D}_{\mathrm{r}}\left(E^{\mathrm{l,r}}_{\mathbf{k}'s}\right)\mathrm{d}E^{\mathrm{l,r}}_{\mathbf{k}s}\mathrm{d}E^{\mathrm{l,r}}_{\mathbf{k}'s} \tag{B.1.15}$$

The tunnelling current in the limit of $T \to 0$ and $V \to 0$ thus becomes:

$$I = 2\pi q^2 V_{\mathrm{a}} C^2 \sum_s \overline{Z}^{\mathrm{l}}_s \overline{Z}^{\mathrm{r}}_s \tag{B.1.16}$$

where $\overline{Z}^{\mathrm{l,r}}_s$ are the k-space averaged renormalisation factors.

It is important to note, that once again (as in section 3.1.4), the density of states of the electrodes, explicitly present in equation B.1.15, cancels with the inverse dependence of the matrix element B.1.4 on the density of states leaving no explicit dependence in the expression for the tunnelling current. Nevertheless, the renormalisation factors remain in, carrying the information for the polarisation of s-like states via their hybridisation with the d-like states.

The realisation of the fact that, the renormalisation factors, rather than the density of states, that influence the tunnelling conductance, gives a way of understanding the experimental fact (evidence mainly from superconducting tunnelling experiments), that the majority (spin-up) electrons have higher transmission coefficients, while having lower density of states at, or close to the Fermi level. As the minority (spin-down) electrons have a lower Fermi energy (are more strongly hybridised), the difference $E^{\mathrm{l,r}}_{\mathbf{k}\downarrow} - {}^{\mathrm{d}}\varepsilon^{\mathrm{l,r}}_{\mathbf{k}\downarrow}$ is smaller, and leads to smaller (see equation B.1.13) renormalisation factors $Z^{\mathrm{l,r}}_{\mathbf{k}\downarrow}$ and correspondingly smaller tunnelling current component.

B.2 Sample preparation and initial characterisation

B.3 Measurement technique

A conventional four-wire DC + AC resistance technique has been used for the simultaneous measurement of both the quasi-static $I-V$ characteristics, and the first and second derivative of voltage drop across the sample with respect to current. A schematic representation of the is shown at figure B.1. The realisation is similar to the one suggested by Hipps & Mazur (2002), with an optional software control of the modulation amplitude. The measurement of differential resistance, instead of differential has several important distinctions:

1. A true four-wire sample leads compensation can be realised (to the level of the device chip, only).

2. Low noise JFET pre-amplifiers can be used, preserving satisfactory level of impedance matching, and therefore better noise performance.

3. A higher level of protection against electrical breakthrough of the junction under test may be achieved when actively limiting the maximal current, thus avoiding overheating problems.

4. The current sourcing (both DC and AC parts) can be readily bypassed, preserving the current limits upon connection and disconnection of a device to the measurements system. As the device connections are essentially all shorted to the system ground during bypassing, the level of electrostatic safety is considerably improved.

5. As DC resistance and AC differential resistance are the natively determined parameters, the determination of DC and AC conductance has to be done numerically. For example, if the first and second derivative of the voltage drop with respect to current are known (or evaluated numerically), the second derivative can be computed like (see Wolf & Losee (1970)):

$$\frac{\partial^2 J}{\partial V^2} = -\frac{\partial^2 V}{\partial J^2}\left(\frac{\partial V}{\partial J}\right)^{-2} \tag{B.3.1}$$

The sample environment has been provided in a Quantum Design, PPMS[1] system, equipped with a 14 T superconducting magnet, and a He vapour flow temperature control system, with an in-vacuum sample space. The data acquisition and control software has been written specifically for this class of measurement platforms, and allows for full system monitoring,

[1] Physical Property Measurement System

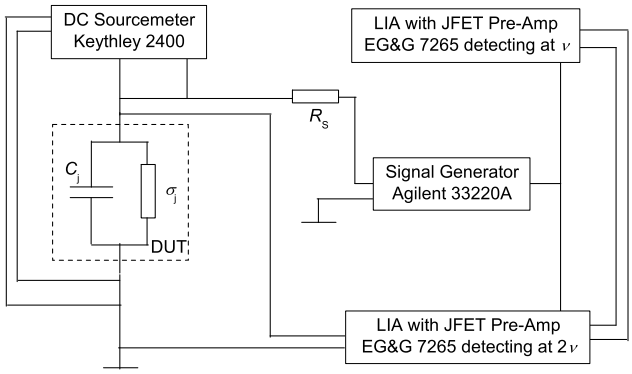

Figure B.1: Schematic diagram of the setup used for four-wire DC resistance and AC differential resistance measurements.

control and programming. Detail on the design of the control system are given in appendix B.5.

An important verification of the technique and instrumentation, that is normally performed before each measurement cession, is the bias dependence of a standard low-noise metal thin film resistor. Example of such a procedure is shown on figure B.2. It is readily seen, that

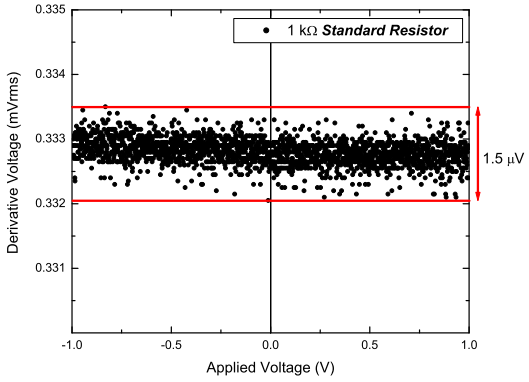

Figure B.2: Voltage dependence of the differential resistance of a 1 kΩ standard resistor. The noise band is shown for a time constant of 0.1 s.

the measured differential resistance is constant with respect to the statistical dispersion of the data, as expected. The band noise shown, is primarily determined by the imperfections in the shielding of the screened twisted pairs used for connection to the devise under test (interference pick-up from other subsystems in the same measurement platform), while the sample and pre-amplifier noise, are often not a point of concern. Of course, in situations, where there is a large

impedance mismatch between the measured junction and the amplifiers (both measurement and current/voltage sourcing ones), excessive noise can become an issue. Therefore, care must be taken in order to both, select proper pre-amplifiers, and select working frequencies and frequency filtering strategies, that would guarantee minimal interference and optimal amplifier noise-figures. Moreover, conditioned current and voltage signals have been monitored directly on a digital oscilloscope, in order to exclude the possibility of sporadic or systematic interferences of large magnitude interfering with the signal of interest and influencing the detected amplitudes or their current and instrumental broadening.

Examples of electromagnetic interference, as coupled to a standard grounded chassis 50 Ω BNC connector are shown on figures B.3 and B.4. As anticipated, the most prominent

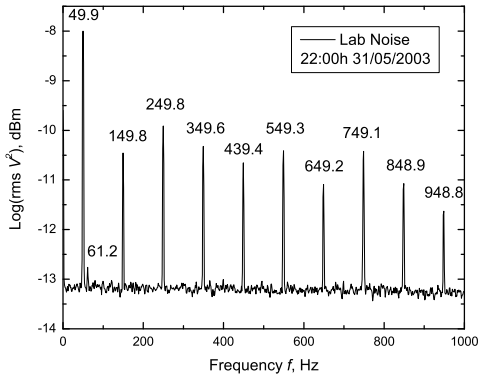

Figure B.3: Electromagnetic interference as coupled to a standard BNC connector, in a normal laboratory environment, in the frequency window where mains interference is dominant.

sources of interference are the mains power supply units, both with conventional rectifiers and pulsed-width modulation ones. The frequencies that should be avoided are thus the mains frequency (50 Hz in this particular case) and its odd harmonics[1], and some frequencies generated by pulse-width modulation power supplies (26, 64, 66 kHz). In synchronous, heterodyne detectors, lock-in amplifiers, etc., where notch filters are used to reduce mains interference, often, useful frequencies for modulation are in the region above 500 Hz. Elevated working frequencies also have the advantage of providing smaller minimal integration time constant, and therefore faster data acquisition, on the expense of complications related to the capacitive and inductive components of the impedances in the measurement circuit.

[1]The generation of predominantly odd harmonics, is only the case, when close to ideal rectifiers are used, as the Fourier transform of a generally asymmetric transfer function (neither odd, not even), contains both odd and even harmonics.

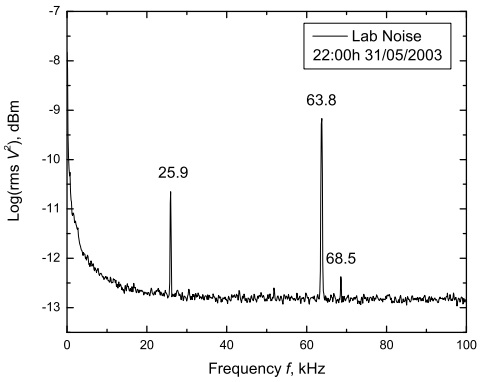

Figure B.4: Electromagnetic interference as coupled to a standard BNC connector, in a normal laboratory environment.

B.4 Ferromagnet - Superconductor tunnelling

Below a summary, within the classical semi-empirical model , is given of the basic features of the tunnelling process between a superconductor and a ferromagnetic metal. This is important, as the techniques developed in this respect are still a source of basic information about the spin-polarisation in ferromagnetic metals (see Meservey *et al.* (1970) and Tedrow & Meservey (1973)), but also in order to point-out the differences in the tunnelling process (mainly the influence of the density of states).

The current is expressed through matrix element in the normal state like:

$$J = \frac{2\pi q}{\hbar}|\mathcal{T}|^2\mathcal{D}_{\rm l}(0)\mathcal{D}_{\rm r}(0)\int_{-\infty}^{\infty}\rho_{\rm sup}(E)\left[f(E)-f(E-qV_{\rm a})\right]{\rm d}E \tag{B.4.1}$$

where $\rho_{\rm sup}$ is the BCS theory[1] energy dependence of the state density given (neglecting the thermal smearing by):

$$\begin{aligned}\rho_{\rm sup}(E) &= \frac{|E|}{\sqrt{E^2-\Delta_{\rm s}^2}}, \quad |E|\geq\Delta_{\rm s}\\ \rho_{\rm sup}(E) &= 0, \quad |E|<\Delta_{\rm s}\end{aligned} \tag{B.4.2}$$

where the superconducting gap is given by $2\delta_{\rm s}$.

Conventionally, the dependence of the tunnel current on the normal-state density is taken care of by normalising the differential conductance measured in the superconducting state for

[1] Bardeen Cooper Schreiffer theory of conventional superconductivity

one of the electrodes, to the one measured with both electrodes in the normal state, like:

$$\frac{\sigma_{\mathrm{j}}^{\mathrm{sup}}}{\sigma_{\mathrm{j}}^{\mathrm{norm}}} = \int_{-\infty}^{\infty} \rho_{\mathrm{sup}}(E) \frac{1}{kT} \frac{\exp\left(\frac{E-qV_{\mathrm{a}}}{kT}\right)}{\left[1+\exp\left(\frac{E-qV_{\mathrm{a}}}{kT}\right)\right]^2} \mathrm{d}E \tag{B.4.3}$$

for the case of non-ferromagnetic electrodes, or simply as a convolution of the superconducting density of states with the conventional Fermi-smearing kernel (see equation 3.2.37), which reduces to a delta function in the limit $T \to 0$, leaving the normal conductance directly proportional to the superconducting density of states. For a ferromagnetic second electrode, neglecting interactions that would generate spin-flip transitions (for example spin-orbit interaction), i.e. making the independent spin-channel approximation, the normalised differential conductivity can be expressed as:

$$\begin{aligned}\frac{\sigma_{\mathrm{j}}^{\mathrm{sup}}}{\sigma_{\mathrm{j}}^{\mathrm{norm}}} = &\int_{-\infty}^{\infty} \left(\frac{\alpha^{\mathrm{s}}+1}{2}\right) \rho_{\mathrm{sup}}(E+g\mu_{\mathrm{B}}B) \frac{1}{kT} \frac{\exp\left(\frac{E-qV_{\mathrm{a}}}{kT}\right)}{\left[1+\exp\left(\frac{E-qV_{\mathrm{a}}}{kT}\right)\right]^2} \mathrm{d}E \\ &+ \int_{-\infty}^{\infty} \left(\frac{1-\alpha^{\mathrm{s}}}{2}\right) \rho_{\mathrm{sup}}(E-g\mu_{\mathrm{B}}B) \frac{1}{kT} \frac{\exp\left(\frac{E-qV_{\mathrm{a}}}{kT}\right)}{\left[1+\exp\left(\frac{E-qV_{\mathrm{a}}}{kT}\right)\right]^2} \mathrm{d}E\end{aligned} \tag{B.4.4}$$

where α^{s} is, as customary, the static density of states polarisation of the ferromagnetic electrode, at the Fermi level. Equation B.4.4 represents one of the most valuable methods for determination of the static polarisation of Ferromagnetic metals at low temperatures.

There are couple of factors that contribute to the difficulty of observing density of states effects in normal metal - ferromagnet junctions, or direct relation of density of states polarisation and conductivity for ferromagnet - ferromagnet tunnelling. One is the step-like density of states is a peculiarity if the superconducting state (or other similar gapped states), which allows for the clear separation of the individual spin-channel contributions, under the application of external magnetic field[1]. Another is the intrinsic conflict, between the demands for reasonable spectroscopic resolution, that should be comparable to the zeeman splittings accessible experimentally, and high Curie temperature, which is necessary for both practical applicability and in order to provide an advantage over the cryogenic methods.

An open possibility still remains, for the observation of density-of-states related effects in normal metal - low Curie point ferromagnet tunnel junctions, which can be readily driven

[1] For example, similar effects are difficult or impossible to observe in semiconductor-ferromagnet tunnelling, as the typical semiconductor gaps are of the order of 100 meV, and the externally applied bias V_{a}, tends to create extended voltage drop across metal-semiconductor junctions, due to the relatively low carrier densities in semiconductors, and accordingly worse charge screening.

through a sharp transition; or the utilisation of semimetal - ferromagnet junctions, should the semi-metal have a low-enough density of states at the Fermi level, while preserving sufficient conductivity (i.e. very high mobility) at low temperature. True half-metals may also be applied as selective electrodes, however, there is limited evidence for sharp features in the tunnelling involving alleged half-metals like (LaSr)MnO_3 (see Mukhopadhyay *et al.* (2005) and references thereof).

B.5 Physical Property Measurement System Controller Software Package

The following is a brief description of the functionality offered in the *PPMS Controller* software package.

The package is aimed at providing all basic functionality of the standard *MultiVu* software package supplied together with the Physical Property Measurement System[1] (PPMS) measurement platform. Apart from providing means of direct dialog control of all functional parameters of the system the software package provides means of monitoring, logging and some safety features like command parameter control and low He level system shutdown.

There are three major differences between the *PPMS Controller* and *MultiVu*[2]:

1. *PPMS Controller* is able to acquire data at much higher rates than the *MultiVu*. The inherent parallelism of the program allows for data rates as high as 50 Hz[3], while monitoring and logging the system status at say 1 Hz.

2. *PPMS Controller* is able to control equipment external to the PPMS system, connected on RS-232[4], GPIB[5], USB[6] or any other Windows^{tm} compatible interface.

3. *PPMS Controller* has a far more sophisticated scripting language, allowing for variables, cycles, labels, branching, floating point and boolean computation, among others.

The grammar is non-context sensitive (in its dominant part) - second level[7], mainly agglutinating, and partially inflecting language (see Chomsky (2006)). The execution is done line by

[1] Quantum Design Inc., San Diego, CA, USA

[2] *MultiVu* is the software package supplied with the PPMS system and well established among the user community.

[3] Actual experimental rate, when polling four independent full-speed GPIB compatible devices.

[4] Historic, but widely used, low speed, serial interface standard.

[5] General Purpose Interface Bus

[6] Universal Serial Bus

[7] The actual level may be considered as high as 2.5.

line, unless required by cycles or branching. The sequence can be terminated by user request, by a stop command or by an system event - like a low He level alarm. The grammar is not case sensitive nor space (tab) sensitive. The commands can be abbreviated to the shortest distinguishable symbol sequence.

B.5.1 Control Commands

The following is a list of all control commands available in Version 1.0 of *PPMS Controller*

' - Remark command - anything on the same line after this symbol is not executed.

% *variable* = *expression* - Changes the value of variable or defines a new variable and sets its value to expression.

"*string***"** - Represents a *string* contained inside the quotation marks.

afn(*string*) - Adds to the name (leaving the extension untouched) of the present file the contents of string or any variable cited inside the brackets.

clr - Clears all presently defined dynamic variables.

end - Unconditionally discontinues the execution of the sequence.

hll(*level* | **en**able | **dis**able) - Enables, disables or sets the Low Helium Level action and trigger level at *level* (the *PPMS Controller* will perform the action independently of whether the sequence is running or not).

sd - Brings the system into Shutdown state.

sf(*set field*, *field rate*, *approach mode*, *final state*) - Sets the magnetic field, where *set field* can take any value between -140000 and 140000, in Oe, *field rate* can take any value between 0.001 and 133.1, in Oe/s, *approach mode* can be any of the following: **lin**ear, **no**vershoot and **osc**illate, *final state* can be either **p**ersistent or **d**riven.

sim(**on** | **off**) - Switches on or off the simulation mode (in simulation mode the sequence is executed as usual, though no actual commands are send to the system).

sp(*setangle*, *speed*) - Sets the angular position of the horizontal rotator to *setangle* degrees at speed defined as a number between 0 and 15, 0 corresponding to fastest speed of about 1 degree per second.

st(*setpoint* , *temp rate*, *approach*) - Sets the system's temperature to *setpoint*, any value between 1.8 and 400, at *temp rate*, any value between 0.01 and 20, in K/s, and regulates the *approach* to be **f**ast or **no**overshoot.

sv(*variable*, *value*) - Sets the value of the *variable* to *value*. If the *variable* is not existant - it will be created.

wait(*wait time*) - The execution of the sequence is paused for *wait time* number of milliseconds.

wf(*time*, *timeout*) - Waits until the system field has been stable for more than *time* number of seconds. The execution will continue either if the first condition is satisfied or if more than *timeout* number of seconds elapse since the command has been issued. A *timeout* of 0 requires the satisfaction of the condition with an indefinite timeout.

wp(*time*, *timeout*) - Waits until the system angular position has been stable for more than *time* number of seconds. The execution will continue either if the first condition is satisfied or if more than *timeout* number of seconds elapse since the command has been issued. A *timeout* of 0 requires the satisfaction of the condition with an indefinite timeout.

wt(*time*, *timeout*) - Waits until the system temperature has been stable for more than *time* number of seconds. The execution will continue either if the first condition is satisfied or if more than *timeout* number of seconds elapse since the command has been issued. A *timeout* of 0 requires the satisfaction of the condition with an indefinite timeout.

B.5.2 Data Taking Commands

The following is a list of all data taking commands available in Version 1.0 of *PPMS Controller*

log(**on** | **off**) - Switches on or off the log information saving mode (logging is performed in the default data file).

save(**on** | **off**) - Switches on or off the fast data saving mode.

saveone - Saves one data point (all data and status information, that has been selected for saving).

readone - Acquires one data point (all selected devices are polled).

runf(*max iter*, *max speed*) - Starts a fast data acquisition process of *max iter* number of data points at *max speed* data taking speed in Hz.

stopf - Stops the fast data aquisition process started with **runf**.

B.5.3 Cycling Commands

The following is a list of all cycle commands available in Version 1.0 of *PPMS Controller*

for(*variable*, *start value*, *end value*, *step*) - Starts a cycle on the variable from *start value* to *end value* inclusive, at a step defined by *step*. The cycle contains all sequence lines before the first encountered next operator. A sequence may contain a number of nested cycles of various types.

next - Delimits the last open **for** cycle.

repeat - Initiates a cycle on all lines in the present sequence to the next **until** command.

until *condition* - Delimits a cycle initiated by the **repeat** command if *condition* is not true.

wend - Delimits the last open **while** cycle.

while *condition* **do** - Cycles all lines to the next **wend** command upon the *condition* being true.

B.5.4 Branching Commands

The following is a list of all branching commands available in Version 1.0 of *PPMS Controller*

{*label***}** - Labels the following command with *label*. The *label* can be any string that does not contain a valid command.

if *condition* **then** *label* **else** *label* - Jumps to first *label* upon the *condition* being true otherwise jumps to the second *label* if the **else** clause is present or to the next line if it is omitted.

B.5.5 Expressions

The following is a list of all expressions available in Version 1.0 of *PPMS Controller* in a modified Backus-Naur Form (see Naur (1960)).

expression ::=	*constant* |	- any numeric constant
	% *variable* |	- any already defined variable
	expression ***** *expression* |	- standard multiplication
	expression **/** *expression* |	- standard division
	expression **+** *expression* |	- standard addition
	expression **-** *expression* |	- standard subtraction
	expression **^** *expression* |	- arbitrary power
	log *expression* |	- decimal logarithm
	ln *expression* |	- natural logarithm
	(*expression* **)** |	- standard bracketing
	expression **** *expression* |	- integer division
	expression **mod** *expression* |	- remanent after division
	exp *expression* |	- standard exponent
	sin *expression* |	- standard sine
	cos *expression* |	- standard cosine
	tan *expression* |	- standard tangent
	atn *expression* |	- standard arcus tangent

	abs *expression* |	- absolute value
	int *expression* |	- integer part
	sgn *expression* |	- the signum of the expression
	sqr *expression*	- standard square-root
bool expr ::=	**true**|	- logical true
	false |	- logical false
	(*bool expr*) |	- standard bracketing
	not *bool expr* |	- logical not (inversion)
	bool expr **and** *bool expr* |	- logical and (conjunction)
	bool expr **or** *bool expr* |	- logical or (disjunction)
	bool expr **xor** *bool expr* |	- logical exclusive or
	bool expr **imp** *bool expr* |	- logical implication
	bool expr **eqv** *bool expr* |	- logical equivalence
	expression > *expression* |	- greater than
	expression < *expression* |	- less than
	expression >= *expression* |	- greater or equal
	expression <= *expression* |	- less or equal
	expression = *expression* |	- strictly equal
	expression <> *expression* |	- strictly not equal
string ::=	” *string const* ” |	- string constant *string const*
	string + *string*	- concatenation of two strings

B. APPENDIX B

Appendix C

Appendix D

C.1 Experimental setup and samples for direct magnetic detection of spin injection

The experimental setup is presented on the top panel of figure 4.1. The samples have been dimensioned to make optimal use of the second-order gradiometer in a Quantum Design MPMS 5 XL SQUID based magnetometer system. The main parameters being the on-axis-approximation decorrelation length of 1.00 cm (see C.3) and the maximal accessible sample translation (12 cm).

The samples, schematically visualised on figure C.1, are prepared on either 200 µm borosilicate glass substrates, 5.5 mm wide, 25 mm long (Sample 1), or on 1 mm high purity (5N5) fused silica rod 18 cm long (Sample 2). Gold contacts 40 nm thick are first evaporated in a AUTO 306 thermal evaporator in a dry vacuum of $5 \cdot 10^{-7}$ mbar, using set of shadow masks. The two injection electrodes (Fe, Co, Ni or Zn) 10 nm thick, either 2 mm $\times$ 5.5 mm (Sample 1) or 0.5 mm $\times$ 1 mm (Sample 2), with a centre spacing of 20 mm are evaporated next. The aluminium strip, either 20 mm $\times$ 5.5 mm $\times$ 40 nm, or 20 cm $\times$ 1mm $\times$ 500nm, is deposited last. Bare gold wires 35 µm in diameter are attached to the gold contacts using indium solder.

The samples are mounted in clear drinking straws and connected to a double twisted pair or oxygen-free copper wires for electrical measurements. Care is taken to orthogonalise any potential current loops with respect to the measurement axis of the system, in order to minimise the mutual inductance with the gradiometer. Current is supplied, either by a Keithley 2400

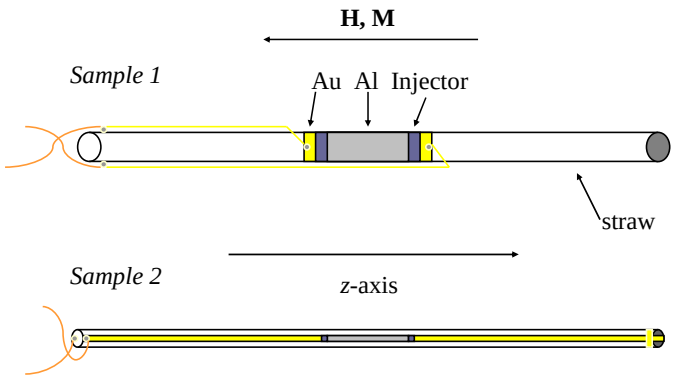

Figure C.1: Schematic representation of the two types of samples used to investigate the possibilities for direct magnetic detection of injected spin polarisation.

source-meter for DC measurements or by a TGA 1242 arbitrary waveform generator and EG&G 5209 lock-in amplifier for AC measurements.

The measurements are performed by translating the sample assembly with a maximum displacement of 80 mm along the gradiometer axis and either digitising the amplified voltage proportional to the flux coupled to the gradiometer (DC method) or by acquiring the in-phase and out-of-phase components with respect to the excitation current for zero, positive or negative constant current bias (AC method). The choice of low-pass filter (nominally 12 dB/Octave at 80 Hz) determined the electronic drift in the DC method. The maximal applied field (along the z-axis of the assembly) has been limited to 500 mT and is determined by the flux drift due to the field inhomogeneity in the sample region. A minimal applied field of 20 mT is chosen in order to guarantee the stability of the magnetisation in the Fe injection electrodes.

C.2 Materials used in the spin injection experiment

Below are notes on the magnetic properties of some of the materials used in the construction of the samples used in the experiments described in section 4.4.

The temperature dependence of the magnetic susceptibility of the Al source material used is an important factor that ultimately limit the maximal temperature elevation of the samples used for magnetic detection of spin-injection. The measured magnetic susceptibility is dominated by the Pauli paramagnetic contribution, and agrees well with existing data on pure Al and dilute Al-Mn alloys, in the pure Al limit (see Hedgcock & Li (1970)) of $2.07 \cdot 10^{-5}$, as evidenced by figure C.2.

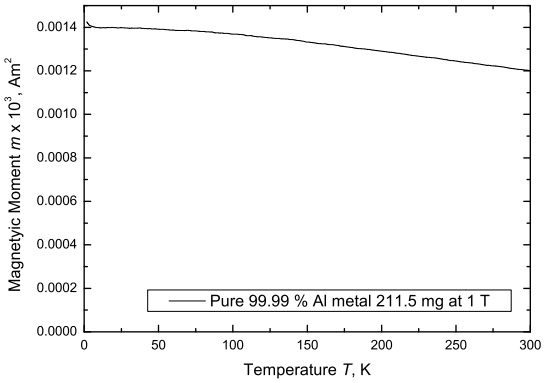

Figure C.2: Magnetic moment as a function of temperature, measured in a field of 1 T, for a 4N pure Al sample of mass 211.5 mg.

Aluminium exhibits a relatively large quadratic in temperature correction to the dominant constant term in the Pauli susceptibility (the Fermi energy of Al is about 10 eV) as has been first noted by Wheeler (1968). This has been illustrated on figure C.3. Systematically repro-

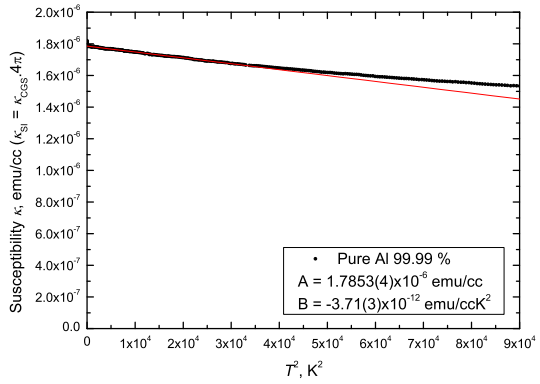

Figure C.3: The dataset of figure C.2, replotted in order to illustrate the quadratic temperature dependence of the magnetic susceptibility.

ducible low-temperature upturn of the paramagnetic susceptibility is also commonly observed in aluminium. The temperature dependence is Curie-like, as evidenced on figure C.4, but is unlikely to be due to the paramagnetism of isolated impurity ions, because of their high Kondo temperature in Al, and is considered an effect intrinsic to the electronic structure of the material (see Cooper & Miljak (1976); Hedgcock & Li (1970)).

A reasonable agreement between the experimental data and a combined model, including

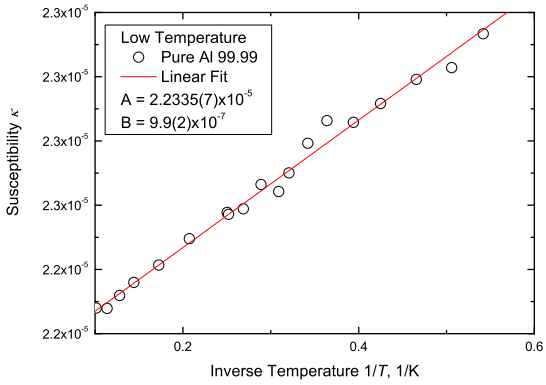

Figure C.4: The dataset of figure C.2, replotted in order to illustrate the low temperature Curie-like temperature dependence of the magnetic susceptibility.

Pauli paramagnetism and Curie-like term at low temperature, is achieved in temperature region 1.8 - 300 K, as evidenced on figure C.5.

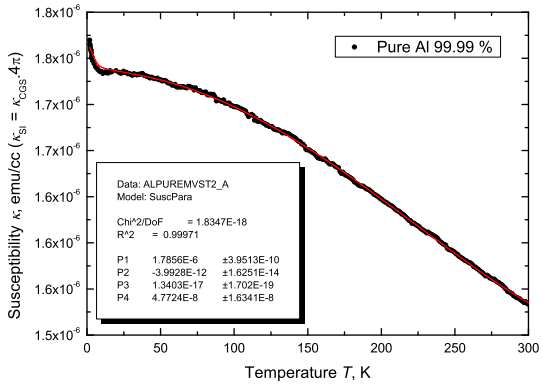

Figure C.5: A fit to the dataset of figure C.2, including the temperature dependence of the Pauli susceptibility and the Curie-like low temperature upturn.

The susceptibility of the borosilicate glass substrates used, has been found to be a superposition of a diamagnetic and paramagnetic (with some evidence of interaction effects) terms of comparable magnitudes, as shown on figure C.6. Compensation is reached for temperatures in the region of 10 K. The strong, hyperbolic temperature dependence of the susceptibility is a major factor, preventing samples prepared on these substrates to be used for optimal resolution spin-injection experiments.

The magnetic susceptibility of the fused silica rods, used to prepare the support for Sample

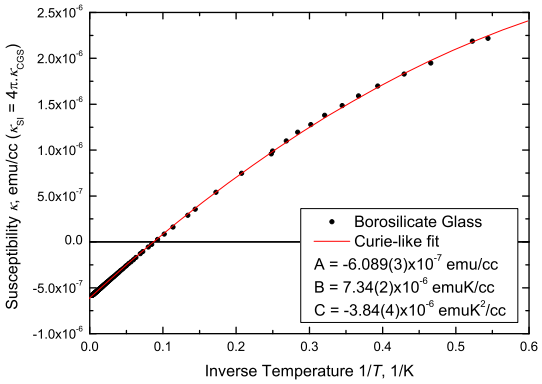

Figure C.6: Magnetic susceptibility as a function of temperature for a borosilicate glass sample.

2, has been found to be diamagnetic and essentially temperature independent as expected (see figure C.7). The experimental dimensionless susceptibility of $\kappa_{SiO_2} = 1.52(3) \cdot 10^{-5}$ (in SI units) agrees well with the standard value of $1.55 \cdot 10^{-5}$ (see Keyser & Jefferts (1989)). The temperature stability of the susceptibility and its high uniformity throughout the material used ensures optimal suppression of spurious effects due to sample heating.

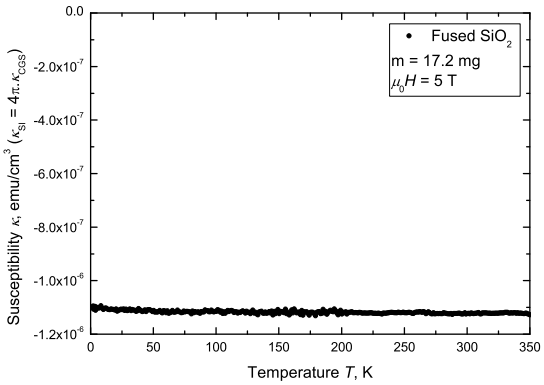

Figure C.7: Magnetic susceptibility as a function of temperature for a 5N pure fused SiO_2 rod sample. The data has not been corrected for an absolute sensitivity calibration factor of 1.085(1) valid at the time of the measurement.

C.3 Magnetisation Measurements Using Second Order Gradiometers

C.3.1 Gradiometers for magnetisation measurements

The increasing requirements, mainly in solid-state physics, for characterisation of small or weekly magnetic samples, such as thin films, has tightened the requirements on high-sensitivity vibrating sample (VSM) and SQUID[1] magnetometers. Various first and second order gradiometer coil assemblies have been optimized to measure the different components of the magnetic moment of a sample. For their better suppression of external interferences second order gradiometers are generally preferred. They are widely used in the popular single axis SQUID based magnetometer.

A number of theoretical works describe procedures for calculating the response functions of various pick-up assemblies under more-or-less severe restrictions. Very often the sample is approximated by an ideal dipole perfectly positioned in the centre of the sample holder; extended samples are often considered to be homogeneously magnetised. Detrimental effects relating to the mechanical orientation and translation of the sample or the existence of image effects (due to the presence of superconducting material in the form of shields or coils) are neglected. A review of works, on both image and sample geometry effects, is provided by Zieba (1993).

The following analysis is illustrated with a particular example of a SQUID magnetometer (Quantum Design Magnetic Property Measurement System MPMS XL [2]), equipped with longitudinal pickup coils, although the approach used can be readily generalized and exploited for simulating the response of any other induction-based magnetometer.

C.3.2 Second-order gradiometer analysis

The second-order gradiometer under consideration is depicted on the inset in figure C.8. It consists of four single turns of superconducting wire wound on a cylindrical support and connected as (- + + -). In order to calculate the response of a second-order gradiometer pick-up coil assembly one may estimate the induction **B** at an arbitrary point **r** outside the sample with

[1] Superconducting Quantum Interference Device

[2] Quantum Design Magnetic Property Measurement System MPMS XL, Quantum Design, 6325 Lusk Boulevard - San Diego, CA 92121-3733, USA

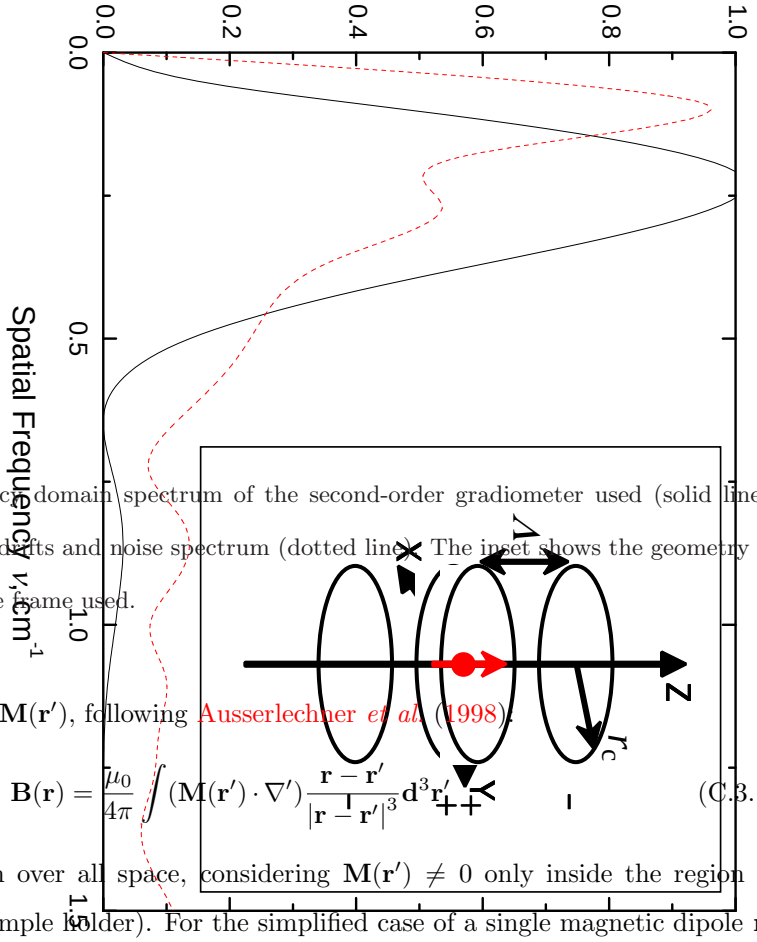

Figure C.8: Spatial frequency domain spectrum of the second-order gradiometer used (solid line), compared to the background drifts and noise spectrum (dotted line). The inset shows the geometry of gradiometer and the reference frame used.

magnetisation distribution $\mathbf{M}(\mathbf{r}')$, following Ausserlechner *et al.* (1998):

$$\mathbf{B}(\mathbf{r}) = \frac{\mu_0}{4\pi} \int (\mathbf{M}(\mathbf{r}') \cdot \nabla') \frac{\mathbf{r} - \mathbf{r}'}{|\mathbf{r} - \mathbf{r}'|^3} \mathrm{d}^3\mathbf{r}' \tag{C.3.1}$$

where the integral is taken over all space, considering $\mathbf{M}(\mathbf{r}') \neq 0$ only inside the region of interest (i.e. sample and sample holder). For the simplified case of a single magnetic dipole $\mathbf{m}$ in the centre of the coordinate system, (see for example Garachtchenko *et al.* (1992)), equation C.3.1 reduces to the well-known expression for the field of a point dipole:

$$\mathbf{B}\left(\mathbf{m}, \mathbf{r}\right) = \frac{\mu_0}{4\pi} \left[\frac{3(\mathbf{m} \cdot \mathbf{r})\mathbf{r}}{r^5} - \frac{\mathbf{m}}{r^3} \right] \tag{C.3.2}$$

The z-component of the magnetic induction couples to the pick-up coils and is given in any point by:

$$B_z(m_z, \mathbf{r}) = \frac{\mu_0}{4\pi} \left(\frac{3m_z z^2}{r^5} - \frac{m_z}{r^3} \right) \tag{C.3.3}$$

The resulting flux through any of the four coils can be obtained by analytical or numerical integration over the area of the loops:

$$\Phi_{\mathrm{tot}} = \sum_{i=0}^{3} \Phi_i = \sum_{i=0}^{3} \int_{A_i} B_z \mathrm{d}A_i \tag{C.3.4}$$

the area of the of the four coils being denoted as A_i $(i = 0 \ldots 3)$, with $\mathrm{d}A = \mathrm{d}x\mathrm{d}y$. For this particular geometry, taking into account the dimensions of the gradiometer and translating the sample, so that it is situated on the z-axis at point ζ, the total flux Φ_{tot} threading the pick-up

assembly is:

$$\Phi_{\text{tot}} = m_z \frac{\mu_0}{2} \left\{ 2\frac{r_c^2}{\left[r_c^2+\zeta^2\right]^{3/2}} - \frac{r_c^2}{\left[r_c^2+(\zeta+\Lambda)^2\right]^{3/2}} - \frac{r_c^2}{\left[r_c^2+(\zeta-\Lambda)^2\right]^{3/2}} \right\} \tag{C.3.5}$$

where r_c is the radius of the coils, and Λ is the base distance of the gradiometer. This function is plotted on C.9 As this flux is coupled via a superconducting transformer and consecutively converted to measurable voltage using a SQUID device (see for example Gallop & Petley (1976)). Introducing a constant calibration factor S, the response of the system is thus described by:

$$V = m_z S \left\{ 2\left[r_c^2+\zeta^2\right]^{-\frac{3}{2}} - \left[r_c^2+(\zeta+\Lambda)^2\right]^{-\frac{3}{2}} - \left[r_c^2+(\zeta-\Lambda)^2\right]^{-\frac{3}{2}} \right\} \tag{C.3.6}$$

Expression C.3.6 is valid exactly only when the sample is adequately represented by a point dipole on the measurement axis of the system (i.e. a homogeneously magnetised sample that occupies only few per cent of the volume of the pick-up coils assembly and is properly centred), and only after the background signal due to the sample mounting has been properly subtracted (SMC (2000)) or its contribution minimised (Hautot *et al.* (2005); Kamenev *et al.* (2006); Lewis & Bussmann (1996); Sesé *et al.* (2007)). For real-life samples the above requirements are rarely satisfied, it is therefore useful to look at the different imperfections in more detail in the following section.

C.3.3 Data regression algorithms

There are three distinct, commonly-used procedures for data reduction based on equation C.3.6:

1. The *full scan* algorithm is based on the facts that the function C.3.5 has a compact carrier and is proportional to m_z, so that its norm over the entire z-axis (or the entire scan length, as Φ_{tot} decays quickly outside the gradiometer volume), is given by:

$$\sqrt{\int \Phi_{\text{tot}}\left(\zeta\right)^2 \mathrm{d}\zeta} = C_{\text{fs}}|m_z| \tag{C.3.7}$$

   where C_{fs} is a constant that can be either evaluated analytically, calculated numerically for given pick-up coil dimensions or combined with S and calibrated experimentally using a standard sample. In the example followed here, $C_{\text{fs}} = 1.182 \cdot 10^{-5}$ Wb $\cdot$ m$^{1/2}$/Am^2 for a point dipole oriented along z (the value is strictly valid only in this case). The integral can be substituted by a root mean average over discreet set of data points and the magnitude of the z-axis projection of the dipole moment thereby evaluated (ODR (2001)).

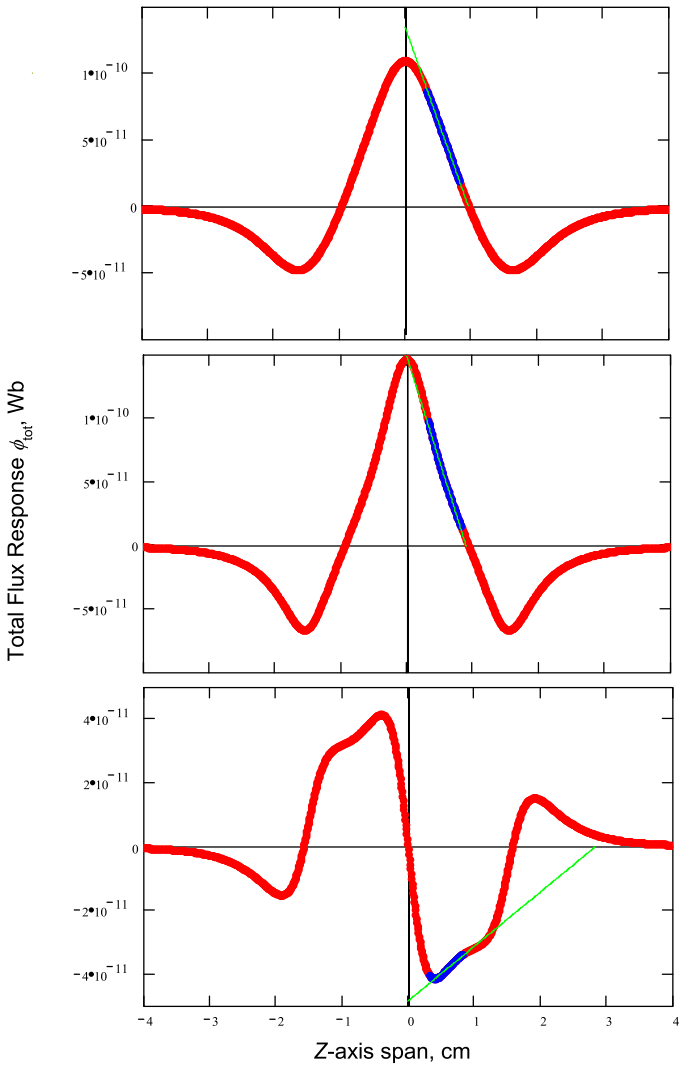

Figure C.9: The total coupled flux due to a point dipole of $1 \cdot 10^{-6}$ Am^2: situated in the centre of the system and oriented along the z-axis (top panel); radially offset at $\rho = 0.5$ cm and oriented along the z-axis (middle panel); radially offset at $\rho = 0.5$ cm and oriented perpendicular to the z-axis (bottom panel). Linear fits around the right-hand-side maximal derivative position are also shown, together with the actual z-axis spans used.

2. An alternative approach is based on the fact, that close to its maximum derivative position, the function C.3.6 can be approximated by a straight line (see C.9). Again as Φ_{tot} is proportional to m_z, the slope of the measured curve C.3.6 will be given by:

$$\max\left[\frac{\mathrm{d}V(\zeta)}{\mathrm{d}\zeta}\right] = C_{\text{lr}} m_z \tag{C.3.8}$$

where C_{lr} is a constant that can be estimated numerically or calibrated experimentally using a standard sample. In our example, C_{lr} can be readily evaluated, for the case of point dipole oriented along z, to be $C_{\text{lr}} = 1.399 \cdot 10^{-2}$ $\text{Wbm}^{-1}/\text{Am}^2$. The actual projection of the sample dipole moment can thus be inferred from the slope of the *linear regression* fit to the experimental data in a narrow region around the maximal derivative position of $\Phi_{\text{tot}}(\zeta)$.

3. The third standard approach is based on a non-linear least squares regression using the function C.3.6 to fit the data in a roughly centred interval around the sample position. Extra degrees of freedom can be added in order to account for constant, or linear on z-axis coordinate, background, as well as to correct for small misplacements of the sample along the axis of the gradiometer (ODR (2001)).

C.3.4 Various imperfections

Below the various imperfections associated with the limited validity of simple analytical expressions, like equation C.3.6, are discussed.

C.3.4.1 Sample shape and size

Finite sample size invalidates the use of equation C.3.1 to describe the induction field. The general expression C.3.2 is still applicable, but direct analytical integration is not generally possible. A number of different approaches are possible, some are described briefly.

Green's function for the magnetic scalar potential For certain high symmetry sample and coil geometries (i.e. cylindrical), it is possible to derive analytical expressions for the Greens function $G(\mathbf{r}, \mathbf{r}')$ for the magnetic scalar potential due to the sample magnetisation, and calculate the scalar potential as:

$$\Psi(\mathbf{r}) = -\int \left[\nabla \cdot \mathbf{M}(\mathbf{r}')\right] G(\mathbf{r}, \mathbf{r}') \mathrm{d}^3\mathbf{r}' \tag{C.3.9}$$

The magnetic flux density is then given as:

$$\mathbf{B}(\mathbf{r}) = -\mu_0 \nabla \Psi(\mathbf{r}) \tag{C.3.10}$$

The total flux Φ_{tot} can be thus calculated by integration, as defined in equation C.3.4. An example of application of this approach can be found in reference (Osterman & Williamson (1983)), together with a comparison with experimental data for a first-order gradiometer coil.

Analytic multipole expansion The non-linearity of the integrand in equation C.3.1 can be handled at reasonably large distances from the sample by expanding the term $\frac{\mathbf{r}-\mathbf{r}'}{|\mathbf{r}-\mathbf{r}'|^3}$ as a Taylor series in $\mathbf{r}'$, thus making use of a multipole expansion of the sample magnetisation. At large distances $|\mathbf{r}| \gg |\mathbf{r}'|$ the lowest order term in the series (the dipole moment of the magnetic configuration) is sufficient to describe the magnetic field profile. The higher order multipole terms are, however, necessary to accurately describe the near-field contributions, as they contain the detailed information about the size, shape and structure of the magnetisation distribution. This procedure is described in great detail by Ausserlechner *et al.* (1998), together with analysis of the region of applicability for of the approximations.

Finite element analysis A different approach is to approximate the sample by a set of point dipoles (not necessarily placed on the z-axis), and calculate the superposition of the induction created by the individual elements. The resulting total flux through the gradiometer of interest can then be evaluated numerically using equation C.3.4. This method contains the hidden disadvantage that the magnetic induction vector has to be calculated over a reasonably fine grid spanning the coil areas A_i, and at each point the contributions of all elementary dipoles to be superposed.

Semi-analytical finite element analysis A modification of the above scheme is to use exact analytical expressions (these are often obtainable when the pick-up coils have a particular, for example cylindrical, symmetry) or approximate solutions for the flux created by the individual point dipoles (ideally, situated at an arbitrary position and having arbitrary magnitude and orientation, so as to represent the sample magnetisation state correctly), and then obtain the total flux threading the gradiometer as a direct scalar sum. Examples of the expressions for pickup coils with cylindrical symmetry and a single point dipole can be found in reference (Miller (1996)). The computational problem is thus linear with the number of elementary dipoles N, and relatively free of the convergence problems often encountered in the multipole expansion method, apart of a small region of space close to the pickup windings. Strictly, the expressions for the total flux components should only be divergent if there are point dipoles (elements of the representation) coincident with the coils.

Results of the calculated response using the standard data regression algorithms for some common sample shapes and orientations are presented in table C.10. The relative errors, regardless of the regression procedure, are smaller than 4 %, except for the case of paramagnetic

film on diamagnetic substrate, where the errors can be very large, as explained later. Similar calculations can, in principle, provide correction factors for already processed data or, at least, set the minimal possible absolute uncertainty of moments extracted using the standard regression routines.

Deconvolution and spatial frequency domain analysis While the above three procedures can be readily applied to solve the direct problem (to evaluate the response of the system if the sample shape, position and magnetisation distribution are known), there are a number of cases of interest, when some of these key parameters are not well defined (i.e. weakly magnetic and inhomogeneous materials specimens or elongated biological membranes). In these situations the signal obtained upon translation of the sample through the pick-up coils is a convolution of the z-axis magnetisation distribution with the single dipole response function (point spread function), which in the example considered here, is a normalised version of equation C.3.6. This is strictly valid for a homogeneous magnetisation distribution with a carrier on the z-axis, as elsewhere the response function may contain components odd on z, or be different in shape from the standard model. Under this approximation, following Blott & Daniell (1993), for continuous a distribution $m_z(\zeta)$ the convolution is:

$$V(z) = S\left[\int_{-\infty}^{\infty} m_z(\zeta)\Phi_{\text{tot}}(z-\zeta)\mathrm{d}\zeta + \eta(z)\right] \tag{C.3.11}$$

where $\eta(z)$ is the residual noise in the data. In Fourier space, the same process can be expressed as:

$$v(k) = \phi(k)M_z(k) + N(k) \tag{C.3.12}$$

with $v(k)$, $\phi(k)$, $M_z(k)$ and $N(k)$ being the Fourier transform of $V(z)$, Φ_{tot}, $m_z(z)$ and $\eta(z)$, respectively. Neglecting the noise, equation C.3.12 can be solved for $M_z(k)$ giving:

$$M_z(k) = v(k)\phi(k)^{-1} \tag{C.3.13}$$

The real space distribution can then be recovered via an inverse Fourier transform, and if necessary, $m_z(\zeta)$ integrated over a region containing the sample, to recover the total magnetic moment, though, as pointed out by Blott & Daniell (1993), equation C.3.13 is practically useless, due to the rapid noise expansion, mainly due to the high spatial frequency noise often contained in the data, as well as various backgrounds and drifts (mechanical, electronic, etc.) Results are not satisfactory even when band-pass spatial frequency-domain filtering is used, because of the relatively large possible overlap between Fourier transform of the point spread function and some high-frequency electronic noise components and low-frequency flux-drift components (see

Symbol	Sample Description	Geometrical Average	Linear Regression	Iterative Regression
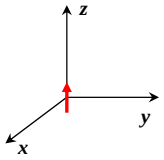	Ideal Dipole	5.912 0.00 %	5.782 0.00 %	5.872 0.00 %
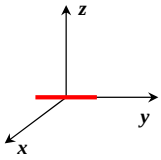	Line	6.008 1.62 %	5.901 2.06 %	5.967 1.62 %
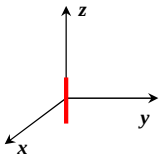	Line	5.726 -3.15 %	5.532 -4.32 %	5.686 -3.17 %
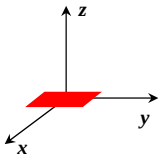	Plane	6.107 3.29 %	6.018 4.08 %	6.064 3.27 %
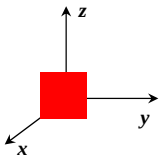	Plane	5.816 -1.62 %	5.661 -2.09 %	5.777 -1.62 %

Figure C.10: Calculated total coupled flux quoted in 10^{-11} Wb (numbers on top), and deviations relative to a point dipole (numbers on bottom) for different geometrical distributions of magnetic moment. The three columns correspond to the three standard data reduction procedures discussed in the text. The total sample moment is set to $1 \cdot 10^{-6}$ Am^2. The sizes are 0.5 cm in all dimensions, as appropriate, apart from the film on substrate examples where the substrate thickness is 0.5 mm and the ratio of the paramagnetic moment of the film to the diamagnetic moment of the substrate is 1:2. Continued on pages 320 and 321.

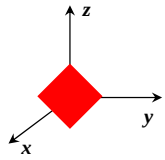	Plane	5.820 -1.56 %	5.653 -2.23 %	5.781 -1.55 %
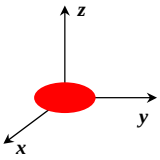	Disc	6.045 2.25 %	5.946 2.84 %	6.004 2.25 %
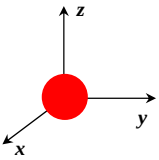	Disc	5.847 -1.09 %	5.697 -1.47 %	5.807 -1.11 %
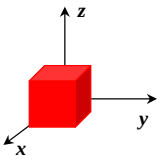	Cube	5.909 -0.05 %	5.789 0.12 %	5.869 -0.05 %
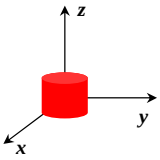	Cylinder	5.851 -1.03 %	5.710 -1.25 %	5.811 -1.04 %
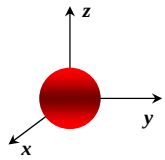	Sphere	5.912 0.00 %	5.782 0.00 %	5.872 0.00 %

Figure C.11: Continued from page 319.

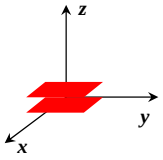	Film on Substrate	7.312 23.68 %	4.536 -21.55 %	7.229 23.11 %
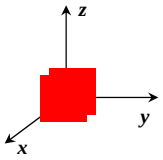	Film on Substrate	5.820 -1.56 %	5.667 -1.98 %	5.781 1.54 %
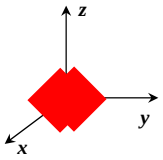	Film on Substrate	5.824 -1.49 %	5.659 -3.68 %	5.785 -1.48 %

Figure C.12: Continued from page 320.

figure C.8). Additional information is necessary in order to recover useful distributions of the magnetisation.

One possible approach is a matched filter deconvolution procedure described by Blott & Daniell (1993). For a discreet data set d_i, $i = 1 \ldots N$, magnetic moment distribution m_i and residual noise of each data point n_i , the convolution process C.3.11 is given by:

$$\mathbf{d} = \mathbf{wm} + \mathbf{n} \tag{C.3.14}$$

where $\mathbf{w}$ is the convolution matrix for the discreet version of the point spread function. As the direct inversion

$$\mathbf{m} = \mathbf{w}^{-1}\mathbf{d} \tag{C.3.15}$$

is practically inapplicable because $\mathbf{w}$ is often close to singular, using a postulated noise model with an autocovariance $\mathbf{R}$, the best value for the magnetisation distribution is given as:

$$\mathbf{a} = \boldsymbol{\rho}\mathbf{w}^{\mathrm{T}}\mathbf{R}^{-1}\mathbf{d} \tag{C.3.16}$$

where

$$\boldsymbol{\rho} = \left(\mathbf{w}^{\mathrm{T}}\mathbf{R}^{-1}\mathbf{w} + \frac{1}{\sigma_{\mathrm{m}}^2}\mathbf{1}\right)^{-1} \tag{C.3.17}$$

and $\mathbf{R} = \mathbf{R}(\alpha, \sigma_{\mathrm{b}}, \sigma_{\mathrm{n}})$. For the case described by Blott & Daniell (1993), σ_{b} and σ_{n} are the standard deviations of a semi-stochastic process describing the background drift and uncorrelated Gaussian noise, respectively. The α parameter is a constant close to unity determining

the smoothness of the background noise distribution, and σ_{m} is the standard deviation of the Gaussian distribution assumed *a priori* for $\mathbf{m}$. The above variances may be estimated from the data using convergent iterative procedure. The errors of resulting total moments depend on how close the actual distribution of $\mathbf{m}$ is to the postulated one and the various constraints imposed on the deconvolution procedure (i.e. maximal sample size).

Within reasonable constraints, *direct least squares multi-parameter fitting* can be employed to reduce the experimental data. A detailed look at the normalised autocorrelation function defined as:

$$C(z) = \frac{\int_{-\infty}^{\infty} V(\zeta)V(\zeta - z)\mathrm{d}\zeta}{\int_{-\infty}^{\infty} V(\zeta)^2\mathrm{d}\zeta} \tag{C.3.18}$$

and plotted at figure C.13, of the gradiometer response clarifies the criteria that have to

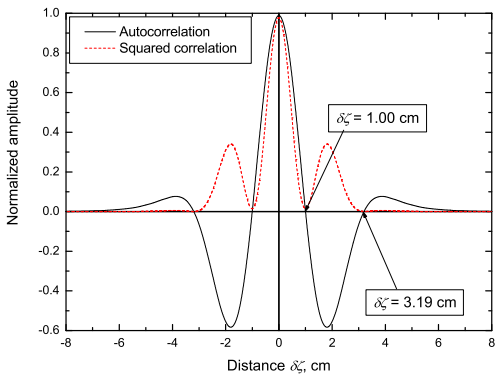

Figure C.13: Autocorrelation function (solid line) and the squared correlation function (dotted line) for the response function of the gradiometer used. The distances at which two point dipoles are independent are given with arrows.

be satisfied. It is clear that the response of the pickup to closely situated dipoles is strongly correlated. For the example considered here, the responses of the system to two point dipoles are linearly independent when they are situated at distances $\delta\zeta = 1.00, 3.19$ cm and, naturally, for distances larger than the maximal z-axis span. The response of the system can, therefore, be approximated by a system of point dipoles $m(z_i)$, with $|z_i| \leq L$ situated at $\delta z = z_{i+1} - z_i \geq \kappa \min(\delta\zeta)$, where for practical purposes $\kappa \geq 0.5$ is a number depending on the level of high spatial frequency noise in the data, as well as the ratio of the total number of independent data samplings to the total number of free parameters in the fit. The maximal value of L depends on the magnetometer system hardware, though it is often possible to define a more compact

region where $m(z) \neq 0$. Any other independent constraint, which can be imposed on the fitting parameters, further increases the limiting signal to noise ratio limit for practical applicability of the method. An example of the deconvolution procedure output is shown on C.14. The

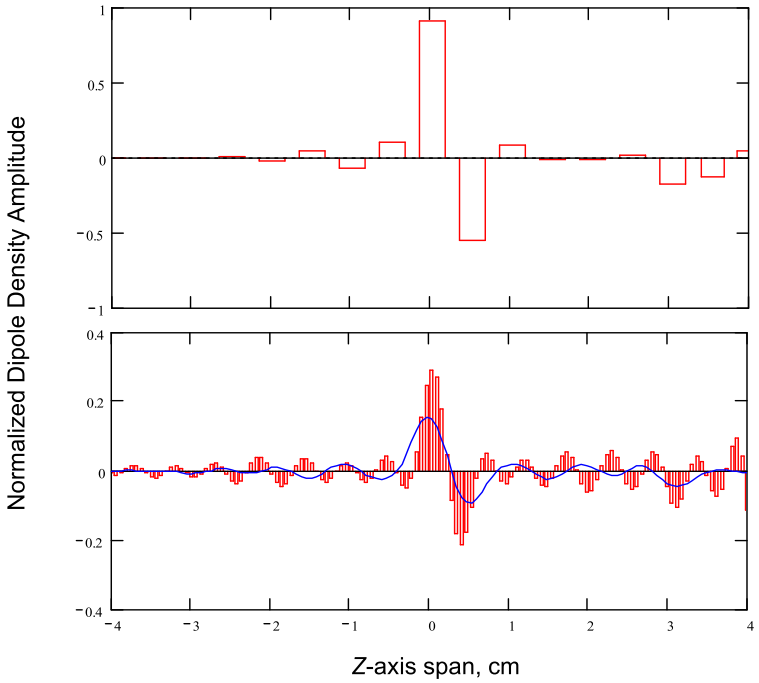

Figure C.14: Calculated and deconvoluted z-axis profile of the magnetisation distribution, by multi-parameter regression (top panel), and by abruptly filtered SVD deconvolution (bottom panel, bars) and smoothly filtered SVD (bottom panel, line); for a system of three point dipoles of magnitudes 1, -0.5 and -0.25, situated at positions z = 0, 0.45 and 3.19 cm , respectively. The simulated random noise background is 0.1 % of the signal amplitude.

algorithm yields errors generally smaller than 2 % in the determination of the total magnetic moment $m_{\text{tot}} = \sum_i m(z_i)$, for uni-directionally magnetised distributions compact on a scale close to or larger than $\delta\zeta$, with peak-peak noise of 1 %. A particularly disadvantageous case is a distribution $m(z)$, which abruptly changes sign on a scale smaller than $\delta\zeta$. With the above noise floor requirements, errors exceeding 20 % are often observed.

Another possibility is to employ the singular value decomposition - *SVD matrix inversion method* to solve the inversion C.3.15 by factoring out the singular values of $\mathbf{w}$ as:

$$\mathbf{w} = \mathbf{U} diag(\mathbf{s}) \mathbf{V}^{\mathrm{T}} \tag{C.3.19}$$

where for a square matrix $\mathbf{w}$, the matrices $\mathbf{U}$ and $\mathbf{V}$ are orthogonal, and $diag(\mathbf{s})$ is a diagonal matrix containing the singular values of $\mathbf{w}$ (see for example reference Press *et al.* (1992)). In order to limit the detrimental noise expansion effects, due the fact that the response matrix is ill-conditioned (its condition number, defined as the ratio $\gamma = \max(\mathbf{s})/\min(\mathbf{s})$ is rather large, or $1/\gamma \rightarrow \max|\mathbf{n}|/\max|\mathbf{m}|$), the vector of its singular values can be filtered, so as to exclude from the solution the eigenvectors whose eigenvalues are close to zero. This can be done by zeroing the elements of $diag(\mathbf{s})^{-1}$, which correspond to small singular values, or in other words, define a filtered vector $\mathbf{f}$ of singular values as:

$$f_i = \begin{vmatrix} 0 & , & s_i < threshold \\ \frac{1}{s_i} & , & otherwise \end{vmatrix} \tag{C.3.20}$$

where the constant *threshold* is larger than zero and should be determined in accordance with the signal-to-noise ratio of the data. The inverse of the modified response matrix is then given by:

$$\hat{\mathbf{w}}^{-1} = \mathbf{V} diag(\mathbf{f}) \mathbf{U}^{\mathrm{T}} \tag{C.3.21}$$

and the distribution $\mathbf{m}$ may be recovered using C.3.15 to be:

$$\mathbf{m} = \hat{\mathbf{w}}^{-1}\mathbf{d} \tag{C.3.22}$$

The result of such a filtering process is virtually analogous to low-pass filtering of the spatial Fourier transform of the response as can be seen on figure C.14. As with any perfectly sharp filter this causes 'ringing' of the output signal. In order to achieve smooth filtering of the vector of sorted singular values, a modified analytical form may be used instead of equation C.3.20:

$$\hat{f} = \frac{s_i^{-1}}{2}\left[1 - \tanh\left(\frac{i - cutoff \cdot N}{slope \cdot N}\right)\right] \tag{C.3.23}$$

where $cutoff$ and $slope$ are constants ranging between zero and unity, that characterise the filter and have to be determined with respect to the width of the singular values spectrum of the response matrix, and the signal to noise ratio of the data. The application of equation C.3.23, as can be evidenced from figure C.14, leads to satisfactory profiles of the z-axis magnetisation density. More importantly, the total magnetic moment can often be recovered with an error of less than 2 %, provided the peak to peak noise amplitude in the data vector does not exceed 3 %. An example of the performance under realistic conditions is demonstrated on figure C.15. This algorithm, also, has the advantage of being relatively insensitive to abrupt changes in sign in $m(z)$. Though it is generally not possible to resolve opposing dipoles situated less than $\delta\zeta/2$ apart, the total magnetic moment m_{tot} is recovered within the above-stated limits. It is important to note that without the filtering action of equation C.3.20 or C.3.23, this approach

is as bad as the direct matrix inversion in amplifying the noise in the data vector. As the use of inversion C.3.21 can be treated as modification of the response matrix, the singular value selection should be done so as to conserve the norm of the data vectors in the sense of equation C.3.7.

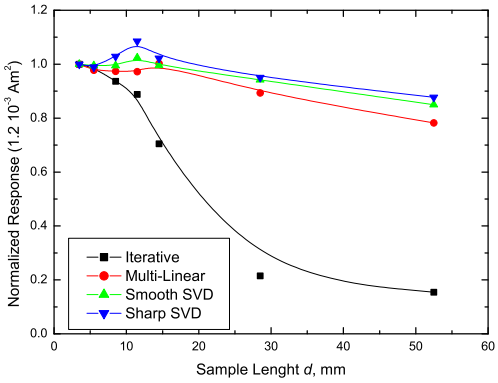

Figure C.15: Normalised total magnetic moment response of various deconvolution procedures, compared with the standard iterative regression procedure, for a system consisting of a spring of 99.9 % pure Ag wire (ϕ 0.5 mm, m = 124.5 mg), elongated to different lengths d. Note relative stability of response of the smooth-filtered SVD deconvolution procedure.

It is often useful to assume that the magnetic moment distribution is either only positive or only negative, thus imposing constrains on the deconvolution process. A simple iterative process can be used employing equation C.3.13, so as to keep the same sign for all the elements of **m**. The procedure can be described as follows:

1. use equations C.3.11 and C.3.13 to recover an estimate of **m**;

2. calculate the vector of the error as $\mathbf{e} = \mathbf{d} - \mathbf{f}$, where **d** is the measured vector of the coupled flux distribution, and **f** is the recovered one;

3. convert, using equation C.3.12, the error vector **e** to obtain the residual moment vector **u**, then use **u** to correct the estimate for **m** like $\mathbf{m} \rightarrow \mathbf{m} + \eta\mathbf{u}$, where $\eta < 1$ is a number, that will determine the rate of convergence;

4. zero any elements in **m** that are not satisfying assumption for the sign and use the new guess for **m** to calculate a new estimate for the coupled flux distribution **f**;

5. go to step 2, unless the maximal element of the error vector is below a predefined threshold or the difference between two consecutive guesses for **m** is below a predefined value; otherwise stop.

This process is rapidly converging to a reasonable estimate for **m** and is normally numerically stable, as it is free from the direct inversion problems encountered when using equation C.3.15 without modifying the response matrix $\hat{\mathbf{w}}$. An example of application of this procedure is discussed later.

C.3.4.2 Sample position and orientation

The errors falling into this category have been analysed in detail for the case of a point dipole, studied by Miller (1996), and classified under the following three categories: radial off-centreing of a correctly oriented dipole, angular misalignment of a centred dipole and angular misalignment of a radially off-centred dipole. Here we would like to point out that the rotation of a radially-centred dipole, due to the symmetry of the coil assembly yields the angular dependence of the measured projection m_z, and therefore may not be considered an imperfection. Nevertheless, the misplacement of the sample in the xy-plane can give rise to an odd component in the response function, which is zero when the dipole lies on the z-axis, due to the symmetry of the gradiometer.

The influence of the radial displacement on the response function (for a gradiometer similar to our example) has been demonstrated by Miller (1996), for the case of a point dipole. Analytical generalisations of equation C.3.6 for this more general case are unattainable. Therefore numerical integration must be used to evaluate the modified response function in every particular case. Nevertheless, it is instructive to analyse the response of an individual coil (i.e. one of the central coils of the second-order gradiometer) to a point dipole as plotted on figure C.16. The area of the resulting peak of the coupled flux $\Phi_{tot}(\zeta)$ is virtually constant for different radial offsets $\rho \in [0, 9]$ mm, changing by less than 0.2 % (the error being attributed to the small but non-zero coupled flux at both ends of the finite integration interval of ± 4 cm). The width W of the peak is a quadratic function of the radial offset of the form $W = 14.8(8)$ mm $- 0.167(2)$ mm^{-1} ρ^2, as demonstrated on the inset of Fig. 6 for the coil dimensions of our example.

This general notion can be propagated using C.3.4 for the case of complete gradiometer assembly. Both the positive and the negative peaks of the response function are, therefore getting narrower with increasing ρ, keeping the total integral on z approximately constant. Generally,

increased radial offset ρ, makes the response function more sensitive to the high frequency components in the spatial Fourier transform of the measured magnetisation distribution.

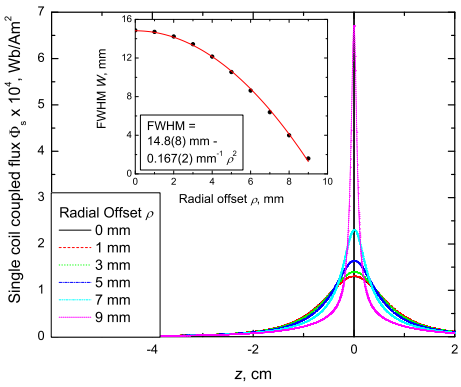

Figure C.16: Single coil response function at different radial offsets ρ. The inset shows the dependence of the width of the response peak on the radial offset (dots) and a quadratic fit for its dependence on ρ (line). The radius of the coil is $r_c = 0.97$ cm.

The dependence of the observable total flux on the radial displacement is plotted on figure C.17. The results coincide with the ones calculated for the least squares fitting procedure 9, within 5 % error due to the slightly different coil dimensions used. It can be noted that the error in the apparent flux is smallest for the linear regression algorithm. A typical curve flux profile for a radially misplaced sample is shown on figure C.9 (middle panel). An example of the response to a dipole oriented perpendicular to the z-axis and radially displaced is demonstrated also on figure C.9 (bottom panel).

Although, radial misplacements are generally considered imperfections, on-purpose introduced displacements of sufficiently small samples can yield information for the both axial M_z and radial M_ρ components of the magnetisation, as demonstrated on figure C.18. The base-set (F_z, F_ρ) can be readily calculated either in point dipole approximation or using finite element analysis. An example for radial offset $\rho = 2.5$ mm is shown on figure C.19. The applicability of such an approach to vector magnetisation measurements is limited by the fact that the orthogonal to the z-axis component is sensed with at least three times smaller amplitude, compared to the axial one, and therefore is prone to background noise and sample holder contributions. The success of this procedure is ultimately limited by the homogeneity of the field source along the z-axis, as the sample has to be translated at large lengths during the measurement (otherwise the radial base-function R_ρ wound not be sufficiently de-correlated from the linear electronic and background drifts).

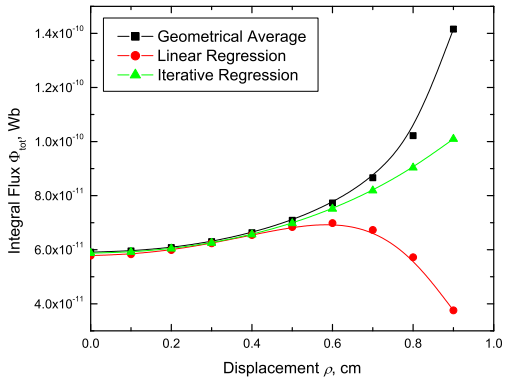

Figure C.17: The response of the three standard regression procedures to a point dipole of $1 \cdot 10^{-6}$ Am^2, radially displaced at a distance ρ.

Better understanding of the various regression procedures' response to elongated samples is achieved by studying a model system consisting of two point dipoles situated at a distance Z on the z-axis. As can be seen on C.20, the response is roughly analogous in shape to the autocorrelation function, though the amplitudes of the dependencies and their symmetry are algorithm dependent.

C.3.4.3 Non-uniform magnetisation distribution

As pointed out by Ribeiro *et al.* (1987), a gradiometer acts as a spatial high-pass filter, and is thus particularly sensitive to high spatial frequency components in the measured distribution of the magnetic moment of the sample and the holder. A common example of an inhomogeneous magnetisation distribution is a sample consisting of a ferromagnetic film on a diamagnetic substrate. This case is particularly troublesome when the two opposing moments are of similar magnitude. The calculated effect on a non-linear magnetisation curve is shown on figure C.21a. together with an experimental example of the observation of this imperfection on figure C.21b, for a thin film of $Sn_{0.95}Co_{0.05}O$ on Al_2O_3 substrate. It is instructive to study the normalised response of the different regression algorithms to a system of opposing dipoles with a different base distances d, as plotted on figures C.22, C.23 and C.24. It is should be emphasised that the divergences in the response of the geometric averaging and iterative regression procedure are greater than the one observed with the linear regression algorithm. It is therefore advantageous to use a linear fit around the maximal derivative position in such cases.

When the distribution of the magnetisation is not known, but is radially confined to a reasonable approximation around the z-axis of the system, often deconvolution may provide

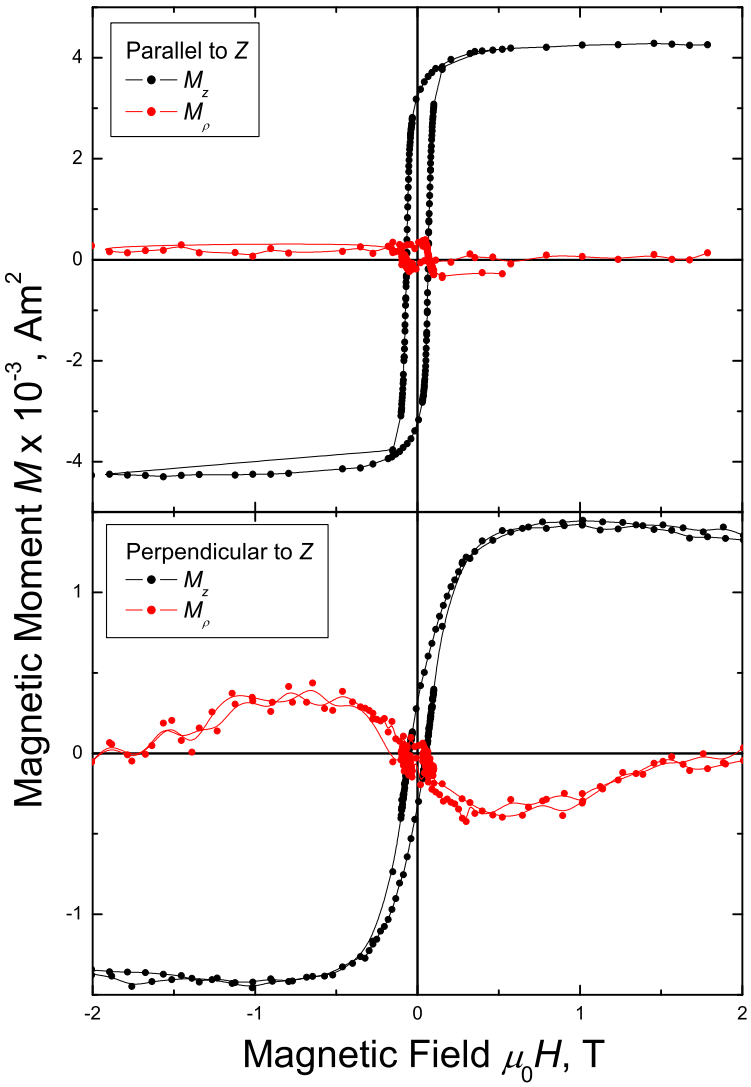

Figure C.18: Magnetisation curves for pieces of CrO_2 commercial magnetic recording tape situated at a radial offset $\rho = 2.5$ mm, and oriented parallel (top panel) and perpendicular (bottom panel) to the z-axis. Both the axial m_z and radial m_ρ components of the magnetic moment are extracted.

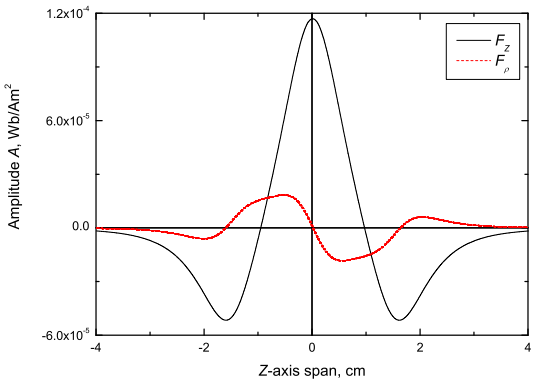

Figure C.19: Base-set functions for a point dipole situated at a radial offset $\rho = 2.5$ mm: on axis component F_z (solid line) and radial component F_ρ (dotted line).

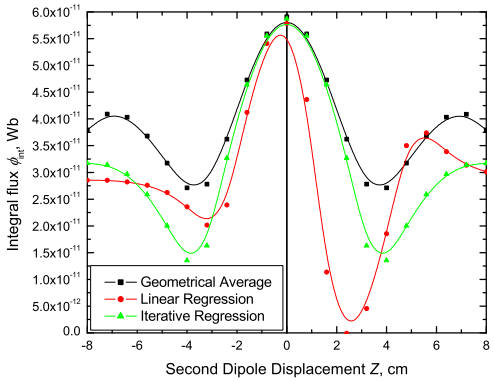

Figure C.20: Response of the three standard regression procedures to a system of two point dipoles of $0.5 \cdot 10^{-6}$ Am^2 each, one of which is situated at the centre of the system and the other one is placed at a distance Z along the z-axis.

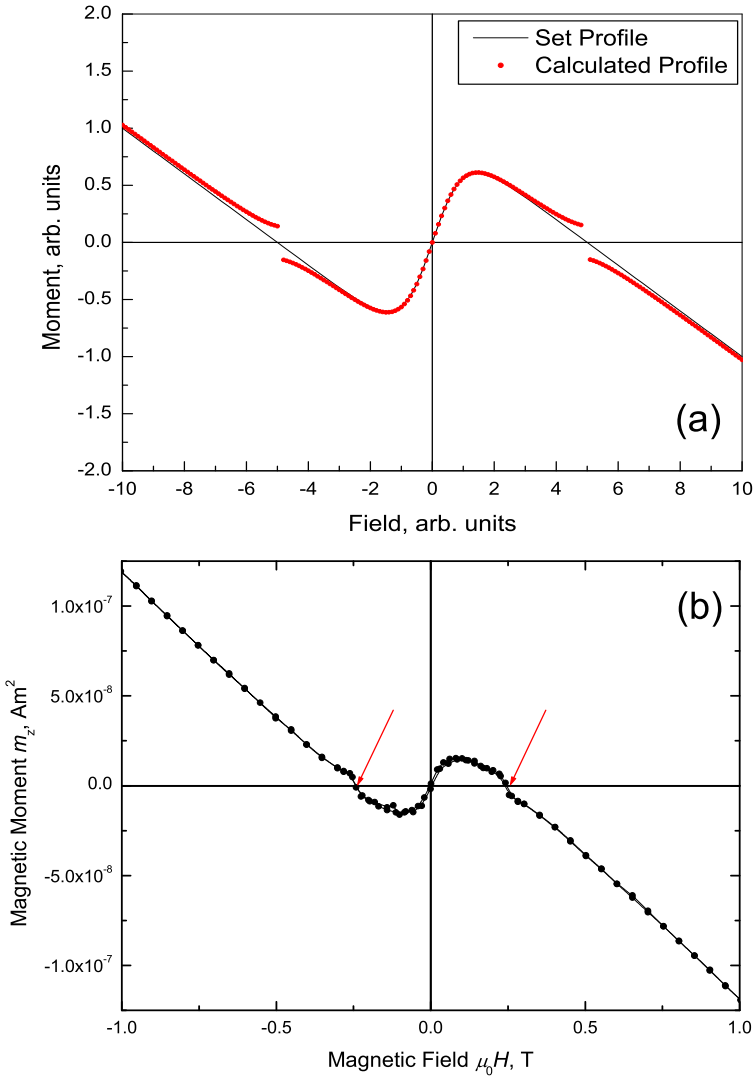

Figure C.21: (a) Arbitrary non-linear magnetisation curve (solid line) of a system of two point dipoles situated 0.5 mm apart, one of which positive and saturating in applied field, and the other one negative and linear in applied field. The calculated response of the iterative regression procedure is shown as (dots). Note the large deviations around zero total magnetic moment. (b) Magnetisation curve at 300 K for 100 nm thick $Sn_{0.95}Co_{0.05}O$ film on R-cut Al_2O_3 substrate (0.5 x 5 x 5 mm). Please, note the deviations pointed out in the regions where the total z-axis dipole moment m_z is close to zero.

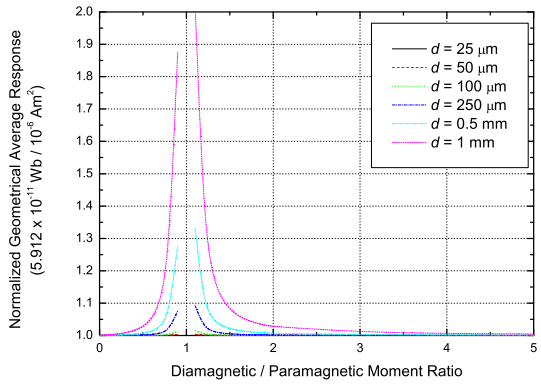

Figure C.22: Response of the geometrical average data regression procedure, for a system of two point dipoles of opposite signs and various magnitudes, for different distance d between them.

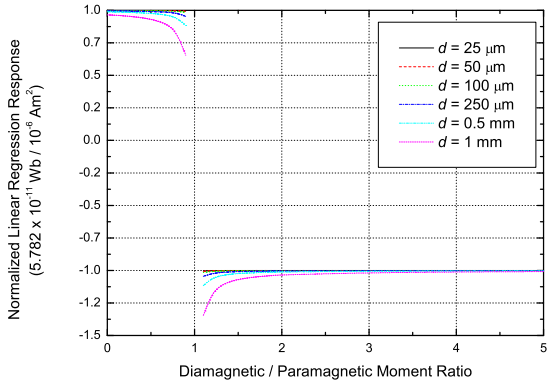

Figure C.23: Response of the linear data regression procedure, for a system of two point dipoles of opposite signs and various magnitudes, for different distance d between them.

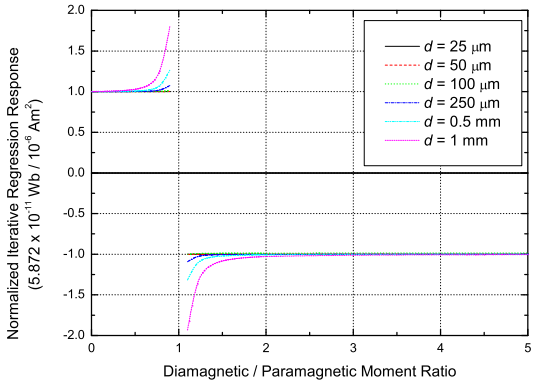

Figure C.24: Response of the iterative data regression procedure, for a system of two point dipoles of opposite signs and various magnitudes, for different distance d between them.

a good estimate of the total magnetic moment of the sample (see figure C.15). If the signal-to-noise ratio permits, an experimental profile of the on-axis magnetisation distribution can be often obtained, as shown on figure C.18, for a discreet set of magnetic moments (small pieces of magnetic recording tape). The best results are achieved with, constrained to either positively-defined or negatively-defined magnetisation distribution, deconvolution, which can yield resolution of approximately L/N (1.7 mm for our example), where N (64 in our example) is the maximal number of data points in a full z-axis scan. As evidenced from figure C.25, the distribution $m_z(z)$ is not only recovered qualitatively, but also the magnitudes of the moments, relative to the largest one, (0.48, 1.00, 0.61, 0.31) are reproduced as (0.43, 1.00, 0.59, 0.23). of Multi-parameter fitting, for comparison, can reach resolution of 2L/N. Magnetisation distribution profiles recovered by non-constrained deconvolution are generally harder to interpret, as they are prone to background noise and drifts. Unknown non-uniform distributions combined with large radial displacements are not trivial to analyse.

C.3.5 Calculation details

A semi-analytical finite element analysis code has been developed in Mathcad, Maple and C, to simulate the response of a second order gradiometer pick-up coil assembly (for example, the Quantum Design Magnetic Property Measurement System MPMS XL). The flux integrals are computed for a given sample shape, orientation and position, arbitrary direction of the magnetisation and magnetic moment spatial distribution, and their axial distributions analysed using all three standard regression procedures (geometrical average, linear regression, non-linear least squares).

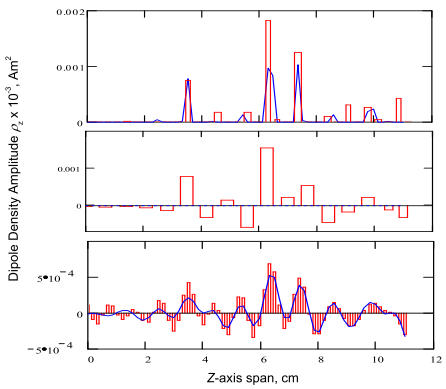

Figure C.25: Measured and deconvoluted z-axis profile of the magnetisation distribution, by constrained to positive dipole density multi-linear fitting (top panel, bars) and SVD deconvolution (top panel, line), by multi-parameter regression (middle panel), and by abruptly filtered SVD deconvolution (bottom panel, bars) and smoothly filtered SVD (bottom panel, line); for a system of four dipoles of relative magnitudes 0.48, 1.00, 0.61 and 0.31, situated at positions z = 3.3, 6.2, 7.2 and 9.6 cm, respectively. The sample consists of pieces of standard CrO_2 magnetic recording tape. Total moment is $4.4 \cdot 10^{-6}$ Am^2.

The dimensions of the pick-up assembly relevant to our example are r_c = 0.97 cm and Λ = 1.519 cm (see SSH (2002)). The virtual measurement is done by translating the sample along the z-axis with a maximal scan amplitude with respect to the centre of the gradiometer L = 4 cm. For the calculation of the systems response, the samples were discretized on a regular 1, 2 or 3-dimensional grid, containing at least n = 20 nodes per dimension. The sample is described by a set of matrices containing the three coordinates of each elementary dipole, the magnitude and the direction of the magnetisation. The orientation and position of the sample are specified by the radius vector of the centre of the discretization grid r_{shift}, and three angles of rotation around the x, y and z-axis of the stationary frame connected to the gradiometer. The amplitude of the span used in the linear regression moment extraction algorithm was a = 0.5 cm. Unless otherwise specified, the total magnetic moment of the samples is set to $m = 1 \cdot 10^{-6}$ Am^2. All numerical results are valid to at least 0.1 %.

C.3.6 Experimental details

The experiments have been performed on a commercial SQUID magnetometer[1]. The samples have been mounted either in drinking straws or in 20 cm long fused quartz tubes. Both standard stepping transport mechanism and a servo transport mechanism have been used as appropriate. Whenever the non-linear least squares algorithm have been used, the sample has been scanned with amplitude of 1 cm around the central position. Whenever the linear regression algorithm has been used the sample has been oscillated with and amplitude of 0.5 cm around the maximal derivative position.

C.3.7 Experimental precautions

For homogeneously magnetized samples that are well centred and occupying only a few percent (< 5 %) of the gradiometer volume, no corrections to the standard point dipole approximation are normally necessary. When the magnetic moment of interest is small, compared to the background of the sample holder, the latter should be properly subtracted in accordance with SSH (2002), provided the sample can be removed from the sample holder without damage, or better the very construction of the holder changed so as to produce minimal background (see for example SMC (2000), Roy *et al.* (1982) and Bedanta *et al.* (2005)).

When the sample position on the z-axis is unlikely to change (for example due to the thermal expansion of the sample rod), measurements done by oscillating the sample with small amplitude around the maximal derivative position of the response function are to be preferred, because of their relative insensitivity to the exact magnetisation state of the sample and better noise suppression (in the case when lock-in detection and filtering are used).

In the case of extended samples of a well-defined geometry, pre-calculated correction factors can be introduced on data already processed by one of the standard methods using one of the exact or approximate methods described. A better approach is to recalculate a modified response function and use it instead of the standard point-dipole approximation in the regression procedure of choice for the measurement. Reproducible and small radial off-centring can also be accounted for employing one of the above approaches, assuming that the sample is magnetised along the z-axis of the gradiometer. As a last resource, a suitable deconvolution method may be applied. Similar remarks can be made about non-idealities related to inhomogeneous magnetisation distribution.

One of the most problematic imperfections is the existence of net dipole component of the sample magnetic moment that is substantially radially off-centred and orthogonal to the z-axis

[1] Quantum Design MPMS XL

of the pickup assembly. If the reliability of the background subtraction permits, it may be possible to avail for the odd component in the response function and even extract an estimate for the radial component of the sample magnetisation.

C.3.8 Conclusions

Finite sample size, misorientation and other imperfections may and do become important under extreme circumstances - large samples, large spatial offsets, non-uniform or non-collinear local magnetisation, and lead to substantial absolute errors in the deduced magnetic moments, even for statistically acceptable (i.e. judged by the regression value RVA (2001)) experimental data. The expected response profiles can be estimated and the errors involved in making various approximations predicted. These allow for higher absolute accuracy of the actual magnetisation measurements, virtually limited by the flux noise levels, the electronic and mechanical noise and, to a great extent, by the reproducibility and the scale of the relative contribution of the sample mounting. A possibility is also defined for measurement of transverse components of the magnetisation without a second coil assembly, provided that the sample is sufficiently small and situated off the central axis of the system.

Appendix D

Appendix E

D.1 Sample preparation and characterisation

The magneto-transport in Co-doped ZnO, including data up to 20 T, have been investigated at three different magnet/cryostat cites, a 5 T superconducting magnet with a vapour flow cryostat (Quantum Design, USA), a 14 T superconducting magnet with a in-vacuum cryostat (Quantum Design, USA), and magnet cite M3, at the Grenoble High Magnetic Fields Laboratory, with a vapour flow cryostat. The samples have been measured either in the Van der Pauw geometry or as patterned by wet-etching Hall bars. Contacts have been prepared by thermal evaporation of Al/Au bi-layer.

A multitude of samples have been studied, with $x = 0$, with $x = 0.04$ prepared in different conditions and couple with $x = 0.25$. All samples have been prepared by pulsed laser deposition on sapphire substrates, maintained at fixed temperatures, between 400 °Cand 700 °C. It can be argued, that there is a narrow process window of substrate temperature around 450 °C, where films on c - cut Al_2O_3 exhibit ferromagnetism. They all show <001> texture with $a = 0.316$ nm, $c = 0.524$ nm. The film thickness is 80 - 100 nm, as determined by optical transmission/reflection measurements (see figure D.1), and by grazing incidence x-ray diffraction (Phillips X'Pert Pro).

The films with $x = 0.25$ and one of the two with $x = 0.04$ are ferromagnetic with Curie temperatures well above room temperature and moments of 0.5 μ_B/Co and 0.1 μ_B/Co, respectively. The other films with $x = 0.04$ or $x = 0.05$ are paramagnetic.

Co metal clusters have been detected by XRD in a sample with $x = 0.25$, with an average size of 18 ± 1 nm, while clusters have not been resolved in the films with $x = 0.04$ prepared

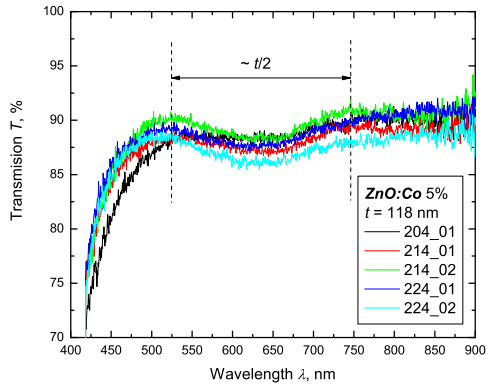

Figure D.1: Approximate thickness determination from the optical transmission of a seres of 5 % Co doped ZnO films made at different occasions.

and measured in the same conditions. Four times thicker films, analogous to the ones used in the present study, but with $x = 0.05$, have been found to co contain a detectable by XRD concentration of Co metal clusters with average size 7 ± 1 nm. Therefore, no perfect substitution is expected for the Co ions, even in the films with $x = 0.04$. Judging from recent experimental data by Denardin *et al.* (2005), the blocking temperature can be expected to be above room temperature, already for Co clusters of average size 3.5 nm. The oxidation state of Co in films with x ¡ 0.05, analogous to the ones used in the present study, has been found to be 2+ by Fitzgerald *et al.* (2005).

Optical absorption spectroscopy has been performed on two different setups. One is a commercial dual beam system (Perkin-Elmer, Lambda 800). The other is a home made fibre-optic coupled system with two different spectrometer units: S1000 and S2000 by Ocean Optics, Holland. An example of absorption spectrum is given on figure D.2.

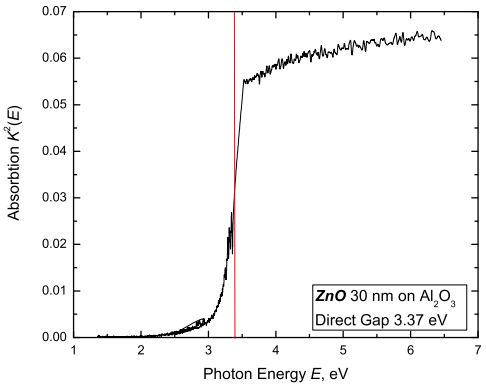

Figure D.2: Optical absorption spectrum in the NIR-VIS-NUV region. The data is a combination of two data sets measured with S1000 and S2000, fibre-optic coupled spectrometers.

D. APPENDIX E

Appendix E

Appendix C

E.1 Samples Information

HOPG samples have been obtained from the Graphite Research Institute, Moscow, Russia, and Advanced Ceramics (formerly Union Carbide), USA. The samples investigated have been of different grades - ZYA, ZYB and ZYH graphite of nominal 5N5 purity with Mosaic spread of around 0.3 °, for the best grade. The samples are cut with a diamond blade and cleaved before contacting (for the transport samples) with 30 nm thick, evaporated gold pads.

The multi-walled carbon nanotubes used have been produced by the standard He ark technique from 5N5 pure graphite ingot, and are on average 1-3 μm long, with a mean diameter of about 20 nm.

E.2 Magnetisation Measurements

Magnetisation measurements have been performed on a SQUID-based magnetometer (Quantum Design XL 5). The maximal applied field was 5 T with reproducibility of around 0.01 mT. The temperature in which is controlled with a He vapour-flow cryostat in the range 1.7 - 300 K. The samples have been mounted in clear drinking straws using gelatine capsules, ensuring that no air was trapped in the sample space (as oxygen is strongly paramagnetic at low temperature). Linear regression at the maximal slope position, data processing strategy has been employed for measurements performed at fixed temperature. Iterative regression and automatic sample tracking have been used for the measurements performed as a function of temperature.

E.3 Transport Measurements

Transport measurements at small fields (up to 5 T) have been performed in system described in point section E.2, using a resistance bridge (Linear Research-200 series) and source-meter (Keithley 2400). Transport measurements at high fields (up to 23 T) have been performed at Grenoble High Magnetic Field Laboratory (magnet site M3), using two different set-ups - a He^4 bath cryostat with a biaxial rotation stage, and a He^3 cryostat with uniaxial rotation stage, in the temperature range 0.3 - 5 K. Vernier Lock-in amplifiers (EG&G 58xx series) detection has been used with an arbitrary moderate DC bias for removal of the zero-bias contact abnormalities.

E.4 Many-carrier transport model

Below, a simple recollection of the many-carrier transport model is given. Conductivity tensors corresponding to the individual carrier types can be written (in their own coordinate system) as:

$$\hat{\sigma}^i = \begin{bmatrix} \sigma^i_{xx} & \sigma^i_{xy} \\ \sigma^i_{yx} & \sigma^i_{yy} \end{bmatrix} \tag{E.4.1}$$

where i indexes the carrier types, the magnetic field is assumed to be applied along the z-axis, and the external potential difference along the x-axis, so that nominally the component σ^i_{xx} is due to the sample resistivity, and the component σ^i_{xy} to the Hall effect.

Because of symmetry of the transport coefficients with respect to time reversal, the corresponding tensors are normally antisymmetric:

$$\sigma^i_{xx} = \sigma^i_{yy} \tag{E.4.2}$$

$$\sigma^i_{xy} = -\sigma^i_{yx} \tag{E.4.3}$$

and are, most simply, defined as:

$$\sigma^i_{xx} = \frac{\rho^i}{\left(\rho^i\right)^2 + \left(R^i_{\mathrm{H}}B\right)^2} \tag{E.4.4}$$

$$\sigma^i_{xy} = \frac{-\left(R^i_{\mathrm{H}}B\right)}{\left(\rho^i\right)^2 + \left(R^i_{\mathrm{H}}B\right)^2} \tag{E.4.5}$$

where ρ^i are the resistivities of the individual carrier types, which within the Druide model, may be expressed as:

$$\rho^i = \frac{m^\star_i}{q^2 n^i \tau^i} \tag{E.4.6}$$

and R^i are the corresponding Hall coefficients:

$$R^i = \frac{1}{q^i n^i} \tag{E.4.7}$$

where $q^i = \pm q$ with the sign being $(-)$ for electron-like carriers, and $(+)$ for hole-like carriers, n^i are the carriers' concentrations, $m_i^\star$ the corresponding effective masses, and τ^i the corresponding scattering times.

If charge conservation is obeyed, and in the linear regime, the conductivity tensor for the entire system is given simply by:

$$\hat{\sigma} = \sum_i \hat{\sigma}^i \tag{E.4.8}$$

where i runs over all carriers types. The resistivity tensor can be then calculated as the inverse:

$$\hat{\rho} = \hat{\sigma}^{-1} \tag{E.4.9}$$

and the resulting functional dependence used for fitting and other data-regression purposes.

E. APPENDIX C

Appendix F

List of Publications

1. *On the direct magnetic detection of spin injection and adiabatic depolarization in aluminum*
   Journal of Magnetism and Magnetic Materials, **320**, 403-406, (2008)
   P. Stamenov and J. M. D. Coey

2. *Magnetic and structural properties of Co-doped ZnO thin films*
   Journal of Magnetism and Magnetic Materials, **310**, 2087-2088 (2007)
   L.S. Dorneles, M. Venkatesan, R. Gunning, P. Stamenov, J. Alaria, M. Rooney, J.G. Lunney and J. M. D. Coey

3. *Magnetic, magnetotransport, and optical properties of Al-doped $Zn_{0.95}Co_{0.05}O$ thin films*
   Applied Physics Letters, **90**, 242508 (2007)
   M. Venkatesan, P. Stamenov, L. S. Dorneles, R. D. Gunning, B. Bernoux, and J. M. D. Coey

4. *Sample size, position, and structure effects on magnetization measurements using second-order gradiometer pickup coils*
   Review or Scientific Instruments, **77**, 015106 (2006)
   P. Stamenov and J. M. D. Coey

5. *Magnetoresistance of Co-doped ZnO thin films*
   Journal of Applied Physics, **99**, 08M124 (2006)

P. Stamenov, M. Venkatesan, L. S. Dorneles, D. Maude, and J. M. D. Coey

6. *Vector vibrating-sample magnetometer with permanent magnet flux source*
   Journal of Applied Physics, **99**, 08D912 (2006)
   P. Stamenov and J. M. D. Coey

7. *Magnetization of electrodeposited nickel: Role of interstitial carbon*
   Journal of Applied Physics, **99**, 08J301 (2006)
   C. O'Reilly, S. Sanvito, F. M. F. Rhen, P. Stamenov, and J. M. D. Coey

8. *Magnetism in dilute magnetic oxide thin films based on SnO_2*
   Physical Review B, **74**, 115307 (2006)
   C. B. Fitzgerald, M. Venkatesan, L. S. Dorneles, R. Gunning, P. Stamenov, J. M. D. Coey, P. A. Stampe, R. J. Kennedy, E. C. Moreira, and U. S. Sias

9. *Magnetic susceptibility of carbon - experiment and theory*
   Journal of Magnetism and Magnetic Materials, **290-291**, 279-285 (2005)
   P. Stamenov and J. M. D. Coey

10. *Shubnikov - de Haas and Hall quantum oscillations in graphite*
    Journal of Magnetism and Magnetic Materials, **290-291**, 1402-1404 (2005)
    P. Stamenov, V. Krstic and J. M. D. Coey

11. *Oriented cobalt nanowires prepared by electrodeposition in a porous membrane*
    Journal of Magnetism and Magnetic Materials, **290-291**, 1210-1213 (2005)
    N. B. Chaure, P. Stamenov, F. M. F. Rhen and J. M. D. Coey

12. *Magnetism in hafnium dioxide*
    Physical Review B, **72**, 024450 (2005)
    J. M. D. Coey, M. Venkatesan, P. Stamenov, C. B. Fitzgerald, and L. S. Dorneles

13. *Anisotropy of the magnetization of a dilute magnetic oxide*
    Journal of Magnetism and Magnetic Materials, **290-291**, 1405-1407 (2005)
    J.M.D. Coey, M. Venkatesan, C.B. Fitzgerald, L.S. Dorneles, P. Stamenov and J.G. Lunney

14. *Structural distortions and charge/orbital ordering in* $Bi_{0.25}Ho_{0.25}Ca_{0.5}MnO_3$
    Physica B: Condensed Matter, **350**, E13-E17 (2004)
    K. Krezhov, D. Kovacheva, E. Svab, F. Bourée and P. Stamenov

15. *Nonlinear oscillator derived from the Lorenz chaotic system*
    Comptes Rendu de l'Academie Bulgare des Sciences, **54**, 11 (2001)
    S. Panchez, T. Spasova, P. Stamenov

References

(2000). *Sample mounting considerations*. Quantum Design, 6325 Lusk Boulevard San Diego, CA 92121-3733, USA, mpms application note 1014-201 edn. 314, 335

(2001). *Outline of data regression routines*. Quantum Design, 6325 Lusk Boulevard San Diego, CA 92121-3733, USA, mpms application note 1014-203 edn. 314, 316

(2001). *Regression value algorithm*. Quantum Design, 6325 Lusk Boulevard San Diego, CA 92121-3733, USA, mpms application note 1014-214 edn. 336

(2002). *Subtracting sample holder background from dilute samples*. Quantum Design, 6325 Lusk Boulevard San Diego, CA 92121-3733, USA, mpms application note 1014-213 edn. 334, 335

Abrahams, E., Anderson, P.W., Licciardello, D.C. & Ramakrishnan, T. (1979). Scaling theory of localization: Absence of quantum diffusion in two dimansions. *Phys. Rev. Lett.*, **42**, 673. 206

Adams, E.N. (1953). Magnetic susceptibility of a diamagnetic electron gas - the role of small effective electron mass. *Phys. Rev.*, **89**, 633. 234

Adler, J.G., Kreuzer, H.J. & Straus, J. (1975). Nonequilibrium electron tunneling in metal-insulator-metal junctions. *Phys. Rev. B*, **11**, 2812. 116

Åkerman, J.J., Escuedo, R., Leighton, C., Kim, S., Rabson, D.A., Dave, R.W., Slaughter, J.M. & Schuller, I.K. (2002). Criteria for ferromagnetic-insulator-ferromagnetic tunneling. *Journ. Magn. Magn. Mat.*, **240**, 86. 147

Åkerman, J.J., Roshchin, I.V., Slaughter, J.M., Dave, R.W. & Schuller, I.K. (2003). Origin of the temperature dependence in tunneling magnetoresistance. *Europhys. Lett.*, **63**, 104. 132

Alavi, M., Reinhard, D.K. & Yu, C.C.W. (1987). Minority-carrier injection in pt-si schottky-barrier diodes at high current densities. *IEEE Trans. Electron Dev.*, **ED-34**, 1134. 22

Albrecht, J.D. & Smith, D.L. (2002). Electron spin injection at a schottky contact. *arXiv:cond-mat*, **1**, 0202131. 7

Albrecht, J.D. & Smith, D.L. (2003). Spin-polarized electron transport at ferromagnet/semiconductor schottky contacts. *arXiv:cond-mat*, **1**, 0302457. 7

Almashary, B. (2004). Genetic algorithm based diode model parameters extraction. *IEEE Semiconductor Devices Conference 2004*, **1**, 545. 38

Altshuler, B.L. & Aronov, A.G. (1979). Zero bias anomaly in tunnel resistance and electron-electron interaction. *Solid State Comm.*, **30**, 115. xix, 113, 115, 162, 163, 166

Altshuler, B.L. & Aronov, A.G. (1981). Magnetoresistance of thin films and wires in longtitudinal magnetic fields. *JETP Lett.*, **33**, 515–518. 206

Altshuler, B.L. & Aronov, A.G. (1983). Anomalies of the tunnel conductance at small bias in magnetic field. *JETP Lett.*, **37**, 145. 115

Altshuler, B.L. & Aronov, A.G. (1993). Zero bias anomaly in tunnel resistance and electron-electron interaction. *Solid-State Comm.*, **88**, 1033. 113

Altshuler, B.L., Aronov, A.G. & Lee, P.A. (1980). Interaction effects in disordered fermi systems in two dimensions. *Phys. Rev. Lett.*, **44**, 1288. 113

Amaral, V.S. (1990). On the contribution of magnetic scattering to weak localization magnetoresistance. *J. Phys.: Condens. Matter*, **2**, 8201–8204. 206

Anderson, J.R., O'Sullivan, W.J., Schirber, J.E. & Soule, D.E. (1967). Effect of pressure on the fermi surface of graphite. *Phys. Rev.*, **164**, 1038. 237, 249

Anderson, P.W. (1966). Localized magnrtic states and fermi-surface annomalies in tunneling. *Phys. Rev. Lett.*, **17**, 95. 113

Andrearczyk, T., Jaroszynski, J., Gabecki, G., Dietl, T., Fukumura, T. & Kawasaki, M. (2005). Spin-related magnetoresistance of n-type zno:al and $zn_{1-x}mn_xo$:al thin films. *Phys. Rev. B*, **72**, 121309(R). 209

Andrews, J.M. & Phillips, J.C. (1975). Chemical bonding and structure of metal-semiconductor interfaces. *Phys. Rev. Lett.*, **35**, 56. 12

Appelbaum, J. (1966). "s-d" exchange model of zero-bias tunneling anomalies. *Phys. Rev. Letters*, **17**, 91. 113, 142, 153

Appelbaum, J., Phillips, J.C. & Tzouras, G. (1967). Microscopic theory of tunneling anomalies. *Phys. Rev.*, **160**, 554. 113

Appelbaum, J.A. (1967). Exchange model of zero-bias tunneling anomalies. *Phys. Rev.*, **154**, 633. 113

Appelbaum, J.A. & Brinkman, W.F. (1970). Interface effects in normal metal tunneling. *Phys. Rev. B*, **2**, 907. 113

Appelbaum, J.A. & Shen, L.Y.L. (1971). Zero-bias-conductance-peak anomaly of ta-*i*-al tunnel junctions at 0.3 k and 90 kg. *Phys. Rev. B*, **5**, 544. 113

Argyres, P.N. (1962). Theory of tunneling and its dependence on a longtitudinal magnetic field. *Phys. Rev.*, **126**, 1386. 238

Aronov, A.G. (1976). Spin injection in metals and its influence on the nuclear polarisation. *JETP Lett.*, **24**, 37. 183, 185, 186, 189, 198

Aronov, A.G. & Linda-Geller, U.B. (1989). Nuclear electrical resonance and carrier spin orientation in electric field. *JETP Lett.*, **50**, 398–400. 183

Aronov, A.G. & Pikus, G.E. (1976). Spin injection into semiconductors. *Sov. Phys. Semicond.*, **6**, 134. 183

Ashcroft, N.W. & Mermin, N.D. (1976). *Solid State Physics*. Brooks/Cole. 13, 54, 57, 276

Aspnes, D.E. & Studna, A.A. (1973). Schottky-barrier electroreflectance: application to gaas. *Phys. Rev. B*, **7**, 4605. 59

Ausserlechner, U., Kasperkovitz, P. & Steiner, W. (1998). A theoretical discussion of vector pick-up systems for squid magnetometers. *Meas. Sci. Technol.*, **9**, 989. 313, 317

Averkiev, N.S., Golub, L.E. & Pikus, G.E. (1999). Weak localization in semiconductors with complicated valence band structure, www.ioffe.rssi.ru/PAPERS/97w10.pdf. 207

REFERENCES

Ayyildiz, E., Türüt, A., Efeoğlu, H., Tüzemen, S., Sağlam, M. & Yoğurtcu, Y.K. (1996). Effect of series resistance on the forward current-voltage characteristics of schottky diodes in the presence of interfacial layer. *Solid-State Electronics*, **39**, 83. 30

Bachtold, A., Strunk, C., Salvetat, J.P., Bonard, J.M., Forró, L., Nussbaumer, T. & Schönenberger, C. (1999). Aharonov-bohm oscillations in carbon nanotubes. *Nature*, **397**, 673. 233

Badila, M. & Georgescu, S. (2002). Integrated schottky diode parameters extraction. *Proceedings of the Semicinductors Conference CAS 2002*, **1**, 431. 30

Bae, S.Y. & Wang, S.X. (2002). Transport in magnetically doped magnetic tunnel junctions. *IEEE Trans. Magn.*, **38**, 2721. 142

Bandow, S. (1996). Magnetic properties of nested carbon nanostructures studied by electron spin resonance and magnetic susceptibility measurements. *J. Appl. Phys.*, **80**, 1020. 233

Bandow, S., Kokai, F., Takahashi, K., Yudasaka, M. & Iijima, S. (2001). Unique magneism observed in single-walled carbon nanohorns. *Appl. Phys. A: Mat. Sci. Process.*, **73**, 281–285. 233

Banwell, T.C. & Jayakumar, A. (2000). Exact analytical solution for current flow through diode with series resistance. *Electronics Lett.*, **36**, 291. 31

Barabash, S.V. & Stroud, D. (2001). Negative magnetoresistance produced by hall fluctuations in a ferromagnetic domain structure. *Appl. Phys. Lett.*, **79**, 979. 203

Bardeen, J. (1961). Tunnelling from a many-particle point of view. *Phys. Rev. Lett.*, **6**, 57. 104, 110, 112, 136

Bardou, F. (1997). Rare events in quantum tunneling. *Europhys. Lett.*, **39**, 239–244. 135

Barret, C., Chekir, F. & Vapaille, A. (1983). Study of metal-semiconductor interface states using schottky capacitance spectroscopy. *Journ. Phys. C: Solid State Phys.*, **16**, 2421. 17

Bass, J. & Pratt-Jr, W.P. (2007). Spin-diffusion lengths in metals and alloys, and spin-flipping at metal/metal interfaces: an experimentalist's critical review. *J. Phys.: Condens. Matter*, **19**, 183201. 198

Bauer, G.E.W., Tserkovnyak, Y., Brataas, A., Ren, J., Xia, K., Xia, K., Zwierzycki, M. & Kelly, P.J. (2005). Spin accumulation and decay in magnetic schottky barriers. *Phys. Rev. B.*, **72**, 155304. 7

Baxter, D.V., Sumanasekera, G.U. & Carini, J.P. (1996). Transport anisotropy and dimensional crossover in ag/ge multilayers. *Journ. Magn. Magn. Mat.*, **156**, 359–361. 208

Bedanta, S., Petracic, O., Aderholz, M. & Kleemann, W. (2005). A sample holder design for high temperature measurements in superconducting quantum interference device magnetometers. *Rev. Sci. Instr.*, **76**, 083910. 335

Belevtsev, B.I., Beliayev, E.Y., Komnik, Y.F. & Kopiechenko, E.Y. (1998). Negative magnetoresistance in the nearest-neighbour hopping conduction in granular gold film. *Physica B*, **254**, 260–266. 202, 203

Bennet, R.J. (1987). Interpretation of forward bias behaviour of schottky barriers. *IEEE Trans. Electron. Dev.*, **34**, 935. 37

Bergmann, G. (1982a). Measurement of magnetic scattering time by weak localization. *Phys. Rev. Lett.*, **49**, 162. 206

Bergmann, G. (1982b). Quantative analysis of weak localization in mg films by magnetoresistance measurements. *Phys. Rev. B*, **25**, 2937. 207

Bergmann, G. (1983a). Consistent temperature and field dependence in weak localization. *Phys. Rev. B*, **28**, 515. 207

Bergmann, G. (1983b). Physical interpretation of weak localization: A time-of-flight experiment with conduction electrons. *Phys. Rev. B*, **28**, 2914. 206

Bergmann, G. (1984). Weak localizationin thin films. *Physics Reports*, **107**, 1–58. 206

Bergmann, G. (1986). Weak localization in thin films. *Physica Scripta*, **T14**, 99. 206

Bergmann, G. & Horriat-Esser, C. (1985). Spin-orbit scattering in thin films and on surfaces measured by weak localization. *Phys. Rev. B*, **31**, 1161. 206

Berhod, C., Binggeli, N. & Baldereschi, A. (2003). Schottky barrier heights at polar metal/semiconductor interfaces. *arXiv:cond-mat*, **1**, 0306404. 9

Berlincourt, T.G. & Steele, M.C. (1953). Oscillatory hall effect, magnetoresistance, and magnetic susceptibility of a graphite single crystal. *Phys. Rev.*, **98**, 956. 235

Bernard, W., Goldstein, S., Roth, H., Straub, W.D. & Jr., J.E.M. (1968). Oscillatory behaviour of the tunneling current in germanium in a longtitudinal magnetic field. *Phys. Rev.*, **166**, 785. 238

Berthod, C. (1998). *Electronic Properties of Ideal and Engineered Metal/Semiconductor Interfaces*. Ph.D. thesis, Department of Physics, Ecolé Polytechnique Féderalé de Lausanne. 11, 28

Bezák, V. & Selim, M.M. (2001). Tunneling across an inhomogenious delta-barrier. *Czechoslovak Journ. Phys.*, **51**, 829. 38

Bibes, M., Laukhin, V., Valencia, S., Martinez, B., Fortcuberta, J., Gorbenko, O.Y., Kaul, A.R. & Martinez, J.L. (2005). Anisotropic magnetoresistance and anomalous hall effect in manganite thin films. *J. Phys.: Condens. Matter*, **17**, 2733–2740. 205

Bickerton, R.J. & von Engel, A. (1955). The positive column in a longtitudinal magnetic field. *Proc. Phys. Soc.*, **LXIX**, 468. 44

Biercuk, M.J., Mason, N., Chow, J.M. & Marcus, C.M. (2004). Locally adressable tunnel barriers within a cabon nanotube. *Nano Lett.*, **4**, 2499–2502. 234

Bland, J.A.C., Steinmuller, S.J., Hirohata, A., Cho, W.S., Xu, Y.B., Guertler, C.M., Wastlbauer, G., Ionescu, A., Trypiniotis, T. & Holmes, S.N. (2003). Electron spin filtering in ferromegnet/semiconductor heterostructures. *J. Phys. D: Appl. Phys.*, **36**, 2204. 7

Blott, B.H. & Daniell, G.J. (1993). The determination of magnetic moments of extended samples in a squid magnetometer. *Meas. Sci. Technol.*, **4**, 462. 318, 321

Blundell, S.J. & Singleton, J. (1996). Semiclassical description of angle-dependent magnetoresistance oscillations in quasi-one-dimensional metals. *Phys. Rev. B*, **53**, 5609. 205

Bondarenko, V.B., Kudinov, J.A., Ershov, S.G. & Korablev, V.V. (1998). Natural inhomogeneities of the schottky barrier height. *Phys. Tech. Semicond.*, **32**, 554. 40

Boon, M. (1973). Negative magnetoresistance in doped semiconductors. *Phys. Rev. B*, **7**, 761. 203

Bozhkov, V.G. & Zaitsev, S.E. (2005a). A model of the intimate metal-semiconductor schottky-barrier contact. *Russ. Phys. Journ.*, **48**, 1085. 12

Bozhkov, V.G. & Zaitsev, S.E. (2005b). On the current-voltage characteristic of an ideal metal-semiconductor schottky-barrier contact. *Russ. Phys. Journ.*, **48**, 312. 28

Bozhkov, V.G. & Zaitsev, S.E. (2006). On the current-voltage characteristic of a tunnel metal-semiconductor schottky-barrier contact. *Russ. Phys. Journ.*, **49**, 251. 29

Bozhkov, V.G. & Zaitsev, S.E. (2007). Current-voltage and noise characteristics of an inhomogeneous schottky-barrier contact. *Journ. Comm. Tech. Electr.*, **52**, 87. 38

Bratkovsky, A.M. & Osipov, V.V. (2003). Spin extraction from a nonmagnetic semiconductor: Tunneling of electrons from semiconductors into ferromagnets through a modified schottky barrier. *arXiv:cond-mat*, **2**, 0307656. 51

Brillson, L.J. (1978). Transition in schottky barrier formation with chemical reactivity. *Phys. Rev. Lett.*, **40**, 260. 12

Brinkman, W.F., Dynes, R.C. & Rowell, J.M. (1970). Tunneling conductance of asymmetrical barriers. *Journ. Appl. Phys.*, **41**, 1915. 112

Bruno, M., Bonani, F. & Ghione, G. (2007). Transfer matrix method modelling of inhomogeneous schottky barrier diodes on silicon carbide. *Solid-State Electronics*, **51**, 466. 282

Budhani, R., Pant, P., Rakshit, R., Senapati, K., Mandal, S., Pandey, N. & Kumar, J. (2005). Magnetotransport in epitaxial films of the degenerate semiconductor zncoo. *J. Phys.: Condens. Matter*, **17**, 75. 209

Buess, M., Knowles, T.P., Ramsperger, U., Pescia, D. & Back, C.H. (2004). Phase-resolved pulsed precessional motion at a schottky barrier. *Phys. Rev. B*, **69**, 174422. 7

Butler, W.H., Zhang, X.G., Schulthess, T.C. & Maclaren, J.M. (2001). Spin-dependent tunneling conductance of fe|mgo|fe sandwiches. *Phys. Rev. B*, **63**, 054416. 122

Büttiker, M. (1988). Symmetry of electrical conduction. *IBM J. Res. Dev.*, **32**, 317. 129, 254

Byszewski, P. (1997). Carbon tubes discussed in a metalic ring model. *J. Phys. Chem. Solids*, **58**, 1685. 255, 256, 261

Byszewski, P. & Baran, M. (1995). Magnetic susceptibility of carbon nanotubes. *Europhys. Lett.*, **31**, 363–366. 257

Calawa, A.R., Rediker, R.H., Lax, B. & McWhorter, A.L. (1960). Magneto-tunneling in insb. *Phys. Rev. Lett.*, **5**, 55. 238

Carlo, A.D., Vogl, P. & Pötz, W. (1994). Theory of zener tunneling and wannier-stark states in semiconductors. *Phys. Rev. B*, **50**, 8358. 237

Caroline, D. (1969). The high-field magnetoresistance of lead. *J. Phys. C: Solid St. Phys.*, **2**, 308. 205

Céspedes, O., Ferreira, M.S., Sanvito, S., Kociak, M. & Coey, J.M.D. (2004). Contact induced magnetism in carbon nanotubes. *J. Phys.: Cond. Mat.*, **16**, L115. 231

Chand, S. (2002). An accurate approach for analysing inhomogenious schottky diode with a gaussian distribution of barrier heights. *Semicond. Sci. Technol.*, **17**, L36. 38

Chand, S. & Kumar, J. (1997). Effects of barrier height distribution on the behaviour of a schottky diode. *Journ. Appl. Phys.*, **82**, 5005. 39

Chantis, A.N., Belashenko, K.D., Tsymbal, E.Y. & van Schillfgaarde, M. (2007). Tunneling anisotropic magnetoresistance driven by resonant surface states: First-proncipled calculations on an fe(001) surface. *Phys. Rev. Lett.*, **98**, 046601. 131

Chatterjee, A. & Marshak, A.H. (1981). Theory of abrupt heterojunctions in equilibrium. *Solid-State Electronics*, **24**, 1111. 13

Chattopadhyay, P. (1995). A new technique for the determination of barrier height of schottky barrier diodes. *Solid-State Electr.*, **38**, 739. 34

Chattopadhyay, P. (1996). The effect of shunt resistance on the electrical characteristics of schottky barrier diodes. *Journ. Phys. D: Appl. Phys.*, **29**, 823. 30, 31

Chauvet, O., Forro, L., Bacsa, W., Ugarte, D., Doudin, B. & de Heer, W.A. (1995). Magnetic anisotropies of aligned carbon nanotubes. *Phys. Rev. B*, **52**, R6963. 233

Chazalviel, J.N. (1975). Spin relaxation of conduction electrons in n-type indium antimonide at low temperature. *Phys. Rev. B*, **11**, 1555. 183

Chen, T.P., Au, H.L., Lee, T.C., Ling, C.C., Beling, C.D. & Fung, S. (1993a). Numerical study of the decay of photovoltage at metal-semiconductor interfaces. *Solid State Comm.*, **87**, 1163. 61

Chen, T.P., Lee, T.C., Fung, S. & Beling, C.D. (1993b). A photovoltaic study of current transport and its influence on the determination of the schottky barrier height in schottky diodes. *Semicond. Sci. Technol.*, **8**, 2085. 60

Chen, T.P., Fung, S. & Beling, C.D. (1994). A study of recombination current in schottky contacts by photovoltage measurements. *Semicond. Sci. Technol.*, **9**, 2101. 61

Chiang, W.C., Chang, Y.M., Ho, C.H., Yao, Y.D. & Lin, M.T. (2005). Field orientation dependnce of magnetoresistancein spin-dependent tunnel junctions. *IEEE Trans. Magn.*, **41**, 896. 131

Chomsky, N. (2006). *Language and Mind*. Cambridge. 301

Choo, S.C. (1995). Theory of surface photovoltage in a semiconductor with a schottky contact. *Solid-State Electronics*, **38**, 2085. 60

Christopher, J.E., Coleman, R.V., Isin, A. & Morris, R.C. (1968). Experiments with tunnel junctions using ferromagnetic metals. *Phys. Rev.*, **172**, 485. 113

Chui, S.T. (1997). Bias dependence in spin-polarized tunneling. *Phys. Rev. B*, **55**, 5600. 122

Chynoweth, A.G., Logan, R.A. & Wolff, P.A. (1960). Effect of landau levels upon tunnel currents in indium antimonide. *Phys. Rev. Lett.*, **5**, 548. 238

Ciuti, C., McGuire, J.P. & Sham, L.J. (2002). Spin polarisation of semiconductor carriers by reflection off a ferromagnet. *Phys. Rev. Lett.*, **89**, 156601. 7

Clark, W.G. & Feher, G. (1963). Nuclear polarisation in insb by a dc current. *Phys. Rev. Lett.*, **10**, 134. 183

Coey, J.M.D. (1999). Powder magnetoresistance. *Journ. Appl. Phys.*, **85**, 5576. 264

Collection (2007). Semiconductors reference database. http://www.iofe.ru/SVA/NSM/Semicond/, hTML Resource. 63

Cooper, J.D., Smith, J.P., Woore, J. & Young, D.A. (1970). Shubnikov - de haas oscillations in neutron-irradiated graphite. *J. Phys. C: Solid St. Phys.*, **4**, 442. 237, 249

Cooper, J.R. & Miljak, M. (1976). Single impurity behaviour and interaction effects in the magnetic susceptibility of almn and alcr alloys. *J. Phys. F: Metal Phys.*, **6**, 2151. 309

Crowell, C.R. & Rideout, V.L. (1969). Notmalized thermionic emission in metal-semiconductor (schottky) barriers. *Solid-State Electron.*, **12**, 89. 280

Crowell, C.R. & Sze, S.M. (1966a). Current transport in metal-semiconductor barriers. *Solid St. Electron.*, **9**, 1035. 18, 28

Crowell, C.R. & Sze, S.M. (1966b). Quantum-mechanical reflection of electrons at metal-semiconductor barriers: Electron transport in semiconductor-metal-semiconductor structures. *Journ. Appl. Phys.*, **37**, 2683. 27

da Silva, R.R., Torres, J.H.S. & Kopelevich, Y. (2001). Indication of superconductivity at 35 k in graphite-sulfur composites. *Phys. Rev. Lett.*, **87**, 147001. 231

Danner, G.M., Kang, W. & Chaikin, P.M. (1994). Measuring the fermi surface of quasi-one-dimensional metals. *Phys. Rev. Lett.*, **72**, 3714. 205

Darling, R.B. (1996). Current-voltage characteristics of schottky barrier diodes with dynamic interfacial defect state occupancy. *IEEE Trans. Electr. Dev.*, **46**, 1153. 20

Dartora, C.A. & Cabrera, G.G. (2004). Ferromagnetic tunneling junctions at low voltages: Elastic *versus* inelastic scattering at t=0 k. *Journ. Appl. Phys.*, **95**, 6058–6064. 140

Davis, A.H. & MacLaren, J.M. (2000). Spin dependent tunneling at finite bias. *J. Appl. Phys.*, **87**, 5224. 122

Denardin, J.C., Knobel, M., Dorneles, L.S. & Schelp, L. (2005). Structural, magnetic and transport properties of discontinuous granular multi-layers. *Journ. Magn. Magn. Mat.*, **294**, 206. 338

Devoret, M.H., Esteve, D., Garabert, H., Ingold, G.L., Pothier, H. & Urbina, C. (1990). Effect of the electromagnetic environment on the coulomb blockade in ultrasmall tunnel junctions. *Phys. Rev. Lett.*, **64**, 1824. 166

Dietl, T., Ohno, H., Matsukura, F., Cibert, J. & Ferrand, D. (2000). Zener model description of ferromagnetism in zinc-blende magnetic semiconductors. *Science*, **287**, 1019. 208

Dimopoulos, T., Gieres, G., Wecker, J., Luo, Y. & Samwer, K. (2004). Analysis of the magnetotransport channels in tunnel junctions with amorphous cofeb. *Europhys. Lett.*, **68**, 706–712. 140, 141

Ding, H.F., Wulfhekel, W., Hen, J., Bruno, P. & Kirschner, J. (2003). Absence of zero-bias anomaly in spin-polarized vacuum tunneling in co(0001). *Phys. Rev. Lett.*, **90**, 116603. 142

Dmitruk, N.L., Borkovskaya, O.Y. & Mamykin, S.V. (1997). Measurement of diffusion length of minority charge carriers using real schottky barriers. *Semiconductors*, **31**, 661. 59

Domaingo, A. & Schürrer, F. (2004). Simulation of schottky barrier diodes with a direct solver for the boltzmann-poisson system. *Journal of Computational Electronics*, **3**, 221. 15, 26

Donoval, D., Drobny, V. & Luza, M. (1998). A contribution to the analysis of the $i - v$ characteristic of schottky structures. *Solid-State Electronics*, **42**, 235. 31

Dragulescu, A., Yakovenko, V.M. & Singh, D.J. (1999). Theory of angular magnetoresistance oscillations in $tl_2ba_2cuo_6$. *Phys. Rev. B*, **60**, 6312–6315. 205

Dresselhaus, M.S. & Mavroides, J.G. (1964). The fermi surface of graphite. *IBM Journ. Res. Dev.*, **8**, 262. 235

Du, X., Tsai, S.W., Maslov, D.L. & Hebard, A.F. (2004). Unconventinal magnetotransport in graphite. *arXiv:cond-mat*, **1**, 0404725. 232, 243

Du, X., Tsai, S.W., Maslov, D.L. & Hebard, A.F. (2005). Metal-insulator-like behaviour in semimetallic bismuth and graphite. *Phys. Rev. Lett.*, **94**, 166601. 232, 243

Dugaev, V.K., Bruno, P. & Barnas, J. (2001). Weak localization i ferromagnes with spin-orbit interaction. *Phys. Rev. B*, **64**, 144423. 206

Eastman, D.E. (1970). Photoelectric work functions of transition, rare-earth and noble metals. *Phys. Rev. B*, **2**, 1. xv, 85

Eastman, D.E. & Freeouf, J.L. (1975). Relation of schottky barriers to empty surface states on iii-v semiconductors. *Phys. Rev. Lett.*, **34**, 1624. 85

Edahiro, T., Fujimura, N. & Ito, T. (2003). Formation of two-dimensional electron gas and the magnetotransport behaviour of znmno/zno heterostructure. *Journ. Appl. Phys.*, **93**, 7673. 209

Eddrief, M., Marangolo, M., Corlevi, S., Giuchar, G.M., Etgens, V.H., Mattana, R., Mosca, D.H. & Sirotti, F. (2002). Fe/znse(001) schottky-barrier height evaluated by photoemission. *Appl. Phys. Lett.*, **81**, 4553. 57

Epstein, R.J., Malajovich, I., Kawakami, R.K., Chye, Y., Hanson, M., Petroff, P.M., Gossard, A.C. & Awschalom, D.D. (2002). Spontaneous spin coherence in n-gaas produced by ferromagnetic proximity polarization. *Phys. Rev. B*, **65**, 121202. 7

Epstein, R.J., Stephens, J., Hanson, M., Chye, Y., Gossard, A.C., Petroff, P.M. & Awschalom, D.D. (2003). Voltage control of nuclear spin in ferromagnetic schottky diodes. *Phys. Rev. B*, **68**, 041305. 7

Esaki, L. & Stiles, P.J. (1965). Study of electronic band structures by tunelling spectroscopy: Bismuth. *Phys. Rev. Lett.*, **14**, 902. 156

Esaki, L. & Stiles, P.J. (1966a). Bisb alloy tunnel junctions. *Phys. Rev. Lett.*, **16**, 574. 156

Esaki, L. & Stiles, P.J. (1966b). New type of negative resistance in barrier tunneling. *Phys. Rev. Lett.*, **16**, 1108. 156

Esquinazi, P., Setzer, A., Höhne, R., Semmelhack, C., Kopelevich, Y., Spemann, D., Butz, T., Kohlstrunk, B. & Lösche, M. (2002). Ferromagnetism in oriented graphite samples. *Phys. Rev. B*, **66**, 024429. 231

Esquinazi, P., Spermann, D., Höhne, R., Setzer, A., Han, K.H. & Butz, T. (2003). Induced magnetic ordering by proton irradiation in graphite. *Phys. Rev. Lett.*, **91**, 227201. 231

Fadnis, A.N., Trudeau, M.L., Joly, A. & Baxter, D.V. (1993). Anisotropic electron diffusion and weak localization in cu/al multilayers. *Phys. Rev. B*, **48**, 12202. 208

Faure-Vincent, J., Tiusan, C., Jougulet, E., Canet, F., Sajiaddine, M., Bellouard, C., Popova, E., Hehn, M., Montaigne, F. & Schuhl, A. (2003). High tunnel magnetoresistance in epitaxial fe/mgo/fe tunnel junctions. *Appl. Phys. Lett.*, **82**, 4507. 142

Feher, G. (1959). Nuclear polarization via "hot" conduction electrons. *Phys. Rev. Lett.*, **3**, 135. 183, 186

Ferhat-Hamida, A., Ouennoughi, Z., Hoffmann, A. & Weiss, R. (2001). Extraction of schottky diode parameters including parallel conductance using a vertical optimization method. *Solid-State Electron.*, **46**, 615. 37

Fischbach, D.B. (1961). Diamagnetic susceptibility of pyrolitic graphite. *Phys. Rev.*, **123**, 1613. 238

Fitzgerald, C.B., Venkatesan, M., Lunney, J.G., Dorneles, L.S. & Coey, J.M.D. (2005). Cobalt-doped zno - a room temperature dilute magnetic semiconductor. *Appl. Surf. Sci.*, **247**, 493. 338

Flood, D.J. (1969). Magnetothermal oscillations in pressure-annealed pyrolytic graphite. *Phys. Lett. A*, **30**, 178. 249

Floyd, R.B. & Walmsley, D.G. (1978). Tunnelling conductance of clean and doped al-i-pb junctions. *J. Phys. C: Solid State Phys.*, **11**, 4601. 124

Fortunato, E.M.C., Barquinha, P.M.C., Pimentel, A.C.M.B.G., Goncalves, A.M.F., Marques, A.J.S., Martins, R.F.P. & Pereira, L.M.N. (2004). Wide-bandgap high-mobility zno thin-film transistors produced at room temperature. *Appl. Phys. Lett.*, **85**, 2541. 210

Fowler, R.H. (1931). The analysis of photoelectric sensitivity curves for clean metals at various temperatures. *Phys. Rev.*, **38**, 45. 56, 57

Frenkel, J. (1938). On pre-breakdown phenomena in insulators and electronic semiconductors. *Phys. Rev.*, **54**, 647. 272

Fuchs, G.D., Katine, J.A., Kiselev, S.I., Mauri, D., Wooley, K.S., Ralph, D.C. & Buhrman, R.A. (2006). Spin torque, tunnel-current spin polarization, and magnetoresistance in mgo magnetic tunnel junctions. *Phys. Rev. Lett.*, **96**, 186603. 143

Fujiwara, A., Tomiyama, K., Suematsu, H., Yumura, M. & Uchida, K. (1999). Quantum interference of electrons in multiwall carbon nanotubes. *Phys. Rev. B*, **60**, 13492. 233

Fukuda, Y., Elam, W.T. & Park, R.L. (1977). Absolute $2p_{3/2}$ core binding energies and work functions of $3d$ transition-metal surfaces. *Phys. Rev. B*, **16**, 3322. 85

Fukumura, T., Jin, Z., Ohtomo, A., Koinuma, H. & Kawasaki, M. (1999). An oxide-diluted magnetic semiconductor: Mn-doped zno. *Appl. Phys. Lett.*, **75**, 3366. 208

Fukumura, T., Toyosaki, H. & Yamada, Y. (2005). Magnetic oxide semiconductors. *Semicond. Sci. Technol.*, **20**, S103–S111. 208, 209

Gallop, J. & Petley, B. (1976). Squids and their applications. *Journal of Physics E: Scien. Instr.*, **9**, 417. 314

Garachtchenko, A., Matlashov, A. & Jr., R.H.K. (1992). Baseline distance optimisation for squid gradiometers. *IEEE Trans. On Appl. Supercond.*, **9**, 3676. 313

Garbarczyk, J., Krukowska-Fulde, B., Langer, T. & Langer, J.M. (1978). Determination of the barrier height in metal - CdF_2 schottky diodes. *J. Phys. D: Appl. Phys.*, **11**, L17. 17

Ghosh, S., Sih, V., Lau, W.H., Awschalom, D.D., Bae, S.Y., Wang, S., Vaidya, S. & Chapeline, G. (2005). Room-temperature spin coherence in zno. *Appl. Phys. Lett.*, **86**, 232507. 209

Giaever, I. (1960a). Electron tunneling between two superconductors. *Phys. Rev. Lett.*, **5**, 464. 109

Giaever, I. (1960b). Energy gap in superconductors measured by electron tunneling. *Phys. Rev. Lett.*, **5**, 147. 109

Giddings, A.D., Khalid, M.N., Jungwirth, T., Wunderlich, J., Yasin, S., Campion, R.P., Edmonds, K.W., Sinova, J., Ito, K., Wang, K.Y., Williams, D., Gallager, B.L. & Foxon, C.T. (2005). Large tunneling anisotropic magnetoresistance in (ga,mn)as nanoconstrictions. *Phys. Rev. Lett.*, **94**, 127202. 131

Giraud, R., Gryglas, M., Thevenard, L., Lemaitre, A. & Faini, G. (2005). Voltage-controlled tunneling anisotropic magnetoresistance of a ferromagnetic p^{++}-(ga, mn)as/n^{+}-gaas zener-esaki diode. *Appl. Phys. Lett.*, **87**, 242505. 131

Godfrey, R. & Johnson, M. (2006). Spin injection in mesoscopic silver wires: Experimental test of resistance mismatch. *Phys. Rev. Lett.*, **96**, 136601. 183

Gomila, G. (1999). Effects of interface states in the non-stationery transport properties of schottky contacts and metal-insulator-semiconductor tunnel diodes. *Journ. Phys. D: Appl. Phys.*, **32**, 64. 27

Goodman, A.M. (1961). A method for the measurement of short minority carrier diffusion lengths in semiconductors. *Journ. Appl. Phys.*, **32**, 2550. 60

Goto, H., Shi, W., Suzuki, T., Sawaki, N., Ito, H. & Hara, K. (1995). Negative magnetoresistance in si atomic-layer-doped gaas. *Journ. Cryst. Growh*, **271-276**, 271–276. 202

Gould, C., Rüstler, C., Jungwirth, T., Girgis, E., Schott, G.M., Giraud, R., Brunner, K., Schmidt, G. & Molenkamp, L.W. (2004). Tunneling anisotropic magnetoresistance: A spin-valve-like tunnel magnetoresistance using a single magnetic layer. *Phys. Rev. Lett.*, **93**, 117203. 131

Goze-Bac, C., Latil, S., Lauginie, P., Jourdain, V., Conard, J., Duclaux, L., Rubio, A. & Bernier, P. (2002). Magnetic interaction in carbon nanostructures. *Carbon*, **40**, 1825–1842. 232

GREMPEL, D.R. (1987). Lacalisation in the presence of spin-dependent scattering: a renormalisation group study. *J. Phys. C: Solid State Phys.*, **20**, 3143–3153. 208

GRIMALDI, C. & PIETRONERO, L. (1999). Pauli susceptibility of nonadiabatic fermi liquids. *Europhys. Lett.*, **47**, 681–687. 187

GROVE, A.S. (1967). *Physics and Technology of Semiconductor Devices*. New York: Wiley. 21

GUNEA, F., SÁNCHEZ-DEHESA, J. & FLORES, F. (1983). Schottky barrier formation: I. abrupt metal-semiconductor junctions. *J. Phys. C: Solid State Phys.*, **16**, 6499. 12

HACHATUROV, A.I. (2005a). Manifestation of the band structure in tunnel characteristics of materials with low fermi energies. *Low Temperature Physics*, **31**, 109. 124, 139, 162

HACHATUROV, A.I. (2005b). Qualitative analysis of the spin-dependent tunelling in ferromagnetic metal - insulator - ferromagnetic metal junctions. *JETP Lett.*, **82**, 728. 122, 128, 130

HADDON, R.C. (1994). Magnetism of carbon clusters. *Phys. Rev. B*, **50**, 16459. 232

HAERING, R.R. & MILLER, P.B. (1961). Oscillations in the longtitudinal tunnel current of tunnel diodes. *Phys. Rev. Lett.*, **6**, 269. 238

HALPERIN, B.I. (1982). Quantized hall conductanc, current-carrying edge states, and the existance of extended states in a two-dimensional disordered potential. *Phys. Rev. B*, **25**, 2185. 231

HAN, K.H., SPEMANN, D., ESQUINAZI, P., HÖHNE, R., RIEDE, V. & BUTZ, T. (2004). Magnetic signals of proton irradiated spots created on highly oriented pyrolytic graphite surface. *Journ. Magn. Magn. Materials*, **272-276**, 1190–1191. 231

HAN, X.F., YU, A.C.C., OOGANE, M., MURAI, J., DAIBOU, T. & MIYAZAKI, T. (2001). Analyses of intrinsic magnetoelectric properties in spin-valve-type tunnel junctions with high magnetoresistance and low resistance. *Phys. Rev. B*, **63**, 224404. 140, 142

HANBICKI, A.T., VAN 'T ERVE, O.M.J., MAGNO, R., KIOSEOGLOU, G., LI, C.H., JONKER, B.T., ITSKOS, G., MALLORY, R., YASAR, M. & PETROU, A. (2003). Analysis of the transport process providing spin injection through an fa/algaas schottky barrier. *Appl. Phys. Lett.*, **82**, 4092. 7

HARIGAYA, K., KOBAYASHI, Y., TAKAI, K., RAVIER, J. & ENOKI, T. (2002). Novel electronic wave interference patterns in nanographene sheets. *J. Phys.: Condens. Matter*, **14**, L605–L611. 233

Harrison, W.A. (1961). Tunneling from an independent-particle point of view. *Phys. Rev.*, **123**, 85. 53, 107, 108, 109, 111, 122

Hassan, M.M.S. (2000). Characteristic of an epitaxial schottky barrier diode for all levels of injection. *Solid-State Electonics*, **44**, 1111. 22, 24

Hassenkam, T., Pedersen, S., Baklanov, K., Kristensen, A., Sorensen, C.B., Lindelof, P.E., Pikus, F.G. & Pikus, G.E. (1997). Spin- splitting and weak localization in (110) gaas/al$_x$ga$_{1-x}$as quantum wells. *Phys. Rev. B*, **55**, 9298. 206

Hautot, D., Pankhurst, Q.A. & Dobson, J. (2005). Superconducting quantum interference device measurements of dilute magnetic materiels in biological samples. *Rev. Sci. Instrum.*, **76**, 045101. 314

Hayashi, T., Katsumoto, S., Hashimoto, Y., Endo, A., Kawamura, M., Zalalutdinov, M. & Iye, Y. (2000). Anisotropy and barkhausen umps i diluted magnetic semiconductor (ga,mn)as. *Physica B*, **284-288**, 1175–1176. 205

Hedgcock, F.T. & Li, P.L. (1970). Magnetic susceptibility of dilute al-mn alloys. *Phys. Rev. B*, **2**, 1342. 308, 309

Heiliger, C., Zahn, P., Yavorsky, B.Y. & Merdig, I. (2005). Influence of the interface structure on the bias dependence of tunneling magnetoresistance. *Phys. Rev. B*, **72**, 180406(R). 143

Heilinger, C., Zahn, P., Yavorsky, B.Y. & Mertig, I. (2006). Interface structure and bias dependence of fe/mgo/fe tunnel junctions: *Ab initio* calculations. *Phys. Rev. B*, **73**, 214441. 143

Heine, V. (1965). Theory of surface states. *Phys. Rev.*, **138**, A1689. 11, 12

Henk, J. & Bruno, P. (2003). Bias voltage dependence of the magnetoresistance in ballistic vacuum tunneling: Theory and application to planar co(0001) junctions. *Phys. Rev. B*, **68**, 174430. 142

Heremans, J., Olk, C.H. & Morelli, D.T. (1994). Magnetic susceptibility of carbon structures. *Phys. Rev. B*, **49**, 15122. 233

Hipps, K.W. & Mazur, U. (2002). *Handbook of Vibrational Spectroscopy*, chap. Inelastic Tunneling Spectroscopy, 1. John Wiley & Sons Ltd. 296

Hirohata, A., Xu, Y.B., Guertler, C.M. & Bland, J.A.C. (1999). Spin-dependent electron transport at the ferromagnetit/semiconductor interface. *Journ. Appl. Phys.*, **85**, 5804. 7

Hirose, K., Ohndomari, I. & Uda, M. (1988a). Schottky-barrier heights of transition-metal-silicide-silicon contacts studied by x-ray photoemission spectroscopy measurements. *Phys. Rev. B*, **37**, 6929. 85

Hirose, K., Tsuda, T. & Mizutani, T. (1988b). Al/n-gaas schottky barrier height modified with rare-earth metal interlayer. *Journ. Appl. Phys.*, **64**, 6575. 85

Hoch, M.J.R., Lu, J., Kuhns, P.L., Moulton, W.G. & Reyes, A.P. (2005). Current-induced dynamic nuclear polarisation in gaas. *Phys. Rev. B*, **72**, 233204. 183

Höhne, R., K. H. Han, P.E., Setzer, A., Semmelhack, H., Spemann, D. & Butz, T. (2004). Magnetism of pure, disordered carbon films prepared by pulsed laser deposition. *Journ. Magn. Magn. Materials*, **272-276**, e839–e840. 231

Hornmark, E.T., Lyon, S.A., Poindexter, E.H. & Young, C.F. (2000). New features of electrically detected magnetic resonance in silicon p-n diodes. *Solid-State Comm.*, **116**, 279. 47

Hove, J.E. (1955). Theory of the magnetic susceptibility of graphite. *Phys. Rev.*, **100**, 645. 235

Hsu, C.Y. & Huang, J.C.A. (2005). Characterisation of interfacial properties in magnetic tunnel junctions by bias-dependent complex impedence spectroscopy. *IEEE Trans. Magn.*, **41**, 3643. 164

Huang, J.C. & Hsu, C.Y. (2004). Complex capacitance spectroscopy as a probe for oxidation process of alo$_x$-based magnetic tunnel junctions. *Appl. Phys. Lett.*, **85**, 5947. 164

Imry, Y. & Ovadyahu, Z. (1982). Density-of-states anomalies in a disordered conductor: A tunneling study. *Phys. Rev. Lett.*, **49**, 841. 113

Inoue, J., Nishimura, N. & Itoh, H. (2002). Influence on tunnel magnetoresistance of spin configurations localized within insulators. *Phys. Rev. B*, **65**, 104433. 113

Isakovic, A.F., Carr, D.M., Strand, J., D.Schultz, B., Palmstrøm, C.J. & Crowell, P.A. (2002). Optically pumped transport in ferromagnet-semiconductor schottky diodes. *Journ. Appl. Phys.*, **91**, 7261. 7

Jacšić, Z. & Durić, Z. (2000). Optimized high-frequency performance of auger-suppressed magnetoconcentration photoconductors. *Microelectronics Journal*, **31**, 981. 49

Jaffrés, H., Lacour, D., Dau, F.N.V., Briatico, J., Petroff, F. & Vaurés, A. (2001). Angular dependence of the tunnel magnetoresistance in transition-metal-based junctions. *Phys. Rev. B*, **64**, 064427. 131

Jaklevic, R.C. & Lambe, J. (1969). *Molecular Excitations in Barriers II*, chap. Chapter 18, 243. Plenum Press - New York. 118

Jang, M. & Lee, J. (2002). Analysis of schottky barrier height in small contacts using a thermionic-field emission model. *ETRI Journal*, **24**, 455. 281

Jang, M., Cho, W., Jung, W., Lee, S., Park, K., Lee, J. & Cha, J. (2003). Extraction of schottky barrier height in highly boron doped small size metal-silicon contact. *Journ. Korean Phys. Soc.*, **42**, S189. 40, 281

Jansen, R. & Moodera, J.S. (2000). Magnetoresistance in doped magnetic tunnel junctions: Effect os spin scattering and impurity assisted transport. *Phys. Rev. B*, **61**, 9047. 142

Jedema, F.J., Nijboer, M.S., Filip, A.T. & van Wees, B.J. (2003). Spin injection and spin accumulation in all-metal mesoscopic spin valves. *Phys. Rev. B*, **67**, 085319. 183

Jervase, J.A., Bourdoucen, H. & Al-Lawati, A. (2001). Solar cell parameter extraction using genetic algorithms. *Meas. Sci. Technol.*, **12**, 1922. 38

Jin, Z., Hasegawa, K., Fukumura, T., Yoo, Y.Z., Hasegawa, T., Koinuma, H. & Kawasaki, M. (2001). Magnetoresistance of 3d transition-metal-doped epitaxial zno thin films. *Physica E: Low-dim. Systems Nanostruct.*, **10**, 256. 209

Jin, Z., Fukumura, T., Hasegawa, K., Yoo, Y., Ando, K., Sekiguchi, T., Ahmet, P., Chikyow, T., Hasegawa, T., Koinuma, H. & Kawasaki, M. (2002). Optical and electrical properties of co-doped epitaxial zno films. *J. Cryst. Growth*, **237-239**, 548. 209

Johnson, M. (1993). Spin accumulation in gold films. *Phys. Rev. Lett.*, **70**, 2142. 183

Johnson, M. (2000). Dynamic nuclear polarization by spin injection. *Appl. Phys. Lett.*, **77**, 1680. 183

Johnson, M. & Byers, J. (2003). Charge and spin diffusion in mesoscopic metal wires and at ferromagnet/nonmagnet interfaces. *Phys. Rev. B*, **67**, 125112. 183, 185

Johnson, M. & Silsbee, R.H. (1985). Interfacial charge-spin coupling: Injection and detection of spin magnetisation in metals. *Phys. Rev. Lett.*, **55**, 1790. 183, 186

Johnson, M. & Silsbee, R.H. (1987). Thermodynamic analysis of interfacial transport and of the thermomagnetoelectric system. *Phys. Rev. B*, **35**, 4959. 183, 185, 186

Johnson, M. & Silsbee, R.H. (1988a). Coupling of electronic charge and spin at a ferromagnetic-paramagnetic metal interface. *Phys. Rev. B*, **37**, 5312. 183, 198

Johnson, M. & Silsbee, R.H. (1988b). Spin-injection experiment. *Phys. Rev. B*, **37**, 5326. 183, 198

Johnson, M. & Silsbee, R.H. (1989). Nonlocal resistance and magnetoresistance in bulk metals. *Phys. Rev. B*, **39**, 8169. 183

Jullière, M. (1975). Tunneling between ferromagnetic films. *Phys. Lett.*, **54A**, 225. 121, 122, 130, 141, 142

Jungwirth, T., Abolfath, M., Sinova, J., Kucera, J. & MacDonald, A.H. (2002). Boltzmann theory of engineered anisotropic magnetoresistance in (ga, mn)as. *Appl. Phys. Lett.*, **81**, 4029. 205

Jungwirth, T., Sinova, J., Wang, K.Y., Edmonds, K.W., Campion, R.P., Gallagher, B.L., Foxon, C.T., Niu, Q. & MacDonald, A.H. (2003). Dc-transport properties of ferromagnetic (ga,mn)as semiconductors. *Appl. Phys. Lett.*, **83**, 320. 205

Kalameĭtsev, A.V., Romanov, D.A., Kovchavtsev, A.P., Kuryshev, G.L., Postnikov, K.O. & Subbotin, I.M. (1997). Negative differential resistivity of a nonideal schottky barrier based on indium arsenide. *Semiconductors*, **31**, 308. 53, 281

Kaltsas, G., Travlos, A., Salamouras, N., Nassiopoulos, A.G., Revva, P. & Traverse, A. (1996). Erbium silicide films on (100) silicon, grown in high vacuum. fabrication and properties. *Thin Solid Films*, **275**, 87. 93

Kamarinos, G. & Viktorovitch, P. (1976). Scchottky diode magnetic sensor of high sensitiveness. *Proc. 1976 Inter. Electron Dev. Meeting*, **1**, 271. 49

Kamenev, K.V., Tancharakorn, S., Robertson, N. & Harrison, A. (2006). Long symmetric high-pressure cell for magnetic measurements in superconducting quantum interference device magnetometer. *Rev. Sci. Instrum.*, **77**, 073905. 314

Kaminski, A., Marchand, J.J., Fave, A. & Laugier, A. (1997). New method of parameters extraction from dark $i - v$ curve. 37

Kane, E.O. (1969). *Tunneling Phenomena in Solids*, chap. 1, 1–11. Plenum Press - New York. 104

Kartsovnik, M.V., Laukhin, V.N., Pesotskii, S.I., Schegolev, I.F. & Yakovenko, V.M. (1991). Angular magnetoresistance oscillations and the shape of the fermi surface in β-$(et)_2ibr_2$. *J. Phys. I France*, **2**, 89. 205

Kartsovnik, M.V., Kovalev, A.E., Laukhin, V.N. & Pesotskii, S.I. (1992). Giant angular magnetoresistance oscillations in $(bedt\text{-}ttf)_2tlhg(scn)_4$: the warped plane fermi surface effect. *J. Phys. I France*, **2**, 223–338. 205

Katkar, R.A. & Tait, G.B. (2004). Modelling of current density boundery conditions for a heterodimensional contact of 3d-metal to 2d-semiconductor. *Journ. Comput. Electronics*, **3**, 5. 26

Kauppinen, J.P. & Pekola, J.P. (1996). Charging in solitary, voltage biased tunnel junctions. *Phys. Rev. Lett.*, **77**, 3889. 166

Kawakami, R.K., Kato, Y., Hanson, M., Malajovich, I., Stephens, J.M., Johnston-Halperin, E., Salis, G., Gossard, A.C. & Awschalom, D.D. (2001). Ferromagnetic imprinting of nuclear spins in semiconductors. *Science*, **294**, 131. 7

Kempa, H., Kopelevich, Y., Mrowka, F., Setzer, A., Torres, J.H.S., Hohne, R. & Esquinazi, P. (2000). Magnetic-field-driven superconductorinsulator-type transition in graphite. *Solid State Comm.*, **115**, 539. 231

Keyser, P.T. & Jefferts, S.R. (1989). Magnetic susceptibility of some materials used for apparatus construction (at 295 k). *Rev. Sci. Instrum.*, **60**, 2711. 311

Khmelevskyi, S., Palotás, K., Szunyogh, L. & Weinberger, P. (2003). *Ab initio* calculation of the anisotropic magnetoresistance in $ni_{1-c}fe_c$ bulk alloys. *Phys. Rev. B*, **68**, 012402. 205

Khveshchenko, D.V. (2001a). Ghost excitonic insulator transition in layered graphite. *Phys. Rev. Lett.*, **87**, 246802. 231

Khveshchenko, D.V. (2001b). Magnetic-field-induced insulating behaviour in highly oriented pyrolitic graphite. *Phys. Rev. Lett.*, **87**, 206401. 231

Kim, J.R., So, H.M., Kim, J.J. & Kim, J. (2002). Spin-dependent transport properties in a single-walled carbon nanotube with mesoscopic co contacts. *Phys. Rev. Lett.*, **66**, 233401. 264

Kimura, T., Hamrle, J. & Otani, Y. (2005). Estimation of spin-diffusion length from the magnitude of current absorption: multiterminal ferromagnetic/nonferomagnetic hybrid structures. *Phys. Rev. B*, **72**, 014461. 183

Kimura, T., Otani, Y. & Hamrle, J. (2006). Switching magnetisation of a nanoscale ferromagnetic particle using nonlocal spin injection. *Phys. Rev. Lett.*, **96**, 037201. 184

Kinchin, G.H. (1953). The electrical properties of graphite. *Proc. Royal Soc. London*, **217**, 9–26. 240

Kirley, J.R. & Hansma, P.K. (1975). Effect of the second metal electrode on vibrational spectra in inelastic-electron-tunneling spectroscopy. *Phys. Rev. B*, **12**, 531. 176

Kirtley, J., Scalapino, D.J. & Hansma, P.K. (1976). Theory of vibrational mode intensities in inelastic electron tunneling spectroscopy. *Phys. Rev. B*, **14**, 3177. 118

Kittel, C. (1996). *Introduction to Solid State Physics*. Wiley. 6, 18, 107

Klaua, M., Ullmann, D., Barthel, J., Wulfhekel, W., Kirschner, J., Urban, R., Monchesky, T.L., Enders, A., Cochran, J.F. & Heinrich, B. (2001). Growth, structure, electronic, and magnetic properties of mgo/fe(001) bilayers and fe/mgo/fe(001) trilayers. *Phys. Rev. B*, **64**, 134411. 142

Klein, J., Léger, A., Belin, M., Défourneau, D. & Sangster, M.J.L. (1973). Inelastic-electron-tunneling spectroscopy of metal-insulator-metal junctions. *Phys. Rev. B*, **7**, 2336. 134, 177

Kobayashi, K. & Osada, T. (2005). Quantum features of angular dependent magnetoresistance oscillations in quasi-two-dimensional conductors near high magnetic field quantim limit. *Synthetic Metals*, **155**, 670–673. 205

Köhler, U., Ziese, M., bollero, A., Höhne, R. & Esquinazi, P. (2004). On the road to an all-oxide spin-transistor: study of magnetotransport properties of magnetite/nb:sto interfaces. *Journ. Magn. Magn. Mat.*, **272-276**, e1437. 42

Kohlhepp, J.T., LeClair, P., Swagten, H.J.M. & de Jonge, W.J.M. (2002). Interfacial sensitivity and zero-bias anomalies in magnetic tunnel junctions. *Phys. Stat. Sol. A*, **189**, 585–589. 142

Kopelevich, Y., Esquinazi, P., Torres, J.H.S., da Silva, R.R. & Kempa, H. (2003a). Graphite as a highly correlated electron liquid. *Adv. Solid State Phys.*, **43**, 207–222. 231, 246

Kopelevich, Y., Esquinazi, P., Torres, J.H.S., da Silva, R.R., Kempa, H., Mrowka, F. & Ocana, R. (2003b). Metal-insulator-metal transitions, superconductivity and magnetism in graphite. *Studies of High Temperature Superconductors*, **45**, 59–106. 231

Korošak, D. & Cvikl, B. (2004). On possible spin injection at non-ideal schottky contacts. *Solid. State Comm.*, **130**, 765. 52

Kotelnikov, I.N., Rilik, A.S. & Shulman, A.J. (1993). Magnetooscillations ad anisotropy of the zero-bias anomaly of tunell barriers n-gaas/au in quantising magnetic fields. *JETP Lett.*, **58**, 831. 53

Kotelnikov, I.N., Shulman, A.J., Maude, D.K. & Portal, J.C. (1994). Tunneling in quantising magnetic field and many-particle peculiarities in the tunneling spectra of schottky barriers. *JETP Lett.*, **60**, 849. 53

Kotosonov, A.S. (1999). Texture and magnetic anisotropy of carbon nanotubes found in cathode discharge residues. *JETP Letters*, **70**, 476. 233, 257

Kotosonov, A.S. & Kuvshinnikov, S.V. (1997). Diamagnetism of some quasi-two-dimensional graphites and multiwall carbon nanotubes. *Phys. Lett. A*, **229**, 377. 233, 257

Lake, R. (1997). Self-consistent calculation of the electrostatic potential. http://www.cfdrc.com/nemo/pubs, open HTML resource. 15

Landau, L. & Livshitz, E. (1982). *Electrodynamics*. Nauka - Moskow. 232, 256

Landau, L.D. & Liphshitz, E.M. (1976). *Theoretical Physics - Volume 9 - Condensed Matter Theory*. Nauka - Moskva. 249, 294

Landau, L.D., Liphshitz, E.M. & Pitaevskii, L.P. (1989). *Theoretical Physics - Volume 4 - Quantum Electrodynamics*. Nauka- Moskow. 113

Landauer, R. (1957). Spatial variation ofcurrents and fields due to localized scatterers in metallic conduction. *IBM J. Res. Dev.*, **1**, 223. 129

Laughlin, R.B. (1981). Quantized hall conductivity in two dimensiones. *Phys. Rev. B*, **23**, 5632. 231

Lawes, G., Risbud, A., Ramirez, A. & Seshadri, R. (2005). Absence of ferromagnetism in co and mn substituted polycrystalline zno. *Phys. Rev. B*, **71**, 045201. 208

Lebed, A.G. & Bagnet, N.N. (1997). Nonanalytical magnetoresistance, the third angular effect, and a method to investigate fermi surfaces in quasi-two-dimensional conductors. *Phys. Rev. B*, **55**, R8654. 205

Lebed, A.G., Bagmet, N.N. & Naughton, .J. (2004). Magic angle effects and angular magnetoresistance oscillations as dimensional crossovers. *Phys. Rev. Lett.*, **93**, 157006. 205

LeClair, P., Kohlhepp, J.T., Swagten, H.J.M. & de Jonge, W.J.M. (2001). Interfacial density of states in magnetic tunnel junctions. *Phys. Rev. Lett.*, **86**, 1066. 142

Lee, J.I., Brini, J. & Dimitriadis, C.A. (1998). Simple parameter extraction method for non-ideal schottky barrier diodes. *Electronics Letters*, **34**, 1268. 35

Lee, K.I., Joo, S.J., Lee, J.H., Rhie, K., Kim, T.S., Lee, W.Y., Shin, K.H., Lee, B.C., LeClair, P., Lee, J.S. & Park, J.H. (2007). Kondo effect in magnetic tunnel junctions. *Phys. Rev. Lett.*, **98**, 107202. 113, 147

Lee, P.A. & Ramakrishnan, T.V. (1982). Magnetoresistance of weakly disordered electrons. *Phys. Rev. B*, **26**, 4009. 208

Lehovec, K. (1948). The photo-voltaic effect. *Phys. Rev.*, **74**, 463. 55, 58

Leo, J. & MacDonald, A.H. (1990). Disorder-assisted tunneling through a double-barrier structure. *Phys. Rev. Lett.*, **64**, 817. 139

Leo, R.D. (2005). First-principle generation of stereographic maps for high-field magnetoresistance in normal metals: an application to au and ag. *Physica B: Cond. Matt.*, **362**, 62–75. 205

Lévy, L.P., Dolan, G., Dunsmuir, J. & Bouchiat, H. (1990). Magnetization of mesoscopic copper rings: Evidence for persistent currents. *Phys. Rev. Lett.*, **64**, 2074. 255

Lewis, L.H. & Bussmann, K. (1996). A sample holder design and calibration technique for the quantum design magnetic properties measurement system superconducting quantum interference device magnetometer. *Rev. Sci. Instrum.*, **67**, 3537. 314

Li, Y. & Li, D.Y. (2004). Experimental studies on relationships between the electron work function, adhesion, and friction for 3d transition metals. *Journ. Appl. Phys.*, **95**, 7961. 85

Lien, C.D., So, F.C.T. & Nicolet, M.A. (1984). An improved forward $i - v$ method for nonideal schottky diodes with high sries resistance. *IEEE Trans. Electron Dev.*, **ED-31**, 1502. 33

Likodimos, V., Glenis, S., Guskos, N. & Lin, C.L. (2003). Magnetic and electronic properties of multiwall carbon nanotubes. *Phys. Rev. B*, **68**, 045417. 233

Liu, S.S. & Guo, G.Y. (2000). Voltage-dependence of magnetoresistance in ferromagnetic tunneling junctions: a rigorous free electron model study. *Journ. Magn. Magn. Mat.*, **209**, 135. 128

Lopes, J.V., dos Santos, J.M.B.L. & Pogorelov, Y.G. (2002). Dipolar interactions and anisotropic magnetoresistance in metallic granular systems. *Phys. Rev. B*, **66**, 064416. 205

Losee, D.L. & Wolf, E.L. (1969). Tunneling spectroscopy of cds schottky-barrier junctions. *Phys. Rev.*, **187**, 925. 113

Lou, X., Adelmann, C., Furis, M., Crooker, S.A. & Palmstrøm, C.J. (2006). Electrical detection of spin accumulation at a ferromagnet-semiconductor interface. *Phys. Rev. Lett.*, **96**, 176603. 7

Lou, Y.S. & Wu, C.Y. (1994). A self-consistent characterisation methodology for schottky-barrier diodes and ohmic contacts. *IEEE Trans. Electron Dev.*, **41**, 558. 20

Low, G.G.E. (1955). A pulse method for measuring the injection ratio of metal-semiconductor contacts. *Proc. Phys. Soc. B*, **68**, 447. 22

Luk'yanchuk, I.A. & Kopelevich, Y. (2004). Phase analysis of quantum oscillations in graphite. *Phys. Rev. Lett.*, **93**, 166402. 237, 249

Lundstrøm, M.S. & Schuelke, R.J. (1982). Modeling semiconductiong heterojunctions in equilibrium. *Solid-State Electron.*, **25**, 683. 28

Luo, Y., Esseling, M., Käufler, A., Samwer, K., Dimopolous, T., Gieres, G., Vieth, M., Rührig, M., Wecker, J., Rudolf, C., Niermann, T. & Seibt, M. (2005). Co-rich magnetic amorphous films and their application in magnetoelectronics. *Phys. Rev. B*, **72**, 014426. 143

Lyanda-Geller, Y., Chun, S.H., Salamon, M.B., Goldbart, P.M., Han, P.D., Tomioka, Y., Asamitsu, A. & Tokura, Y. (2001). Charge transport in manganites: Hopping conduction, the anomalous hall effect, and universal scaling. *Phys. Rev. B*, **63**, 184426. 205

MacLaren, J.M., Zhang, X.G. & Butler, W.H. (1997). Validity of the julliere model of spin-dependent tunneling. *Phys. Rev. B*, **56**, 11827. 129, 130

Makarova, T.L., Sundqvist, B., Höhne, R., Esquinazi, P., Kopelevich, Y., Scharff, P., Davydov, V., Kashevarova, L.S. & Rakhmanina, A.V. (2001). Magnetic carbon. *Nature*, **413**, 716–718. 231

Makarova, T.L., Han, K.H., Esquinazi, P., da Silva, R.R., Kopelevich, Y., Zakharova, I.B. & Sundqvist, B. (2003). Magnetism in photopolymerized fullerenes. *Carbon*, **41**, 1575–1584. 231

Malozemoff, A.P. (1985). Anisotropic magnetoresistance of amorphous and concentrated polycrystalline iron alloys. *Phys. Rev. B*, **32**, 6080. 203

Malozemoff, A.P. (1986). Anisotropic magnetoresistance with cubic anisotropy and weak ferromagnetism: A new paradigm. *Phys. Rev. B*, **34**, 1853. 205

Mal'shukov, A.G., Froltsov, V.A. & Chao, K.A. (1999). Crystal anisotropy effects on the weak-localization magnetoresistance of a iii-v semiconductor quantum well in a magnetic field parallel to interfaces. *Phys. Rev. B*, **59**, 5702. 208

Manchon, A., Strelkov, N., Ryzhanova, N., Vedyaev, A., Dieny, B. & Slonczewski, J.C. (2007). Theoretical investigation of the relationship between spin torque and magnetoresistance in spin-valves and magnetic tunnel junctions. *Journ. Magn. Magn. Mat.*, **316**, e977–e979. 129

Many, A. (1954). Measurements of minority carrier lifetime and contact injection ratioon transistor materials. *Proc. Phys. Soc. B*, **67**, 636. 22

Matsumoto, R., Hamada, Y., Mizuguchi, M., Shiraishi, M., Maehara, H., Tsunekawa, K., Djayaprawira, D.D., Watanabe, N., Kurosaki, Y., Nagahama, T., Fukushima, A., Kubota, H., Yuasa, S. & Suzuki, Y. (2005). Tunneling spectra of sputter-deposited cofeb/mgo/cofeb magnetic tunnel junctions showing giant tunneling magnetoresistance effect. *Solid State Comm.*, **1136**, 611–615. 143

MAYERGOYZ, I.D. (1986). Solutionn to the nonlinear poisson equation of semiconductor device theory. *J. Appl. Phys.*, **59**, 195. 17

MAZIN, I.I. (1999). How to define and calculate the degree of spin polarization in ferromagnets. *Phys. Rev. Lett.*, **83**, 1427. 6

MCCANN, E. & FAL'KO, V.I. (2004). A tunnel junction between a ferromagnet and a normal metal: magnon-assisted contribution to thermopower and conductance. *Journ. Magn. Magn. Mat.*, **268**, 123–131. 112

MCCARTHY, K.T., ARNASON, S.B. & HEBARD, A.F. (1999). Frequency-dependent interface capacitance of al-al_2o_3-al tunnel junctions. *Appl. Phys.Lett.*, **74**, 302. 164

MCCLURE, J.W. (1956). Diamagnetism of graphite. *Phys. Rev.*, **104**, 666. 235

MCCLURE, J.W. (1957). Band structure of graphite and de haas - van alphen effect. *Phys. Rev.*, **108**, 612. 235

MCCLURE, J.W. (1958). Analysis of multicarrier galvanomagnetic data for graphite. *Phys. Rev.*, **112**, 715. 235

MCCLURE, J.W. (1960). Theory of diamagnetism of graphite. *Phys. Rev.*, **119**, 606. 235

MCCLURE, J.W. (1964). Energy band structure of graphite. *IBM Journ. Res. Dev.*, **8**, 255. 235

MCGUIRE, T.R. & POTTER, R.I. (1975). Anisotropic magnetoresistance in ferromagnetic 3d alloys. *IEEE Trans. Magn.*, **MAG-11**, 1018. 204

MCKENZIE, R.H. & MOSES, P. (1998). Incoherent interlayer transport and angular-dependent magnetoresistance oscillations in layered metals. *Phys. Rev. Lett.*, **81**, 4492. 205

MCLEAN, A.B. (1986). Limitations to the norde $I - V$ plot. *Semicond. Sci. Technol.*, **1**, 177. 34

MCLEAN, A.B., DHARMADASA, I.M. & WILLIAMS, R.H. (1986). Schottky-barrier height determination in the presence of interfacial disorder. *Semicond. Sci. Technol.*, **1**, 137. 30

MENZEL, D.H., ed. (1960). *Fundamental Formulas of Physics*. Dover. 27, 109, 273

MESERVEY, R., TEDROW, P.M. & FULDE, P. (1970). Magnetic field splitting of the quasi-particle states in superconducting aluminium films. *Phys. Rev. Lett.*, **25**, 1270. 299

Mezei, F. (1969). Coherence length effects in zero bias tunneling anomalies. *Solid State Comm.*, **7**, 771. 113

Miao, G.X., Chetry, K.B., Gupta, A., Butler, W.H., Tsunekawa, K., Djayaprawira, D. & Xiao, G. (2006). Inelastic tunneling spectroscopy of magnetic tunnel junctions based on cofeb/mgo/cofeb with mg insertion layer. *Journ. Appl. Phys.*, **99**, 08T305. 143, 177

Mikhelashvili, V. & Eisenstein, G. (1999). The influence of image forces on the extraction of physical parameters in schottky barrier diodes. *Journ. Appl. Phys.*, **86**, 6965. 37

Mikhelashvili, V., Eisenstein, G., Garber, V., Fainleib, S., Bahir, G., Ritter, D., Orenstein, M. & Peer, A. (1999). On the extraction of linear and nonlinear physical parameters in nonideal diodes. *Journ. Appl. Phys.*, **85**, 6873. 37

Mikhelashvili, V., Eisenstein, G. & Uzdin, R. (2001). Extraction of schottky diode parameters with a bias dependent barier height. *Solid-State Electron.*, **45**, 143. 37

Miller, D.J. & Lobb, J. (1994). Sharp variation in the magnetoresistance of a si schottky diode. *Appl. Phys. Lett.*, **65**, 1391. 47, 48

Miller, L.L. (1996). The response of longitudinal and transverse pickup coils to a misaligned magnetic dipole. *Rev. Sci. Instrum.*, **67**, 3201. 317, 326

Min, B.C., Motohashi, K., Lodder, C. & Jansen, R. (2006). Tunable spin-tunnel sontacts to silicon using low-work-function ferromagnets. *Nature Materials*, **5**, 817. 85

Minot, E., Yaish, Y., Sazonova, V. & McEuen, P.L. (2004). Determination of electron orbital magnetic moments in carbon nanotubes. *Nature*, **428**, 536. 233, 234

Miyazaki, T. & Tezuka, N. (1995). Giant magnetic tunneling effect in fe/al$_2$o$_3$fe junction. *Journ. Magn. Magn. Mat.*, **139**, L231–L234. 131

Mizuguchi, M., Hamada, Y., Matsumoto, R., Nishioka, S., Maehara, H., Tsunekawa, K., Djayaprawira, D.D., Watanabe, N., Nagahama, T., Fukushima, A., Kubota, H., Yuasa, S., Shiraishi, M. & Suzuki, Y. (2006). Tunneling spectroscopy of magnetic tunnel junctions: Comparison between cofeb/mgo/cofeb and cofeb/al-o/cofeb. *Journ. Appl. Phys.*, **99**, 08T309. 143

Mohaghegh, A., CristoLoveanu, S. & de Pontcharra, J. (1981). Double-injection phenomena under magnetic field in sos films: A new generation of magnetosensitive microdevices. *IEEE Trans. Electron Dev.*, **ED-28**, 237. 49

Monsterleet, J., Capoen, B. & Biskupski, G. (1997). Negative magnetoresistance in insulating n-type gaas and localized magnetic moments. *Solid State Comm.*, **101**, 525. 202, 203

Montaigne, F., Hehn, M. & Schuhl, A. (2001). Tunnel barrier parameters and magnetoresistance in the parabolic band model. *Phys. Rev. B*, **64**, 144402. 128

Moodera, J.S., Kinder, L.R., Wong, T.M. & Meservey, R. (1995). Large magnetoresistance at room temperature in ferromagnetic thin film tunnel junctions. *Phys. Rev. Lett.*, **74**, 3273. 157

Moodera, J.S., Nowak, J. & van de Veerdonk, R.J.M. (1998). Interface magnetism and spin wave scattering in ferromagnet-insulator-ferromagnet tunnel junctions. *Phys. Rev. Lett*, **80**, 2941. 141

Morelli, D.T. & Uher, C. (1984). T^2 dependence of the in-plane resistivity of graphite at very low temperature. *Phys. Rev. B*, **30**, 1080. 240

Moriyama, T., Ni, C., Wang, W.G., Zhang, X. & Xiao, J.Q. (2006). Tunneling magnetoresistance in (001)-oriented feco/mgo/feco magnetic tunnel junctions grown by sputtering deposition. *Appl. Phys. Lett.*, **88**, 222503. 143

Mott, N.F. & Zinamon, Z. (1970). The metal-nonmetal transition. *Rep. Prog. Phys.*, **33**, 881. 202

Mukhopadhyay, S., Das, I., Pai, S.P. & Raychaudhuri, P. (2005). Anomalous bias dependence of tunnel magnetoresistance in a magnetic tunnel junction. *Appl. Phys. Lett.*, **86**, 152108. 301

Mullen, K., Ben-Jacob, E., Jaclevic, R.C. & Schuss, Z. (1988). $i - v$ characteristics of coupled ultrasmall-capacitance normal tunnel junctions. *Phys. Rev. B*, **37**, 98. 166

Murai, J., Ando, Y., Daibou, T., Yaoita, K., Han, H.F. & Miyazaki, T. (2001). Magnon excitations of cofe/al-oxide/cofe ferromagnetic tunnel junctions. *Journ. Magn. Magn. Mat.*, **226-230**, 922–923. 142

Myburg, G., Auret, F.D., Meyer, W.E., Louw, C.W. & van Staden, M.J. (1998). Summary of schottky barrier height data on epitaxially grown n- and p-gaas. *Thin Solid Films*, **325**, 181. 85

Nagahama, T., Yuasa, S. & Suzuki, Y. (2003). Quantum size effect in magnetic tunnel junctions with single-crystal ultrathin electrodes. *Proc. Inter. Conf. MEMS, Nano and Smart Systems*, **ICMENS'03**, 7695. 177

Nagasaka, K., Varga, L., Shimizu, Y., Eguchi, S. & Tanaka, A. (2000). The temperature dependence of exchange anisotropy in ferromagnetic/pdptmn bilayers. *Journ. Appl. Phys.*, **87**, 6433. 143

Nakagawa, N., Asai, M., Mukunoki, Y., Susaki, T. & Hwang, H.Y. (2005). Magnetocapacitance and exponential magnetoresistance in manganite-titanate heterojunctions. *Appl. Phys. Lett.*, **86**, 082504. 46

Nam, M.S., Bundell, S.J., Ardavan, A., Symington, J.A. & Singleton, J. (2001). Fermi surface shape and angle-dependent magnetoresistance oscillations. *J. Phys.: Condens. Matter*, **13**, 2271. 205

Naur, P. (1960). *Revised Report on the Algorithmic Language ALGOL 60*, chap. Vol 3, 299–314. Communications of the ACM. 304

Netzer, F.P. (1995). Rare earth overlayers on silicon. *Journ. Phys.: Condens. Matter*, **7**, 991. 85

Newson, D.J. & Pepper, M. (1985). Anisotropic negative magnetoresistance in a variable-thickness electron gas. *J. Phys. C: Solid State Phys.*, **18**, L1049–L1055. 208

Ng, W.T., Liang, S. & Salama, C.A.T. (1990). Schottky barrier diode characteristics under high level injection. *Solid-State Electron.*, **33**, 39. 22

Nielsen, P. (1969). Zero bias anomalies produced by controlled amounts of cr in al-i-al tunnel junctions. *Solid State Comm.*, **7**, 1429. 113

Nielsen, P. (1970). Conductance changes produced by the controlled addition of foreign atoms to the barrier of al-insulator-metal tunnel junctions. *Phys. Rev. B*, **2**, 3819. 113

Norde, H. (1979). A modified forward $i-v$ plot for schottky diodes with high series resistance. *Journ. Appl. Phys*, **50**, 5052. 33

Norde, H., de Sousa Pires, J., d'Heurle, F., Pesavento, F., Petersson, S. & Tove, P.A. (1981). The schottky-barrier height of the contacts between some rare-earth metals (and silicides) and p-type silicon. *Appl. Phys. Lett.*, **38**, 865. 93

Noziéres, P. (1958). Cyclotron resonance in graphite. *Phys. Rev.*, **109**, 1510. 235

Ocana, R., Esquinazi, P., Kempa, H., Torres, J.H.S. & Kopelevich, Y. (2003). Magnetothermal conductivity of highly oriented pyrolytic graphite in the quantum limit. *Phys. Rev. B*, **68**, 165408. 237

Ono, K., Daibou, T., Ahn, S.J., Sakuraba, Y., Miyakoshi, T., Morita, T., Kikuchi, Y., Oogane, M., Ando, Y. & Miyazaki, T. (2006). Tunneling spectroskopy in cofeb/mgo/cofeb magnetic tunnel junctions. *Journ. Appl. Phys.*, **99**, 08A905. 143

Ortiz-Conde, A. & Sánchez, F.J.G. (2005). Extraction of non-ideal junction model parameters from the explicit analytic solution of its $i-v$ characteristic. *Solid-State Electronics*, **49**, 465. 31

Ortiz-Conde, A., Sánchez, F.J.G., Liou, J.J., Andrian, J., Laurence, R.J. & Schmidt, P.E. (1995). A generalized model for a two-terminal device and its applications to parameter extraction. *Solid-State Electron.*, **38**, 265. 37

Ortiz-Conde, A., Ma, Y., Thomson, J., Santos, E., Liou, J.J., Sánchez, F.J.G., Lei, M., Finol, J. & Layman, P. (1999). Direct extraction of semiconductor device parameters using lateral optimization method. *Solid-State Electron.*, **43**, 843. 37

Ortiz-Conde, A., Ma, Y., Thomson, J., Santos, E., Liou, J.J., Sánchez, F.J.G., Lei, M., Finol, J. & Layman, P. (2000). Parameter extraction using lateral and vertical optimization. *Proc. 22nd International Conference on Microelectronics*, **1**, 165. 37

Ortiz-Conde, A., Estrada, M., Sánchez, A.C.F.J.G. & Mercato, G.D. (2001). Modeling real junctions by a series combination of two ideal diodes with parallel resistance and its parameter extraction. *Solid-State Electron.*, **45**, 223. 38

Osada, T., Kagoshima, S. & Miura, N. (1996). Third angular effect of magnetoresistance in quasi-one-dimensional conducors. *Phys. Rev. Lett.*, **77**, 5261. 205

Osipov, V.V. & Bratkovsky, A.M. (2004a). Efficient nonlinear room-temperature spin injection from ferromagnets into semiconductors through a modified schottky barrier. *Journ. Appl. Phys.*, **96**, 4525. 51

Osipov, V.V. & Bratkovsky, A.M. (2004b). Eficient nonlinear room-temperature spin injection from ferromagnets into semiconductors through a modified schhottky barrier. *Phys. Rev. B.*, **70**, 205312. 51

Osterman, D.P. & Williamson, S.J. (1983). Effect of sample and magnetometer dimensions on the flux detected by a squid magnetometer. *Rev. Sci. Instrum.*, **54**, 1380. 317

Ostling, D., Tomanek, D. & Rosen, A. (1997). Electronic structure of single-wall, multi-wall, and filled carbon nanotubes. *Phys. Rev. B*, **55**, 13980. 231

Osvald, J. (2004). Comment on"negative schottky barrier between titanium ans n-type si(001) for low-resistance ohmic contacts". *Solid-State Electronics*, **48**, 2347. 85

Osvald, J. (2006a). Influence of lateral current spreading on the apparent barrier parameters of inhomogenious schottky diodes. *Journ. Appl. Phys.*, **99**, 033708. 39

Osvald, J. (2006b). Series resistance influence on intersecting behaviour of inhomogeneous schottky diodes $i - v$ curves. *Solid-State Electronics*, **50**, 228. 39

Osvald, J. & Dobročka, E. (1996). Generalized approach to the parameter extraction from $i - v$ characteristics of schottky diodes. *Semicond. Sci. Technol.*, **11**, 1198. 38

Otani, Y., Ishiyama, T., Kim, S.G. & Fukamichi, K. (2000). Hall effect due to spin injection in co/al planar junctions. *Journ. Appl. Phys.*, **87**, 6995. 183

Ottaviani, G., Tu, K.N. & Mayer, J.W. (1980). Interfacial reaction and schottky barrier in metal-silicon systems. *Phys. Rev. Lett.*, **44**, 284. 88

Padovani, F.A. & Stratton, R. (1966). Field and thermionic emission in schottky barriers. *Solid-State Electron.*, **9**, 695. 281

Pakhomov, A., Roberts, B., Tuan, A., Shutthanandan, V., McCready, D., Thevuthasan, S., Chambers, A. & Krishnan, K. (2004). Studies of two- and three-dimensional zno:co structures through different synthetic routes. *Journ. Appl. Phys.*, **95**, 7393. 209

Pal, B.P. (1974). Hot-electron magnetic susceptibility of degenerate semiconductors at low temeperatures: Effect of non-parabolicity. *Phys. Stat. Sol.*, **63**, 739. 187

Pal, B.P. & Sharma, S.K. (1974). Hot-electron magnetic susceptibility of degenerate semiconductors at low temperatures. *Journ. Appl. Phys.*, **45**, 1287. 187

Palasantzas, G., Barnas, J. & Hosson, T.M.D. (2000). Self-affine roughness effects on electron transmission and electric current in tunnel junctions. *J. Appl. Phys.*, **88**, 927. 139

Pannetier, B., Chaussy, J., Rammmal, R. & Gandit, P. (1985). First observation of altshuler-aronov-spivak effect in gold and copper. *Phys. Rev. B*, **31**, 3209. 255

Park, J.H., Kim, M.G., Jang, H.M. & Ryu, S. (2004). Co-metal clustering as the origin of ferromagnetism in co-doped zno thin films. *Appl. Phys. Lett.*, **84**, 1338. 209

Parkin, S.S.P., Kaiser, C., Panchula, A., Rice, P.M., Hughes, B., Samant, M. & Yang, S.H. (2004). Giant tunneling magnetoresistance at room temperature with mgo (100) tunnel barriers. *Nature Materials*, **3**, 862. 142

Pikus, F.G. & Pikus, G.E. (1996). Weak localization and negative magnetoresistance in wurzite-type crystals. *Solid State Comm.*, **100**, 95–99. 207

Pinnick, H.T. (1954). Magnetic susceptibility of carbon and polycrystalline graphites. i. *Phys. Rev.*, **94**, 319. 238

Pinnick, H.T. & Kiive, P. (1956). Magnetic susceptibility of carbon and polycrystalline graphites. ii. *Phys. Rev.*, **102**, 58. 238

Pipnis, P.A., Rimeĭka, A.K. & Lapeĭka, V.A. (1998). Temperature dependence of the reverse current in schottky barrier diodes. *Semiconductors*, **32**, 785. 33

Plesiewicz, W. & Adler, J.G. (1986). Inelastic electron-tunneling study of mgo barriers. *Phys. Rev. B*, **34**, 4583. 176

Potter, R.I. (1974). Magnetoresistance anisotropy in ferromagnetic nicu alloys. *Phys. Rev. B*, **10**, 4626. 205

Press, W., Teukolsky, S., Vetterling, W. & Flannery, B. (1992). *Numerical Recipies in C: the art of scientific computing*, chap. Chapter 2, Singular Value Decomposition. Cambridge University Press. 144, 324

Prohorov, A.M., ed. (1988). *Physics Encyclopaedia*. Narod. 63

Prokopyev, A.I. & Mesheryakov, S.A. (1999). Static characteristics of high-barrier schottky diode under high injection level. *Solid-State Electron.*, **43**, 1747. 22

Prokopyev, A.I. & Mesheryakov, S.A. (2003). Restrictions of forward $i - v$ methods for determination of schottky diode parameters. *Measurement*, **33**, 135. 34

Prokopyev, A.I. & Mesheryakov, S.A. (2005). Fast extraction of static parameters of schottky diodes from forward $i - v$ characteristic. *Measurement*, **37**, 149. 22

Quade, W., Schöll, E., Rossi, F. & Jacoboni, C. (1994). Quantum theory of impact ionization in coherent high-field semiconductor transport. *Phys. Rev B*, **50**, 7398. 237

Racko, J., Germanová, A. & Breza, J. (1996). Extended thermionic emission-diffusion theory of charge transport through a schottky diode. *Solid-State Electronics*, **39**, 391. 281

Racko, J., Grmanová, A., Parízek, J. & Breza, J. (1997). Thermionic emission-tunneling theory of charge transport through a schottky contact. *Czech. Journ. Phys.*, **47**, 649. 281

Ramirez, A. (1994). Defects in carbon nanostructures. *Science*, **265**, 84. 233

Ramirez, A.P., Haddon, R.C., Zhou, O., Fleming, R.M., Zhang, J., McClure, S.M. & Smalley, R.E. (1994). Magnetic susceptibility of molecular carbon: Nanotubes and fullerite. *Science*, **265**, 84. 232

Rashba, E.I. (2000). Theory of electrical spin injection: Tunnel contacts as a solution of the conductivity mismatch problem. *Phys. Rev. B*, **62**, R16267. 7

Reine, M., Vrehen, Q.H.F. & Lax, B. (1966). Photon-assisted magnetotunneling in parallel and crossed fields. *Phys. Rev. Lett.*, **17**, 582. 59

Reizer, M. (1998). Zero-bias anomaly in asymetric contacts. *Phys. Rev. B*, **58**, 15789. 166

Ren, M.J., Yan, S.S., Ji, G., Chen, Y.X., Song, H.Q. & Mei, L.M. (2003). Magnetic and trasport properties of zno/co nanomultilayers. *Chin. Phys. Lett.*, **12**, 2239. 209

Rhoderick, E.H. & Williams, R.H. (1988). *Metal-Semiconductor Contacts*. Oxford: Clarendon. 15, 18, 26, 64, 67, 280

Ribeiro, P.C., Bruno, A.C. & Paulsen, C.C. (1987). Spatial fourier transform method for evaluating squid gradiometers. *Rev. Sci. Instrum.*, **58**, 1580. 328

Rijks, T.G.S.M., Coehoorn, R., de Jong, M.J.M. & de Jonge, W.J.M. (1995). Semi-classical calculations of the anisotropic magnetoresistance of nife-based thin films, wires and multilayers. *Phys. Rev. B*, **51**, 283. 205

Rochon, P. & Fortin, E. (1975). Photovolaic effect and interband magneto-optical transitions in inp. *Phys. Rev. B*, **12**, 5803. 58

Rochon, P. & Fortin, E. (1976). Photovoltaic spectra and magneto-optical transitions in insb. *Phys. Rev. B*, **15**, 2025. 58

Rode, A.V., Gamaly, E.G., Christy, A.G., Gerald, J.G.F., Hyde, S.T., Elliman, R.G., Luther-Davies, B., Veinger, A.I., Androulakis, J. & Giapintzakis, J. (2004). Unconventional magnetism in all-carbon nanofoam. *Phys. Rev. B*, **70**, 054407. 232

Rollbühler, J. & Grabert, H. (2001). Coulomb blockade of tunneling between disordered conductors. *Phys. Rev. Lett.*, **87**, 126804. 166

Roth, H., Bernard, W., Straub, W.D. & Jr., J.E.M. (1966). Magnetic-field dependence of direct interband tunneling in germanium. *Phys. Rev.*, **145**, 667. 238

Rottländer, P., Helm, M. & Schuhl, A. (2002). Determining the interfacial barrier height and its relation to tunnel magnetoresistance. *Phys. Rev. B*, **65**, 054422. 159

Rowell, J.M. & Shen, L.Y.L. (1966). Zero-bias anomalies in normal metal tunnel junctions. *Phys. Rev. Lett.*, **17**, 15. 112

Roy, A., Buchanan, D., Ginsberg, D. & Roach, P. (1982). Sample holder for measurement of small magnetic moments using squid magnetometers. *Rev. Sci. Instr.*, **53**, 1053. 335

Ruüster, C., Gould, C., Jungwirth, T., Sinova, J., Schott, G.M., Giraud, R., Brunner, K., Schmidt, G. & Molenkamp, L. (2005). Very large tunneling anisotropic magnetoresistance of a (ga,mn)as/gaas/(ga,mn)as stack. *Phys. Rev. Lett.*, **94**, 027203. 131

Saito, H., Yuasa, S. & Ando, K. (2005). Origin of te tunnel anisotropic magnetoresistance in $ga_{1-x}mn_xas/znse/ga_{1-x}mn_xas$ magnetic tunnel junctions of ii-vi/iii-v heterostructures. *Phys. Rev. Lett.*, **95**, 086604. 131

Saito, M., Sasaki, T. & Fukuyama, H. (2003). A theoretical study on orbital magnetism of mesoscopic ring systems. *Physica E*, **18**, 362–363. 255

Saito, R., Dresselhaus, G. & Dresselhaus, M. (1998). *Physical Properties of Carbon Nanotubes*. Cambridge. 256

Savitski, V.G. & Sokolovsky, B.S. (1995). Interfacial recombination of current carriers: influence on magnetoconcentration effect in semiconductor heterostructure. *Vacuum*, **46**, 505. 49

Scharfetter, D.L. (1965). Minority carrier injection and charge storage in epitaxial schottky-barrier diodes. *Solid-State Electron.*, **8**, 299. 22

Schlüter, M. (1978). Chemical trends in metal-semiconductor barrier heights. *Phys. Rev. B*, **17**, 5044. 12

Schmalhorst, J., Kämmerer, S., Reiss, G. & Hütten, A. (2005). Inelastic electron tunneling spectroscopy and bias voltage dependence of magnetic tunnel junctions with polycrystalline co$_2$mnsi electrode. *Appl. Phys. Lett.*, **86**, 052501. 177

Schmidt, G., Ferrand, D., Molenkamp, L.W., Filip, A.T. & van Wees, B.J. (2000). Fundamental obstacle for electrical spin injection from a ferromagnetic metal into a diffusive semiconductor. *Phys. Rev. B*, **62**, R4790. 7

Sercheli, M.S., Kopelevich, Y., da Silva, R.R., Torres, J.H.S. & Rettori, C. (2002). Evidence for internal field in graphite: a conduction electron spin resonance study. *Solid State Comm.*, **121**, 579–583. 231

Sesé, J., Bartolomé, J. & Rillo, C. (2007). Disposable sample holder for high tempperature measurements in mpms superconducting quantim interference device magnetometers. *Rev. Sci. Instrum.*, **78**, 046101. 314

Shamir, N., Sheinman, B., Ritter, D. & Gershoni, D. (2001). Comparison of titanium and platinum schottky barrier heights to $Ga_{0.47}In_{0.53}As$ obtained from franz keldysh oscillations and schottky diode characteristics. *Solid-State Electronics*, **45**, 475. 59

Shang, C.H., Nowak, J., Jansen, R. & Moodera, J.S. (1998). Temperature dependence of magnetoresistance and surface magnetisation in ferromagnetic tunnel junctions. *Phys. Rev. B*, **58**, R2917. 140

Sharma, M., Wang, S.X. & Nickel, J.H. (1999). Inversion of spin polarization and tunneling magnetoresistance in spin-dependent tunneling junctions. *Phys. Rev. Lett.*, **82**, 616. 128

Sharma, M.P., Johnson, L.G. & McClure, J.W. (1974). Diamagnetism of graphite. *Phys. Rev. B*, **9**, 2467. 235

Shen, L.Y.L. & Rowell, J.M. (1967). Magnetic field and temperature dependence of the "zero bias tunneling anomaly". *Solid. State Comm.*, **5**, 189. 113

Shen, L.Y.L. & Rowell, J.M. (1968). Zero-bias tunneling anomalies - temperature, voltage and magnetic field dependence. *Phys. Rev.*, **165**, 566. 113

Shen, M., Saikin, S. & Cheng, M.C. (2004). Monte carlo modelling of spin injection through a schottky barrier and spin transport in a semiconductor quantum well. *Journ. Appl. Phys.*, **96**, 4319. 52

shen Yan, S., Ren, C., Wang, X., Xin, Y., Zhou, Z.X., Mei, L.M., Ren, M.J., Chen, Y.X., Liu, Y.H. & Garmestani, H. (2004). Ferromagnetism and magnetoresistance of co-zno inhomogeneous magnetic semiconductors. *Appl. Phys. Lett.*, **84**, 2376. 209

Shenai, K. & Dutton, R.W. (1988). Current transport mechanisms in atomically abrupt metal-semiconductor interfaces. *IEEE Trans. Electron Dev.*, **35**, 468. 280

Sheng, L., Xing, D.Y. & Sheng, D.N. (2004). Theory of the zero-bias anomaly in magnetic tunnel junctions: Inelastic tunneling via impurities. *Phys. Rev. B*, **70**, 094416. 115

Shibkov, A., Ershov, M. & Ryzhii, V. (1992). Numerical simulation of carrier transport in schottky barrier diodes. *Electronics Lett.*, **28**, 1841. 19

Shklovskij, V.A. (1980). Hot electrons in metals at low temperatures. *Journ. Low Temp. Physics*, **41**, 375. 187

Simmons, J.G. (1963). Generalized formula for the elecric tunnel effect between similar electrodes separated by a this insulating film. *J. Appl. Phys.*, **34**, 1793. 100, 101, 158

Simmons, J.G. (1969). *Tunneling Phenomena in Solids*, chap. 10, 135–148. Plenum Press - New York. xxi, 99, 101, 102, 176, 177

Slonczewski, J.C. (1989). Conductance and exchange coupling of two ferromagnets separated by a tunneling barrier. *Phys. Rev. B*, **39**, 6995. 128, 129, 130, 141

Slonczewski, J.C. (2005). Currents, torques, and polarisation factors in magnetic tunnel junctions. *Phys. Rev. B*, **71**, 024411. 128

Slonczewski, J.C. & Sun, J.Z. (2007). Theory of voltage-driven current and torque in magnetic tunnel junctions. *Journ. Magn. Magn. Mat.*, **310**, 169–175. 178

Smith, D.L. & Silver, R.N. (2001). Electron spin injection into semiconductors. *Phys. Rev. B*, **64**, 045323. 7

Song, S.N., Wang, X.K., Chang, R.P.H. & Ketterson, J.B. (1994). Electronic properties of graphite nanotubes from galvanomagnetic effects. *Phys. Rev. Lett.*, **72**, 697. 264

Sood, B.R. (1982). Magnetic-field-dependent zero-bias anomaly in al-oxide-ga (granular) thin-film tunnel junctions. *Phys. Rev. B*, **25**, 6064. 113

Soule, D.E. (1958). Analysis of galvanomagnetic de haas-van alphen type oscillations in graphite. *Phys. Rev.*, **112**, 708. 236

Soule, D.E. (1964). Change in fermi surfaces of graphite by dilute acceptor doping. *IBM Journ. Res. Dev.*, **8**, 268. 235

Soule, D.E., McClure, J.W. & Smith, L.B. (1964a). Study of the schubnikov - de haas effect. determination of the fermi surfaces in graphite. *Phys. Rev.*, **134**, A453. 249

Soule, D.E., McClure, J.W. & Smith, L.R. (1964b). Study of the shubnikov - de haas effect. determination of the fermi surfaces in graphite. *Phys. Rev.*, **134**, A453. 236

Spaldin, N.A. (2004). Search for ferromagnetism in transition-metal-doped piezoelectric zno. *Phys. Rev. B*, **69**, 125201. 208

Stephens, J., Berezovsky, J., McGuire, J.P., Sham, L.J., Gossard, A.C. & Awschalom, D.D. (2004). Spin accumulation in forward-biased mnas/gaas schottky diodes. *Phys. Rev. Lett.*, **93**, 097602. 7

Stratton, R. (1964). Electron tunneling with diffuse boundary conditions. *Phys. Rev.*, **136**, A837. 136

Sun, Z.G., Mizuguchi, M., Manago, T. & Akinaga, H. (2004). Magnetic-field-controllable avalanche breackdown and giant magnetoresistive effects in gold/semi-insulating-gaas schottky diode. *Appl. Phys. Lett.*, **85**, 5643. 54

Suzuura, H. & Ando, T. (2000). Huge magnetoresistance by phonon scattering in carbon nanotubes. *Physica E*, **6**, 864–867. 264

Swami, R. & Tantry, B. (1972). Effect of an intense magnetic field on the diffusion of minority carriers in semiconductors. *J. Phys. D: Appl. Phys.*, **5**, 639. 44

Sze, J.J. & Cheng, H.C. (1995). A new analytical expression for the interface index of metal-schottky contacts on semiconductors. *Solid-State Electronics*, **38**, 1059. 12

Sze, S.M. (1981). *Physics of Semiconductor Devices*. John Wiley & Sons. 18, 277

Szopa, M., Margańska, M. & Zipper, E. (2002). Persistent currents in carbon nanotubes. *Phys. Lett. A*, **299**, 593–600. 255

Tang, J.G. & Adams, T.W. (1989). Computer simulation of boundary condition for schottky barrier diodes. *Electronics Letters*, **25**, 1098. 19

Tang, X., Katcki, J., Dubois, E., Reckinger, N., Ratajczak, J., Larrieu, G., Lourmaye, P., Nisole, O. & Bayot, V. (2003). Very low schottky barrier to n-type silicon with pter-stack silicide. *Solid-State Electronics*, **47**, 2105. 85

Tao, M. & Zhu, J. (2004). Response to "comment on 'negative schottky barrier between titanium and n-type si(001) for low resistance ohmic contacts"'. *Solid-State Electronics*, **48**, 2351. 85

Tao, M., Udeshi, D., Agarwal, S., Maldonado, E. & Kirk, W.P. (2004). Negative schottky barrier betwen titanium and n-type si(001) for low-resistance ohmic contacts. *Solid-State Electronics*, **48**, 335. 85

Tatar, R.C. & Rabii, S. (1982). Electronic properties of graphite: A unified theoretical study. *Phys. Rev. B*, **25**, 4126. 235

Tedrow, P.M. & Meservey, R. (1973). Spin polarisation of electrons tunneling from films of fe, co, ni and gd. *Phys. Rev. B*, **7**, 318. 299

Tersoff, J. (1984). Schottky barrier heights and the contiuum of gap states. *Phys. Rev. Lett.*, **52**, 465. 8

Tersoff, J. & Harrison, W.A. (1987). Trensition-metal impurities in semiconductors - their connection with band lineups and schottky barrier. *Phys. Rev. Lett.*, **58**, 2367. 85

Tezuka, N., Oogane, M. & Miyazaki, T. (1999). Applied voltage and temperature dependence of tunneling magnetoresistance. *Journ. Magn. Magn. Mat.*, **198-199**, 149–151. 142

Tiusan, C., Dimopoulos, T., Ounadjela, K., Hehn, M., van den Berg, H.A.M., da Costa, V. & Henry, Y. (2000). Correlation between micromagnetism and tunnel magnetoresistance in magnetic tunnel junctions using artificial ferrimagnets. *Phys. Rev. B*, **61**, 580. 131

Tiusan, C., Faure-Vincent, J., Belloard, C., Hehn, M., Jouguelet, E. & Schuhl, A. (2004). Interfascial ressonance state probed by spin-polarized tunneling in epitaxial fe/mgo/fe tunnel junctions. *Phys. Rev. Lett.*, **93**, 106602. 142

Tiusan, C., Greullet, F., Sicot, M., Hehn, M., Bellouard, C., Montaigne, F., Andrieu, S. & Schuhl, A. (2006a). Engineering of spin filtering in double epitaxial tunnel junctions. *Journ. Appl. Phys.*, **99**, 08A903. 143

Tiusan, C., Sicot, M., Faure-Vincent, J., Hehn, M., Bellouard, C., Montaigne, F., Andrieu, S. & Schuhl, A. (2006b). Static and dynamic aspects of spin tunneling in crystalline magnetic tunnel junctions. *J. Phys.: Condens. Matter*, **18**, 941–956. 143

Tkachov, G. (2007). Nonmonotonic inelastic tunneling spectra due to emission of surface magnons in itinerant electron ferromagnetic junctions. *arXiv:cond-mat*, **2**, 0401460. 140

Torkhov, N.A. (2001). Effect of ballistic electron transport in metal-n-gaas-n^+gaas schottky-barrier structures. *Semiconductors*, **35**, 788. 274

Tsui, D.C., Dietz, R.E. & Walker, L.R. (1971). Multiple magnon excitation in nio by electron tunneling. *Phys. Rev. Lett.*, **27**, 1729. 177

Tsui, F., Jin, L. & Zhou, O. (2000). Anisotropic magnetic susceptibility of multiwalled carbon nanotubes. *Appl. Phys. Lett.*, **76**, 1452. 233

Tsukagoshi, K., Alphenaar, B.W. & Ago, H. (1999). Coherent transport of electron spin in a ferromagnetically contacted carbon nanotube. *Nature*, **401**, 572–574. 264

Tsunekawa, K., Djayaprawira, D.D., Nagai, M., Maehara, H., Yamagata, S., Watanabe, N., Yuasa, S., Suzuki, Y. & Ando, K. (2005). Giant tunneling magnetoresistance effect in low-resistance cofeb/mgo(001)/cofeb magnetic tunnel junctions for read-head applications. *Appl. Phys. Lett.*, **87**, 072503. 142

Tsymbal, E.Y. & Pettifor, D.G. (1998). Spin-polarized electron tunneling across a disordered insulator. *Phys. Rev. B*, **58**, 432. 99

Tu, K.N., Thompson, R.D. & Tsaur, B.Y. (1981). Low schottky barrier of rare-earth silicide on n-si. *Appl. Phys. Lett.*, **38**, 626. 93

Urech, M., Johansson, J., Korenivski, V. & Haviland, D.B. (2004). Spin injection in ferromagnet-superconductor/normal-ferromagnet structures. *Journ. Magn. Magn. Mat.*, **272-276**, e1469–e1470. 184, 186

Urech, M., Korenivski, V., Poli, N. & Haviland, D.B. (2006). Direct demonstration of decoupling of spin and charge currents in nanostructures. *Nano Letters*, **6**, 871–874. 184

v. Kiltzing, K., Dorda, G. & Pepper, M. (1980). New method for high-accuracy determination of the fine-structure constant based on quantized hall resistance. *Phys. Rev. Lett.*, **45**, 494. 231

Veal, T.D., Jefferson, P.H., Piper, L.F.J., McConville, C.F., Joyce, T.B., Chalker, P.R., Considine, L., Lu, H. & Schaff, W.J. (2006). Transition from electron accumulation to depletion at ingan surfaces. *Appl. Phys. Lett.*, **89**, 202110. 283

Vega, R.A. (2006). Comparison study of tunneling models for schottky field effect transistors and the effect of schottky barrier lowering. *IEEE Trans. Electron Dev.*, **53**, 1593. 282

Velev, J., Sabirianov, R.F., Jaswal, S.S. & Tsymbal, E.Y. (2005). Ballistic anisotropic magnetoresistance. *Phys. Rev. Lett.*, **94**, 127203. 205

Voskoboynikov, A., Liu, S.S. & Lee, C.P. (1998). Spin-dependent electronic tunneling at zero magnetic field. *Phys. Rev. B*, **58**, 15397. 122

Wagner, L.F. & Chuang, C.T. (1985). Probing the minority-carrier quasi-fermi level in epitaxial schottky-barrier diodes. *IEEE Trans. Electr. Dev.*, **ED-32**, 753. 22

Walker, M.B. (1999). Theory of tunneling for thick junctions with rough interfaces. *Phys. Rev. B*, **60**, 9283. 138

Wallis, R.H. & Wyatt, A.F.G. (1972). Evidence for interactions in magnetically doped tunnel junctions. *Phys. Rev. Lett.*, **29**, 479. 112

Wang, J., Gu, Z., Lu, M., Wu, D., Yuan, C., Zhang, S., Chen, Y., Zhu, S. & Zhu, Y. (2006a). Giant magnetoresistance in transition-metal-doped zno films. *Appl. Phys. Lett.*, **88**, 252110. 209

Wang, L., Davids, P.S., Saxema, A. & Bishop, A.R. (1992). Quasiparticle energy spectra and magnetic response of certain curved graphitic geometries. *Phys. Rev. B*, **46**, 7175. 263

Wang, X., Liu, Z.X., Zhang, Y.L., Li, F.Y., Yu, R.C. & Jin, C.Q. (2002). Evolution of magnetic behaviour in the graphitisation process of glossy carbon. *J. Phys.: Condens. Matter.*, **14**, 10265–10272. 232

Wang, X., Xu, J., Zhang, B., Yu, H., Wang, J., Zhang, X., Yu, J. & Li, Q. (2006b). Signature of intrinsic high-temperature ferromagnetism in cobal-doped zinc oxide nanocrystals. *Advanced Materials*, **18**, 2476–2480. 208

Wang, X.R., Ma, S.C. & Xie, X.C. (1999). The level shifting induced negative magnetoresistance in the nearest-neighbour hopping conduction. *Europhys. Lett.*, **45**, 368–373. 202

Weger, M. (1963). Nucler polarization in homogeneous insb by a direct current. *Phys. Rev.*, **132**, 581. 183, 187

Wei, W., Rosenbaum, R. & Bergmann, G. (1989). Magnetic scattering in auco and agco with weak localization. *Phys. Rev. B*, **39**, 4568. 206

Wellstood, F.C., Urbina, C. & Clarke, J. (1994). Hot-electron effects in metals. *Phys. Rev. B*, **49**, 5942. 187

Werner, J.H. (1988). Schottky barrier and pn-junction i/v plots - small signal evaluation. *Appl. Phys. A*, **47**, 291. 35

Wheeler, J.C.G. (1968). Magnetic susceptibility of al-mn alloys between 2 and 300 k. *Phys. Lett.*, **28A**, 437. 309

Williamson, S.J., Foner, S. & Dresselhaus, M.S. (1965). de haas-van alphen effect in pyrolytic and single-crystal graphite. *Phys. Rev.*, **140**, A1429. 249

Wingbermühle, J., Stein, S. & Kohlstedt, H. (2002). Magnon scattering and tunneling through localized states in magnetic tunnel junctions. *Journ. Appl. Phys.*, **92**, 7261. 140

Wittmer, M. (1990). Current transport in high-barrier irsi/si schottky diodes. *Phys. Rev. B*, **42**, 5249. 21

Wittmer, M. (1991). Conduction mechanism in ptsi/si schottky diodes. *Phys. Rev. B*, **43**, 4385. 21

Woan, G. (2000). *The Cambridge Handbook of Physics Formulas*. Cambridge University Press. 13, 15, 105, 106, 280

Woerlee, P.H., Verkade, G.C. & Jansen, A.G.M. (1983). An experimental investigation on weak localization, spin-orbit and interaction effects in thin bismuth films. *J. Phys. C: Solid State Phys.*, **16**, 3011–3024. 206

Wolf, E.L. & Losee, D.L. (1970). Spectroscopy of kondo and spin-flip scattering: High-field tunneling studies of schottky-barrier junctions. *Phys. Rev. B*, **2**, 3660. 296

Wong, H. & Lam, W.H. (2001). A robust parameter extraction method for diode with series resistance. *Proceedings of 2001 Electron Devices Meeting IEEE*, **1**, 38. 36

Wood, R.A., Lewis, M.H., Lees, M.R., Bennington, S.M., Cain, M.G. & Kitamura, N. (2002). Ferromagnetic fullerene. *J. Phys.: Condens. Matter*, **14**, L385–L391. 231

Woods, J.F. & Chen, C.Y. (1964). Negative magnetoresistance in impurity conduction. *Phys. Rev.*, **135**, A1462. 202

Woollam, J.A. (1970). Spin splitting, fermi energy changes, and anomalous g shifts in single-crystal and pyrolytic graphite. *Phys. Rev. Lett.*, **25**, 810. 235, 237

Woollam, J.A. (1971a). Graphite carrier localisation and quantum transport to 10 t (100 kg). *Phys. Rev. B*, **3**, 1148. 237

Woollam, J.A. (1971b). Minority carriers in graphite. *Phys. Rev. B*, **4**, 3393. 235, 249

Wu, C.Y. (1982). Interfacial layer-thermionic emission-diffusion theory for the schottky barrier diodes. *Journ. Appl. Phys.*, **53**, 5947. 20

Wulfhekel, W., Klaua, M., Ullmann, D., Zavaliche, F., Kirschner, J., Urban, R., Monchesky, T. & Heinrich, B. (2001). Single-crystal magnetotunnel junctions. *Appl. Phys. Lett.*, **78**, 509. 142

Wunderlich, J., Jungwirth, T., Kaestner, B., Irvine, A.C., Shick, A.B., Wang, K., Stone, N., Rana, U., Giddings, A.D., Foxon, C.T., Campion, R.P., Williams, D.A. & Gallagher, B.L. (2006). Coulomb blockade anisotropic magnetoresistance effect in a (ga, mn)as single electron transistor. *Phys. Rev. Lett.*, **97**, 077201. 205

Xiang, X.H., Zhu, T., Du, J. & Xiao, J.Q. (2003a). Conductance anomaly and density of states effects in magnetic tunnel junctions. *Journ. Appl. Phys.*, **93**, 8053. 142

Xiang, X.H., Zhu, T., Landry, G., Du, J., Zhao, Y. & Xiao, J.Q. (2003b). Spin-dependent conductance minima in magnetic tunnel junctions. *Appl. Phys. Lett.*, **83**, 2826. 112

Xu, Q., Hartmann, L., Schmidt, H., Hochmuth, H., Lorenz, M., Schmidt-Grund, R., Spemann, D., Rahm, A. & Grundmann, M. (2006a). Magnetoresistance in pulsed laser deposited 3d transition matel doped zno films. *Thin Solid Films*, **215**, 2549–2554. 209

Xu, X.H., Blythe, H.J., Ziese, M., Behan, A.J., Neal, J.R., Mokhtari, A., Ibrahim, R.M., Fox, A.M. & Ghering, G.A. (2006b). Carrier-induced ferromagnetism in n-type znmnalo and zncoalo thin films at room temperature. *New Journal of Physics*, **8**, 135. 209

Yavorsky, B.Y. & Mertig, I. (2006). Noncolinear interface magnetism and ballistic transport in fe/feo/mgo/fe tunnel junctions: *Ab initio* calculations using the kkr method. *Phys. Rev. B*, **74**, 174402. 143

Young, R.C. (1982). The high-field magnetoresistance of gd, y and pr. *J. Phys. F: Met. Phys.*, **12**, 1931. 205

Yu, L.S., Liu, Q.Z., Xing, Q.J., Qiao, D.J., Lau, S.S. & Redwing, J. (1998). The role of the tunneling component in the current-voltage characteristis of metal-gan schottky diodes. *Journ. of App. Phys.*, **84**, 2099. 21

Yu, Z.G. & Flatté, M.E. (2002a). Electric-field dependent spin diffusion and spin injection into semiconductors. *Phys. Rev. B*, **66**, 201202(R). 7

Yu, Z.G. & Flatté, M.E. (2002b). Spin diffusion and injection in semiconductor structures: Electric field effects. *Phys. Rev. B*, **66**, 235302. 7

Yuan, L., Liou, S.H. & Wang, D. (2006). Temperature dependence of magnetoresistance in magnetic tunnel junctions with different free layer structures. *Phys. Rev. B*, **73**, 134403. 143

Yuasa, S., Sato, T., Tamura, E., Suzuki, Y., Yamamori, H., Ando, K. & Katayama, T. (2000). Magnetic tunnel junctions with single-crystal electrodes: A crystal anisotropy of tunnel magnetoresistance. *Europhysics Lett.*, **52**, 344. 130

Yuasa, S., Nagahama, T., Fukushima, A., Suzuki, Y. & Ando, K. (2004). Giant room-temperature magnetoresistance in single-crystal fe/mgo/fe magnetic tunnel junctions. *Nature Materials*, **3**, 868. 143

Yuasa, S., Katayama, T., Nagahama, T., Fukushima, A., Kubota, H., Suzuki, Y. & Ando, K. (2005). Giant tunneling magnetoresistance in fully epitaxial body-centered-cubic co/mgo/fe magnetic tunnel junctions. *Appl. Phys. Lett.*, **87**, 222508. 143

Yuasa, S., Fukushima, A., Kubota, H., Suzuki, Y. & Ando, K. (2006). Giant tunneling magnetoresistance up to 410 epitaxial co/mgo/co magnetic tunnel junctions with bcc co(001) electrodes. *Appl. Phys. Lett.*, **89**, 042505. 142

Yung-Song Lou, C.Y.W. (1994). A self-consistent characterisation methodology for schottky barrier diodes and ohmic contacts. *IEEE Trans. Electr. Dev.*, **41**, 558. 15

Zav'ialov, V.V. & Radantsev, V.F. (1994). Tunneling in pb-p-hgcdte schottky barriers in longtitudinal and transverse magnetic fields. *Semicond. Sci. Technol.*, **281-288**, 281–288. 54

Zawadzki, W. & Kowalski, J. (1971). Small-gap semiconductors in crossed magnetic and electric fields. *Phys. Rev. Lett.*, **27**, 1713. 238

Zeghbroeck, B.V. (1997). Accumulation at the metal-semiconductor interface. http://ece-www.colorado.edu/~bart, online HTML resource. 283

Zhang, C., Zhang, X.G., Krstić, P.S., ping Cheng, H., Butler, W.H. & MacLaren, J.M. (2004a). Electronic structure and spin-dependent tunneling conductance under a finite bias. *Phys. Rev. B*, **69**, 134406. 122

Zhang, S. & Levy, P.M. (1999). Models for magnetoresistance in tunnel junctions. *Eur. Phys. J. B*, **10**, 599. 121, 293

Zhang, S., Levy, P.M., Marley, A.C. & Parkin, S.S.P. (1997a). Quenching of magnetoresistance by hot electrons in magnetic tunnel junctions. *Phys. Rev. Lett.*, **79**, 3744. 141

Zhang, X., Li, B.Z., Sun, G. & Pu, F.C. (1997b). Spin-polarized tunelling and magnetoresistance in ferromagnet/insulator(semiconductor) single and double tunnel junctions subjected to an electric field. *Phys. Rev. B*, **56**, 5484. 129, 140

Zhang, Z., Xue, Q.Z. & Zhu, D.D. (2004b). Positive and negative linear magnetoresistance of graphite. *Phys. Lett. A*, **320**, 471–477. 264

Zhu, C.Y., Wang, C.D., Feng, L.F., Zhang, G.Y., Yu, L.S. & Shen, J. (2006). A novel method of electrical characterisation of a semiconductor diode at forward bias. *Solid-State Electronics*, **50**, 821. 17

Zhu, H.J., Ramsteiner, M., Kostial, H., Wassermeier, M., Schönherr, H.P. & Ploog, K.H. (2001). Room-temperature spin injection from fe into gaas. *Phys. Rev. Lett.*, **87**, 016601. 7

Zieba, A. (1993). Image and sample geometry effects in squid magnetometers. *Rev. Sci. Instrum.*, **64**, 3357. 312

Ziese, M. & Sena, S.P. (1998). Anisotropic magnetoresistance of thin $la_{0.7}ca_{0.3}mno_3$ films. *J. Phys.: Cond. Matter*, **10**, 2727. 205

Ziese, M. & Thornton, M.J., eds. (2001). *Spin Electronics*. Springer-Verlag. 5, 41

Ziese, M., Köhler, U., Bollero, A., Höhne, R. & Esquinazi, P. (2005). Sshottky barrier and spin polarization at the $Fe_3O_4 - Nb : SrTiO_3$ interface. *Phys. Rev. B*, **71**, 180406(R). 42

ZIMAN, J.M. (1965). *Principles of the theory of solids*. Cambridge. 237, 255

ZVEZDIN, A.K. (1966). Nuclear polarisation in semiconductors and semimetals by a direct current. *Sov. Phys. JETP*, **22**, 907. 183, 187, 195

ZVEZDIN, A.K. (1967). Theory of nuclear spin polarization induced by hot electrons. *Sov. Phys. JETP*, **24**, 546. 183, 187

Index

2DEG, 10

accumulation, 282, 283
Andreev reflection, 6

ballistic transport, 273
band
    bending, 8
    conduction, 8
    rigid, 7
    valence, 8
bands
    rigid, 42
barrier
    lowering, 29
barrier height
    determination, 17
Bethe
    model, 18
bipolar generation, 55
Bohr
    magneton, 42
    radius, 13
Boltzmann
    equation, 25
    statistics, 186
Boltzmann-Poisson, 15
borosilicate, 310
Bose
    statistics, 25
Bose-Einstein
    statistics, 140

capacitance
    junction, 17
CESR, 183
conductivity
    mismatch, 52
contacts, 7, 10

dark current, 56
De Broglie
    wavelength, 27
Debye
    length, 283
deconvolution, 189
delta doping, 280
density of states, 13
depletion region, 9
diffusion
    coefficient, 16
    velocity, 19
Dirac
    delta, 6
drift-diffusion, 184

EDMR, 47
effective mass, 18
Einstein
    relation, 44, 276

electron
affinity, 8

Fermi
function, 51
golden rule, 280
level, 5, 8, 198
pinning, 8, 11
wave vector, 13
Fermi-Dirac
distribution, 56
FID, 183
Fowler's hypothesis, 56
Fowler-Nordheim, 271
Franz-Keldysh effect, 59
fudge factor, *see* ideality factor
full depletion, 274
fused silica, 310

gradiometer, 312

half-metal, 6
Hanle effect, 7, 198
hot electrons, 187

ideality factor, 29
impact ionisation, 54

Kondo
scattering, 147

Lambert's function, 31
Landau
levels, 59
Lande g-factor, 41
Larmor
frequency, 44

localised spins, 187

minority current, 21

NMR, 183
non-local
geometry, 184
resistance, 184

ohmic contact, 9
oxide layer, 26

Poisson equation, 16
Poole-Frenkel, 272

quantum
reflection, 27

recombination
centre, 19
current, 91
velocity, 19
Richardson
constant, 18

silicides, 64
space-charge, 272
spin
injection, 183
temperature, 186
spin electronics, 5
spin injection, 7
spin-filter, 7
spin-flip, 186
time, 184, 185
spin-orbit
scattering, 186
SQUID, 183, 312

Sze model, 18

Taylor
    series, 42, 43
theory
    Bethe, 16
    Schottky, 16
thermal
    activation, 89, 92
Thomas-Fermi, 13
    wave vector, 13
Townsend
    expression, 44
tunnelling
    current, 21

uni-polar generation, 55

VSM, 312

WKB, 271
WKB approximation, 279
work function, 8

Zeeman
    energy, 44
Zener
    effect, 54